MICROALGAE AS BIOREFINERY: DEVELOPMENT OF PROCESSES FOR THE GREEN EXTRACTION OF HIGH ADDED VALUE ANTIOXIDANTS

Davide Liberti

Dottorato in Biotecnologie – XXXV ciclo

Università di Napoli Federico II

Dottorato in Biotecnologie – XXXV ciclo

Università di Napoli Federico II

MICROALGAE AS BIOREFINERY: DEVELOPMENT OF PROCESSES FOR THE GREEN EXTRACTION OF HIGH ADDED VALUE ANTIOXIDANTS

Davide Liberti

Dottorando: Davide Liberti

Relatore: Prof.ssa Daria Maria Monti

Coordinatore: Prof. Marco Moracci

Settore Scientifico Disciplinare: BIO/10

Index

Riassunto

Le risorse naturali della Terra sono sottoposte ad un tremendo stress a causa della crescita demografica e dei cambiamenti climatici; da qui la necessità urgente di dare priorità alla sostenibilità rispetto alla produttività. Uno dei principi fondamentali dello sviluppo sostenibile è la riduzione, o addirittura l'eliminazione completa, dei rifiuti che sono prodotti durante un processo industriale. Partendo dalla definizione di “Sostenibilità” da parte della Commissione Mondiale per l'Ambiente e lo Sviluppo delle Nazioni Unite ("lo sviluppo che soddisfa le esigenze del presente senza compromettere la capacità delle generazioni future di soddisfare i propri bisogni"), l'idea innovativa di Economia Circolare (EC) ha guadagnato popolarità dalla metà degli anni 2000. In sintesi, il concetto alla base della EC è l'utilizzo di materie prime rinnovabili come fonte alternativa per l’ottenimento di *bulk chemicals* e carburanti, con la produzione di rifiuti biodegradabili che possono essere considerati materie prime seconde. La EC è strettamente legata al concetto di bioraffineria, che elude i convenzionali processi lineari di trasformazione della biomassa. L'approccio di bioraffineria intende infatti utilizzare la biomassa in modo completo, utilizzando un approccio in cascata, con conseguente minimizzazione dei rifiuti.

In questo contesto, le microalghe hanno suscitato molto interesse per la loro vasta gamma di applicazioni. Tali microrganismi eucariotici possono vivere in diversi ecosistemi, sono in grado di svolgere la fotosintesi, grazie alla quale convertono la CO_2 atmosferica in energia e O_2 e sono una fonte rinnovabile di molecole ad alto valore aggiunto. Le microalghe hanno un'efficienza di conversione dell'energia solare in biomassa circa tre volte più alta rispetto alle piante, il che le rende una materia prima unica. Come le piante, le microalghe hanno requisiti nutrizionali minimi e possono crescere in varie risorse idriche, comprese acque dolci, marine e persino reflue. Le microalghe rappresentano una collezione di organismi estremamente diversi, la cui diversità non è stata ancora completamente esplorata. Oltre a poter catturare il carbonio, le microalghe sono un’incredibile risorsa di molecole con una vasta gamma di applicazioni, dalla produzione di biocarburanti all'industria cosmeceutica e nutraceutica. Tuttavia, l'analisi della produzione su larga scala evidenzia che le tecnologie proposte per produrre biocarburanti a partire dalle microalghe non sono ancora economicamente sostenibili. In particolare, i costi di coltivazione (circa 3-10 euro/kg, a seconda della specie e delle tecniche di coltivazione) non sono compensati dai ricavi. Inoltre, il successivo

trattamento presenta ancora una serie di ostacoli. Una possibile soluzione può essere l'applicazione del concetto di bioraffineria alle microalghe, come recentemente riportato da alcuni esempi in letteratura. Tuttavia, questi processi sono ancora su scala di laboratorio, sebbene la ricerca abbia come obiettivo l'applicabilità di questi processi in campo industriale.

L'obiettivo del presente progetto di dottorato è stato sviluppare e applicare un approccio in cascata in grado di sfruttare appieno la coltura microalgale di *Porphyridium cruentum*. Il processo di bioraffineria, così come è stato pensato e progettato, ha permesso di ottenere quattro bioprodotti: esopolisaccaridi solfati (s-EPSs), ficoeritrina (PE), carotenoidi e lipidi. Tutte le molecole sono state ottenute senza influenzare significativamente le rese complessive e la loro bioattività.

Dal terreno di coltura esausto, generalmente considerato uno scarto, sono stati isolati gli esopolisaccaridi solfati (s-EPS). Grazie alla loro composizione, gli s-EPSs sono risultati dotati di attività antiossidante, antinfiammatoria e cicatrizzante, determinate con esperimenti basati su cellule umane immortalizzate.

Il primo bioprodotto isolato dalla biomassa di *P. cruentum* è stato la ficoeritrina (PE), proteina nota per le sue attività biologiche speciali. Sono state valutate diverse procedure di estrazione proteica con solventi acquosi (sonicazione, macerazione, congelamento/scongelamento e French Press), e tra queste, la sonicazione è stata scelta per l'elevata resa in PE, il minor contenuto in termini di proteine contaminanti presenti nell'estratto totale, e il risparmio di tempo. L'estrazione è stata ulteriormente ottimizzata confrontando la resa e il grado di purezza della PE a partire da tre biomasse: (i) fresca; (ii) congelata; (iii) raccolta mediante flocculazione. I risultati hanno suggerito che le condizioni di conservazione non influiscono sull'estrazione della PE, conferendo un'elevata versatilità al processo. La PE è stata poi purificata all'omogeneità applicando un unico passaggio di purificazione che ha permesso di ottenere la proteina ad un livello di purezza elevato, tale da determinarne la struttura cristallografica (1.6 Å di risoluzione) e la relativa sequenza. La PE si è dimostrata essere attiva contro lo stress ossidativo indotto dai raggi UVA e contro l'infiammazione. Attraverso esperimenti basati su cellule eucariotiche immortalizzate, è stato determinato un nuovo ruolo della PE nel campo della rimarginazione delle ferite.

I carotenoidi sono stati estratti dalla biomassa come seconda classe di molecole. L'estrazione è stata effettuata in parallelo sulla biomassa grezza e sulla biomassa residua, ovvero la biomassa recuperata dopo l'estrazione della PE. Le rispettive rese di carotenoidi

sono risultate essere simili tra di loro e le analisi HPLC effettuate su entrambi gli estratti hanno rivelato che l'estratto ottenuto dalla biomassa residua è arricchito in β-carotene, un noto antiossidante.

Infine, i lipidi sono stati isolati e frazionati come ultima classe di molecole dalla biomassa di *P. cruentum*. La frazione lipidica era più ricca di acidi grassi saturi (SFA) rispetto a quella ottenuta dalla biomassa grezza. Gli SFA sono chimicamente stabili, sono biocompatibili e hanno un punto di fusione ben definito. Grazie a queste proprietà, negli ultimi anni, gli SFA stanno guadagnando spazio come molecole per il rilascio controllato di farmaci o agenti antibatterici.

Nonostante l'elevata rilevanza dei bioprodotti per molte industrie, lo sfruttamento commerciale delle microalghe deve attualmente affrontare gravi ostacoli scientifici e operativi. Complessivamente, in letteratura sono presenti diversi esempi di bioraffineria, ma pochissimi sono gli esempi, o i tentativi, di progettare processi completi. Sia i processi a monte che quelli a valle della crescita microalgale devono essere semplificati e integrati per diventare fattibili e sostenibili. Tuttavia, è importante ricordare che qualsiasi tecnologia progettata per l'ottenimento di un singolo prodotto dovrebbe sempre essere completata da una valutazione dell'impatto del processo nel suo complesso. Numerosi studi di *Life Cycle Assesment* sulla coltivazione di microalghe evidenziano diversi colli di bottiglia, dove la raccolta, lo stoccaggio e l'estrazione sono tra i principali responsabili dei consumi di energia all'interno del processo complessivo.

In conclusione, la composizione di *P. cruentum*, l'elevato valore aggiunto dei prodotti ottenuti e l'assenza di prodotti di scarto hanno reso possibile un concreto approccio di bioraffineria. Tuttavia, molti fattori, come la scalabilità e l'analisi dei costi complessivi, devono ancora essere messi a punto e chiariti per rendere questo processo una realtà industriale.

Esperienze all’estero:

Gli esperimenti per la caratterizzazione dell’attività antiossidante e antinfiammatoria *in vitro* sono stati effettuati presso il Centre of Marine Sciences (CCMAR), Università dell’Algarve, Faro, Portogallo, presso il laboratorio della Prof. L. Barreira, dal 18 Febbraio 2022 al 18 Agosto 2022.

Summary

Nowadays, the strategy of biorefinery perfectly fits with the circular bioeconomy concept and microalgae can be considered excellent candidates for their use in biorefinery approaches. Indeed, microalgae are a reliable source of natural compounds with different biological activities, they perform carbon capture and can grow in lands which do not compete with food production.

The aim of the present PhD project was the complete exploitation of *Porphyridium cruentum* culture to obtain different high value products in a cascade approach.

Sulphated exopolysaccharides (s-EPSs) were isolated from the culture medium and a chemical characterization was obtained.

Different procedures to harvest the biomass were compared, and biomass storage was analyzed in the context of phycoerythrin (PE) yield.

Phycoerythrin isolation was defined upon evaluation of different techniques. The obtained purity grade of the protein was so high that its X-ray structure was determined at 1.60 Å resolution and the protein sequence was determined. Then, carotenoids and lipids were extracted from the residual biomass in two sequential steps and a complete chemical characterization was achieved.

In-vitro and cell-based assays were performed to assess the biological activities of these compounds. The s-EPSs, thanks to the presence of sulphate groups, showed biocompatibility on immortalized eukaryotic cell lines and a high antioxidant activity on cell-based systems. PE showed powerful antioxidant activity both *in vitro* and on cell-based systems, but its purification is mandatory for its safe use. Finally, both molecules showed anti-inflammatory activity comparable to that of Ibuprofen and helped tissue regeneration.

The obtained results could boost the industrial utilization of *P. cruentum* offsetting the high downstream processes cost. Moreover, the simultaneous microalgae culture valorization and carbon capture can contribute to the sustainable expansion of microalgae market.

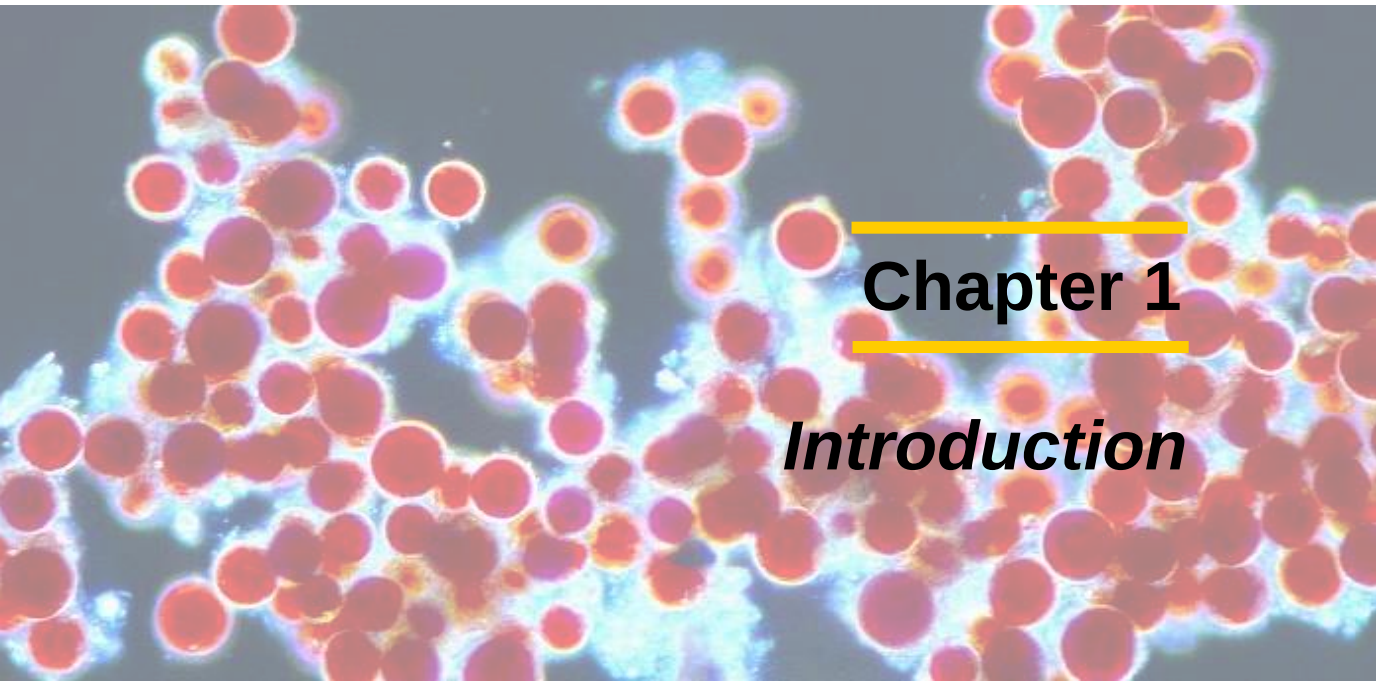

Chapter 1

Introduction

1.1 Circular economy, biorefinery and microalgae

Earth's natural resources are under tremendous stress for the growing population and climate change. The need to prioritize sustainability over productivity is fostered by these catastrophic circumstances. One of the fundamental tenets of sustainable development is lowering, or even completely eradicate, wastes (Omer, 2008). Starting from the definition of sustainability by the UN World Commission on Environment and Development ("the development that meets the demands of the present without compromising the ability of future generations to satisfy their own needs"), the innovative idea of the Circular Economy (CE) has gained popularity since middle 2000's (Ghisellini et al., 2016). Briefly, the concept underlying CE is the utilization of renewable materials as an alternative source of chemicals and fuels, with the production of biodegradable wastes which can be considered as secondary raw materials. CE is strictly linked to the biorefinery concept, which dodges the conventional linear processes of biomass transformation. Indeed, a biorefinery is intended as a process aimed at obtaining different class of molecules from a single biomass, using sustainable approaches. However, the first-generation of biorefinery-derived companies obtained only one product, but they defined themselves as biorefinery company because biomass was used as feedstock. Then, the focus shifted from a single-product approach to the obtainment, from the same biomass, of more than one bio-product, using a cascade approach and where no wastes were produced (González-Delgado and Kafarov, 2011).

In this context, microalgae gained much interest among scientists for their wide range of applications. These eukaryotic microorganisms can live in different ecosystems and are able to carry out photosynthesis, thanks to which they convert atmospheric CO_2 into energy and O_2 (Roy et al., 2022). They have about 3-fold better solar energy to biomass conversion efficiency than plants, making them a unique feedstock (Melis, 2009). Microalgae, like plants, have minimum nutritional requirements and can flourish in various water resources, including fresh, marine, and even wastewaters (Fan et al., 2020). Microalgae represent an extremely diverse collection of organisms, still not fully explored (Kselíková et al., 2022; Lovejoy et al., 2006; Luche et al., 2007). Besides being able to do carbon capture, microalgae are an incredible reservoir of other molecules which can find different applications, from biofuel production (Mata et al., 2010; Ruiz et al., 2016), to cosmeceutical and nutraceutical industries. However, the analysis of the large-scale production points out that the technologies

proposed to produce biofuels are still not self-sustainable from an economic point of view. This is mainly due to their cultivation costs (about 3-10 Euros/kg, depending from species and cultivation techniques) (Ruiz et al., 2016) that are not compensated by revenues.

A possible solution can be the application of the biorefinery concept to microalgae, as recently reported by few examples present in literature (Dineshkumar and Sen, 2020; Gallego et al., 2019; Imbimbo et al., 2019; Mehariya et al., 2021). However, these processes are still on laboratory level and an upscale is sought. Indeed, microalgae and cyanobacteria have to be exploited for the enormous variety of molecules they can synthetize and that can find applications in different fields. A brief description of some of them is reported below.

1.2 Sulphated exopolysaccharides

Polysaccharides are produced by all living organisms and most of them are made of a relatively limited class of hexoses (such as glucose, galactose or mannose) and pentoses (such as xylose and arabinose). They show a variety of properties, leading them to industrial exploitation as hydrocolloids, bio-sourced materials and biological active agents (Soanen et al., 2016).

To date, the use of microalgal exopolysaccharides is very limited, compared to those extracted from terrestrial plants (pectins, starch, galactomannans, arabic gum), macroalgae (carrageenans, alginate, agars or fucoidans) or non-photosynthetic microorganisms (chitosan, xanthan, scleroglucan, gellan or curdlan) (Venugopal, 2016). However, the mucilage from marine microalgae is a very complex polysaccharidic exopolymeric structure, partially soluble into the extracellular medium (Arad and Levy-Ontman, 2010; Villay et al., 2013). The mucilage (**Figure 1**) protects cells from fluctuations of the environment (salinity, desiccation, pH, temperature) and/or from predators (De Philippis and Vincenzini, 1998; Ferreira et al., 2021). With the exception of some oligosaccharidic sequences, most of the exopolymeric structures has not yet been elucidated (Geresh et al., 2002). It is known that they are high molecular weight molecules (between $8 \cdot 10^5$ and $26 \cdot 10^5$ g/mol), often composed of a pentose (xylose) and four main hexoses: galactose, glucose, rhamnose and glucuronic acid (Geresh et al., 2002; Villay et al., 2013). They are generally sulfated (between 6% and 10%) and linked by β-(1,3) and β-(1,4) glycosidic bonds (Filomena et al., 2021). *Porphyridium*, *Dixioniella* and *Rhodella* strains have been described in literature as the main exopolysaccharide producers (Arad and Levy-Ontman, 2010; Filomena

et al., 2021).

The cost of their isolation, which is higher than that of other polysaccharides from plants, macroalgae, or non-photosynthetic microorganisms, is the principal obstacle for their industrial use.

Figure 1. Microalgae enveloped in exopolysaccharides. Exopolysaccharides protect cells from desiccation, temperature, pH, and salinity (Copyright 1995-2018 Protist Information Server).

1.3 Phycoerythrin

Phycoerythrin (PE) is a light harvesting protein, which helps chlorophyll pigments during photosynthesis. PE is found in the outer layer of phycobilisome (PBS), a huge light harvesting antenna complex, which is associated to the cytoplasmic surface of the thylakoid membrane (**Figure 2**) (Glazer, 1994). PE is composed by α and β monomers, assembled into disc-shaped hexamers $(\alpha\beta)_6$ or trimers $(\alpha\beta)_3$ with 3/2 or 3 symmetry and enclosing a central channel. In PBS, each trimer or hexamer contains at least one linker protein located in central channel. B-phycoerythrin (B-PE) and R-phycoerythrin (R-PE), found in red algae, contain also a third subunit, γ, which functions as a linker and has light-harvesting functions (Ficner and Huber, 1993). PE

is a red colored protein, fluorescent, which can be used in food, cosmetic, pharmaceutical industries, or as a fluorescent biomarker in immunology (Qiu et al., 2004). Moreover, PE has antioxidant, anti-inflammatory and anti-bacterial activity, thus the worldwide PE market is estimated to reach US $ 6.3 million by 2025 (Ardiles et al., 2020).

Since PE is an intracellular metabolite assembled on the thylakoid membrane of chloroplasts, the procedures generally applied to extract it from the biomass involve cell and chloroplast membranes disruption (Gantt, 1969). Several methods have been tested for the extraction of B-PE, such as high-pressure homogenization (Jubeau et al., 2013), sonication (Benavides and Rito-Palomares, 2006; Bermejo et al., 2001) or bead-mill, but all of them are very impactful, as they fully destroy the biomass, rendering PE purification very difficult.

Consequently, when a high purity level is required, such as immunology biomarking, several purification steps have to be used, thus increasing its production cost. As an example, Benavides and Palomares performed a polyethylene glycol precipitation before applying an aqueous two-phase purification system (Benavides and Rito-Palomares, 2004). Román and collegues performed two different selective precipitations (Román et al., 2002), and Marcati and coworkers applied two steps of membrane filtration (Marcati et al., 2014).

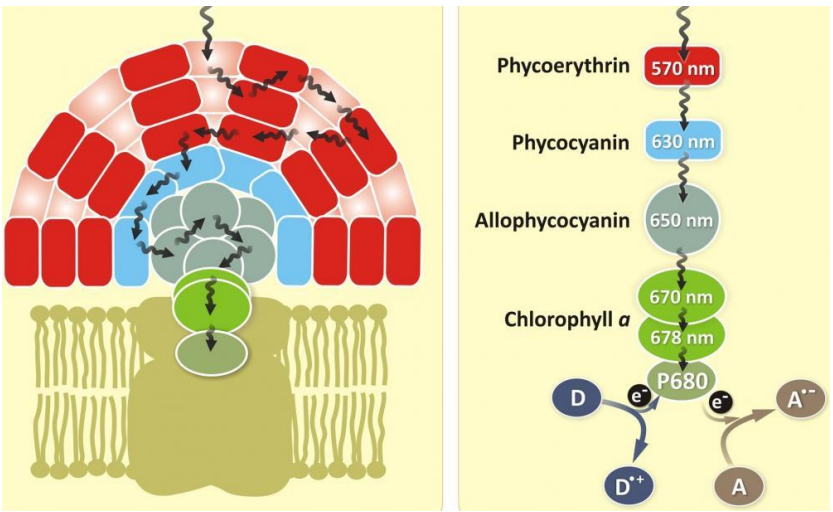

Figure 2. Graphic representation of the phycobilisome. Allophycocyanins (grey circles) are close to the photosystem and aid in the transport of energy during photosynthesis. The core is connected to six rods of phycocyanins and phycoerythrin. Hexamers of

phycocyanin (cyan rectangles) and phycoerythrin (red rectangles) are organized to reflect the resonance energy transfer pathway.

1.4 Carotenoids

Carotenoids (**Figure 3**) play key roles in light harvesting and energy transfer during photosynthesis and in the protection of the photosynthetic apparatus against photo-oxidative damage (Choudhury et al., 2022). Several studies have demonstrated that carotenoids are among the main responsible for the antioxidant capacity of microalgae (Cichoński and Chrzanowski, 2022). Thanks to their inherent antioxidant activity and a role in preventing harmful human health disorders, carotenoids have drawn big attention since the last ten years. Indeed, carotenoids can quench singlet oxygen and free radicals, which are responsible for cell damage. Moreover, carotenoids can aid in the prevention and treatment of numerous diseases, including cancer, heart disease, diabetes, and osteoporosis (Kohlmeier et al., 1997; Rao and Rao, 2007; Shaish et al., 2006). They are frequently used as a natural colorant in the food sector because of their remarkable color, antioxidant, and preservative properties (Nwoba et al., 2020). Carotenoids are lipophilic molecules; thus, they are utilized as a coloring agent especially when making foods with high levels of fatty acids (such margarine, butter, soft drinks, cakes, and milk-based products). Thanks to their wide application, global carotenoids market reached a value of 2 US $ billion by 2019 (Martínez-Cámara et al., 2021). The average content of carotenoids in microalgae is about 0.1-0.2% dry weight but some species are able to produce up to 14% of β-carotene under stressed growth conditions (nitrogen starvation) (Borowitzka, 2013). For example, the majority of the β-carotene used in the food industry is extracted from the microalga *Dunaliella salina* (Novoveská et al., 2019).

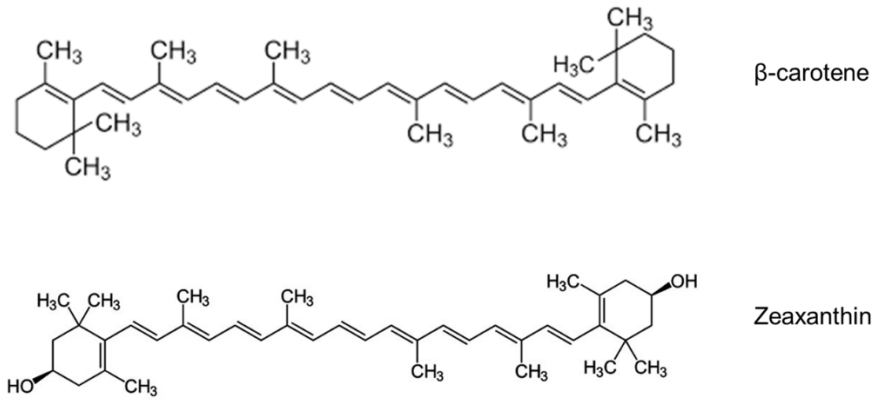

Figure 3. Molecular structure of carotenoids. With the chemical formula $C_{40}H_{56}$, β-carotene is the most prevalent carotenoid, member of the family of isoprenoids and a precursor of vitamin A. Zeaxanthin ($C_{40}H_{56}O_2$) is a carotenoid derived from β-carotene and it is involved in the xanthophyll cycle.

1.5 Lipids

Depending on the growth conditions, microalgae can change their metabolism and start accumulating lipids. Fatty acids (FAs) and sterols are the main lipid molecules that can be isolated from microalgae (Cuellar-Bermudez et al., 2015) and can find applications in different fields: biofuel production, food products, feed, aquaculture, food additives, etc. (Maltsev and Maltseva, 2021). FAs are involved in the metabolic pathways of formation and conversion of most lipid classes, and their composition largely determines their properties and practical use. Depending on the species and on the growth conditions adopted, total lipids usually represent 20-50% of total biomass dry weight (Richmond and Hu, 2013; Seyed Yagoubi et al., 2018). FAs may find different applications based on their chemical composition: ω-3 and ω-6 are used as food supplements (D'Alessandro and Antoniosi Filho, 2016) or as a vegetarian alternative to fish oil (Bartek et al., 2021), poly- and mono- unsaturated fatty acids may be used for biofuel production (Peng et al., 2020), whereas saturated FAs have recently gained attention as drug delivery molecules or as antibacterial agents (Xue et al., 2021; Yoon et al., 2018). In 2019, the market value of microalgal lipids reached 2.49 US $ billion (Oliver et al., 2020). Currently,

traditional extraction methods, such as Bligh & Dyer (Bligh and Dyer, 1959) or Soxhlet extraction are used, but they need a dry biomass and conventional organic solvents, such as chloroform, acetone, methanol, and diethyl ether.

1.6 *Porphyridium cruentum*

Rhodophyta, also known as red algae, are eukaryotic microorganisms characterized by: (i) the presence of the phycobilisome as photosynthetic accessory machine, (ii) chloroplasts containing non-linked thylakoids, (iii) floridoside cytoplasmic granules used as storage product, (iv) cell-wall composed of a microfibrillar layer of cellulose or xylan and amorphous polysaccharidic mucilages, and (v) the absence of flagella. Among the different genera of red microalgae, the best known are *Porphyridium, Rhodella* and *Rhodosorus*. Their morphology is the simplest of all the red algae. In particular, *Porphyridium cruentum* (**Figure 4**) is a mesophile microalga that belongs to the class of *Porphyridiophyaceae,* with a spherical shape and a cell lacking cell wall and with PE which provides the characteristic red color. *P. cruentum* secretes sulphated exopolysaccharides, which cause the cultures to become viscous, especially under limiting growth conditions. Besides PE and exopolysaccharides, the biomass contains carotenoids and polyunsaturated and saturated fatty acids (e.g. arachidonic acid, eicosapentaenoic acid and palmitic acid), as high value molecules (Gallego et al., 2019; Medina-Cabrera et al., 2020).

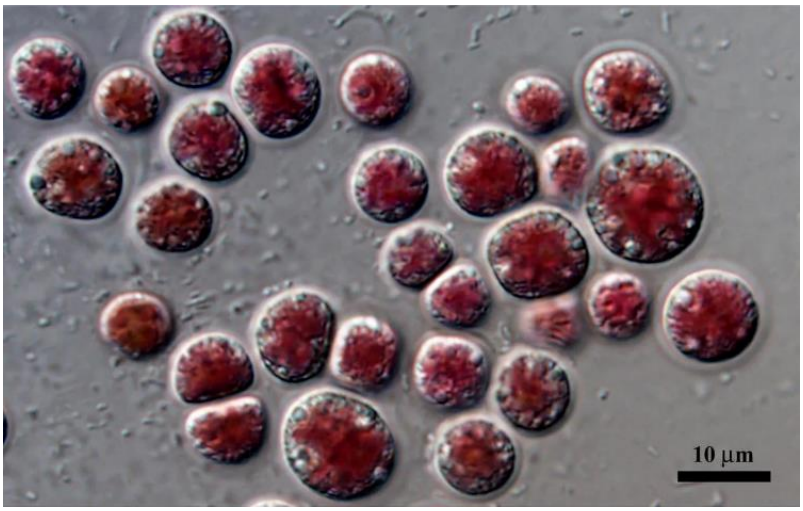

Figure 4. Microscopic image of *Porphyridium cruentum*. (https://algaeresearchsupply.com/products/copy-of-algae-culture-porphyridium-cruentum).

1.7 Aim of the thesis

The general aim of present PhD thesis was the use of a commercial microalgal strain, *Porphyridium cruentum* (CCALA415) to obtain high-added value bioproducts in a cascade approach. To fully exploit not only the biomass, but also the exhausted culture medium, EPSs were recovered from the medium, whereas PE, carotenoids and lipids were isolated, sequentially, from the biomass. The reason for the selected extraction order was due to some considerations: (i) PE is the most valuable product; (ii) the solvent for protein extraction is an aqueous buffer, so that it would not affect the residual molecules present in the biomass (such as carotenoids and lipids); (iii) lipids extraction requires the use of well-known toxic solvents, able to affect the structural properties of other class of molecules; (iv) lipids were the class of molecules with the lowest market value. The research activities are explained below:

1. **Optimization of growth conditions, biomass harvesting procedures and phycoerythrin extraction (Chapter 2).**
   The growth conditions for *P. cruentum* culture were set up. Then, different procedures to harvest the biomass were used, and PE extraction was set up, evaluating different

techniques. Analyses on the storage of the biomass were done to improve the process from an economical point of view.

2. **Set up of the biorefinery from *Porphyridium cruentum* and purification of the isolated class of molecules (Chapter 3).**
   EPSs were isolated from the culture medium and a chemical characterization was performed. Different approaches to purify PE were carried out and the sequence and the structure of the protein were obtained. Then, two different class of molecules were extracted from the residual biomass in two sequential steps: carotenoids and lipids. Finally, the chemical characterization of the obtained molecules was performed.

3. **Bioactivity evaluation of s-EPSs and PE (Chapter 4).**
   Biocompatibility of EPSs and PE was carried out on immortalized eukaryotic cell lines. Then, antioxidant and anti-inflammatory activities were evaluated by different *in vitro* and cell-based assays. Finally, the wound healing effect was evaluated by scratch assay on human immortalized keratinocytes.

1.8 References

Arad, S., Levy-Ontman, O., 2010. Red microalgal cell-wall polysaccharides: Biotechnological aspects. Curr. Opin. Biotechnol. 21, 358–364. https://doi.org/10.1016/j.copbio.2010.02.008

Ardiles, P., Cerezal-Mezquita, P., Salinas-Fuentes, F., Órdenes, D., Renato, G., Ruiz-Domínguez, M.C., 2020. Biochemical composition and phycoerythrin extraction from red microalgae: A comparative study using green extraction technologies. Processes 8, 1628.

Bartek, L., Strid, I., Henryson, K., Junne, S., Rasi, S., Eriksson, M., 2021. Life cycle assessment of fish oil substitute produced by microalgae using food waste. Sustain. Prod. Consum. 27, 2002–2021.

Benavides, J., Rito-Palomares, M., 2006. Simplified two-stage method to B-phycoerythrin recovery from *Porphyridium cruentum*. J. Chromatogr. B Anal. Technol. Biomed. Life Sci. 844, 39–44. https://doi.org/10.1016/j.jchromb.2006.06.029

Benavides, J., Rito-Palomares, M., 2004. Bioprocess intensification: A potential aqueous two-phase process for the primary recovery of B-phycoerythrin from *Porphyridium cruentum*. J. Chromatogr. B Anal. Technol. Biomed. Life Sci. 807, 33–38. https://doi.org/10.1016/j.jchromb.2004.01.028

Bermejo, R., Talavera, E.M., Alvarez-Pez, J.M., 2001. Chromatographic purification and characterization of B-phycoerythrin from *Porphyridium cruentum* - Semipreparative high-performance liquid chromatographic separation and characterization of its subunits. J. Chromatogr. A 917, 135–145. https://doi.org/10.1016/S0021-9673(01)00692-6

Bligh, E.G., Dyer, W.J., 1959. A rapid method of total lipid extraction and purification. Can. J. Biochem. Physiol. 37, 911–917. https://doi.org/10.1139/o59-099

Borowitzka, M.A., 2013. High-value products from microalgae-their development and commercialisation. J. Appl. Phycol. 25, 743–756. https://doi.org/10.1007/s10811-013-9983-9

Choudhury, S., Goswami, S., Choudhury, A.R., Paul, S., 2022. Light-Harvesting Antenna Complex and Its Role in Environmental Stress, in: Photosynthesis and Respiratory Cycles during Environmental Stress Response in Plants. Apple Academic Press, pp. 79–97.

Cichoński, J., Chrzanowski, G., 2022. Microalgae as a Source of Valuable Phenolic Compounds and Carotenoids. Molecules 27, 8852.

Cuellar-Bermudez, S.P., Aguilar-Hernandez, I., Cardenas-Chavez, D.L., Ornelas-Soto, N., Romero-Ogawa, M.A., Parra-Saldivar, R., 2015. Extraction and purification of high-value metabolites from microalgae: Essential lipids, astaxanthin and phycobiliproteins. Microb. Biotechnol. 8, 190–209. https://doi.org/10.1111/1751-7915.12167

D'Alessandro, E.B., Antoniosi Filho, N.R., 2016. Concepts and studies on lipid and pigments of microalgae: A review. Renew. Sustain. Energy Rev. 58, 832–841.

De Philippis, R., Vincenzini, M., 1998. Exocellular polysaccharides from cyanobacteria and their possible applications. FEMS Microbiol. Rev. 22, 151–175.

Dineshkumar, R., Sen, R., 2020. A sustainable perspective of microalgal biorefinery for co-production and recovery of high-value carotenoid and biofuel with CO2 valorization. Biofuels, Bioprod. Biorefining 14, 879–897.

Fan, H., Wang, K., Wang, C., Yu, F., He, X., Ma, J., Li, X., 2020. A

comparative study on growth characters and nutrients removal from wastewater by two microalgae under optimized light regimes. Environ. Technol. Innov. 19, 100849. https://doi.org/10.1016/J.ETI.2020.100849

Ferreira, A.S., Mendonça, I., Póvoa, I., Carvalho, H., Correia, A., Vilanova, M., Silva, T.H., Coimbra, M.A., Nunes, C., 2021. Impact of growth medium salinity on galactoxylan exopolysaccharides of *Porphyridium purpureum*. Algal Res. 59, 102439.

Ficner, R., Huber, R., 1993. At 0 . 23-Nm Resolution and Localization of the Y Subunit 106, 103–106.

Filomena, M., Raposo, D.J., Maria, A., Bernardo, M., Manuel, R., Costa, S., 2021. Polysaccharides, Polysaccharides. https://doi.org/10.1007/978-3-319-03751-6

Gallego, R., Martínez, M., Cifuentes, A., Ibáñez, E., Herrero, M., 2019. Development of a Green Downstream Process for the Valorization of *Porphyridium cruentum* Biomass. Molecules 24. https://doi.org/10.3390/molecules24081564

Gantt, E., 1969. Properties and Ultrastructure of Phycoerythrin From *Porphyridium cruentum* . Plant Physiol. 44, 1629–1638. https://doi.org/10.1104/pp.44.11.1629

Geresh, S., Adin, I., Yarmolinsky, E., Karpasas, M., 2002. Characterization of the extracellular polysaccharide of *Porphyridium sp*.: Molecular weight determination and rheological properties. Carbohydr. Polym. 50, 183–189. https://doi.org/10.1016/S0144-8617(02)00019-X

Ghisellini, P., Cialani, C., Ulgiati, S., 2016. A review on circular economy: the expected transition to a balanced interplay of environmental and economic systems. J. Clean. Prod. 114, 11–32.

Glazer, A.N., 1994. Phycobiliproteins - a family of valuable, widely used fluorophores. J. Appl. Phycol. 6, 105–112. https://doi.org/10.1007/BF02186064

González-Delgado, Á.-D., Kafarov, V., 2011. Biorefinery : Issues. CT&F - Ciencia, Tecnol. y Futur. 4, 5–22.

Imbimbo, P., Romanucci, V., Pollio, A., Fontanarosa, C., Amoresano, A., Zarrelli, A., Olivieri, G., Monti, D.M., 2019. A cascade extraction of active phycocyanin and fatty acids from *Galdieria phlegrea*. Appl. Microbiol. Biotechnol. 103, 9455–9464. https://doi.org/10.1007/s00253-019-10154-0

Jubeau, S., Marchal, L., Pruvost, J., Jaouen, P., Legrand, J., Fleurence, J., 2013. High pressure disruption: A two-step treatment for selective extraction of intracellular components from the microalga *Porphyridium cruentum*. J. Appl. Phycol. 25, 983–989.

https://doi.org/10.1007/s10811-012-9910-5
Kohlmeier, L., Kark, J.D., Gomez-Gracia, E., Martin, B.C., Steck, S.E., Kardinaal, A.F.M., Ringstad, J., Thamm, M., Masaev, V., Riemersma, R., 1997. Lycopene and myocardial infarction risk in the EURAMIC Study. Am. J. Epidemiol. 146, 618–626.
Kselíková, V., Singh, A., Bialevich, V., Čížková, M., Bišová, K., 2022. Improving microalgae for biotechnology—From genetics to synthetic biology–Moving forward but not there yet. Biotechnol. Adv. 58, 107885.
Lovejoy, C., Massana, R., Pedrós-Alió, C., 2006. Diversity and distribution of marine microbial eukaryotes in the arctic ocean and adjacent seas. Appl. Environ. Microbiol. 72, 3085–3095. https://doi.org/10.1128/AEM.72.5.3085-3095.2006
Luche, H., Weber, O., Rao, T.N., Blum, C., Fehling, H.J., 2007. Faithful activation of an extra-bright red fluorescent protein in “knock-in” Cre-reporter mice ideally suited for lineage tracing studies. Eur. J. Immunol. 37, 43–53. https://doi.org/10.1002/eji.200636745
Maltsev, Y., Maltseva, K., 2021. Fatty acids of microalgae: Diversity and applications. Rev. Environ. Sci. Bio/Technology 20, 515–547.
Marcati, A., Ursu, A.V., Laroche, C., Soanen, N., Marchal, L., Jubeau, S., Djelveh, G., Michaud, P., 2014. Extraction and fractionation of polysaccharides and B-phycoerythrin from the microalga *Porphyridium cruentum* by membrane technology. Algal Res. 5, 258–263. https://doi.org/10.1016/j.algal.2014.03.006
Martínez-Cámara, S., Ibañez, A., Rubio, S., Barreiro, C., Barredo, J.-L., 2021. Main carotenoids produced by microorganisms. Encyclopedia 1, 1223–1245.
Mata, T.M., Martins, A.A., Caetano, N.S., 2010. Microalgae for biodiesel production and other applications: A review. Renew. Sustain. Energy Rev. 14, 217–232. https://doi.org/10.1016/j.rser.2009.07.020
Medina-Cabrera, E.V., Rühmann, B., Schmid, J., Sieber, V., 2020. Optimization of growth and EPS production in two *Porphyridium* strains. Bioresour. Technol. Reports 11, 100486. https://doi.org/10.1016/j.biteb.2020.100486
Mehariya, S., Goswami, R.K., Verma, P., Lavecchia, R., Zuorro, A., 2021. Integrated approach for wastewater treatment and biofuel production in microalgae biorefineries. Energies 14, 2282.
Melis, A., 2009. Solar energy conversion efficiencies in photosynthesis: Minimizing the chlorophyll antennae to maximize efficiency. Plant Sci. 177, 272–280. https://doi.org/10.1016/J.PLANTSCI.2009.06.005

Novoveská, L., Ross, M.E., Stanley, M.S., Pradelles, R., Wasiolek, V., Sassi, J.-F., 2019. Microalgal carotenoids: A review of production, current markets, regulations, and future direction. Mar. Drugs 17, 640.

Nwoba, E.G., Ogbonna, C.N., Ishika, T., Vadiveloo, A., 2020. Microalgal pigments: a source of natural food colors, in: Microalgae Biotechnology for Food, Health and High Value Products. Springer, pp. 81–123.

Oliver, L., Dietrich, T., Marañón, I., Villarán, M.C., Barrio, R.J., 2020. Producing omega-3 polyunsaturated fatty acids: A review of sustainable sources and future trends for the EPA and DHA market. Resources 9, 148.

Omer, A.M., 2008. Energy, environment and sustainable development. Renew. Sustain. energy Rev. 12, 2265–2300.

Peng, L., Fu, D., Chu, H., Wang, Z., Qi, H., 2020. Biofuel production from microalgae: a review. Environ. Chem. Lett. 18, 285–297.

Qiu, J., Madoz-Gurpide, J., Misek, D.E., Kuick, R., Brenner, D.E., Michailidis, G., Haab, B.B., Omenn, G.S., Hanash, S., 2004. Development of Natural Protein Microarrays for Diagnosing Cancer Based on an Antibody Response to Tumor Antigens. J. Proteome Res. 3, 261–267. https://doi.org/10.1021/pr049971u

Rao, A.V., Rao, L.G., 2007. Carotenoids and human health. Pharmacol. Res. 55, 207–216.

Richmond, A., Hu, Q., 2013. Handbook of microalgal culture: applied phycology and biotechnology. John Wiley & Sons.

Román, R.B., Alvárez-Pez, J.M., Fernández, F.G.A., Grima, E.M., 2002. Recovery of pure b-phycoerythrin from the microalga *Porphyridium cruentum*. J. Biotechnol. 93, 73–85. https://doi.org/10.1016/S0168-1656(01)00385-6

Roy, A., Gogoi, N., Yasmin, F., Farooq, M., 2022. The use of algae for environmental sustainability: trends and future prospects. Environ. Sci. Pollut. Res. 1–11.

Ruiz, J., Olivieri, G., De Vree, J., Bosma, R., Willems, P., Reith, J.H., Eppink, M.H.M., Kleinegris, D.M.M., Wijffels, R.H., Barbosa, M.J., 2016. Towards industrial products from microalgae. Energy Environ. Sci. 9, 3036–3043. https://doi.org/10.1039/c6ee01493c

Seyed Yagoubi, A., Shahidi, F., Mohebbi, M., Varidi, M., Golmohammadzadeh, S., 2018. Preparation, characterization and evaluation of physicochemical properties of phycocyanin-loaded solid lipid nanoparticles and nanostructured lipid carriers. J. Food Meas. Charact. 12, 378–385. https://doi.org/10.1007/s11694-017-9650-y

Shaish, A., Harari, A., Hananshvili, L., Cohen, H., Bitzur, R., Luvish, T., Ulman, E., Golan, M., Ben-Amotz, A., Gavish, D., 2006. 9-cis β-carotene-rich powder of the alga *Dunaliella bardawil* increases plasma HDL-cholesterol in fibrate-treated patients. Atherosclerosis 189, 215–221.

Soanen, N., Da Silva, E., Gardarin, C., Michaud, P., Laroche, C., 2016. Improvement of exopolysaccharide production by *Porphyridium marinum*. Bioresour. Technol. 213, 231–238.

Venugopal, V., 2016. Marine polysaccharides: Food applications. CRC Press.

Villay, A., Laroche, C., Roriz, D., El Alaoui, H., Delbac, F., Michaud, P., 2013. Optimisation of culture parameters for exopolysaccharides production by the microalga *Rhodella violacea*. Bioresour. Technol. 146, 732–735.

Xue, K., Lv, S., Zhu, C., 2021. Bringing naturally-occurring saturated fatty acids into biomedical research †. J. Mater. Chem. B 9, 6973–6987. https://doi.org/10.1039/d1tb00843a

Yoon, B.K., Jackman, J.A., Valle-González, E.R., Cho, N.J., 2018. Antibacterial Free Fatty Acids and Monoglycerides: Biological Activities, Experimental Testing, and Therapeutic Applications. Int. J. Mol. Sci. 2018, Vol. 19, Page 1114 19, 1114. https://doi.org/10.3390/IJMS19041114

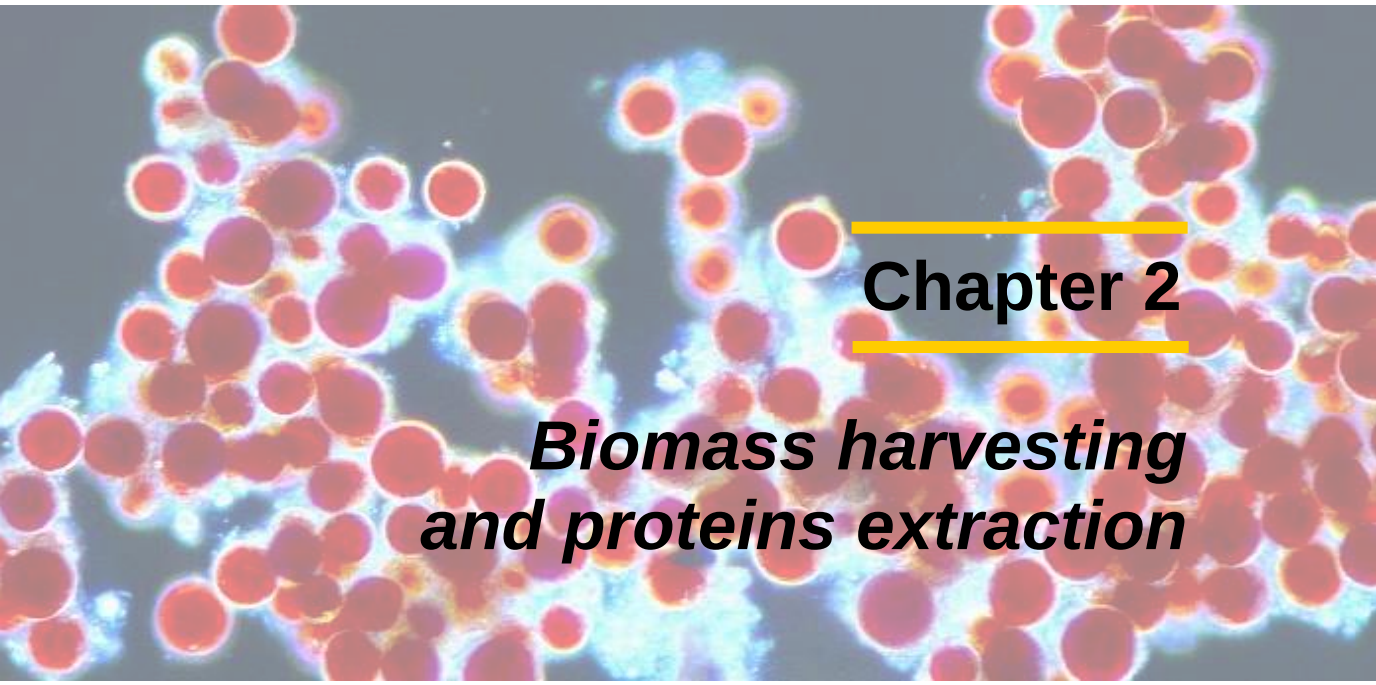

Chapter 2

Biomass harvesting and proteins extraction

2.1 Introduction

The obtainment of products economically viable from microalgae, such as biofuels, bioactive compounds, food or feed, is still enclosed in niche markets due to the high energy input and downstream processes costs for biomass treatment. Among the main issues that affect the overall costs of microalgae products, harvesting, biomass storage and cell disruption method are very impactful.

Dewatering accounts for up to 30% of the overall cost of biomass production (Bamba et al., 2021; Mkpuma et al., 2022). Why is so difficult to harvest microalgae? Because microalgal cultures never reach high density (usually the concentration reached is lower than 0.5 g/L) (Manirafasha et al., 2016; Mkpuma et al., 2022), and their cell is characterized by a small cell size (up to 20 μm). The identification of the suitable harvesting method for microalgae needs to consider many factors. As an example, to obtain high-value products, centrifugation is used, but this technique cannot be applied when processing large volumes. Thus, centrifugation cannot be used when bulk products, such as biofuels, are needed, as a huge amount of biomass is required (Najjar and Abu-Shamleh, 2020). To harvest large amount of biomass, there are few techniques that can be considered: filtration, sedimentation and flocculation. Filtration does not affect the quality of the end-product, as no chemicals are added, but its progress is hindered by the requirement of different size of filters, and, most importantly, by fouling (Mkpuma et al., 2022). Gravity sedimentation is simple, with low operation costs, but it is very time-consuming and with a low yield; moreover, due to the long time required, it can induce cell deterioration (Ma et al., 2022). Flocculation can be considered as effective, low costs, with low energy consumption and technically feasible (Li et al., 2020).

Flocculation can be classified as: (i) physical, if electricity, magnetism or ultrasounds are used to harvest the biomass, but these techniques require high-cost special equipment (Li et al., 2020); (ii) chemical, when inorganic (metal ions) or organic (polymers) compounds are added to the culture to form bridges among microalgae cells. However, the addition of such molecules to the culture may affect the activity/purity of the bio-products (Raina et al., 2022); (iii) bio-flocculation, in which flocculation is achieved by adding different microorganisms, including bacteria, fungi, yeast, as well as extracellular polymeric molecules secreted by them (Alam et al., 2016). However, this approach is specific for each strain and time

consuming, as it is strictly dependent on the microorganism adopted (Mathimani and Mallick, 2018).

After harvesting, microalgal biomass must be easily packaged and transported. Indeed, companies that sell products from microalgae must store the biomass, in dried or freeze-dried form, thus increasing the overall costs (Nemer et al., 2021). Depending on the desired final product(s), drying could help or hinder extraction, thus the extraction procedure has to be carefully chosen. Ultrasonication, bead milling and high-speed homogenization are extraction methods used on an industrial level today (Günerken et al., 2015). Nonetheless, research is directed towards the improvement of these technologies, or even to the development of new ones, such as pressurized liquid extraction and ionic liquid extraction systems (Callejón et al., 2022; Imbimbo et al., 2020; Ong et al., 2021; Rezaei Motlagh et al., 2020), to improve selectivity and, as a consequence, the purity of the obtained products. It is urgently needed to find low-cost technologies to render microalgal products sustainable.

Here, we exploited different approaches to overcome some of the abovementioned bottlenecks in microalgal downstream process, in order to push its commercialization.

2.2 Materials and Methods

2.2.1 Reagents

All chemicals, solvents, and reagents, unless differently specified, were from Sigma-Aldrich (St Louis, MO, USA).

2.2.2 Microalgal strains

Porphyridium cruentum strain (CCALA 415) was acquired from Culture Collection of Autotrophic Organism (CCALA, Centre for Phycology, Institute of Botany of the AS CR, Dukelská 135, TŘEBOŇ CZ-379 82, Czech Republic). *Galdieria phlegrea* (ACUF 009), *Synechococcus bigranulatus* (ACUF 680) and *Pseudococcomyxa simplex* (ACUF 127) were kindly provided by Algal Collection of the University Federico II (ACUF, University of Naples Federico II, Department of Biology, Naples, Italy, www.acuf.net).

2.2.3 *Porphyridium cruentum* cultivation and dry weight determination

Pre-cultures (50 mL, 0.09 ± 0.01 O.D./mL) of *P. cruentum* were inoculated in Porphyridium medium (**Table 1**) (Brody and Emerson, 1959) in 1L bubble column photobioreactors (working volume 800 mL) in autotrophic condition and without CO_2, changing different parameters:

- in a room with constant temperature (37 ± 1 °C) and light (fluorescent lamps with an intensity of 100 ± 1 PAR $\left[\frac{\mu mol_{photons}}{m^2}/s\right]$)
- in a room with constant temperature (25 ± 1 °C) and light (fluorescent lamps with an intensity of 100 ± 1 PAR)
- in a room with constant temperature (25 ± 1 °C), light (fluorescent lamps with an intensity of 100 ± 1 PAR) and 300 rpm agitation
- in a room with constant temperature (25 ± 1 °C) and light (fluorescent lamps with an intensity of 13 ± 1 PAR).

Unless different specified, the culture was mixed by bubbling air through a sintered glass tube placed at the bottom of each reactor. Algal growth was monitored by measuring the absorbance at 730 nm. The O.D. values were converted into biomass amount by experimentally correlating O.D. and dry cell weight. The conversion factor is 1 O.D. = 0.64 $mg_{D.W.}$.

Table 1. Porphyridium medium composition.

Porphyridium Medium (Brody and Emerson, 1959)	
Component	**g/L**
KCl	4
NaCL	3.13
KNO_3	1.24
$MgSO_4 * 7 H_2O$	2.5
K_2HPO_4	0.66
$Ca(NO_3)_2 * 4 H_2O$	0.17
KI	0.05
KBr	0.05
Fe_3-EDTA	18.4
Oligoelements	**mg/L**
H_3BO_3	30.9
$MnSO_4 * 4 H_2O$	12
$CoSO_4 * 7 H_2O$	14
$CuSO_4 * 5 H_2O$	12.4
$ZnSO_4 * 7 H_2O$	14.3
$(NH_4)_6Mo_7O_{24} * 4 H_2O$	18.4

2.2.4 Algal growth media

P. simplex was grown in the inorganic medium Bold Basal Medium (BBM) (Bold, 1949), *S. bigranulatus* in Blue-Green medium (BG-11) (Rippka et al., 1979) and *G. Phlegrea* in Allen medium (Allen, 1968).

2.2.5 Chemical flocculation

At the end of cultivation, increasing concentrations of chitosan (CS) or sodium glutamate (SG) (from 50 to 300 mg/L) were added to each culture. Flocculation was carried out at the pH measured at the end of cell growth (7 for *P. cruentum*, 1.5 for *G. phlegrea*, 8 for *S. bigranulatus* and 8 for *P. simplex*), or at pH 10, by adding 0.1 N NaOH. After adding the flocculating agent, each culture was stirred for 30 seconds at 1000 rpm and then the O.D. of the solution was measured at 730 nm. Time-course experiments were performed by measuring the O.D. after 10, 20, 30, 60 and 120 minutes from incubation with 50 mg/L of either CS or SG.

Flocculation efficiency was calculated as percentage (%) using the formula:

$$Flocculation\ effinciency\ (\%) = \left(1 - \frac{O.D._{\cdot Sample}}{O.D._{\cdot Culture}}\right) \times 100$$

where $O.D._{sample}$ is the O.D. measured after the treatment and $O.D._{culture}$ is the value measured before treatment (Chua et al., 2020; Praharyawan and Putri, 2017).

2.2.6 Cell disruption and protein quantification

Fresh biomass was harvested by centrifugation at 1200*g* for 30 min at room temperature and resuspended at 10 $mg_{D.W.}$/mL in PBS pH 7.4. Cell disruption was achieved by: (i) maceration; (ii) freeze and thaw; (iii) French-Press and (iv) sonication. For maceration, the biomass was kept at 4° C in agitation for 24 h. For the freeze and thaw method, the biomass was frozen (-80 °C) and then thawed (37° C) for five cycles. For the French Press, two cycles were performed at a pressure of 2 kbar. Ultrasound method was performed by operating with MS73 tip at 40% amplitude of the instrument (Bandelin Sonoplus HD 3200) for different length of times, from 4 to 20 minutes (30'' on, 30'' off), on ice. At the end of each step, samples were centrifuged at 5000*g* at 4 °C for 30 min, proteins were recovered in the supernatant, total proteins were determined by BCA Protein Assay Kit (Thermo Scientific) and then SDS-PAGE analysis followed by Coomassie staining was performed. Phycobiliproteins concentration was determined by the Bennet & Bogorad equations (Bennett and Bogobad, 1973):

$$C_{PC} = \frac{[Abs_{615nm} - (0.474 \times Abs_{652})]}{5.34}$$

$$C_{Apc} = \frac{[Abs_{652nm} - (0.208 \times Abs_{620nm})]}{5.09}$$

$$C_{Pe} = \frac{[Abs_{562nm} - (2.41 \times C_{Pc}) - (0.849 \times C_{Apc})]}{9.62}$$

The reported wavelengths (562 nm, 615 nm and 652 nm) correspond to the maximum of absorption of Phycoerythrin, Phycocyanin and Allophycocyanin, respectively.

2.2.7 Statistical analyses

Results are reported as mean of results obtained after three independent experiments (mean ± SD) and compared by one-way ANOVA according to the Bonferroni's method (posthoc) using Graphpad Prism for Windows, version 6.01.

2.3 Results and Discussion

2.3.1 Optimization of growth parameters

To establish *P. cruentum* best growth conditions, the strain was grown under different experimental conditions, summarized in **Table 2**.

Table 2. *P. cruentum* experimental growth conditions

Condition	Temperature	Illumination	Agitation
I	37 ± 1 °C	100 ± 1 PAR	No
II	25 ± 1 °C	100 ± 1 PAR	No
III	25 ± 1 °C	100 ± 1 PAR	300 rpm
IV	25 ± 1 °C	13 ± 1 PAR	No

In the 1st condition, high temperature and light intensity induced cell bleaching. The 2nd condition used the same illumination conditions, but a lower temperature. In this experimental set up, the produced exopolysaccharides induced cell adhesion to the photobioreactor and microalgae formed lumps (Garza Rodríguez,

2022). As shown in **Figure 1A**, under these circumstances it was not possible to calculate cell growth, as sampling was not accurate (high heterogeneity of the culture).

Thus, a 3rd condition was used, identical to the 2nd but with agitation. In this case, according to literature (Rossi and De Philippis, 2015), cell damage was induced as the absence of exopolysaccharides affected microalgal growth, resulting in a very low biomass production (**Figure 1B**). The last experimental condition analyzed was the number 4, with low temperature, low light intensity and no extra agitation. As shown in **Figure 1C**, the culture was homogeneous and the growth curve was obtained. Under this condition, the concentration of biomass, at the end of growth, was about 600 ± 27 mg/L.

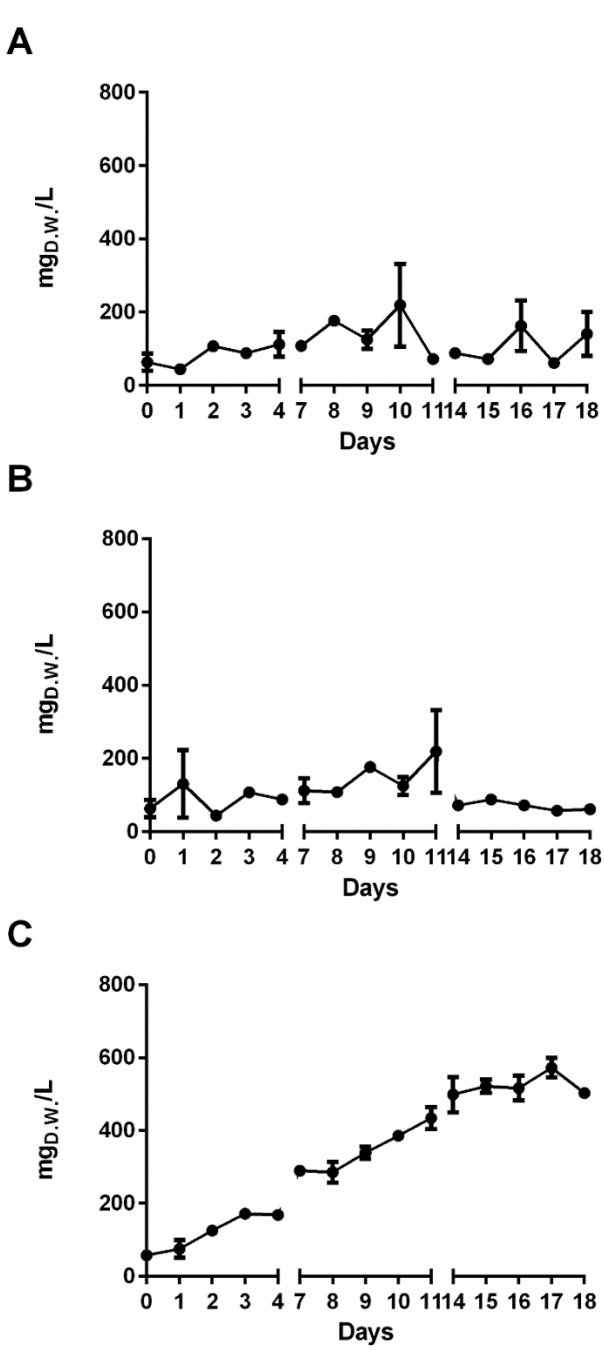

Figure 1. Growth of *Porphyridium cruentum* under different conditions. Cells were grown in bubble column photobioreactors with different parameters. **A:** 25 ± 1 °C, 100 ± 1 PAR; **B**: 25 ± 1 °C, 100 ± 1 PAR, 300 rpm agitation; **C**: 25 ± 1 °C, 13 ± 1 PAR.

2.3.2 Harvesting

In order to set up the best flocculation parameters, increasing concentrations of either CS or SG were added to different microalgal cultures. A chlorophyta (*P. simplex*), a cyanobacterium (*S. bigranulatus*) and two red microalgae strains (*G. phlegrea* and *P. cruentum*) were used, in order to get a general understanding of the procedure. In the case of first two strains, as reported in **Table 3**, SG did not produce any flocculation at any of the analyzed pH, thus indicating that SG is not suitable for their flocculation. On the other hand, CS induced 98% of flocs formation on *P. simplex* culture starting from the lowest concentration tested (50 mg/L), independently from the pH used. Different was the case of *S. bigranulatus* culture, in which a 40% of flocculation was observed at pH 8 and about 50% at pH 10.

Table 3. Flocculation efficiency (%) of *P. simplex* and *S. bigranulatus* cultures. Values are reported as % of flocculated biomass. CS indicates chitosan and SG indicates sodium glutamate. Data are obtained by mean of three independent experiments (mean ± S.D.).

Flocculation efficiency (%)								
	P. simplex				*S. bigranulatus*			
	pH 8		pH 10		pH 8		pH 10	
mg/L	CS	SG	CS	SG	CS	SG	CS	SG
50	98 ± 1	3 ± 2	97 ± 1	3 ± 1	41 ± 3	3 ± 1	46 ± 5	4 ± 2
100	98 ± 1	1 ± 3	97 ± 1	2 ± 1	36 ± 1	4 ± 1	52 ± 4	5 ± 1
150	98 ± 1	2 ± 4	96 ± 1	1 ± 3	30± 10	5 ± 2	50 ± 4	6 ± 3
200	94 ± 2	4 ± 4	93 ± 1	4 ± 4	40 ± 2	5 ± 3	50 ± 2	4 ± 1
250	87 ± 2	2 ± 1	90 ± 1	5 ± 1	31 ± 3	5 ± 1	47 ± 2	4 ± 1
300	78 ± 1	3 ± 2	84 ± 1	4 ± 4	34 ± 2	6 ± 1	49 ± 4	8 ± 4

The same procedure was used on rodophyta, as shown in **Table 4**. In this case, CS induced a complete flocculation of *P. cruentum* culture when tested at 200 mg/L at pH 7. When the procedure was performed at pH 10, the amount of chitosan needed to obtain flocculation was halved. This result is in contrast with literature, according to which the alkaline environment should reduce the

flocculation capacity of chitosan (Li et al., 2020). Noteworthy, SG had no effect on the flocculation, at either pH tested.

As for *G. phlegrea* culture, either CS or SG did not produce any effect under each condition tested.

Table 4. Flocculation efficiency (%) of two rodophyta strains. Values are reported as % of flocculated biomass. CS indicates chitosan and SG indicates sodium glutamate. Data are obtained by mean of three independent experiments (mean ± S.D.).

Flocculation efficiency (%)								
	G. phlegrea				*P. cruentum*			
	pH 1.5		pH 10		pH 7		pH 10	
mg/L	CS	SG	CS	SG	CS	SG	CS	SG
50	14 ± 7	16 ± 1	11 ± 2	17 ± 2	54 ± 2	3 ± 1	53 ± 1	3 ± 1
100	13 ± 1	18 ± 1	15 ± 2	17 ± 1	71 ± 4	4 ± 1	99 ± 1[a]	4 ± 1
150	17 ± 1	19 ± 1	16 ± 1	17 ± 1	96 ± 4[a]	5 ± 2	98 ± 1	5 ± 2
200	18 ± 2	19 ± 2	14 ± 1	19 ± 2	99 ± 1[a]	5 ± 3	99 ± 1	5 ± 3
250	9 ± 4	19 ± 2	13 ± 1	19 ± 1	99 ± 1	5 ± 1	99 ± 1	5 ± 1
300	13 ± 4	20 ± 5	15 ± 1	19 ± 1	99 ± 1	6 ± 1	99 ± 1	6 ± 1

[a]indicates $p \leq 0.05$ with respect to biomass flocculated with 50 mg/mL of chitosan.

A time course (0-120 min) of the flocculation efficiency was then performed using either CS or SG at 50 mg/L. The flocculation efficiency, measured at the pH values recorded at the end of each growth (as reported in Materials and Method section) is reported in **Table 5**, whereas flocculation performed at pH 10 is reported in **Table 6**. With the exception of *G. phlegrea* culture, in which no flocculation occurred, all the other strains showed almost complete flocculation already after 10 min. In particular, in the case of *S. bigranulatus*, more than 90% flocculation occurred at both pH values (94 ± 1% and 94 ± 1% at pH 8 and 10, respectively). In the case of *P. simplex*, the results confirmed the minimum amount of chitosan needed to obtain flocculation. *P. cruentum*, instead, showed an increase from 78 ± 5% after 10 min incubation, to 88 ± 2% after 120 min at pH 7, and from 86 ± 1% to 90 ± 1% at pH 10. Finally, a rough estimation of the cost of the process was performed. Considering the results obtained, the amount of CS needed to completely flocculate 1 kg of *P. cruentum*

biomass is about 10% (w/w) of the biomass. The price of low molecular weight CS, at laboratory scale, ranges between 850 and 1750 US $/kg, depending on the purity grade and on seller company, so that the cost to flocculate 1 kg of biomass would be around 85/175 US $. It has to be considered, however, that different prices would be applied for industrial amount of CS.

Table 5. Flocculation efficiency (%) over time. Values are reported as % of flocculated biomass at pH values measured at the end of cell growth. Data are obtained by mean of three independent experiments (mean ± S.D.).

Flocculation efficiency (%) over time				
min	*P. simplex*	*S. bigranulatus*	*P. cruentum*	*G. phlegrea*
0	29 ± 7	39 ± 5	54 ± 1	5 ± 1
10	90 ± 2[a]	94 ± 2[a]	78 ± 5	3 ± 2
20	98 ± 3	95 ± 2	82 ± 4	4 ± 4
30	99 ± 1	96 ± 1	86 ± 4	2 ± 2
60	98 ± 1	98 ± 1	87 ± 3	4 ± 3
120	99 ± 1	99 ± 1	88 ± 2	5 ± 1

[a]indicates $p \leq 0.05$ with respect to biomass flocculated at 0 min.

Table 6. Flocculation efficiency (%) over time at pH 10. Values are reported as % of flocculated biomass at pH 10. Data are obtained by mean of three independent experiments (mean ± S.D.).

Flocculation efficiency (%) over time, pH 10				
min	*P. simplex*	*S. bigranulatus*	*P. cruentum*	*G. phlegrea*
0	32 ± 1	35 ± 3	54 ± 2	6 ± 2
10	91 ± 2[a]	94 ± 2[a]	86 ± 1	3 ± 1
20	98 ± 1	95 ± 1	87 ± 2	7 ± 5
30	99 ± 1	96 ± 1	88 ± 1	2 ± 1
60	98 ± 1	98 ± 1	89 ± 3	8 ± 2
120	99 ± 1	99 ± 1	90 ± 1	12 ± 4

[a]indicates $p \leq 0.01$ with respect to biomass flocculated at 0 min.

2.3.3 Phycoerythrin extraction optimization

PE extraction was performed on *P. cruentum* biomass, by testing different extraction procedures: Maceration, Sonication, Freeze & thaw and French Press, as described in Materials and Methods. All the procedures allowed to obtain a red colored and fluorescent solution, suggesting that PE was successfully extracted (**Figure 2**). Then, total protein concentration was determined by colorimetric assay (BCA), whereas PE, phycocyanin (PC) and allophycocyanin (APC) concentration were obtained using the Bennet & Bogorad equations (as reported in Material and Methods section). The amount of PE, reported in **Table 7**, showed no significant differences among the analyzed samples, whereas PC and APC were found to be most abundant only in the extract obtained by French Press. Indeed, the presence of APC and PC in the French Press extract halved the purity grade of the extract with respect to those obtained for the other three extracts.

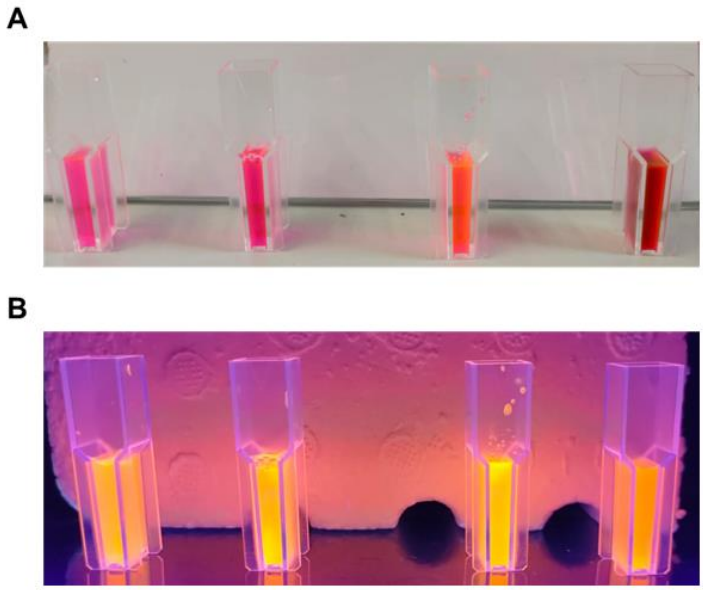

Figure 2. Supernatants obtained from *P. cruentum* by different extraction protocols. Normal light exposed (**A**) and UVA light exposed (**B**) extracts obtained by different methods. From left to right: Freeze and thaw; Maceration; Sonication; French Press.

Table 7. Total protein concentration, phycobiliproteins concentration, extraction yield and phycoerythrin purity grade. Total protein concentration was obtained by BCA assay and total PE, PC and APC concentration by Bennett & Bogorad equations. Yields are expressed as $g_{protein}/g_{d.w.biomass}$. The PE purity grade was calculated from Abs_{562nm}/Abs_{280nm} ratio.

	Maceration	Sonication	Freeze & thaw	French Press
Protein yield (%)	44 ± 5	35 ± 4	35 ± 3	37 ± 6
PE yield (%)	1.8 ± 0.1	1.8 ± 0.8	1.8 ± 0.5	1.4 ± 0.7
PE Purity grade (Abs_{562nm}/Abs_{280nm})	0.8 ± 0.1	0.9 ± 0.1	1.1 ± 0.1	0.4 ± 0.2
PC yield (%)	0.14 ± 0.02	0.48 ± 0.1	0.2 ± 0.1	1.4 ± 0.5
APC yield (%)	0.13 ± 0.1	0.2 ± 0.1	0.5 ± 0.1	1.1 ± 0.2

Supernatants were also analyzed by SDS-PAGE followed by Coomassie staining (**Figure 3A**) and UVA light exposure, taking advantage of chromophores present in PE (**Figure 3B**). The analyses revealed two major bands, whose molecular weights corresponded to PE α and β subunits (17 kDa) and γ subunit (30 kDa), in each lane. Results suggested ultrasounds as the most promising method.

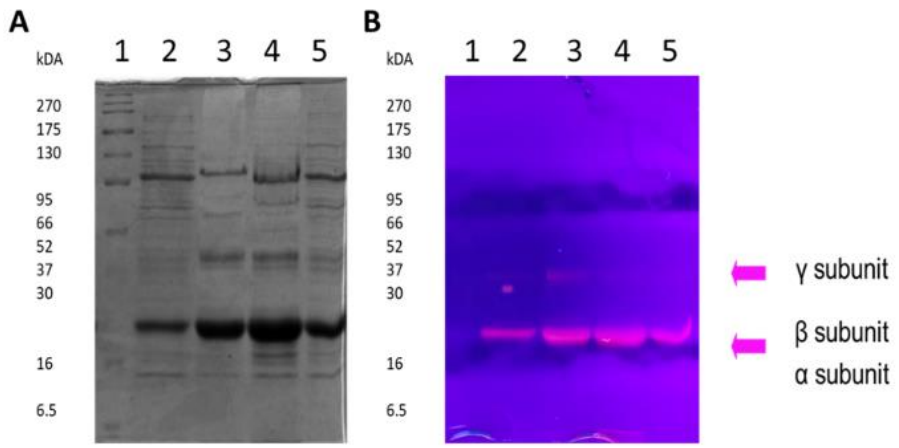

Figure 3. SDS-PAGE analysis of *P. cruentum* extracts. Coomassie staining (**A**) and UVA light exposed of unstained (**B**) SDS-PAGE of total proteins extracted with different techniques. Lane 1:

protein molecular weight markers; lane 2: Freeze & thaw extract; lane 3: Sonication extract; lane 4: Maceration extract; lane 5: French Press extract. 30 µg of total proteins were loaded in each lane.

2.3.4 Biomass storage

As biomass storage is a crucial step in industrial-scale processes, also from a logistically point of view (Gruber-Brunhumer et al., 2016), extractions were performed on either fresh or frozen biomass (stored at –80 °C). Ultrasounds were used for different length of time (from 4 to 20 min) to lyse cells. At the end of each extraction, the disrupted biomass was analyzed by SDS-PAGE (**Figure 4**). Supernatants obtained after 20 min extraction seemed to be best choice of extraction for fresh biomass, as 4 min extraction allowed to recover a PE content of 1.8% (**Table 7**) with a purity grade of 0.9 (**Table 7**), whereas 20 min of sonication on fresh biomass allowed to recover a PE content of 3.0 ± 0.4% with a purity grade of 1.5 ± 0.3. These extraction values are higher with respect to those obtained, after 20 min of sonication, from the frozen biomass: PE yield varied from 2.2 ± 0.2% to 3.0 ± 0.4% for frozen and fresh biomass, respectively, and a PE purity grade was 1.0 ± 0.2 and 1.5 ± 0.3 for frozen and fresh biomass, respectively. Thus, 20 min sonication were selected for further experiments.

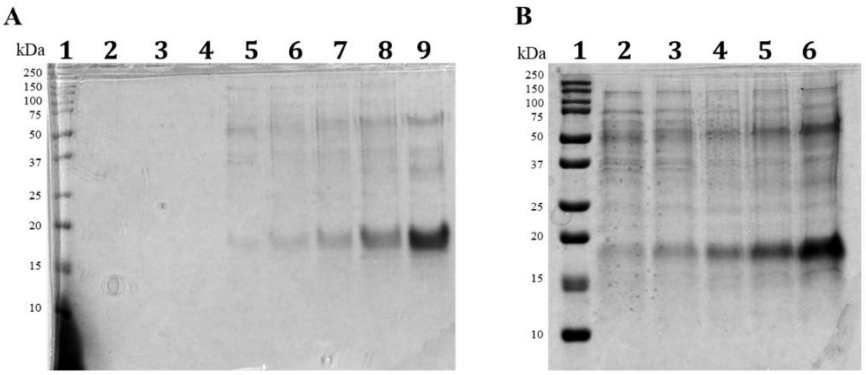

Figure 7. Coomassie staining of SDS-PAGE. Proteins were extracted by ultrasounds for different times from (A) fresh and (B) frozen biomass. A: Lane 1: protein molecular weight markers; lanes 2-4: empty lanes; lanes 5-9: proteins extracted for 4, 8, 12, 16, and 20 minutes, respectively. **B:** Lane 1: protein molecular weight

markers; lanes 2-6: proteins extracted for 4, 8, 12, 16, and 20 minutes, respectively.

Finally, flocculation was combined to 20 min sonication to evaluate if flocculation could affect PE extraction. As a control, the biomass harvested by centrifugation was used. At the end of sonication, samples were centrifuged and total protein content, PE content and its purity grade were calculated from both supernatants. The extract obtained from the flocculated biomass showed similar protein yield (36 ± 2%), PE yield (3.0 ± 0.2%) and purity grade (1.6 ± 0.2) compared to the extract obtained from the biomass harvested by centrifugation (35 ± 4% protein content, 3.0 ± 0.4% PE yield, 1.5 ± 0.3 purity grade), thus suggesting that flocculation could be adopted as harvesting method without affecting the extraction of proteins.

2.4 Conclusions

Here, we defined the starting point of the biorefinery process to fully valorize *Porphyridium cruentum* biomass (**Figure 8**). The optimization of growth parameters was set up, allowing obtaining a homogenous culture. Sonication was chosen as the best extraction technique and no significant difference was found between fresh and frozen biomass, allowing reducing the cost of the biomass storage. Finally, since harvesting represents a huge issue that hampers the economic viability of microalgal products, here it was demonstrated that a low amount of chitosan allows the flocculation of the biomass, without affecting the subsequent extraction of proteins. It has to be considered, however, that the best conditions to flocculate biomass are strain dependent and no general rules can be applied.

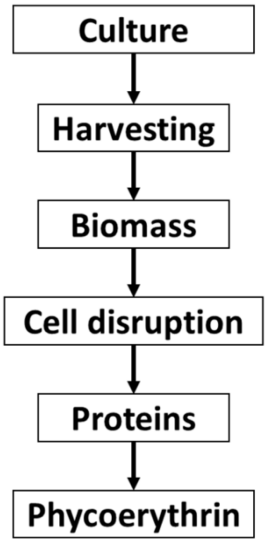

Figure 8. Schematic representation of the applied process.

Some data have been published on: Inside out *Porphyridium cruentum*: beyond the conventional biorefinery concept, ACS Sustainable Chemistry and Engineering (2022), https://doi.org/10.1021/acssuschemeng.2c05869

2.5 References

Alam, M., Vandamme, D., Chun, W., Zhao, X., Foubert, I., Wang, Z., Muylaert, K., Yuan, Z., 2016. Bioflocculation as an innovative harvesting strategy for microalgae. Rev. Environ. Sci. Bio/Technology 15, 573–583.

Allen, M.M., 1968. Simple conditions for growth of unicellular blue-green algae on plates 1, 2. J. Phycol. 4, 1–4.

Bamba, B.S.B., Tranchant, C.C., Ouattara, A., Lozano, P., 2021. Harvesting of Microalgae Biomass Using Ceramic Microfiltration at High Cross-Flow Velocity. Appl. Biochem. Biotechnol. 193, 1147–1169. https://doi.org/10.1007/S12010-020-03455-Y

Bennett, A., Bogobad, L., 1973. Complementary chromatic adaptation in a filamentous blue-green alga. J. Cell Biol. 58, 419–435. https://doi.org/10.1083/jcb.58.2.419

Bold, H.C., 1949. The morphology of Chlamydomonas

chlamydogama, sp. nov. Bull. Torrey Bot. Club 101–108.
Brody, M., Emerson, R., 1959. the Effect of Wavelength and Intensity of Light on the Proportion of Pigments in *Porphyridium Cruentum*. Am. J. Bot. 46, 433–440. https://doi.org/10.1002/j.1537-2197.1959.tb07034.x
Callejón, M.J.J., Medina, A.R., Sánchez, M.D.M., Moreno, P.A.G., López, E.N., Cerdán, L.E., Grima, E.M., 2022. Supercritical fluid extraction and pressurized liquid extraction processes applied to eicosapentaenoic acid-rich polar lipid recovery from the microalga *Nannochloropsis sp.* Algal Res. 61, 102586.
Chua, E.T., Shekh, A.Y., Eltanahy, E., Thomas-Hall, S.R., Schenk, P.M., 2020. Effective harvesting of Nannochloropsis microalgae using mushroom chitosan: a pilot-scale study. Front. Bioeng. Biotechnol. 8, 771.
Garza Rodríguez, Z.B., 2022. Characterization of the effect of UV-A light and agitation on the exopolysaccharide production of *Chlorella vulgaris* and *Porphyridium cruentum*.
Gruber-Brunhumer, M.R., Jerney, J., Zohar, E., Nussbaumer, M., Hieger, C., Bromberger, P., Bochmann, G., Jirsa, F., Schagerl, M., Obbard, J.P., Fuchs, W., Drosg, B., 2016. Associated effects of storage and mechanical pre-treatments of microalgae biomass on biomethane yields in anaerobic digestion. Biomass and Bioenergy 93, 259–268. https://doi.org/10.1016/J.BIOMBIOE.2016.07.013
Günerken, E., D'Hondt, E., Eppink, M.H.M., Garcia-Gonzalez, L., Elst, K., Wijffels, R.H., 2015. Cell disruption for microalgae biorefineries. Biotechnol. Adv. 33, 243–260. https://doi.org/10.1016/j.biotechadv.2015.01.008
Imbimbo, P., Bueno, M., D'Elia, L., Pollio, A., Ibañez, E., Olivieri, G., Monti, D.M., 2020. Green compressed fluid technologies to extract antioxidants and lipids from *Galdieria phlegrea* in a Biorefinery Approach. ACS Sustain. Chem. Eng. 8, 2939–2947.
Li, S., Hu, T., Xu, Y., Wang, J., Chu, R., Yin, Z., Mo, F., Zhu, L., 2020. A review on flocculation as an efficient method to harvest energy microalgae: mechanisms, performances, influencing factors and perspectives. Renew. Sustain. Energy Rev. 131, 110005.
Ma, C., Wang, G., Liu, X., Li, Y., Huang, J., Zhang, P., Chu, X., Wang, L., Zhao, B., Zhang, Z., 2022. A novel gravity sedimentation-Forward osmosis hybrid technology for microalgal dewatering. Chemosphere 308, 136300.
Manirafasha, E., Ndikubwimana, T., Zeng, X., Lu, Y., Jing, K., 2016. Phycobiliprotein: Potential microalgae derived pharmaceutical

and biological reagent. Biochem. Eng. J. 109, 282–296.
Mathimani, T., Mallick, N., 2018. A comprehensive review on harvesting of microalgae for biodiesel–key challenges and future directions. Renew. Sustain. Energy Rev. 91, 1103–1120.
Mkpuma, V.O., Moheimani, N.R., Ennaceri, H., 2022. Microalgal dewatering with focus on filtration and antifouling strategies: A review. Algal Res. 61, 102588. https://doi.org/10.1016/J.ALGAL.2021.102588
Najjar, Y.S.H., Abu-Shamleh, A., 2020. Harvesting of microalgae by centrifugation for biodiesel production: A review. Algal Res. 51, 102046.
Nemer, G., Louka, N., Vorobiev, E., Salameh, D., Nicaud, J.-M., Maroun, R.G., Koubaa, M., 2021. Mechanical cell disruption technologies for the extraction of dyes and pigments from microorganisms: A review. Fermentation 7, 36.
Ong, H.C., Tiong, Y.W., Goh, B.H.H., Gan, Y.Y., Mofijur, M., Fattah, I.M.R., Chong, C.T., Alam, M.A., Lee, H.V., Silitonga, A.S., 2021. Recent advances in biodiesel production from agricultural products and microalgae using ionic liquids: Opportunities and challenges. Energy Convers. Manag. 228, 113647.
Praharyawan, S., Putri, S.A., 2017. Optimasi Efisiensi Flokulasi Pada Proses Panen Mikroalga Potensial Penghasil Biodiesel Dengan Flokulan Ion Magnesium-(Optimization of Flocculation Efficiency in the Harvesting Process of Potential Biodiesel Producing Microalgae by Using Magnesium Ions). Biopropal Ind. 8, 89–98.
Raina, D., Kumar, V., Saran, S., 2022. A critical review on exploitation of agro-industrial biomass as substrates for the therapeutic microbial enzymes production and implemented protein purification techniques. Chemosphere 133712.
Rezaei Motlagh, S., Harun, R., Radiah Awang Biak, D., Hussain, S.A., A. Elgharbawy, A., Khezri, R., Wilfred, C.D., 2020. Prediction of potential ionic liquids (ILs) for the solid–liquid extraction of docosahexaenoic acid (DHA) from microalgae using COSMO-RS screening model. Biomolecules 10, 1149.
Rippka, R., Deruelles, J., Waterbury, J.B., Herdman, M., Stanier, R.Y., 1979. Generic assignments, strain histories and properties of pure cultures of cyanobacteria. Microbiology 111, 1–61.
Rossi, F., De Philippis, R., 2015. Role of cyanobacterial exopolysaccharides in phototrophic biofilms and in complex microbial mats. Life 5, 1218–1238.

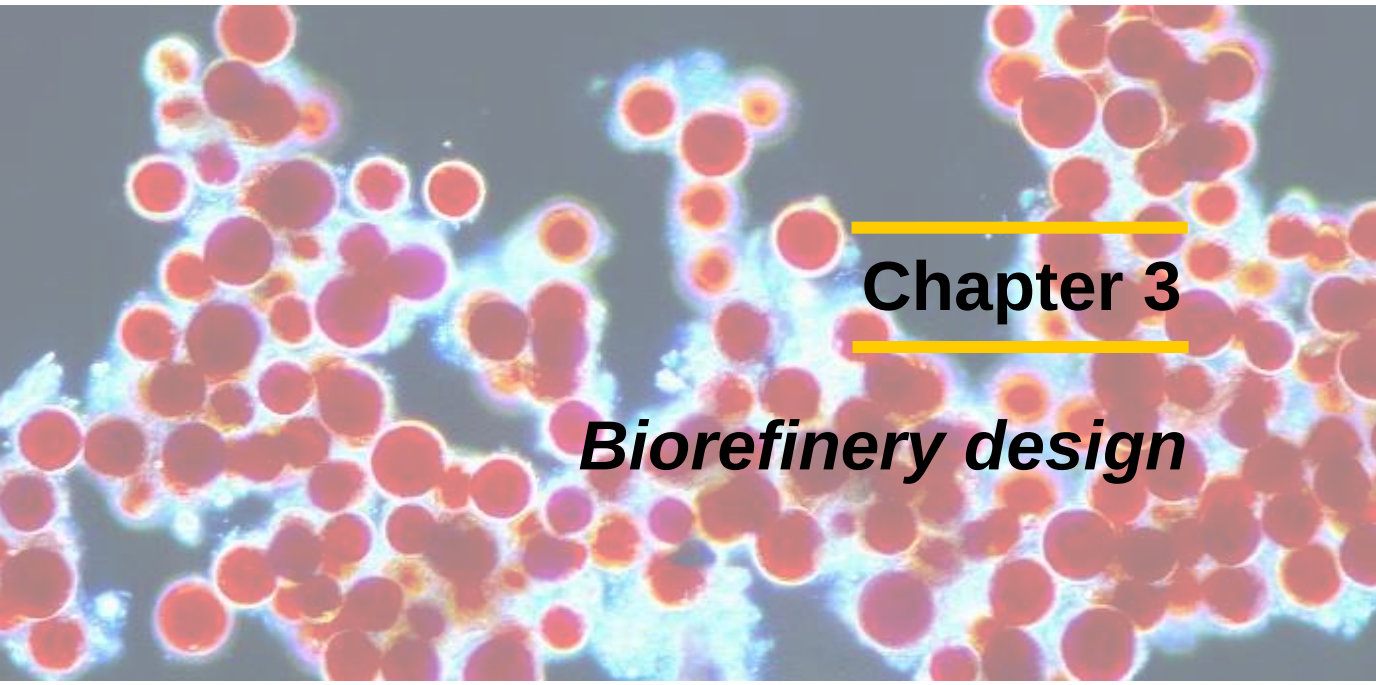

Chapter 3

Biorefinery design

3.1 Introduction

Microalgae capture carbon dioxide during their growth to perform photosynthesis: this implies the production of oxygen and the reduction of carbon dioxide emissions (Zhang and Liu, 2021). Noteworthy, microalgae are used as a reliable source of food and high added-value products (Bhalamurugan et al., 2018). Microalgae can be considered perfect candidates for their use in biorefinery approaches (Yen et al., 2013), as they can grow in lands which do not compete with food production, and with higher growth rate with respect to conventional crops. From a theoretical point of view, a biorefinery is a combination of multiple integrated processes able to convert the biomass into a variety of high added-value products, in an economical and environmentally sustainable approach (Gallego et al., 2019). This is in line with the principles of circular economy, fostered by international organizations and promoted by European Union (https://eur-lex.europa.eu/legal-content/EN/ALL/?uri=CELEX%3A52015DC0614). Unfortunately, in the microalgae field, a real biorefinery has been demonstrated only for few strains (Imbimbo et al., 2020), and most of the present literature is focused on the extraction of one or two classes of molecules, thus suggesting that the process is not economically feasible.

Porphyridium cruentum is a red marine microalga, reservoir of potentially high added-value molecules, such as carotenoids, sulfated exopolysaccharides (EPSs), B-phycoerythrin (PE) and lipids (Di Lena et al., 2019; Feller et al., 2018; Gaignard et al., 2019; Rebolloso Fuentes et al., 2000). Carotenoids are well-known antioxidants, also able to counteract many disorders, from type 2 diabetes, to degenerative diseases or cancer (Rodriguez-Concepcion et al., 2018). Sulfated EPSs have a chemical structure which confer them peculiar rheological properties (Xiao and Zheng, 2016) and many biological activities (De Jesus Raposo et al., 2013), such as antimicrobial, anti-inflammatory (Mišurcová et al., 2012), hypocholesterolemic (Dvir et al., 2009), antiviral activities (Huheihel et al., 2002), skin protective activity (Meléndez-Martínez et al., 2018). PE, the main protein found in *P. cruentum*, has a good market value for different reasons: (i) in biomedical and molecular applications for its natural fluorescence; (ii) as a natural red-colored protein to be used as a dye for food and cosmetics, and (iii) in pharmaceutical industry thanks to its antioxidant activity (Qiu et al., 2004). Finally, recent literature exploited the use of saturated fatty acids as antimicrobial agents and as drug delivery systems (Xue et al., 2021; Yoon et al., 2018).

Thus, taking advantage of the chemical composition of *P. cruentum*, here we propose a real biorefinery. For the first time, not only the biomass, but also the exhausted medium, were fully exploited to recover: EPSs from the medium and PE, carotenoids and lipids from the biomass. Molecules were extracted sequentially, starting from the most valuable one, without affecting the activity of the molecules in the residual biomass.

3.2 Materials and Methods

3.2.1 Reagents

All chemicals, solvents and reagents, unless differently specified, were from Sigma-Aldrich (St Louis, MO, USA).

3.2.2 Exopolysaccharides isolation and quantization

To process a high volume of medium, the latter was concentrated 10 times by lyophilization, prior to add pure ethanol (1:2 v/v); EPSs were then recovered by centrifugation (12000*g*, 30 min, 4 °C), collected and lyophilized. Total carbohydrates were quantified by the phenol-sulfuric acid method, according to Geresh et al. (Geresh et al., 2002), with some modifications, as reported in Gallego (Gallego et al., 2019). A reference curve was obtained by using glucose (0.03-1.0 mg/mL).

3.2.3 Determination of monosaccharide composition

Lyophilized EPSs (2 mg) were solubilized with 1 mL of HCl/CH_3OH (1.25 M) for 16 h at 80 °C (Ricciardelli et al., 2019). Then, the sample was dried and acetylated with 25 µL of acetic anhydride and 25 µL of pyridine and kept at 100 °C for 30 min. The mixture was analyzed by Gas Chromatography-Mass Spectrometry (GC-MS) by using an Agilent Technologies instrument (GC 7820A, MS 5977B), equipped with a HP-5MS 30m, 0.25mm, 0.25µm capillary column. The following temperature program was used to analyze acetylated methyl glycosides: 140 °C for 3 min, 140 °C → 240 °C at 3 °C/min.

3.2.4 Total Carbon, Hydrogen, Nitrogen and Sulfur

The determination of total carbon (C), hydrogen (H), nitrogen (N) and sulfur (S) in EPSs recovered from *P. cruentum* medium was carried

out by performing total combustion, using the FlashSmart Elemental Analyzer, according to Álvarez-Gómez and colleagues (Álvarez-Gómez et al., 2019). Elements (C, H, N, S) were expressed as % with respect to the sample's total weight.

3.2.5 Phycoerythrin purification

PE purification was performed by comparing three techniques: anion-exchange chromatography, gel filtration and ultrafiltration. The anion-exchange chromatography was carried out by using a Nuvia-Q resin equilibrated with PBS pH 7.4 and elution was performed using 0.25 M NaCl. Gel filtration was performed by using a Sephadex G-75 equilibrated in PBS pH 7.4. Ultrafiltration was carried out with a 10 kDa molecular weight cut-off membrane and the process was performed at 4 °C. The fractions obtained by anion-exchange and gel filtration, as well as the retentate obtained by ultrafiltration, were collected and analyzed by SDS-PAGE followed by Coomassie staining and PE purity grade was calculated by measuring the ratio Abs_{562nm}/Abs_{280nm}.

3.2.6 Crystallization, data collection, structure solution and refinement of Phycoerythrin

PE crystals were grown by hanging drop vapor diffusion method (Russo Krauss et al., 2013) using a drop containing 10 mg/mL PE in 0.25 M ammonium sulphate, 25 mM potassium phosphate at pH 5.0, equilibrated with a reservoir containing 0.5 M ammonium sulphate, 50 mM potassium phosphate at pH 5.0. Red crystals were visible after one week.

The crystals were soaked in a cryoprotectant solution containing 30% (v/v) glycerol in the reservoir solution and cooled at -173 °C. Starting from one crystal, a high-resolution data set was collected at the XRD2 beamline at the Elettra synchrotron in Trieste, Italy, at -173 °C. Data were processed and scaled using Autoproc (Vonrhein et al., 2011). The crystal was trigonal, space group R3, with unit cell parameters a=b= 186.59 Å, c=59.19 Å, α=β=90°, γ=120°. For data collection statistics, see **Table S1** (**Appendix I**). The structure of PE was solved by molecular replacement using PHASER(McCoy et al., 2007), solved at 1.85 Å resolution and deposited in the protein Data Bank under the accession 3V58 (Camara-Artigas et al., 2012), as a starting model. The structure shows the presence of two (αβ) dimers in the asymmetric unit. Visual inspection and model improvements were carried out using Coot (Emsley and Cowtan, 2004). Refinements were

carried out using Refmac 5.0 (Murshudov et al., 1997). R factor and R free values were used to optimize the refinement strategy. The final model, which has good geometries and refinement statistics (**Table S1, Appendix I**), was deposited in the Protein Data Bank under the accession code 8B4N. Pymol (www.pymol.org) was used to obtain molecular-graphics figures.

3.2.7 *In situ* digestion

A single PE crystal was solubilized in water and analyzed by SDS-PAGE. For in-gel hydrolysis, SDS-PAGE bands were excised from the gel lane, destained by consecutive cycles of 0.1 M NH_4HCO_3 at pH 8.0 and acetonitrile (ACN), followed by reduction (10 mM DTT in 100 mM NH_4HCO_3, 45 min, at 56 °C) and alkylation (55 mM IAM in 100 mM NH_4HCO_3, 30 min, at room temperature). The gel pieces were washed with 0.1 M NH_4HCO_3 of pH 8.0 and ACN and subjected to the enzymatic hydrolysis by covering them with 40 µL sequencing grade modified trypsin (10 ng/µL trypsin; 10 mM NH_4HCO_3) overnight at 37 °C. Peptide mixtures were eluted, vacuum-dried, and resuspended in 2% ACN acidified with 0.1% HCOOH. Tryptic peptide mixtures were analysed by MALDI-TOF (AB SCIEX, Milan, Italy) to reveal the amino acid sequence of the three phycoerythrin chains.

3.2.8 Mass Spectrometry Analyses

Matrix-assisted laser desorption/ionization (MALDI) mass spectrometry (MS) experiments were performed on a 5800 MALDI-TOF-TOF ABSciex equipped with a nitrogen laser (337 nm) (AB SCIEX, Milan, Italy). Starting from each band, aliquots of peptide mixture (0.5 µL) were mixed (1:1, v/v) with alphacyano hydroxycinnamic acid (10 mg/mL) in acetonitrile: 55mM citric acid (70:30) solution. Calibration was done by using a calibration mixture from AB SCIEX (Monoisotopic $(M + nH)^{n+}$: 904.46 Da des-Arg-Bradykinin, 1296.68 Da Angiotensin I, 1570.67 Da Glu-Fibrinopeptide B, 2093.08 Da ACTH (clip 1–17), 2465.19 Da ACTH (clip 18–39), 3657.92 Da ACTH (clip 7–38)). Peptides were identified by MS spectra, acquired using a mass (m/z) range of 400–4000 Da. Peptide mass fingerprinting was performed by MS digest of homologue phycoerythrin sequences. Matrix-assisted laser desorption/ionization (MALDI) mass spectrometry (MS) experiments were performed on a 5800 MALDI-TOF-TOF ABSciex equipped with a nitrogen laser (337 nm) (AB SCIEX, Milan, Italy). The instrument operated with an accelerating voltage of 20 kV, a grid

voltage at 66% of the source voltage and a delay time at 200 ns. Laser power was set to 3500 V for the spectra acquisition. Each spectrum represents the sum of 10000 laser pulses from randomly chosen positions on the same target place. The data were reported as monoisotopic masses.

3.2.9 Carotenoids extraction and characterization

Carotenoids were extracted from the dry biomass, either raw or after proteins extraction. Extractions were performed in ethanol, as reported by Aremu, with some modifications (Aremu et al., 2016). Briefly, for each extraction, 200 mg of freeze-dried biomass was suspended in pure ethanol (4 mL) and sonicated (40% amplitude, 4 min on ice, Bandelin Sonoplus HD 3200, tip MS73). Mixture volume was then adjusted to 20 mL and shaken for 24 h at 250 rpm in a dark room at 4 °C. The supernatant was collected by centrifugation at 12000*g* for 10 min, dried under nitrogen stream and then stored at -20 °C. Carotenoids identification was performed by HPLC-DAD-APCI-QTOF-MS/MS, whereas quantization was done by calibration curves obtained by using commercial zeaxanthin and β-carotene, according to a method previously described (Imbimbo et al., 2020), with some modifications. The analysis of the extracts was carried out in an Agilent 1290 UHPLC system (Ultrahigh Performance Liquid Chromatography) equipped with a diode-array detector (DAD), coupled to Agilent 6540 quadrupole-time-of-flight mass spectrometer (q-TOF MS) equipped with an atmospheric pressure chemical ionization (APCI) source, all from Agilent Technologies (Santa Clara, CA, USA). Extracts were solubilized in ethanol (5 mg/mL), filtered through 0.45 µm nylon filters and then analyzed under positive ionization mode, using the following parameters: capillary voltage, 3.5 kV; drying temperature, 350 °C; vaporizer temperature, 400 °C; drying gas flow rate, 8 L/min; nebulizer gas pressure, 40 psi; corona current (which sets the discharge amperage for the APCI source), 4000 nA. The mass spectrometer was operated in MS and tandem MS modes for the structural analysis of all compounds. The MS and Auto MS/MS modes were set to acquire m/z values ranging between 50-1100 and 50-800, respectively, at a scan rate of 5 spectra per second.

3.2.10 Lipids extraction and characterization

Lipids were extracted from the dried biomass. Both the raw and the two residual biomasses (I and II residual biomass) were dried at 60

°C for 24 h. Lipids were obtained as reported by Bligh & Dyer (Bligh and Dyer, 1959). Nitrogen flux was used to dry, recover and weigh lipids. Lipids fractionation was performed by solubilizing them in chloroform and using a commercial pre-packed column containing a stationary phase made of Florisil. Neutral lipids were eluted with chloroform:methanol (2:1, v/v); fatty acids with 2% acetic acid in diethyl-ethere, whereas phospholipids were eluted with 100% methanol. The recovered fatty acids were then characterized by GC-MS, as previously reported (Imbimbo et al., 2019).

3.2.11 Statistical analyses

Results are reported as mean of results obtained after three independent experiments (mean ± SD) and compared by one-way ANOVA according to the Bonferroni's method (posthoc) using Graphpad Prism for Windows, version 6.01.

3.3 Results and Discussion

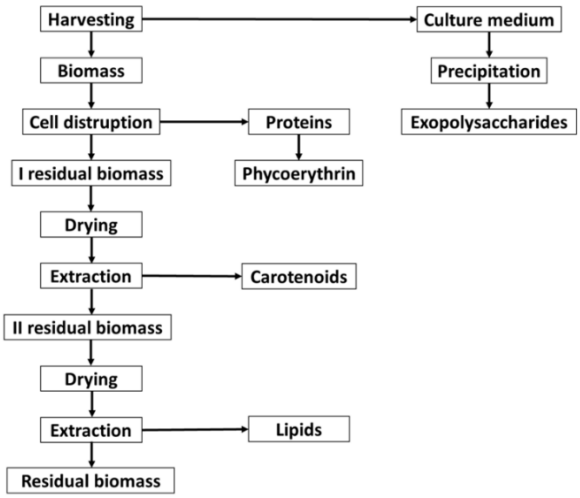

Figure 1. Schematic representation of the applied process.

3.3.1 Exopolysaccharides recovery and characterization

Considering the promising results obtained in Chapter 2, an intensification of the process was performed to fully valorize *P. cruentum* culture. **Figure 1** reports the extraction strategy used to

recover different molecules from *P. cruentum*. At the end of cell growth, medium, generally regarded as waste, was collected and polysaccharides were isolated by precipitation using ethanol or 2-propanol. The EPSs content was measured by the phenol–sulfuric acid method and no significant difference between the two applied solvents was observed (ethanol yield 0.100 ± 0.020 and 2-propanol 0.116 ± 0.020 mg/mL), thus ethanol was selected because of its wide range of applications (Melo et al., 2021). The EPSs yield was found to be 300 ± 67 mg/L of culture medium, which corresponds to EPS yield of 0.53 $g/g_{d.w.biomass}$. The monosaccharide composition was achieved by GC-MS analysis, after derivatization as acetylated methyl glycosides (AMGs). The GC-MS chromatogram disclosed the presence of mainly xylose (Xyl), galactose (Gal), and glucose (Glc). Finally, traces of rhamnose (Rha), glucuronic acid (GlcA), glucosamine (GlcN) were detected (**Figure 2**).

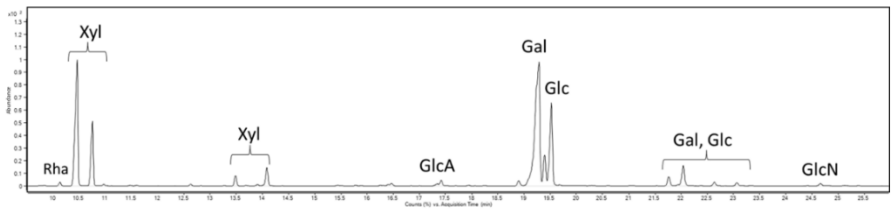

Figure 2. GC-MS chromatogram of the AMG of *P. cruentum* exopolysaccharides recovered from the culture medium. In the graph the relative ion current abundance is reported as a function of retention time (min).

Since the EPSs from *P. cruentum* are known to be sulfated, the elemental composition analysis was performed. Results, reported in **Table 1**, indicate that the % of sulfur present in the sample is similar to that reported in literature (7.4% ± 0.2%) (Ben Hlima et al., 2021; Bernaerts et al., 2018). No proteins were detected.

Table 1. Elemental composition and protein content of EPS. Elements were measured by elemental analyzer. Oxygen % was calculated by subtracting the % of the other elements from 100%. % are expressed as mg of each element/mg of analyzed EPS. Protein content was measured by colorimetric assay.

O (%)	N (%)	H (%)	C (%)	S (%)	Protein content (mg/mL)
76.0 ± 2.4	1.1 ± 0.6	2.6 ± 0.4	13.1 ± 1.3	7.4 ± 0.2	N.D.

3.3.2 Phycoerythrin purification and structure determination

. Once set up PE extraction procedure (Chapter 2), its purification was performed by comparing three techniques: anion-exchange chromatography, gel filtration and ultrafiltration. The results of the different techniques are reported in Supporting Information (**Figure S2 E-G, Appendix I**). Only the size-exclusion chromatography allowed obtaining pure PE; in particular, this purification step allowed to recover about 80% of PE and to reach a purity grade of 4.0. It is known that a purity grade ≥ 4.0 indicates a protein to be used in analytical grade (Fernández-Rojas et al., 2014). According to the overall results, this approach allowed obtaining high purity grade PE by only one step extraction and purification. To the best of our knowledge, this is the first time that PE was extracted and purified with such a purity grade by using only a single purification step (Nguyen et al., 2020; Serucňik et al., 2020; Ulagesan et al., 2021; Vicente et al., 2019).

Figure 3. PE crystals. Crystals were grown by hanging drop vapor diffusion method using a drop containing 10 mg/mL PE in 0.250 M ammonium sulphate, 0.025 M potassium phosphate at pH 5.0, equilibrated with a reservoir containing 0.500 M ammonium sulphate, 0.050 M potassium phosphate at pH 5.0.

To determine the protein identity and purity, PE was crystallized (**Figure 3**), and its X-ray structure determined at 1.60 Å resolution. The X-ray structure is constituted by 5990 atoms, including five phycoerythrobilin (PEB) chromophores for each αβ dimer, one methylated Asn in position β72 (**Figure 4A**) for each β subunit, two sulphate ions and 324 water molecules, and refines to R-factor/Rfree values of 0.222/0.256. The structure confirms the formation of the $(\alpha\beta)_3$ hexamer (**Figure 4C-D**) but does not allow to identify the exact location of the γ subunit (**Figure 4E**). Similar results were obtained in previous works (Ficner and Huber, 1993; Ritter et al., 1999) and were attributed to rotational disorder of the γ subunit within the protein crystal and to the finding that the electron density of this subunit is averaged out by the threefold crystallographic symmetry. The α subunit contains 164 residues, the β subunit 177 residues. The overall structure of the protein is very similar to that previously reported and deposited in the Protein Data Bank under accession code 3V58, obtained from crystals grown under different experimental conditions, but at the same pH. After superposition, the 164 CA atoms of the α subunit have a root-mean-square (r.m.s.) deviation of 0.146 Å, and the 177 CA atoms of β subunit have a r.m.s. deviation of 0.142 Å. Each αβ dimer has five PEBs in position α82, α139, β61, β82, and β158. The first PEB, which adopts two alternate conformations in our structure, is covalently attached to the side chain of Cys82 of the α subunit by ring A. The second PEB is bound to Cys139 of the same subunit. The other three PEBs are found in the β subunit. They are bound to the side chains of Cys61, Cys82 and Cys158. The stereochemistry of the chromophores and their interaction with protein residues are basically identical to that observed in the starting model (Camara-Artigas et al., 2012) and previously described. An example of the well-defined electron density maps of the chromophores is reported in **Figure 4B**.

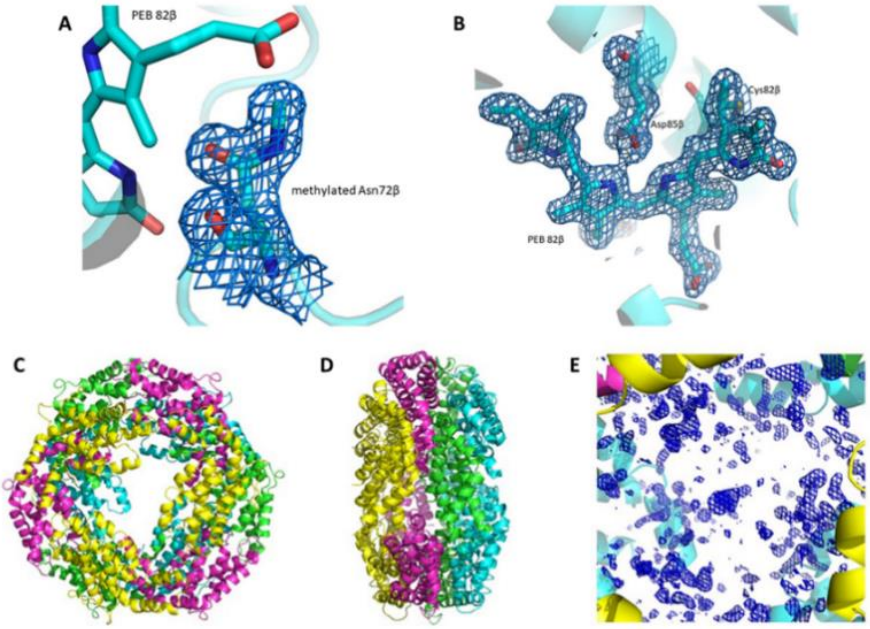

Figure 4. PE crystal structure. A, 2Fo-Fc electron density map (1.0 σ) of the methylated Asn72β in the structure of PE. **B**, 2Fo-Fc electron density maps contoured at 1.0 σ of one of the five PEB chromophores found in the structure of PE. **C**, $(\alpha\beta)_3$ hexamer shown from the upper view and the lateral view (**D**). Electron density of the central cavity is shown in panel **E**. This segment of electron density should contain information on the location of the γ subunit.

To verify the presence of γ subunit, PE crystals were dissolved and analyzed by UV-vis absorption spectroscopy, SDS-PAGE analyses and mass spectrometry. The UV-vis absorption spectrum (**Figure 5A**) showed the peculiar shoulder at 498 nm, ascribed to the phycourobilin chromophore of the γ subunit. SDS-PAGE analysis (**Figure 5B)** showed the presence of two molecular species, whose molecular mass were compatible with α and β subunits (double bands at about 17 kDa) and with γ subunit (30 kDa). *In-situ* digestion was performed on the bands and the peptide mixtures were analysed by MALDI-TOF; peptide mass fingerprinting was performed by MS digest of homologue phycoerythrin sequences. The assignment of each mass spectrometry signal allowed highlighting the peptide sequence along the entire protein sequence.

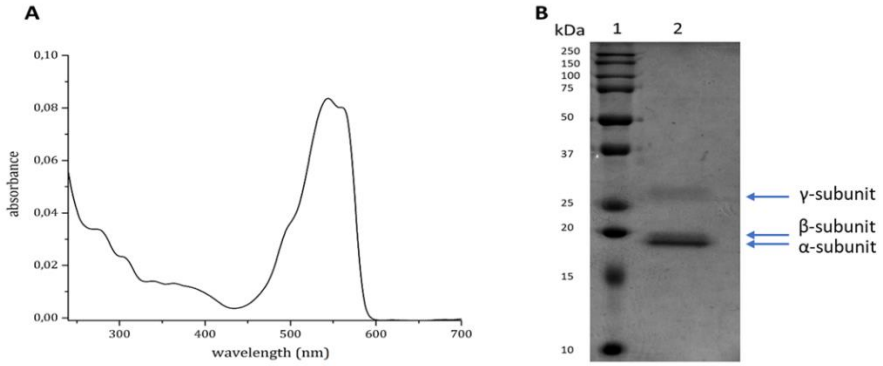

Figure 5. Analyses of PE dissolved crystals. A, UV-vis spectrum obtained from PE dissolved crystals. Spectrum was acquired at 25 °C, in the range 190–700 nm. **B**, SDS-PAGE analyses of PE dissolved crystals. Lane 1: molecular weight markers; lane 2: 20 μL of PE dissolved crystals.

As shown in **Figure 6 A-B**, the MS analysis of the lower band enabled to trace the peptide sequence (labelled in bold and underlined) for the α and β chains, displaying a sequence coverage of 64% and 61%, respectively. The MS analysis of the higher band, on the other hand, revealed that the signals were attributed to two γ-chains with comparable sequence coverage (59.3% and 43.5%), as shown in **Figure 6 C-D**. The presence of the two γ subunits has been previously found in the structure of the entire phycobilisome solved by electron microscopy (PDB code 6KGX) (Ma et al., 2020). The heptameric structures of PE, with the two different γ subunits, extracted from PDB code 6KGX are reported in **Figure 7**, with the same orientation.

Figure 6. α, β and γ chain sequences of *P. cruentum* detected by MALDI-TOF analysis. A, α chain sequence displaying the different peptides (bold and underlined) compared to P11392 (PHEA_PORPP) sequence on UniProt. **B**, β chain sequence displaying the different peptides (bold and underlined) compared to P11393 (PHEB_PORPP) sequence on UniProt. **C**, γ chain sequence displaying the different peptides (bold and underlined) compared to A0A5J4YX19 (PHEB_PORPP) sequence on UniProt. **D**, γ chain sequence displaying the different peptides (bold and underlined) compared to A0A5J4YZM7 (PHEB_PORPP) sequence on UniProt.

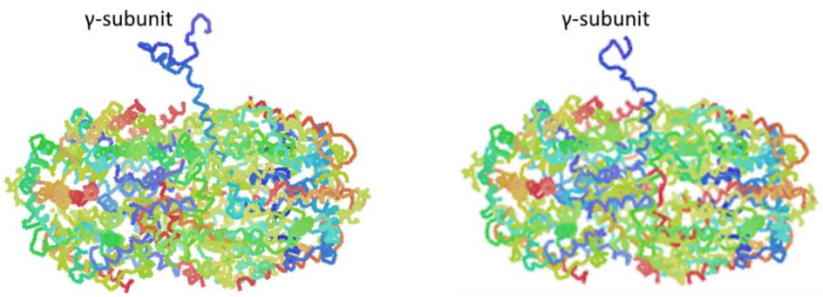

Figure 7. The heptameric $(\alpha\beta)_3\gamma$ structures observed in the phycobilisome from *P. cruentum.*

3.3.3 Carotenoids extraction and characterization

Carotenoids extraction was performed by using a conventional method on both residual biomass (herein referred as I residual biomass) and on the raw one, used as benchmark (as reported in Materials and Methods section). HPLC analyses (**Figure 8**) revealed that zeaxanthin and β-carotene were the major pigments present in the two extracts. Quantification analyses for the two carotenoids are reported in **Table 3** and indicate that all the zeaxanthin isoforms present in the I residual biomass represented about 55% of those present in the raw biomass, whereas β-carotene isoforms recovery was about 210% with respect to the raw biomass. It is important to point out that the carotenoids yield obtained from the I residual biomass was comparable to the one obtained by innovative green extractions performed on the residual biomass of the same species (Gallego et al., 2019), thus suggesting the feasibility of the proposed process.

Table 3. Comparison between zeaxanthin, β-carotene and their isomers in the raw and I residual extracts.

Peak number	Retention time (min)	Peak identification	Raw biomass ($mg/g_{extract}$)	I residual biomass ($mg/g_{extract}$)
5	7.668	Zeaxanthin isomer I	1.03	0.64
6	8.057	Zeaxanthin	21.37	11.79
7	9.826	Zeaxanthin isomer II	2.84	1.69
13	18.701	β-Carotene	0.20	0.44
14	18.892	β-Carotene isomer	0.04	0.07

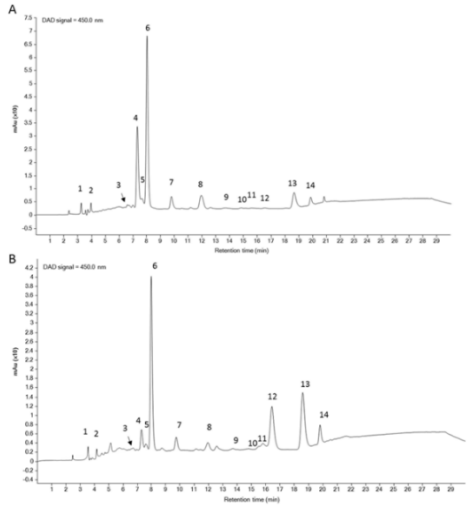

Fig. 8. Representative HPLC−DAD chromatograms of carotenoids extracted from *P. cruentum* biomass. A, raw biomass; **B**, I residual biomass (after PE extraction). Peak numbers and their identification are reported in **Table S2, Appendix I**.

3.3.4 Lipids extraction and characterization

According to the strategy described in **Figure 1**, lipids extraction represented the last class of the proposed process, after a drying step. To verify if the previous extractions could affect lipids composition, control experiments were performed by determining the composition of the lipid fraction obtained after PE extraction (I residual biomass) and after PE and carotenoids extraction (II residual biomass). The extractions were performed according to Bligh & Dyer (Bligh and Dyer, 1959), followed by a solid phase extraction (SPE). As shown in **Table 4**, a 14% yield of total lipids was obtained from the raw biomass whereas about 29% were extracted from the I residual biomass (i.e. after protein extraction). Nevertheless, when lipids were extracted from the II residual biomass (i.e. after protein and carotenoid extractions), the yield (14.1%) was comparable to those calculated for the raw biomass. Interestingly, the gas chromatography analysis of the fatty acids (FAs) fraction revealed a clear trend: while polyunsaturated fatty acids (PUFA) decreased during the cascade extractions (from 26% to 14% to 4%), a clear increase in the yield of saturated fatty acids (SFA) was observed (from 72% to 76% to 93%). The yields of PUFA and SFA obtained from the raw biomass are in agreement with those reported by Kim and coworkers, who evaluated the lipids accumulation in

microalgae under different sources of light (Kim et al., 2019). SFAs are considered now as an interesting new class of molecules, thanks to their chemical stability, responsible for their well-defined melting points and biocompatibility.

Thus, they have been proposed as new materials for drug-controlled release or simply as antibacterial molecules (Xue et al., 2021; Yoon et al., 2018).

Table 4. Total lipids yields. Lipids mean yields are reported as the percentage of the ratio between each lipidic class after SPE and dried raw biomass.

	Lipid yield (%)	Neutral lipids (%)	Phospholipids (%)	Fatty acids (%)	PUFA (%)	SFA (%)
Raw biomass	14.0 ± 2.6	11.2 ± 1.5	12.0 ± 4.0	3.7 ± 0.3	25.8 ± 4.6	71.7 ± 13.6
I Residual biomass	28.8 ± 1.5[a]	10.2 ± 0.3	10.6 ± 0.3	2.5 ± 0.2	14.4 ± 1.9	76.3 ± 5.8
II Residual biomass	14.1 ± 0.4[b]	9.1 ± 0.6	3.8 ± 0.4	1.6 ± 0.2	4.3 ± 0.8	92.8 ± 7.2

[a]indicates $p \leq 0.05$ with respect to raw biomass.
[b]indicates $p \leq 0.05$ with respect to I residual biomass.

3.4 Conclusions

The strategy proposed in **Figure 1** was found to be effective, since an innovative and reliable strategy was set up to sequentially recover high-added value products from *P. cruentum* culture. In particular: (i) *P. cruentum* culture is completely employed to recover intra- and extra- cellular class of high-added value molecules; (ii) the yield of each extracted class of molecules is similar to those obtained when extractions are performed to recover single class of molecules; (iii) according to the biorefinery principles, all the class of molecules have been recovered starting from the one with the highest market value. In particular, the extracted proteins, carotenoids and lipids represented 35%, 8.5% and 14% of total biomass, respectively; PE in particular was 2% of biomass; the leftover biomass was about 40%. However, the production of s-EPSs (0.53 $g/g_{d.w.biomass}$) should also be taken into account, since their production represents an energy and nutrients consumption. The relationship with potential selling prices and

the amount of recovered molecules could give an idea of the overall value of the biomass. As an example, *P. cruentum* raw biomass price, depending on the culture conditions and on the final application, ranges between 200 and 1500 US$/kg (Llamas et al., 2021); Sigma-Aldrich company sells PE at about 140 US$/mg. With the proposed extraction strategy, it is possible to recover about 20 g of PE/kg of biomass, with a consequent revenue of about 3 million US$. However, the purchase of PE with such a high purity grade is restricted to laboratories which use it to perform analyses, therefore the amount purchased would never reach big amounts. A similar analysis should be done for all the other bioproducts obtained, in order to have a general idea of the profitability of the process. Generally speaking, the simultaneous microalgae culture valorization and carbon capture can contribute to the sustainable expansion of microalgae market.

3.5 References

Álvarez-Gómez, F., Korbee, N., Casas-Arrojo, V., Abdala-Díaz, R.T., Figueroa, F.L., 2019. UV Photoprotection, Cytotoxicity and Immunology Capacity of Red Algae Extracts. Mol. . https://doi.org/10.3390/molecules24020341

Aremu, A.O., Masondo, N.A., Molnár, Z., Stirk, W.A., Ördög, V., Van Staden, J., 2016. Changes in phytochemical content and pharmacological activities of three *Chlorella* strains grown in different nitrogen conditions. J. Appl. Phycol. 28, 149–159. https://doi.org/10.1007/s10811-015-0568-7

Ben Hlima, H., Smaoui, S., Barkallah, M., Elhadef, K., Tounsi, L., Michaud, P., Fendri, I., Abdelkafi, S., 2021. Sulfated exopolysaccharides from *Porphyridium cruentum*: A useful strategy to extend the shelf life of minced beef meat. Int. J. Biol. Macromol. 193, 1215–1225. https://doi.org/10.1016/J.IJBIOMAC.2021.10.161

Bernaerts, T.M.M., Kyomugasho, C., Van Looveren, N., Gheysen, L., Foubert, I., Hendrickx, M.E., Van Loey, A.M., 2018. Molecular and rheological characterization of different cell wall fractions of *Porphyridium cruentum*. Carbohydr. Polym. 195, 542–550. https://doi.org/10.1016/J.CARBPOL.2018.05.001

Bhalamurugan, G.L., Valerie, O., Mark, L., 2018. Valuable bioproducts obtained from microalgal biomass and their commercial applications: A review. Environ. Eng. Res. 23, 229–241.

Bligh, E.G., Dyer, W.J., 1959. A rapid method of total lipid extraction and purification. Can. J. Biochem. Physiol. 37, 911–917.

https://doi.org/10.1139/o59-099
Camara-Artigas, A., Bacarizo, J., Andujar-Sanchez, M., Ortiz-Salmeron, E., Mesa-Valle, C., Cuadri, C., Martin-Garcia, J.M., Martinez-Rodriguez, S., Mazzuca-Sobczuk, T., Ibañez, M.J., Allen, J.P., 2012. PH-dependent structural conformations of B-phycoerythrin from *Porphyridium cruentum*. FEBS J. 279, 3680–3691. https://doi.org/10.1111/j.1742-4658.2012.08730.x
De Jesus Raposo, M.F., De Morais, R.M.S.C., De Morais, A.M.M.B., 2013. Bioactivity and applications of sulphated polysaccharides from marine microalgae. Mar. Drugs 11, 233–252. https://doi.org/10.3390/md11010233
Di Lena, G., Casini, I., Lucarini, M., Lombardi-Boccia, G., 2019. Carotenoid profiling of five microalgae species from large-scale production. Food Res. Int. 120, 810–818. https://doi.org/10.1016/J.FOODRES.2018.11.043
Dvir, I., Stark, A.H., Chayoth, R., Madar, Z., Arad, S.M., 2009. Hypocholesterolemic Effects of Nutraceuticals Produced from the Red Microalga *Porphyridium sp*. in Rats. Nutr. . https://doi.org/10.3390/nu1020156
Emsley, P., Cowtan, K., 2004. Coot: Model-building tools for molecular graphics. Acta Crystallogr. Sect. D Biol. Crystallogr. 60, 2126–2132. https://doi.org/10.1107/S0907444904019158
Feller, R., Matos, Â.P., Mazzutti, S., Moecke, E.H.S., Tres, M. V., Derner, R.B., Oliveira, J. V., Junior, A.F., 2018. Polyunsaturated ω-3 and ω-6 fatty acids, total carotenoids and antioxidant activity of three marine microalgae extracts obtained by supercritical CO2 and subcritical n-butane. J. Supercrit. Fluids 133, 437–443. https://doi.org/10.1016/J.SUPFLU.2017.11.015
Fernández-Rojas, B., Hernández-Juárez, J., Pedraza-Chaverri, J., 2014. Nutraceutical properties of phycocyanin. J. Funct. Foods 11, 375–392. https://doi.org/10.1016/J.JFF.2014.10.011
Ficner, R., Huber, R., 1993. Refined crystal structure of phycoerythrin from *Porphyridium cruentum* at 0.23-nm resolution and localization of the gamma subunit. Eur. J. Biochem. 218, 103–106.
Gaignard, C., Gargouch, N., Dubessay, P., Delattre, C., Pierre, G., Laroche, C., Fendri, I., Abdelkafi, S., Michaud, P., 2019. New horizons in culture and valorization of red microalgae. Biotechnol. Adv. 37, 193–222. https://doi.org/10.1016/J.BIOTECHADV.2018.11.014
Gallego, R., Martínez, M., Cifuentes, A., Ibáñez, E., Herrero, M., 2019. Development of a green downstream process for the valorization of *Porphyridium cruentum* biomass. Molecules 24, 1564.

Geresh, S., Adin, I., Yarmolinsky, E., Karpasas, M., 2002. Characterization of the extracellular polysaccharide of *Porphyridium sp*.: Molecular weight determination and rheological properties. Carbohydr. Polym. 50, 183–189. https://doi.org/10.1016/S0144-8617(02)00019-X

Huheihel, M., Ishanu, V., Tal, J., Arad, S., 2002. Activity of *Porphyridium sp*. polysaccharide against herpes simplex viruses in vitro and in vivo. J. Biochem. Biophys. Methods 50, 189–200. https://doi.org/10.1016/S0165-022X(01)00186-5

Imbimbo, P., Bueno, M., D'Elia, L., Pollio, A., Ibañez, E., Olivieri, G., Monti, D.M., 2020. Green compressed fluid technologies to extract antioxidants and lipids from *Galdieria phlegrea* in a Biorefinery Approach. ACS Sustain. Chem. Eng. 8, 2939–2947.

Imbimbo, P., Romanucci, V., Pollio, A., Fontanarosa, C., Amoresano, A., Zarrelli, A., Olivieri, G., Monti, D.M., 2019. A cascade extraction of active phycocyanin and fatty acids from *Galdieria phlegrea*. Appl. Microbiol. Biotechnol. 103, 9455–9464. https://doi.org/10.1007/s00253-019-10154-0

Kim, S.H., Sunwoo, I.Y., Hong, H.J., Awah, C.C., Jeong, G.-T., Kim, S.-K., 2019. Lipid and unsaturated fatty acid productions from three microalgae using nitrate and light-emitting diodes with complementary LED wavelength in a two-phase culture system. Bioprocess Biosyst. Eng. 42, 1517–1526.

Llamas, B., Suárez-Rodríguez, M.C., González-López, C. V, Mora, P., Acién, F.G., 2021. Techno-economic analysis of microalgae related processes for CO2 bio-fixation. Algal Res. 57, 102339.

Ma, J., You, X., Sun, S., Wang, X., Qin, S., Sui, S.F., 2020. Structural basis of energy transfer in *Porphyridium purpureum* phycobilisome. Nature 579, 146–151. https://doi.org/10.1038/s41586-020-2020-7

McCoy, A.J., Grosse-Kunstleve, R.W., Adams, P.D., Winn, M.D., Storoni, L.C., Read, R.J., 2007. Phaser crystallographic software. J. Appl. Crystallogr. 40, 658–674. https://doi.org/10.1107/S0021889807021206

Meléndez-Martínez, A.J., Mapelli-Brahm, P., Stinco, C.M., 2018. The colourless carotenoids phytoene and phytofluene: From dietary sources to their usefulness for the functional foods and nutricosmetics industries. J. Food Compos. Anal. 67, 91–103. https://doi.org/10.1016/J.JFCA.2018.01.002

Melo, T., Figueiredo, A.R.P., da Costa, E., Couto, D., Silva, J., Domingues, M.R., Domingues, P., 2021. Ethanol extraction of polar lipids from *Nannochloropsis oceanica* for food, feed, and

biotechnology applications evaluated using lipidomic approaches. Mar. Drugs 19. https://doi.org/10.3390/md19110593

Mišurcová, L., Škrovánková, S., Samek, D., Ambrožová, J., Machů, L., 2012. Health benefits of algal polysaccharides in human nutrition. Adv. Food Nutr. Res. 66, 75–145.

Murshudov, G.N., Vagin, A.A., Dodson, E.J., 1997. Refinement of macromolecular structures by the maximum-likelihood method. Acta Crystallogr. Sect. D Biol. Crystallogr. 53, 240–255. https://doi.org/10.1107/S0907444996012255

Nguyen, H.P.T., Morançais, M., Déléris, P., Fleurence, J., Nguyen-Le, C.T., Vo, K.H., Dumay, J., 2020. Purification of R-phycoerythrin from a marine macroalga *Gracilaria gracilis* by anion-exchange chromatography. J. Appl. Phycol. 32, 553–561. https://doi.org/10.1007/S10811-019-01947-X/FIGURES/7

Qiu, J., Madoz-Gurpide, J., Misek, D.E., Kuick, R., Brenner, D.E., Michailidis, G., Haab, B.B., Omenn, G.S., Hanash, S., 2004. Development of Natural Protein Microarrays for Diagnosing Cancer Based on an Antibody Response to Tumor Antigens. J. Proteome Res. 3, 261–267. https://doi.org/10.1021/pr049971u

Rebolloso Fuentes, M.M., Acién Fernández, G.G., Sánchez Pérez, J.A., Guil Guerrero, J.L., 2000. Biomass nutrient profiles of the microalga *Porphyridium cruentum*. Food Chem. 70, 345–353. https://doi.org/10.1016/S0308-8146(00)00101-1

Ricciardelli, A., Casillo, A., Vergara, A., Balasco, N., Corsaro, M.M., Tutino, M.L., Parrilli, E., 2019. Environmental conditions shape the biofilm of the Antarctic bacterium *Pseudoalteromonas haloplanktis* TAC125. Microbiol. Res. 218, 66–75. https://doi.org/10.1016/j.micres.2018.09.010

Ritter, S., Hiller, R.G., Wrench, P.M., Welte, W., Diederichs, K., 1999. Crystal Structure of a Phycourobilin-Containing Phycoerythrin at 1.90-Å Resolution. J. Struct. Biol. 126, 86–97. https://doi.org/https://doi.org/10.1006/jsbi.1999.4106

Rodriguez-Concepcion, M., Avalos, J., Bonet, M.L., Boronat, A., Gomez-Gomez, L., Hornero-Mendez, D., Limon, M.C., Meléndez-Martínez, A.J., Olmedilla-Alonso, B., Palou, A., Ribot, J., Rodrigo, M.J., Zacarias, L., Zhu, C., 2018. A global perspective on carotenoids: Metabolism, biotechnology, and benefits for nutrition and health. Prog. Lipid Res. 70, 62–93. https://doi.org/10.1016/J.PLIPRES.2018.04.004

Russo Krauss, I., Merlino, A., Vergara, A., Sica, F., 2013. An Overview of Biological Macromolecule Crystallization. Int. J. Mol. Sci. . https://doi.org/10.3390/ijms140611643

Serucňik, M., Vicente, F.A., Brecko, Ž., Coutinho, J.A.P., Ventura, S.P.M., Žnidaršič-Plazl, P., 2020. Development of a microfluidic platform for R-Phycoerythrin purification using an aqueous micellar two-phase system. ACS Sustain. Chem. Eng. 8, 17097–17105. https://doi.org/10.1021/ACSSUSCHEMENG.0C05042/ASSET/IMAGES/LARGE/SC0C05042_0007.JPEG

Ulagesan, S., Nam, T.J., Choi, Y.H., 2021. Extraction and Purification of R-Phycoerythrin Alpha Subunit from the Marine Red Algae *Pyropia Yezoensis* and Its Biological Activities. Mol. 2021, Vol. 26, Page 6479 26, 6479. https://doi.org/10.3390/MOLECULES26216479

Vicente, F.A., Cardoso, I.S., Martins, M., Gonçalves, C.V.M., Dias, A.C.R.V., Domingues, P., Coutinho, J.A.P., Ventura, S.P.M., 2019. R-phycoerythrin extraction and purification from fresh: *Gracilaria sp*. using thermo-responsive systems. Green Chem. 21, 3816–3826. https://doi.org/10.1039/c9gc00104b

Vonrhein, C., Flensburg, C., Keller, P., Sharff, A., Smart, O., Paciorek, W., Womack, T., Bricogne, G., 2011. Data processing and analysis with the autoPROC toolbox. Acta Crystallogr. Sect. D Biol. Crystallogr. 67, 293–302. https://doi.org/10.1107/S0907444911007773

Xiao, R., Zheng, Y., 2016. Overview of microalgal extracellular polymeric substances (EPS) and their applications. Biotechnol. Adv. 34, 1225–1244. https://doi.org/10.1016/J.BIOTECHADV.2016.08.004

Xue, K., Lv, S., Zhu, C., 2021. Bringing naturally-occurring saturated fatty acids into biomedical research †. J. Mater. Chem. B 9, 6973–6987. https://doi.org/10.1039/d1tb00843a

Yen, H.W., Hu, I.C., Chen, C.Y., Ho, S.H., Lee, D.J., Chang, J.S., 2013. Microalgae-based biorefinery - From biofuels to natural products. Bioresour. Technol. 135, 166–174. https://doi.org/10.1016/j.biortech.2012.10.099

Yoon, B.K., Jackman, J.A., Valle-González, E.R., Cho, N.J., 2018. Antibacterial Free Fatty Acids and Monoglycerides: Biological Activities, Experimental Testing, and Therapeutic Applications. Int. J. Mol. Sci. 2018, Vol. 19, Page 1114 19, 1114. https://doi.org/10.3390/IJMS19041114

Zhang, S., Liu, Z., 2021. Advances in the biological fixation of carbon dioxide by microalgae. J. Chem. Technol. Biotechnol. 96, 1475–1495.

https://eur-lex.europa.eu/legal-content/EN/ALL/?uri=CELEX%3A52015DC0614

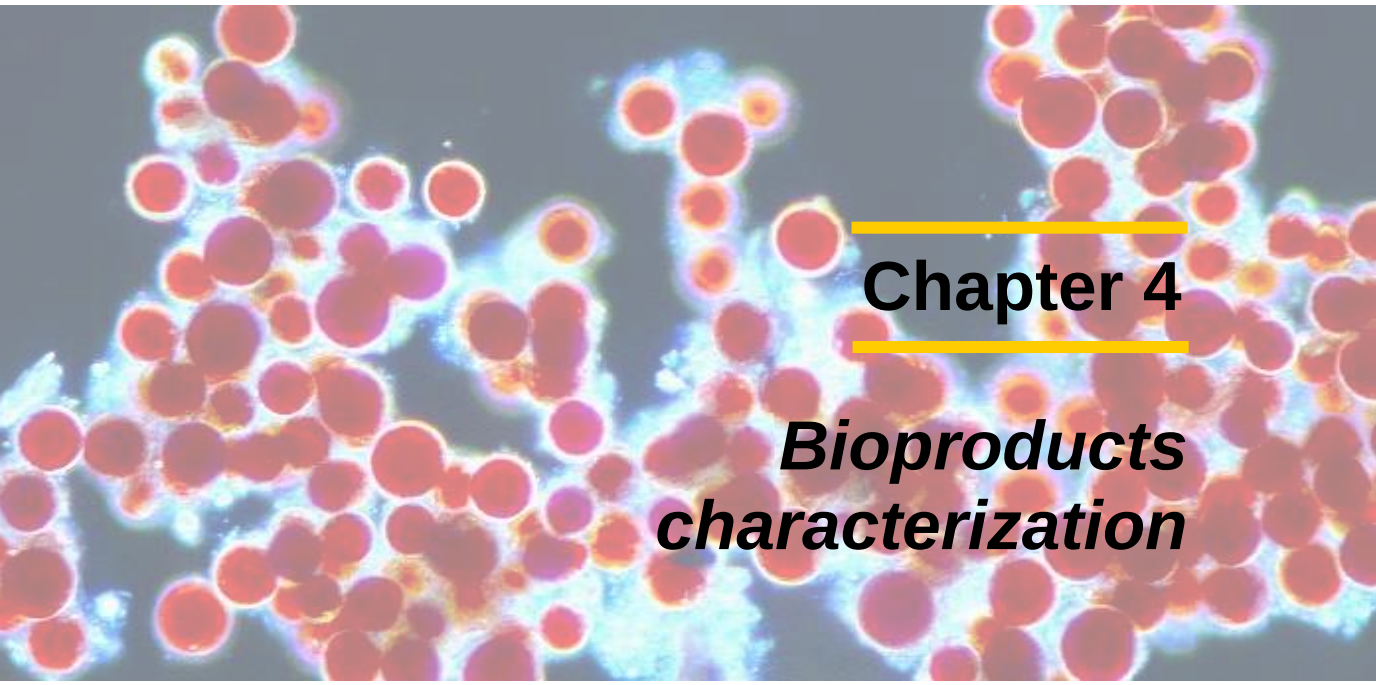

Chapter 4

Bioproducts characterization

4.1 Introduction

Microalgae are ubiquitous eukaryotic photosynthetic microorganisms, able to live in different environments, either in single colonies, in chains or groups and, depending on the species, their size can vary from few to hundreds micrometers (Alam et al., 2014; Mobin and Alam, 2017; Suganya et al., 2016). The biodiversity of microalgae is mainly due to their unique ability to adapt and grow even under unfavorable growth conditions (e.g., extreme temperatures, variable salinity, and low/high light intensity) and produce a wide range of interesting chemical compounds with novel structures and biological activities (Anbuchezhian et al., 2015; Herrero et al., 2013). Among microalgae, the red marine microalga *Porphyridium cruentum*, could be pointed as a commercial source of various high-value bioproducts (Mobin and Alam, 2017), to be recovered from the same culture, in order to make the whole process economically feasible (Di Lena et al., 2019; Feller et al., 2018; Gaignard et al., 2019; Liberti et al., 2022; Rebolloso Fuentes et al., 2000). In particular, *P. cruentum* produces sulfated exopolysaccharides (S-EPSs) that are accumulated in a layer surrounding the cytoplasmic membrane. These exopolysaccharides act as a mucilage, since *P. cruentum* is deprived of a well-defined cell wall (Dvir et al., 2009). They are composed of glucuronic acid and several major neutral monosaccharides, such as D- and L-Gal, D-Glc, D-Xyl, D-GlcA, and sulfate groups. S-EPSs from *P. cruentum* have antioxidant (Ben Hlima et al., 2021), immunomodulatory, anti-inflammatory, hypocholesterolemic, antimicrobial, and antiviral activity (Gallego et al., 2019; Mišurcová et al., 2012). S-EPSs from *P. cruentum* exhibit also specific rheological properties that can be exploited in food applications (Ben Hlima et al., 2021; Medina-Cabrera et al., 2021). Besides exopolysaccharides, *P. cruentum* produces a broad range of colored pigments, including chlorophylls, carotenoids and phycobilins, pigments commercially utilized in the food, pharmaceutical and cosmetic industries (Sudhakar et al., 2015). Amongst them, Phycoerythrin (PE) is a light-harvesting protein with a structure of $(\alpha\beta)_6\gamma$ complex and a MW ranging from 240 to 260 kDa. Due to its unique biological properties, PE gained much attention from food to pharmaceutical industry and in the molecular biology field (Ganesan et al., 2020; García et al., 2021; Hsieh-Lo et al., 2019; Kannaujiya et al., 2019; Manirafasha et al., 2016; Simovic et al., 2022).

Here, starting from our previous results (Chapter 3) (Liberti et al., 2022), a comprehensive study on the biological activities of s-EPSs and purified PE was carried out, in order to verify if the extraction techniques

could have affected their biological activities.

4.2 Materials and Methods

4.2.1 Reagents

All solvents, reagents and chemicals were purchased from Sigma-Aldrich (St Louis, MO, USA).

4.2.2 Biocompounds isolation

S-EPSs and PE were isolated and purified from the culture of *Porphyridium cruentum* (CCALA415) as previously described (**Chapter 2 and 3**). Briefly, at the end of cell growth, the culture was centrifuged to recover s-EPSs in the supernatant. The s-EPSs were precipitated adding pure ethanol (1:2 v/v) and centrifuging the sample (12,000 *g*, 30 min, 4 °C). The supernatant was discarded, and the precipitate was freeze-dried. S-EPSs yield was 300 ± 67 g/L, which corresponds to 0.53 $g/g_{d.w.\ biomass}$. In the case of PE, a crude aqueous extract was obtained *via* sonication (40% amplitude, 20 min, 30 sec on, 30 sec off) from the harvested biomass. PE was then isolated *via* one step purification procedure as reported in section 3.2.5 (**Chapter 3**) up to a purity grade of 4.

4.2.3 Eukaryotic cell culture and biocompatibility assay

Immortalized human keratinocytes (HaCaT, Innoprot, Derio Spain) and immortalized murine fibroblasts Balb/c-3T3 (ATCC, Virginia, USA) were cultured in 10% foetal bovine serum in Dulbecco's modified Eagle's medium, in the presence of 1% penicillin/streptomycin and 2 mM L-glutamine, in a 5% CO_2 humidified atmosphere at 37 °C. To verify the biocompatibility of the crude extract, of s-EPSs and of purified PE, cells were seeded in 96-well plates at a density of 2 $\times 10^3$/well and, 24 h after seeding, were incubated with increasing concentrations of the extract/compounds (5 to 75 µg/mL for EPS, 5 to 500 µg/mL of total proteins for crude extracts and 5 nM to 100 nM for purified PE) for 72 h. At the end of the incubation period, cell viability was assessed by the MTT assay. Cell survival was expressed as the percentage of viable cells in the presence of compounds, compared with control cells (represented by the average obtained between untreated cells and cells supplemented with the highest concentration of buffer).

4.2.4 *In vitro* antioxidant assays

Antioxidant activity of the extract/compounds was tested by measuring their ability to scavenge the free radicals 1,1-Diphenyl-2-picrylhydrazyl radical and 2,2′-azinobis-[3-ethylbenzthiazoline-6-sulfonic acid] (DPPH and ABTS, respectively) and to reduce or chelate redox active iron and copper (ferric reducing antioxidant power - FRAP; iron chelating activity - ICA and copper chelating activity - CCA respectively). DPPH and FRAP assay were done following the procedure reported by Rodrigues and colleagues (Rodrigues et al., 2016) and ascorbic acid and butylhydroxytoluene (BHT), respectively, were used as positive controls at the same concentrations of the sample under test. The ability of the extract/compounds to scavenge the ABTS radical was assessed as previously reported (Re et al., 1999). Results were compared to a calibration curve obtained using Trolox (6-hydroxy-2,5,7,8-tetramethylchromane-2-carboxylic acid) as standard. ICA and CCA were determined by measuring the formation of the Fe^{2+}-ferrozine complex and by using pyrocatechol violet (PV) respectively, according to the method reported by Megias (Megías et al., 2009). EDTA was used as a standard, at a final concentration of 100 µg/mL. S-EPSs or purifed PE were tested between 0.05 to 120 µg/mL and 0.2 to 270 nM, respectively. Results are expressed as IC_{50}, i.e. the concentration required to scavenge 50% of the free radical or as the highest % achieved.

4.2.5 Determination of intracellular ROS levels on eukaryotic cell lines by DCFDA assay

The protective effect of s-EPSs (from 5 to 75 µg/mL) or purified PE (10 nM) against oxidative stress was measured by determining the intracellular reactive oxygen species (ROS) levels, following the protocol used by Imbimbo (Imbimbo et al., 2019).

4.2.6 Determination of intracellular glutathione levels (DTNB assay) and lipid peroxidation levels (TBARS assay) on eukaryotic cell lines

Intracellular GSH levels and lipid peroxidation levels were measured by following the procedure described by Petruk (Petruk et al., 2017). 12 µg/mL of s-EPSs or 10 nM of purified PE were used.

4.2.7 Anti-inflammatory activity

The anti-inflammatory activity of the compounds was tested by their ability to inhibit cyclooxygenase-2 (COX-2). S-EPSs or purified PE were tested at different concentrations (4 and 167 µg/mL for s-EPSs or 10 and 27 nM for purified PE) using a commercial inhibitory screening assay kit, Cayman test kit-560131 (Cayman Chemical Company, Ann Arbor, MI, USA). Ibuprofen was used as positive control. Results were expressed as a percentage of inhibition of COX-2.

4.2.8 Wound healing assay

Wound healing was assessed by a scratch assay. HaCaT cells were seeded at a cell density of 3×10^5 cells/cm^2 for 24 h, to allow cells to reach about 95% of confluence. Then, cells were washed with PBS, scratched manually with a 200-µL pipet tip, and incubated with 12 µg/mL of s-EPSs or 10 nM of purified PE. The scratch size was monitored at 0 h and 24 h by acquiring images by using an optical microscopy (Zeiss LSM 710, Zeiss, Germany) at 10x magnification. The width of the wound was measured by using Zen Lite 2.3 software (Zeiss, Germany). Results are expressed as reduction of area (fold) compared to untreated cells.

4.2.9 Statistical analyses

All the experiments were performed in triplicate. Results are presented as mean of results obtained after three independent experiments (mean ± SD) and compared by one-way ANOVA according to the Bonferroni's method (post-hoc) using Graphpad Prism for Windows, version 6.01 (Dotmatics, California, USA).

4.3 Results and Discussion

S-EPSs and PE were extracted from the culture of *P. cruentum*, as previously described in **Chapter 2**. PE was then isolated *via* one step purification procedure, as reported in **Chapter 3**, up to a purity grade of 4. Here, both biocompounds were characterized for their biological activity to check if the process applied could affect their activity.

4.3.1. S-Exopolysaccharides characterization

4.3.1.1 s-EPSs biocompatibility on cell-based model

S-EPSs were tested for their biocompatibility on two eukaryotic immortalized cell lines: HaCaT (human keratinocytes) and Balb/c-3T3 (murine fibroblasts) cells. 24 h after seeding, cells were incubated with increasing amounts of s-EPSs (from 5 to 75 µg/mL). After 72 h incubation, cell viability was assessed by the MTT assay and cell survival expressed as the percentage of viable cells in the presence of s-EPSs compared to that of control samples (i.e., untreated cells). The results in **Figure 1** show that, under all the experimental conditions, s-EPSs were fully biocompatible on both cell lines analyzed.

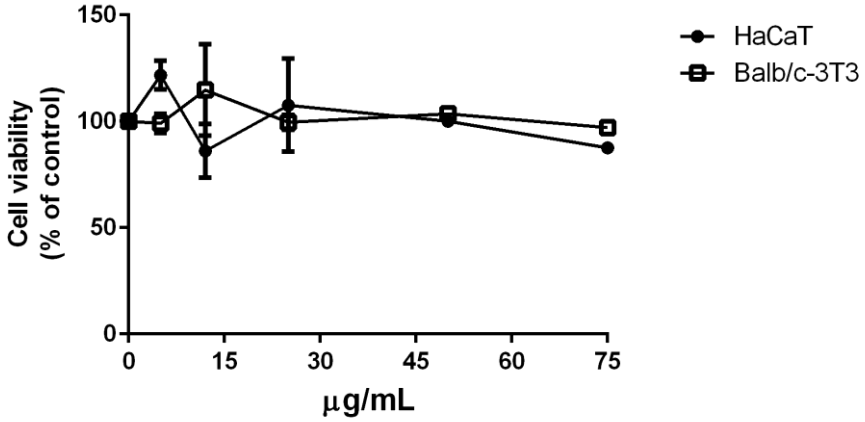

Figure 1. Effect of s-EPSs from *P. cruentum* on cell viability. Dose-response curves of HaCaT (black dots) and Balb/c-3T3 (empty squares) cells after 72 h incubation with increasing concentrations of exopolysaccharides (5-75 µg/mL). Cell viability is reported as a function of s-EPS concentration.

4.3.1.2 s-EPSs *in vitro* antioxidant activity

It is generally believed that polysaccharides with high-sulfated content have biological activities (Wang et al., 2019), such as antioxidant (Marques, 2007). Thus, the antioxidant activity of s-EPS was evaluated by different *in vitro* analyses: ABTS, DPPH, FRAP, iron and copper chelating assays. It is known that antioxidant molecules can bind metal ions forming metal ion complexes, and that the presence of

sulfate groups could increase the metal binding capacity of the carbohydrates by donating an electron pair or by losing a proton, thus stabilizing the complex (Andrew and Jayaraman, 2020; Bhunia et al., 2018).

As shown in **Table 1**, s-EPSs were not able to scavenge the ABTS and DPPH radicals, whereas a slight but significant activity was observed for the chelation of iron and for ferric ion reduction assays. Both tests are based on the ability to act on iron: the former measures the ability of the compounds under test to bind Fe^{2+}, whereas the latter analyzes the ability to reduce Fe^{3+} to Fe^{2+}. As for copper chelating assay, the highest activity reached, at the highest concentration tested, was 9 ± 3%, a value much lower than the one obtained by testing the positive control molecule at the same concentration.

In agreement with Wang and colleagues, we found that s-EPSs had no radical scavenging activity against DPPH, whereas they showed antioxidant activity in the ABTS assay, with IC_{50} values ranging from 6.59 to 8.92 mg/mL (Wang et al., 2021).

Table 1. *In vitro* antioxidant and chelating activity of s-EPSs. Results are expressed as percentage of inhibition. The concentration evaluated is referred to the final concentration of s-EPSs or positive control used in the well. ICA, Iron Chelating Activity; CCA, Copper Chelating Activity.

Test	Concentration (µg/mL)	s-EPSs Activity (%)	C+ Activity (%)
FRAP	120	34 ± 3	97 ± 1
ABTS	25	2 ± 2	98 ± 2
DPPH	50	1 ± 1	52 ± 1
ICA	55	66 ± 3	91 ± 1
CCA	45	9 ± 3	91 ± 2

4.3.1.3 s-EPSs antioxidant activity on a cell-based model

The antioxidant activity of s-EPSs was also evaluated on HaCaT cells. To this purpose, cells were incubated with increasing concentrations of s-EPSs (from 5 to 50 µg/mL) for 2 h, and then oxidative stress was induced by UVA irradiation (100 J/cm^2). Immediately after irradiation, intracellular ROS levels were measured by using H_2DCFDA as a probe. For each set of experiments, untreated cells were used as a control. As shown in **Figure 2**, UVA treatment significantly increased the DCF fluorescence (black bars, p <0.001). In

the absence of stress, s-EPSs induced a slight but significant increase in intracellular ROS level (**Figure 2**, white, dashed grey and dark grey bars on the left part of the graph). Interestingly, when cells were pre-incubated with s-EPSs, prior to be stressed, only 5 and 12 µg/mL were able to protect cells from ROS formation (**Figure 2**, light grey and white bars on the right part of the graph), whereas the higher concentrations had no protective effect. This result is in agreement with Giordano and colleagues (Giordano et al., 2020), as antioxidants act at low concentrations, whereas, at high concentrations they may work as prooxidants. Based on these results, s-EPSs were used at 12 µg/mL for further experiments.

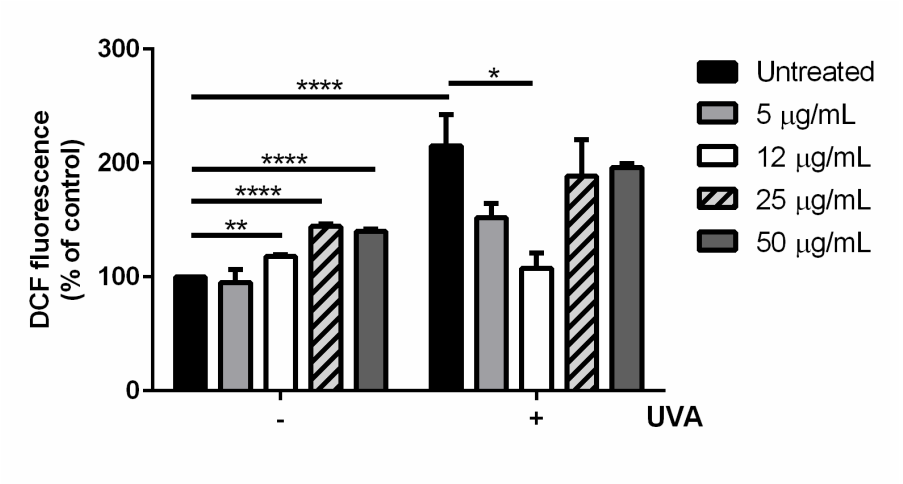

Figure 2. Antioxidant activity of s-EPSs on UVA-stressed HaCaT cells. Intracellular ROS levels were determined by DCFDA assay. Cells were pre-incubated in the presence of increasing amount (from 5 to 50 µg/mL) of s-EPSs for 2 h, prior UVA irradiation (100 J/cm^2). Results are expressed as percentage with respect to untreated cells. Black bars refer to untreated cells; light grey bars refer to cells incubated with 5 µg/mL of s-EPSs; white bars to cells incubated with 12 µg/mL; dashed bars to cells incubated with 25 µg/mL; dark grey bars refer to cells incubated with 50 µg/mL of s-EPSs, in the absence (-) or in the presence (+) of UVA stress. Data shown are means ± S.D. of three independent experiments. * indicates p <0.05, ** indicates p <0.01, **** indicates p <0.001.

To deeply analyze the protective effect of s-EPSs, intracellular glutathione levels and lipid peroxidation levels were determined by the DTNB and TBARS assay, respectively. In the absence of any

treatment, a significant decrease (p <0.01) in GSH levels was observed after UVA exposure (**Figure 3A**), and s-EPSs (grey bars) were able to inhibit GSH oxidation, thus confirming a protective effect against oxidative stress. As for the TBARS assay, a significant increase (p <0.05) in lipid peroxidation levels was observed after UVA treatment (black bars, **Figure 3B**), but, notably, this effect was inhibited upon pretreatment with s-EPSs (grey bars). Treatment of cells with exopolysaccharides did not significantly alter both glutathione and lipid peroxidation levels in the absence of UVA treatment (-). Taken together, the results clearly indicate that s-EPSs are able to protect cells form oxidative damage.

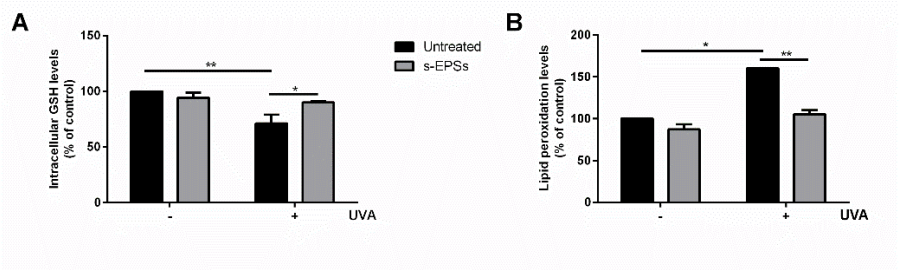

Figure 3. Protective effect of s-EPSs on HaCaT cells. Intracellular GSH levels determined by the DTNB assay (**A**) and lipid peroxidation levels determined by the TBARS assay (**B**). Cells were pre-incubated in the presence of 12 µg/mL of s-EPSs for 2 h, prior UVA irradiation (100 J/cm^2). GSH and lipid peroxidation levels were measured after 90 min from UVA irradiation. Black bars refer to untreated cells and grey bars refer to cells incubated with s-EPSs, in the absence (-) or in the presence (+) of UVA stress. Values are expressed as percentage with respect to untreated cells. Data shown are means ± S.D. of three independent experiments. * Indicates p <0.05, ** indicates p <0.01.

Interestingly, despite the low antioxidant activity observed *in vitro*, s-EPSs were active on a cell-based system at a concentration almost 600 times lower than that measured *in vitro*. This result is in agreement with literature, as it is well-known that *in vitro* assays should not be compared to cell-based ones, since antioxidants provide their function by different mechanisms of action, so that bioavailability, stability, retention, or reactivity of the compound under test in a complex system, such as that of eukaryotic cells, could not be either mimicked or evaluated *in-vitro* (López-Alarcón and Denicola, 2013). Our results indicated that s-EPSs were able not only to inhibit the intracellular ROS

production, but also to prevent GSH depletion and lipid peroxidation.

4.3.1.4 *In vitro* anti-inflammatory activity of s-EPSs

As inflammation is a condition strictly linked to oxidative stress, the anti-inflammatory activity of s-EPSs was measured by evaluating their capacity to inhibit the enzyme COX-2. When inflammation occurs, COX-2 is able to enhance the prostanoids production (Landa et al., 2009). As reported in **Table 2**, surprisingly, s-EPSs showed no significant differences compared to ibuprofen, used as positive control, when tested at the same concentration, thus suggesting a new role of s-EPSs in inflammation control.

Table 2. *In vitro* s-EPSs anti-inflammatory activity.

	Concentration (µg/mL)	Inhibition (%)
s-EPSs	167	77 ± 8
Ibuprofen	167	99 ± 1

4.3.2 Phycoerythrin characterization

4.3.2.1 Phycoerythrin biocompatibility on immortalized eukaryotic cells

Following biomass lysis, phycoerythrin (PE) had a purity grade of 1.5 (Liberti et al., 2022). This value is considered as a reagent grade, thus indicating that the protein can be used as it is also for food applications (Fernández-Rojas et al., 2014). In order to verify the safeness of the protein on eukaryotic cells, a MTT assay was performed by comparing the crude extract with the purified protein (purity grade of 4). Results from the MTT assay, reported in **Figure 4**, clearly shows that only purified PE was fully biocompatible on both cell lines (**Figure 4B**), while the crude extract exerted a dose dependent toxicity (**Figure 4A**). These results clearly indicate that PE needs to be purified to a higher purity grade before being used on cell-based models, or, at least, that it cannot be applied, when present in the extract, at concentrations higher than a certain threshold (100 µg/mL).

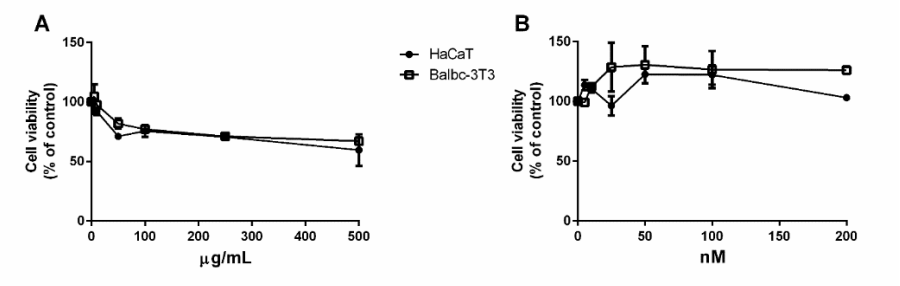

Figure 4. Biocompatibility of total extract (A) and purifed PE (B) on eukaryotic cells. Dose-response curves of HaCaT (black dots) and Balb/c-3T3 cells (empty squares) after 72 h incubation with increasing concentrations of total extract (**A**) and purified PE (**B**). Cell viability was assessed by the MTT assay and reported as a function of extract/protein concentration.

4.3.2.2. *In vitro* antioxidant activity

In vitro analysis of the antioxidant activity of purified PE was carried out by the experimental procedures abovementioned. As reported in **Table 3**, purified PE was not able to scavenge the DPPH radical or chelate copper ions. However, it demonstrated a high capacity to scavenge the ABTS radical ion as well as reduce ferric iron or chelate iron with considerably low IC_{50} values (0.072 ± 0.004 and 0.084 ± 0.012 µM, 0.084 ± 0.004 µM, respectively). Noteworthy, purified PE IC_{50} values were about 160, 1000 and 600 times lower with respect to the IC_{50} values obtained with positive control molecules (Trolox, 12 ± 1 µM in the ABTS; BHT, 90 ± 4 µM in the FRAP, and EDTA, 51 ± 3 µM in the ICA).

Table 3. *In vitro* antioxidant and chelating activity of purified PE. Results are expressed as IC_{50} values, µM. ICA, Iron Chelating Activity; CCA, Copper Chelating Activity.

Test	Purified PE	Positive control
	IC_{50} (µM)	
ABTS	0.072 ± 0.004	12 ± 1
DPPH	> 0.27	29 ± 2
FRAP	0.084 ± 0.012	90 ± 4
ICA	0.084 ± 0.004	51 ± 3
CCA	> 0.1	63 ± 2

Differently from s-EPSs, purified PE was found to be a very powerful antioxidant agent on both *in vitro* and on a cell-based system. The ABTS assay was in line with that observed by Sonani on a PE from a different source (IC_{50} of 72 ± 4 nM vs 101 nM , respectively) (Sonani et al., 2014), whereas the PE prepared by this author had lower DPPH scavenging (930 nM) and Iron chelating abilities (484 nM) than the purified PE prepared in this study. We hypothesize that the higher antioxidant activity measured in our experimental system may rely on the source, or strain, used.

4.3.2.3 Cell-based antioxidant activity of PE

Starting from the encouraging results obtained *in vitro*, purified PE was tested on the UVA-stressed HaCaT experimental system used for s-EPSs. Cells were treated with 2.5 µg/mL (10 nM) of purified PE for 2 h, and then oxidative stress was induced by UVA irradiation (100 J/cm^2). At the end of the irradiation, intracellular ROS levels were evaluated. As shown in **Figure 5**, UVA induced a significant increase in intracellular ROS levels (black bars, 200%) with respect to untreated cells ($p < 0.001$). When cells were treated with purified PE (grey bars), no increase in intracellular ROS levels was observed. Interestingly, when cells were incubated with purified PE, prior the UVA exposure, an inhibition in the intracellular ROS production was observed.

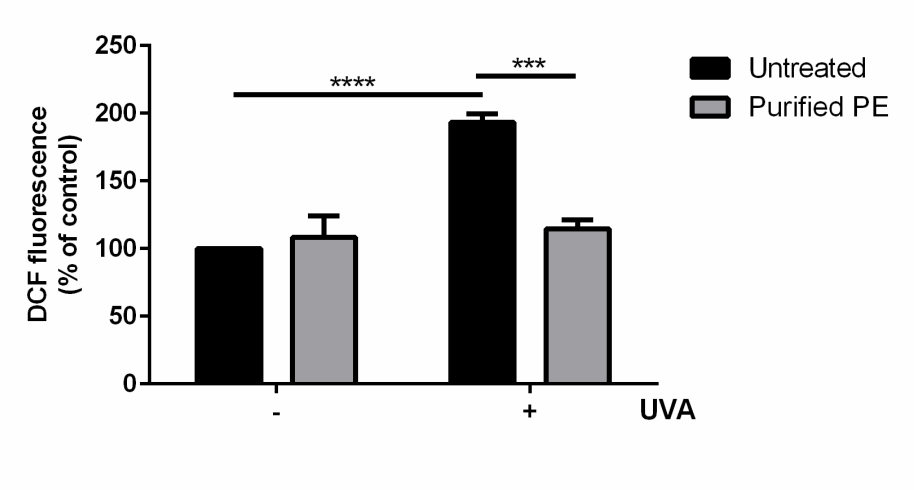

Figure 5. Protective effect of purified PE on UVA-stressed HaCaT cells. Intracellular ROS levels were determined by DCFDA assay. Cells were pre-incubated in the presence of 10 nM of purified

PE (grey bars) for 2 h, prior UVA irradiation (100 J/cm^2). Black bars refer to untreated cells in the absence (-) or in the presence (+) of UVA stress. Values are expressed as percentage with respect to untreated cells. Data shown are means ± S.D. of three independent experiment. *** indicates $p < 0.005$, **** indicates $p < 0.001$ with respect to UVA treated cells.

The effect of purified PE on GSH and lipid peroxidation was also assessed. As shown in **Figure 6**, PE was able to fully protect cells from oxidative stress, as no alteration in both GSH levels (**Figure 6A**) or in lipid peroxidation levels (**Figure 6B**) was found when cells were pretreated with purified PE prior to stress cells, thus confirming the protective effect of the protein against UVA irradiation at concentration in the low nanomolar range (10 nM).

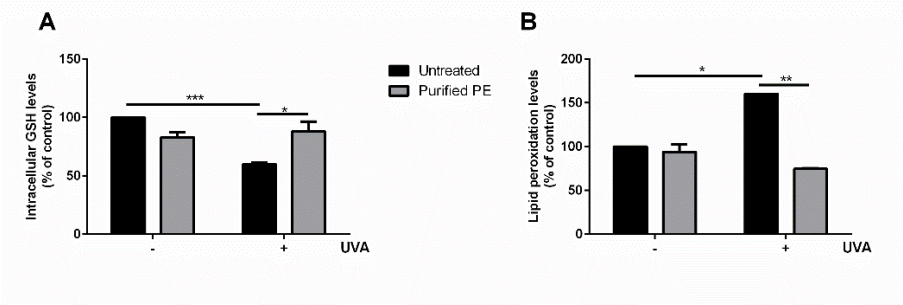

Figure 6. Analysis of intracellular GSH and lipid peroxidation levels on HaCaT cells. Cells were preincubated with 10 nM of purified PE for 2 h before UVA irradiation (100 J/cm^2). **A**, determination of intracellular GSH levels; **B**, analysis of lipid peroxidation levels. In both experiments, measurements were done 90 min after UVA-induced stress. Values are expressed as % with respect to control (i.e., untreated) cells. Data shown are means ± S.D. of three independent experiment. * indicates $p < 0.05$, ** indicates $p < 0.01$, *** indicates $p < 0.005$.

4.3.2.4 *In vitro* PE anti-inflammatory activity

Purified PE was also able to inhibit COX-2 (**Table 4)** by about 75%, although the level of inhibition attained with ibuprofen 24 nM could not be achieved, at any of the analyzed concentrations.

Table 4. COX-2 inhibition by purified PE.

Sample	Concentration (nM)	Inhibition (%)
Phycoerythrin	27	75 ± 8
	10	72 ± 8
Ibuprofen	24	96 ± 1

4.3.3 Effect of s-EPSs and purified PE on wound healing

Finally, a scratch assay was carried out on HaCaT cells to test the ability of s-EPSs and purified PE to induce cell migration, related to wound repairing. Results are reported in **Figure 7** and **Table 5**. In the absence of any treatment, cells spontaneously migrated to induce the re-epithelialization. Interestingly, when cells were treated with either s-EPSs or purified PE, a significant enhancement in the wound closure was observed after 24 h. Indeed, s-EPSs reduced the scratched area by 2.50 ± 0.17 fold and purified PE by 2.40 ± 0.13 fold, with respect to untreated cells (1.80 ± 0.02 fold reduction).

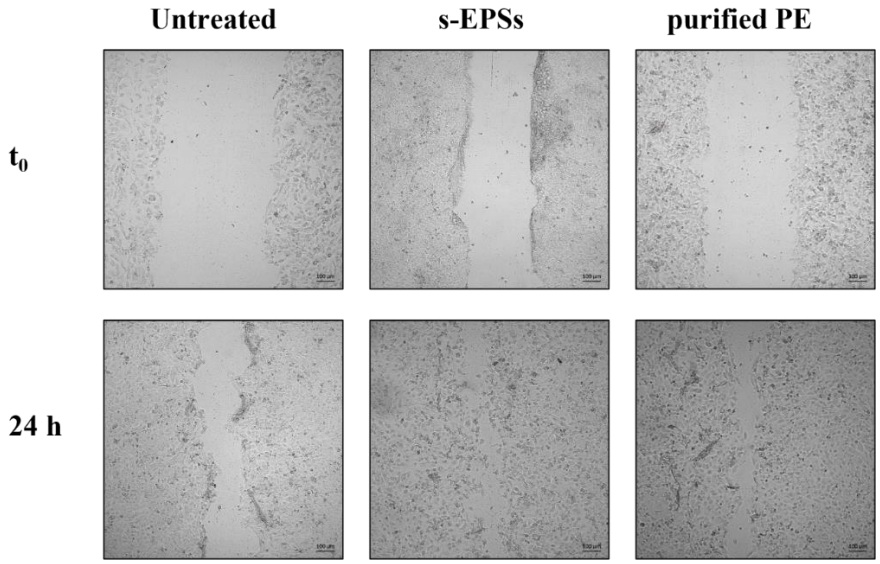

Figure 7. Effect of s-EPSs and purified PE on wound healing. Confluent HaCaT cells were scratched and treated with either 12 µg/mL s-EPSs or 10 nM purified PE for 24 h. Optical microscopy images were acquired at 10x magnification at the beginning (t_0) and at the end of the

incubation (24 h).

Table 5. Reduction of area (fold) of wound closure upon 24 h incubation with either s-EPSs or purified PE. Data shown are means ± S.D. of three independent experiments. For each experiment, at least 10 images were acquired. * indicates $p < 0.05$.

Sample	Reduction of area (fold)
Untreated	1.80 ± 0.02
s-EPSs	2.50 ± 0.17*
Purified PE	2.40 ± 0.13*

* = $p < 0.05$

Our results well fit with the mechanism of action of antioxidants, which prevent the generation of free radicals which, in turn, can significantly affect some physiological processes, including wound healing. In particular, ROS generation can damage tissues and slow down the regeneration process. The presence of antioxidants should counteract chronic inflammation and at the same time contribute to promote tissue regeneration (Alvarez et al., 2021). Considering that both s-EPSs and PE were able to inhibit one of the key enzymes in the inflammation process (COX-2) and to induce a significant faster scratch closure with respect to untreated cells, we can conclude that these bioproducts obtained by *P. cruentum* can represent an excellent ingredient for new biomaterials, such as medical patches.

4.4 Conclusions

As the use of synthetic molecules is known to be harmful in the long run, the search for new natural compounds, endowed with beneficial properties, is urgent (Montégut et al., 2022). In this context, antioxidants from microalgae could represent an excellent alternative, but microalgae upstream and downstream processes costs are still too high (Coulombier et al., 2021).

We recently set up a cascade approach to recover four class of molecules from *P. cruentum* culture: s-EPSs, PE, carotenoids, and saturated fatty acids. Among them, here we evaluated the biological activity of s-EPSs and PE. These molecules showed a remarkable antioxidant activity in a cell-based system, higher than that obtained by *in vitro* assays, thus suggesting that the reliability of *in vitro* assays has to be overhauled. Moreover, both molecules showed anti-inflammatory characteristics comparable with ibuprofen and a significant ability in

promoting cell proliferation.

4.5 References

Alam, F., Date, A., Rasjidin, R., Mobin, S.M.A., Moria, H., Baqui, A., 2014. Biofuel from Algae: Is It a Viable Alternative? Adv. Biofuel Prod. Aquat. Plants 32742–33487.

Alvarez, X., Alves, A., Ribeiro, M.P., Lazzari, M., Coutinho, P., Otero, A., 2021. Biochemical characterization of *Nostoc sp*. exopolysaccharides and evaluation of potential use in wound healing. Carbohydr. Polym. 254, 117303. https://doi.org/10.1016/J.CARBPOL.2020.117303

Anbuchezhian, R., Karuppiah, V., Li, Z., 2015. Prospect of marine algae for production of industrially important chemicals, in: Algal Biorefinery: An Integrated Approach. Springer, pp. 195–217.

Andrew, M., Jayaraman, G., 2020. Structural features of microbial exopolysaccharides in relation to their antioxidant activity. Carbohydr. Res. 487, 107881.

Ben Hlima, H., Smaoui, S., Barkallah, M., Elhadef, K., Tounsi, L., Michaud, P., Fendri, I., Abdelkafi, S., 2021. Sulfated exopolysaccharides from *Porphyridium cruentum*: A useful strategy to extend the shelf life of minced beef meat. Int. J. Biol. Macromol. 193, 1215–1225. https://doi.org/10.1016/J.IJBIOMAC.2021.10.161

Bhunia, B., Uday, U.S.P., Oinam, G., Mondal, A., Bandyopadhyay, T.K., Tiwari, O.N., 2018. Characterization, genetic regulation and production of cyanobacterial exopolysaccharides and its applicability for heavy metal removal. Carbohydr. Polym. 179, 228–243.

Coulombier, N., Jauffrais, T., Lebouvier, N., 2021. Antioxidant compounds from microalgae: A review. Mar. Drugs 19. https://doi.org/10.3390/md19100549

Di Lena, G., Casini, I., Lucarini, M., Lombardi-Boccia, G., 2019. Carotenoid profiling of five microalgae species from large-scale production. Food Res. Int. 120, 810–818. https://doi.org/10.1016/J.FOODRES.2018.11.043

Dvir, I., Stark, A.H., Chayoth, R., Madar, Z., Arad, S.M., 2009. Hypocholesterolemic Effects of Nutraceuticals Produced from the Red Microalga *Porphyridium sp*. in Rats. Nutr. . https://doi.org/10.3390/nu1020156

Feller, R., Matos, Â.P., Mazzutti, S., Moecke, E.H.S., Tres, M. V., Derner, R.B., Oliveira, J. V., Junior, A.F., 2018. Polyunsaturated

ω-3 and ω-6 fatty acids, total carotenoids and antioxidant activity of three marine microalgae extracts obtained by supercritical CO2 and subcritical n-butane. J. Supercrit. Fluids 133, 437–443. https://doi.org/10.1016/J.SUPFLU.2017.11.015

Fernández-Rojas, B., Hernández-Juárez, J., Pedraza-Chaverri, J., 2014. Nutraceutical properties of phycocyanin. J. Funct. Foods 11, 375–392. https://doi.org/10.1016/J.JFF.2014.10.011

Gaignard, C., Gargouch, N., Dubessay, P., Delattre, C., Pierre, G., Laroche, C., Fendri, I., Abdelkafi, S., Michaud, P., 2019. New horizons in culture and valorization of red microalgae. Biotechnol. Adv. 37, 193–222. https://doi.org/10.1016/J.BIOTECHADV.2018.11.014

Gallego, R., Martínez, M., Cifuentes, A., Ibáñez, E., Herrero, M., 2019. Development of a green downstream process for the valorization of Porphyridium cruentum biomass. Molecules 24, 1564.

Ganesan, A.R., Subramani, K., Shanmugam, M., Seedevi, P., Park, S., Alfarhan, A.H., Rajagopal, R., Balasubramanian, B., 2020. A comparison of nutritional value of underexploited edible seaweeds with recommended dietary allowances. J. King Saud Univ. 32, 1206–1211.

García, A.B., Longo, E., Murillo, M.C., Bermejo, R., 2021. Using a B-phycoerythrin extract as a natural colorant: Application in milk-based products. Molecules 26, 297.

Giordano, M.E., Caricato, R., Lionetto, M.G., 2020. Concentration dependence of the antioxidant and prooxidant activity of trolox in hela cells: Involvement in the induction of apoptotic volume decrease. Antioxidants 9, 1058.

Herrero, M., Mendiola, J.A., Plaza, M., Ibañez, E., 2013. Screening for bioactive compounds from algae, in: Advanced Biofuels and Bioproducts. Springer, pp. 833–872.

Hsieh-Lo, M., Castillo, G., Ochoa-Becerra, M.A., Mojica, L., 2019. Phycocyanin and phycoerythrin: Strategies to improve production yield and chemical stability. Algal Res. 42, 101600.

Imbimbo, P., Romanucci, V., Pollio, A., Fontanarosa, C., Amoresano, A., Zarrelli, A., Olivieri, G., Monti, D.M., 2019. A cascade extraction of active phycocyanin and fatty acids from *Galdieria phlegrea*. Appl. Microbiol. Biotechnol. 103, 9455–9464. https://doi.org/10.1007/s00253-019-10154-0

Kannaujiya, V.K., Kumar, D., Pathak, J., Sinha, R.P., 2019. Phycobiliproteins and their commercial significance, in: Cyanobacteria. Elsevier, pp. 207–216.

Landa, P., Kokoska, L., Pribylova, M., Vanek, T., Marsik, P., 2009. In

vitro anti-inflammatory activity of carvacrol: Inhibitory effect on COX-2 catalyzed prostaglandin E2 biosynthesisb. Arch. Pharm. Res. 32, 75–78. https://doi.org/10.1007/s12272-009-1120-6

Liberti, D., Imbimbo, P., Giustino, E., D'elia, L., Ferraro, G., Casillo, A., Illiano, A., Pinto, G., Di Meo, M.C., Alvarez-Rivera, G., Corsaro, M.M., Amoresano, A., Zarrelli, A., Ibáñez, E., Merlino, A., Monti, D.M., 2022. Inside out *Porphyridium cruentum*: Beyond the Conventional Biorefinery Concept. ACS Sustain. Chem. Eng. https://doi.org/10.1021/acssuschemeng.2c05869

López-Alarcón, C., Denicola, A., 2013. Evaluating the antioxidant capacity of natural products: A review on chemical and cellular-based assays. Anal. Chim. Acta 763, 1–10. https://doi.org/10.1016/j.aca.2012.11.051

Manirafasha, E., Ndikubwimana, T., Zeng, X., Lu, Y., Jing, K., 2016. Phycobiliprotein: Potential microalgae derived pharmaceutical and biological reagent. Biochem. Eng. J. 109, 282–296.

Marques, C., 2007. Antioxidant activities of sulfated polysaccharides from brown and red seaweeds. J. Appl. Phycol. 19, 153–160.

Medina-Cabrera, E.V., Gansbiller, M., Rühmann, B., Schmid, J., Sieber, V., 2021. Rheological characterization of *Porphyridium sordidum* and *Porphyridium purpureum* exopolysaccharides. Carbohydr. Polym. 253, 117237.

Megías, C., Pastor-Cavada, E., Torres-Fuentes, C., Girón-Calle, J., Alaiz, M., Juan, R., Pastor, J., Vioque, J., 2009. Chelating, antioxidant and antiproliferative activity of *Vicia sativa* polyphenol extracts. Eur. Food Res. Technol. 230, 353–359.

Mišurcová, L., Škrovánková, S., Samek, D., Ambrožová, J., Machů, L., 2012. Health benefits of algal polysaccharides in human nutrition. Adv. Food Nutr. Res. 66, 75–145.

Mobin, S., Alam, F., 2017. Some promising microalgal species for commercial applications: a review. Energy Procedia 110, 510–517.

Montégut, L., de Cabo, R., Zitvogel, L., Kroemer, G., 2022. Science-Driven Nutritional Interventions for the Prevention and Treatment of Cancer. Cancer Discov. 12, 2258–2279.

Petruk, G., Di Lorenzo, F., Imbimbo, P., Silipo, A., Bonina, A., Rizza, L., Piccoli, R., Monti, D.M., Lanzetta, R., 2017. Protective effect of *Opuntia ficus-indica* L. cladodes against UVA-induced oxidative stress in normal human keratinocytes. Bioorg. Med. Chem. Lett. 27, 5485–5489.

Re, R., Pellegrini, N., Proteggente, A., Pannala, A., Yang, M., Rice-Evans, C., 1999. Antioxidant activity applying an improved ABTS radical cation decolorization assay. Free Radic. Biol. Med. 26,

1231–1237.
Rebolloso Fuentes, M.M., Acién Fernández, G.G., Sánchez Pérez, J.A., Guil Guerrero, J.L., 2000. Biomass nutrient profiles of the microalga Porphyridium cruentum. Food Chem. 70, 345–353. https://doi.org/10.1016/S0308-8146(00)00101-1
Rodrigues, M.J., Neves, V., Martins, A., Rauter, A.P., Neng, N.R., Nogueira, J.M.F., Varela, J., Barreira, L., Custódio, L., 2016. In vitro antioxidant and anti-inflammatory properties of *Limonium algarvense* flowers' infusions and decoctions: A comparison with green tea (Camellia sinensis). Food Chem. 200, 322–329.
Simovic, A., Combet, S., Velickovic, T.C., Nikolic, M., Minic, S., 2022. Probing the stability of the food colourant R-phycoerythrin from dried Nori flakes. Food Chem. 374, 131780.
Sonani, R.R., Singh, N.K., Kumar, J., Thakar, D., Madamwar, D., 2014. Concurrent purification and antioxidant activity of phycobiliproteins from *Lyngbya sp*. A09DM: An antioxidant and anti-aging potential of phycoerythrin in *Caenorhabditis elegans*. Process Biochem. 49, 1757–1766. https://doi.org/10.1016/j.procbio.2014.06.022
Sudhakar, M.P., Jagatheesan, A., Perumal, K., Arunkumar, K., 2015. Methods of phycobiliprotein extraction from *Gracilaria crassa* and its applications in food colourants. Algal Res. 8, 115–120. https://doi.org/10.1016/j.algal.2015.01.011
Suganya, T., Varman, M., Masjuki, H.H., Renganathan, S., 2016. Macroalgae and microalgae as a potential source for commercial applications along with biofuels production: a biorefinery approach. Renew. Sustain. Energy Rev. 55, 909–941.
Wang, W.-N., Li, Y., Zhang, Y., Xiang, W.-Z., Li, A.-F., Li, T., 2021. Comparison on characterization and antioxidant activity of exopolysaccharides from two Porphyridium strains. J. Appl. Phycol. 33, 2983–2994. https://doi.org/10.1007/s10811-021-02518-9
Wang, Y., Xing, M., Cao, Q., Ji, A., Liang, H., Song, S., 2019. Biological activities of fucoidan and the factors mediating its therapeutic effects: A review of recent studies. Mar. Drugs 17, 183.

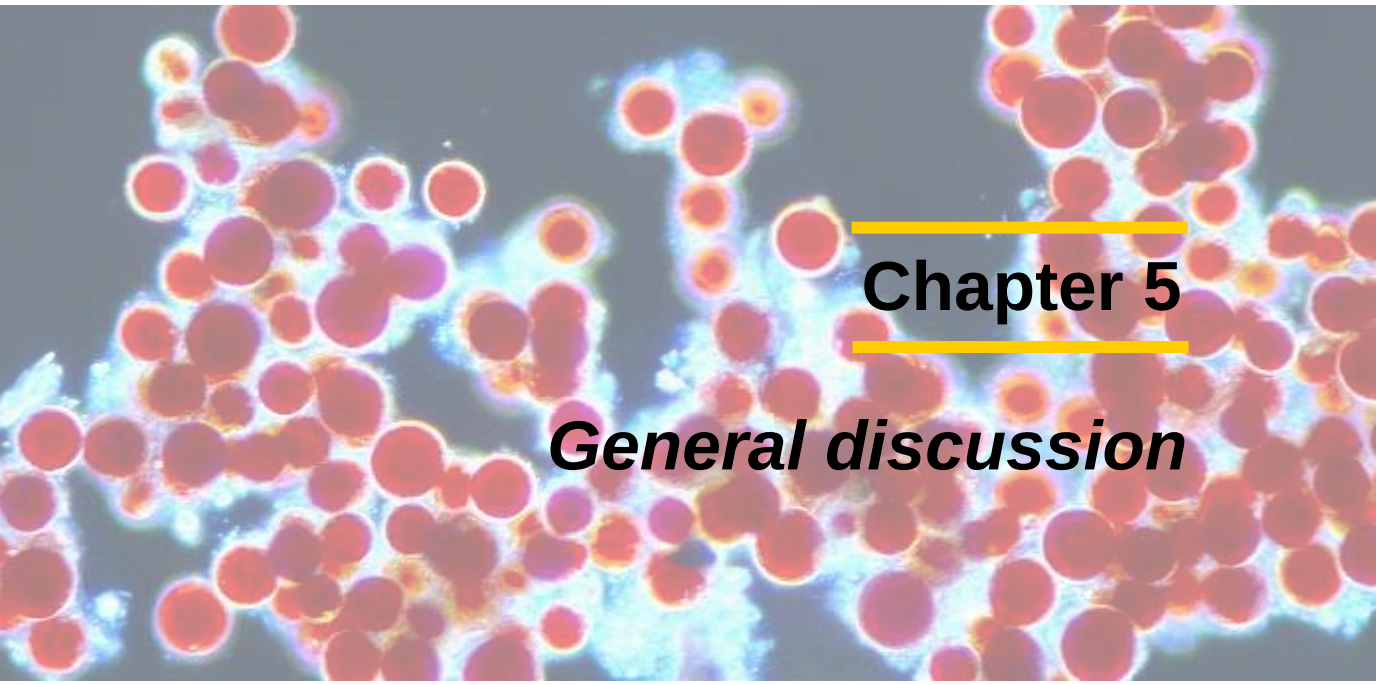

Chapter 5

General discussion

5.1 General discussion

Overpopulation, global warming, and reduction of natural resources are among the main problems of our time. The adoption of policies and procedures that have sustainability as starting point can help in alleviating some of the above-mentioned problems. Sustainability is a concept promoted by various world organizations, and it entails using both old and new resources, without producing waste and/or affecting the needs of future generations (Hummels and Argyrou, 2021; Ngan et al., 2019).

In this context, the concept of biorefinery could find its spot. Sustainability and biorefinery are two closely connected concepts; in fact, the implementation of a biorefinery approach might be seen as sustainability's ultimate goal. The international energy agency has defined biorefinery as: “the sustainable processing of biomass into a spectrum of bio-based products (food, feed, chemicals, materials) and bioenergy (biofuels, power and/or heat)" (de Jong et al., 2012). Biorefineries can provide multiple chemicals by fractioning an initial raw material (biomass) into multiple intermediates (e.g. carbohydrates, proteins, triglycerides), by a cascade approach, that can be further converted into value-added products (Cherubini, 2010).

Microalgae have gained wide interest in recent years, as they can be pointed out as consumers of CO_2 (Wu et al., 2022), producers of secondary metabolites with a variety of applications (Khaligh and Asoodeh, 2022) and do not require the use of arable lands to be cultivated (Dębowski et al., 2020). Nowadays, there are several microalgae products already on the market, but their marketability is still low due to their high production costs. Despite the fact that many researchers have reported the obtainment of products within a biorefinery framework, the economic viability is unreached and the microalgal biorefinery is, at the moment, still too much expensive (Tang et al., 2020; Zhou et al., 2017).

The general objective of the PhD project was to develop and apply a cascade approach able to fully exploit the microalgal culture of *Porphyridium cruentum*.

Since *P. cruentum* is already commercialized, in recent years, some studies have been carried out trying to improve its marketability. For instance, Gallego and colleagues applied two different subsequent extraction steps to obtain carotenoids and proteins from the same biomass (Gallego et al., 2019); Guihéneuf and Stengel carried out strategies to improve the co-production of different compounds from *P. cruentum* (Guihéneuf and Stengel, 2015). However, the majority of

research is focused on the obtainment of only one product (Di Lena et al., 2019; Martínez et al., 2019).

Differently from the abovementioned studies, the present biorefinery process, as it was thought and designed, allowed obtaining, in a cascade approach, four bioproducts: sulphated exopolysaccharides (s-EPSs), phycoerythrin (PE), carotenoids and lipids. All of them were obtained without significantly affecting the overall yields and the bioactivity of the other isolated compounds. Here, a brief discussion of the four molecules is reported, highlighting the drawbacks and pros of the available techniques.

Sulphated exopolysaccharides. Sulphated exopolysaccharides (s-EPSs) were isolated from the exhausted culture medium, generally regarded as waste, and were found to be endowed with antioxidant, anti-inflammatory and wound healing activities.

To date, very few s-EPSs are commercialized, and they are mostly used in the cosmetics sector. According to Keristovesky and colleagues (Keristovesky et al., 1993), *P. cruentum* s-EPSs are not hydrolyzed in the digestive tract. Indeed, the Solazyme company, in 2007, formulated biologically active nutraceutics with s-EPS, as they showed antioxidant and anti-inflammatory activities (Dillon et al., 2007). Due to the lack of bioavailability and the high viscosity of s-EPS solutions, their potential application as dietary fibers may be of interest. Additionally, recently, Alvarez and colleagues demonstrated the use of s-EPSs as hydrocolloid dressing in wound treatment, by preventing the exude of liquids from the wound and enhancing skin regeneration (Alvarez et al., 2021).

Unfortunately, the recovery of s-EPSs from the culture medium starts by removing the biomass by centrifugation, and then ethanol precipitation and diafiltration are performed (Ravishankar and Ambati, 2019), with an increase in the overall costs. Thus, their marketability is restricted to the niche of the high-value compounds. Recently, s-EPSs have been proposed as flocculating agent (Babiak and Krzemińska, 2021), but this kind of application could represent an economic loss. Specific, innovative, and green downstream processes could help the microalgae biorefinery to achieve the breakeven point, allowing s-EPSs to find many other applications, such as in the food, cosmetics, pharmaceuticals, and agricultural industries.

Phycoerythrin. The first bioproduct isolated from *P. cruentum* biomass was phycoerythrin (PE). Different protein aqueous extraction procedures were evaluated (sonication, maceration, freeze and thaw and French press) to isolate the protein. Among them, sonication was chosen for PE yield, the lower content of contaminating proteins and it

was time-saving. The extraction was further optimized by comparing the yield and the purity grade of PE starting from three feedstocks: (i) fresh biomass; (ii) frozen biomass; (iii) biomass collected by flocculation. Results suggested that storage conditions did not affect PE extraction, giving high versatility to the process. PE was then isolated by applying a single purification step, which allowed to obtain the protein with a high purity level, so high that its crystallographic structure and sequence were obtained. The highly purified PE was active against UVA-induced oxidative stress and inflammation. Interestingly, a new role for PE was found, i.e. in re-epithelization.

Noteworthy, the purity grade of the protein is important for its applications, as a significant toxicity of PE was found when the purity grade was lower than 4. Needless to say, the higher the number of steps needed to purify the protein, the higher the purity grade, the higher the market value, but the higher the overall costs (Ghosh and Mishra, 2020; Ma et al., 2020; Phuong et al., 2022). During the different extraction steps, care has to be given to heat and mechanical shear forces which can cause a loss in terms of PE amount (Mishra et al., 2011). At the same time, stability to pH, temperature and time have to be considered for its large-scale production and shelf life (Hsieh-Lo et al., 2019; Kannaujiya et al., 2019). Nevertheless, several companies commercialize PE produced in microalgae, such as: Europa Bioproducts, Sigma-Aldrich, Jackson Immuno Research, Thermo Fisher Scientific, SETA BioMedicals, Binmei Biotechnology, Algapharma Biotech, Phyco-Biotech, Norland Biotech, Columbia Bioscience and Dainippon Ink and Chemicals. Depending on the ultimate purity level and the proposed application, the market price of purified PE can vary between $180 and $250 per milligram, with an estimation of the total market of about $6.3 million by 2025 (Ardiles et al., 2020). Future Market Insights Inc. estimated that the market value of $2.6 billion overall in 2022 might quadruple by 2032 (https://www.futuremarketinsights.com/reports/phycoerythrin-market).

Carotenoids. To valorize the residual biomass, after PE extraction, carotenoids were obtained. The extract from the residual biomass gave a similar yield, compared to the one obtained from the raw biomass, but it was enriched in β-carotene, a well-known antioxidant (Feller et al., 2018).

Carotenoids have a wide range of applications, from food, feed, nutraceutics up to cosmetics. Because of their color and nutritional benefits, carotenoids have been used in the food and feed sectors since many years. With a 47% market share, the animal feed industry was the higher consumer of carotenoids in 2014

(https://www.marketsandmarkets.com/Market-Reports/carotenoid-market-158421566.html). Similarly, carotenoids have been added to the diet of aquatic organisms, in aquaculture, to enhance the pink/red color of crustaceans, salmonids, and other farmed fish (Lorenz and Cysewski, 2000). This feed industry is expected to grow at a very high rate in the world ($4.4 billion by 2030) (Ottinger et al., 2016). Indeed, in 2019, the carotenoids industry reached the fastest growth in the health and nutraceutical market, which was about $440 million with a compound annual growth rate (CAGR) of 3.7% (https://www.marketsandmarkets.com/Market-Reports/carotenoid-market-158421566.html). To obtain natural carotenoids, different extraction techniques can be used, from the most classical, including physical grinding, milling, ultrasound- and microwave-assisted extraction, freeze-thawing, solvent extraction (Ambati et al., 2019), up to the most innovative and green ones, such as enzyme-assisted extractions, green solvents, subcritical water extraction, and super-critical CO_2 extraction (Saini and Keum, 2018). Even if technologies are rapidly evolving, synthetic carotenoids can be produced more quickly and inexpensively. For instance, the cost of a carotenoid isolated from microalgae can be as high as $7,500/kg (Koller et al., 2014), whereas its synthetic equivalent may only cost half as much (Li et al., 2011). However, recent data are showing that synthetic carotenoids can be harmful in the long run (Montégut et al., 2022). As an example, in 2011, EU banned the use of the chemical ethoxyquin (EQ), used as a feed additive (https://eur-lex.europa.eu/legal-content/EN/TXT/?uri=CELEX:32017R0962). EQ was employed as a stabilizer, preventing from combusting during storage and transport. Thus, it is important the search for the obtainment of natural carotenoids. Unfortunately, microalgae are able to produce only low amount of carotenoids (up to 10% of biomass dry weight) (Di Caprio et al., 2020), so that the microalgae-based carotenoids market still represents the 1% of the total market (Novoveská et al., 2019).

Lipids. Finally, lipids were isolated and fractionated as last class of molecules from the residual biomass of *P. cruentum*. The lipid fraction was richer in saturated fatty acids (SFAs) with respect to that obtained from the raw one. SFAs are chemically stable, have a well-defined melting point and are biocompatible, so that they are emerging as an intriguing new family of compounds, to be used as controlled drug-release molecules or antibacterial agents (Xue et al., 2021; Yoon et al., 2018).

One of the primary issues within the lipid industry is the extraction process (Gifuni et al., 2019). Organic solvents like hexane,

chloroform, acetone, methanol, and diethyl ether are frequently used (Saini and Keum, 2018). These conventional extractions often require significant volumes of solvents, extended extraction time, and a dry biomass (Mansour et al., 2019). Additionally, the pretreatment phase is frequently necessary before the extraction, with consequences on the overall costs (Chen et al., 2013; Kadir et al., 2018). The harvesting-dewatering process represents a bottleneck for microalgae-based industry, as the commonly used techniques, such as centrifugation or filtration (Branyikova et al., 2018; Fuad et al., 2018; Tan et al., 2020), have a high cost (20-30% of the total cost) and cannot be applied when the biomass is needed for bulk products (biofuels) (Najjar and Abu-Shamleh, 2020). A new generation of extraction methods started developing, without the use of hazardous solvents, resulting in a more environmentally friendly approach (Armenta et al., 2019; Chemat et al., 2012). Additionally, without altering chemical structure, the novel approaches enable shorter extraction times and higher extraction yields (Dixon and Wilken, 2018). Currently, only a few algae strains, including *Spirulina*, *Chlorella*, *Dunaliella salina*, *Aphanizomenon flosaquae*, *Haematococcus pluvialis*, *Crypthecodinium cohnii*, and *Shizochytrium* (Brennan and Owende, 2010; De Luca et al., 2021; Kothari et al., 2017), are used for large-scale production of polyunsaturated fatty acids (PUFAs). PUFAs are normally used for human nutrition, or for biodiesel production. In particular, research and development efforts in the field of microalgae are mostly motivated by energy-related trends, even if this driving force was lost after 2015 as a result of the popularity and acceptance of electric vehicles (Li et al., 2020) and of the fall in oil price. To date, PUFAs are mostly used as nutritional supplements, for functional food, and in the pharmaceutical industry (Ratledge and Cohen, 2008). Several companies, such as Oceans Alive (USA), Blue Biotech (Germany), Flora Health (USA) and InnovalG (France), produce ω3-PUFA from microalgae as dietary supplements or food additives (Ambati et al., 2019). The global market for ω3-PUFA was assessed to be worth $16.2 billion in 2020, and it is forecasted that this market would expand to $36.9 billion by 2027, with a CAGR of 12.5% (https://www.strategyr.com/).

Despite the high relevance of bio-based products for many industries, the commercial exploitation of microalgae currently faces severe scientific and operational obstacles. Overall, several examples of particular biorefinery stages are recorded in literature, but there have been very few attempts to design complete processes. Both upstream and downstream processes must be simplified and integrated to become feasible and sustainable. However, it is important to remember

that any technology designed for the obtainment of a single product should always be followed by an assessment of the impact of the process as a whole. Numerous Life Cycle Assessment studies on microalgae production highlight several bottlenecks, with harvesting, storage and extraction as major energy consumers within the overall process (Razon and Tan, 2011; Soratana et al., 2014; Xu et al., 2011).

Although microalgae have the potential to contribute to a wide range of markets, their present use is restricted to medium- and high-value related markets, such as nutraceuticals, food, biopesticides and biostimulants, due to economic and technological constraints. In feed-related applications, microalgae can be used as an additive as they cannot entirely substitute other raw materials (Llamas et al., 2021).

The price of *P. cruentum* biomass can range from few to several hundred dollars per kilogram, depending on the supplier and the growth conditions. From its biomass it is possible to recover Phycoerythrin, whose price can range from several hundred to several thousand dollars per gram, depending on the supplier and the purity of the product, related to the purification steps required. It is important to note that the prices of PE and *P. cruentum* biomass can fluctuate over time due to market demand and supply chain factors. As research continues to explore the potential uses of these products in various industries, their prices may change accordingly.

In conclusion, the composition of *P. cruentum*, summarized in Chapter 3, section 3.4, the consequent high value added to 1 kg of biomass, and the absence of waste products made a concrete biorefinery approach possible, even though still many other factors need to be fine-tuned and clarified to make this process an industrial reality.

5.2 References

Alvarez, X., Alves, A., Ribeiro, M.P., Lazzari, M., Coutinho, P., Otero, A., 2021. Biochemical characterization of *Nostoc sp*. exopolysaccharides and evaluation of potential use in wound healing. Carbohydr. Polym. 254, 117303. https://doi.org/10.1016/J.CARBPOL.2020.117303

Ambati, R.R., Gogisetty, D., Aswathanarayana, R.G., Ravi, S., Bikkina, P.N., Bo, L., Yuepeng, S., 2019. Industrial potential of carotenoid pigments from microalgae: Current trends and future prospects. Crit. Rev. Food Sci. Nutr. 59, 1880–1902.

Ardiles, P., Cerezal-Mezquita, P., Salinas-Fuentes, F., Órdenes, D., Renato, G., Ruiz-Domínguez, M.C., 2020. Biochemical

composition and phycoerythrin extraction from red microalgae: A comparative study using green extraction technologies. Processes 8, 1628.

Armenta, S., Garrigues, S., Esteve-Turrillas, F.A., de la Guardia, M., 2019. Green extraction techniques in green analytical chemistry. TrAC Trends Anal. Chem. 116, 248–253.

Babiak, W., Krzemińska, I., 2021. Extracellular polymeric substances (EPS) as microalgal bioproducts: A review of factors affecting EPS synthesis and application in flocculation processes. Energies 14, 4007.

Branyikova, I., Prochazkova, G., Potocar, T., Jezkova, Z., Branyik, T., 2018. Harvesting of microalgae by flocculation. Fermentation 4, 93.

Brennan, L., Owende, P., 2010. Biofuels from microalgae-A review of technologies for production, processing, and extractions of biofuels and co-products. Renew. Sustain. Energy Rev. 14, 557–577. https://doi.org/10.1016/j.rser.2009.10.009

Chemat, F., Vian, M.A., Cravotto, G., 2012. Green extraction of natural products: Concept and principles. Int. J. Mol. Sci. 13, 8615–8627.

Chen, P.H., Oswald, W.J., Marsolek, M.D., Kendall, E., Thompson, P.L., Shuman, T.R., Prajapati, S.K., Kaushik, P., Malik, A., Vijay, V.K., Sambusiti, C., Bellucci, M., Zabaniotou, A., Beneduce, L., Monlau, F., Heaven, S., Milledge, J., Zhang, Y., Alzate, M.E., Muñoz, R., Rogalla, F., Fdz-Polanco, F., Pérez-Elvira, S.I., Keymer, P., Ruffell, I., Pratt, S., Lant, P., Schwede, S., Rehman, Z.U., Gerber, M., Theiss, C., Span, R., Passos, F., Uggetti, E., Carrère, H., Ferrer, I., González-Fernández, C., Sialve, B., Bernet, N., Steyer, J.P., Salim, S., Bosma, R., Vermuë, M.H., Wijffels, R.H., Divakaran, R., Pillai, V.N.S., Shanmugam, P., Horan, N.J., Kafarov, V., Schmid-staiger, U., González-Fernández, C., Sialve, B., Bernet, N., Steyer, J.P., Angelidaki, I., Alves, M., Bolzonella, D., Borzacconi, L., Campos, J.L., Guwy, a. J., Kalyuzhnyi, S., Jenicek, P., Van Lier, J.B., 2013. Algae Biorefinery - Concepts Microalgae - microscopic small „ plants “. Bioresour. Technol. 44, 471–474.

Cherubini, F., 2010. The biorefinery concept: using biomass instead of oil for producing energy and chemicals. Energy Convers. Manag. 51, 1412–1421.

de Jong, E., Higson, A., Walsh, P., Wellisch, M., 2012. Bio-based Chemicals Value Added Products from. IEA Bioenergy | Task 42 Biorefinery 1–33.

De Luca, M., Pappalardo, I., Limongi, A.R., Viviano, E., Radice, R.P., Todisco, S., Martelli, G., Infantino, V., Vassallo, A., 2021. Lipids from microalgae for cosmetic applications. Cosmetics 8, 52.

Dębowski, M., Zieliński, M., Kazimierowicz, J., Kujawska, N., Talbierz, S., 2020. Microalgae cultivation technologies as an opportunity for bioenergetic system development—advantages and limitations. Sustainability 12, 9980.

Di Caprio, F., Altimari, P., Pagnanelli, F., 2020. Sequential extraction of lutein and β-carotene from wet microalgal biomass. J. Chem. Technol. Biotechnol. 95, 3024–3033.

Di Lena, G., Casini, I., Lucarini, M., Lombardi-Boccia, G., 2019. Carotenoid profiling of five microalgae species from large-scale production. Food Res. Int. 120, 810–818. https://doi.org/10.1016/J.FOODRES.2018.11.043

Dillon, H., Somanchi, A., Rao, K., 2007. Methods and compositions for reducing inflammation and preventing oxidative damage.

Dixon, C., Wilken, L.R., 2018. Green microalgae biomolecule separations and recovery. Bioresour. Bioprocess. 5, 1–24.

Feller, R., Matos, Â.P., Mazzutti, S., Moecke, E.H.S., Tres, M. V., Derner, R.B., Oliveira, J. V., Junior, A.F., 2018. Polyunsaturated ω-3 and ω-6 fatty acids, total carotenoids and antioxidant activity of three marine microalgae extracts obtained by supercritical CO2 and subcritical n-butane. J. Supercrit. Fluids 133, 437–443. https://doi.org/10.1016/J.SUPFLU.2017.11.015

Fuad, N., Omar, R., Kamarudin, S., Harun, R., Idris, A., WAKG, W.A., 2018. Mass harvesting of marine microalgae using different techniques. Food Bioprod. Process. 112, 169–184.

Gallego, R., Martínez, M., Cifuentes, A., Ibáñez, E., Herrero, M., 2019. Development of a Green Downstream Process for the Valorization of *Porphyridium cruentum* Biomass. Molecules 24. https://doi.org/10.3390/molecules24081564

Ghosh, T., Mishra, S., 2020. Studies on Extraction and Stability of C-Phycoerythrin From a Marine Cyanobacterium. Front. Sustain. Food Syst. 4, 102.

Gifuni, I., Pollio, A., Safi, C., Marzocchella, A., Olivieri, G., 2019. Current Bottlenecks and Challenges of the Microalgal Biorefinery. Trends Biotechnol. 37, 242–252. https://doi.org/10.1016/j.tibtech.2018.09.006

Guihéneuf, F., Stengel, D.B., 2015. Towards the biorefinery concept: Interaction of light, temperature and nitrogen for optimizing the co-production of high-value compounds in *Porphyridium purpureum*. Algal Res. 10, 152–163.

Hsieh-Lo, M., Castillo, G., Ochoa-Becerra, M.A., Mojica, L., 2019. Phycocyanin and phycoerythrin: Strategies to improve production yield and chemical stability. Algal Res. 42, 101600.

Hummels, H., Argyrou, A., 2021. Planetary demands: Redefining sustainable development and sustainable entrepreneurship. J. Clean. Prod. 278, 123804.

Kadir, W.N.A., Lam, M.K., Uemura, Y., Lim, J.W., Lee, K.T., 2018. Harvesting and pre-treatment of microalgae cultivated in wastewater for biodiesel production: a review. Energy Convers. Manag. 171, 1416–1429.

Kannaujiya, V.K., Kumar, D., Pathak, J., Sinha, R.P., 2019. Phycobiliproteins and their commercial significance, in: Cyanobacteria. Elsevier, pp. 207–216.

Keristovesky, G., Simon, B., Barak, Z., Geresh, S., 1993. Biodegradation of the sulphated polysaccharide of *Porphyridium* by soil bacteria. Phytochemistry 32, 287–290.

Khaligh, S.F., Asoodeh, A., 2022. Recent advances in the bio-application of microalgae-derived biochemical metabolites and development trends of photobioreactor-based culture systems. 3 Biotech 12, 1–19.

Koller, M., Muhr, A., Braunegg, G., 2014. Microalgae as versatile cellular factories for valued products. Algal Res. 6, 52–63.

Kothari, R., Pandey, A., Ahmad, S., Kumar, A., Pathak, V. V, Tyagi, V. V, 2017. Microalgal cultivation for value-added products: a critical enviro-economical assessment. 3 Biotech 7, 1–15.

Li, D., Du, W., Fu, W., Cao, X., 2020. A Quick Look Back at the Microalgal Biofuel Patents: Rise and Fall. Front. Bioeng. Biotechnol. 8, 1035.

Li, J., Zhu, D., Niu, J., Shen, S., Wang, G., 2011. An economic assessment of astaxanthin production by large scale cultivation of Haematococcus pluvialis. Biotechnol. Adv. 29, 568–574.

Llamas, B., Suárez-Rodríguez, M.C., González-López, C. V, Mora, P., Acién, F.G., 2021. Techno-economic analysis of microalgae related processes for CO2 bio-fixation. Algal Res. 57, 102339.

Lorenz, R.T., Cysewski, G.R., 2000. Lorentz 2000 18, 160–167.

Ma, J., You, X., Sun, S., Wang, X., Qin, S., Sui, S.F., 2020. Structural basis of energy transfer in *Porphyridium purpureum* phycobilisome. Nature 579, 146–151. https://doi.org/10.1038/s41586-020-2020-7

Mansour, E.A., Abo El-Enin, S.A., Hamouda, A.S., Mahmoud, H.M., 2019. Efficacy of extraction techniques and solvent polarity on lipid recovery from domestic wastewater microalgae. Environ. Nanotechnology, Monit. Manag. 12, 100271. https://doi.org/10.1016/j.enmm.2019.100271

Martínez, J.M., Delso, C., Álvarez, I., Raso, J., 2019. Pulsed electric

field permeabilization and extraction of phycoerythrin from *Porphyridium cruentum*. Algal Res. 37, 51–56. https://doi.org/10.1016/j.algal.2018.11.005

Mishra, S.K., Shrivastav, A., Mishra, S., 2011. Preparation of highly purified C-phycoerythrin from marine cyanobacterium *Pseudanabaena sp*. Protein Expr. Purif. 80, 234–238.

Montégut, L., de Cabo, R., Zitvogel, L., Kroemer, G., 2022. Science-Driven Nutritional Interventions for the Prevention and Treatment of Cancer. Cancer Discov. 12, 2258–2279.

Najjar, Y.S.H., Abu-Shamleh, A., 2020. Harvesting of microalgae by centrifugation for biodiesel production: A review. Algal Res. 51, 102046.

Ngan, S.L., How, B.S., Teng, S.Y., Promentilla, M.A.B., Yatim, P., Er, A.C., Lam, H.L., 2019. Prioritization of sustainability indicators for promoting the circular economy: The case of developing countries. Renew. Sustain. Energy Rev. 111, 314–331.

Novoveská, L., Ross, M.E., Stanley, M.S., Pradelles, R., Wasiolek, V., Sassi, J.-F., 2019. Microalgal carotenoids: A review of production, current markets, regulations, and future direction. Mar. Drugs 17, 640.

Ottinger, M., Clauss, K., Kuenzer, C., 2016. Aquaculture: Relevance, distribution, impacts and spatial assessments–A review. Ocean Coast. Manag. 119, 244–266.

Phuong, H., Massé, A., Dumay, J., Vandanjon, L., Mith, H., Legrand, J., Arhaliass, A., 2022. Enhanced Liberation of Soluble Sugar, Protein, and R-Phycoerythrin Under Enzyme-Assisted Extraction on Dried and Fresh *Gracilaria gracilis* Biomass. Front. Chem. Eng 4, 718857.

Ratledge, C., Cohen, Z., 2008. Microbial and algal oils: do they have a future for biodiesel or as commodity oils? Lipid Technol. 20, 155–160.

Ravishankar, G.A., Ambati, R.R., 2019. Handbook of Algal Technologies and Phytochemicals: Volume I Food, Health and Nutraceutical Applications. CRC Press.

Razon, L.F., Tan, R.R., 2011. Net energy analysis of the production of biodiesel and biogas from the microalgae: *Haematococcus pluvialis* and *Nannochloropsis*. Appl. Energy 88, 3507–3514.

Saini, R.K., Keum, Y.-S., 2018. Carotenoid extraction methods: A review of recent developments. Food Chem. 240, 90–103.

Soratana, K., Barr, W.J., Landis, A.E., 2014. Effects of co-products on the life-cycle impacts of microalgal biodiesel. Bioresour. Technol. 159, 157–166.

Tan, J. Sen, Lee, S.Y., Chew, K.W., Lam, M.K., Lim, J.W., Ho, S.-H., Show, P.L., 2020. A review on microalgae cultivation and harvesting, and their biomass extraction processing using ionic liquids. Bioengineered 11, 116–129.

Tang, D.Y.Y., Khoo, K.S., Chew, K.W., Tao, Y., Ho, S.-H., Show, P.L., 2020. Potential utilization of bioproducts from microalgae for the quality enhancement of natural products. Bioresour. Technol. 304, 122997.

Wu, W., Tan, L., Chang, H., Zhang, C., Tan, X., Liao, Q., Zhong, N., Zhang, X., Zhang, Y., Ho, S.-H., 2022. Advancements on process regulation for microalgae-based carbon neutrality and biodiesel production. Renew. Sustain. Energy Rev. 112969.

Xu, L., Brilman, D.W.F.W., Withag, J.A.M., Brem, G., Kersten, S., 2011. Assessment of a dry and a wet route for the production of biofuels from microalgae: energy balance analysis. Bioresour. Technol. 102, 5113–5122.

Xue, K., Lv, S., Zhu, C., 2021. Bringing naturally-occurring saturated fatty acids into biomedical research †. J. Mater. Chem. B 9, 6973–6987. https://doi.org/10.1039/d1tb00843a

Yoon, B.K., Jackman, J.A., Valle-González, E.R., Cho, N.J., 2018. Antibacterial Free Fatty Acids and Monoglycerides: Biological Activities, Experimental Testing, and Therapeutic Applications. Int. J. Mol. Sci. 2018, Vol. 19, Page 1114 19, 1114. https://doi.org/10.3390/IJMS19041114

Zhou, W., Wang, J., Chen, P., Ji, C., Kang, Q., Lu, B., Li, K., Liu, J., Ruan, R., 2017. Bio-mitigation of carbon dioxide using microalgal systems: Advances and perspectives. Renew. Sustain. Energy Rev. 76, 1163–1175.

https://www.futuremarketinsights.com/reports/phycoerythrin-market

https://www.marketsandmarkets.com/Market-Reports/carotenoid-market-158421566.html

https://eur-lex.europa.eu/legal-content/EN/TXT/?uri=CELEX:32017R0962

https://www.strategyr.com/

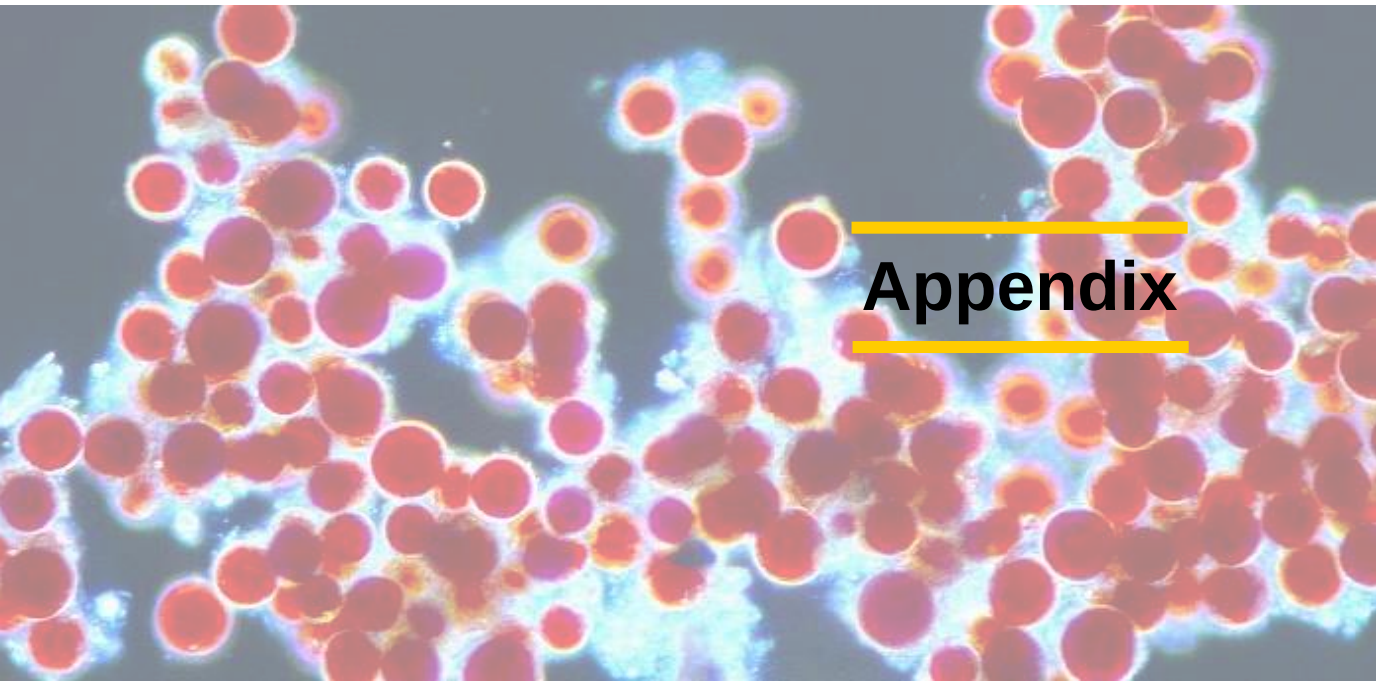

Appendix

List of scientific publications:

I. **Liberti, D.**, Alfieri, M.L., Monti, D.M., Panzella, L., Napolitano, A.. ***A melanin-related phenolic polymer with potent photoprotective and antioxidant activities for dermo-cosmetic applications.*** Antioxidants, 2020, 9(4), 270. doi.org/10.3390/antiox9040270

II. Imbimbo, P., D'Elia, L., **Liberti, D.**, Olivieri, G., Monti, D.M.. ***Towards green extraction methods from microalgae learning from the classics.*** Applied Microbiology and Biotechnology, 2020, 104(21), pp. 9067-9077. doi.org/10.1007/s00253-020-10839-x

III. D'Elia, L., Imbimbo, P., **Liberti, D.**, Bolinesi, F., Pollio, A., Mangoni, O., Brilman, W., Monti, D. M.. ***Switchable Solvent Selective Extraction of Hydrophobic Antioxidants from Synechococcus bigranulatus.*** ACS Sustainable Chemistry & Engineering, 2021. doi.org/10.1021/acssuschemeng.1c04400

IV. Annunziata, A., **Liberti, D.**, Bedini, E., Cucciolito, M. E., Loreto, D., Monti, D. M., Merlino, A., Ruffo, F.. ***Square-Planar vs. Trigonal Bipyramidal Geometry in Pt (II) Complexes Containing Triazole-Based Glucose Ligands as Potential Anticancer Agents.*** International journal of molecular sciences, 2021, 22(16), 8704, doi.org/10.3390/ijms22168704

V. Srećković, N. Z., Nedić, Z. P., **Liberti, D.**, Monti, M. D., Mihailović, N. R., Katanić Stanković, J. S., Dimitrijević, S., Mihailović, V. B.. ***Application potential of biogenically synthesized silver nanoparticles using Lythrum salicaria L. extracts as pharmaceuticals and catalysts for organic pollutant degradation***. RCS Advances, 2021, 11, 35585-35599, DOI: 10.1039/D1RA05570D

VI. D'Elia, L., Imbimbo, P., **Liberti, D.**, Olivieri, G., Pollio, A., Monti, D.M.. ***Thermo resistant antioxidants from photoautotrophic microorganism: screening and characterization.*** World Journal of Microbiology and Biotechnology, 2021, 37, 1-13, doi.org/10.1007/s11274-021-03180-6

Appendix

VII. Argenziano, R., Alfieri, M. L., Arntz, Y., Castaldo, R., **Liberti, D.**, Monti, D. M., Gentile, G., Panzella, L., Crescenzi, O., Ball, V., Napolitano, A., d'Ischia, M.. ***Non-covalent small molecule partnership for redox-active films improving polydopamine coating technology.*** Journal of Colloid and Interface Science, 2022, 624, pp. 400–410, doi.org/10.1016/j.jcis.2022.05.123

VIII. Moccia F, **Liberti D**, Giovando S, Caddeo C, Monti DM, Panzella L, Napolitano A. ***Chestnut Wood Mud as a Source of Ellagic Acid for Dermo-Cosmetic Applications.*** Antioxidants, 2022, Vol. 11: 1681. doi.org/doi.org/10.3390/antiox11091681

IX. **Liberti, D.**, Imbimbo, P., Giustino, E., D'Elia, L., Ferraro, G., Casillo, A., Illiano, A., Pinto, G., Di Meo, M.C., Alvarez-Rivera, G., Corsaro, M.M., Amoresano, A., Zarrelli, A., Ibáñez, E., Merlino, A., Monti, D.M.. ***Inside out Porphyridium cruentum: Beyond the Conventional Biorefinery Concept.*** ACS Sustainable Chemistry & Engineering, 2022. doi.org/10.1021/acssuschemeng.2c05869

I. **Liberti, D**., Imbimbo, P., Giustino, E., D'Elia, L., Silva, M., Barreira, L., Monti, D.M.. ***Shedding light on the hidden benefit of Porphyridium cruentum culture.*** Antioxidants, 2023. doi.org/10.3390/antiox12020337

List of scientific communications:

1- **Liberti, D.**, Imbimbo, P., Giustino, E., D'Elia, L., Ferraro, G., Casillo, A., Illiano, A., Pinto, G., Di Meo, M.C., Alvarez-Rivera, G., Corsaro, M.M., Amoresano, A., Zarrelli, A., Ibáñez, E., Merlino, A., Monti, D.M.. Inside out Porphyridium cruentum: Beyond the Conventional Biorefinery Concept. Meeting sezione SIB Campania 2022 (Naples, Italy, October 26th, 2022) Oral communication

2- **Liberti, D.**, Imbimbo, P., Giustino, E., D'Elia, L., Ferraro, G., Casillo, A., Illiano, A., Pinto, G., Di Meo, M.C., Alvarez-Rivera, G., Corsaro, M.M., Amoresano, A., Zarrelli, A., Ibáñez, E., Merlino, A., Monti, D.M.. Inside out Porphyridium cruentum: Beyond the Conventional Biorefinery Concept. Meeting sezione SIB Campania 2022 (Naples, Italy, October 26th, 2022) Poster presentation

3- Giustino, E, Imbimbo, P., **Liberti, D.**, Rossi, M., Monti, D.M.. Algaceutical: when microalgae application meets innovation. Meeting sezione SIB Campania 2022 (Naples, Italy, October 26th, 2022) Poster presentation
4- Imbimbo, P.,Bueno, M., D'Elia, L., **Liberti, D.**, Ibañez, E., Monti, D.M.. Microalgae as factory of high added bioproducts. Meeting sezione SIB Campania 2022 (Naples, Italy, October 26th, 2022) Poster presentation
5- **Liberti, D.**, Imbimbo, P., Giustino, E., D'Elia, L., Ferraro, G., Casillo, A., Illiano, A., Pinto, G., Di Meo, M.C., Alvarez-Rivera, G., Corsaro, M.M., Amoresano, A., Zarrelli, A., Ibáñez, E., Merlino, A., Monti, D.M.. Inside out Porphyridium cruentum: Beyond the Conventional Biorefinery Concept. Convegno AISAM Mario Tredici. (Naples, Italy, October 16-18, 2022) Poster presentation
6- Giustino, E, Imbimbo, P., **Liberti, D.**, Rossi, M., Monti, D.M.. Algaceutical: when microalgae application meets innovation. Convegno AISAM Mario Tredici. (Naples, Italy, October 16-18, 2022) Poster presentation
7- Panzella, L., Moccia, F., **Liberti, D.**, Giovando, S., Caddeo, C., Monti, D. M., Napolitano, A.. Nanoformulated chestnut wood mud as a source of ellagic acid for dermo-cosmetic applications. Polyphenols Applications World Congress, (Valencia, Spain, September 28-30, 2022). Oral communication
8- Argenziano, R., Alfieri, M. L., Arntz, Y., Castaldo, R., **Liberti, D.**, Monti, D. M., Gentile, G., Panzella, L., Crescenzi, O., Ball, V., Napolitano, A., d'Ischia, M.. Functional film from 5,6-dihydroxyindole oligomers and long chains diamines partnership. XXVII National Conference of Società Chimica Italiana (September 14-23, 2021). Oral communication
9- Annunziata, A., **Liberti, D.**, Bedini, E., Cucciolito, M. E., Loreto, D., Monti, D. M., Merlino, A., Ruffo, F.. Square-Planar vs. Trigonal Bipyramidal Geometry in Pt(II) Complexes Containing Triazole-Based Glucose Ligands as Potential Anticancer Agents. XXVII National Congress of the Italian Chemical Society (Web edition, September 14-23, 2021). Oral communication
10- Argenziano, R., Alfieri, M. L., Arntz, Y., Castaldo, R., **Liberti, D.**, Monti, D. M., Gentile, G., Panzella, L., Crescenzi, O., Ball, V., Napolitano, A., d'Ischia, M.. Antioxidant activity of film forming systems based on melanins from 5,6-

dihydroxyindole derivatives. 1st International E-Conference on Antioxidants in Health and Disease (CADH) (Web edition, December 1-15, 2020). Oral communication

11- Organizing committe ""In"equalities in science: a mirror of the society. An environmental pollution overview" (Naples, Web edition, December 18th, 2020)

12- Oral communication ""In"equalities in science: a mirror of the society. An environmental pollution overview" (Naples, Web edition, December 18th, 2020)

13- Argenziano, R., Alfieri, M. L., Arntz, Y., Castaldo, R., **Liberti, D.**, Monti, D. M., Gentile, G., Panzella, L., Crescenzi, O., Ball, V., Napolitano, A., d'Ischia, M.. 5,6-dihydroxyindole derivatives for melanin-based functional antioxidant and film forming systems. 1st Virtual Symposium for Young Organic Chemists of Società Chimica Italiana (October 29, 2020). Oral communication

14- D'Elia, L., Imbimbo, P., **Liberti, D.**, Olivieri, G., Pollio, A., Monti, D.M.. Identification of a potential microalgal strain for thermo resistant antioxidants production. AlgaEurope Conference France (Paris, France, December 3-5, 2019). Poster presentation

Experience in foreign laboratories:

Visiting period at University of Algarve, Faro, Portugal, from February 18th ,2022 to August 18th ,2022 in the Centre of Marine Sciences (CCMAR) under supervision of Prof. L. Barreira

Appendix A

antioxidants

MDPI

Article

A Melanin-Related Phenolic Polymer with Potent Photoprotective and Antioxidant Activities for Dermo-Cosmetic Applications

Davide Liberti, Maria Laura Alfieri, Daria Maria Monti *, Lucia Panzella * and Alessandra Napolitano

Department of Chemical Sciences, University of Naples "Federico II", Via Cintia 4, I-80126 Naples, Italy; davide.liberti@unina.it (D.L.); marialaura.alfieri@unina.it (M.L.A.); alesnapo@unina.it (A.N.)

* Correspondence: mdmonti@unina.it (D.M.M.); panzella@unina.it (L.P.); Tel.: +39-081-679150 (D.M.M.); +39-081-674131 (L.P.)

Received: 26 February 2020; Accepted: 23 March 2020; Published: 25 March 2020

check for updates

Abstract: Eumelanins, the dark variant of skin pigments, are endowed with a remarkable antioxidant activity and well-recognized photoprotective properties that have been ascribed to pigment components derived from the biosynthetic precursor 5,6-dihydroxyindole-2-carboxylic acid (DHICA). Herein, we report the protective effect of a polymer obtained starting from the methyl ester of DHICA (MeDHICA-melanin) against Ultraviolet A (UVA)-induced oxidative stress in immortalized human keratinocytes (HaCaT). MeDHICA-melanin was prepared by aerial oxidation of MeDHICA. At concentrations as low as 10 μg/mL, MeDHICA-melanin prevented reactive oxygen species accumulation and partially reduced glutathione oxidation in UVA-irradiated keratinocytes. Western blot experiments revealed that the polymer is able to induce the translocation of nuclear factor erythroid 2–related factor 2 (Nrf-2) to the nucleus with the activation of the transcription of antioxidant enzymes, such as heme-oxygenase 1. Spectrophotometric and HPLC analysis of cell lysate allowed to conclude that a significant fraction (ca. 7%), consisting mainly of the 4,4′-dimer of MeDHICA (ca. 2 μM), was internalized in the cells. Overall these data point to the potential use of MeDHICA-melanin as an antioxidant for the treatment of skin damage, photoaging and skin cancers.

Keywords: melanins; 5,6-dihydroxyindole-2-carboxylic acid; antioxidant; photoprotection; UVA; HaCaT cells; reactive oxygen species; glutathione; Nrf-2

1. Introduction

Melanins are the primary determinants of skin, hair and exoskeletal pigmentation in mammals, birds and insects [1–6], and their importance has been growing over the past few years not only from a biological point of view, related to their role in the human body, but also for the exploitation of their unique properties in biomedicine or in the cosmetic and health sectors [7–16]. These pigments are biosynthesized in melanocytes, starting with the oxidation of tyrosine to dopaquinone catalyzed by the enzyme tyrosinase (Figure 1) [1,17,18]. Dopaquinone may then undergo cyclization leading, after a further oxidation step, to 5,6-dihydroxyindole (DHI) or 5,6-dihydroxyindole-2-carboxylic acid (DHICA) whose oxidative polymerization ultimately leads to melanin pigments brown or dark in color, known as eumelanins [1,9,18]. On the other hand, entrapment of dopaquinone by cysteine, a process which is under genetic control, gives rise to isomeric cysteinyldopas whose polymerization is responsible for the biosynthesis of the reddish-brown pigments known as pheomelanins, typical of the red hair phenotype [1,19,20] (Figure 1).

Appendix A

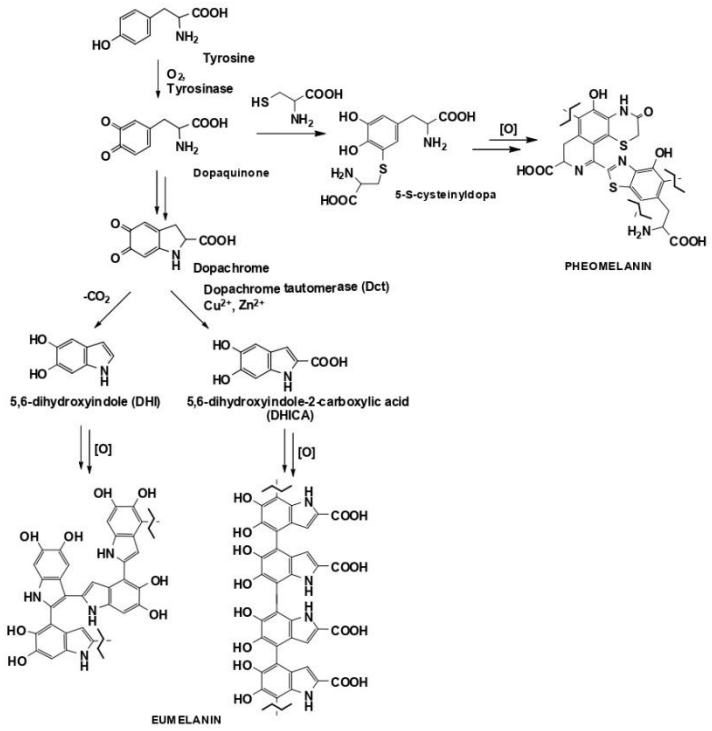

Figure 1. Biosynthetic pathways leading to eumelanins and pheomelanins.

Traditionally, eumelanins have been attributed a role as antioxidant and photoprotective agents in dark-skinned phenotypes, whereas pheomelanins have been implicated in the enhanced susceptibility to skin cancer of individuals belonging to the red-hair phenotype due to their photosensitizing and pro-oxidant properties [1,9,21–26]. Among eumelanins, bionspired synthetic pigments obtained by oxidative polymerization of DHICA have shown remarkable antioxidant properties, and have been proposed as a plausible explanation for the high content of DHICA-related units in natural eumelanins [27,28]. Indeed, DHICA-melanin is able to act as a potent hydroxyl radical scavenger in the Fenton reaction [29] and has been found to act as an efficient antioxidant and radical scavenger also in the 2,2-diphenyl-1-picrylhydrazyl (DPPH), 2,2′-azinobis(3-ethylbenzothiazoline-6-sulfonic acid) (ABTS) and nitric oxide scavenging assays [30]. DHICA-melanin also exhibited inhibition properties against in vitro lipid peroxidation [31], whereas silica/DHICA-melanin hybrid nanoparticles exerted protecting effects against hydrogen peroxide-induced cytotoxicity [32]. More recently, the higher antioxidant activity of DHICA-melanin compared to DHI-melanin has also been confirmed by the Folin–Ciocalteu assay [33].

The antioxidant properties of DHICA-melanin seem to also play a role in the maintenance of immune hyporesponsiveness to melanosomal proteins of relevance for the onset of autoimmune

Appendix A

vitiligo [34]. Recently, a natural pigment isolated from marine *Aspergillus nidulans* and tentatively identified as a DHICA-melanin exhibited protective effects against Ultraviolet B (UVB)-induced oxidative stress in cellular and mice models [35,36]. UV radiations are known to be very harmful for the human skin, as they induce reactive oxygen species (ROS) production. Both Ultraviolet A (UVA) and UVB are able to induce DNA damages [37,38]. UVB radiations induce DNA dimerization reactions between adjacent pyrimidine bases, whereas UVA radiations, weakly absorbed by DNA, can excite endogenous chromophores, leading to mispairing of DNA bases with consequent translation of mutated proteins [39].

In this context, the remarkable antioxidant properties of DHICA-melanin and its chromophoric characteristics, allowing significant absorption in the UVA region [1,9,30], would suggest its use in dermo-cosmetic formulations with photoprotective action.

Yet, full exploitation of DHICA-melanin has so far been hampered by the low solubility in lipophilic or hydroalcoholic solvents usually employed in cosmetics, and the relatively high susceptibility to (photo)degradation [40,41]. On these bases, we recently developed a variant of DHICA-melanin which was obtained by oxidative polymerization of the methyl ester of DHICA (MeDHICA-melanin) and shown to consist of a collection of intact oligomers from the dimer up to the heptamer by MALDI-MS analysis (Figure 2) [42]. The material was characterized by an intense and broad absorption band centered at 330 nm and proved to be soluble in water miscible organic solvents. Moreover, MeDHICA-melanin retained the antioxidant properties of DHICA-melanin, proving indeed even more active. It was also stable to prolonged oxidation or exposure to a solar simulator [42].

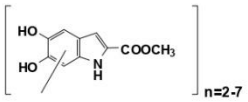

Figure 2. Structure proposed for the methyl ester of 5,6-dihydroxyindole-2-carboxylic acid (MeDHICA)-melanin based on MALDI-MS analysis [42].

Here, we report the protective effect of MeDHICA-melanin, prepared by aerial oxidation of MeDHICA, on oxidative photodamage of immortalized human keratinocytes (HaCaT) induced by UVA-exposure. Keratinocytes represent the most exposed cellular layer in the epidermis, functioning as a protective barrier from environmental stimuli, pathogens and radiation, and it is now generally recognized that molecules endowed with antioxidant activity, especially polyphenols, can strengthen the barrier function of keratinocytes from photoaging [43,44].

2. Materials and Methods

2.1. Reagents

MeDHICA was prepared as described in [42]. MeDHICA-melanin was prepared by aerial oxidation of MeDHICA in phosphate buffer at pH 8.5, as previously reported [42]. Phosphate buffer saline (PBS), Dulbecco's modified Eagle's medium (DMEM), fetal bovine serum (HyClone), 3-(4,5-dimethylthiazol-2-yl)-2,5-diphenyltetrazolium bromide (MTT), 2′,7′-dichlorodihydrofluorescein diacetate (H_2DCFDA), L-glutamine, trypsin-EDTA, Triton, 5,5′-dithiobis-2-nitrobenzoic acid (DTNB), thiobarbituric acid (TBA), and Bradford reagent were from Sigma-Aldrich (St. Louis, MI, USA). Bicinchoninic acid (BCA) protein assay kit was from Thermo Scientific (Waltham, MA, USA). Antibodies against nuclear factor erythroid 2–related factor 2 (Nrf-2) and heme oxygenase 1 (HO-1) were from Cell Signal Technology (Danvers, MA, USA). Antibodies against B-23 and β-actin and the chemiluminescence detection system (SuperSignal® West Pico) were from Thermo Fisher Scientific (Waltham, MA, USA).

Appendix A

2.2. Cell Culture

Human immortalized keratinocytes (HaCaT) were from Innoprot (Derio, Spain). Cells were cultured in DMEM, supplemented with 10% fetal bovine serum, 2 mM L-glutamine and antibiotics in a 5% CO_2 humidified atmosphere at 37 °C. Every 48 h, cells were refreshed in a ratio 1:5. The culture medium was removed and cells were rinsed with PBS and then detached with trypsin-EDTA. After centrifugation (5 min at 1000 rpm), cells were diluted in fresh medium.

2.3. Analysis of Cell Viability

Cells were seeded in 96-well plates (100 µL/well) at a density of 2.5×10^3 cells/cm^2. 24 h after seeding, cells were incubated with increasing concentrations (0.1, 1, 5 and 10 µg/mL) of MeDHICA-melanin. Mother solutions of MeDHICA-melanin were prepared in DMSO at a concentration of 0.2 mg/mL and proper aliquots were added to the incubation medium to get the desired concentration. After 24 h and 48 h incubation, cell viability was assessed by the MTT assay. The MTT reagent, dissolved in DMEM without phenol red, was added to the cells (0.5 mg/mL). After 4 h at 37 °C, the culture medium containing MTT was removed and the resulting formazan salt was dissolved in 2-propanol containing 0.01 M HCl (100 µL/well). Absorbance values of blue formazan were determined at 570 nm using an automatic plate reader (Microbeta Wallac 1420, Perkin Elmer, Milano, Italy). Cell survival was expressed as the percentage of viable cells in the presence of MeDHICA-melanin compared to the controls, represented by untreated cells and cells supplemented with identical volumes of DMSO, in order to exclude a possible effect of DMSO on cell viability.

2.4. UVA irradiation and H_2DCFDA Assay

To evaluate the protective effect of MeDHICA-melanin against oxidative stress, cells were plated at a density of 3.5×10^4 cells/cm^2 (in 60 mm eukaryotic cell plates), pre-incubated in the presence of increasing concentration (0.1–10 µg/mL) of MeDHICA-melanin for different lengths of time (from 5 to 120 min) and stressed by UVA light for 10 min (100 J/cm^2) [45]. Then, cells were incubated with the cell permeable, redox-sensitive fluorophore H_2DCFDA at a concentration of 20 µM for 30 min at 37 °C. Cells were then washed with cold PBS 2 times, detached by trypsin, centrifuged at 1000 rpm for 10 min and resuspended in PBS containing 30 mM glucose, 1 mM $CaCl_2$, and 0.5 mM $MgCl_2$ (PBS plus) at a cell density of 1×10^5 cells/mL. H_2DCFDA is nonfluorescent until it is hydrolyzed by intracellular esterases, and in the presence of ROS it is readily oxidized to the highly fluorescent 2′,7′-dichlorofluorescein (DCF). DCF fluorescence intensity was measured at an emission wavelength of 525 nm with excitation wavelength set at 488 nm using a Perkin-Elmer LS50 spectrofluorometer (Perkin Elmer, Milano, Italy). Emission spectra were acquired at a scanning speed of 300 nm/min, with 5 slit widths for excitation and emission. ROS production was expressed as percentage of DCF fluorescence intensity of the sample under test, with respect to the untreated sample.

2.5. Western Blot Analysis

HaCaT cells were plated at a density of 3.5×10^4 cells/cm^2 (100 mm eukaryotic cell plates) in complete medium for 24 h and then treated with 10 µg/mL of MeDHICA-melanin for 5, 15, 30 and 60 min. To extract nuclear proteins, cells were first incubated with PBS buffer containing 0.1% Triton and protease inhibitors to extract cytosolic proteins. After centrifugation at 1200 rpm for 10 min, nuclear pellet was obtained and proteins were extracted by resuspending the pellet in radioimmunoprecipitation assay buffer (RIPA) buffer (150 mM NaCl, 1% NP-40, 0.1% SDS, proteases inhibitors in 50 mM Tris-HCl pH 8.0). Proteins were quantified by BCA protein assay kit. Western blotting was used to analyze 100 µg of proteins, as reported [46]. Nuclear factor erythroid 2–related factor 2 (Nrf-2) and heme oxygenase 1 (HO-1) levels were detected by using specific antibodies. To normalize protein intensity levels, specific antibodies against B-23 and β-actin were used for nuclear and cytosolic extracts, respectively. Signals were detected by using the chemiluminescence detection system.

Appendix A

2.6. Catalase Assay

HaCaT cells were plated at a density of 3.5×10^4 cells/cm^2 (in a 100 mm eukaryotic cell plate) in complete medium for 24 h and then treated with 10 μg/mL of MeDHICA-melanin for 60 min. At the end of the experiment, total cell lysate was obtained by resuspending each cell pellet in 50 μL of lysis buffer (100 mM Tris-HCl, 300 mM NaCl and 0.5% NP-40 at pH 7.4 with addition of inhibitors of proteases and phosphatases). Proteins were quantified by BCA protein assay kit. To measure catalase activity, a procedure reported in the existing literature was followed [47]. Briefly, cell lysates (50 μg of proteins) were incubated for 30 min at room temperature in 1 mL of hydrogen peroxide solution (50 mM potassium phosphate buffer, pH 7.0, 0.036% *w/w* H_2O_2). Then, the hydrogen peroxide concentration in solution was determined by measuring the absorbance at 240 nm. The percentage of peroxide removed was calculated as following:

$$\%\ H_2O_2 \text{ reduced} = 1 - OD_{240nm} \text{ sample}/OD_{240nm} \text{ standard}$$

Standard is referred to the hydrogen peroxide solution in the absence of lysate and measured at 240 nm after 30 min of incubation.

2.7. Determination of Intracellular Glutathione (GSH) Levels

HaCaT cells were plated at a density of 3.5×10^4 cells/cm^2 (60 mm eukaryotic cell plates) in complete medium for 24 h and then treated with 10 μg/mL of MeDHICA-melanin for 60 min. At the end of the photoirradiation experiment, cells were lysed, and protein concentration was determined by the Bradford colorimetric assay. Proteins (50 μg) were incubated in the presence of 3 mM EDTA, 144 μM DTNB in 30 mM Tris-HCl at pH 8.2, and centrifuged at 13,000 rpm for 5 min at 4 °C. Supernatants were collected, and the absorbance was measured at 412 nm by using a multiplate reader (Bio-Rad, Hercules, CA, USA). GSH levels were expressed as % of the sample under test with respect to the untreated sample.

2.8. Analysis of Lipid Peroxidation Levels

HaCaT cells were seeded at a density of 3.5×10^4 cells/cm^2 (100 mm eukaryotic cell plates) in complete medium for 24 h and then treated with 10 μg/mL of MeDHICA-melanin for 120 min. After UVA irradiation, cells were kept at 37 °C for 90 min, before performing the thiobarbituric acid reactive substances (TBARS) assay as described [48]. Briefly, cells were detached and 5×10^4 cells suspended in 0.67% TBA containing 20% trichloroacetic acid (TCA) (1:1 *v/v*). After heating for 30 min at 100 °C, samples were centrifuged at 2500 rpm for 5 min at 4 °C, and supernatants spectrophotometrically analyzed at 532 nm.

2.9. Quantification of Internalized Melanin

HaCaT cells were plated at a density of 3.5×10^4 cells/cm^2 (100 mm eukaryotic cell plates) in complete medium for 24 h and then treated with 10 μg/mL of MeDHICA-melanin for 60 min. After treatment, total cell lysate was obtained, 50 μg of proteins (Bradford assay) were diluted in 1 mL of potassium phosphate buffer (50 mM, pH 7.0) and UV-vis spectra were recorded. The amount of MeDHICA-melanin internalized by the cells was determined by using a calibration curve obtained with pure MeDHICA-melanin. In particular, increasing concentrations (0.6–20 μg/mL) of MeDHICA-melanin, alone or in the presence of 50 μg of cell lysate, were used to record the UV-vis spectra. The calibration curve was built by plotting values of absorbance at 330 nm against MeDHICA-melanin concentration.

2.10. HPLC and LC-MS Analysis of Cell Lysate

HPLC analysis was performed on an instrument (Agilent 1100, Santa Clara, CA, USA) equipped with a binary pump and a SPD-10AV VP UV-vis detector set at 300 nm. The chromatographic separation was achieved on a Sphereclone octadecylsilane-coated column, 250 mm × 4.6 mm, 5 μm particle size

Appendix A

(Phenomenex, Torrance, CA, USA) at 0.7 mL/min using binary gradient elution conditions as follows: 0.1% formic acid (solvent A), acetonitrile (solvent B) from 35% to 70%, 0–45 min. LC-MS analyses were run on a LC-MS ESI-TOF 1260/6230DA Agilent instrument operating in positive ionization mode in the following conditions: Nebulizer pressure 35 psig; drying gas (nitrogen) 5 L/min, 325 °C; capillary voltage 3500 V; fragmentor voltage 175 V. An Eclipse Plus C18 column, 150 × 4.6 mm, 5 µm (Agilent), at a flow rate of 0.4 mL/min was used, using the same eluant as above. The cell lysate, obtained as described in Section 2.9, was lyophilized and subjected to acetylation treatment with acetic anhydride (500 µL) and pyridine (75 µL) overnight. After repeated washings with methanol to remove solvents, the residue was taken up in methanol and analyzed by HPLC and LC-MS. A control lysate sample obtained in the absence of MeDHICA-melanin was also analyzed.

2.11. Statistical Analysis

In all the experiments, each sample was tested in three independent analyses, each carried out in triplicate. The results are presented as mean of results obtained (mean ± SD) and compared by one-way ANOVA following Tukey's multiple comparison test using Graphpad Prism for Windows, version 6.01 (San Diego, CA, USA).

3. Results and Discussion

3.1. Biocompatibility of MeDHICA-Melanin on Keratinocytes

In order to assess the possible use of MeDHICA-melanin for cosmetic applications, its biocompatibility was tested on immortalized human keratinocytes (HaCaT), as these cells are normally present in the outermost layer of the skin. Increasing amounts of MeDHICA-melanin (from 0.1 to 10 µg/mL) were incubated with the cells for 24 and 48 h. At the end of each incubation, cell viability was assessed by the MTT assay. As shown in Figure 3, cell viability was not affected at any of the experimental conditions tested, neither after 24 h nor after 48 h incubation, thus suggesting that MeDHICA-melanin was fully biocompatible on HaCaT cells.

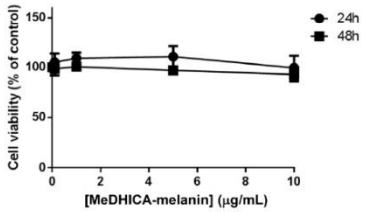

Figure 3. Effects of MeDHICA-melanin on HaCaT cells viability. Dose-response curves after 24 h (black circles) and 48 h (black squares) incubation of HaCaT cells with increasing concentration of MeDHICA-melanin (0.1–10 µg/mL). Cell viability was assessed by the MTT assay and cell survival expressed as percentage of viable cells in the presence of MeDHICA-melanin, with respect to control cells (i.e., cells grown in the absence of the melanin). The results shown are means ± SD of three independent experiments.

3.2. Inhibition of UVA-Induced Damage on HaCaT Cells by MeDHICA-Melanin

To assess the protective effect of MeDHICA-melanin against photoinduced oxidative stress, irradiation with UVA was chosen as a source of stress as this has been shown to induce many side effects on human skin [49]. A dose-response experiment was first performed to evaluate the optimal MeDHICA-melanin concentration to be used. HaCaT cells were incubated with increasing

Appendix A

concentrations of MeDHICA-melanin (0.1–10 μg/mL) for 2 h prior to UVA irradiation treatment, and immediately after irradiation ROS production was evaluated by the H_2DCFDA assay.

As shown in Figure 4A, DCF fluorescence was significantly increased after UVA irradiation (2.3 fold increase, $p < 0.005$), whereas MeDHICA-melanin had no effect on ROS levels on non-irradiated cells. Interestingly, when cells were preincubated with MeDHICA-melanin prior to UVA exposure, ROS production was decreased in a dose dependent manner, and reached the levels observed in non-irradiated cells when the melanin was tested at 10 μg/mL ($p < 0.005$) (Figure 4A).

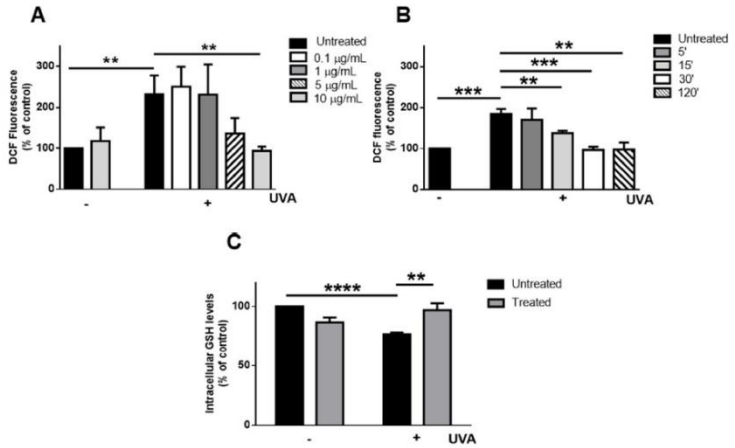

Figure 4. Antioxidant effects of MeDHICA-melanin on UVA-stressed HaCaT cells. (**A**) Dose-response analysis of intracellular ROS levels by 2′,7′-dichlorodihydrofluorescein diacetate (H_2DCFDA) assay. Cells were pre-incubated with increasing concentrations of MeDHICA-melanin for 2 h prior to UVA irradiation (100 J/cm^2) for 10 min. Cells were incubated with 0.1 μg/mL (white bars), 1 μg/mL (dark grey bars), 5 μg/mL (dashed bars) or 10 μg/mL (light grey bars) MeDHICA-melanin. Black bars refer to untreated cells. (**B**) Time-course analysis of intracellular ROS levels by H_2DCFDA assay. Cells were incubated for 5 min (dark grey bars), 15 min (light grey bars), 30 min (white bars) or 120 min (dashed bars) with MeDHICA-melanin before being irradiated by UVA. Black bars are referred to untreated cells. (**C**) Intracellular GSH levels evaluated by 5,5′-dithiobis-2-nitrobenzoic acid (DTNB) assay. Cells were pre-incubated with MeDHICA-melanin (10 μg/mL) for 1 h before UVA irradiation. Values are expressed as % with respect to control (i.e. untreated) cells. Data shown are means ± SD of three independent experiments. ** indicates $p < 0.005$, *** indicates $p < 0.0005$, **** indicates $p < 0.0001$.

The effect of the preincubation time with MeDHICA-melanin on ROS production was also evaluated (Figure 4B). A significant protection against UVA damage was observed already after 15 min of incubation with 10 μg/mL of MeDHICA-melanin ($p < 0.005$). These data confirmed the potent antioxidant activity of MeDHICA-melanin [42] also in a cellular model, further highlighting its potential as an active ingredient in cosmetic formulations when compared to other natural or synthetic materials, such as phenol-rich plant extracts or other melanin-related samples. As an example, 10-fold higher concentrations (100 μg/mL) and longer pre-incubation times (1 h) have been reported in the case of a water extract from red grapevine leaves containing high levels of polyphenols to observe an effect comparable to that of the present study on the decrease of ROS generation in HaCaT cells irradiated with lower doses of UVA (25 J/cm^2) [38]. Also, the activity of silymarin was much lower than that

Appendix A

observed with MeDHICA-melanin: 30 min of pre-incubation with 250 μg/mL of the compound were able to reduce the ROS produced by irradiating HaCaT cells with 20 J/cm^2 UVA by only 30% [50].

Based on these promising results, subsequent experiments were carried using 10 μg/mL MeDHICA-melanin.

The intracellular levels of GSH were evaluated in view of the important role of this biomolecule in the cellular redox balance, and the decrease associated to oxidative stress [51]. Following UVA irradiation, a 25% decrease ($p < 0.0001$) of intracellular GSH levels was observed with respect to control cells, whereas GSH levels were unaltered in cells preincubated with MeDHICA-melanin (Figure 4C). Similar effects have been reported on UVA-irradiated HaCaT cells for phenol-rich extracts from *Eugenia uniflora* [52] and *Syzygium aqueum* [53] leaves, which, however, had to be tested at higher concentrations (50 μg/mL) and for a longer time (2 h) to show a protective effect.

The different behavior of all these samples compared to MeDHICA-melanin can be ascribed to differences in the chemical structures of the compounds tested, determining crucial variations not only in the intrinsic antioxidant activity, but also in the cell-permeation ability as well as in the UVA-interaction properties.

The protective effects of MeDHICA-melanin on HaCaT cells were further confirmed by analyzing the lipid peroxidation levels 90 min after irradiation (Figure S1). The results indicated that MeDHICA-melanin was able to keep lipid peroxidation unaltered. In fact, cells pretreated with MeDHICA-melanin and then exposed to UVA radiation showed a significantly lower intracellular level of lipid peroxidation when compared to untreated cells exposed to UVA (50% decrease, $p < 0.005$) (Figure S1). Notably, a lower protective effect against lipid peroxidation has been reported for the well-recognized antioxidant pterostilbene in 20 J/cm^2 UVA irradiated-HaCaT cells after 24 h pretreatment with 2.5 μg/mL of the compound [54]. However, a significant increase in lipid peroxidation levels was observed in cells incubated only with MeDHICA-melanin (2.4 fold increase), without photoirradiation, an intriguing observation that will be addressed in future studies. In any case, the overall results clearly indicate that MeDHICA-melanin is able to protect HaCaT cells from UVA-induced oxidative stress.

3.3. Induction of Nrf-2 Nuclear Translocation by MeDHICA-Melanin

The MeDHICA-melanin protective effect was analyzed at a molecular level by studying the involvement of Nrf-2. Under normal physiological conditions, the complex between Nrf-2 and Keap-1 keeps Nrf-2 in the cytosol and the protein is degraded through the proteasome. Oxidative stress, or small amounts of antioxidants, induce the dissociation between Keap-1 and Nrf-2, and the latter is translocated to the nucleus. Once in the nucleus, it binds to antioxidant responsive element (ARE) sequences and activates the transcription of several phase-II detoxifying enzymes, such as HO-1 and catalase [55]. Thus, cells were incubated with MeDHICA-melanin for 5, 15 and 30 min and then nuclear Nrf-2 levels were evaluated by Western blot analyses. As shown in Figure 5A, a significant increase of Nrf-2 nuclear levels was observed after 30 min of incubation (about 2 fold increase, $p < 0.005$). Nrf-2 activation was confirmed by measuring HO-1 levels (Figure 5B), which were found to significant increase after 60 min incubation of the cells with MeDHICA-melanin (about 2 fold increase, $p < 0.05$). Nrf-2 activation was also confirmed by measuring consumption of H_2O_2 added to the incubation medium, that could indirectly indicate the activity of catalase. As reported in Figure 5C, the levels of H_2O_2 detected in keratinocyte lysates were lower (33% decrease, $p < 0.05$) in the cells after incubation with MeDHICA-melanin with respect to the control sample.

Appendix A

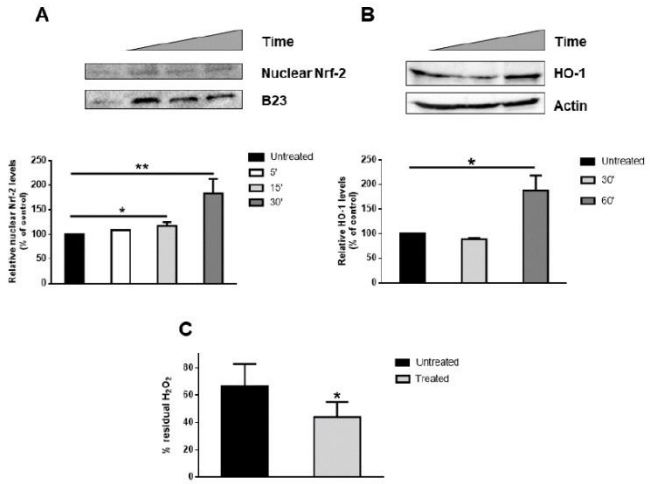

Figure 5. MeDHICA-melanin effects on Nrf-2 activation in HaCaT cells. Cells were incubated with MeDHICA-melanin (10 μg/mL) for different lengths of time, and (**A**) nuclear Nrf-2, or (**B**) cytosolic HO-1 proteins were analyzed by Western blotting. (**A**) HaCaT cells were incubated with MeDHICA-melanin for 5 min (white bars), 15 min (light grey bars) and 30 min (dark grey bars) and then nuclear proteins extracted to perform Western blot analysis of Nrf-2. Nrf-2 was quantified by densitometric analysis and normalized to B-23. (**B**) Western blot analysis for HO-1 performed on cytosolic proteins obtained from HaCaT cells after incubation with MeDHICA-melanin for 30 min (light grey bars) and 60 min (dark grey bars). HO-1 was quantified by densitometric analysis and normalized to β-Actin. (**C**) Cells were incubated with melanin (10 μg/mL) for 1 h and then 50 μg of cell lysate were incubated with 0.036% w/w H_2O_2. Hydrogen peroxide concentration in solution was determined by measuring the absorbance at 240 nm. Black bars are referred to control cells. Data shown are means ± SD of three independent experiments. * indicates $p < 0.05$ ** indicates $p < 0.005$.

3.4. Cellular Uptake of MeDHICA-Melanin

In order to verify whether MeDHICA-melanin was internalized in the cells, HaCaT cells were incubated with MeDHICA-melanin at 10 μg/mL for 60 min, after that the total cell lysate was obtained. UV–vis spectra of lysates from untreated and treated cells were recorded and the amount of melanin internalized by the cells was estimated to be about 7% using a measurement of the absorbance at 330 nm of treated cells lysate and a comparison with the calibration curve obtained by using pure MeDHICA-melanin (Figure 6). This result is in agreement with the by now well-established idea that melanin is internalized by cells to serve as a protective agent [56].

MeDHICA-melanin internalization was further corroborated by HPLC analysis of the cell lysate upon incubation with the pigment. To improve the chromatographic properties and the stability, the cell lysate obtained by HaCaT incubation with 10 μg/mL of MeDHICA-melanin was acetylated with acetic anhydride-pyridine overnight at room temperature and then analyzed by HPLC (Figure 7A).

Comparison of the elutographic properties with those of an authentic standard [42] allowed to identify the compound eluted at 19 min as the acetylated derivatives of the 4,4′-dimer of MeDHICA (ca. 2 μM). The identity of this product was further confirmed by LC-MS analysis ($[M+H]^+$ for acetylated dimer = 581 *m/z*) (Figure 7B,C).

Appendix A

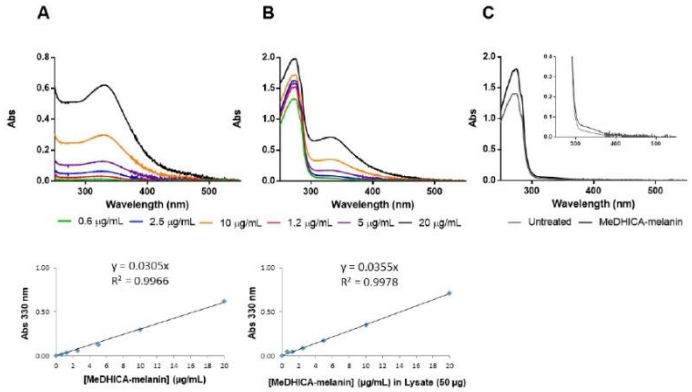

Figure 6. Quantification of internalized MeDHICA-melanin. Increasing concentrations (0.6–20 μg/mL) of MeDHICA-melanin, (**A**) alone, or (**B**) in the presence of 50 μg of cell lysate, were used to record the UV–vis spectra. Calibration curves built by plotting values of absorbance at 330 nm against MeDHICA-melanin concentration are also shown. (**C**) UV–vis spectra of untreated cells (grey line) and MeDHICA-melanin treated (black line) HaCaT cells.

4. Conclusions

UVA radiations are highly harmful as they can penetrate the skin, crossing the epidermis and reaching the dermis. They are responsible for a variety of physiopathological conditions, ranging from inflammation to premature skin aging and skin cancer development [45,57,58]. On the other hand, the antioxidant and photoprotective properties of eumelanins and model pigments from DHICA are well-established [29,30,41,42].

In this paper, MeDHICA-melanin, previously shown to possess marked in vitro antioxidant activity and favorable solubility properties for dermo-cosmetic applications [42], was demonstrated to exert protective effects on a cellular model of immortalized keratinocytes (HaCaT) exposed to UVA radiations. All the endpoint parameters of oxidative stress, i.e., ROS, lipid peroxidation, and intracellular oxidized glutathione levels, were significantly inhibited in cells incubated with MeDHICA-melanin at concentrations compatible with cell viability. Moreover, a comparison with related findings recently reported in the literature on natural phenols or phenol-rich extracts further highlighted the advantages of MeDHICA-melanin.

Similarly to other natural antioxidants [58], MeDHICA-melanin also proved to provide protection by activating the Nrf-2 pathway. Indeed, the nuclear translocation of Nrf-2 was effective, as demonstrated by the activation of downstream genes. To our knowledge, this is the first report on the correlation between the antioxidant activity of melanins and the Nrf-2 pathway. We also demonstrated that MeDHICA-melanin was able to enter keratinocytes, although, as expected, only

Low molecular weight components such as dimeric compounds were appreciably internalized after 1 h incubation. These data provide further confirmation to biological studies indicating that keratinocytes are able to internalize melanins as the result of a cross-talk with melanocytes, mediated by the protease-activated receptor 2 (PAR-2) and the Ras-related protein Rab11 [59,60]. Overall, our findings demonstrate that MeDHICA-melanin is able to enter the cells and activate the antioxidant system to protect skin cells from UVA-induced damage, encouraging its use as an effective component in dermo-cosmetic formulations for the treatment of skin damage, photoaging and skin cancers.

Appendix A

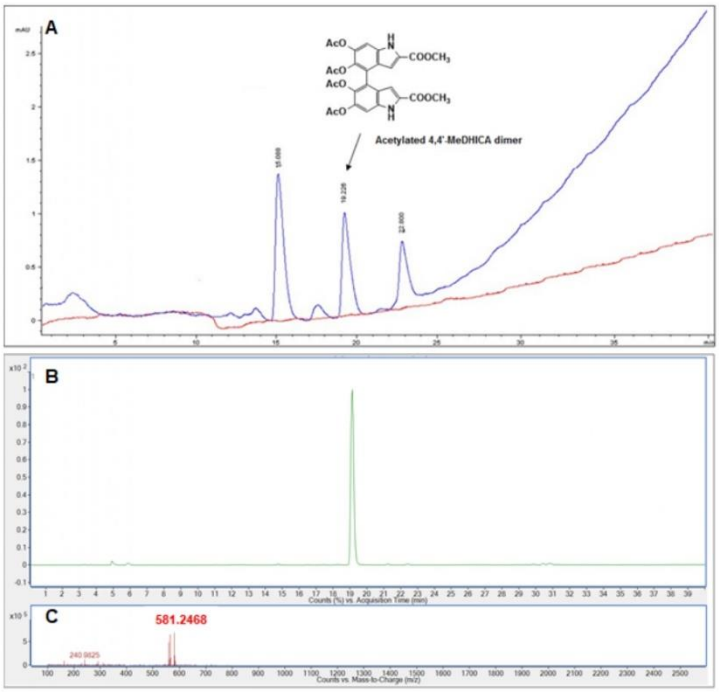

Figure 7. HPLC and LC-MS analysis of cell lysate. (**A**) HPLC profile of acetylated cell lysate (blue trace) and acetylated lysate from control cells (not incubated with MeDHICA-melanin) (red trace). (**B**) LC-MS extracted ion chromatogram (*m/z* 581). (**C**) MS spectrum of the compound eluted at 19 min.

Supplementary Materials: The following are available online at http://www.mdpi.com/2076-3921/9/4/270/s1, Figure S1: Lipid peroxidation levels evaluated by TBARS assay.

Author Contributions: Conceptualization, D.M.M., L.P. and A.N.; methodology, D.M.M., L.P. and A.N.; validation, D.M.M., L.P. and A.N.; investigation, D.L and M.L.A.; data curation, D.M.M., L.P. and A.N.; writing—original draft preparation, D.L., M.L.A, D.M.M and L.P.; writing—review and editing, D.M.M., L.P. and A.N. All authors have read and agreed to the published version of the manuscript.

Funding: This research was funded in part by Kao Corporation.

Conflicts of Interest: The authors declare no conflict of interest.

References

1. Micillo, R.; Panzella, L.; Koike, K.; Monfrecola, G.; Napolitano, A.; D'Ischia, M. "Fifty shades" of black and red or how carboxyl groups fine tune eumelanin and pheomelanin properties. *Int. J. Mol. Sci.* **2016**, *17*, 746. [CrossRef] [PubMed]
2. Galvan, I.; Solano, F. Bird integumentary melanins: Biosynthesis, forms, function and evolution. *Int. J. Mol. Sci.* **2016**, *17*, 520. [CrossRef] [PubMed]

Appendix A

3. Del Bino, S.; Duval, C.; Bernerd, F. Clinical and biological characterization of skin pigmentation diversity and its consequences on UV impact. *Int. J. Mol. Sci.* **2018**, *19*, 2668. [CrossRef] [PubMed]
4. Miyamura, Y.; Coelho, S.G.; Wolber, R.; Miller, S.A.; Wakamatsu, K.; Zmudzka, B.Z.; Ito, S.; Smuda, C.; Passeron, T.; Choi, W.; et al. Regulation of human skin pigmentation and responses to ultraviolet radiation. *Pigment Cell Res.* **2007**, *20*, 2–13. [CrossRef]
5. Ito, S.; Wakamatsu, K. Diversity of human hair pigmentation as studied by chemical analysis of eumelanin and pheomelanin. *J. Eur. Acad. Dermatol. Venereol.* **2011**, *25*, 1369–1380. [CrossRef]
6. Sugumaran, M.; Barek, H. Critical analysis of the melanogenic pathway in insects and higher animals. *Int. J. Mol. Sci.* **2016**, *17*, 1753. [CrossRef]
7. Meredith, P.; Sarna, T. The physical and chemical properties of eumelanin. *Pigment Cell Res.* **2006**, *19*, 572–594. [CrossRef]
8. Xie, W.; Pakdel, E.; Liang, Y.; Kim, Y.J.; Liu, D.; Sun, L.; Wang, X. Natural eumelanin and its derivatives as multifunctional materials for bioinspired applications: A review. *Biomacromolecules* **2019**, *20*, 4312–4331. [CrossRef]
9. Panzella, L.; Ebato, A.; Napolitano, A.; Koike, K. The late stages of melanogenesis: Exploring the chemical facets and the application opportunities. *Int. J. Mol. Sci.* **2018**, *19*, 1753. [CrossRef]
10. D'Ischia, M. Melanin-based functional materials. *Int. J. Mol. Sci.* **2018**, *19*, 228. [CrossRef]
11. Solano, F. Melanin and melanin-related polymers as materials with biomedical and biotechnological applications-cuttlefish ink and mussel foot proteins as inspired biomolecules. *Int. J. Mol. Sci.* **2017**, *18*, 1561. [CrossRef] [PubMed]
12. Huang, L.; Liu, M.; Huang, H.; Wen, Y.; Zhang, X.; Wei, Y. Recent advances and progress on melanin-like materials and their biomedical applications. *Biomacromolecules* **2018**, *19*, 1858–1868. [CrossRef] [PubMed]
13. Barra, M.; Bonadies, I.; Carfagna, C.; Cassinese, A.; Cimino, F.; Crescenzi, O.; Criscuolo, V.; D'Ischia, M.; Maglione, M.G.; Manini, P.; et al. Eumelanin-based organic bioelectronics: Myth or reality? *MRS Adv.* **2016**, *1*, 3801–3810. [CrossRef]
14. D'Ischia, M.; Wakamatsu, K.; Cicoira, F.; Di Mauro, E.; Garcia-Borron, J.C.; Commo, S.; Galvan, I.; Ghanem, G.; Kenzo, K.; Meredith, P.; et al. Melanins and melanogenesis: From pigment cells to human health and technological applications. *Pigment Cell Melanoma Res.* **2015**, *28*, 520–544. [CrossRef] [PubMed]
15. Longo, D.L.; Stefania, R.; Aime, S.; Oraevsky, A. Melanin-based contrast agents for biomedical optoacoustic imaging and theranostic applications. *Int. J. Mol. Sci.* **2017**, *18*, 1719. [CrossRef]
16. D'Ischia, M.; Napolitano, A.; Pezzella, A.; Meredith, P.; Buehler, M.J. Melanin biopolymers: Tailoring chemical complexity for materials design. *Angew. Chem. Int. Ed.* **2019**. [CrossRef]
17. Panzella, L.; Napolitano, A. Natural and bioinspired phenolic compounds as tyrosinase inhibitors for the treatment of skin hyperpigmentation: Recent advances. *Cosmetics* **2019**, *6*, 57. [CrossRef]
18. Ito, S.; Wakamatsu, K.; D'Ischia, M.; Napolitano, A.; Pezzella, A. Structure of Melanins. In *Melanins and Melanosomes*; Borovansky, J., Riley, P.A., Eds.; Wiley: Weinheim, Germany, 2011; pp. 167–185.
19. Ito, S.; Wakamatsu, K. Chemistry of mixed melanogenesis—Pivotal roles of dopaquinone. *Photochem. Photobiol.* **2008**, *84*, 582–592. [CrossRef]
20. Napolitano, A.; Panzella, L.; Leone, L.; D'Ischia, M. Red hair benzothiazines and benzothiazoles: Mutation-inspired chemistry in the quest for functionality. *Acc. Chem. Res.* **2013**, *46*, 519–528. [CrossRef]
21. Kang, M.; Kim, E.; Temocin, Z.; Li, J.; Dadachova, E.; Wang, Z.; Panzella, L.; Napolitano, A.; Bentley, W.E.; Payne, G. Reverse engineering to characterize redox properties: Revealing melanin's redox activity through mediated electrochemical probing. *Chem. Mater.* **2018**, *30*, 5814–5826. [CrossRef]
22. Kim, E.; Panzella, L.; Napolitano, A.; Payne, G.F. Redox activities of melanins investigated by electrochemical reverse engineering: Implications for their roles in oxidative stress. *J. Invest. Dermatol.* **2020**, *140*, 537–543. [CrossRef] [PubMed]
23. Napolitano, A.; Panzella, L.; Monfrecola, G.; D'Ischia, M. Pheomelanin-induced oxidative stress: Bright and dark chemistry bridging red hair phenotype and melanoma. *Pigment Cell Melanoma Res.* **2014**, *27*, 721–733. [CrossRef]
24. Morgan, A.M.; Lo, J.; Fisher, D.E. How does pheomelanin synthesis contribute to melanomagenesis? Two distinct mechanisms could explain the carcinogenicity of pheomelanin synthesis. *BioEssays* **2013**, *35*, 672–676. [CrossRef] [PubMed]

Appendix A

25. Abdel-Malek, Z.A.; Ito, S. Being in the red: A no-win situation with melanoma. *Pigment Cell Melanoma Res.* **2013**, *26*, 164–166. [CrossRef]
26. Ito, S.; Wakamatsu, K.; Sarna, T. Photodegradation of eumelanin and pheomelanin and its pathophysiological implications. *Photochem. Photobiol.* **2018**, *94*, 409–420. [CrossRef]
27. Panzella, L.; Napolitano, A.; D'Ischia, M. Is DHICA the key to dopachrome tautomerase and melanocyte functions? *Pigment Cell Melanoma Res.* **2011**, *24*, 248–249. [CrossRef]
28. Kovacs, D.; Flori, E.; Maresca, V.; Ottaviani, M.; Aspite, N.; Dell'Anna, M.L.; Panzella, L.; Napolitano, A.; Picardo, M.; D'Ischia, M. The eumelanin intermediate 5,6-dihydroxyindole-2-carboxylic acid is a messenger in the cross-talk among epidermal cells. *J. Invest. Dermatol.* **2012**, *132*, 1196–1205. [CrossRef]
29. Jiang, S.; Liu, X.M.; Dai, X.; Zhou, Q.; Lei, T.C.; Beermann, F.; Wakamatsu, K.; Xu, S.Z. Regulation of DHICA-mediated antioxidation by dopachrome tautomerase: Implication for skin photoprotection against UVA radiation. *Free Radic. Biol. Med.* **2010**, *48*, 1144–1151. [CrossRef]
30. Panzella, L.; Gentile, G.; D'Errico, G.; Della Vecchia, N.F.; Errico, M.E.; Napolitano, A.; Carfagna, C.; D'Ischia, M. Atypical structural and π-electron features of a melanin polymer that lead to superior free-radical-scavenging properties. *Angew. Chem. Int. Ed.* **2013**, *52*, 12684–12687. [CrossRef]
31. Blarzino, C.; Mosca, L.; Foppoli, C.; Coccia, R.; De Marco, C.; Rosei, M.A. Lipoxygenase/H_2O_2-catalyzed oxidation of dihydroxyindoles: Synthesis of melanin pigments and study of their antioxidant properties. *Free Radic. Biol. Med.* **1998**, *26*, 446–453. [CrossRef]
32. Silvestri, B.; Vitiello, G.; Luciani, G.; Calcagno, V.; Costantini, A.; Gallo, M.; Parisi, S.; Paladino, S.; Iacomino, M.; D'Errico, G.; et al. Probing the eumelanin-silica interface in chemically engineered bulk hybrid nanoparticles for targeted subcellular antioxidant protection. *ACS Appl. Mater. Interfaces* **2017**, *9*, 37615–37622. [CrossRef] [PubMed]
33. Cecchi, T.; Pezzella, A.; Di Mauro, E.; Cestola, S.; Ginsburg, D.; Luzi, M.; Rigucci, A.; Santato, C. On the antioxidant activity of eumelanin biopigments: A quantitative comparison between free radical scavenging and redox properties. *Nat. Prod. Res.* **2019**, 1–9. [CrossRef] [PubMed]
34. Liu, X.-M.; Zhou, Q.; Xu, S.-Z.; Wakamatsu, K.; Lei, T.-C. Maintenance of immune hyporesponsiveness to melanosomal proteins by DHICA-mediated antioxidation: Possible implications for autoimmune vitiligo. *Free Radic. Biol. Med.* **2011**, *50*, 1177–1185. [CrossRef] [PubMed]
35. Shanuja, S.K.; Iswarya, S.; Gnanamani, A. Marine fungal DHICA as a UVB protectant: Assessment under in vitro and in vivo conditions. *J. Photochem. Photobiol. B* **2018**, *179*, 139–148. [CrossRef]
36. Shanuja, S.K.; Iswarya, S.; Rajasekaran, S.; Dinesh, M.G.; Gnanamani, A. Pre-treatment of extracellular water soluble pigmented secondary metabolites of marine imperfect fungus protects HDF cells from UVB induced oxidative stress. *Photochem. Photobiol. Sci.* **2018**, *17*, 1229–1238. [CrossRef]
37. Baron, Y.; Corre, S.; Mouchet, N.; Vaulont, S.; Prince, S.; Galibert, M.D. USF-1 is critical for maintaining genome integrity in response to UV-induced DNA photolesions. *PLoS Genet.* **2012**, *8*, e1002470. [CrossRef]
38. Marabini, L.; Melzi, G.; Lolli, F.; Dell'Agli, M.; Piazza, S.; Sangiovanni, E.; Marinovich, M. Effects of *Vitis vinifera* L. leaves extract on UV radiation damage in human keratinocytes (HaCaT). *J. Photochem. Photobiol. B* **2020**, *204*, 111810. [CrossRef]
39. Aust, A.E.; Eveleigh, J.F. Mechanisms of DNA oxidation. *Proc. Soc. Exp. Biol. Med.* **1999**, *222*, 246–252. [CrossRef]
40. Szewczyk, G.; Zadlo, A.; Sarna, M.; Ito, S.; Wakamatsu, K.; Sarna, T. Aerobic photoreactivity of synthetic eumelanins and pheomelanins: Generation of singlet oxygen and superoxide anion. *Pigment Cell Melanoma Res.* **2016**, *29*, 669–678. [CrossRef]
41. Ito, S.; Kikuta, M.; Koike, S.; Szewczyk, G.; Sarna, M.; Zadlo, A.; Sarna, T.; Wakamatsu, K. Roles of reactive oxygen species in UVA-induced oxidation of 5,6-dihydroxyindole-2-carboxylic acid-melanin as studied by differential spectrophotometric method. *Pigment Cell Melanoma Res.* **2016**, *29*, 340–351. [CrossRef]
42. Micillo, R.; Iacomino, M.; Perfetti, M.; Panzella, L.; Koike, K.; D'Errico, G.; D'Ischia, M.; Napolitano, A. Unexpected impact of esterification on the antioxidant activity and (photo)stability of a eumelanin from 5,6-dihydroxyindole-2-carboxylic acid. *Pigment Cell Melanoma Res.* **2018**, *31*, 475–483. [CrossRef] [PubMed]
43. Zhao, P.; Alam, M.B.; Lee, S.H. Protection of UVB-induced photoaging by fuzhuan-brick tea aqueous extract via MAPKs/Nrf2-mediated down-regulation of MMP-1. *Nutrients* **2018**, *11*, 60. [CrossRef] [PubMed]

Appendix A

44. Kostyuk, V.; Potapovich, A.; Albuhaydar, A.R.; Mayer, W.; De Luca, C.; Korkina, L. Natural substances for prevention of skin photoaging: Screening systems in the development of sunscreen and rejuvenation cosmetics. *Rejuvenation Res.* **2018**, *2*, 91–101. [CrossRef] [PubMed]
45. Petruk, G.; Illiano, A.; Del Giudice, R.; Raiola, A.; Amoresano, A.; Rigano, M.M.; Piccoli, R.; Monti, D.M. Malvidin and cyanidin derivatives from açai fruit (*Euterpe oleracea* Mart.) counteract UV-A-induced oxidative stress in immortalized fibroblasts. *J. Photochem. Photobiol. B* **2017**, *172*, 42–51. [CrossRef]
46. Galano, E.; Arciello, A.; Piccoli, R.; Monti, D.M.; Amoresano, A. A proteomic approach to investigate the effects of cadmium and lead on human primary renal cells. *Metallomics* **2014**, *6*, 587–597. [CrossRef]
47. Beers, R.F.; Sizer, I.W. A spectrophotometric method for measuring the breakdown of hydrogen peroxide by catalase. *J. Biol. Chem.* **1952**, *195*, 133–140.
48. Del Giudice, R.; Petruk, G.; Raiola, A.; Barone, A.; Monti, D.M.; Rigano, M.M. Carotenoids in fresh and processed tomato (*Solanum lycopersicum*) fruits protect cells from oxidative stress injury. *J. Sci. Food Agric.* **2017**, *97*, 1616–1623. [CrossRef]
49. Haywood, R.; Rogge, F.; Lee, M. Protein, lipid, and DNA radicals to measure skin UVA damage and modulation by melanin. *Free Radic. Biol. Med.* **2008**, *44*, 990–1000. [CrossRef]
50. Fidrus, E.; Ujhelyi, Z.; Fehér, P.; Hegedűs, C.; Janka, E.A.; Paragh, G.; Vasas, G.; Bácskay, I.; Remenyik, E. Silymarin: Friend or foe of UV exposed keratinocytes? *Molecules* **2019**, *24*, 1652. [CrossRef]
51. Aquilano, K.; Baldelli, S.; Ciriolo, M.R. Glutathione: New roles in redox signaling for an old antioxidant. *Front. Pharmacol.* **2014**, *5*, 196. [CrossRef]
52. Sobeh, M.; El-Raey, M.; Rezq, S.; Abdelfattah, M.A.O.; Petruk, G.; Osman, S.; El-Shazly, A.M.; El-Beshbishy, H.A.; Mahmoud, M.F.; Wink, M. Chemical profiling of secondary metabolites of *Eugenia uniflora* and their antioxidant, anti-inflammatory, pain killing and anti-diabetic activities: A comprehensive approach. *J. Ethnopharmacol.* **2019**, *240*, 111939. [CrossRef] [PubMed]
53. Sobeh, M.; Mahmoud, M.F.; Petruk, G.; Rezq, S.; Ashour, M.L.; Youssef, F.S.; El-Shazly, A.M.; Monti, D.M.; Abdel-Naim, A.B.; Wink, M. *Syzygium aqueum*: A polyphenol- rich leaf extract exhibits antioxidant, hepatoprotective, pain-killing and anti-inflammatory activities in animal models. *Front. Pharmacol.* **2018**, *9*, 566. [CrossRef] [PubMed]
54. Deng, H.; Li, H.; Ho, Z.Y.; Dai, X.Y.; Chen, Q.; Li, R.; Liang, B.; Zhu, H. Pterostilbene's protective effects against photodamage caused by UVA/UVB irradiation. *Pharmazie* **2018**, *73*, 651–658. [PubMed]
55. Ma, Q. Role of Nrf2 in oxidative stress and toxicity. *Annu. Rev. Pharmacol. Toxicol.* **2013**, *53*, 401–426. [CrossRef]
56. Huang, Y.; Li, Y.; Hu, Z.; Yue, X.; Proetto, T.; Jones, Y.; Gianneschi, N.C. Mimicking melanosomes: Polydopamine nanoparticles as artificial microparasols. *ACS Cent. Sci.* **2017**, *3*, 564–569. [CrossRef]
57. Kulms, D.; Schwarz, T. Molecular mechanisms of UV-induced apoptosis. *Photodermatol. Photoimmunol. Photomed.* **2000**, *16*, 195–201. [CrossRef]
58. Hseu, Y.-C.; Chou, C.W.; Senthil Kumar, K.J.; Fu, K.T.; Wang, H.M.; Hsu, L.S.; Kuo, Y.H.; Wu, C.R.; Chen, S.C.; Yang, H.L. Ellagic acid protects human keratinocyte (HaCaT) cells against UV-A-induced oxidative stress and apoptosis through the upregulation of the HO-1 and Nrf-2 antioxidant genes. *Food Chem. Toxicol.* **2012**, *50*, 1245–1255. [CrossRef]
59. Moreiras, H.; Lopes-da-Silva, M.; Seabra, M.C.; Barral, D.C. Melanin processing by keratinocytes: A non-microbial type of host-pathogen interaction? *Traffic* **2019**, *20*, 301–304. [CrossRef]
60. Seiberg, M.; Paine, C.; Sharlow, E.; Andrade-Gordon, P.; Costanzo, M.; Eisinger, M.; Shapiro, S.S. The protease-activated receptor 2 regulates pigmentation via keratinocyte-melanocyte interactions. *Exp. Cell Res.* **2000**, *254*, 25–32. [CrossRef]

Appendix A

Supplementary Materials

A Melanin-Related Phenolic Polymer with Potent Photoprotective and Antioxidant Activities for Dermo-Cosmetic Applications

Davide Liberti, Maria Laura Alfieri, Daria Maria Monti,* Lucia Panzella * and Alessandra Napolitano

Department of Chemical Sciences, University of Naples "Federico II", Via Cintia 4, I-80126 Naples, Italy; davide.liberti@unina.it (D.L.); marialaura.alfieri@unina.it (M.L.A.); alesnapo@unina.it (A.N.)

* Correspondence: mdmonti@unina.it (D.M.M.); panzella@unina.it (L.P.); Tel.: +39-081-679150 (D.M.M.); +39-081-674131 (L.P.)

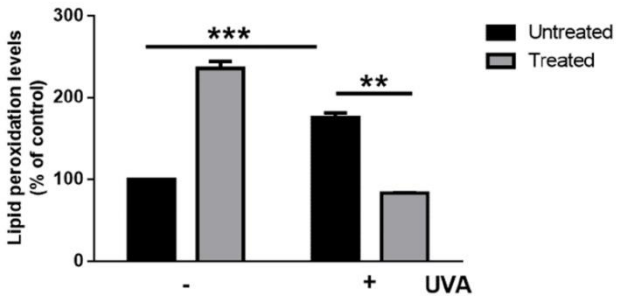

Figure S1. Lipid peroxidation levels evaluated by TBARS assay. Cells were pre-incubated with MeDHICA-melanin (10 μg/mL) for 2 h before UVA irradiation and then incubated for 90 min. Values are expressed as % with respect to control (*i.e.* untreated) cells. Data shown are means ± SD of three independent experiment. ** indicates $p < 0.005$, *** indicates $p < 0.0005$. Black bars refer to control cells and grey bars to cells incubated with MeDHICA-melanin. (−) indicates non irradiated cells; (+) indicates cells exposed to UVA irradiation.

Appendix B

Applied Microbiology and Biotechnology (2020) 104:9067–9077
https://doi.org/10.1007/s00253-020-10839-x

MINI-REVIEW

Towards green extraction methods from microalgae learning from the classics

Paola Imbimbo[1] · Luigi D'Elia[1] · Davide Liberti[1] · Giuseppe Olivieri[2,3] · Daria Maria Monti[1]

Received: 13 May 2020 / Revised: 29 July 2020 / Accepted: 14 August 2020 / Published online: 22 September 2020

Abstract
Microalgae started receiving attention as producers of third generation of biofuel, but they are rich in many bioactive compounds. Indeed, they produce many molecules endowed with benefic effects on human health which are highly requested in the market. Thus, it would be important to fractionate algal biomass into its several high-value compounds: this represents the basis of the microalgal biorefinery approach. Usually, conventional extraction methods have been used to extract a single class of molecules, with many side effects on the environment and on human health. The development of a green downstream platform could help in obtaining different class of molecules with high purity along with low environmental impact. This review is focused on technical advances that have been performed, from classic methods to the newest and green ones. Indeed, it is fundamental to set up new procedures that do not affect the biological activity of the extracted molecules. A comparative analysis has been performed among the conventional methods and the new extraction techniques, i.e., switchable solvents and microwave-assisted and compressed fluid extractions.

Keywords Microalgae · Green chemistry · Switchable solvents · Microwave-assisted extraction · Compressed fluid extraction · Lipids

Introduction

In the last years, high-value bioproducts extracted from microalgae achieved a foothold in the market (Pulz and Gross 2004). Compared with conventional crops, microalgae are considered a fast and continuous source of polyunsaturated fatty acids, carotenoids, and proteins, which exert beneficial effects on humans (Vega-López et al. 2004; Zhang et al. 2014). Despite microalgae representing a huge alternative to conventional feedstocks, three main drawbacks limit their use at large scale: (i) cultivation, (ii) harvesting, and (iii) downstream costs (Günerken et al. 2015; Zhang et al. 2016; Youn et al. 2017; Gifuni et al. 2019).

The main problems related to cultivation are (i) costs associated to the control of growth parameters, especially the temperature, and (ii) risks related to contaminations (Wang et al. 2013; Molina et al. 2019). To control them, microalgae are generally grown in photobioreactors (PBRs), which allow also obtaining high productivity yields and keeping the cultures axenic (Benedetti et al. 2004; Liu et al. 2019). However, as PBRs are very expensive for industrial applications, microalgae are grown in open pond systems (OPS), which are uncontrolled outdoor systems and do not allow a good productivity. OPS have pros (i–iii) and cons (iv–vi), such as (i) a low initial investment (Narala et al. 2016); (ii) a low power demand (Chen et al. 2013); (iii) low operating and maintenance costs (González-Delgado and Kafarov 2011); (iv) high contamination risk (Banerjee and Ramaswamy 2017); (v) requirement of large areas of land (Norsker et al. 2011); and (vi) high water demand to overcome the poor light utilization (Yin et al. 2020). Moreover, cultivations performed in these systems are strongly influenced by weather and

✉ Giuseppe Olivieri
giuseppe.olivieri@wur.nl

✉ Daria Maria Monti
mdmonti@unina.it

[1] Department of Chemical Science, University of Naples Federico II, via Cinthia 4, 80126 Naples, Italy

[2] Bioprocess Engineering Group, Wageningen University and Research, Droevendaalsesteeg 1, 6700AA Wageningen, the Netherlands

[3] Department of Chemical, Materials and Industrial Engineering, University of Naples Federico II, Piazzale Tecchio 80, 80125 Napoli, Italy

Appendix B

environmental conditions. Indeed, controlling the growth parameters, such as temperature, pH, and light intensity is still tricky and may affect the biomass productivity (Carvalho et al. 2006; Slegers et al. 2013; Koley et al. 2019). To face the contaminations, an optimization of highly selective environment is required. Among all the steps involved in the algal biomass production, the harvesting step represents the 20–30% of the overall costs (Rawat et al. 2011; Barros et al. 2015). Thus, the selection of the right technology to harvest the biomass is one of the key issues to make the microalgal exploitation cost-effective at large scale. The high costs are related to several factors, such as the high dilution of the culture that requires an intensive de-watering step; the density of the cells in the medium that is similar to the water density; and the negative charge of algal cells that implies an electrostatic repulsions among them, thus keeping cells in a stable disperse state (Zheng et al. 2012; Hu et al. 2014; Gayen et al. 2019). To date, the most common harvesting industrial procedures are centrifugation, flocculation, coagulation, and immobilization (Drexler and Yeh 2014; Fuad et al. 2018; Hidayah et al. 2019). These techniques present several disadvantages, not only for the elevated energy costs of each operation but also for the low separation efficiency (Danquah et al. 2009; Xu et al. 2010). For these reasons, the optimization of an efficient and economic harvesting procedure is still a challenge.

Another important issue to consider is the selection of the right extraction procedure to be employed. In fact, when extracting molecules from the biomass, one should choose a fully biocompatible buffer which will not alter the bioactivity of the extracted molecule. Currently, conventional extraction techniques involve the use of organic solvents, such as chloroform, acetone, methanol, and diethyl ether to be used in large amounts, for a long time and also the use of dry biomass as a starting material (Ghasemi Naghdi et al. 2016; Saini and Keum 2018; Zhang et al. 2019)

Recently, a new generation of extracting techniques, which do not require the involvement of toxic solvents, is being developed. Much effort has been done to set up green extraction procedures without using toxic solvents, thus minimizing environmental impact (Chemat et al. 2012; Armenta et al. 2019). Moreover, the new techniques allow to reduce the extraction time and to improve the extraction yields, without affecting the biological activity (Esquivel-Hernández et al. 2017; Dixon and Wilken 2018). To date, only few algae strains are considered suitable for the large-scale production (Brennan and Owende 2010; Kothari et al. 2017; De-Luca et al. 2019), such as *Spirulina*, *Chlorella*, *Dunaliella salina*, *Aphanizomenon flosaquae*, *Haematococcus pluvialis*, *Crypthecodinium cohnii*, and *Shizochytrium* (García et al. 2017).

One way to reduce the overall costs of microalgae cultivation on a large-scale production is the valorization of different microalgal biomass components (Lam et al. 2018; Chandra et al. 2019). In the last decades, the linear economy has given way to the circular economy, to promote a better use of resources by utilizing wastes and natural products as starting material, and to develop an integrated platform able to produce different bioproducts from biomasses (Bhalamurugan et al. 2018; Mathimani and Pugazhendhi 2019). In this context, microalgal biorefinery could be considered the most efficient and cost-effective approach to obtain different molecules, starting from the one endowed with the highest market value. This requires an appropriate selection of the extraction procedure to be employed. In this review, we will try to provide an overview on the different extraction techniques used for microalgae with a special focus on the improvements obtained.

Organic-solvent extraction techniques

The extraction step represents one of the main drawbacks in algae-based industries (Gifuni et al. 2019). Lipids and carotenoids are commonly recovered by using organic solvents, such as hexane, chloroform, acetone, methanol, and diethyl ether (Saini and Keum 2018). Conventional extractions usually require large amounts of organic solvent and long extraction times and they generally need dry biomass (Mansour et al. 2019; Sati et al. 2019). Moreover, a pretreatment step is often required before the extraction, thus increasing the overall costs (Alzate et al. 2012; Kadir et al. 2018). A brief description of the conventional methods, generally used to extract lipids, is reported, and the results obtained are summarized in Table 1.

The Folch method

The Folch method (Folch 1957) is one of the oldest methods employed for the extraction of lipids from microalgae and cyanobacteria. This procedure is fast and easy; however, it is less sensitive compared with the most recent procedures (Kumar et al. 2015). It requires chloroform and methanol as solvents, and it still represents one of the most used methods to estimate, spectrophotometrically, algal lipids. Banskota et al. (2019) extracted lipids from several microalgal strains. Extractions were performed starting from freeze-dried biomass using chloroform to methanol (2:1). They found that the method was able to extract from 30 to 40% (w/w of dry biomass) of lipids, with the exception of *Nannochloropsis granulata* in which the lipid content was 49.3 ± 4.0% (w/w of dry biomass). Authors demonstrated also that the lipid content was directly related to ORAC values (Banskota et al. 2019). Schipper et al. (2019) studied novel microalgal strains isolated from extreme desert environments: *Tetraselmis* sp.

Appendix B

Table 1 Different conventional extraction methods and their relative yields

Microalgal species	Extraction method	Solvent	Biomass	Lipid yield (%)	Reference
N. oleoabundans	Folch	Chloroform/methanol	Dry	31.8 ± 6.7	(Banskota et al. 2019)
B. braunii				41.1 ± 5.5	(Banskota et al. 2019)
P. tricornutum				44.8 ± 3.6	(Banskota et al. 2019)
N. granulata				49.3 ± 4.0	(Banskota et al. 2019)
C. sorokiniana				32.3 ± 2.4	(Banskota et al. 2019)
P. aerugineum				30.9 ± 6.1	(Banskota et al. 2019)
S. obliquus				40.5 ± 7.8	(Banskota et al. 2019)
Scenedesmus sp.				36.3 ± 12.5	(Banskota et al. 2019)
T. chui				32.1 ± 5.5	(Banskota et al. 2019)
T. subcordiformis QUCCCM51				25.6 ± 0.9	(Banskota et al. 2019)
P. maculatum QUCCCM127				28.0 ± 2.0	(Banskota et al. 2019)
N. oculata				24.4	(Wei et al. 2014)
T.subcordiformis				22.2	(Wei et al. 2014)
C. acidophila LAFIC-004	Bligh and Dyer	Chloroform/methanol/water	Dry	54.6	(Souza et al. 2017)
I. galbana				25.3 ± 0.2	(Bonfanti et al. 2018)
C. sorokiniana				29.9	(Rasouli et al. 2018)
M. capsulatus				21.8	(Rasouli et al. 2018)
C. vulgaris		Chloroform/methanol		10.4	(Zullaikah et al. 2019)
G. phlegrea	Soxhlet	Chloroform/methanol	Dry	79 ± 26	(Imbimbo et al. 2019)
S. obliquus				17.4 ± 0.4	(Wang et al. 2019)
Chlorophyta sp.		*n*-Hexane/ether		18.3 ± 0.4	(Yusuff 2019)
C. gracilis				12.3	(Kanda et al. 2020)
P. carterae		*n*-Hexane		7.5	(Kanda et al. 2020)
C. vulgaris		Heptane		57.5 ± 0.5	(Minyak et al. 2017)

and *Picochlorum* sp., characterized by their tolerance to high temperature and to high CO_2 concentrations. The species were isolated, and lipid extraction showed that the two novel strains contained significant amounts of lipids, up to 25.6 ± 0.9% and 28.0 ± 2.0% (w/w of dry biomass), for *Tetraselmis* sp. and *Picochlorum* sp., respectively. The method is very reliable as different authors reported the same extraction yield for the same strain (Danquah et al. 2009; Wei et al. 2014).

Bligh and Dyer

The Bligh and Dyer method (Bligh and Dyer 1959) is similar to Folch method. It allows for the extraction of lipids from homogenized cells, generally using a mixture of chloroform/methanol. It is a rapid and effective procedure, thus becoming a standard method for the lipid content determination in biological tissues (Iverson et al. 2001).

Souza and co-workers (Souza et al. 2017) studied the acidophilic microalga *Chlamydomonas acidophila* LAFIC-004 performing a lipid extraction by the Bligh and Dyer method and obtained 54.6% (w/w of dry biomass) of lipids. Bonfanti et al. (2018) performed lipid extraction starting from *Isochrysis galbana*, with a 25.3 ± 0.2% (w/w of dry biomass) yield. Rasouli and co-workers (Rasouli et al. 2018) extracted about 30% of lipids from *Chlorella sorokiniana*, a value similar to that reported using the Folch method (Schipper et al. 2019), thus suggesting that all the methodologies are able to extract the same amount of lipids when the same strain and the same experimental procedure are followed.

Soxhlet extraction

Soxhlet extraction is a conventional procedure employed for the extraction of lipids and carotenoids. It is performed by using solvents at boiling temperature and ambient pressure, and even if it requires high amount of solvents and a long extraction time, it provides high yields and does not affect the bioactivity of the extracted molecules. We recently reported a Soxhlet extraction with chloroform to methanol (2:1) to obtain lipids from *Galdieria phlegrea* (Imbimbo et al. 2019).

Appendix B

This procedure allowed obtaining a recovery of 79 ± 26% (w/w of dry biomass) of lipids starting from the dried biomass (Imbimbo et al. 2019). Yusuff reported an oil extraction performed by Soxhlet from the green microalga *Chlorophyta* sp. The extraction was performed by using *n*-hexane to ether (4:1) mixture and allowed a yield of 18.3 ± 0.4% (w/w of dry biomass) (Yusuff 2019). Kanda and colleagues used two different microalgae strains to extract lipids: *Chaetoceros gracilis* and *Pleurochrysis carterae.* Extractions were performed by Soxhlet using pure *n*-hexane. This technique allowed achieving yields of 12.3% (w/w of dry biomass) for *C. gracilis* and 7.5% (w/w of dry biomass) for *P. carterae* (Kanda et al. 2020).

Green extraction techniques

Recently, the demand for greener, safer, and more natural products that do not require the involvement of toxic solvent increased. The development of green extraction procedures to recover valuable compounds from natural sources represents a significant advance. These eco-friendly techniques allow obtaining bioactive products by reducing or completely replacing toxic solvents, thus minimizing the environmental impact, in agreement with several Green Chemistry principles (Capello et al. 2007; Anastas and Eghbali 2010; Jeevan Kumar et al. 2017). Moreover, a reduction in the extraction time and an improvement in the extraction yields have been obtained. Nevertheless, only few innovative techniques succeeded so far.

Ionic liquids and switchable solvents

Ionic liquids (ILs) are organic solution of salts that can melt at mild temperature (< 100 °C). They are typically composed of a large number of inorganic or organic cations and are characterized by synthetic flexibility and thermal stability. Moreover, they are non-volatile and non-flammable (Vekariya 2017; Harris et al. 2018), being a good alternative to conventional solvents. They are generally employed for lipid extraction; however, to date, only limited papers are available in literature (Motlagh et al. 2019). One of the main drawbacks of ILs is the unrealistic application at industrial scale, due to their costs and the environmental impact (Zhang et al. 2008). Indeed, many ILs have been proved to be not harmful for humans, but their synthesis involves many steps that require expensive, toxic, and volatile reagents (Domínguez de María 2017; Harris et al. 2018; Singh and Savoy 2020). In recent years, a second generation of ILs has been developed: switchable solvents (SSs). First reported by Philipp Jessop et al. (2005), SSs are non-volatile liquids able to switch from hydrophobic to hydrophilic state and vice versa in response to external stimuli, such as temperature or pH variation and/or the addition or removal of a gas (i.e., CO_2) (Al-Ameri and Al-Zuhair 2019; Do Yook et al. 2019). Theoretically, these SSs have many pros: (i) they allow performing cascade extractions of high-value molecules, (ii) it is possible to recover and reuse the solvent; thus, they are considered economically competitive and they require low energy consumption (iii); (iv) they are eco-friendly; (v) they are highly selective; and (vi) they enable extractions in a short time (Pollet et al. 2011; Jeevan Kumar et al. 2017; Clarke et al. 2018). For all these reasons, the second generation of SSs is considered green (Vanderveen et al. 2014; Jeevan Kumar et al. 2017). However, many cons have emerged with respect to solvent loss. This is mainly due to (i) the use of CO_2 in the switching process; (ii) the impossibility to completely remove the solvent from the residual biomass after the process; and (iii) the release of the solvent in water. To improve SS properties, functional groups may be incorporated into the structure during the chemical synthesis, with increase in production costs (Clarke et al. 2018). Nowadays, primary, secondary, and tertiary amines are among the most SSs (Schuur et al. 2019). Table 2 reports a comparison between the lipid yield extraction by using SSs and conventional methods.

Research on SSs is quite recent. In 2018, Cicci et al. (2018) used N,N-dimethyl-cyclohexylamine (DMCHA) on the wet biomass of *Scenedesmus dimorphus* to extract lipids. The lipid yield was 35.6% (w/w of dry biomass), about 1.2-fold more than the yield obtained by Gour and colleagues with a conventional method (Bligh and Dyer) (Gour et al. 2020). Nevertheless, the experimental procedure seemed to be able to extract similar amount of lipids independently from the strain. Indeed, the lipid yields obtained by Cicci et al. (2018) on *Scenedesmus dimorphus* can be compared with the lipid yield obtained by Samorì et al. (2013) on *Tetraselmis suecica* (31.9%). Instead, Du et al. (2013) showed that N-eyhylbutylamine (EBA) was able to extract lipids from *Desmodesmus* sp. with a yield of 16.8% (w/w of dry biomass), a value lower than that obtained by Samorì and colleagues who used DMCHA (29.2%) (Samorì et al. 2013). Indeed, the yield was higher than that obtained by the Bligh and Dyer method (Du et al. 2013; Samorì et al. 2013). Probably, the tertiary amine DMCHA allows a better extraction of the lipid fraction from the biomass, as it is more hydrophobic than the secondary amine EBA. Afterwards, Du et al. (2018) showed that, starting from a stressed culture of *Neochloris oleoabundans*, EBA allowed to obtain an increase in the lipid yield, from 47.0 to 61.3% (w/w of dry biomass), only by increasing the number of extractions. In this case, authors found that EBA extracted about 4 times more lipids than the Bligh and Dyer method. It has to be noticed, however, that the switch back has not been reported in literature yet, so that the use of SSs is still far from being used in a biorefinery approach.

Appendix B

Table 2 Yields obtained with switchable solvent method from different microalgae

Microalgal species	Extraction method	Solvent	Biomass	Lipid yield (%)	Fold increase	Reference
S. dimorphus (UTEX 1237)	Switchable solvent	DMCHA	Wet	35.6 ± 1.9	1.2	(Cicci et al. 2018)
S. dimorphus (Sd12)	Bligh and Dyer	Chloroform/methanol/water	Dry	30.7		(Gour et al. 2020)
N. gaditana	Switchable solvent	DMCHA	Wet	57.9 ± 1.3	1.3	(Samorì et al. 2013)
	Bligh and Dyer	Chloroform/methanol/water	Dry	45.1 ± 0.9		(Samorì et al. 2013)
T. suecica	Switchable solvent	DMCHA	Wet	31.9 ± 1.5	1.3	(Samorì et al. 2013)
	Bligh and Dyer	Chloroform/methanol/water	Dry	25.4 ± 2.6		(Samorì et al. 2013)
D. communis	Switchable solvent	DMCHA	Wet	29.2 ± 0.9	1.6	(Samorì et al. 2013)
	Bligh and Dyer	Chloroform/methanol/water	Dry	17.8 ± 0.1		(Samorì et al. 2013)
Desmodesmus sp.	Switchable solvent	EBA	Wet	16.8 ± 0.5	1.3	(Du et al. 2013)
	Bligh and Dyer	Chloroform/methanol/water	Dry	12.8 ± 0.6		(Du et al. 2013)
N. oleoabundans	Switchable solvent	EBA	Wet	47.0	1	(Du et al. 2017; Du et al. 2018)
	Bligh and Dyer	Chloroform/methanol/water	Dry	13.1		(Du et al. 2017; Du et al. 2018)
Chlorella sp.	Switchable solvent	EBA	Wet	12.3 ± 3.2	3.2* 1.3**	(Al-Ameri and Al-Zuhair 2019)
		DMCHA		13.3 ± 0.4	3.5* 1.4**	(Al-Ameri and Al-Zuhair 2019)
		Dipropylamine		7.0 ± 1.3		(Al-Ameri and Al-Zuhair 2019)
	Conventional	[Bmim][PF6]	Dry	3.8 ± 1.1		(Al-Ameri and Al-Zuhair 2019)
		n-Hexane		9.4 ± 0.7		(Al-Ameri and Al-Zuhair 2019)

*With respect to [Bmim][PF6]

**With respect to *n*-hexane

Microwave-assisted extraction

Microwave-assisted extraction (MAE) involves the use of microwaves to heat up the solvent in contact with the cell thus allowing to extract pigments, lipids, and other bioactive molecules (Juin et al. 2015). The heating is caused by two phenomena: dipole rotation and ionic conduction, which may happen individually or simultaneously (Tatke and Jaiswal 2011). MAE is generally performed in closed systems to avoid heating dissipation. By this way, the heating mechanism is targeted and selective, thus reducing the extraction time and improving the final yield. However, the main limitation of this method is the high temperature required that might affect the bioactivity of the extracted molecules. A study from Mahfud's group indicated that MAE was able to increase by almost 10 times the lipid extraction yield in *Spirulina platensis*, with respect to Soxhlet (Kalsum et al. 2019), when *n*-hexane was used as solvent. These and other results are reported in Table 3, with a comparison with conventional methods.

In the extraction processes using microwave, the use of a mixture of solvents may result in an increase of the yield. As an example, the mixture *n*-hexane/methanol is a non-polar solvent able to solve oils from the matrix cells of microalgae. On the other hand, methanol allows microalgae to absorb more microwave energy with a consequent increase in microalgal disruption (Kalsum et al. 2019).

Krishnan and colleagues studied the importance of different ILs in the MAE extraction system on *Chlorella vulgaris*. Interestingly, they found that the extraction yield increased from 10.9 (Bligh and Dyer method) to 19.2% (w/w of dry biomass) when the 1-octyl-3-methylimidazolium acetate ([Omim][OAc]) was used (Krishnan et al. 2020). In general, they found that the polarity of the ILs and the electronegativity of the anions used played an important role in the type of lipids extracted: the higher the hydrophobicity of the anion used, the higher the extraction of non-polar compounds.

Recently, Zghaibi et al. (2019) found that it was possible to use MAE to extract lipids from *Nannochloropsis* sp. by using only 10% NaCl (6.9% yield). In particular, the lipid extraction yield was similar with respect to Soxhlet extraction (4.5%), and lower with respect to the Bligh and Dyer (18%). However, MAE fully replaced the use of organic and harmful solvents, and, noteworthy, a better quality of lipids was obtained (polyunsaturated fatty acids and omega-3) (Zghaibi et al. 2019). It has to be considered that water, which as a highly polar solvent, can absorb microwave energy, and NaCl can improve the dielectric loss responsible for converting microwave energy into heat. The result is a higher efficiency in PUFA recovery.

Appendix B

Table 3 Yields obtained with MAE method from different microalgae

Microalgal species	Extraction method	Solvent	Biomass	Operative parameters	Lipid yield (%)	Fold increase	Reference
S. platensis	MAE	Methanol/*n*-hexane	Dry	600 W; 40 min	12.5	9.6	(Kalsum et al. 2019)
	Soxhlet	*n*-Hexane			1.3		(Kalsum et al. 2019)
C. vulgaris	MAE	Chloroform/methanol/water [Omim][OAc] 2.5%		700 W; 10 min	19.2	1.8	(Krishnan et al. 2020)
	Bligh and Dyer	Chloroform/methanol/water			10.9		(Krishnan et al. 2020)
Nannochloropsis sp.	MAE	Water/sodium chloride 10%		800 W; 30 min	6.9	1.5*	(Zghaibi et al. 2019)
	Soxhlet	*n*-hexane			4.5	0.38**	(Zghaibi et al. 2019)
	Bligh and Dyer	Chloroform/methanol/water			18		(Zghaibi et al. 2019)

*With respect to Soxhlet

**With respect to Bligh and Dyer

Compressed fluid extractions

Compressed fluid extractions are considered valuable green alternatives to conventional extractions. They include subcritical water extraction (SWE), pressurized liquid extraction (PLE), and supercritical fluid extraction (SFE). Solvents involved in PLE and SWE are maintained at a temperature above the boiling point and at a pressure high enough to keep fluids in their liquid states (Ramos et al. 2002). On the other hand, SFE operates at temperature and pressure above the critical point of the solvent selected (Herrero et al. 2013). These conditions allow for the increase of diffusivity of the solvent, thus improving the penetration of the solvent into the matrix (Phelps et al. 1996). Besides the differences between these techniques, they all require minimum amount of GRAS solvents to perform selective extraction of bioactive compounds, without affecting the bioactivity or the chemical structure (Herrero and Ibañez 2018). Unfortunately, they are still not diffused due to the high investment costs (Herrero and Ibañez 2018). So far, CO_2 is the most used solvent, especially in supercritical extractions (Goto et al. 2015). CO_2 is an economic, non-harmful, non-flammable, and recyclable solvent. Due to its thermodynamic properties, at supercritical conditions, CO_2 shows a high diffusivity and a high density that allow a better penetration into the matrix (Goto et al. 2015; Molino et al. 2020). However, supercritical CO_2 ($ScCO_2$) is limited to the extraction of non-polar or low polar compounds (Gilbert-López et al. 2015; Gallego et al. 2019). To overcome this problem, a low amount of co-solvent (e.g., ethanol) can be used to increase the CO_2 polarity.

According to this, Nobre and co-workers performed a lipid extraction starting from the dried biomass of *Nannochloropsis* sp. (NANNO-2) by using $ScCO_2$ in the presence and in the absence of a co-solvent (20% ethanol). Authors found that $ScCO_2$ combined with ethanol was able to increase lipid yield, as 45% (w/w of dry biomass) of lipid yield was obtained with respect to 32% yield (w/w of dry biomass), in the absence of co-entrainer (Nobre et al. 2013). Moreover, Zullaikah et al. (2019) performed a lipid extraction from the wet raw biomass of *Chlorella vulgaris* by SWE. Besides the co-solvent, time and temperature may also affect the extraction yields. For this reason, experiments were performed in the presence or absence of co-solvents, at different temperatures and different time. In particular, chloroform, methanol, ethanol, ethyl acetate, and *n*-hexane were tested as co-solvents. Extractions were performed at 160 °C, 80 bar, at 160 °C, 180 °C and 200 °C, for 15 min, 30 min, 1 h, 3 h, and 5 h. All the results were then compared with conventional Bligh and Dyer extraction. The study revealed that SWE performed at 200 °C, 80 bar for 30 min, using ethyl acetate as co-solvent, gave the highest lipid yield (65.94%, w/w of dry biomass), while conventional chloroform/methanol extraction allowed for the obtaining of a lipid yield of 10.43% (w/w of dry biomass). Altenhofen da Silva and co-workers evaluated the effect of supercritical carbon dioxide ($ScCO_2$) on freeze-dried biomass of *Desmodesmus subspicatus*. Extractions were performed comparing two different pressures (20 and 30 MPa, that correspond to 200 and 300 bar, respectively) at 60 °C. Authors found out that a direct correlation was observed with pressure and lipid yield, as, at 30 MPa, 45% of lipids were recovered, a value which is almost the double of that obtained at 20 MPa or with Soxhlet (23% at and 20%, respectively) (Altenhofen et al. 2016).

Zimmerer et al. (2019) employed *Phaeodactylum tricornutum* dry biomass for lipid extraction. Cells were disrupted by ultrasonication prior the extraction with $ScCO_2$. Among the different pressures and temperatures tested, 90 °C and 621 bar were found to be the best conditions, as a 25% yield was obtained (w/w of dry biomass). As a reference, lipids were extracted by Folch method, using a mixture of

Appendix B

water, methanol, and chloroform. The lipid yield obtained by the conventional method was 28% (w/w of dry biomass). He and co-workers set up a process to obtain lipids from *Isochrysis* sp. dried biomass. Lipids were extracted by 3 cycles of 5 min each of PLE, at 103 bar, 80 °C, using two different solvents: *n*-hexane and ethanol. Soxhlet extraction (with hexane) and Folch method (with a mixture of chloroform/methanol/water) were performed to compare the extraction yields. PLE with *n*-hexane gave a higher yield (34.42 %) when compared with Soxhlet extraction performed with the same solvent (about 19% yield). However, PLE performed by using ethanol improved the process, as the lipid yield was 38.94% (w/w of dry biomass) (He et al. 2019).

We recently reported a process intensification to obtain three different high-value molecules in a biorefinery approach (Imbimbo et al. 2019). In particular, we improved lipid extraction as the third step of the cascade process. The extraction was performed using pure CO_2 as solvent, at 350 bar, 60 °C for 100 min starting from the wet biomass of *Galdieria phlegrea*. The yield was then compared with the one obtained by a conventional extraction performed with 0.37% NaCl in chloroform/methanol (2:1) on dry biomass. SFE allowed for the obtaining of 18.4% yield (w/w of dry biomass), in comparison with 11% yield (w/w of dry biomass) obtained by the conventional extraction method (Imbimbo et al. 2020). All the extraction yields are reported in Table 4.

Conclusions

Microalgae represent a natural source of bioactive compounds to be used in pharmaceutical, nutraceutical, cosmetic, and food sectors. In particular, many hydrophobic molecules endowed with special biological activity can be extracted from microalgae and used. Of course, during extraction, many parameters have to be considered. An ideal extraction method should allow to operate at low costs and to preserve both the original characteristics of the isolated molecule and of the residual biomass. Green extraction techniques seem to combine environmentally friendly and cost-effective extractions. Most of them are economically and environmentally sustainable and non-toxic and can increase the selectivity and

Table 4 Yields obtained with compressed fluid extraction methods from different microalgae

Microalgal species	Extraction method	Solvent	Biomass	Lipid yield (%)	Fold increase	Reference
Nannochloropsis sp. (NANNO-2)	SFE	CO_2	Dry	34	1.3*	(Nobre et al. 2013)
		CO_2 + 20% ethanol		45		(Nobre et al. 2013)
	Soxhlet	*n*-Hexane		40.7		(Nobre et al. 2013)
		Ethanol		50.6		(Nobre et al. 2013)
	Bligh and Dyer	Chloroform/methanol/water		25.3		(Nobre et al. 2013)
G. phlegrea	SFE	CO_2	Wet	18.4 ± 0.5	1.7	(Imbimbo et al. 2020)
	Conventional	Chloroform/methanol/sodium chloride	Dry	11 ± 0.3		(Imbimbo et al. 2020)
C. vulgaris	SWE	Water/ethyl acetate	Wet	65.9	6.3	(Zullaikah et al. 2019)
	Bligh and Dyer	Chloroform/methanol	Dry	10.4		(Zullaikah et al. 2019)
D. subspicatus	SFE	*n*-Hexane	Dry	45	2.3	(Altenhofen et al. 2016)
	Soxhlet	Chloroform/methanol/water		20		(Altenhofen et al. 2016)
P. tricornutum	SFE	CO_2	Dry	25	0.9	(Zimmerer et al. 2019)
	Folch	Chloroform/methanol/water		28		(Zimmerer et al. 2019)
Isochrysis sp.	PLE	*n*-Hexane	Dry	34.41	1.4** 1.8***	(He et al. 2019)
	PLE	Ethanol		38.94	1.5** 2***	(He et al. 2019)
	Folch	Chloroform/methanol/water		25.36		(He et al. 2019)
	Soxhlet	*n*-Hexane		19		(He et al. 2019)

*With respect to SFE in absence of co-solvent

**With respect to Folch

***With respect to Soxhlet

Appendix B

extraction efficiency (Domínguez de María 2017; Häckl and Kunz 2018; Singh and Savoy 2020). However, all of them have pros and cons with respect to the industrial benchmark of extraction with organic solvent.

In particular, MAE is a green technique used to recover different thermo-stable molecules. Of course, this can be a problem in the case of thermolabile molecules as the experimental conditions used may affect the physical-chemical properties of the isolated molecules. Furthermore, the efficiency of the extraction is often lower with respect to organic solvents.

Compressed fluid extractions can represent an excellent alternative to recover thermolabile molecules. The major advantage resides in the possibility to recover and recycle the solvent. Furthermore, the solvent polarity can be tuned by combining the neutral CO_2 with polar co-solvents, such as ethanol or isopropanol. The major limitation of compressed fluid extractions is represented by its initial investment costs. Lab-scale tests seem efficient when achieving > 300-bar pressure, which is often economically unfeasible at industrial scale. In case of switchable solvents, solvent separation and recycle are the main advantage. Furthermore, the tunability of the polarity allows these solvents to extract both hydrophobic and hydrophilic molecules only by switching a chemical-physical factor. What is still a pending point for SSs is their effect on the residual biomass after the extraction. Unfortunately, there is still much effort to be done to use these solvents, as no evidence of their extraction abilities have been reported after the switch.

Generally speaking, one should keep in mind that microalgae can be used as an excellent source of bioactive molecules provided that a biorefinery approach has to be used. Thus, microalgae costs have to be paid by obtaining more than a class of molecules, starting from the one with the highest market value. So, if the biorefinery approach includes downstream processes able to fulfill the requirements of Green Chemistry, it will end up with a new and sustainable process. With respect to green extraction techniques of lipids and pigments, less is known on two important aspects: the residual amount of solvent in the biomass and, mainly, the effect of the extraction on the other molecules in the leftover spent biomass. This review provides a step further in the extraction knowledge that can help to valorize microalgae biomass by using innovative extraction techniques, which comply with the Green Chemistry principles.

References

Al-Ameri M, Al-Zuhair S (2019) Using switchable solvents for enhanced, simultaneous microalgae oil extraction-reaction for biodiesel production. Biochem Eng J 141:217–224. https://doi.org/10.1016/j.bej.2018.10.017

Altenhofen M, Barbosa H, Brito C, Arjonilla F, Bastos G, Guenter T (2016) Heterotrophic growth of green microalgae *Desmodesmus subspicatus* in ethanol distillation wastewater (vinasse) and lipid extraction with supercritical CO_2. J Chem Technol Biotechnol 92:573–579. https://doi.org/10.1002/jctb.5035

Alzate ME, Muñoz R, Rogalla F, Fdz-Polanco F, Pérez-Elvira SI (2012) Biochemical methane potential of microalgae: influence of substrate to inoculum ratio, biomass concentration and pretreatment. Bioresour Technol 123:488–494. https://doi.org/10.1016/j.biortech.2012.06.113

Anastas P, Eghbali N (2010) Green chemistry: principles and practice. Chem Soc Rev 39:301–312. https://doi.org/10.1039/b918763b

Armenta S, Garrigues S, Esteve-Turrillas FA, de la Guardia M (2019) Green extraction techniques in green analytical chemistry. TrAC Trends Anal Chem 116:248–253. https://doi.org/10.1016/j.trac.2019.03.016

Banerjee S, Ramaswamy S (2017) Dynamic process model and economic analysis of microalgae cultivation in open raceway ponds. Algal Res 26:330–340. https://doi.org/10.1016/j.algal.2017.08.011

Banskota AH, Sperker S, Stefanova R, McGinn PJ, O'Leary SJB (2019) Antioxidant properties and lipid composition of selected microalgae. J Appl Phycol 31:309–318. https://doi.org/10.1007/s10811-018-1523-1

Barros AI, Gonçalves AL, Simões M, Pires JCM (2015) Harvesting techniques applied to microalgae: a review. Renew Sust Energ Rev 41:1489–1500. https://doi.org/10.1016/j.rser.2014.09.037

Benedetti S, Benvenuti F, Pagliarani S, Francogli S, Scoglio S, Canestrari F (2004) Antioxidant properties of a novel phycocyanin extract from the blue-green alga *Aphanizomenon flos-aquae*. Life Sci 75:2353–2362. https://doi.org/10.1016/j.lfs.2004.06.004

Bhalamurugan GL, Valerie O, Mark L (2018) Valuable bioproducts obtained from microalgal biomass and their commercial applications: a review. Environ Eng Res 23:229–241. https://doi.org/10.4491/eer.2017.220

Bligh EG, Dyer WJ (1959) A rapid method of total lipid extraction and purification. Can J Biochem Physiol 37:911–917. https://doi.org/10.1139/y59-099

Bonfanti C, Cardoso C, Afonso C, Matos J, Garcia T, Tanni S, Bandarra NM (2018) Potential of microalga *Isochrysis galbana*: bioactivity and bioaccessibility. Algal Res 29:242–248. https://doi.org/10.1016/j.algal.2017.11.035

Brennan L, Owende P (2010) Biofuels from microalgae—a review of technologies for production, processing, and extractions of biofuels and co-products. Renew Sust Energ Rev 14:557–577. https://doi.org/10.1016/j.rser.2009.10.009

Capello C, Fischer U, Hungerbühler K (2007) What is a green solvent? A comprehensive framework for the environmental assessment of solvents. Green Chem 9:927–934. https://doi.org/10.1039/b617536h

Carvalho AP, Meireles A, Malcata FX (2006) Microalgal reactors: a review of enclosed system designs and performances. Biotechnol Prog 22:1490–1506. https://doi.org/10.1021/bp060065r

Chandra R, Iqbal MN, Vishal G, Lee H, Nagra S (2019) Bioresource technology algal biorefinery: a sustainable approach to valorize algal-based biomass towards multiple product recovery. 278:346–359. https://doi.org/10.1016/j.biortech.2019.01.104

Chemat F, Vian MA, Cravotto G (2012) Green extraction of natural products: concept and principles. Int J Mol Sci 13:8615–8627. https://doi.org/10.3390/ijms13078615

Chen Y, Wang J, Zhang W, Chen L, Gao L, Liu T (2013) Forced light/dark circulation operation of open pond for microalgae cultivation. Biomass Bioenergy 56:464–470. https://doi.org/10.1016/j.biombioe.2013.05.034

Appendix B

Cicci A, Sed G, Jessop PG, Bravi M (2018) Circular extraction: an innovative use of switchable solvents for the biomass biorefinery. Green Chem 20:3908–3911. https://doi.org/10.1039/c8gc01731j

Clarke CJ, Tu WC, Levers O, Bröhl A, Hallett JP (2018) Green and sustainable solvents in chemical processes. Chem Rev 118:747–800. https://doi.org/10.1021/acs.chemrev.7b00571

Danquah MK, Gladman B, Moheimani N, Forde GM (2009) Microalgal growth characteristics and subsequent influence on dewatering efficiency. Chem Eng J 151:73–78. https://doi.org/10.1016/j.cej.2009.01.047

De-Luca R, Bezzo F, Béchet Q, Bernard O (2019) Meteorological data-based optimal control strategy for microalgae cultivation in open pond systems. Complexity 2019:1–12. https://doi.org/10.1155/2019/4363895

Dixon C, Wilken LR (2018) Green microalgae biomolecule separations and recovery. Bioresour Bioprocess 5. https://doi.org/10.1186/s40643-018-0199-3

Do Yook S, Kim J, Woo HM, Um Y, Lee SM (2019) Efficient lipid extraction from the oleaginous yeast *Yarrowia lipolytica* using switchable solvents. Renew Energy 132:61–67. https://doi.org/10.1016/j.renene.2018.07.129

Domínguez de María P (2017) Chapter 6-ionic liquids, switchable solvents, and eutectic mixtures. In: Pena-Pereira F, Tobiszewski MBT-TA of GS in SP (eds) The application of green solvents in separation processes. Elsevier, pp 139–154. https://doi.org/10.1016/B978-0-12-805297-6.00006-1

Drexler ILC, Yeh DH (2014) Membrane applications for microalgae cultivation and harvesting: a review. Rev Environ Sci Biotechnol 13:487–504. https://doi.org/10.1007/s11157-014-9350-6

Du Y, Schuur B, Samorì C, Tagliavini E, Brilman DWF (2013) Secondary amines as switchable solvents for lipid extraction from non-broken microalgae. Bioresour Technol 149:253–260. https://doi.org/10.1016/j.biortech.2013.09.039

Du Y, Schuur B, Brilman DWF (2017) Maximizing lipid yield in *Neochloris oleoabundans* algae extraction by stressing and using multiple extraction stages with N-ethylbutylamine as switchable solvent. Ind Eng Chem Res 56:8073–8080. https://doi.org/10.1021/acs.iecr.7b01032

Du Y, Schuur B, Kersten SRA, Brilman DWF(W) (2018) Multistage wet lipid extraction from fresh water stressed *Neochloris oleoabundans* slurry–Experiments and modelling. Algal Res 31:21–30. https://doi.org/10.1016/j.algal.2018.01.001

Esquivel-Hernández DA, Ibarra-Garza IP, Rodríguez-Rodríguez J, Cuéllar-Bermúdez SP, Rostro-Alanis M d J, Alemán-Nava GS, García-Pérez JS, Parra-Saldívar R (2017) Green extraction technologies for high-value metabolites from algae: a review. Biofuels Bioprod Biorefin 11:215–231. https://doi.org/10.1002/bbb.1735

Folch J (1957) A simple method for the isolation and purification of total lipids from animal tissues. J Biol Chem 266:497–509

Fuad N, Omar R, Kamarudin S, Harun R, Idris A, Wan WA (2018) Mass harvesting of marine microalgae using different techniques. Food Bioprod Process 112:169–184. https://doi.org/10.1016/j.fbp.2018.10.006

Gallego R, Bueno M, Herrero M (2019) Sub- and supercritical fluid extraction of bioactive compounds from plants, food-by-products, seaweeds and microalgae–an update. TrAC - Trends Anal Chem 116:198–213. https://doi.org/10.1016/j.trac.2019.04.030

García JL, de Vicente M, Galán B (2017) Microalgae, old sustainable food and fashion nutraceuticals. Microb Biotechnol 10:1017–1024. https://doi.org/10.1111/1751-7915.12800

Gayen K, Bhowmick TK, Maity SK (Eds.) (2019) Sustainable downstream processing of microalgae for industrial application. CRC Press, Boca Raton

Ghasemi Naghdi F, González González LM, Chan W, Schenk PM (2016) Minireview progress on lipid extraction from wet algal biomass for biodiesel production. Microb Biotechnol 9:718–726. https://doi.org/10.1111/1751-7915.12360

Gifuni I, Pollio A, Safi C, Marzocchella A, Olivieri G (2019) Current bottlenecks and challenges of the microalgal biorefinery. Trends Biotechnol 37:242–252. https://doi.org/10.1016/j.tibtech.2018.09.006

Gilbert-López B, Mendiola JA, Fontecha J, Van Den Broek LAM, Sijtsma L, Cifuentes A, Herrero M, Ibáñez E (2015) Downstream processing of *Isochrysis galbana*: a step towards microalgal biorefinery. Green Chem 17:4599–4609. https://doi.org/10.1039/c5gc01256b

González-Delgado Á-D, Kafarov V (2011) Biorefinery: issues. CT&F - Ciencia, Tecnol y Futur 4(4):5–22

Goto M, Kanda H, Wahyudiono MS (2015) Extraction of carotenoids and lipids from algae by supercritical CO_2 and subcritical dimethyl ether. J Supercrit Fluids 96:245–251. https://doi.org/10.1016/j.supflu.2014.10.003

Gour RS, Garlapati VK, Kant A (2020) Effect of salinity stress on lipid accumulation in *Scenedesmus* sp. and *Chlorella* sp.: feasibility of stepwise culturing. Curr Microbiol. https://doi.org/10.1007/s00284-019-01860-z

Günerken E, D'Hondt E, Eppink MHM, Garcia-Gonzalez L, Elst K, Wijffels RH (2015) Cell disruption for microalgae biorefineries. Biotechnol Adv 33(2):243–260. https://doi.org/10.1016/j.biotechadv.2015.01.008

Häckl K, Kunz W (2018) Some aspects of green solvents. Comptes Rendus Chim 21:572–580. https://doi.org/10.1016/j.crci.2018.03.010

Harris J, Viner K, Champagne P, Jessop PG (2018) Advances in microalgal lipid extraction for biofuel production: a review. Biofuels, Bioprod. Biorefining 12(6):1118–1135

He Y, Huang Z, Zhong C, Guo Z, Chen B (2019) Bioresource technology pressurized liquid extraction with ethanol as a green and efficient technology to lipid extraction of Isochrysis biomass. Bioresour Technol 293:122049. https://doi.org/10.1016/j.biortech.2019.122049

Herrero M, Ibañez E (2018) Green extraction processes, biorefineries and sustainability: recovery of high added-value products from natural sources. J Supercrit Fluids 134:252–259. https://doi.org/10.1016/j.supflu.2017.12.002

Herrero M, Castro-Puyana M, Mendiola JA, Ibañez E (2013) Compressed fluids for the extraction of bioactive compounds. TrAC Trends Anal Chem 43:67–83. https://doi.org/10.1016/j.trac.2012.12.008

Hidayah N, Yasin M, Shafei NI, Rushan NH, Raihana N, Sepian A, Said FM (2019) ScienceDirect the effect of microalgae harvesting on lipid for biodiesel production. Mater Today Proc 19:1582–1590. https://doi.org/10.1016/j.matpr.2019.11.186

Hu Y, Guo C, Wang F, Wang S, Pan F, Liu C (2014) Improvement of microalgae harvesting by magnetic nanocomposites coated with polyethylenimine. Chem Eng J 242:341–347. https://doi.org/10.1016/j.cej.2013.12.066

Imbimbo P, Romanucci V, Pollio A, Fontanarosa C, Amoresano A, Zarrelli A, Olivieri G, Monti DM (2019) A cascade extraction of active phycocyanin and fatty acids from *Galdieria phlegrea*. Appl Microbiol Biotechnol 103:9455–9464. https://doi.org/10.1007/s00253-019-10154-0

Imbimbo P, Bueno M, D'Elia L, Pollio A, Ibañez E, Olivieri G, Monti DM (2020) Green compressed fluid technologies to extract antioxidants and lipids from *Galdieria phlegrea* in a biorefinery approach. ACS Sustain Chem Eng 8:2939–2947. https://doi.org/10.1021/acssuschemeng.9b07505

Iverson SJ, Lang SLC, Cooper MH (2001) Comparison of the bligh and dyer and folch methods for total lipid determination in a broad range of marine tissue. Lipids 36:1283–1287. https://doi.org/10.1007/s11745-001-0843-0

Appendix B

Jeevan Kumar SP, Vijay Kumar G, Dash A, Scholz P, Banerjee R (2017) Sustainable green solvents and techniques for lipid extraction from microalgae: a review. Algal Res 21:138–147. https://doi.org/10.1016/j.algal.2016.11.014

Jessop PG, Heldebrant DJ, Li X, Eckert CA, Liotta CL (2005) Reversible nonpolar-to-polar solvent. Green Chem 436:1101–1102. https://doi.org/10.1038/nature4361101a

Juin C, Chérouvrier JR, Thiéry V, Gagez AL, Bérard JB, Joguet N, Kaas R, Cadoret JP, Picot L (2015) Microwave-assisted extraction of phycobiliproteins from *Porphyridium purpureum*. Appl Biochem Biotechnol 175:1–15. https://doi.org/10.1007/s12010-014-1250-2

Kadir WNA, Lam MK, Uemura Y, Lim JW, Lee KT (2018) Harvesting and pre-treatment of microalgae cultivated in wastewater for biodiesel production: a review. Energy Convers Manag 171:1416–1429. https://doi.org/10.1016/j.enconman.2018.06.074

Kalsum U, Kusuma HS, Roesyadi A, Mahfud M (2019) Lipid extraction from *Spirulina platensis* using microwave for biodiesel production. Korean Chem Eng Res 57:301–304. https://doi.org/10.9713/kcer.2019.57.2.301

Kanda H, Hoshino R, Murakami K, Wahyudiono ZQ, Goto M (2020) Lipid extraction from microalgae covered with biomineralized cell walls using liquefied dimethyl ether. Fuel 262:116590. https://doi.org/10.1016/j.fuel.2019.116590

Koley S, Mathimani T, Bagchi SK, Sonkar S, Mallick N (2019) Microalgal biodiesel production at outdoor open and polyhouse raceway pond cultivations: a case study with *Scenedesmus accuminatus* using low-cost farm fertilizer medium. Biomass Bioenergy 120:156–165. https://doi.org/10.1016/j.biombioe.2018.11.002

Kothari R, Pandey A, Ahmad S, Kumar A, Pathak VV, Tyagi VV (2017) Microalgal cultivation for value-added products: a critical enviro-economical assessment. 3 Biotech 7:243

Krishnan S, Ghani NA, Aminuddin NF, Quraishi KS, Azman NS, Cravotto G, Leveque JM (2020) Microwave-assisted lipid extraction from *Chlorella vulgaris* in water with 0.5%–2.5% of imidazolium based ionic liquid as additive. Renew Energy 149:244–252. https://doi.org/10.1016/j.renene.2019.12.063

Kumar RR, Rao PH, Arumugam M (2015) Lipid extraction methods from microalgae: a comprehensive review. 2:1–9. https://doi.org/10.3389/fenrg.2014.00061

Lam GP, Vermuë MH, Eppink MHM, Wijffels RH, Van Den Berg C (2018) Multi-product microalgae biorefineries: from concept towards reality. Trends Biotechnol 36:216–227. https://doi.org/10.1016/j.tibtech.2017.10.011

Liu W, Chen Y, Wang J, Liu T (2019) Biomass productivity of *Scenedesmus dimorphus* (Chlorophyceae) was improved by using an open pond–photobioreactor hybrid system. Eur J Phycol 54:127–134. https://doi.org/10.1080/09670262.2018.1519601

Mansour EA, Abo El-Enin SA, Hamouda AS, Mahmoud HM (2019) Efficacy of extraction techniques and solvent polarity on lipid recovery from domestic wastewater microalgae. Environ Nanotechnol Monit Manag 12:100271. https://doi.org/10.1016/j.enmm.2019.100271

Mathimani T, Pugazhendhi A (2019) Utilization of algae for biofuel, bio-products and bio-remediation. Biocatal Agric Biotechnol 17:326–330. https://doi.org/10.1016/j.bcab.2018.12.007

Minyak P, Daripada A, Air M, Chlorella T (2017) Algae oil extraction from freshwater microalgae *Chlorella vulgaris*. Malaysian J Anal Sci 21:735–744. https://doi.org/10.17576/mjas-2017-2103-23

Molina D, de Carvalho JC, Júnior AIM, Faulds C, Bertrand E, Soccol CR (2019) Biological contamination and its chemical control in microalgal mass cultures. Appl Microbiol Biotechnol 103:9345–9358. https://doi.org/10.1007/s00253-019-10193-7

Molino A, Mehariya S, Di Sanzo G, Larocca V, Martino M, Leone GP, Marino T, Chianese S, Balducchi R, Musmarra D (2020) Recent developments in supercritical fluid extraction of bioactive compounds from microalgae: role of key parameters, technological achievements and challenges. J CO2 Util 36:196–209. https://doi.org/10.1016/j.jcou.2019.11.014

Motlagh SR, Harun R, Biak DRA, Hussain SA, Ghani WAWAK, Khezri R, Wilfred CD, Elgharbawy AAM (2019) Screening of suitable ionic liquids as green solvents for extraction of eicosapentaenoic acid (EPA) from microalgae biomass using COSMO-RS model. Molecules 24:713. https://doi.org/10.3390/molecules24040713

Narala RR, Garg S, Sharma KK, Thomas-Hall SR, Deme M, Li Y, Schenk PM (2016) Comparison of microalgae cultivation in photobioreactor, open raceway pond, and a two-stage hybrid system. Front Energy Res 4:1–10. https://doi.org/10.3389/fenrg.2016.00029

Nobre BP, Villalobos F, Barragán BE, Oliveira AC, Batista AP, Marques PASS, Mendes RL, Sovová H, Palavra AF, Gouveia L (2013) A biorefinery from *Nannochloropsis* sp. microalga-extraction of oils and pigments. Production of biohydrogen from the leftover biomass. Bioresour Technol 135:128–136. https://doi.org/10.1016/j.biortech.2012.11.084

Norsker NH, Barbosa MJ, Vermuë MH, Wijffels RH (2011) Microalgal production-a close look at the economics. Biotechnol Adv 29(1):24–27. https://doi.org/10.1016/j.biotechadv.2010.08.005

Phelps CL, Smart NG, Wai CM (1996) Past, present, and possible future applications of supercritical fluid extraction technology. J Chem Educ 73:1163–1168. https://doi.org/10.1021/ed073p1163

Pollet P, Eckertabc CA, Liotta CL (2011) Switchable solvents. Chem Sci 2:609–614. https://doi.org/10.1039/c0sc00568a

Pulz O, Gross W (2004) Valuable products from biotechnology of microalgae. Appl Microbiol Biotechnol 65:635–648. https://doi.org/10.1007/s00253-004-1647-x

Ramos L, Kristenson EM, Brinkman UAT (2002) Current use of pressurised liquid extraction and subcritical water extraction in environmental analysis. J Chromatogr A 975:3–29. https://doi.org/10.1016/S0021-9673(02)01336-5

Rasouli Z, Valverde-Pérez B, D'Este M, De Francisci D, Angelidaki I (2018) Nutrient recovery from industrial wastewater as single cell protein by a co-culture of green microalgae and methanotrophs. Biochem Eng J 134:129–135. https://doi.org/10.1016/j.bej.2018.03.010

Rawat I, Kumar RR, Mutanda T, Bux F (2011) Dual role of microalgae: phycoremediation of domestic wastewater and biomass production for sustainable biofuels production. Appl Energy 88:3411–3424. https://doi.org/10.1016/j.apenergy.2010.11.025

Saini RK, Keum Y (2018) Carotenoid extraction methods: a review of recent developments. Food Chem 240:90–103. https://doi.org/10.1016/j.foodchem.2017.07.099

Samorì C, Lòpez Barreiro D, Vet R, Pezzolesi L, Brilman DWF, Galletti P, Tagliavini E (2013) Effective lipid extraction from algae cultures using switchable solvents. Green Chem 15:353–356. https://doi.org/10.1039/c2gc36730k

Sati H, Mitra M, Mishra S, Baredar P (2019) Microalgal lipid extraction strategies for biodiesel production: a review. Algal Res 38:101413. https://doi.org/10.1016/j.algal.2019.101413

Schipper K, Al Muraikhi M, Alghasal GSHS, Saadaoui I, Bounnit T, Rasheed R, Dalgamouni T, Al Jabri HMSJ, Wijffels RH, Barbosa MJ (2019) Potential of novel desert microalgae and cyanobacteria for commercial applications and CO_2 sequestration. J Appl Phycol 31:2231–2243. https://doi.org/10.1007/s10811-019-01763-3

Schuur B, Brouwer T, Smink D, Sprakel LMJ (2019) Green solvents for sustainable separation processes. Curr Opin Green Sustain Chem 18:57–65. https://doi.org/10.1016/j.cogsc.2018.12.009

Singh SK, Savoy AW (2020) Ionic liquids synthesis and applications: an overview. J Mol Liq 297:112038. https://doi.org/10.1016/j.molliq.2019.112038

Appendix B

Slegers PM, Lösing MB, Wijffels RH, van Straten G, van Boxtel AJB (2013) Scenario evaluation of open pond microalgae production. Algal Res 2:358–368. https://doi.org/10.1016/j.algal.2013.05.001

Souza LS, Simioni C, Bouzon ZL, De Cassia R, Schneider S, Gressler P, Miotto MC, Rossi MJ, Rörig LR (2017) Morphological and ultrastructural characterization of the acidophilic and lipid-producer strain *Chlamydomonas acidophila* LAFIC-004 (*Chlorophyta*) under different culture conditions. 1385–1398. https://doi.org/10.1007/s00709-016-1030-7

Tatke P, Jaiswal Y (2011) An overview of microwave assisted extraction and its applications in herbal drug research. Res J Med Plant 5:21–31. https://doi.org/10.3923/rjmp.2011.21.31

Vanderveen JR, Durelle J, Jessop PG (2014) Design and evaluation of switchable-hydrophilicity solvents. Green Chem 16:1187–1197. https://doi.org/10.1039/c3gc42164c

Vega-López S, Kaul N, Devaraj S, Cai RY, German B, Jialal I (2004) Supplementation with ω3 polyunsaturated fatty acids and all-rac alpha-tocopherol alone and in combination failed to exert an anti-inflammatory effect in human volunteers. Metabolism 53:236–240. https://doi.org/10.1016/j.metabol.2003.09.012

Vekariya RL (2017) A review of ionic liquids: applications towards catalytic organic transformations. J Mol Liq 227:44–60. https://doi.org/10.1016/j.molliq.2016.11.123

Wang H, Zhang W, Chen L, Wang J, Liu T (2013) The contamination and control of biological pollutants in mass cultivation of microalgae. Bioresour Technol 128:745–750. https://doi.org/10.1016/j.biortech.2012.10.158

Wang S, Yerkebulan M, Abomohra AEF, El-Khodary S, Wang Q, Souza LS, Simioni C, Bouzon ZL, Schneider RCS, Gressler P, Miotto MC, Rossi MJ, Rörig LR, Schipper K, Al Muraikhi M, Alghasal GSHS, Saadaoui I, Bounnit T, Rasheed R, Dalgamouni T, Al Jabri HMSJ, Wijffels RH, Barbosa MJ, Yusuff AS, Wei L, Huang X, Huang Z (2019) Morphological and ultrastructural characterization of the acidophilic and lipid-producer strain *Chlamydomonas acidophila* LAFIC-004 (Chlorophyta) under different culture conditions. J Appl Phycol 31:121371–122243. https://doi.org/10.1007/s10811-019-01763-3

Wei L, Huang X, Huang Z (2014) Temperature effects on lipid properties of microalgae *Tetraselmis subcordiformis* and *Nannochloropsis oculata* as biofuel resources. Chin J Oceanol Limnol 33:99–106. https://doi.org/10.1007/s00343-015-3346-0

Xu L, Wang F, Li HZ, Hu ZM, Guo C, Liu CZ (2010) Development of an efficient electroflocculation technology integrated with dispersed-air flotation for harvesting microalgae. J Chem Technol Biotechnol 85:1504–1507. https://doi.org/10.1002/jctb.2457

Yin Z, Zhu L, Li S, Hu T, Chu R, Mo F, Hu D, Liu C, Li B (2020) A comprehensive review on cultivation and harvesting of microalgae for biodiesel production: environmental pollution control and future directions. Bioresour Technol 301:122804. https://doi.org/10.1016/j.biortech.2020.122804

Youn S, Muk J, Keun Y, Oh Y (2017) Cell disruption and lipid extraction for microalgal biorefineries: a review. Bioresour Technol 244:1317–1328. https://doi.org/10.1016/j.biortech.2017.06.038

Yusuff AS (2019) Environmental effects extraction, optimization, and characterization of oil from green microalgae *Chlorophyta* species. Energy Sources, Part A Recover Util Environ Eff 1–12 . https://doi.org/10.1080/15567036.2019.1676327

Zghaibi N, Omar R, Kamal SMM, Biak DRA, Harun R (2019) Microwave-assisted brine extraction for enhancement of the quantity and quality of lipid production from microalgae *Nannochloropsis* sp. Molecules 24:1–21. https://doi.org/10.3390/molecules24193581

Zhang Y, Bakshi BR, Demessie ES (2008) Life cycle assessment of an ionic liquid versus molecular solvents and their applications. Environ Sci Technol 42:1724–1730. https://doi.org/10.1021/es0713983

Zhang J, Sun Z, Sun P, Chen T, Chen F (2014) Microalgal carotenoids: beneficial effects and potential in human health. Food Funct 5:413–425. https://doi.org/10.1039/c3fo60607d

Zhang T, Hu H, Wu Y, Zhuang L, Xu X (2016) Promising solutions to solve the bottlenecks in the large-scale cultivation of microalgae for biomass/bioenergy production. Renew Sust Energ Rev 60:1602–1614. https://doi.org/10.1016/j.rser.2016.02.008

Zhang R, Parniakov O, Grimi N, Lebovka N, Marchal L, Vorobiev E (2019) Emerging techniques for cell disruption and extraction of valuable bio-molecules of microalgae *Nannochloropsis* sp. Bioprocess Biosyst Eng 42:173–186. https://doi.org/10.1007/s00449-018-2038-5

Zheng H, Gao Z, Yin J, Tang X, Ji X, Huang H (2012) Harvesting of microalgae by flocculation with poly (c-glutamic acid). Bioresour Technol 112:212–220. https://doi.org/10.1016/j.biortech.2012.02.086

Zimmerer J, Pingen D, Hess SK, Koengeter T, Mecking S (2019) microalgae lipids in supercritical carbon dioxide †. Green Chem 21:2428–2435. https://doi.org/10.1039/c9gc00312f

Zullaikah S, P MCJ, Yasmin M, Rachimoellah M, Wu D (2019) Lipids extraction from wet and unbroken microalgae *Chlorella vulgaris* using subcritical water. Mater Sci Forum 964:103–108. https://doi.org/10.4028/www.scientific.net/MSF.964.103

ACS Sustainable Chemistry & Engineering

pubs.acs.org/journal/ascecg

Research Article

Switchable Solvent Selective Extraction of Hydrophobic Antioxidants from *Synechococcus bigranulatus*

Luigi D'Elia, Paola Imbimbo, Davide Liberti, Francesco Bolinesi, Antonino Pollio, Olga Mangoni, Wim Brilman, Giuseppe Olivieri, and Daria Maria Monti*

Cite This: *ACS Sustainable Chem. Eng.* 2021, 9, 13798−13806

Read Online

ACCESS | Metrics & More | Article Recommendations | Supporting Information

ABSTRACT: Hydrophobic molecules, in particular, carotenoids, have been directly extracted from *Synechococcus bigranulatus* ACUF680 by means of secondary amine switchable solvent *N*-ethylbutylamine (EBA) without any other pretreatment. EBA was able to extract hydrophobic molecules from both fresh and frozen biomass at the same extent of the conventional procedure (about 20% of dry biomass). In particular, selective extraction of a zeaxanthin-enriched fraction (green fraction, GF) and a β-carotene-enriched fraction (orange fraction, OF) was obtained. The ratio between zeaxanthin and β-carotene was 4.4 ± 1.5 for GF, 0.07 ± 0.06 for OF, and about 1 for conventional extraction. These fractions showed *in vitro* antioxidant activity (IC_{50} values of 0.056 ± 0.013 and 0.024 ± 0.008 mg mL^{-1} for GF and OF, respectively) and biocompatibility on immortalized cells. Moreover, OF and GF were able to protect cells from oxidative stress, both before and after thermal treatment. Results clearly indicate that EBA is a good candidate to specifically extract β-carotene and zeaxanthin from the wet biomass of *S. bigranulatus* without affecting their biological activity. Skipping energy-intensive operations to break the cells and using either fresh or frozen biomass may be the driving factors to use EBA switchable solvent on an industrial scale.

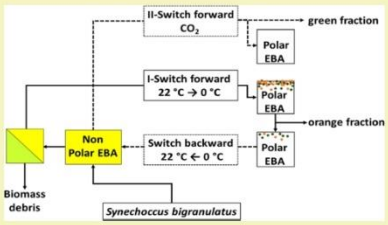

KEYWORDS: *antioxidants, switchable solvents, microalgae, N-ethylbutylamine, green chemistry*

INTRODUCTION

In the last decades, the search for energy from renewable sources and the increasing demand of consumers for healthy foods have driven the attention toward microalgae and cyanobacteria.[1−4] These phototrophic microorganisms can be rich in high-value biological compounds, such as proteins, polysaccharides, polyunsaturated fatty acids, vitamins, and pigments with special biological activities, and thus they can potentially be exploited in several industrial sectors and meet many new consumer wishes.[4−6]

Today, algae and cyanobacteria are used only in the food industry as additives for functional food and as food supplements. In this context, the increasing demand for natural antioxidants, as a healthy alternative to synthetic additives in the food industry, has strengthened the interest for microalgae and cyanobacteria as a valid source of natural antioxidants, such as polyphenols and pigments.[7−14] Among pigments, carotenoids show the highest antioxidant activity. They are divided into two groups: carotenes and xanthophylls. So far, in the global market, the most commercialized carotenoids are astaxanthin, β-carotene, lutein, canthaxanthin, lycopene, and zeaxanthin.[15]

Till date, antioxidant extraction is usually performed by using organic solvents.[10,16,17] However, these benchmark technologies suffer from several drawbacks, making the whole process unsustainable: (i) the use of high amounts of solvent; (ii) the need for a large amount of energy to recover the solvent by evaporation; (iii) the need for more than one extraction step; (iv) the recovery of a mixture of molecules with similar polarity.[18−20]

These drawbacks are even more consistent in the case of antioxidants from microalgae as they already suffer from upstream process costs.[21] Thus, the optimization of a green extraction technique able to replace conventional procedures seems to be a good starting point for lowering the costs. So far, it has been reported that the new green extraction techniques performed at high pressure, such as supercritical fluid extraction and pressurized liquid extraction, are more sustainable and can be competitive in the effectiveness of the extraction of hydrophobic molecules.[22−24] However, these innovative tech-

Received: June 28, 2021
Revised: September 23, 2021
Published: October 6, 2021

https://doi.org/10.1021/acssuschemeng.1c04400
ACS Sustainable Chem. Eng. 2021, 9, 13798−13806

Appendix C

nologies show some disadvantages: (i) need of biomass pretreatment often, (ii) difficulty to extract hydrophilic molecules ; (iii) high investment costs, and (iv) difficulty to scale up the process at an industrial scale.[20,25]

In this context, a new class of solvents is emerging: switchable solvents. Switchable solvents (SSs), first reported by Jessop and Liotta,[26,27] are liquids that can be converted from a nonpolar form to a polar form and vice versa. The switching of the solvent in the hydrophilic form (switch forward) is done by bubbling CO_2 through the solvent. The reverse reaction is induced by completely removing CO_2 from the system with an inert gas, such as N_2, and is enhanced by the heating temperature.[28] This unique feature allows the solvent, when in the nonpolar form, to extract hydrophobic components, and, when in the polar form, to extract hydrophilic components. Furthermore, when in the polar form or in the nonpolar form, the solvent should be easily separated by the hydrophobic or hydrophilic extracts, respectively. Noteworthy, the circularity of the extraction process on the wet biomass involves a significant reduction in energy consumption because the separation of the solvent from the extract is not performed by evaporation.[29,30]

Recently, a study carried out by Du et al. reported that the secondary amine *N*-ethylbutylamine (EBA) shows a lower critical solution temperature (LCST) behavior, which means that a change in EBA polarity is possible only by changing the temperature.[31] This alternative operation is expected to be a cost and energy efficient alternative to the CO_2 switching system.[31] However, the feasibility of the process to effectively and sequentially extract lipids and proteins from microalgae by using a SS characterized by LCST behavior has not been clearly defined yet.[32]

Here, an innovative procedure to selectively extract hydrophobic antioxidants from the cyanobacterium *Synechococcus bigranulatus* was set up. *S. bigranulatus* is a good candidate for the production of thermo-resistant antioxidants as it is able to grow at different temperatures.[33] Experiments were performed by using EBA as the extracting solvent, and three different strategies were tested (Figures S1−S3). Hydrophobic fractions were characterized from a chemical and biological point of view, and the antioxidant activity was tested before and after high-temperature short-time (HTST) pasteurization.

MATERIALS AND METHODS

Reagents. All solvents, reagents, chemicals, and culture media, unless differently specified, were from Sigma-Aldrich (St Louis, MO, USA).

Microalgal Strain and Culture Conditions. *S. bigranulatus* was provided by the Algal Collection of the University Federico II (ACUF number 680).[34] Cells were grown in autotrophic conditions in 800 mL working volume bubble column photobioreactors in BG11 medium. The photobioreactors were housed in a climate chamber at 37 ± 1 °C equipped with fluorescent lamps with a constant light intensity of 300 PAR $\mu mol_{photons}\ m^{-2}\ s^{-1}$. The aeration of cultures was provided by supplying air at the bottom of the photobioreactors. Cell density was inferred from the absorbance measured at a wavelength of 730 nm. The culture was harvested at the end of the exponential phase, and the biomass concentration was about 0.8 g L^{-1}.

Water Content of *S. bigranulatus*. The water content of the harvested wet microalgae paste after centrifugation was determined by weighing the sample before and after drying at 60 °C for 24 h. The water content did not change significantly among samples and was 73.1 ± 3.3%.

Protein Extraction and Quantification. The biomass was harvested by centrifugation at 1200*g* for 30 min at room temperature. Then, 1.5 g of wet biomass, which corresponds to about 400 mg d.w., was resuspended in 50 mM sodium acetate buffer pH 5.5.[35] Cells were disrupted by ultrasonication (30 s on, 30 s off, 40% instrument amplitude) for 45 min on ice. After centrifugation at 5000*g* at 4 °C for 30 min, the proteins were recovered in the supernatant and their concentration was measured by the BCA Assay Kit (Thermo Fisher Scientific, Waltham, MA USA).

Conventional Extraction of Total Hydrophobic Molecules. Conventional extraction of hydrophobic molecules from the dry biomass (∼0.3 g) was performed according to the original Bligh & Dyer (B&D) method.[36]

Hydrophobic Molecule Extraction by EBA. To extract hydrophobic molecules from *S. bigranulatus* by EBA, the wet biomass (∼1.5 g) was mixed with EBA in a ratio of 1:2 (wt/wt). The mixture was magnetically stirred at room temperature for 18 h to ensure extraction of hydrophobic molecules. Then, the mixture was centrifuged at 9000*g* at room temperature, and the supernatant (which contains EBA and hydrophobic molecules) was mixed with water in a ratio of 1:2 (wt/wt), forming a biphasic system. Then, three experimental approaches were followed and are schematically represented in Figures S1−S3.

Strategy 1: CO_2–N_2 Switching Method. CO_2 was insufflated into the biphasic system for 30 min at 2 vvm (volume volume per minute) to allow EBA to switch in its polar form (switching forward). The sample was centrifuged at 9000*g* at room temperature. At the end of centrifugation, EBA and water formed a homogeneous phase (water phase) with a small lipid layer on the top. The hydrophobic molecules were recovered by chloroform. The total amount of the extracted product was measured gravimetrically (after evaporating the solvent) and reported as a percentage of the algae dry weight.

To extract hydrophilic molecules, the water phase was incubated in the presence of the residual biomass for 2 h at room temperature. The sample was centrifuged at 9000*g* at 0 °C for 10 min. Then, to recover the extracted hydrophilic molecules, N_2 was bubbled through the supernatant to remove CO_2 (switch back) and to allow EBA returning in the hydrophobic form. The sample was centrifuged at 9000*g* at room temperature. However, no formation of the two phase system was observed.

Strategy 2: Temperature switching method (LCST). The supernatant was cooled to 0 °C for 2 h to allow the switch of EBA in its polar form. The sample was centrifuged at 9000*g* at 0 °C. The result was a water phase with a hydrophobic layer on the top of the tube. This layer consisted of two parts, a green layer on the top and an orange layer on the wall of the tube. To recover the hydrophobic phase, chloroform was added, mixed, and centrifuged at 9000*g* at 0 °C for 10 min. A two-phase system was observed with the hydrophobic molecules on the bottom. The total amount of the extracted products was measured gravimetrically (after evaporating the solvent) and reported as a percentage of the algae dry weight. To extract hydrophilic molecules, the water phase was incubated in the presence of the residual biomass for 2 h at 0 °C. The sample was centrifuged at 9000*g* at 0 °C for 10 min. Then, to collect hydrophilic molecules, the supernatant was heated to 22 °C to allow EBA switching back to the nonpolar form. The sample was centrifuged at 9000*g* at 0 °C for 10 min to allow the formation of two phases. The aqueous fraction containing hydrophilic molecules was collected, the total proteins were determined by the BCA assay, and then an sodium dodecyl sulfate-polyacrylamide gel electrophoresis (SDS-PAGE) analysis was performed.

Strategy 3: Switch Forward-Switch Back-Switch Forward. To avoid the use of chloroform during the recovery of the hydrophobic molecules, heptane was used. By this procedure, the orange layer was recovered after centrifugation at 9000*g* at 0 °C. The green layer was found to be mixed again with EBA. To recover them, a double switch was needed. Thus, the system was heated to 22 °C to allow EBA switching back to the nonpolar form. The sample was centrifuged at 9000*g* at room temperature to allow the formation of two phases. The upper phase contained EBA and the hydrophobic molecules. The upper phase was transferred to a new tube and mixed with water in a ratio of 1:2 (wt/wt) forming a biphasic system. Then, CO_2 was insufflated into the system for 30 min at 2 vvm, and the sample was centrifuged at 9000*g* at room temperature to recover the green fraction (GF) on the top by chloroform.

https://doi.org/10.1021/acssuschemeng.1c04400
ACS Sustainable Chem. Eng. 2021, 9, 13798−13806

Appendix C

The total amount of the extracted products was measured gravimetrically (after evaporating the solvent) and reported as a percentage of the algae dry weight.

In a parallel experiment, heptane was replaced by methanol.

ABTS Assay. The *in vitro* antioxidant activity of the orange fraction (OF) and GF was evaluated by the 2,2′-azinobis-(3-ethylbenzothiazoline-6-sulfonic acid) ABTS assay according to Rigano et al. with some modifications.[37] Briefly, 7.4 mM $ABTS^{\bullet+}$ was mixed with 140 mM $K_2S_2O_8$, and the solution was stabilized for 16 h at room temperature in the dark. The mixture was then diluted with deionized water to obtain an absorbance of 0.70 ± 0.02 unit at 734 nm using a spectrophotometer. Each extract (50 μL) was allowed to react with 250 μL of diluted $ABTS^{\bullet+}$ solution for 7 min, and then the absorbance was read at 734 nm. The standard curve was linear between 0 and 20 μM Trolox. Results are expressed as IC_{50} (mg mL^{-1}), that is, the concentration required to scavenge 50% of free radical ABTS.

Cell Culture and Biocompatibility Assay. Human immortalized keratinocytes (HaCaT, Innoprot, Spain) and immortalized murine fibroblasts (BALB/c 3T3, ATCC, Manassas, VI, USA) were cultured in 10% fetal bovine serum in Dulbecco's modified Eagle's medium in the presence of 1% antibiotics and 2 mM L-glutamine in a 5% CO_2 humidified atmosphere at 37 °C. HaCaT cells were seeded in 96-well plates at a density of 2×10^3 cells $well^{-1}$, and BALB/c 3T3 were seeded at a density of 3×10^3 cells $well^{-1}$. 24 h after seeding, increasing concentrations of OF and GF (from 10 to 200 μg mL^{-1}) were added to the cells for 48 h. At the end of the incubation, cell viability was measured by the tetrazolium salt colorimetric assay (MTT assay), as previously described.[38] Cell survival was expressed as the percentage of viable cells in the presence of the extracts compared to control cells (represented by the average obtained between untreated cells and cells supplemented with the highest concentration of the buffer). Each sample was tested in three independent analysis, each carried out in triplicate.

HTST Pasteurization. Thermal pasteurization was performed accordingly to the protocol reported by Ferraro et al.[39] Briefly, OF and GF were heated at 75 °C in a water bath. After 10 min incubation, the samples were transferred to a second water bath at 20 °C and then stored at 4 °C until analysis.

Cellular Reactive Oxygen Species Assay. To evaluate the protective effect of OF and GF against oxidative stress, DCFDA assay was carried out according to the protocol reported by Petruk et al.[40] with some modifications. Briefly, 24 h after seeding, the cells were incubated in the presence of 25 μg mL^{-1} of either raw or pasteurized OF and GF for 2 h and irradiated by UVA light for 10 min (100 J cm^{-2}). Fluorescence intensity of the probe (2′, 7′-dichlorofluorescein, DCF) was measured at an emission wavelength of 525 nm and an excitation wavelength of 488 nm using a PerkinElmer LS50 spectrofluorometer. Emission spectra were acquired at a scanning speed of 300 nm min^{-1} with a 5-slit width for both excitation and emission. Reactive oxygen species (ROS) production was expressed as the percentage of DCF fluorescence intensity of the samples under test compared to untreated samples. Three independent experiments were carried out, each one with three determinations.

Pigment Identification by High-Performance Liquid Chromatography. For the determination of the pigment content, the extracts were resuspended in 100% methanol and analyzed by isocratic high-performance liquid chromatography (HPLC) (Hewlett Packard, 1100 Series) in a reverse phase (C8 column 3 μm Hyperloop MOS, 10 cm, 4.6 mm internal diameter, Shandon) as described by Vidussi et al.[41] The mobile phase consisted of MeOH: 0.5 N aqueous ammonium acetate, 70:30% v/v (solvent A) and MeOH (solvent B), with a gradient (time expressed in minutes; percent of solvent A-percent of solvent B): 0:75−25; 1:50−50; 15:0−100; and 19:75−25. For the determination of chlorophylls and carotenoids, a spectrophotometer with a diode array detector was set at 440 nm, making it possible to determine the absorption spectrum of the 350−750 nm interval for each peak in order to check the purity of single pigments. The calibration of the instrument was carried out using external standard pigments provided by the International Agency for 14C determination-VKI Water Quality Institute. The identification of pigments was based considering the retention time, spectral characteristics, and chromatography with certified commercial standards (International Agency for 14C determinations, Denmark). Quantification was based on the absorbance at 440 nm and the factor response (peak area/pigment concentration) value for each pigment, as described in the study by Mantoura and Repeta.[42]

Statistical Analysis. Samples were analyzed in triplicate. Results are presented as mean of results (means ± SD) and compared by one-way ANOVA according to the Bonferroni's method (post hoc) or *t*-test using Graphpad Prism for Windows, version 6.01.

■ RESULTS AND DISCUSSION

Extraction and Recovery of Hydrophobic Molecules from Synechococcus bigranulatus through SSs. To verify the ability of EBA SS to extract hydrophobic molecules from the frozen wet biomass of *S. bigranulatus*, a direct comparison with a reference extraction method (B&D) on dry biomass was performed. Thus, frozen wet biomass was mixed with the solvent. Then, to separate hydrophobic molecules from EBA, the solvent was switched to the hydrophilic form (switch forward) by two procedures: (i) by bubbling CO_2 through the system (SS−CO_2 switch-forward, reported in Figure S1) and (ii) by decreasing the temperature (SS-LCST switch-forward, LCST, reported in Figure S2).

The extracted hydrophobic molecules were measured gravimetrically and reported as percentage with respect to the dry weight biomass (Figure 1). Results clearly show that EBA was

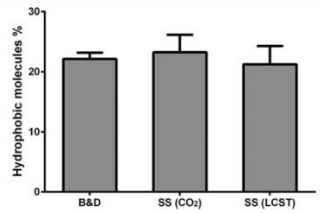

Figure 1. Hydrophobic molecules from *S. bigranulatus* biomass. Yields are reported as % with respect to the dry weight biomass. SS (CO_2) refers to extraction by SS and CO_2; SS (LCST) refers to extraction by SS and LCST. Results are reported as means ± SD of at least three independent experiments.

able to extract hydrophobic molecules from the algae at the same extent of the B&D procedure. This result indicates that it is possible to obtain hydrophobic molecules starting from a wet biomass, thus potentially reducing the costs of the whole process, which are affected by drying, milling, and temperature.

Protein Extraction. After the extraction of hydrophobic molecules, EBA solvent, in its polar form, was used to extract proteins on the residual biomass, as described in the Materials and Method section. In this case, ultrasounds were used as the reference procedure. When the SS-CO_2 switch-forward strategy was performed, no formation of the two-phase system was observed after N_2 insufflation and temperature increase, probably due to stripping of switched (hydrophobic) EBA from the solution by the warm N_2 flow. In the case of SS-LCST switch-forward strategy, in which only the temperature was changed, a hydrophilic phase was recovered and characterized. According to the BCA assay, the SS (LCST-CO_2) method allowed to recover about 10% proteins, a value 3-fold lower than

https://doi.org/10.1021/acssuschemeng.1c04400
ACS Sustainable Chem. Eng. 2021, 9, 13798−13806

Appendix C

in the case of ultrasonication. However, when the samples were analyzed by SDS-PAGE, no proteins were observed in the sample SS (LCST-CO_2) (Figure 2), thus suggesting that, during

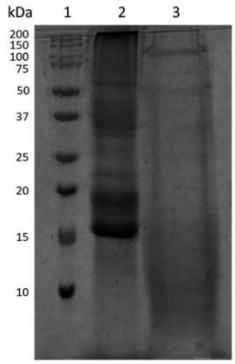

Figure 2. Proteins extracted from *S. bigranulatus*. SDS-PAGE analysis of proteins extracted by ultrasounds and SS (LCST-CO_2) extraction. Lane 1: molecular weight markers; lane 2: soluble proteins extracted by ultrasounds (30 μg); lane 3: soluble proteins extracted by EBA (30 μg). SDS-PAGE was stained by Blue Coomassie.

the extraction with nonpolar EBA, proteins may be degraded and/or unfolded and precipitate in the centrifugation step. The results indicate that the yield calculated by the BCA procedure is affected by the presence of EBA itself. In a parallel experiment, the polar form of EBA was used on the raw biomass to verify its ability to extract hydrophilic molecules. However, no hydrophilic molecules were obtained, maybe because polar EBA was not able to destroy the biomass in the absence of any physical and/or mechanical treatment (data not shown). On the other hand, nonpolar EBA better penetrates the biomass of microalgae with a fragile cell wall, such as the one of *S. bigranulatus*. The cyanobacterium has a cell wall similar to that of Gram-negative bacteria but equipped with a thick peptidoglycan layer.[43,44] Moreover, the absence of cellulose renders the process feasible under mild conditions.

Switch Forward-Switch Back-Switch Forward Strategy. In order to replace chloroform with a green solvent, a third strategy was set up (Figure S3), and the detailed procedure is described in the Materials and Method section. The replacement of chloroform with heptane allowed to recover an OF, whereas the green layer was mixed again with EBA. Thus, the GF was recovered after a second cycle of switch-forward by using chloroform. Fresh and frozen (stored at −20 °C) biomass were analyzed in parallel experiments. As reported in Figure 3, the yields of OF and GF do not show any significant difference between the two starting materials. This result suggests that the extraction can be performed according to the experimental purpose, that is, on either just harvested or stored biomass. Thus, from an industrial point of view, even if storing the biomass can be a cost, it could allow a more flexible scheduling of the downstream process.

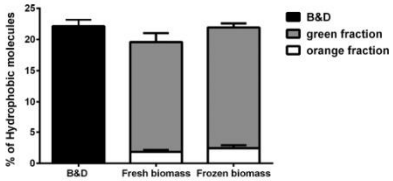

Figure 3. Yields of hydrophobic molecules in OF and GF. Yields are referred to extracts from fresh or frozen biomass and reported as % with respect to the dry weight biomass. Black bar refers to B&D; gray bars refer to the GF; white bars refer to the OF. Results are reported as means ± SD of at least three independent experiments.

HPLC Analysis. HPLC analysis was performed to identify the molecules present in OF and GF. Results are reported in Figure 4 and they clearly show that OF is enriched in β-carotene, whereas GF is enriched in zeaxanthin. Indeed, when the ratio zeaxanthin/β-carotene was measured in both fractions, a ratio of 0.07 ± 0.06 was found in the OF and 4.4 ± 1.5 in the GF, whereas the ratio in the raw extract obtained by conventional extraction was about 1. In particular, zeaxanthin values ranged between 1.3 and 20.7 mg g_{dw}^{-1} in the GF, whereas β-carotene ranged between 0.3 and 0.6 mg g_{dw}^{-1} in the OF. A mean value of 0.37 mg g_{dw}^{-1} was observed instead for both molecules in the extract obtained by a conventional method, suggesting a better extraction yield of at least zeaxanthin with EBA with respect to conventional methods.

ABTS Assay. To verify if the extraction technique affected the biological activity of OF and GF, the *in vitro* antioxidant activity was tested by the ABTS assay. Results are shown in Figure 5 and clearly indicate that both fractions had antioxidant activity. The IC_{50} values, which correspond to the concentration of the extract that can inhibit 50% of the radical, were 0.024 ± 0.008 and 0.056 ± 0.013 mg mL^{-1} for the OF and GF, respectively.

Evaluation of the Biocompatibility of OF and GF on Eukaryotic Cells. The biocompatibility of OF and GF was evaluated by the MTT assay on two immortalized eukaryotic cell lines: HaCaT (human keratinocytes) and BALB/c 3T3 (murine fibroblasts). Cells were incubated in the presence of each extract for 48 h, and cell survival was determined as described in the Materials and Methods section. As shown in Figure 6, the GF did not show cell mortality on both cell lines tested up to 200 μg mL^{-1} (A,B), whereas the OF (C,D) showed a low level of toxicity only on HaCaT cells (IC_{50} value of 152 ± 7 μg mL^{-1}). Noteworthy, the solvent used to recover the OF is important as when methanol was used, cell mortality was achieved at a very low concentration of the extract, with an IC_{50} value of 31 ± 8 μg mL^{-1} and 43 ± 4 μg mL^{-1} on HaCaT cells and BALB/c 3T3 cells, respectively (E,F).

Evaluation of Antioxidant Activity of OF and GF on Eukaryotic Cells. To verify if the two extracts could be used in the food industry and if they are resistant to high-temperature treatments, a comparison between the antioxidant activity of raw and pasteurized extracts (i.e., HTST pasteurization) was performed on a cell-based system. HaCaT cells were stressed by UVA, chosen as a source of oxidative stress. Cells were incubated for 2 h with 25 μg mL^{-1} of each extract prior to UVA exposure. Then, the DCFDA probe was used to measure the

https://doi.org/10.1021/acssuschemeng.1c04400
ACS Sustainable Chem. Eng. 2021, 9, 13798−13806

Appendix C

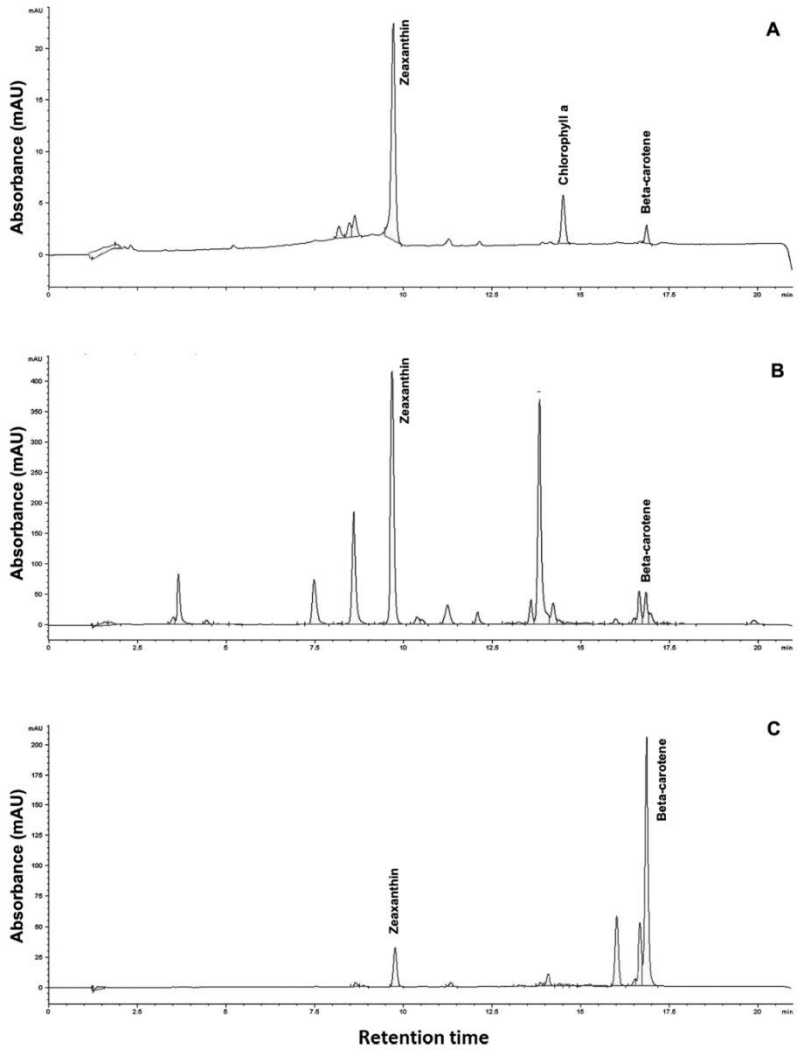

Figure 4. Representative HPLC chromatograms of antioxidants extracted from *S. bigranulatus*. (A) Raw extract obtained by conventional extraction, (B) GF, and (C) OF.

https://doi.org/10.1021/acssuschemeng.1c04400
ACS Sustainable Chem. Eng. 2021, 9, 13798−13806

Appendix C

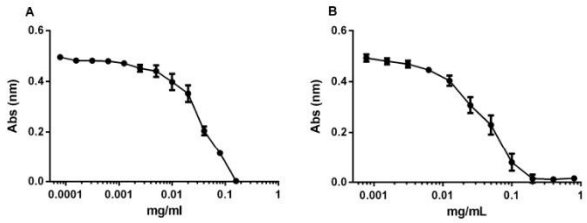

Figure 5. ABTS assay on OF and GF. The ABTS scavenging activity of OF (A) and GF (B) (mg mL^{-1}) from *S. bigranulatus*. Data shown are means ± SD of three independent experiments.

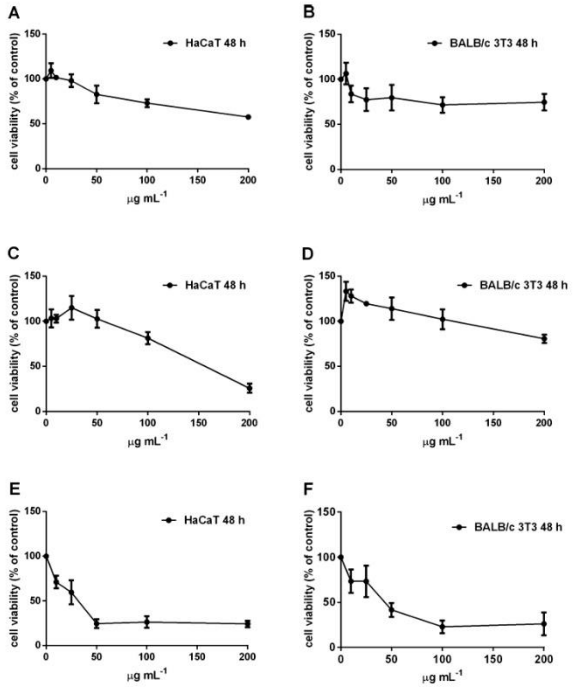

Figure 6. Cell viability of OF and GF on eukaryotic cells. HaCaT and BALB/c 3T3 were incubated for 48 h with increasing concentrations (10−200 μg mL^{-1}) of GF (A,B), OF collected with heptane (C,D), and OF collected with methanol (E,F). Cell viability was assessed by the MTT assay, and cell survival expressed as a percentage of viable cells in the presence of the extracts under test with respect to control cells grown in the absence of the extracts. Data shown are means ± SD of three independent experiments.

ROS levels. As shown in Figure 7, no effect on ROS levels was observed when the cells were incubated with either the raw OF or GF extracts, whereas when the cells were incubated with pasteurized orange and green extracts, an increase in intracellular ROS levels is observed in the absence of any treatment. UVA induced a significant increase in intracellular ROS levels

https://doi.org/10.1021/acssuschemeng.1c04400
ACS Sustainable Chem. Eng. 2021, 9, 13798−13806

Appendix C

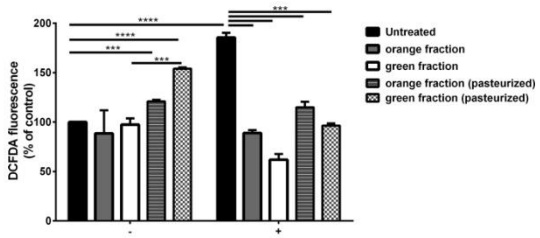

Figure 7. Antioxidant effect of the orange and green extracts from *S. bigranulatus* on UVA-stressed HaCaT cells. Cells were preincubated in the presence of 25 $\mu g\ mL^{-1}$ of raw and pasteurized extracts for 2 h prior to be irradiated by UVA (100 J cm^{-2}). For each experimental condition, ROS production was measured, and the results are reported as percentage with respect to untreated cells. Black bars: untreated cells; gray bars: cells incubated with OF; white bars: cells incubated with GF; gray striped bars: cells incubated with pasteurized OF; white squared bars: cells incubated with pasteurized GF. Data shown are means ± SD of three independent experiments. *** indicates $p < 0.005$; **** indicates $p < 0.0005$.

(180%) with respect to untreated cells (black bars). When cells were preincubated with any of the extract, no alteration in ROS levels was observed, thus suggesting that the extracts were able to protect cells from stress injury. These results indicate that thermal procedures do not affect the antioxidant activity of both fractions.

CONCLUSIONS

SSs are widely used to extract hydrophobic molecules from algae raw biomass.[19,28,45] In this work, the secondary amine EBA was used on the cyanobacterium *S. bigranulatus* to test the ability to sequentially extract hydrophobic and hydrophilic components. Yields of hydrophobic molecules clearly show that EBA has the same extraction power as conventional methods. However, EBA was not able to extract proteins. This result seems to be in contrast with the data reported in the literature as about 40% of proteins have been reported to be extracted from different microalgae by using the tertiary amine *N,N*-dimethyl-cyclohexylamine.[30] Noteworthy, in the present paper, by using the same colorimetric assay, about 10% of proteins seemed to be present in the hydrophilic fraction, but no proteins were observed by SDS-PAGE analysis, thus suggesting an interference of EBA with the colorimetric assay.

Surprisingly, EBA allowed the selective extraction of β-carotene and zeaxanthin. The selectivity found was in agreement with data recently reported on astaxanthin extraction from *Haematococcus pluvialis*.[22] This selectivity allowed obtaining a β-carotene-enriched fraction and a zeaxanthin-enriched fraction, as clearly demonstrated by the HPLC analysis. Furthermore, the yields of both hydrophobic molecules were found to be much higher than those obtained by conventional methods.[19,46] In addition, EBA had the same extraction power on both frozen and fresh biomass. This result is very important from an industrial point of view as it is possible to process the biomass anytime with the same yields and, in case of fresh biomass, to lower the downstream costs.

From a biological point of view, the isolated molecules were fully biocompatible, active as antioxidants, and thermo-stable. In particular, the *in vitro* results showed lower IC_{50} values than those reported in the literature with different microalgae.[47,48] Both fractions were able to protect immortalized human keratinocytes from oxidative stress induced by UVA. This ability was fully maintained also after thermal treatment, that is, pasteurization.

In conclusion, EBA does not affect the biological activity of the extracted molecules, has a higher yield of extraction with respect to conventional methods, and does not require any pretreatment step or energy-intensive equipment to break the cells. Further investigation is instead needed to verify if the extraction of hydrophilic components can be improved by means of any chemical or mechanical pretreatment to make proteins more accessible for the extraction.

ASSOCIATED CONTENT

Supporting Information

The Supporting Information is available free of charge at https://pubs.acs.org/doi/10.1021/acssuschemeng.1c04400.

Schematic representation of the three strategies adopted (PDF)

AUTHOR INFORMATION

Corresponding Author

Daria Maria Monti − *Department of Chemical Science, University of Naples Federico II, Naples 80126, Italy; Istituto Nazionale di Biostrutture e Biosistemi (INBB), Rome 00136, Italy;* orcid.org/0000-0002-1136-0576; Email: mdmonti@unina.it

Authors

Luigi D'Elia − *Department of Chemical Science, University of Naples Federico II, Naples 80126, Italy;* orcid.org/0000-0002-6557-1715

Paola Imbimbo − *Department of Chemical Science, University of Naples Federico II, Naples 80126, Italy*

Davide Liberti − *Department of Chemical Science, University of Naples Federico II, Naples 80126, Italy*

Francesco Bolinesi − *Department of Biology, University of Naples Federico II, Naples 80126, Italy*

Antonino Pollio − *Department of Biology, University of Naples Federico II, Naples 80126, Italy*

Olga Mangoni − *Department of Biology, University of Naples Federico II, Naples 80126, Italy*

Wim Brilman − *Sustainable Process Technology Group (SPT), Green Energy Initiative, Faculty of Science and Technology, University of Twente, AE Enschede 7500, The Netherlands*

Appendix C

Giuseppe Olivieri − *Bioprocess Engineering Group, Wageningen University and Research, Wageningen 6700AA, the Netherlands*

Complete contact information is available at: https://pubs.acs.org/10.1021/acssuschemeng.1c04400

Notes

The authors declare no competing financial interest.

REFERENCES

(1) Spolaore, P.; Joannis-Cassan, C.; Duran, E.; Isambert, A. Commercial Applications of Microalgae. *J. Biosci. Bioeng.* **2006**, *101*, 87−96.

(2) Zhu, L. Biorefinery as a Promising Approach to Promote Microalgae Industry: An Innovative Framework. *Renewable Sustainable Energy Rev.* **2015**, *41*, 1376−1384.

(3) Ruiz, J.; Olivieri, G.; de Vree, J.; Bosma, R.; Willems, P.; Reith, J. H.; Eppink, M. H. M.; Kleinegris, D. M. M.; Wijffels, R. H.; Barbosa, M. J. Towards Industrial Products from Microalgae. *Energy Environ. Sci.* **2016**, *9*, 3036−3043.

(4) Draaisma, R. B.; Wijffels, R. H.; Slegers, P.; Brentner, L. B.; Roy, A.; Barbosa, M. J.; Elsevier Current Trends April, 2013, *24*, pp 169−177. DOI: 10.1016/j.copbio.2012.09.012.Food Commodities from Microalgae. *Curr. Opin. Biotechnol.*

(5) Dolganyuk, V.; Belova, D.; Babich, O.; Prosekov, A.; Ivanova, S.; Katserov, D.; Patyukov, N.; Sukhikh, S. Microalgae: A Promising Source of Valuable Bioproducts. *Biomolecules* **2020**, *10*, 1153.

(6) Pulz, O.; Gross, W. Valuable Products from Biotechnology of Microalgae. *Appl. Microbiol. Biotechnol.* **2004**, *65*, 635−648.

(7) Shebis, Y.; Iluz, D.; Kinel-Tahan, Y.; Dubinsky, Z.; Yehoshua, Y. Natural Antioxidants: Function and Sources. *Food Nutr. Sci.* **2013**, *04*, 643−649.

(8) Ribeiro, J. S.; Santos, M. J. M. C.; Silva, L. K. R.; Pereira, L. C. L.; Santos, I. A.; da Silva Lannes, S. C.; da Silva, M. V. Natural Antioxidants Used in Meat Products: A Brief Review. *Meat Science*; Elsevier Ltd. February, 2019, *148*, pp 181−188.

(9) Goiris, K.; Muylaert, K.; Fraeye, I.; Foubert, I.; De Brabanter, J.; De Cooman, L. Antioxidant Potential of Microalgae in Relation to Their Phenolic and Carotenoid Content. *J. Appl. Phycol.* **2012**, *24*, 1477−1486.

(10) Lourenço, S. C.; Moldão-Martins, M.; Alves, V. D. Antioxidants of Natural Plant Origins: From Sources to Food Industry Applications. *Molecules* **2019**, *24*, 4132.

(11) Zhao, Z.; Rasool, M. A.; Chen, C.; Ma, S.; Wang, L.; Huang, G. Identification and Screening of Multiple Tropical Microalgal Strains for Antioxidant Activity in Vitro. *Food Biosci.* **2020**, *36*, 100649.

(12) Villalobos-Delgado, L. H.; Mateo, J.; Caro, I.; Leal Ramos, M.-Y.; Mendez, N. G.; Cansino, R. G.; González Mondragón, E. G. *Sustainable Meat Production and Processing*; Elsevier, 2019, pp 207−236. DOI: 10.1016/b978-0-12-814874-7.00011-0.Natural Antioxidants in Fresh and Processed Meat

(13) Liu, X.; Luo, G.; Wang, L.; Yuan, W. Optimization of Antioxidant Extraction from Edible Brown Algae Ascophyllum nodosum Using Response Surface Methodology. *Food Bioprod. Process.* **2019**, *114*, 205−215.

(14) Sansone, C.; Brunet, C. Promises and Challenges of Microalgal Antioxidant Production. *Antioxidants* **2019**, *8*, 199.

(15) Jacob-Lopes, E.; Maroneze, M. M.; Deprá, M. C.; Sartori, R. B.; Dias, R. R.; Zepka, L. Q. *Current Opinion in Food Science*; Elsevier Ltd February, 2019, *25*, pp 1−7. DOI: 10.1016/j.cofs.2018.12.003.Bioactive Food Compounds from Microalgae: An Innovative Framework on Industrial Biorefineries

(16) Hidalgo, G.-I.; Almajano, M. Red Fruits: Extraction of Antioxidants, Phenolic Content, and Radical Scavenging Determination: A Review. *Antioxidants* **2017**, *6*, 7.

(17) Selvamuthukumaran, M.; Shi, J. Recent Advances in Extraction of Antioxidants from Plant By-Products Processing Industries. *Food Quality and Safety*; Oxford University Press March, 2017, *1*, pp 61−81.

(18) Mäki-Arvela, P.; Hachemi, I.; Murzin, D. Y. Comparative Study of the Extraction Methods for Recovery of Carotenoids from Algae: Extraction Kinetics and Effect of Different Extraction Parameters. *J. Chem. Technol. Biotechnol.* **2014**, *89*, 1607−1626.

(19) Imbimbo, P.; D'Elia, L.; Liberti, D.; Olivieri, G.; Monti, D. M. Towards Green Extraction Methods from Microalgae Learning from the Classics. *Applied Microbiology and Biotechnology*; Springer Science and Business Media Deutschland GmbH November, 2020, Vol.*104*; pp 9067−9077.

(20) Du, Y.; Schuur, B.; Kersten, S. R. A.; Brilman, D. W. F. Opportunities for Switchable Solvents for Lipid Extraction from Wet Algal Biomass: An Energy Evaluation. *Algal Res.* **2015**, *11*, 271−283.

(21) Peng, L.; Fu, D.; Chu, H.; Wang, Z.; Qi, H. Biofuel Production from Microalgae: A Review. *Environ. Chem. Lett.* **2020**, *18*, 285−297.

(22) Liu, H.; Huang, W.-C.; Guo, N.; Mao, X. Application of Secondary Amine Switchable Hydrophilicity Solvents for Astaxanthin Extraction from Wet Haematococcus pluvialis. *Algal Res.* **2020**, *48*, 101892.

(23) Sanzo, G.; Mehariya, S.; Martino, M.; Larocca, V.; Casella, P.; Chianese, S.; Musmarra, D.; Balducchi, R.; Molino, A. Supercritical Carbon Dioxide Extraction of Astaxanthin, Lutein, and Fatty Acids from Haematococcus pluvialis Microalgae. *Mar. Drugs* **2018**, *16*, 334.

(24) Imbimbo, P.; Bueno, M.; D'Elia, L.; Pollio, A.; Ibañez, E.; Olivieri, G.; Monti, D. M. Green Compressed Fluid Technologies To Extract Antioxidants and Lipids from Galdieria phlegrea in a Biorefinery Approach. *ACS Sustainable Chem. Eng.* **2020**, *8*, 2939−2947.

(25) Pawliszyn, J. Kinetic Model of Supercritical Fluid Extraction. *J. Chromatogr. Sci.* **1993**, *31*, 31−37.

(26) Jessop, P. G.; Heldebrant, D. J.; Li, X.; Eckert, C. A.; Liotta, C. L. Reversible nonpolar-to-polar solvent. *Nature* **2005**, *436*, 1102.

(27) Phan, L.; Andreatta, J. R.; Horvey, L. K.; Edie, C. F.; Luco, A.-L.; Mirchandani, A.; Darensbourg, D. J.; Jessop, P. G. *Switchable-Polarity Solvents Prepared with a Single Liquid Component*; ACS Publications, 2007.

(28) Du, Y.; Schuur, B.; Samorì, C.; Tagliavini, E.; Brilman, D. W. F. Secondary Amines as Switchable Solvents for Lipid Extraction from Non-Broken Microalgae. *Bioresour. Technol.* **2013**, *149*, 253−260.

(29) Du, Y.; Schuur, B.; Brilman, D. W. F. Maximizing Lipid Yield in Neochloris oleoabundans Algae Extraction by Stressing and Using Multiple Extraction Stages with N-Ethylbutylamine as Switchable Solvent. *Ind. Eng. Chem. Res.* **2017**, *56*, 8073−8080.

(30) Cicci, A.; Sed, G.; Jessop, P. G.; Bravi, M. Circular Extraction: An Innovative Use of Switchable Solvents for the Biomass Biorefinery. *Green Chem.* **2018**, *20*, 3908−3911.

(31) Du, Y.; Cyprichová, V.; Hoppe, K.; Schuur, B.; Brilman, W. Process Evaluation of Swing Strategies to Recover N-Ethylbutylamine after Wet Lipid Extraction from Microalgae. *Sep. Purif. Technol.* **2020**, *233*, 115819.

(32) Ismail, M.; Al-Zuhair, S. Thermo-Responsive Switchable Solvents for Simultaneous Microalgae Cell Disruption, Oil Extraction-Reaction, and Product Separation for Biodiesel Production. *Biocatal. Agric. Biotechnol.* **2020**, *26*, 101667.

(33) Davies, F. K.; Fricker, A. D.; Robins, M. M.; Dempster, T. A.; McGowen, J.; Charania, M.; Beliaev, A. S.; Lindemann, S. R.; Posewitz, M. C. Microbiota Associated with the Large-Scale Outdoor Cultivation of the Cyanobacterium Synechococcus sp. *Algal Res.* **2021**, *58*, 102382.

(34) D'Elia, L.; Del Mondo, A.; Santoro, M.; De Natale, A.; Pinto, G.; Pollio, A. Microorganisms from Harsh and Extreme Environments: A Collection of Living Strains at ACUF (Naples, Italy). *Ecol. Quest.* **2018**, *29*, 63−74.

(35) Wu, H.-L.; Wang, G.-H.; Xiang, W.-Z.; Li, T.; He, H. Stability and Antioxidant Activity of Food-Grade Phycocyanin Isolated from Spirulina platensis. *Int. J. Food Prop.* **2016**, *19*, 2349−2362.

(36) Bligh, E. G.; Dyer, W. J. A Rapid Method of Total Lipid Extraction and Purification. *Can. J. Biochem. Physiol.* **1959**, *37*, 911−917.

(37) Rigano, M. M.; Raiola, A.; Tenore, G. C.; Monti, D. M.; Del Giudice, R.; Frusciante, L.; Barone, A. Quantitative Trait Loci Pyramiding Can Improve the Nutritional Potential of Tomato

Appendix C

(Solanum lycopersicum) Fruits. *J. Agric. Food Chem.* **2014**, *62*, 11519−11527.
(38) Petruk, G.; Gifuni, I.; Illiano, A.; Roxo, M.; Pinto, G.; Amoresano, A.; Marzocchella, A.; Piccoli, R.; Wink, M.; Olivieri, G.; et al. Simultaneous Production of Antioxidants and Starch from the Microalga Chlorella sorokiniana. *Algal Res.* **2018**, *34*, 164−174.
(39) Ferraro, G.; Imbimbo, P.; Marseglia, A.; Illiano, A.; Fontanarosa, C.; Amoresano, A.; Olivieri, G.; Pollio, A.; Monti, D. M.; Merlino, A. A Thermophilic C-Phycocyanin with Unprecedented Biophysical and Biochemical Properties. *Int. J. Biol. Macromol.* **2020**, *150*, 38−51.
(40) Petruk, G.; Raiola, A.; Del Giudice, R.; Barone, A.; Frusciante, L.; Rigano, M. M.; Monti, D. M. An Ascorbic Acid-Enriched Tomato Genotype to Fight UVA-Induced Oxidative Stress in Normal Human Keratinocytes. *J. Photochem. Photobiol. B Biol.* **2016**, *163*, 284−289.
(41) Vidussi, F.; Claustre, H.; Bustillos-Guzmàn, J.; Cailliau, C.; Marty, J.-C. Determination of Chlorophylls and Carotenoids of Marine Phytoplankton: Separation of Chlorophyll a from Divinylchlorophyll a and Zeaxanthin from Lutein. *J. Plankton Res.* **1996**, *18*, 2377−2382.
(42) Mantoura, R. F. C.; Repeta, D. J. *Calibration Methods for HPLC*; Jeffrey, S. W.; Mantoura, R. F. C.; Wright, S. W., eds.; UNESCO Publ., Paris: 1997, 407−428.
(43) Callieri, C. Synechococcus Plasticity under Environmental Changes. *FEMS Microbiol. Lett.* **2017**, *364*, 1−8.
(44) Hoiczyk, E.; Hansel, A. Cyanobacterial Cell Walls: News from an Unusual Prokaryotic Envelope. *J. Bacteriol.* **2000**, *182*, 1191−1199.
(45) Samori, C.; López Barreiro, D.; Vet, R.; Pezzolesi, L.; Brilman, D. W. F.; Galletti, P.; Tagliavini, E. Effective Lipid Extraction from Algae Cultures Using Switchable Solvents. *Green Chem.* **2013**, *15*, 353−356.
(46) Fabrowska, J.; Messyasz, B.; Szyling, J.; Walkowiak, J.; Łęska, B. Isolation of Chlorophylls and Carotenoids from Freshwater Algae Using Different Extraction Methods. *Phycol. Res.* **2018**, *66*, 52−57.
(47) Assunção, M. F. G.; Amaral, R.; Martins, C. B.; Ferreira, J. D.; Ressurreição, S.; Santos, S. D.; Varejão, J. M. T. B.; Santos, L. M. A. Screening Microalgae as Potential Sources of Antioxidants. *J. Appl. Phycol.* **2017**, *29*, 865−877.
(48) Guedes, A.; Gião, M.; Seabra, R.; Ferreira, A.; Tamagnini, P.; Moradas-Ferreira, P.; Malcata, F. Evaluation of the Antioxidant Activity of Cell Extracts from Microalgae. *Mar. Drugs* **2013**, *11*, 1256−1270.

https://doi.org/10.1021/acssuschemeng.1c04400
ACS Sustainable Chem. Eng. 2021, 9, 13798−13806

Appendix C

SUPPORTING INFORMATION

Switchable solvent selective extraction of hydrophobic antioxidants from *Synechococcus bigranulatus*

Luigi D'Elia[a], Paola Imbimbo[a], Davide Liberti[a], Francesco Bolinesi[b], Antonino Pollio[b], Olga Mangoni[b], Wim Brilman[c], Giuseppe Olivieri [d], Daria Maria Monti [a,e]*

[a] Department of Chemical Science, University of Naples Federico II, via Cinthia 4, 80126, Naples, Italy

[b] Department of Biology, University of Naples Federico II, via Cinthia 4, 80126, Naples, Italy

[c] University of Twente, Sustainable Process Technology Group (SPT), Green Energy Initiative, Faculty of Science and Technology, PO Box 217, 7500 AE Enschede, The Netherlands

[d] Bioprocess Engineering Group, Wageningen University and Research, Droevendaalsesteeg 1, 6700AA, Wageningen, the Netherlands

[e] Istituto Nazionale di Biostrutture e Biosistemi (INBB), Rome 00136, Italy

* Corresponding author: mdmonti@unina.it

Table of contents:

Appendix C

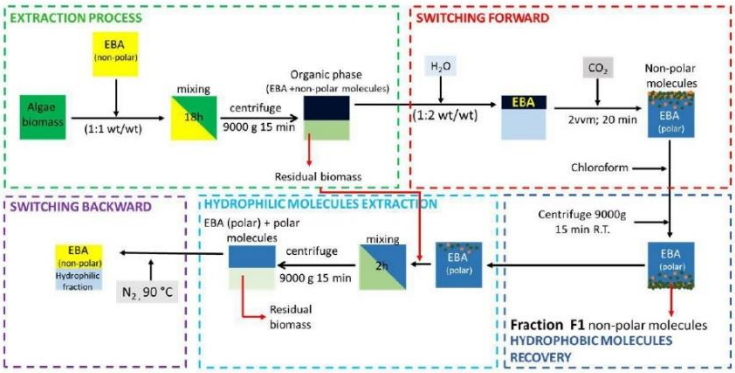

Figure S1. Schematic representation of strategy 1. The CO_2-N_2 switching method was used, named SS (CO_2).

Appendix C

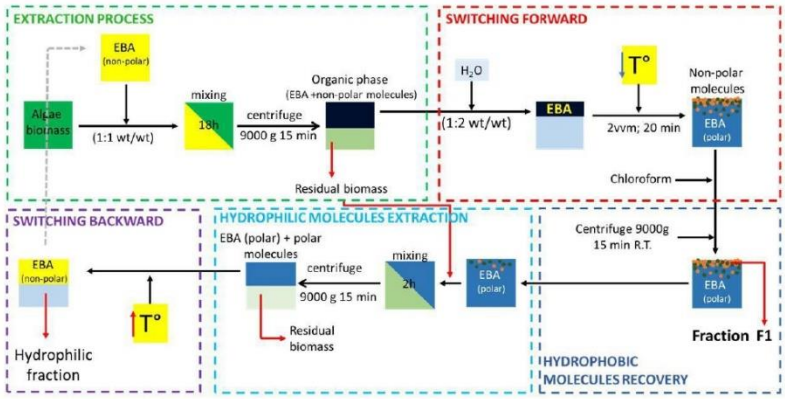

Figure S2. Schematic representation of strategy 2. The temperature switching method (Lower Critical Solution Temperature) was used, named SS (LCST).

Appendix C

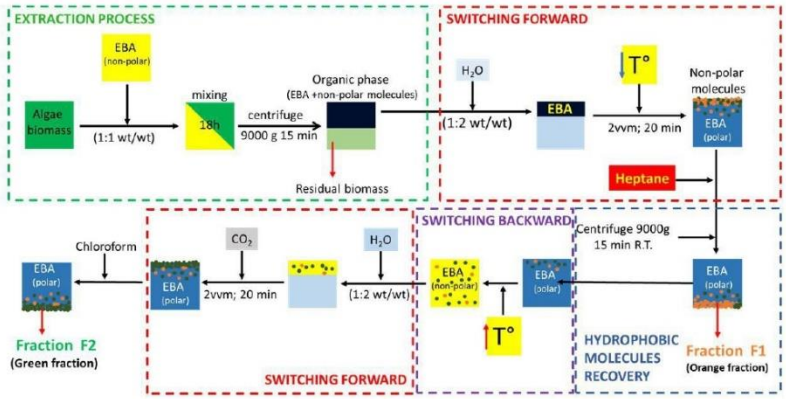

Figure S3. Schematic representation of strategy 3. The switch forward-switch back-switch forward method was used, named SS (LCST-CO_2).

Appendix D

International Journal of *Molecular Sciences*

MDPI

Article

Square-Planar vs. Trigonal Bipyramidal Geometry in Pt(II) Complexes Containing Triazole-Based Glucose Ligands as Potential Anticancer Agents

Alfonso Annunziata, Davide Liberti, Emiliano Bedini, Maria Elena Cucciolito, Domenico Loreto, Daria Maria Monti, Antonello Merlino and Francesco Ruffo *

Dipartimento di Scienze Chimiche, Università di Napoli Federico II, Complesso Universitario di Monte S. Angelo, Via Cintia 21, 80126 Napoli, Italy; alfonso.annunziata@unina.it (A.A.); davide.liberti@unina.it (D.L.); emiliano.bedini@unina.it (E.B.); cuccioli@unina.it (M.E.C.); domenico.loreto@unina.it (D.L.); mdmonti@unina.it (D.M.M.); antonello.merlino@unina.it (A.M.)
* Correspondence: ruffo@unina.it

Abstract: This article describes the synthesis, characterization, and biological activity of novel square-planar cationic platinum(II) complexes containing glucoconjugated triazole ligands and a comparison with the results obtained from the corresponding five-coordinate complexes bearing the same triazole ligands. Stability in solution, reactivity with DNA and small molecules of the new compounds were evaluated by NMR, fluorescence, and UV–vis absorption spectroscopy, together with their cytotoxic action against pairs of immortalized and tumorigenic cell lines. The results show that the square-planar species exhibit greater stability than the corresponding five-coordinate ones. Furthermore, although the square-planar complexes are less cytotoxic than the latter ones, they exhibit a certain selectivity. These results simultaneously demonstrate that overall stability is a fundamental prerequisite for preserving the performance of the agents and that coordinative saturation constitutes a point in favor of their biological action.

Keywords: platinum(II); square-planar complexes; glycoconjugation; cytotoxic activity; DNA binding

Citation: Annunziata, A.; Liberti, D.; Bedini, E.; Cucciolito, M.E.; Loreto, D.; Monti, D.M.; Merlino, A.; Ruffo, F. Square-Planar vs. Trigonal Bipyramidal Geometry in Pt(II) Complexes Containing Triazole-Based Glucose Ligands as Potential Anticancer Agents. *Int. J. Mol. Sci.* **2021**, *22*, 8704. https://doi.org/10.3390/ijms22168704

Academic Editor: Cristina Angeloni

Received: 30 July 2021
Accepted: 10 August 2021
Published: 13 August 2021

1. Introduction

Organometallic complexes have been currently considered valid anticancer agents due to their unique features [1–3]. Platinum compounds play a prevalent role in metal-based anticancer therapies, with cisplatin, carboplatin, and oxaliplatin used all over the world in clinics despite general low selectivity and drug resistance often limiting their efficacy [4,5]. To date, the efforts of the scientific community have multiplied to prepare increasingly effective agents, aimed at reducing the numerous and unpleasant side effects of cisplatin and its close derivatives [6–16]. One of the most successful strategies is the introduction of bio-active molecules in the coordination environment of the metal, capable of increasing its versatility and selectivity [17,18]. Among these, sugars are an excellent example due to their biocompatibility, the possibility of modulating their chemico-physical properties, and the ability of selective recognition by cancer cells, known as the Warburg effect [19–28]. In this context, over the last few years, our research group has proposed new organometallic glycoconjugate platinum complexes as innovative anticancer agents [29–33].

In particular, we intensely explored five-coordinate platinum(II) complexes (Figure 1) characterized by trigonal bipyramidal geometry, with the equatorial plane occupied by the bidentate ligand 2,9-dimethyl-1,10-phenantroline (dmphen) and ethylene, while the sugar fragment occupies one of the axial positions [34]. These species combine glycoconjugation with coordinative saturation, a prerogative that is supposed to increase the stability of the structure and preserve its integrity up to the cellular target. The biological results confirmed the expectations because **1Pt** [30] and **2Pt** [31] showed, in some cases, remarkable activity

Appendix D

and selectivity towards pairs of tumor and healthy cell lines, while the entire panel of complexes **3Pt** [29] displayed high activity, although poor selectivity.

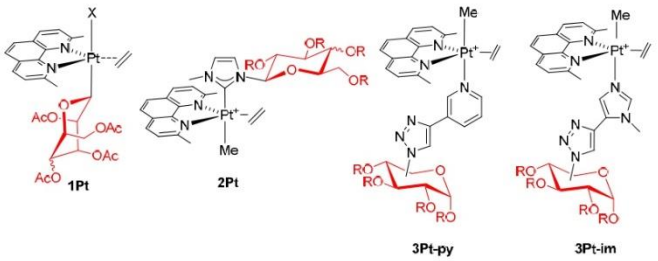

Figure 1. Structure of the five-coordinate platinum(II) complexes **1Pt**, **2Pt**, and **3Pt** (R=H, OAc).

Since the versatility of platinum organometallic chemistry allows us to span between different coordination numbers and geometries, we were stimulated to synthesize new carbohydrate-based platinum agents, **4Pt** (Figure 2), to better understand the effect of the coordination environment on cytotoxicity as well as selectivity:

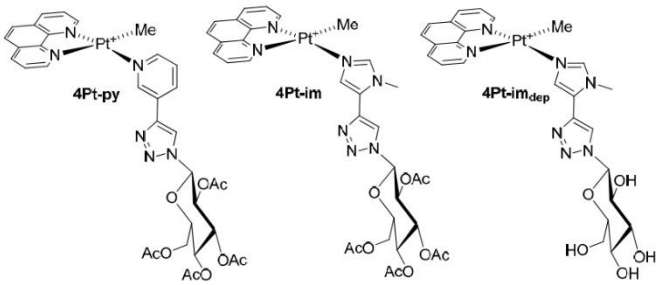

Figure 2. Structure of the four-coordinate platinum(II) complex **4Pt**.

These compounds share with the five-coordinate **3Pt** agents the oxidation state II of Pt, a positive charge, a glycoconjugate ligand, and a methyl group. On the other hand, they are four-coordinate, and the bidentate nitrogen chelate dmphen is replaced with 1,10-phenanthroline (phen), which does not introduce steric hindrance in the coordination plane and, hence, is more suitable in square-planar environments. It is noteworthy that the planarity of the molecules, combined with the presence of aromatic moieties, phen, and triazo-pyridine/imidazole ligands, makes the family of **4Pt** potential metallo-intercalating agents, capable of intercalating in DNA base pairs by π–π stacking and weak electrostatic interactions [35–38]. Representative complexes present, respectively, pyridine (**4Pt-py**) and imidazole (**4Pt-im**), decorated with a peracetylated glucose and a ligand in which the sugar is completely deprotected (**4Pt-im$_{dep}$**). To the best of our knowledge, this is a rare example of a homogeneous comparison between two classes of Pt-based anticancer agents sharing an oxidation state and the nature of the ligands in two different molecular geometries [39].

In this paper, we describe the synthesis and spectroscopic characterization of the new compounds, their in-solution stability and reactivity with DNA, and their cytotoxic activity in comparison with **3Pt** analogs.

Appendix D

2. Results

2.1. Synthesis and Characterization of Complexes of Type 4Pt

The sugar ligands **py**, **im**, and **im$_{dep}$** were obtained through a click chemistry reaction between peracetylated 1-azido-β-D-glucose and the appropriate heterocyclic precursor 3-ethynylpiridine or 5-ethynyl-1-methyl-1H-imidazole. The peracetylated platinum(II) complexes were then prepared, starting from the chloro-precursor [PtClMe(phen)], by exchanging halogen in the presence of silver triflate, as exemplified in Scheme 1 for **4Pt-im** (path i):

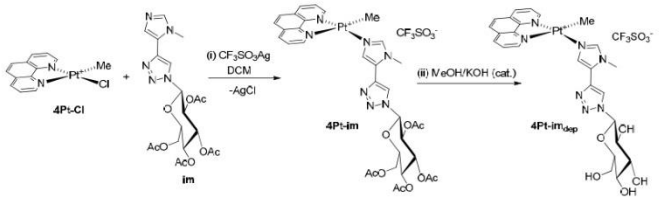

Scheme 1. Synthesis of the four-coordinate platinum(II) complex **4Pt-im**.

After filtration of the precipitated silver chloride, the complexes were isolated as yellow powder by reducing the volume of the filtrate and adding diethyl ether. The corresponding deprotected species, **4Pt-im$_{dep}$**, was prepared by treatment of **4Pt-im** in methanol containing a catalytic amount of potassium hydroxide. Attempts to isolate the square-planar dmphen analogs were performed by reacting the chloro–dmphen precursor in the same conditions reported in Scheme 1. Unfortunately, the reaction mixture showed no clear presence of the desired product. The unsuccessful outcome of the synthesis is probably due to the steric hindrance brought into the plane by the methyl groups, which prevents the formation of the square-planar complex. Finally, complex **4Pt-py** was prepared uneventfully with a procedure analogous to the synthesis of **4Pt-im**. The characterization of the products was carried out through mono- and bi-dimensional NMR spectroscopy (Figures S1–S9), which allowed the unequivocal assignment to the entire panel of protons. Figure 3 shows the proton spectrum of **4Pt-im**.

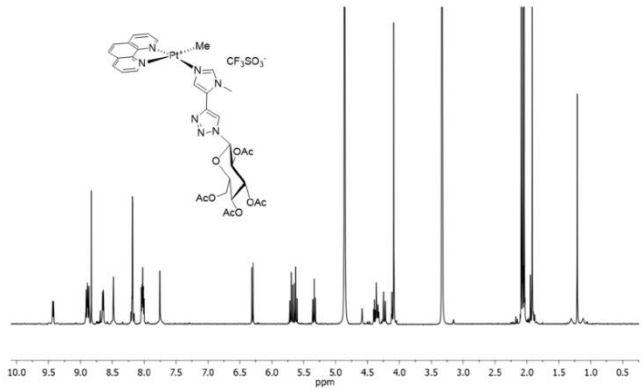

Figure 3. ^{1}H NMR spectrum of **4Pt-im** in MeOD at 400 MHz and 25 °C.

Appendix D

As expected, the two halves of the phen ligand are not equivalent. The signal of the methyl on platinum shifts to higher frequencies (δ 1.2–1.3) than the five-coordinate species (δ 0–0.5) [29,40], and is affected by the coupling with the ^{195}Pt nuclei of ca. 70 Hz, typical of square-planar Pt-complexes containing *N*,*N*′-chelating ligands [41]. The sugar proton signals exhibit the characteristic pattern of the $^{4}C_1$ glucose chair, with the glucose in the β-configuration. The compounds were unequivocally identified by HRMS (ESI/QTOF), carried out in methanol. In the spectra, it was possible to observe peaks relative to the cationic platinum complex at m/z 869.2225, 866.2106, and 701.1802, attributable to **4Pt-im, 4Pt-py**, and **4Pt-im$_{dep}$**, respectively (Figures S10–S12).

2.2. In-Solution Behaviour and Reactivity with Model Nucleophiles

As mentioned before, **3Pt** complexes are highly cytotoxic but poorly selective. Furthermore, similar IC_{50} values were recorded for the entire panel of compounds, regardless of the nature of the sugar ligand [29]. This behavior suggests that the neutral nitrogen ligands in **3Pt** are vulnerable to substitution in a physiological environment, according to the equation (L= **py** or **im**):

3Pt-L + solvent = **3Pt-solvent** + L

Some experiments have demonstrated the ease of substitution in coordinating solvents that is plausibly facilitated by the *trans*-effect of the Me ligand [29]. Therefore, the active species likely do not contain the sugar label anymore, and their activities are very similar.

To compare the solution stability of the complexes, ^{1}H-NMR and UV–vis spectra over time were recorded for **4Pt** type species dissolved in diverse aqueous (phosphate buffer, PB; pH 7.4): organic solvent mixtures, i.e., 1:1 *v*/*v* D_2O:acetone-d_6; 9:1 *v*/*v* PB:DMSO-d_6; 1:1 *v*/*v* PB:DMSO-d_6 and DMSO-d_6. These solvents were selected to verify the stability in pseudo-physiological conditions in the presence of solvents with different coordinating properties and concentrations.

No appreciable structural variations were observed in the 1:1 *v*/*v* D_2O:acetone-d_6 mixture over 3 days. As an example, Figure 4 reports the ^{1}H-NMR spectra recorded over time for **4Pt-im**.

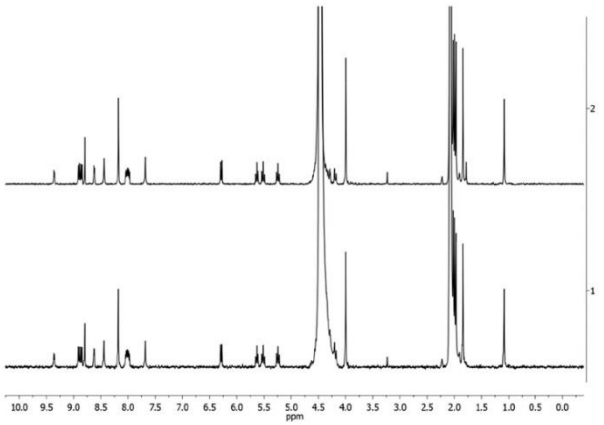

Figure 4. ^{1}H NMR spectra of **4Pt-im** in 1:1 *v*/*v* D_2O:acetone-d_6 over time at 400 MHz, 298K (trace 1 = start, 2 = 72 h).

Appendix D

Analogous results were obtained in 9:1 *v/v* PB:DMSO-d_6, where only traces of complex **4Pt-dmso-d$_6$** were observed after 48 h (Figure 5).

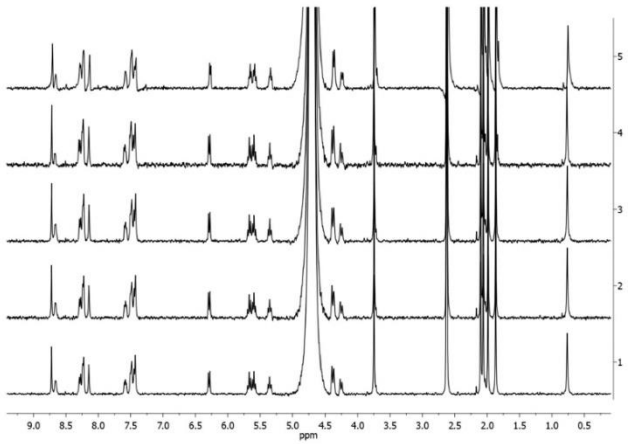

Figure 5. ^{1}H-NMR spectra of **4Pt-im** in 9:1 *v/v* PB:DMSO-d_6 (1 mM) at 37 °C at different times (1 = start, 2 = 1 h, 3 = 3 h, 4 = 24 h, 5 = 48 h).

These results demonstrate that coordinating molecules such as water or acetone do not change the nature of the compounds, different from the corresponding five-coordinate **3Pt** complexes that are not stable in these solvents [29].

Upon increasing the amount of DMSO-d_6, type **4Pt** complexes slowly undergo the following exchange:

4Pt-L + DMSO-d_6 = **4Pt-DMSO-d$_6$** + **L**

From the spectra recorded in 1:1 *v/v* PB:DMSO-d_6 (Figure 6), it is possible to appreciate the appearance of the signals (δ 6.15, 7.23, 7.68, and 8.55) relating to the free sugar ligand **im**, whose intensity increases over time. After 24 h, an equilibrium is reached. Analog results were collected for **4Pt-py** (Figures S15–S19). The exchange rate was, however, much higher for the analogous five-coordinate species **3Pt-im**, to the point that equilibrium was established in the solution within an hour.

These results were confirmed by UV–vis absorption spectra collected in pure DMSO and in 9:1 *v/v* PBS:DMSO-d_6 (Figure 7) as a function of time. Indeed, data collected in pure DMSO show significant variations of the spectral profiles, which can be explained by the exchange of a metal ligand with a solvent molecule. On the contrary, spectra collected in the mixed solvent indicate that the compounds remain rather stable in PBS, with a minimal variation of absorbance that can be explained by slight precipitation.

Appendix D

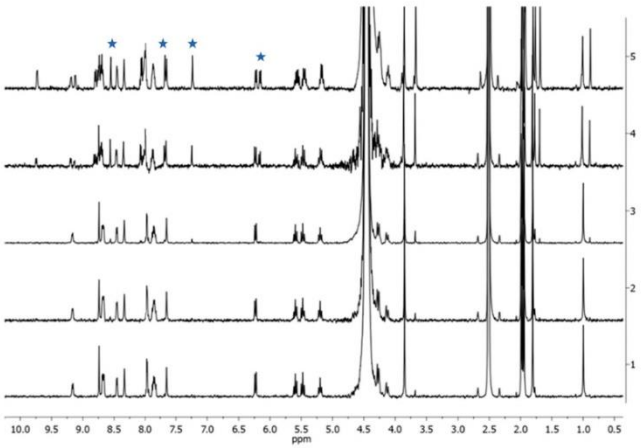

Figure 6. ^{1}H NMR spectra of **4Pt-im** in 1:1 *v/v* PB:DMSO-d_6 over time at 37 °C (trace 1 = start, 2 = 1 h, 3 = 3 h, 4 = 24 h, 5 = 48 h). Stars indicate the signals of free **im**.

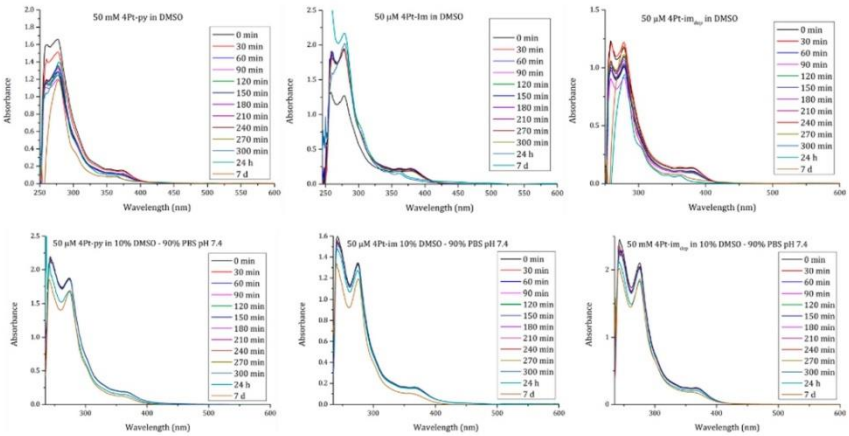

Figure 7. Time course UV–vis spectra of 50 µM **4Pt-im**, **4Pt-im$_{dep}$**, and **4Pt-py** in PBS (pH 7.4):DMSO-*d6* 90:10 (**down**) and pure DMSO (**up**).

These results demonstrate that four-coordinate complexes preserve their structure more efficiently than the corresponding five-coordinate species in mixed solvents. This behavior can be interpreted by considering the different *trans*-effects experienced by the sugar ligand in the two types of compounds. In five-coordinate complexes, the presence of a methyl destabilizes the Pt–N bond and facilitates the substitution. In the case of square-planar complexes, one phenanthroline nitrogen occupies the *trans* coordination site,

Appendix D

and it is therefore reasonable to observe a lower reactivity of the complexes. This result, therefore, encourages the valuation of the biological activity of **4Pt** complexes, with the expectation of a possible recognition action exerted by the sugar portion on the cellular target and a consequent beneficial effect on selectivity.

2.3. Cytotoxicity Studies

The biological effect of the Pt-compounds was tested on two human tumor cell lines, MCF-7 (breast cancer cells) and A431 (epidermoid carcinoma cells), and two non-tumorigenic cell lines, H9c2 (rat cardiomyoblast cells), and HaCaT (human keratinocyte cells), using the MTT assay. After 48 h of incubation, a cytotoxic effect was observed in all the analyzed cell lines, as indicated by the IC_{50} values (the amount of drug able to induce 50% cell death) reported in Table 1A. In line with the different stability in solution, the square-planar species of type **4Pt** exhibit different biological activity compared to that of the corresponding five-coordinate compounds of **3Pt**. Indeed, due to their inertness towards the substitution of the sugar ligand, their biological activity can be influenced by the nature of the sugar ligand, whose presence in the complex can affect its internalization or mechanism of action once inside the cell. On the other hand, in the case of the five-coordinate complexes, the loss of the sugar tag plausibly determines their substantial leveling of activities [29]. Indeed, as demonstrated by the selectivity index (Table 1B), the square-planar complexes exhibit a certain degree of selectivity, much higher than that obtained in the case of cisplatin and the corresponding five-coordinate **3Pt** compounds. Although the general cytotoxicity of square-planar species of type **4Pt** is reduced when compared to the coordinatively saturated **3Pt** species, **4Pt-py** showed much higher IC_{50} values on immortalized cells than cisplatin, and a strong decrease in the IC_{50} value, with respect to cisplatin, was observed for A431 cells. The behavior of **4Pt-im** was very similar to that of **4Pt-py**. No toxic activity was observed with **4Pt-im$_{dep}$**, thus confirming the importance of sugar protection, as already observed in other studies [31].

Table 1. (**A**) IC_{50} values (μM) obtained for Pt-derived drugs on immortalized and cancer cells after 48 h incubation. (**B**) Selectivity index, indicated by the ratio between the IC_{50} values of immortalized cells and cancer cells.

A. MTT IC_{50} 48 h (μM)				
Cell Line	**HaCaT**	**A431**	**H9c2**	**MCF7**
4Pt-py	66 ± 11	12 ± 2	22 ± 10	35 ± 4
4Pt-im	27 ± 7	16 ± 8	53 ± 11	43 ± 7
4Pt-im$_{dep}$	>200	>200	>200	>200
3Pt-py[29]	0.80 ± 0.14	1.10 ± 0.14	0.35 ± 0.07	0.88 ± 0.11
3Pt-im[29]	1.03 ± 0.25	1.10 ± 0.01	0.38 ± 0.04	0.63 ± 0.11
3Pt-im$_{dep}$[29]	0.58 ± 0.04	1.00 ± 0.14	0.35 ± 0.07	0.60 ± 0.09
Cisplatin	6.6 ± 0.3[31]	39 ± 12[31]	8 ± 2.1	18 ± 1.6
B. $Selectivity\ Index = IC_{50}^{immortalized\ cells} / IC_{50}^{cancer\ cells}$				
Cell Line	**HaCaT/A431**	**HaCaT/MCF7**	**H9c2/ A431**	**H9c2/ MCF7**
4Pt-py	5.5	1.88	1.83	0.63
4Pt-im	1.69	0.63	3.3	1.23
4Pt-im$_{dep}$	N.A.	N.A.	N.A.	N.A.
3Pt-py[29]	0.72	0.89	0.32	0.39
3Pt-im[29]	0.91	1.59	0.34	0.6
3Pt-im$_{dep}$[29]	0.58	0.96	0.35	0.58
Cisplatin	0.17	0.82	0.2	0.44

Appendix D

The cell death mechanism induced by **4Pt-py** was analyzed on A431 cells. First, the internalization process of **4Pt-py** was evaluated by studying the involvement of GLUT receptors. In particular, **4Pt-py** internalization and cytotoxicity were tested using quercetin as a glucose transporter inhibitor [24,30,42]. Cells were incubated in the presence or absence of 5 μM quercetin (a non-lethal concentration, data not shown), and a dose–response assay was performed with **4Pt-py**. As shown in Figure 8A, no inhibition of cytotoxicity was observed in the presence of quercetin, thus excluding the involvement of GLUT receptors in the internalization pathway of **4Pt-py**. Necrosis was also excluded as no LDH release was observed after **4Pt-py** cell incubation with an increasing amount of the drug (Figure 8B). The 10 μM concentration used was very similar to the IC_{50} value, and then, a double value (20 μM) was also used to definitely exclude necrosis at very high concentrations.

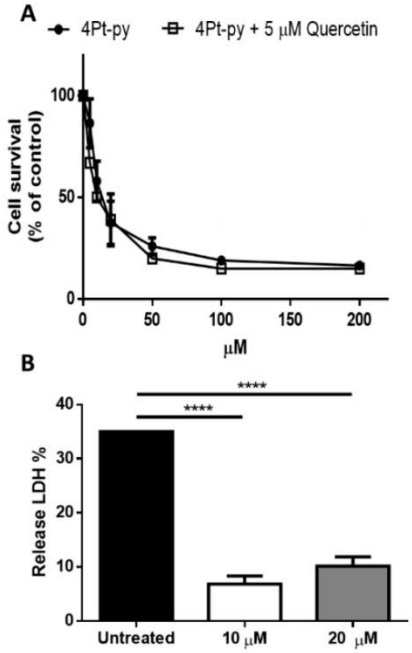

Figure 8. Analysis of the mechanism of action of **4Pt-py**. (**A**) Glucose-transporter-dependent cytotoxicity of **4Pt-py** on A431 cells. Cells were incubated with increasing amounts of **4Pt-py** in the absence (black circles) or presence (empty squares) of 5 μM quercetin. Cell viability was assessed using the MTT assay after 48 h incubation. Values are given as mean ± SD. (**B**) Cells were incubated with increasing amounts of **4Pt-py** for 48 h, and the release of LDH was measured. Data shown are the means ± SD of three independent experiments; **** indicates $p < 0.001$ with respect to untreated cells. The % of LDH release was calculated as described in the Materials and Methods section.

The activation of the apoptotic pathway was analyzed by Western blotting and an analysis of the mitochondrial potential as it is well known that mitochondrial outer membrane permeabilization is essential to initiate mitochondrial apoptosis. Cells were incubated for

Appendix D

48 h in the presence of 12 μM **4Pt-py** (the concentration of **4Pt-py** at which the IC_{50} value was obtained), and the activation of caspase-3 and caspase-9 was analyzed. As shown in Figure 9A,B, a small but significant decrease in the signal associated with both pro-caspases was observed. Accordingly, when the mitochondrial potential (Δψm) was measured, a significant decrease in A431 cells was observed at both the IC_{50} value and the doubled amount (20 μM) (Figure 9C).

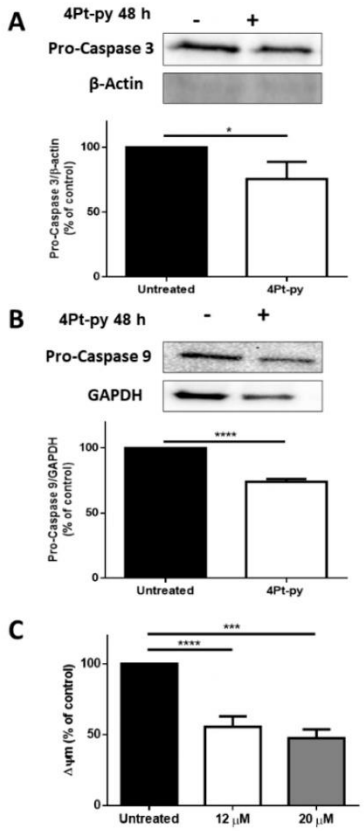

Figure 9. Analysis of 4Pt-py-induced cell death. A431 cells were incubated with 12 μM of **4Pt-py** for 48 h. (**A**,**B**) Analysis by Western blotting of pro-caspase-3 and -9. B-actin or GAPDH was used as the loading control. The densitometric analysis is reported below each Western blotting. (**C**) Changes in mitochondrial membrane potential (Δψm) after 48 h incubation with an increasing amount of **4Pt-py**. The fluorescence intensity of the probe, related to Δψm, is reported as a percentage of the control (%). Data shown are the means ± SD of three independent experiments; * indicates $p < 0.05$, *** indicates $p < 0.005$, and **** indicates $p < 0.001$ with respect to untreated cells.

Appendix D

2.4. DNA Binding Properties

Since the main target of Pt-based drugs is DNA, we evaluated the ability of the compounds to interact with nucleobases and double helixes.

To evaluate the ability of the compounds to interact with double-helix DNA, ethidium bromide (EtBr) displacement fluorescence assays using calf-thymus DNA (ctDNA) were carried out. Attempts to collect circular dichroism spectra of ctDNA in the presence of the compounds failed due to the formation of a yellow precipitate. Results of the fluorescence assay clearly demonstrate that the compounds belonging to the **4Pt** series displace the intercalating agent EtBr from ctDNA (Figure 10). These results indicate that the compounds bind DNA [43].

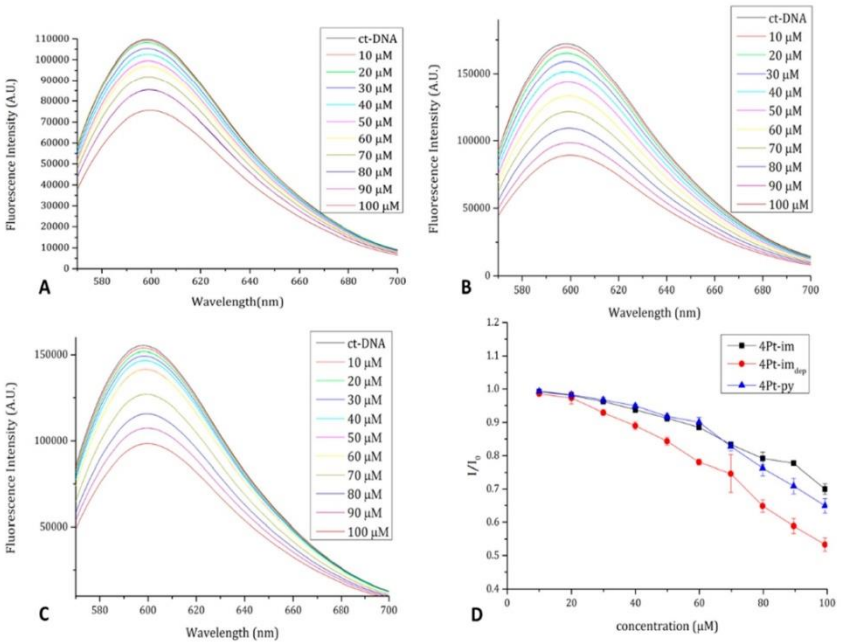

Figure 10. Fluorescence emission spectra of the ct-DNA-EtBr complex upon titration with a solution of **4Pt-im** (**A**), **4Pt-im$_{dep}$** (**B**), and **4Pt-py** (**C**), In panel (**D**), I/Io as a function of compound concentration is reported.

To shed light on the interaction between the complexes and DNA, the interaction with the model nucleobase 2′-deoxyguanosine-5′-monophosphate (dGMP) was studied by ^{1}H-NMR spectroscopy and ESI mass spectrometry. Indeed, N7 in guanine residues are known to be the main binding sites for platinum complexes. Complexes **4Pt-im** and **4Pt-py** were incubated at 37 °C in 9:1 *v/v* PB:DMSO-d_6 in the presence of 2.5 eq of dGMP, and NMR spectra were recorded over time (Figure 11).

Appendix D

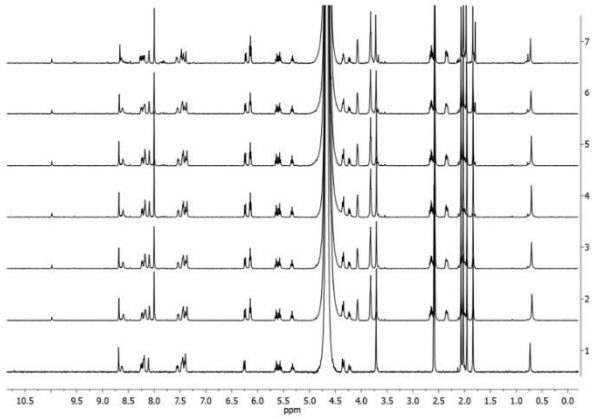

Figure 11. ^{1}H-NMR spectra over time of **2Pt-im** in 9:1 *v/v* PB:DMSO-d_6 (trace 1) and in the presence of 2.5 eq. of dGMP at 37 °C (trace 2 = start, 3 = 2 h, 4 = 4 h, 5 = 6 h, 6 = 24 h, 7 = 48 h).

After 48 h, no coordination of dGMP to the platinum center was observed, while traces to the complex **4Pt–DMSO** were found. Such results were also confirmed by ESI mass spectrometry experiments performed in 9:1 *v/v* H_2O:DMSO. The analysis of the reaction mixture at t = 0 (Figure 12A) and after 48 h of incubation at 37 °C (Figure 12B) confirmed the lack of coordination by dGMP and the formation of the **4Pt-DMSO** complex. Analog results were obtained for the **4Pt-py** complex (Figure S19).

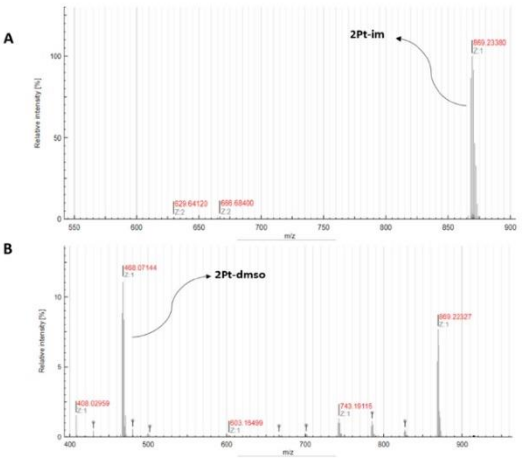

Figure 12. ESI-MS spectrum of **2Pt-im** incubated with dGMP in 9:1 *v/v* H_2O:DMSO recorded at t = 0 (**A**) and after 48 h at 37 °C (**B**).

Appendix D

Such results, combined with the suppressed ligand exchange in aqueous media (see Section 2.2), may indicate that the family of **4Pt** agents interacts in vitro with DNA through an intercalation mechanism [44]. Indeed, classical Pt(II)-based drugs (e.g., cisplatin and its derivatives), upon the hydrolysis of leaving ligands, can be coordinated by nucleobases, resulting in covalent adducts. The inertness of **4Pt** complexes toward ligand exchange, along with their planarity and the presence of aromatic phenanthroline and triazo-imidazole/pyridine ligands, can favor non-covalent interactions with the double helix [45–48].

2.5. Reactivity with S-Donor Molecules

Due to its softness, platinum forms stable bonds with sulfur-donor nucleophiles, which are ubiquitous in biological environments and play an important role in the fate of platinum-based drugs. Reduced glutathione (GSH) is a tripeptide involved in essential processes in the cell, such as redox balance and detoxification [49]. Platinum complexes promptly react with the thiol group of GSH, forming adducts that are often no longer active. Similarly, the thioether moiety of *L*-methionine is often involved in the sequestration of platinum complexes by proteins [50,51]. Hence, the study of the reactivity of the synthesized complexes with GSH and methionine can help to rationalize and clarify their biological activity. The interaction between compounds **4Pt-im** and **4Pt-py**, incubated at 37 °C in the presence of 2.5 eq. of methionine in 9:1 *v/v* D_2O (PBS, pH 7.4):DMSO-d_6, was monitored by ^{1}H-NMR spectroscopy. Spectra collected over time show no sign of coordination of methionine within 48 h (Figures S20 and S21).

Conversely, the compounds react with GSH in the same conditions as indicated by ^{1}H-NMR and ESI-MS. In the NMR spectra (Figure 13) recorded at different times for **4Pt-im**, it is possible to observe from the point of t = 0 the appearance of new signals in the aromatic and glucose regions.

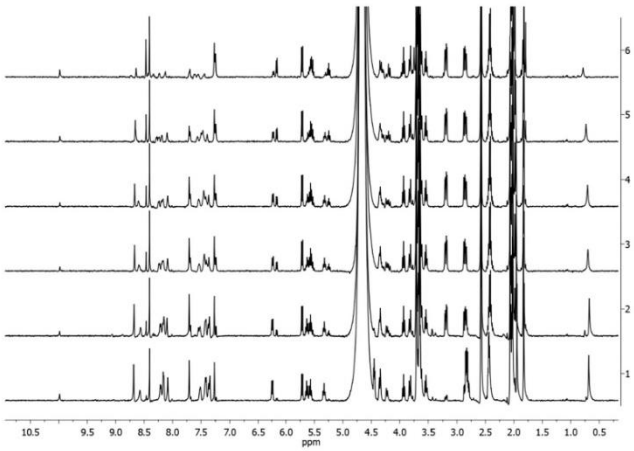

Figure 13. ^{1}H-NMR spectra of **2Pt-im** incubated with GSH in 9:1 *v/v* PB:DMSO-d_6 (1 mM of Pt, 2.5 eq of GSH) at 37 °C at different times (1 = start, 2 = 2 h, 3 = 4 h, 4 = 6 h, 5 = 24 h, 6 = 48 h).

Such resonances can be attributed to the release of the imidazole ligand and the consequent formation of unidentified species. Such peaks decrease in intensity over time until they almost disappear (in the case of **4Pt-py**, completely; Figure S22), probably

Appendix D

because of the precipitation of decomposition products. The reaction mixture analyzed by ESI-MS immediately after the incubation of **4Pt-im** with GSH at 37 °C in 9:1 *v/v* H_2O:DMSO showed the presence of the intact complex at m/z 869.22. The analysis, repeated after 48 h, revealed the presence of multiple peaks (Figure 14 and Table S1) attributable to several species, including mono- and di-nuclear platinum complexes with one or two deprotonated GSH molecules, probably with bridging sulfur atoms in the di-nuclear one, as previously reported for other phenantroline Pt(II) complexes [51].

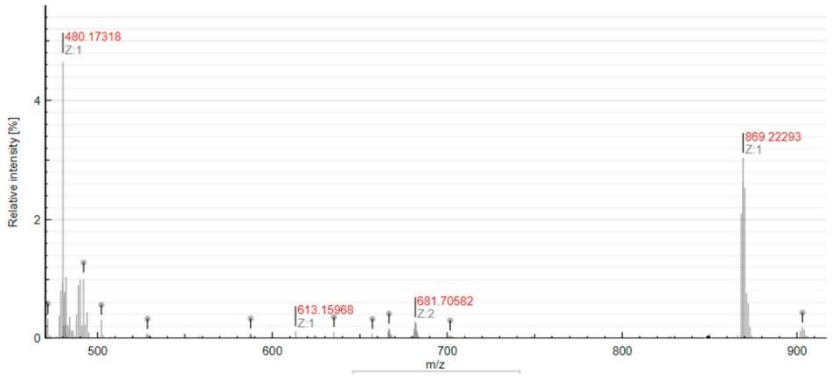

Figure 14. ESI-MS spectrum of **2Pt-im** incubated with GSH in 9:1 *v/v* H_2O:DMSO, recorded after 48 h at 37 °C.

3. Materials and Methods

Solvents and reagents were purchased from Sigma-Aldrich and used without further purification. NMR spectra were recorded using a 400 Bruker AvanceUltrashielded™ or 500 Varian Inova spectrometer. The chemical shifts are provided in parts per million (ppm, δ), referring to the solvent (^{1}H NMR: CHD_2OD, δ = 3.34 ppm; ^{13}C NMR: $^{13}CHD_2OD$, δ = 49 ppm). Coupling constants are expressed in Hz. The following abbreviations describe NMR multiplicities: singlet (s), doublet (d), triplet (t), quartet (q), double doublet (dd), broad (br), and multiplet (m). ESI-MS spectra were recorded on a Xevo G2-S QTOF instrument (Waters) in positive ion mode. MS spectra were analyzed using the open-source software *Aom2S* [52].

3.1. Synthesis of 4Pt-py and 4Pt-im

An equimolar solution (5.0 mL) of the appropriate ligand in dichloromethane and a suspension of [PtClMe (1,10-phen)] (0.10 g, 0.22 mmol) and CF_3SO_3Ag (0.058 g, 0.22 mmol) in dichloromethane (3.0 mL) were stirred at RT for 24 h. After that, the reaction mixture was filtered on Celite®, and the filtrate was concentrated under vacuum; diethyl ether was added to afford a yellow microcrystalline solid. The solid was then isolated, washed with diethyl ether, and then vacuum dried (yield: 70–75%).

4Pt-py ^{1}H NMR (400 MHz, CD_3OD) ^{1}H NMR (400 MHz, MeOD) δ 9.55 (d, $J_{H2Py\text{-}H4Py}$ = 1.9 Hz, J_{Pt} = 46 Hz, 1H, H2Py), 9.47 (dd, 1H, H2, or H9 phen), 9.03 (dd, $J_{H6Py\text{-}H5Py}$ = 5.6 Hz, $J_{H6Py\text{-}H4Py}$ = 1.3 Hz, 1H, H6Py), 9.01 (s, 1H, H-Triazole), 8.97 (dd, 1H, H4, or H7 phen), 8.93 (dd, 1H, H7, or H4 phen), 8.64 (ddd, $J_{H4Py\text{-}H5Py}$ = 8 Hz, 1H, H4Py), 8.48 (dd, 1H, H9, or H2 phen), 8.26 (ABq, 2H, H5, and H6 phen), 8.09 (dd, 1H, H3, or H8 phen), 8.04 (dd, 1H, H8, or H3 phen), 7.83 (ddd, 1H, H5Py), 6.29 (d, $J_{H1\text{-}H2}$ = 8.8 Hz, 1H, H1-glu), 5.66 (t, $J_{H2\text{-}H3}$ = 9.3 Hz, 1H, H2-glu), 5.61 (t, $J_{H3\text{-}H4}$ = 9.3 Hz, 1H, H3-glu), 5.32 (t, $J_{H4\text{-}H5}$ = 9.4 Hz, 1H, H4-glu), 4.39 (dd, $J_{H6\text{-}H6'}$ = 12 Hz, $J_{H5\text{-}H6}$ = 5.0 Hz, 1H, H6-glu), 4.33 (ddd, $J_{H5\text{-}H6'}$ = 1.7 Hz,

Appendix D

1H, H5-glu), 4.23 (dd, 1H, H6′-glu), 2.09 (s, 3H, OAc), 2.07 (s, 3H, OAc), 2.04 (s, 3H, OAc), 1.90 (s, 3H, OAc), 1.32 (s, 3H, J_{Pt} = 81 Hz).

^{13}C NMR (101 MHz, MeOD) δ 170.8, 170.0, 169.8, 169.2, 152.7, 150.0 (x2), 148.5, 147.5, 145.0, 142.7, 139.4, 138.7, 135.4, 131.0, 130.7, 130.3, 127.7, 127.6, 127.5, 126.6, 125.61, 121.9, 120.4 (q, $J_{C\text{-}F}$ = 319 Hz), 85.4, 74.7, 72.6, 70.8, 67.8, 61.6, 19.2, 19.1 (x2), 18.7, −12.1.

HRMS (ESI/QTOF) m/z 866.2106, [**4Pt-py**—$CF_3SO_3^-$].

4Pt-im ^{1}H NMR (400 MHz, CD_3OD) δ ^{1}H NMR (400 MHz, MeOD) δ 9.44 (dd, J_{Pt} = 53 Hz, 1H, H2, or H9 phen), 8.92 (dd, 1H, H4, or H7 phen), 8.88 (dd, 1H, H7, or H4 phen), 8.83 (s, 1H, H-Triazole), 8.66 (dd, 1H, H9, or H2 phen), 8.49 (br, 1H, H-Imidazole), 8.18 (ABq, 2H, H5, and H6 phen), 8.04 (dd, 1H, H3, or H8 phen), 8.02 (dd, 1H, H8, and H3 phen), 7.76 (d, 1H, H-imidazole), 6.30 (d, $J_{H1\text{-}H2}$ = 9.4 Hz, 1H, H1-glu), 5.70 (t, 1H, $J_{H2\text{-}H3}$ = 9.4 Hz, H2-glu), 5.62 (t, $J_{H3\text{-}H4}$ = 9.4 Hz, 1H, H3-glu), 5.34 (t, $J_{H4\text{-}H5}$ = 9.4 Hz, 1H, H4-glu), 4.42–4.32 (m, 2H, H5-glu, and H6-glu), 4.23 (dd, $J_{H5\text{-}H6'}$ = 11.8 Hz, $J_{H6\text{-}H6'}$ = 1.3 Hz, 1H, H6′-glu), 4.09 (s, 3H, Me-Imidazole), 2.09 (s, 3H, OAc), 2.06 (s, 3H, OAc), 2.04 (s, 3H, OAc), 1.92 (s, 3H, OAc), 1.21 (s, 3H, J_{Pt} = 74 Hz).

^{13}C NMR (101 MHz, MeOD) δ 170.8, 170.0, 169.8, 169.2, 149.6, 148.7, 147.7, 145.2, 141.6, 138.9, 138.3, 136.3, 131.0, 130.6, 128.5, 127.6 (x2), 127.4, 126.4, 125.6, 122.3, 120.4 (q, $J_{C\text{-}F}$ = 320 Hz) 85.5, 74.7, 72.5, 70.8, 67.8, 61.6, 33.6, 19.1 (x3), 18.7, −14.0.

HRMS (ESI/QTOF), m/z 869.2225, [**4Pt-im**—$CF_3SO_3^-$].

3.2. Synthesis of 4Pt-im$_{dep}$

Complex **4Pt-im** (0.065 g, 0.064 mmol) was treated in 5.0 mL of methanol containing 5% mol of KOH. After 1 h of stirring, the complex was crystallized by slow addition of diethyl ether to the reaction mixture (yield 90%).

^{1}H NMR (400 MHz, CD_3OD) δ ^{1}H NMR (400 MHz, MeOD) δ 9.46 (d, J_{Pt} = 49 Hz, 1H, H2, or H9 phen), 8.94 (d, 1H, H4, or H7 phen), 8.90 (d, 1H, H7, or H4 phen), 8.71 (s, 1H, 1H, H-Triazole), 8.68 (dd, 1H, H9, or H2 phen), 8.49 (s, 1H, 1H, H-Imidazole), 8.22 (ABq, 2H, H5, and H6 phen), 8.05 (dd, 1H, H3, or H8 phen), 8.03 (dd, 1H, H8, or H3 phen), 7.75 (s, 1H, H-Triazole), 5.76 (d, $J_{H1\text{-}H2}$ = 9.2 Hz, 1H, H1-glu), 4.09 (s, 3H, Me-Imidazole), 4.01 (t, $J_{H2\text{-}H3}$ = 9.1 Hz, 1H, H2-glu), 3.95 (dd, $J_{H6\text{-}H6'}$= 11.6 Hz, $J_{H6\text{-}H5}$ = 1.4 Hz, 1H, H6-glu), 3.79 (dd, $J_{H6'\text{-}H5}$ = 5.3 Hz, 1H, H6′-glu), 3.70 3.50 (m, 2H, H3-glu, and H4-glu), 1.26 (s, 3H, J_{Pt} = 76 Hz).

^{13}C NMR (101 MHz, MeOD) δ 149.8, 148.8, 147.4, 145.2, 141.5, 139.0, 138.1, 135.8, 131.0, 130.7, 128.6, 127.6, 127.4, 126.4, 125.9, 125.6, 122.5, 120.5 ($J_{C\text{-}F}$ = 317 Hz), 88.6, 79.9, 77.0, 72.42, 69.9, 60.8, 33.2, −13.7.

HRMS (ESI/QTOF) m/z 701.1802, [**4Pt-im$_{dep}$**—$CF_3SO_3^-$].

3.3. UV–Vis Absorption Spectroscopy

UV–vis absorption spectra of the compounds as a function of time were collected in PBS (pH 7.4):DMSO-*d6* 90:10 and pure DMSO using a Jasco V-650 UV–vis spectrophotometer. Spectra were collected at room temperature using a compound concentration of 50 μM and 1 cm path length cuvettes. The other experimental settings were: 240–450 nm wavelength range, 400 nm/min scanning speed, 2.0 nm bandwidth, and 1.0 nm data pitch.

3.4. Cell Culture and the MTT Test

A431, H9c2, and MCF7 cells were purchased from American Type Culture Collection (ATCC). HaCaT cells were from Innoprot (Derio, Spain). Cells were cultured in DMEM (Sigma-Aldrich, St. Louis, MO, USA), supplemented with 10% fetal bovine serum (HyClone, Thermo Scientific, Logan, UT, USA) and antibiotics in a 5% CO_2 humidified atmosphere at 37 °C. The growth medium of H9c2 cells was implemented with 2 mM L-glutamine and 2 mM sodium pyruvate. Cells were seeded in 96-well plates at a density of 2.5 × 10^3 cells per well. Different drugs were added at increasing concentrations 24 h after seeding for dose-dependent assays. For the GLUT1-inhibitor-mediated cytotoxicity assay, 24 h after seeding, the cells were treated with 0.5–200 μM **4Pt-py** in the presence or

Appendix D

absence of 5 μM quercetin. Quercetin alone was used as the control. After 48 h incubation, cell viability was assessed by MTT assay, as described in a previous study [30]. Control experiments were performed by either growing cells in the absence of the compound or by supplementing the cell cultures with identical volumes of buffer (water:acetone, 1:1 *v*/*v*). Each value is the mean of three independent experiments, each with three determinations. Significance was determined by Student's *t*-test.

3.5. LDH Release

The occurrence of necrosis was determined by measuring the release of lactate dehydrogenase (LDH) in the culture medium, as described by Sucha et al. [53]. The LDH content of the medium from untreated cells was referred to as a spontaneous release, whereas the LDH total cellular content was determined upon cell lysis. The percentage of LDH release was calculated as:

$$\text{LDH release } (\%) = [(\text{experimental} - \text{spontaneus release})/(\text{total content} - \text{spontaneous release})] \times 100 \quad (1)$$

Each value is the mean of three independent experiments, each with three determinations. Significance was determined by Student's *t*-test.

3.6. Western Blot Analyses

A431 cells were plated at a density of 3×10^5 cells cm^{-2} in a complete medium for 24 h and then treated for 48 h with 12 μM **4Pt-py**. At the end of the incubation, both untreated and treated cells were analyzed, as described previously for Western blot analyses [30]. Upon the determination of total protein concentration in the supernatant by the Bradford assay, samples were analyzed by SDS-PAGE and Western blot using specific antibodies directed towards procaspase-3 or -9 (Cell Signal Technology, Danvers, MA, USA). β-actin (Sigma-Aldrich) or GAPDH (Thermo Fisher, Rockford, IL, USA) was used as the loading control. Each value is the mean of three independent experiments, each with three determinations. Significance was determined by Student's *t*-test.

3.7. Analysis of Mitochondrial Membrane Potential

Mitochondrial membrane potential (Δψm) was measured as we described [31]. Cells were plated at a density of 2×10^4 cells per well, and, after 24 h, cells were incubated for 48 h with 12–20 μM **4Pt-py**. At the end of the treatment, the cells were incubated with 200 nM of the cationic lipophilic dye tetramethylrhodamine ethyl ester (TMRE) for 20 min at 37 °C. Then, the cells were gently washed with 0.2% BSA in PBS three times, and the fluorescence was measured in a microplate reader with peak λ(ex)/λ(em) = 549/575 nm. Each value is the mean of three independent experiments, each with three determinations. Significance was determined by Student's *t*-test.

3.8. Ethidium Bromide Displacement Fluorescence Assay

Fluorescence spectra were collected on a HORIBA Fluoromax-4 spectrofluorometer at 25 °C using 1 cm path length cuvettes. ctDNA was incubated with ethidium bromide (EtBr) in a 1:50 molar ratio for 30 min at room temperature. Then, the complex was diluted in 10 mM ammonium acetate buffer at pH 7.5 up to a ctDNA final concentration of 200 μM. The ctDNA–EtBr complex was then titrated with a **4Pt** solution (final concentration from 10 to 100 μM, stock concentration 15 mM). Fluorescence emission spectra were recorded at excitation at 545 nm after an equilibration time of 5 min following each addition of the Pt complex.

3.9. ^{1}H-NMR and ESI-MS In-Solution Studies

The appropriate **4Pt** complex (5 mg) was dissolved in 0.5 mL of DMSO-d_6 or acetone-d_6. Calculated volumes of solution were diluted to 600 μL with the appropriate volumes of PB in D_2O (25 mM, pH 7.4) and/or DMSO-d_6 to provide a 1 mM solution of the complex

Appendix D

with the appropriate *v/v* ratio of solvents. Samples were incubated at 37 °C, and NMR spectra were recorded at different times.

To study the reactivity with dGMP, L-methionine, and GSH, stock solutions (10 mM) in PB of each nucleophile were prepared and the correct volume was added to a freshly prepared solution of the complexes in 9:1 *v/v* PB:DMSO-d_6 to afford a final concentration of 1 mM of the Pt complex and 2.5 eq. of the nucleophile.

Samples for ESI-MS analysis were prepared as described for NMR samples, using DMSO and H_2O instead of deuterated solvents. Prior to analysis, an aliquot of the reaction mixture was withdrawn and diluted with water to get 0.1 mM of Pt-complex solutions.

4. Conclusions

This work is part of broad research aimed at studying the biological activity of platinum(II) complexes containing glycoconjugated neutral ligands. The expertise of this team in favoring four- or five-coordination complexes through small structural modifications of the ligands allowed a homogeneous comparison between the activity of analogous cationic complexes in the two different coordination environments. In line with expectations, the two classes of compounds revealed profound differences, starting with the higher stability of the square-planar species with respect to the substitution of the sugar ligand. This aspect determines that their biological activity depends on the nature of the latter, whereas, in the case of five-coordinate complexes, the loss of the sugar tag plausibly provokes the substantial leveling of activities. This also implies that only the square-planar complexes exhibit a certain degree of selectivity, although with reduced cytotoxicity. The ensemble of results, also accompanied by the demonstration that the complexes interact with DNA, adds a piece to the knowledge of the properties of antitumor agents based on platinum(II), highlighting how the optimization of their performance requires the careful choice of ligands in the appropriate coordination geometry.

Supplementary Materials: The following are available online at https://www.mdpi.com/article/10.3390/ijms22168704/s1.

Author Contributions: Conceptualization, D.M.M., A.M., and F.R.; methodology, A.A., D.L. (Davide Liberti), and D.L. (Domenico Loreto); validation, E.B. and M.E.C.; investigation, A.A., D.L. (Davide Liberti), and D.L. (Domenico Loreto); data curation, A.A., D.L. (Davide Liberti), and D.L. (Domenico Loreto); writing—original draft preparation, A.A., E.B., and M.E.C.; writing—review and editing, D.M.M., A.M., and F.R.; supervision, F.R.; funding acquisition, E.B., D.M.M., and F.R. All authors have read and agreed to the published version of the manuscript.

Funding: This research was funded by Università di Napoli Federico II, grant number 000023_ALTRI_CDA_75_2021_FRA_RUFFO.

Conflicts of Interest: The authors declare no conflict of interest.

References

1. Mjos, K.D.; Orvig, C. Metallodrugs in Medicinal Inorganic Chemistry. *Chem. Rev.* **2014**, *114*, 4540–4563. [CrossRef] [PubMed]
2. Zhang, P.; Sadler, P.J. Advances in the Design of Organometallic Anticancer Complexes. *J. Organomet. Chem.* **2017**, *839*, 5–14. [CrossRef]
3. Anthony, E.J.; Bolitho, E.M.; Bridgewater, H.E.; Carter, O.W.L.; Donnelly, J.M.; Imberti, C.; Lant, E.C.; Lermyte, F.; Needham, R.J.; Palau, M.; et al. Metallodrugs Are Unique: Opportunities and Challenges of Discovery and Development. *Chem. Sci.* **2020**, *11*, 12888–12917. [CrossRef]
4. Oun, R.; Moussa, Y.E.; Wheate, N.J. The Side Effects of Platinum-Based Chemotherapy Drugs: A Review for Chemists. *Dalton Trans.* **2018**, *47*, 6645–6653. [CrossRef]
5. Ghosh, S. Cisplatin: The First Metal Based Anticancer Drug. *Bioorg. Chem.* **2019**, *88*, 102925. [CrossRef]
6. Živković, M.D.; Kljun, J.; Ilic-Tomic, T.; Pavic, A.; Veselinović, A.; Manojlović, D.D.; Nikodinovic-Runic, J.; Turel, I. A New Class of Platinum(II) Complexes with the Phosphine Ligand Pta Which Show Potent Anticancer Activity. *Inorg. Chem. Front.* **2018**, *5*, 39–53. [CrossRef]
7. Qin, Q.-P.; Wang, Z.-F.; Huang, X.-L.; Tan, M.; Luo, Z.; Wang, S.; Zou, B.-Q.; Liang, H. Two Telomerase-Targeting Pt(II) Complexes of Jatrorrhizine and Berberine Derivatives Induce Apoptosis in Human Bladder Tumor Cells. *Dalton Trans.* **2019**, *48*, 15247–15254. [CrossRef]

Appendix D

8. Dutta, P.K.; Sharma, R.; Kumari, S.; Dubey, R.D.; Sarkar, S.; Paulraj, J.; Vijaykumar, G.; Pandey, M.; Sravanti, L.; Samarla, M.; et al. A Safe and Efficacious Pt(II) Anticancer Prodrug: Design, Synthesis, in Vitro Efficacy, the Role of Carrier Ligands and in Vivo Tumour Growth Inhibition. *Chem. Commun.* **2019**, *55*, 1718–1721. [CrossRef] [PubMed]
9. Eskandari, A.; Kundu, A.; Ghosh, S.; Suntharalingam, K. A Triangular Platinum(II) Multinuclear Complex with Cytotoxicity Towards Breast Cancer Stem Cells. *Angew. Chem. Int. Ed.* **2019**, *58*, 12059–12064. [CrossRef]
10. Singh, K.; Gangrade, A.; Jana, A.; Mandal, B.B.; Das, N. Design, Synthesis, Characterization, and Antiproliferative Activity of Organoplatinum Compounds Bearing a 1,2,3-Triazole Ring. *ACS Omega* **2019**, *4*, 835–841. [CrossRef]
11. Maji, M.; Karmakar, S.; Gupta, A.; Mukherjee, A. Oxamusplatin: A Cytotoxic Pt(II) Complex of a Nitrogen Mustard with Resistance to Thiol Based Sequestration Displays Enhanced Selectivity towards Cancer. *Dalton Trans.* **2020**, *49*, 2547–2558. [CrossRef]
12. Tham, M.J.R.; Babak, M.V.; Ang, W.H. PlatinER: A Highly Potent Anticancer Platinum(II) Complex That Induces Endoplasmic Reticulum Stress Driven Immunogenic Cell Death. *Angew. Chem. Int. Ed.* **2020**, *59*, 19070–19078. [CrossRef]
13. Imran, M.; Rehman, Z.; Hogarth, G.; Tocher, D.A.; Chaudhry, G.-S.; Butler, I.S.; Bélanger-Gariepy, F.; Kondratyuk, T. Two New Monofunctional platinum(ii) Dithiocarbamate Complexes: Phenanthriplatin-Type Axial Protection, Equatorial-Axial Conformational Isomerism, and Anticancer and DNA Binding Studies. *Dalton Trans.* **2020**, *49*, 15385–15396. [CrossRef]
14. Adams, M.; Sullivan, M.P.; Tong, K.K.H.; Goldstone, D.C.; Hanif, M.; Jamieson, S.M.F.; Hartinger, C.G. Mustards-Derived Terpyridine–Platinum Complexes as Anticancer Agents: DNA Alkylation vs Coordination. *Inorg. Chem.* **2021**, *60*, 2414–2424. [CrossRef] [PubMed]
15. Hyeraci, M.; Scalcon, V.; Folda, A.; Labella, L.; Marchetti, F.; Samaritani, S.; Rigobello, M.P.; Dalla Via, L. New Platinum(II) Complexes Affecting Different Biomolecular Targets in Resistant Ovarian Carcinoma Cells. *Chem. Med. Chem.* **2021**, *16*, 1956–1966. [CrossRef]
16. Ding, S.; Hackett, C.L.; Liu, F.; Hackett, R.G.; Bierbach, U. Evaluation of a Platinum–Acridine Anticancer Agent and Its Liposomal Formulation in an in Vivo Model of Lung Adenocarcinoma. *Chem. Med. Chem.* **2021**, *16*, 412–419. [CrossRef] [PubMed]
17. Johnstone, T.C.; Suntharalingam, K.; Lippard, S.J. The Next Generation of Platinum Drugs: Targeted Pt(II) Agents, Nanoparticle Delivery, and Pt(IV) Prodrugs. *Chem. Rev.* **2016**, *116*, 3436–3486. [CrossRef] [PubMed]
18. Kenny, R.G.; Marmion, C.J. Toward Multi-Targeted Platinum and Ruthenium Drugs—A New Paradigm in Cancer Drug Treatment Regimens? *Chem. Rev.* **2019**, *119*, 1058–1137. [CrossRef]
19. Szablewski, L. Expression of Glucose Transporters in Cancers. *Biochim. Biophys. Acta (BBA) Rev. Cancer* **2013**, *1835*, 164–169. [CrossRef] [PubMed]
20. Pettenuzzo, A.; Pigot, R.; Ronconi, L. Metal-Based Glycoconjugates and Their Potential in Targeted Anticancer Chemotherapy. *Metallodrugs* **2016**, *1*, 36–61. [CrossRef]
21. Hartinger, C.; Nazarov, A.; Ashraf, S.; Dyson, P.; Keppler, B. Carbohydrate-Metal Complexes and Their Potential as Anticancer Agents. *Curr. Med. Chem.* **2008**, *15*, 2574–2591. [CrossRef]
22. Patra, M.; Johnstone, T.C.; Suntharalingam, K.; Lippard, S.J. A Potent Glucose-Platinum Conjugate Exploits Glucose Transporters and Preferentially Accumulates in Cancer Cells. *Angew. Chem. Int. Ed.* **2016**, *55*, 2550–2554. [CrossRef] [PubMed]
23. Han, J.; Gao, X.; Liu, R.; Yang, J.; Zhang, M.; Mi, Y.; Shi, Y.; Gao, Q. Design, Synthesis of Novel Platinum(II) Glycoconjugates, and Evaluation of Their Antitumor Effects. *Chem. Biol. Drug Des.* **2016**, *87*, 867–877. [CrossRef]
24. Wu, M.; Li, H.; Liu, R.; Gao, X.; Zhang, M.; Liu, P.; Fu, Z.; Yang, J.; Zhang-Negrerie, D.; Gao, Q. Galactose Conjugated Platinum(II) Complex Targeting the Warburg Effect for Treatment of Non-Small Cell Lung Cancer and Colon Cancer. *Eur. J. Med. Chem.* **2016**, *110*, 32–42. [CrossRef] [PubMed]
25. Gao, X.; Liu, S.; Shi, Y.; Huang, Z.; Mi, Y.; Mi, Q.; Yang, J.; Gao, Q. Mechanistic and Biological Characteristics of Different Sugar Conjugated 2-Methyl Malonatoplatinum(II) Complexes as New Tumor Targeting Agents. *Eur. J. Med. Chem.* **2017**, *125*, 372–384. [CrossRef]
26. Liu, R.; Li, H.; Gao, X.; Mi, Q.; Zhao, H.; Gao, Q. Mannose-Conjugated Platinum Complexes Reveals Effective Tumor Targeting Mediated by Glucose Transporter 1. *Biochem. Biophys. Res. Commun.* **2017**, *487*, 34–40. [CrossRef]
27. Hildebrandt, J.; Trautwein, R.; Kritsch, D.; Häfner, N.; Görls, H.; Dürst, M.; Runnebaum, I.B.; Weigand, W. Synthesis, Characterization and Biological Investigation of Platinum(II) Complexes with Asparagusic Acid Derivatives as Ligands. *Dalton Trans.* **2019**, *48*, 936–944. [CrossRef] [PubMed]
28. Bononi, G.; Iacopini, D.; Cicio, G.; Di Pietro, S.; Granchi, C.; Di Bussolo, V.; Minutolo, F. Glycoconjugated Metal Complexes as Cancer Diagnostic and Therapeutic Agents. *Chem. Med. Chem.* **2021**, *16*, 30–64. [CrossRef]
29. Cucciolito, M.E.; D'Amora, A.; De Feo, G.; Ferraro, G.; Giorgio, A.; Petruk, G.; Monti, D.M.; Merlino, A.; Ruffo, F. Five-Coordinate Platinum(II) Compounds Containing Sugar Ligands: Synthesis, Characterization, Cytotoxic Activity, and Interaction with Biological Macromolecules. *Inorg. Chem.* **2018**, *57*, 3133–3143. [CrossRef]
30. Cucciolito, M.E.; De Luca Bossa, F.; Esposito, R.; Ferraro, G.; Iadonisi, A.; Petruk, G.; D'Elia, L.; Romanetti, C.; Traboni, S.; Tuzi, A.; et al. *C* -Glycosylation in Platinum-Based Agents: A Viable Strategy to Improve Cytotoxicity and Selectivity. *Inorg. Chem. Front.* **2018**, *5*, 2921–2933. [CrossRef]
31. Annunziata, A.; Cucciolito, M.E.; Esposito, R.; Imbimbo, P.; Petruk, G.; Ferraro, G.; Pinto, V.; Tuzi, A.; Monti, D.M.; Merlino, A.; et al. A Highly Efficient and Selective Antitumor Agent Based on a Glucoconjugated Carbene Platinum(II) Complex. *Dalton Trans.* **2019**, *48*, 7794–7800. [CrossRef]

Appendix D

32. Annunziata, A.; Amoresano, A.; Cucciolito, M.E.; Esposito, R.; Ferraro, G.; Iacobucci, I.; Imbimbo, P.; Lucignano, R.; Melchiorre, M.; Monti, M.; et al. Pt(II) versus Pt(IV) in Carbene Glycoconjugate Antitumor Agents: Minimal Structural Variations and Great Performance Changes. *Inorg. Chem.* **2020**, *59*, 4002–4014. [CrossRef] [PubMed]
33. Annunziata, A.; Cucciolito, M.E.; Imbimbo, P.; Silipo, A.; Ruffo, F. A Hydrophilic Olefin Pt(0) Complex Containing a Glucoconjugated 2-Iminopyridine Ligand: Synthesis, Characterization, Stereochemistry and Biological Activity. *Inorg. Chim. Acta* **2021**, *516*, 120092. [CrossRef]
34. Annunziata, A.; Cucciolito, M.E.; Esposito, R.; Ferraro, G.; Monti, D.M.; Merlino, A.; Ruffo, F. Five-coordinate Pt(II) Compounds as Potential Anticancer Agents. *Eur. J. Inorg. Chem.* **2020**, *11-12*, 918–929. [CrossRef]
35. Wang, F.-Y.; Liu, R.; Huang, K.-B.; Feng, H.-W.; Liu, Y.-N.; Liang, H. New Platinum(II)-Based DNA Intercalator: Synthesis, Characterization and Anticancer Activity. *Inorg. Chem. Commun.* **2019**, *105*, 182–187. [CrossRef]
36. Pages, B.J.; Garbutcheon-Singh, K.B.; Aldrich-Wright, J.R. Platinum Intercalators of DNA as Anticancer Agents: Platinum Intercalators of DNA as Anticancer Agents. *Eur. J. Inorg. Chem.* **2017**, *2017*, 1613–1624. [CrossRef]
37. Zhang, S.; Yao, X.; Watkins, N.H.; Rose, P.K.; Caruso, S.R.; Day, C.S.; Bierbach, U. Discovery of a Chiral DNA-Targeted Platinum–Acridine Agent with Potent Enantioselective Anticancer Activity. *Angew. Chem. Int. Ed.* **2020**, *59*, 21965–21970. [CrossRef] [PubMed]
38. Zhang, K.; Yam, V.W.-W. Platinum(II) Non-Covalent Crosslinkers for Supramolecular DNA Hydrogels. *Chem. Sci.* **2020**, *11*, 3241–3249. [CrossRef]
39. De Pascali, S.A.; Migoni, D.; Papadia, P.; Muscella, A.; Marsigliante, S.; Ciccarese, A.; Fanizzi, F.P. New Water-Soluble Platinum(II) Phenanthroline Complexes Tested as Cisplatin Analogues: First-Time Comparison of Cytotoxic Activity between Analogous Four- and Five-Coordinate Species. *Dalton Trans.* **2006**, *42*, 5077–5087. [CrossRef]
40. Calvanese, L.; Cucciolito, M.E.; D'Amora, A.; D'Auria, G.; Esposito, A.; Esposito, R.; Falcigno, L.; Ruffo, F. Recognition of Prochiral Sulfides in Five-Coordinate PtII Complexes. *Eur. J. Inorg. Chem.* **2015**, *2015*, 4068–4075. [CrossRef]
41. Esposito, R.; Calvanese, L.; Cucciolito, M.E.; D'Auria, G.; Falcigno, L.; Fiorini, V.; Pezzella, P.; Roviello, G.; Stagni, S.; Talarico, G.; et al. Oxidative Coupling of Imino, Amide Platinum(II) Complexes Yields Highly Conjugated Blue Dimers. *Organometallics* **2017**, *36*, 384–390. [CrossRef]
42. Vera, J.C.; Reyes, A.M.; Velásquez, F.V.; Rivas, C.I.; Zhang, R.H.; Strobel, P.; Slebe, J.C.; Núñez-Alarcón, J.; Golde, D.W. Direct Inhibition of the Hexose Transporter GLUT1 by Tyrosine Kinase Inhibitors. *Biochemistry* **2001**, *40*, 777–790. [CrossRef]
43. Guo, Y.; He, Y.; Wu, S.; Zhang, S.; Song, D.; Zhu, Z.; Guo, Z.; Wang, X. Enhancing Cytotoxicity of a Monofunctional Platinum Complex via a Dual-DNA-Damage Approach. *Inorg. Chem.* **2019**, *58*, 13150–13160. [CrossRef]
44. Dabbish, E.; Russo, N.; Sicilia, E. Rationalization of the Superior Anticancer Activity of Phenanthriplatin: An In-Depth Computational Exploration. *Chem. Eur. J.* **2020**, *26*, 259–268. [CrossRef]
45. Liu, F.; Suryadi, J.; Bierbach, U. Cellular Recognition and Repair of Monofunctional–Intercalative Platinum–DNA Adducts. *Chem. Res. Toxicol.* **2015**, *28*, 2170–2178. [CrossRef]
46. Aseman, M.D.; Aryamanesh, S.; Shojaeifard, Z.; Hemmateenejad, B.; Nabavizadeh, S.M. Cycloplatinated(II) Derivatives of Mercaptopurine Capable of Binding Interactions with HSA/DNA. *Inorg. Chem.* **2019**, *58*, 16154–16170. [CrossRef]
47. Li, C.; Xu, F.; Zhao, Y.; Zheng, W.; Zeng, W.; Luo, Q.; Wang, Z.; Wu, K.; Du, J.; Wang, F. Platinum(II) Terpyridine Anticancer Complexes Possessing Multiple Mode of DNA Interaction and EGFR Inhibiting Activity. *Front. Chem.* **2020**, *8*, 210. [CrossRef]
48. Lozada, I.B.; Huang, B.; Stilgenbauer, M.; Beach, T.; Qiu, Z.; Zheng, Y.; Herbert, D.E. Monofunctional Platinum(II) Anticancer Complexes Based on Multidentate Phenanthridine-Containing Ligand Frameworks. *Dalton Trans.* **2020**, *49*, 6557–6560. [CrossRef] [PubMed]
49. Montero, D.; Tachibana, C.; Rahr Winther, J.; Appenzeller-Herzog, C. Intracellular Glutathione Pools Are Heterogeneously Concentrated. *Redox Biol.* **2013**, *1*, 508–513. [CrossRef]
50. Oehlsen, M.E.; Qu, Y.; Farrell, N. Reaction of Polynuclear Platinum Antitumor Compounds with Reduced Glutathione Studied by Multinuclear (^{1}H, ^{1}H−^{15}N Gradient Heteronuclear Single-Quantum Coherence, and ^{195}Pt) NMR Spectroscopy. *Inorg. Chem.* **2003**, *42*, 5498–5506. [CrossRef] [PubMed]
51. Kemp, S.; Wheate, N.J.; Pisani, M.J.; Aldrich-Wright, J.R. Degradation of Bidentate-Coordinated Platinum(II)-Based DNA Intercalators by Reduced L-Glutathione. *J. Med. Chem.* **2008**, *51*, 2787–2794. [CrossRef] [PubMed]
52. Ortiz, D.; Gasilova, N.; Sepulveda, F.; Patiny, L.; Dyson, P.J.; Menin, L. Aom 2S: A New Web-based Application for DNA/RNA Tandem Mass Spectrometry Data Interpretation. *Rapid Commun. Mass Spectrom.* **2020**, *34*, e8927. [CrossRef] [PubMed]
53. Sucha, L.; Hroch, M.; Rezacova, M.; Rudolf, E.; Havelek, R.; Sispera, L.; Cmielova, J.; Kohlerova, R.; Bezrouk, A.; Tomsik, P. The cytotoxic effect of α-tomatine in MCF-7 human adenocarcinoma breast cancer cells depends on its interaction with cholesterol in incubation media and does not involve apoptosis induction. *Oncol. Rep.* **2013**, *30*, 2593–2602. [CrossRef] [PubMed]

Appendix D

Square-planar *vs.* trigonal bipyramidal geometry in Pt(II) complexes containing triazole-based glucose ligands as potential anticancer agents

Alfonso Annunziata [1], Davide Liberti [1], Emiliano Bedini [1], Maria Elena Cucciolito [1], Domenico Loreto [1], Daria Maria Monti [1], Antonello Merlino [1] and Francesco Ruffo [1,*]

[1] Dipartimento di Scienze Chimiche, Università di Napoli Federico II, Complesso Universitario di Monte S. Angelo, via Cintia 21, 80126 Napoli (Italy)
* Correspondence: ruffo@unina.it

Content

Appendix D

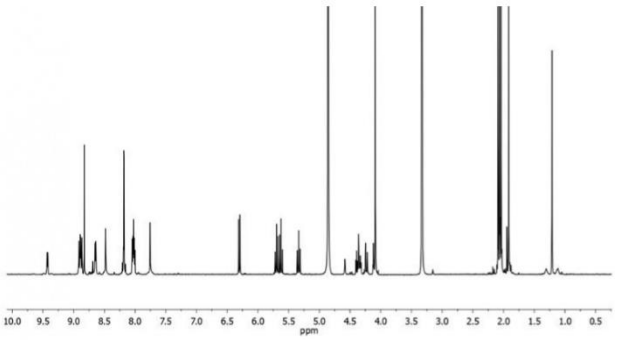

Figure S1. ^{1}H-NMR spectrum of **4Pt-im** in MeOD at 25 °C

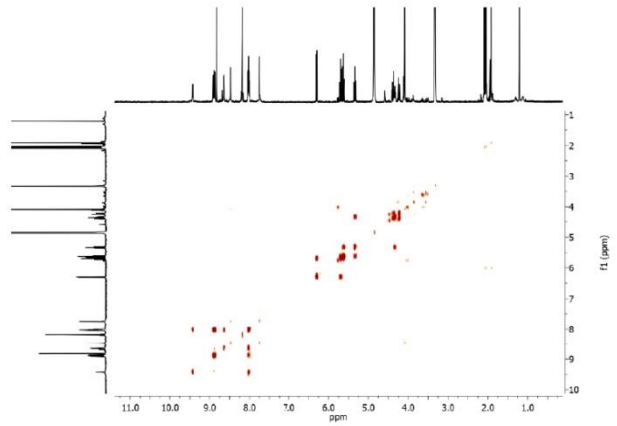

Figure S2. COSY NMR spectrum of **4Pt-im** in MeOD at 25 °C

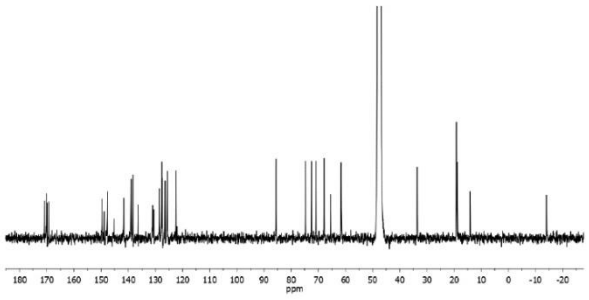

Figure S3. ^{13}C NMR spectrum of **4Pt-im** in MeOD at 25 °C

Appendix D

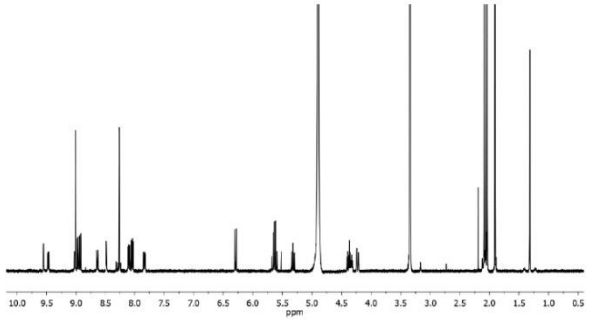

Figure S4. ^{1}H-NMR spectrum of **4Pt-py** in MeOD at 25 °C

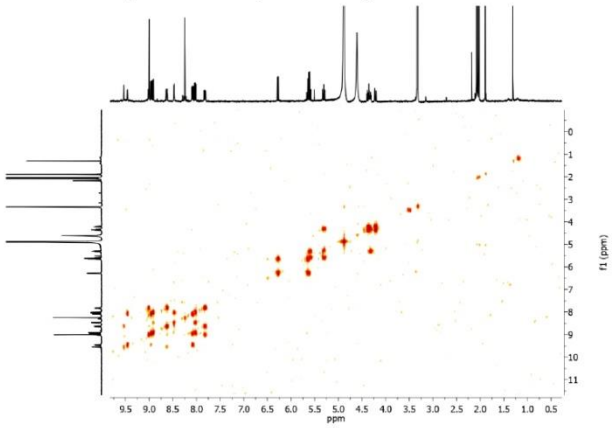

Figure S5. COSY NMR spectrum of **4Pt-py** in MeOD at 25 °C

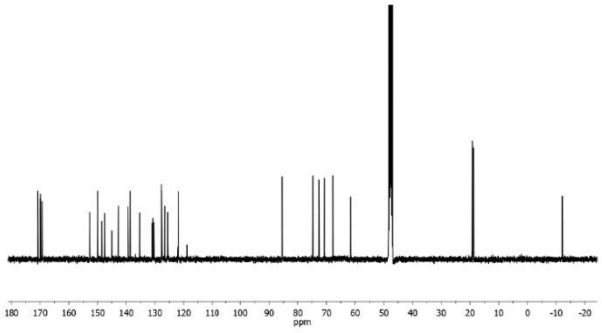

Figure S6. ^{13}C NMR spectrum of **4Pt-py** in MeOD at 25 °C

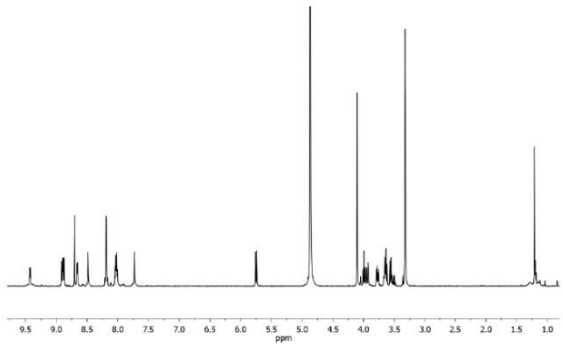

Figure S7. ^{1}H-NMR spectrum of **4Pt-im$_{dep}$** in MeOD at 25 °C

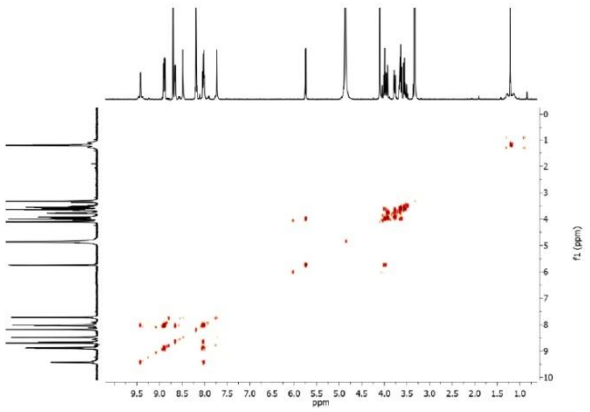

Figure S8. COSY NMR spectrum of 4Pt-im$_{dep}$ in MeOD at 25 °C

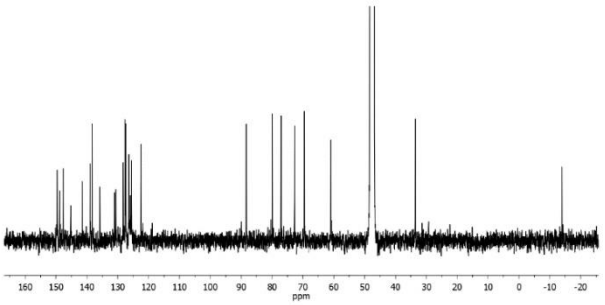

Figure S9. ^{13}C NMR spectrum of **4Pt-im$_{dep}$** in MeOD at 25 °C

Appendix D

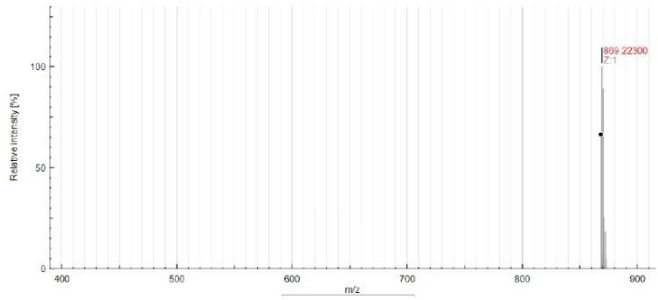

Figure S10. ESI-MS spectrum of **4Pt-im** in MeOH

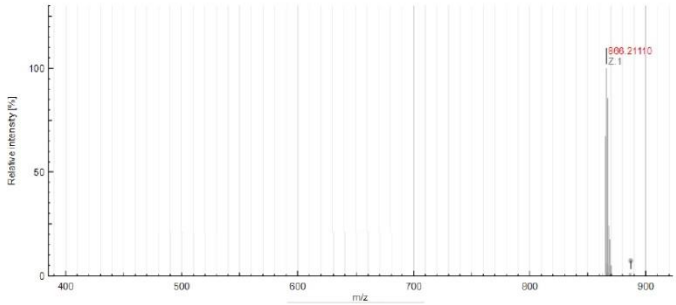

Figure S11 ESI-MS spectrum of **4Pt-py** in MeOH

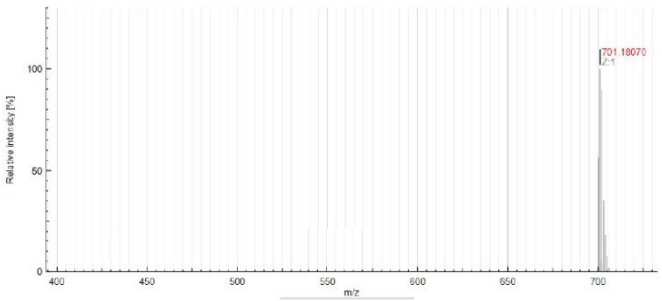

Figure S12 ESI-MS spectrum of **4Pt-im$_{dep}$** in MeOH

Appendix D

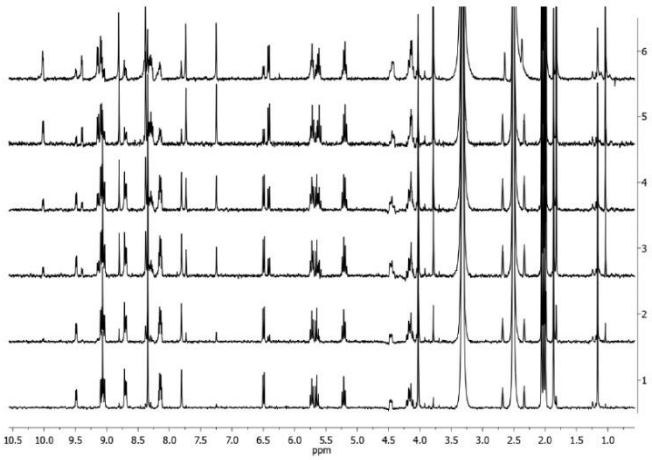

Figure S13. ^{1}H-NMR spectra over time of **4Pt-im** in DMSO (1 mM) at 37 °C (1 = start, 2 =1h, 3 = 3h, 4 = 5h, 5 = 24h, 6 =48 h).

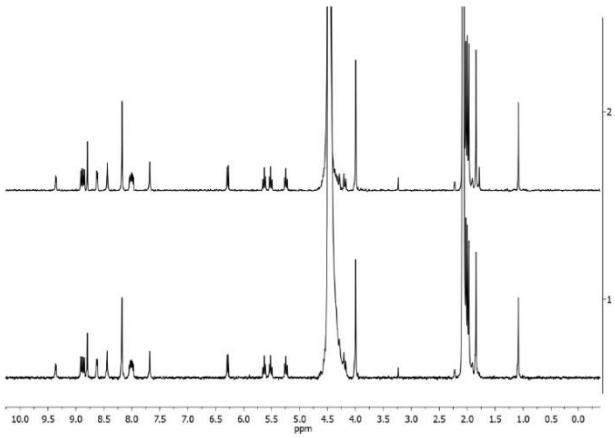

Figure S14. ^{1}H-NMR spectra over time of **4Pt-im** in 1:1 v/v D_2O : acetone-d_6 (1 mM) at 37 °C (1 = start, 2 =72 h).

Appendix D

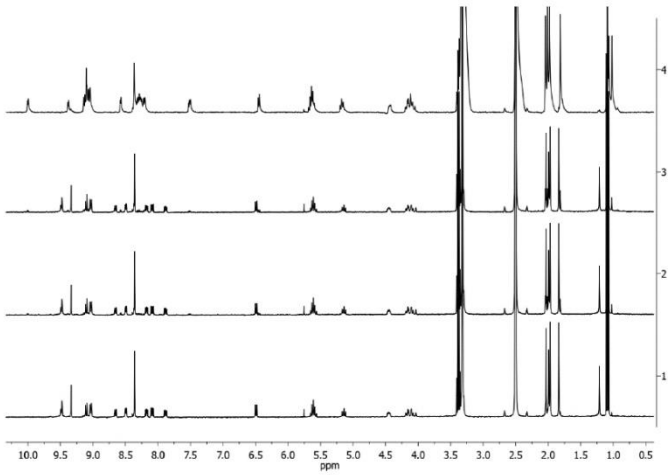

Figure S15. ^{1}H-NMR spectra over time of **4Pt-py** in DMSO (1 mM) at 37 °C (1 = start, 2 =1h, 3 = 2h, 4 = 48 h).

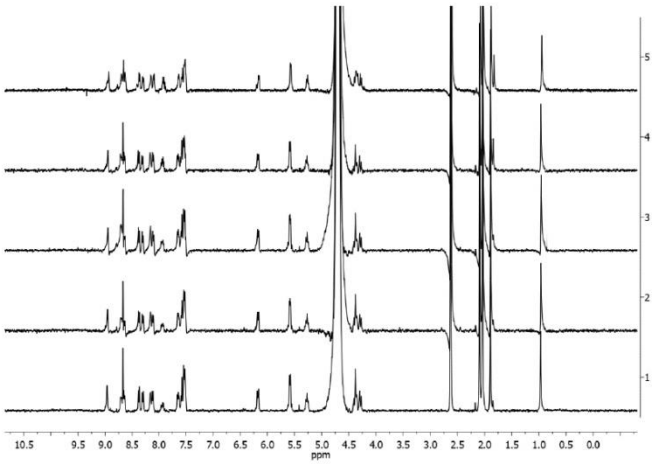

Figure S16. ^{1}H-NMR spectra over time of **4Pt-py** in 9:1 v/v PB : DMSO-d_6 (1 mM) at 37 °C (1 = start, 2 =1h, 3 = 3h, 4 = 24h, 5 =48 h).

Appendix D

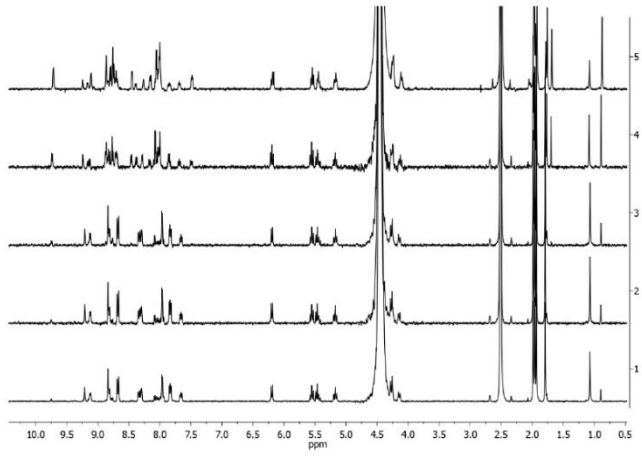

Figure S17. ^{1}H-NMR spectra over time of **4Pt-py** in 1:1 v/v PB : DMSO-d_6 (1 mM) at 37 °C (1 = start, 2 =1h, 3 = 3h, 4 = 24h, 5 =48 h).

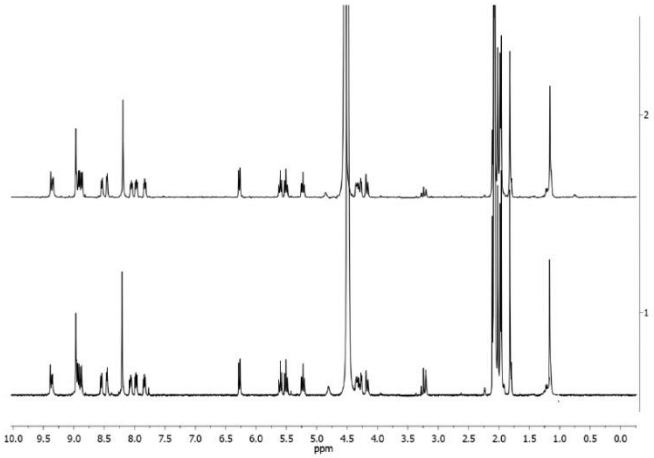

Figure S18. ^{1}H-NMR spectra over time of **4Pt-py** in 1:1 v/v D$_2$O : acetone-d_6 (1 mM) at 37 °C (1 = start, 2 =72 h).

Appendix D

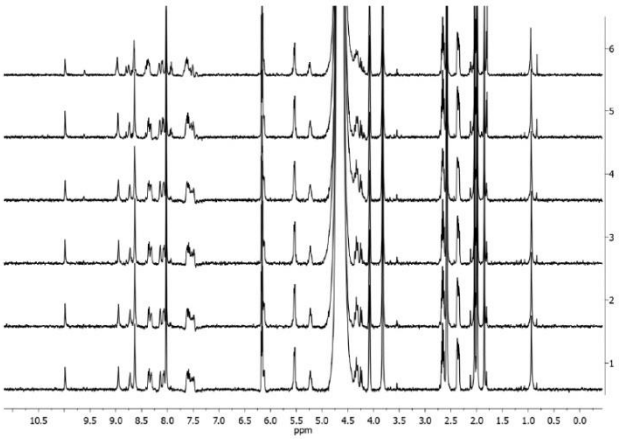

Figure S19. ^{1}H-NMR spectra of **4Pt-py** incubated with dGMP in 9:1 v/v PB:DMSO-d_6 (1 mM of Pt, 2.5 eq of dGMP) at 37 °C at different time (1 = start, 2 = 2h, 3 = 4h, 4 = 6h, 5 = 24 h, 6 = 48 h).

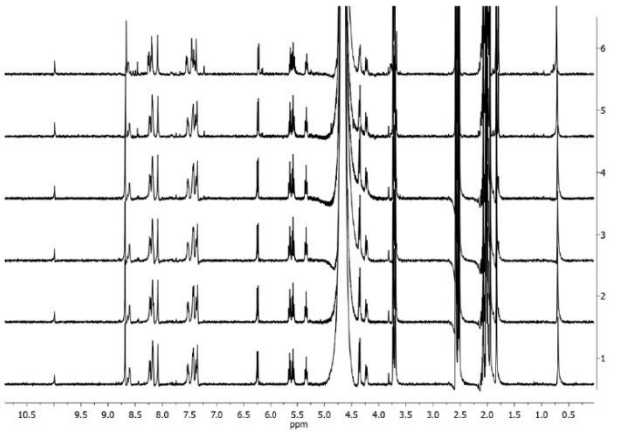

Figure S20. ^{1}H-NMR spectra of **4Pt-im** incubated with L-methionine in 9:1 v/v PB : DMSO-d_6 (1 mM of Pt, 2.5 eq of L-methionine) at 37 °C at different time (1 = start, 2 = 2h, 3 = 4h, 4 = 6h, 5 = 24 h, 6 = 48 h).

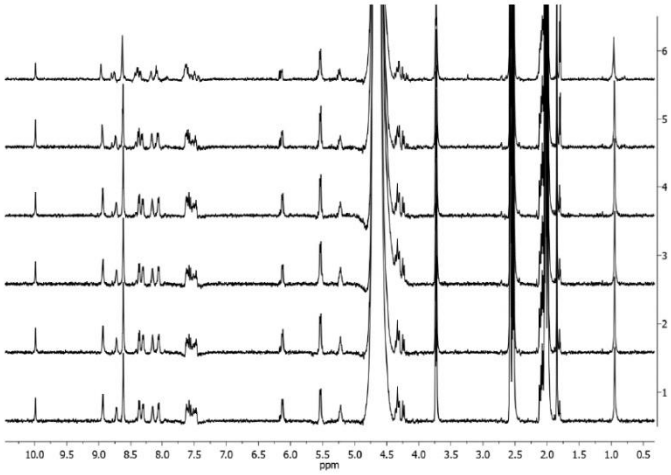

Figure S21. ^{1}H-NMR spectra of **4Pt-py** incubated with L-methionine in 9:1 v/v PB:DMSO-d_6 (1 mM of Pt, 2.5 eq of L-methionine) at 37 °C at different time (1 = start, 2 = 2h, 3 = 4h, 4 = 6h, 5 = 24 h, 6 = 48 h).

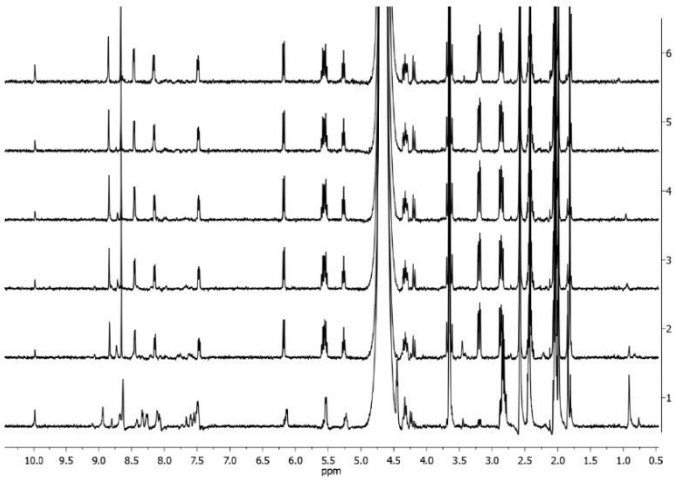

Figure S22. ^{1}H-NMR spectra of **4Pt-py** incubated with GSH in 9:1 v/v PB:DMSO-d_6 (1 mM of Pt, 2.5 eq of GSH) at 37 °C at different time (1 = start, 2 = 2h, 3 = 4h, 4 = 6h, 5 = 24 h, 6 = 48 h).

Appendix D

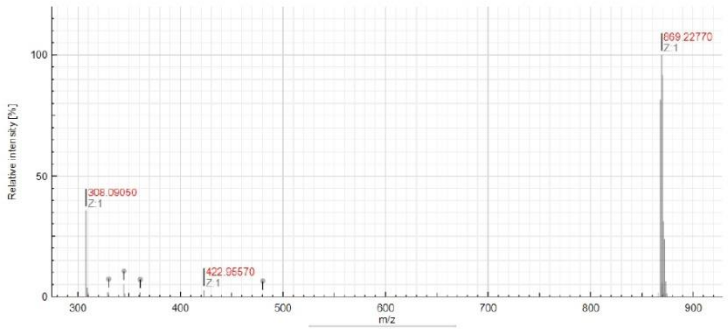

Figure S23. ESI-MS spectrum of **2Pt-im** incubated with GSH in 9:1 v/v H_2O : DMSO recorded after the dissolution.

Table S1. List of peaks found in the ESI-MS spectrum of the reaction mixture between **4Pt-im** and GSH (2.5 eq.) after 48 h of at 37 °C

Sequence	MF	Ionization	MF Mass	m/z	ppm	Intensity	Similarity
[PtPhenL2]	$C_{52}H_{58}N_{12}O_{18}Pt$	(+)2	1333.364	666.6814	1.355398	0.161499	0.987963
[4Pt-im]	$C_{33}H_{36}N_7O_9Pt$	(+)	869.2222	869.2217	1.418583	3.040044	0.980387
[Pt2Phen2GSH2-2H]	$C_{44}H_{48}N_{10}O_{12}Pt_2S_2$	(+)2	1362.219	681.109	1.774932	0.039036	0.968953
[PtMePhen]	$C_{13}H_{11}N_2Pt$	(+)	390.057	390.0565	-0.04174	0.087498	0.959729
[PtMePhenDmso]	$C_{15}H_{17}N_2OPtS$	(+)	468.071	468.0704	1.125112	2.147419	0.930783
[PtPhenGSH-H]	$C_{22}H_{23}N_5O_6PtS$	(H+)	680.1017	681.109	1.774932	0.039036	0.893688
[im + H]	$C_{20}H_{25}N_5O_9$	(H+)	479.1652	480.1725	1.405306	4.714523	0.951694

RSC Advances

ROYAL SOCIETY OF CHEMISTRY

PAPER

View Article Online
View Journal | View Issue

Check for updates

Cite this: *RSC Adv.*, 2021, **11**, 35585

Application potential of biogenically synthesized silver nanoparticles using *Lythrum salicaria* L. extracts as pharmaceuticals and catalysts for organic pollutant degradation†

Nikola Z. Srećković,[a] Zoran P. Nedić,[b] Davide Liberti,[c] Daria Maria Monti,[c] Nevena R. Mihailović,[a] Jelena S. Katanić Stanković,[d] Silvana Dimitrijević[e] and Vladimir B. Mihailović *[a]

This study was designed to evaluate the optimal conditions for the eco-friendly synthesis of silver nanoparticles (AgNPs) using *Lythrum salicaria* L. (Lythraceae) aqueous extracts and their potential application and safe use. AgNPs synthesized using *L. salicaria* aerial parts (LSA-AgNPs) and root extract (LSR-AgNPs) were characterized by UV-Vis spectrophotometry, Fourier transform infrared spectroscopy (FTIR), scanning electron microscopy (SEM/EDS), and X-ray powder diffraction (XRPD). Dynamic light scattering (DLS) was used for the determination of the size distribution profiles of the obtained nanoparticles. Both *L. salicaria* extracts showed high phenolic content, while the flavone *C*-glucosides orientin, vitexin, and isovitexin were detected in extracts using HPLC. The synthesized AgNPs displayed growth inhibition of the tested bacteria and fungi in concentrations between 0.156 and 1.25 mg mL^{-1}. The studied nanoparticles also showed antioxidant potential and gained selectivity at different concentrations on different cancer cell lines. Concentrations of LSA-AgNPs were found to be 20.5 and 12 μg mL^{-1} towards A431 and SVT2, respectively, while LSR-AgNPs were effective only against A431 cancer cells (62 μg mL^{-1}). The hemolytic activity of LSA-AgNPs in concentrations up to 150 μg mL^{-1} was not observed, while LSR-AgNPs in the highest applied concentration hemolyzed 2.8% of erythrocytes. The degradation possibility of Congo red and 4-nitrophenol using LSA-AgNPs and LSR-AgNPs as catalysts was also proven. The results indicate that *L. salicaria* may be used for the eco-friendly synthesis of AgNPs with possible applications as antimicrobial and selective cytotoxic agents towards cancer cell lines, as well as in catalytic degradation of pollutants.

Received 20th July 2021
Accepted 22nd October 2021

DOI: 10.1039/d1ra05570d

rsc.li/rsc-advances

1. Introduction

Nanoparticle's research is a topic of dynamic scientific exploration nowadays, emphasizing nanoparticle application in various fields such as electronics, catalysis, biosensors, wastewater treatment, biomedicine, pharmaceuticals, and cosmetics.[1] Due to the rising industrial uses of nanoparticles, their production volume is constantly increasing, and their synthesis is mainly based on physical and chemical methods that consume a lot of energy or need the use of potentially environmentally harmful chemical compounds.[2] Nanobiotechnology aims to establish low-cost and environmentally suitable methods for use of some biological components or live organisms and their products for the fabrication of different nanoparticles. It has been reported that bacteria, fungi, molds, and plants may be used for the successful synthesis of nanoparticles in an environmentally acceptable manner.[3,4] However, the use of some natural resources such as microorganisms in nanoparticle synthesis risks possible negative effects on health and environmental contamination. Some plant extracts or phytochemicals, particularly obtained from medicinal herbs and spices, have greater potential in nanoparticle synthesis compared with microorganisms. In addition to provide environmentally friendly reducing and stabilizing agents for the formation of the nanoparticles, these plant-originated products may possess beneficial biological characteristics and transfer their properties to nanoparticles during synthesis.[5] Plant

[a]*University of Kragujevac, Faculty of Science, Department of Chemistry, Radoja Domanovića 12, 34000 Kragujevac, Serbia. E-mail: vladimir.mihailovic@pmf.kg.ac.rs*
[b]*University of Belgrade, Faculty of Physical Chemistry, Studentski trg 12-16, P.O. Box 47, 11159 Belgrade, Serbia*
[c]*University of Naples Federico II, Complesso Universitario Monte Sant'Angelo, Department of Chemical Sciences, via Cinthia 4, 80126, Naples, Italy*
[d]*University of Kragujevac, Institute for Information Technologies Kragujevac, Department of Science, Jovana Cvijića bb, 34000 Kragujevac, Serbia*
[e]*Mining and Metallurgy Institute Bor, Zeleni bulevar 35, 19210 Bor, Serbia*

† Electronic supplementary information (ESI) available. See DOI: 10.1039/d1ra05570d

Appendix E

phenolic compounds are well-known secondary metabolites with valuable pharmacological properties and their emphasized redox characteristics. Their redox capacity provides them an opportunity to be used as reducing agents of metal ions during plant-mediated synthesis of metal nanoparticles, while their structure is responsible for stabilizing obtained nanoparticles.[6]

Among different metal-based nanoparticles that are in use, silver nanoparticles (AgNPs) have a long history of application primarily because they possess antimicrobial properties.[7] AgNPs are used in cosmetic preparations, as a catalyst in the chemical industry, for biomedical purposes, and preparation of material with antimicrobial properties.[8] The use of AgNPs for medicinal or food packaging purposes is in increase and their synthesis using plant extracts could be a great advantage considering the ecological aspect of the synthesis process and supplementing of nanoparticles themselves with biologically important compounds.[9,10]

Different nanoparticles, including AgNPs, have been reported as effective catalysts in the degradation of harmful diazo dyes from various industries.[11] Oxidation or photolysis is not a common pathway of degradation of stable azo dyes and they can remain unchanged for years.[12] Therefore, the treatment of wastewater containing such dyes is essential for the preservation of the environment.[13]

Lythrum salicaria L. (Lythraceae) is native in Europe and Asia, as well as in some areas in Africa and Australia. In North America, *L. salicaria* (purple loosestrife) has been introduced and now it is on the red list because of its strong invasive ability. Purple loosestrife is also known for its traditional use in the treatments of inflammatory disorders (dysentery, hemorrhoids, intestinal catarrh, and eczema).[14] Previously published results showed that *L. salicaria* possesses high polyphenolic content and excellent antioxidant properties. Its root is particularly rich in tannins, while the aerial part contains characteristic *C*-glycosides vitexin, orientin, isovitexin, and isoorientin.[14,15] *L. salicaria* aerial part extract was used in a previous study conducted by Mohammadalinejhad *et al.* for synthesis of AgNPs for the fabrication of nanohybrids with cellulose, chitosan, and lignocellulose.[16] However, the root extract of *L. salicaria* which possesses high antioxidant potential[15] has not been studied for nanoparticle synthesis, as well as detailed biological properties of *L. salicaria* fabricated nanoparticles have not been examined so far. The main goal of this study is to determine and optimize the conditions for the ecologically friendly synthesis of AgNPs using aerial part (LSA) and root (LSR) aqueous extracts of *L. salicaria*. Considering the invasiveness of *L. salicaria* and due to the need for reduction of its population in some areas (especially in North America), the focus of this research was the prospective application of *L. salicaria* in the environmentally friendly synthesis of AgNPs and potential applications of obtained nanoparticles as antimicrobial, antioxidant, and cytotoxic agents. Considering catalytic properties of AgNPs, degradation of Congo red day and 4-nitrophenol in presence of obtained nanoparticles was also determined.

2. Methods and materials

2.1. Materials

The chemicals used in this study (sodium borohydride ($NaBH_4$), silver nitrate ($AgNO_3$), 2,2′-azino-bis(3-ethylbenzthiazoline-6-sulfonic acid) (ABTS), sodium dodecyl sulfate (SDS), 2,2-diphenyl-1-picrylhydrazyl 1,1-diphenyl-2-picrylhydrazyl radical (DPPH), referent phenolic standards, and methanol) were procured from Sigma-Aldrich Chemicals (Deisenhofen, Germany). Substrates and components (Nutrient agar (NA), Sabouraud Dextrose Agar (SDA), Müller–Hinton broth (MHB), and Sabouraud Dextrose Broth (SDB)) for microorganisms' cultivation and determination of antimicrobial activity are provided from Torlak Institute of Virology, Vaccines, and Sera (Belgrade, Serbia). The resazurin salt was supplied from Acros Organics (New Jersey, USA). Solvents used in high-performance liquid chromatography (HPLC) analyses were obtained from Roth (Karlsruhe, Germany).

2.2. Preparation of *L. salicaria* extracts

L. salicaria was collected in village Veliko Krčmare (Central Serbia) in August 2017. The plant material was identification at the Herbarium of the Department of Biology and Ecology, Faculty of Science, University of Kragujevac, Serbia (voucher number 130/018). To remove any impurities, the plant material was rinsed with deionized water, dried at room temperature in a dark area, and powdered using a laboratory mill. The powdered dried aerial (LSA) and root (LSR) plant materials (10 g) were separately added to 100 mL of boiling deionized water. After 1 h, the obtained extract was filtered with Macherey-Nagel 85/70 mm filter paper. Aqueous extracts were stored at 4 °C for further use within a week.

2.3. Phytochemical assessment of *L. salicaria* aqueous extracts

Total phenolic and flavonoid contents were estimated spectrophotometrically as described previously.[15] Total phenolic content expressed as milligrams of gallic acid equivalents per gram of dry plant weight (mg GAE per g dry plant) was determined using the Folin–Ciocalteu reagent. The quantification of total flavonoids in extracts expressed in milligrams of quercetin per gram of dry plant weight (mg QUE per g dry plant) was determined using the method with aluminum chloride as reagents for the formation of yellow compounds with flavonoid compounds. All experiments for the determination of total phenolic and flavonoid contents were performed in three replications.

The chromatographic analyses of phenolic compounds in *L. salicaria* aqueous extracts were performed using the HPLC system (Shimadzu Prominence, Kyoto, Japan) configured with a Photodiode Array Detector (SPD-M20A). For separation of phenolic compounds, a Phenomenex Kinetex® (Phenomenex, Torrance, CA, US) C18 column (100 × 4.6 mm, 2.6 μm particle size) thermostated at 40 °C was used. The mobile phase used for the separation of phenolic compounds was Millipore water (phase A) and acetonitrile (phase B) with the addition of trifluoroacetic acid (0.1% in both phases). Gradient mode 0–1 min 5% B, 1–10 min 5–30% B, and 10–15 min 100% B was applied. The solvent flow rate during chromatographic separation was 2 mL min^{-1} after injection of 10 μL of sample extracts.[17] The chromatograms were recorded at wavelengths 280, 325, and 360 nm and analyzed using LC Solution software version 1.24 SP1 (Shimadzu, Kyoto, Japan).

For the identification of compounds in extracts, the retention times and UV-Vis absorption spectra obtained for reference

standards were compared with corresponding data obtained for chromatograms of extracts. The calibration lines for vitexin, isovitexin, and orientin were drawn using different concentrations of corresponding referent standards and used for quantification of these compounds in extracts.

2.4. Biosynthesis of AgNPs

Different reaction conditions were applied for the synthesis of nanoparticles using the aerial part (LSA-AgNPs) and root (LSR-AgNPs) extracts of *L. salicaria*. Silver nitrate was dissolved in diluted (2.5, 5, 10, and 20%, v/v) LSA and LSR aqueous extracts to obtain different concentrations of $AgNO_3$ (0.5, 1, 10, and 20 mM). The reaction mixtures were stirred on a magnetic stirrer and heated at different temperatures (25, 50, and 80 °C) until metal nanoparticles were formed. To modify the pH of the reaction mixture (pH 2, 6, and 12) 1 M HNO_3 or 1 M NaOH were used. Visual color change (from light yellow to dark brown) and UV-Vis spectrophotometry were used to observe the production of AgNPs throughout the synthesis. The best conditions for the highest LSA-AgNPs yield production were: 20 mM concentration of $AgNO_3$, 5% (v/v) aerial part extract concentration, a reaction temperature of 25 °C, pH 12, and reaction time of 30 min for synthesis. The best reaction conditions for the LSR-AgNPs production were as follows: 10 mM $AgNO_3$ concentration, root extract concentration 10% (v/v), a reaction temperature of 80 °C, pH 12, and reaction time 30 min. After the synthesis of AgNPs, the suspensions were centrifuged at 12 000 rpm for 10 min. Obtained residue after centrifugation resuspended in demineralized water, centrifugated again, and the precipitated nanoparticles were then dried in a hot air oven (40 °C) and stored at 4 °C.

2.5. Characterization of synthesized AgNPs

A double beam spectrophotometer Halo DB-20S (Dynamica GmbH, Switzerland) was used to monitor the synthesis of AgNPs in the wavelength range 300–800 nm with a resolution of 0.5 nm. The X-ray diffractometer (PHILIPS PW 1710) set at a voltage of 40 kV and 30 mA with CuKα radiation of 1.54178 Å was used to analyze the crystal structure of the biosynthesized nanoparticles. The samples were tested in the range of 10–90° 2θ with a step of 0.02° and a retention time of 0.25 s at each step. A scanning electron microscope (SEM) JOEL JSM IT 300LV with EDS detector (OXFORD Instruments, X-max) was used to examine the surface and elemental composition of nanoparticles. The samples for SEM were prepared in JOEL FC-TM20 auto coating thickness controller. For the determination of nanoparticles size, dynamic light scattering (DLS) measurements were carried out using Mastersizer 2000 from Malvern Panalytical. Obtained nanoparticles samples, as well as dry extract used in their synthesis, were subjected to Fourier transform infrared spectroscopy (FTIR) for the detection of functional groups of molecules present in samples.

2.6. Antioxidant activity

The antioxidant activity of AgNPs was studied using two $ABTS^{\bullet+}$ and $DPPH^{\bullet}$ scavenging assays.[15] Different concentrations of LSA-AgNPs and LSR-AgNPs aqueous solutions were mixed with ABTS methanol solution. After 30 minutes of incubation at room temperature in the dark, the absorbance was measured at 734 nm. Similarly, serial dilutions of obtained nanoparticles in water were mixed with the same volume of $DPPH^{\bullet}$ solution to test the ability of nanoparticles to neutralize the DPPH radicals. After standing in the dark place for 30 min the absorbance of the solution mixture of DPPH radicals and nanoparticles was measured spectrophotometrically at 517 nm. As a reference antioxidant butylated hydroxytoluene (BHT) was used in both radical scavenging methods. Using the dose–response sigmoidal curve produced with OriginPro8 software (OriginLab, Northampton, Massachusetts, USA), the results for both procedures were reported as the concentration of samples giving 50% of radical scavenging activity (IC_{50}).

2.7. Antimicrobial activity of LSA-AgNPs and LSR-AgNPs

The antimicrobial activity of synthesized AgNPs by the aqueous leaf and root extracts of *L. salicaria* was tested on five Gram-negative and six Gram-positive bacterial strains. Antifungal effects of synthesized AgNPs were tested on the nine fungal species, eight molds and yeast *Candida albicans*. For the determination of AgNPs' antimicrobial activity, bacterial species were obtained from the Institute for Public Health in Kragujevac, Serbia, while fungal species were obtained from the Laboratory for Microbiology, Department of Biology and Ecology, Faculty of Science, University of Kragujevac, Serbia. Nutrient agar (NA) and Sabouraud Dextrose Agar (SDA) were used for the cultivation of bacterial strains and *C. albicans*, respectively, whereas potato glucose agar (PDA) was used for fungal strains growth before antimicrobial testing of AgNPs.

The antimicrobial activity of AgNPs was determined using the microdilution method for the determination of minimal inhibitory concentrations (MIC) described by Sarker *et al.*[18] The MIC determination assay was carried out by a serial dilution technique in 96-well microtiter plates using a Müller–Hinton broth (MHB) for bacterial and Sabouraud Dextrose Broth (SDB) for fungi and *C. albicans* testing. Fresh overnight cultures of bacteria and *C. albicans* were suspended in 5% DMSO and diluted with sterilized water to obtain a concentration of 1.0×10^6 CFU mL^{-1}.[19] The cell suspension of examined molds was diluted with 5% DMSO solution to obtain a concentration of 5×10^4 CFU mL^{-1} following NCCLS recommendations[20] for antifungal determination of AgNPs. For determination of MICs, AgNPs and antibiotic/antimycotic were dissolved in sterile water and 10 μL of these solutions were transferred to 96-microtiter wells containing 70 μL of MHB or SDB. The solution of resazurin (10 μL, 0.6 mg mL^{-1}), then, was added to 96-microtiter wells as an indicator of bacterial growth. In samples for antifungal determination, SBD was added instead of resazurin solution. Lastly, 10 μL of microorganisms' cell suspension was added to all the wells. The sterility control without suspension of microorganisms and growth control without antimicrobial compounds addition were also performed in each used 96-microtiter plate. The final concentration of tested AgNPs was in the range 0.156–20 mg mL^{-1}, while the concentrations of tested antibiotic (erythromycin) and antimycotic (nystatin) for MIC determination were in the range 0.3125–40 μg mL^{-1}. The lowest concentration of test sample in the well without color change of resazurin or visible growth was taken as the MIC value.

Appendix E

2.8. MTT cell proliferation assay

For determination of cytotoxicity of synthesized AgNPs, cancer cell lines Balb/c-3T3 mouse fibroblasts transformed by SV40 virus (SVT2 cells) and human epidermoid carcinoma cells (A431), as well as immortalized murine fibroblasts (Balb/c-3T3) and human keratinocytes (HaCaT) were used. Dulbecco's Modified Eagle's Medium with the addition of 2 mM L-glutamine, 10% fetal bovine serum, and streptomycin and penicillin was used for cell cultivation. Cells were cultured in an incubator containing 5% CO_2 at 37 °C. The cytotoxic activity of LSA-AgNPs and LSR-AgNPs was determined in 96-well plates with a cells density of 3×10^3 per well for immortalized cells and 2×10^3 per well for cancer cells. The solutions of LSA-AgNPs, in a concentration range from 1 to 25 μg mL^{-1} and LSR-AgNPs in a concentration range from 1 to 100 μg mL^{-1}, were added to 96-well plates, 24 h after plating the cells. The MTT (3-(4,5-dimethylthiazol-2-yl)-2,5-diphenyltetrazolium bromide) solution was added to each well (final MTT concentration MTT of 0.5 mg mL^{-1}) after 48 h of incubation.[21] Then plates were incubated at 37 °C for 4 h. After incubation, the solution of 2-propanol containing 0.01 N HCl was added to dissolve obtained formazan crystals. The absorbance at 570 nm of solution in each well was measured using an automatic plate reader (Microbeta Wallac 1420, PerkinElmer, Basel, Switzerland). The percentage of cell survival was calculated based on the percentage of viable cells in the presence of the tested AgNPs relative to untreated cells and cells supplied with equivalent quantities of the buffer. Each sample was tested in three independent assays.

2.9. Hemolytic activity of synthesized nanoparticles

The possible hemolytic activities of LSA-AgNPs and LSR-AgNPs were determined using erythrocyte cells and monitoring the level of released hemoglobin during incubation of tested samples with erythrocytes under simulated physiological conditions.[22] The human blood sample was collected from healthy volunteers in a sterile container with an anticoagulant (ethylenediaminetetraacetic acid). The blood sample was centrifugated at 2500 rpm for 10 min for isolation of erythrocytes. Obtained precipitates (red blood cells) were then washed three times using phosphate buffer saline (PBS, pH 7.4) and centrifuged. For determination of hemolytic properties, 1 mL of LSA-AgNPs or LSR-AgNPs solution in PBS was added in 1 mL of 5% red blood cells (RBCs) dissolved in PBS to obtain the final concentration of nanoparticles of 150, 120, 90, 60, 30, and 10 μg mL^{-1}. Negative control was prepared using PBS instead of nanoparticles solution, while the positive control contained 1 mL of RBCs and 1 mL 1% sodium dodecyl sulfate (SDS). The samples were incubated at 37 °C for 1 h and then centrifugated at 1200 rpm for 15 min. After centrifugation, the absorbance of the supernatant was measured spectrophotometrically at 540 nm. The following equation was used for the determination of the percentage of hemolyzed RBCs:

$$\%\ \text{Hemolysis} = \frac{(A_{\text{AgNPs}} - A_0) - A_k}{A_{\text{SDS}} - A_k} \times 100$$

where A_{AgNPs} is the absorbance of samples with AgNPs, A_0 is the absorbance of corresponding concentration of AgNPs in PBS, A_{SDS} is positive control with SDS solution, and A_k is negative control (only RBSs in PBS).

2.10. Catalytic degradation of Congo red and 4-nitrophenol

The evaluation of the catalytic activity of synthesized LSA-AgNPs and LSR-AgNPs was determined by the reduction of aqueous solutions of Congo red (CR) in the presence of $NaBH_4$ as described by Umamaheswari *et al.*[13] In this reaction, 1 mL of water solution of LSA-AgNPs or LSR-AgNPs (0.1 mg mL^{-1}) was mixed with 5 mL of 10 μM CR solution and 1.5 mL of 1 mM $NaBH_4$ solution. The rate of the catalytic degradation process of Congo red at different time intervals was monitored using a UV-Vis spectrophotometer (λ_{max} was at 497 nm).

The catalytic reduction of 4-nitrophenol (4-NP) using $NaBH_4$ in the presence of LSA-AgNPs and LSR-AgNPs was determined according to the method described by Desai *et al.*[23] Reaction solution was prepared by adding 0.5 mL of nanoparticles solution (0.3 mg mL^{-1}) to the mixture of 0.5 mL of $NaBH_4$ (0.05 mg mL^{-1}) and 5 mL of 4-NP (10 μg mL^{-1}) solutions. The reaction was monitored spectrophotometrically at 25 °C in the wavelength range from 250 to 550 nm.

The constant of reaction rate '*k*' was calculated for catalytic degradation of CR and 4-NP using the following equation:

$$\ln\left(\frac{A_0}{A_t}\right) = kt$$

where 'A_0' is the absorbance at 0 min, 'A_t' is the absorbance at different times, '*k*' is a constant of reaction, and '*t*' is reaction time.

3. Results and discussion

3.1. UV-Vis spectral analysis

The generation of AgNPs in solution during their synthesis using extracts was monitored spectrophotometrically. The color change of solutions from light yellow to dark brown and the appearance of the characteristic peak in UV-Vis spectra characteristic for AgNPs as a result of surface plasmon resonance (SPR) effect were observed. This process in a time-dependent manner was shown in Fig. 1A. The UV-Vis absorption spectra of formed nanoparticles were recorded (300–800 nm) and the highest peaks were positioned within 395–415 nm (characteristic peak for AgNPs), suggesting the formation of AgNPs. The maximum absorption values during biosynthesis were obtained at 30 min, and thereafter the absorption peaks did not increase, thus indicating the end of the synthesis process. Then, the influence of concentration of $AgNO_3$, extracts concentrations, temperature, and pH on the biosynthesis of nanoparticles using LSA and LSR aqueous extracts were evaluated. Initial conditions for the synthesis of both types of nanoparticles were 5 mM $AgNO_3$, 25 °C, 10% extracts concentration without adjustment of pH values. The separate UV spectra of the aerial part and root aqueous extracts are presented in Fig. 1S (ESI†). For the determination of the best conditions in the synthesis of AgNPs using

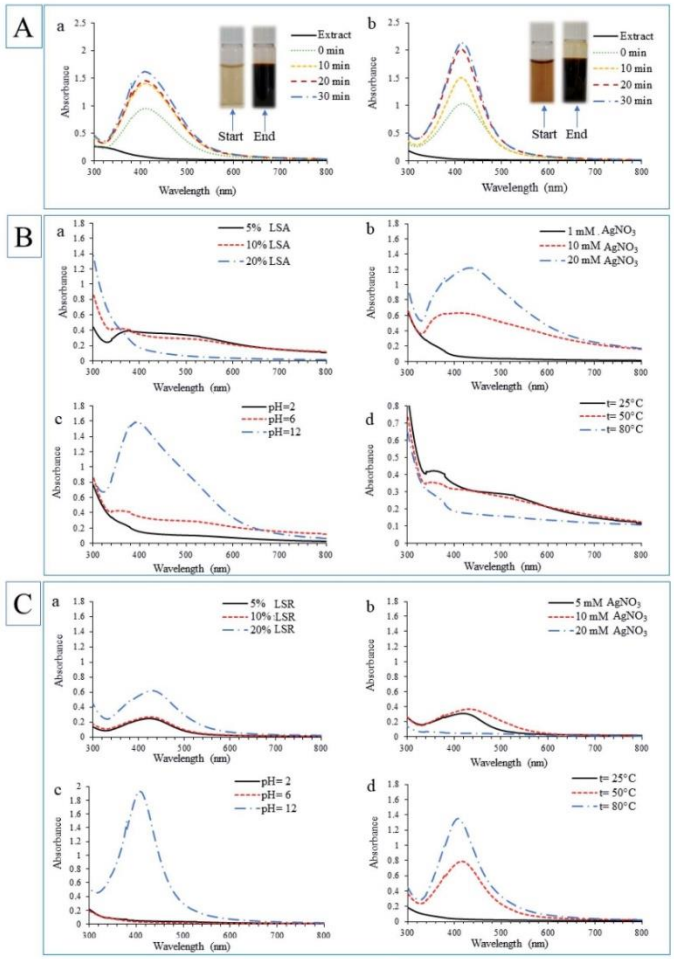

Fig. 1 (A) Time-dependent UV-Vis absorption spectra of AgNPs biosynthesized by *L. salicaria* aerial part (a) and root (b) extracts, (B) UV-Vis absorption spectra of LSA-AgNPs as a function of extract concentration (a), salt concentration (b), pH value of extract solution (c), and different temperatures (d), (C) UV-Vis absorption spectra of the LSR-AgNPs as a function of extract concentration (a), salt concentration (b), pH value of extract solution (c), and different temperatures (d).

LSA and LSR, the parameters were changed one by one. Fig. 1B shows the UV-Vis spectra for the LSA-AgNPs when applied different extract concentrations (a), salt concentrations (b), pH values (c), and temperatures (d). The concentration of 5% (v/v) of LSA extract was the most effective for AgNPs synthesis (Fig. 1B(a)), while higher concentrations of the extract caused agglomeration of nanoparticles and their precipitation. The sharpest peak of LSA-AgNPs was obtained using a higher salt

Appendix E

concentration (20 mM $AgNO_3$) (Fig. 1B(b)). Moreover, the application of 1 mM $AgNO_3$ did not lead to a high yield in nanoparticles synthesis. Increasing the pH value of LSA extract solution led to the augmentation of absorption values for LSA-AgNPs (Fig. 1B(c)). This can be explained by the assumption that the hydroxyl groups attract hydrogens of the phenolic and carboxyl groups (from flavonoids and phenolic acids) and thus increase the partial negative charge of oxygens which then more easily reduce the silver ions and stabilize formed nanoparticles.[24] It is also shown that the concentration of NaOH in solution during Ag^+ bioreduction has an effect on the size, shape, monodispersity, and yield of formed nanoparticles.[25] No nanoparticle formation was observed at pH 2, however, nanoparticles were successfully formed by increasing pH. The fast nanoparticle formation, with high intensity of SPR band at 394 nm, was observed at pH 12, indicating that alkaline conditions could be responsible for the activation of the compounds from the extract and make them more suitable electron donors. Also, Anigol *et al.* have shown that the synthesis of nanoparticles in an acidic medium produces a wide absorbance peak and a wide range of nanoparticles sizes. With the pH increase during synthesis, the peak was narrower and higher, while at pH 9 a more pronounced uniform nanoparticles size was observed.[26] Another study confirmed that pH change does not affect their shape while with increasing pH the size of nanoparticles decreases, for example, the average particle sizes of AgNPs on the pH 5, 7, and 9 range are 45, 29, and 20 nm, respectively.[27] The biosynthesis of LSA-AgNPs was also performed at different temperatures and based on the obtained absorption maximums, it can be concluded that temperature does not have an influence on the formation of nanoparticles using LSA. However, at lower temperatures, slightly higher peaks intensity in the UV-Vis absorption spectrum of LSA-AgNPs were noticed (Fig. 1B(d)). This may be an advantage of using LSA in the synthesis of nanoparticles compared with LSR, due to lower energy consumption during the synthesis process.

The spectrophotometric data for LSR-AgNPs synthesis under different conditions are shown in Fig. 1C. It was noticed that the absorption peaks for LSR-AgNPs increased dose-dependently with the increase of the extract concentration (Fig. 1C(a)). The sharpest peaks were obtained using 10 mM $AgNO_3$ for LSR-AgNPs synthesis. However, when a higher concentration of $AgNO_3$ (20 mM) was used for LSR-AgNPs synthesis, large, dispersed particles appeared, causing a lower absorption maximum in the UV-Vis spectrum (Fig. 1C(b)). As with the

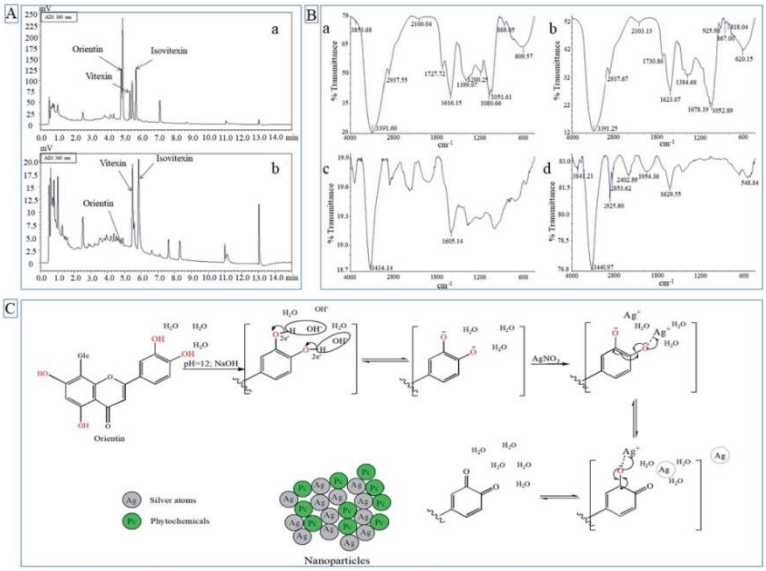

Fig. 2 (A) HPLC-PDA chromatograms of *L. salicaria* aerial part (a) and root (b) aqueous extracts, (B) FT-IR spectra of *L. salicaria* aerial part (a) and root extracts (b) and synthesized nanoparticles LSA-AgNPs (c) and LSR-AgNPs (d), (C) proposed mechanism of orientin Ag(I) reduction during nanoparticle synthesis.

Table 1 HPLC quantification of phenolic compounds and total phenolics (TP) and flavonoids (TF) content of *L. salicaria* aqueous extracts (LSA and LSR)[a]

	HPLC results (μg mL^{-1})			Spectrophotometric results	
Extracts	Orientin	Vitexin	Isovitexin	TP (mg GAE per g d.p.)	TF (mg QUE per g d.p.)
LSA	15.23 ± 0.06	6.94 ± 0.02	11.77 ± 0.17	99.56 ± 2.14	18.29 ± 0.95
LSR	0.357 ± 0.02	0.83 ± 0.02	1.46 ± 0.09	26.44 ± 0.81	0.19 ± 0.02

[a] d.p. – dry plant.

synthesis of nanoparticles using the aerial part extract, the influence of the pH value on LSR-AgNPs synthesis is clearly shown in Fig. 1C(c). Temperature change had a significant effect on the synthesis of LSR-AgNPs, in contrast to the synthesis of LSA-AgNPs. The UV-Vis absorption peak of the solution during LSR-AgNPs synthesis was much higher at 80 °C than at 50 and 25 °C, considering the same reaction conditions (Fig. 1C(d)).

Based on the presented results, the following conditions were used for further experiments. The synthesis of LSA-AgNPs was the most successful using the 5% aqueous extract, 20 mM $AgNO_3$ concentration, without heating, and pH 12, while the most favorable conditions for the synthesis of LSR-AgNPs are as follows, 20% aqueous extract, 10 mM $AgNO_3$, with heating at 80 °C for 30 min, and pH 12.

Our research is in accordance with studies conducted by Mohammadalinejhad *et al.* about the use of *L. salicaria* aerial part extract for the synthesis of AgNPs and AgNPs-organic nanohybrids.[16] The synthesis of nanoparticles using *L. salicaria* root extract, as well as the investigation of optimal conditions for the application of this plant in the synthesis of nanoparticles, their cytotoxic and photocatalytic activities, on the other hand, has never been reported before.

3.2. Phytochemical characterization of *L. salicaria* aqueous extracts

Aqueous extract of *L. salicaria* aerial part and root, used for the synthesis of AgNPs, contained total phenolic compounds in the concentration of 99.56 and 26.44 mg GAE per g of dry plant weight, respectively. Also, the aerial part of the plant had higher flavonoid content (18.29 mg QUE per g dry plant) than the root (0.19 mg QUE per g dry plant). These results, higher total phenolic and flavonoid content in aerial part, can explain the use of a lower concentration of LSA extract for AgNPs synthesis in comparison with the concentration of LSR extract. HPLC chromatograms of *L. salicaria* aerial part and root aqueous extracts are presented in Fig. 2A (a and b, respectively) while the quantification of identified phenolic compounds in extracts is given in Table 1. *C*-glucoflavones orientin, vitexin, and isovitexin were identified in both LSA and LSR aqueous extracts utilized for AgNPs synthesis. The presence of free hydroxyl groups in the structure of these compounds, which are responsible for the redox potential of polyphenolics, suggests that these *C*-glucoflavones may be one of the main compounds in extracts responsible to produce AgNPs. Plants with high antioxidant potential are strongly effective in converting metallic ions to metallic nanoparticles.[28] It is also well known that phenolic compounds are one of the most responsible metabolites for the antioxidant activity of plants, thus phenolics are considered as main contributors in the reduction of metal ions and the synthesis of nanoparticles using plant extracts.[29] HPLC analyses showed that LSA extract was richer in all identified compounds compared with LSR. In previous research published by Srećković *et al.* *C*-glucoflavones orientin and vitexin were also identified in *L. salicaria* methanol extracts as the main phenolic compounds.[15]

3.3. Characterization of synthesized AgNPs

3.3.1. XRPD analysis. The crystalline structure of the biosynthesized AgNPs was checked by XRPD analysis, and spectra of LSA-AgNPs and LSR-AgNPs are shown in Fig. 3A(a and b). Based on the obtained values of I/I_{max} intensities, mutual distances d, comparison with the literature data, and ICDD PDF-2 standards, the presence of the crystalline phases was confirmed.[30]

The most represented crystal phase in both samples was Ag (PDF 87-0597) and the next crystal phase by representation was an AgCl (PDF 31-1238). In the case of LSA-AgNPs (Fig. 5A), the characteristic Bragg reflection peaks appeared at position 38.19°, 44.42°, 64.53° and 77.46° in the 2θ range between 10° and 80°, which could be analog to the (111), (200), (220) and (311) planes of face-centered cubic (fcc) crystalline AgNPs.[1] The peaks at 27.80°, 32.24°, 46.24° correspond to the formation of AgCl phases. Silver in LSR-AgNPs had a lower crystallinity than silver chloride and lower crystallinity than silver in the LSA-AgNPs sample. However, the content of silver chloride in LSR-AgNPs was lower than in the LSA-AgNPs sample. The formation of the crystalline phase of silver chloride may be a consequence of the presence of chloride ions in plant extracts.

3.3.2. FTIR analysis. FT-IR spectra of the dried aqueous aerial part and root extracts of *L. salicaria* were compared with the spectrum of synthesized AgNPs (Fig. 2B). It was observed that the main peaks in the spectra of synthesized nanoparticles (Fig. 2B(c and d)) coincide with peaks of the corresponding extracts (Fig. 2B (a and b)). The absorption band at 3391.60 cm^{-1} for LSA and 3391.25 cm^{-1} for LSR extracts is the characteristic stretching vibration of –OH groups from phenolic compounds (flavonoids, phenolic acids, and other phenolic derivatives). The small band at 2937.55 cm^{-1} and 2937.67 cm^{-1} for LSA and LSR, respectively, may be a consequence of aliphatic

Appendix E

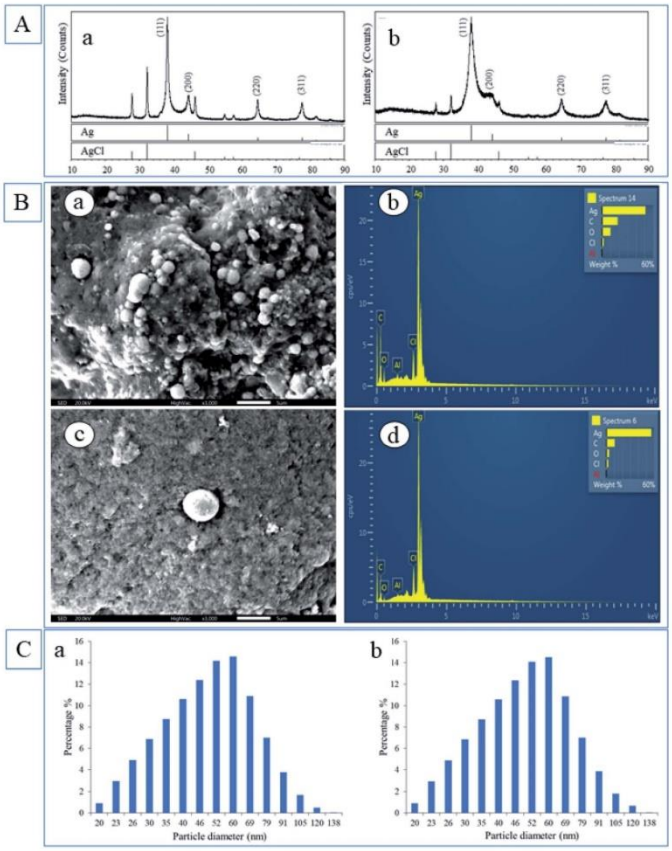

Fig. 3 (A) XRPD pattern of synthesized LSA-AgNPs (a) and LSR-AgNPs (b), (B) SEM image of biosynthesized LSA-AgNPs (a), LSR-AgNPs (c), and their corresponding EDX spectra (b and d), (C) particle size distributions of LSA-AgNPs (a) and LSR-AgNPs (b).

C–H stretching. Also, in the IR spectrum of the LSA and LSR extracts (Fig. 2B(a and b)), bands at 1727.72 and 1730.86 cm^{-1} indicate the presence of –C=O groups. The appearance of pronounced bands at 1616.15 cm^{-1} and 1623.07 cm^{-1} corresponds to the –C=C– of an aromatic ring. FTIR spectra of LSA-AgNPs (c) and LSR-AgNPs (d) were compared with the spectrum of LSA (a) and LSR (b). Based on Fig. 2B it is clear that LSA-AgNPs and LSR-AgNPs possessed bands that originated from plant extract. LSA-AgNPs and LSR-AgNPs possess bands at 3434.14 and 3440.97 cm^{-1}, respectively, which correspond to the alcohol groups, whereas LSR-AgNPs have bands at 2925.80 cm^{-1} that correspond to the C–H from alkanes. The appearance of these bands in LSA-AgNPs and LSR-AgNPs FTIR spectra implies that compounds from *L. salicaria* extracts be involved in the formation of nanoparticles' capping layer. However, peaks attributed to the –C=O group in the nanoparticles' spectra were reduced and almost merged with the intensive band corresponding to aromatic –C=C– vibrations (Fig. 2B(c and d)). The decrease in the peak intensity characteristic for the carbonyl group in nanoparticle spectra may be

attributed to the low concentration of compounds with this group were involving in the stabilization of nanoparticles. Also, the interaction of AgNPs with the carbonyl group (silver–carboxylate interactions) can decrease the intensity and position of –C=O peak in the FTIR spectrum.[31] Additionally, characteristic peaks at 1605.14 and 1629.55 cm^{-1} in obtained nanoparticles may correspond to –C=C– of an aromatic ring as confirmed in the extracts. Finally, the intense bands located at 1051.61–1052.89 cm^{-1} (Fig. 2B(a and b)) which correspond to the ether groups (C–O bond stretch) were present in LSA and LSR extracts (a and b) but not in LSR-AgNPs, so it can be assumed that compounds with an ether group are not responsible for the stabilization of root nanoparticles. The mentioned peaks in FTIR spectra of LSA-AgNPs and LSR-AgNPs characteristic for polyphenolic compounds indicate that flavonoids or other phenolic compounds form protective capping layers on the surface of the obtained nanoparticles. The disappearance of the bands at 1052.89, 1078.19, and 1384.68 cm^{-1} in LSR-AgNPs compared with LSR extract, proves that some compounds present in the extract do not participate in the stabilization of nanoparticles or may be chemically changed during bioreduction of metal ions.

3.3.3. SEM/EDX analysis. The results of SEM and EDX analyses for LSA-AgNPs and LSR-AgNPs are presented in Fig. 3B (a, b and c, d, respectively). The additional information about the structural morphology of green synthesized AgNPs was provided by SEM analysis, while EDX analysis was used to identify the elements included in LSA-AgNPs and LSR-AgNPs. Based on SEM results, it has been confirmed that the obtained nanoparticles possess a spherical shape, also a lower degree of agglomeration was observed. The observed large agglomerated nanoparticles probably occurred as a result of the evaporation of solvent during sample preparation.[32]

The EDX detection displayed intense signals of silver atoms in both types of nanoparticles, and it is around 3 KeV, which corresponds to the previously published value.[1] In addition to the Ag atoms as the main component of nanoparticles, the presence of C and O in LSA-AgNPs and LSR-AgNPs (Fig. 3B(b and d)) was also confirmed. The occurrence of C and O in nanoparticles may be the consequence of the presence of compounds from *L. salicaria* extracts incorporated into the nanoparticle structure. The elemental analysis of LSA-AgNPs and LSR-AgNPs by EDX (Fig. 3B (b and d)) showed that Ag is the main constituent, and it is found to be 50.92% and 45.66% respectively. The mineral content of the plant materials, which is mostly dependent on the soil of the plant habitat, results in the identification of Al traces in both types of nanoparticles. Vardanyan and Ingole confirmed the presence of Al in *L. salicaria*, which suggests the possibility of incorporation of these metal atoms into the structure of the obtained nanoparticles.[33] The Cl content may originate from plant extracts. Also, the increased content of C and O in the nanoparticles synthesized by the aerial part of the plant (LSA-AgNPs) corresponds to the higher phenolic content of the aerial part.

3.3.4. Particle dispersion characterization. For the determination of the size distribution profiles of LSA-AgNPs and LSR-AgNPs in solutions, DLS measurements were carried out. Besides the influence of the pH and temperature during the reaction of the synthesis, many biomolecules from the plant extracts (proteins, flavonoids, terpenoids, and other polyphenols) may have significant effects on the nanoparticle size, structure, and morphology.[8,34,35] Many studies have shown that the size of AgNPs is important for their stability, biocompatibility, and antibacterial activity.[36]

According to DLS analysis, LSA-AgNps and LSR-AgNPs possessed similar sizes, ranging from 20 to 138 nm (Fig. 3C). The size of the most formed LSA-AgNPs and LSR-AgNPs ranged between 35 and 60 nm (60.52 and 60.25% respectively), whereby 75.88% of particles were under 60 nm for both synthesized nanoparticles (Fig. 3C(a and b)). The complexity of the chemical composition of *L. salicaria* extracts may have significant effects on the agglomeration and deposition of the AgNPs.[14]

It is possible that the alkaline environment leads to an increase of negative charge of oxygen on the phenolic hydroxyl groups, which contributes to a better interaction between phytochemicals and silver ions, and therefore faster reduction time, and stabilization. Fig. 2C shows the possible mechanism of nanoparticles synthesis using orientin, one of the phenolic compounds (flavonoid) identified in both extracts used for nanoparticle synthesis. Bhutto *et al.* suggested a mechanism of AgNPs synthesis using gallic acid as an example of a phenolic compound, explaining that phenolic groups are oxidized to quinones.[37] Another study confirmed that flavonoids with 1 to 3 OH groups react only at pH values 9 and/or 10, while flavonoids with four and more hydroxyl groups, such as luteolin (aglycon of orientin), can reduce Ag^{+} relatively fast in the solution with pH around 7. The high reactivity of flavonoids in this process is conditioned by the presence of hydroxyl groups on the B ring which can be oxidized. Further, additional hydroxyl groups of flavonoids and their obtained oxidation forms after reduction reaction are important for attaching flavonoids molecules to obtained nanoparticles and for nanoparticles stabilization.[38] The orientin possesses these properties and may be one of the molecules in *L. salicaria* extracts that contributes to the formation and stabilization of AgNPs.

3.4. Antioxidant potential of *L. salicaria* aqueous extracts and synthesized nanoparticles

The antioxidant potential of the extracts was assessed using DPPH and ABTS methods. Butylated hydroxytoluene (BHT) was used as a referent standard and obtained results are presented in Table 2. The biosynthesized LSA-AgNPs and LSR-AgNPs displayed lower antioxidant activity in the DPPH method compared with LSA and LSR. It has been noticed that the IC_{50} value of the LSR-AgNPs in the ABTS assay was lower (127.78 μg mL^{-1}) compared with the IC_{50} value of LSA-AgNPs (141.66 μg mL^{-1}). Moreover, LSR-AgNPs showed higher antioxidant activity against $ABTS^{\cdot+}$ compared with the root aqueous extract (LSR).

As shown in Table 2 the aqueous extract of the aerial part had a slightly higher ABTS radical scavenging potential compared to the corresponding LSA-AgNPs nanoparticles. Interestingly, the nanoparticles synthesized by root extract (LSR-AgNPs) have approximately the two-fold ABTS radical scavenging potential

Appendix E

Table 2 *In vitro* antioxidant activity of *L. salicaria* aerial and root aqueous extracts and synthesized nanoparticles[a]

Samples and standards	IC_{50} values (μg mL^{-1}) DPPH˙ scavenging activity	$ABTS^{\cdot+}$ scavenging activity
LSA	86.38 ± 0.13	65.33 ± 2.08
LSA-AgNPs	>100	141.66 ± 17.05
LSR	175.26 ± 6.31	198.36 ± 11.75
LSR-AgNPs	>100	127.78 ± 13.52
BHT	13.08 ± 0.97	21.29 ± 1.98

[a] LSA – *L. salicaria* aerial aqueous extract, LSR – *L. salicaria* root aqueous extract, LSA-AgNPs – silver nanoparticles synthesized by *L. salicaria* aerial part extract, LSR-AgNPs – silver nanoparticles synthesized by *L. salicaria* root extract.

Table 3 Antibacterial and antifungal activity of AgNPs synthesized by *L. salicaria* aerial part (LSA-AgNPs) and root (LSR-AgNPs) extracts

Bacterial strains	MIC (mg mL^{-1}) LSA-AgNPs	LSR-AgNPs	MIC (μg mL^{-1}) Erythromycin
E. coli	0.625	2.5	2.5
B. cereus	0.3125	0.3125	<0.156
P. aeruginosa	<0.156	0.3125	20
E. faecalis	0.3125	0.625	1.25
B. subtilis	0.156	0.625	10
M. lysodeikticus	0.625	0.156	<0.156
S. typhimurium	1.25	0.625	2.5
S. enteritidis	1.25	0.625	20
S. epidermidis	<0.156	0.3125	0.625
S. aureus	0.3125	0.625	1.25
K. pneumoniae	0.3125	0.625	10

Fungal strains	MIC (mg mL^{-1}) LSA-AgNPs	LSR-AgNPs	MIC (μg mL^{-1}) Nystatin
C. albicans	0.625	1.25	1.25
T. longibrachiatum	1.25	1.25	5
T. harzianum	1.25	0.625	5
P. canescens	0.3125	0.625	2.5
P. cyclopium	<0.156	0.625	2.5
D. stemonitis	2.5	0.625	2.5
A. alternata	1.25	0.3125	1.25
F. oxysporum	10	0.625	2.5
A. brasiliensis	10	0.3125	1.25

compared to the aqueous root extract. Previous studies have confirmed that nanoparticles synthesized using plant extracts possessed significantly higher antioxidant potential than nanoparticles obtained using conventional methods indicating that plant compounds bound to nanoparticles are responsible for the higher antioxidant potential.[39] The higher antioxidant potential of LSR-AgNPs, compared with the value obtained with LSR, may suggest that this extract has antioxidant compounds that can be incorporated very efficiently on the surface of the nanoparticles.

3.5. Antimicrobial activity

The employment of silver as an antimicrobial agent against infections has been known since ancient Greek and Roman times. Numerous studies have confirmed the antimicrobial properties of AgNPs on different microbes, fungi, and parasites.[2,40] According to our knowledge, most studies dealing with the antimicrobial activity of AgNPs used the disk diffusion test to determine the antimicrobial activity of nanoparticles samples. The disk diffusion test is used to determine the antimicrobial susceptibility of microorganisms against antimicrobial drugs, while the dilution method provides significantly more accurate results, and obtained MIC values are used for the determination of drug dosage for infection treatment.[41] In this study, the microdilution method was used for the determination of the antimicrobial activity of synthesized LSA-AgNPs and LSR-AgNPs and the results are presented in Table 3. The obtained nanoparticles showed potent antibacterial activity with MIC values below 1 mg mL^{-1} against the tested bacteria. Antibacterial activities of LSR-AgNPs and LSA-AgNPs were similar and most of their MIC values were in the range from 0.156 to 0.625 mg mL^{-1}. Obtained nanoparticles showed less antifungal activity compared with their antibacterial potential, especially LSA-AgNPs. The concentrations that inhibit fungal growth were considerably lower for tested LSR-AgNPs compared with LSA-AgNPs which showed MIC values for six fungal species above 1 mg mL^{-1}.

It may be interesting to point out that AgNPs synthesized using LSA and LSR extracts showed higher inhibitory potential on the growth of *P. aeruginosa* compared to AgNPs synthesized using *P. hibiscicola* in research conducted by Punjabi *et al*[42] Another Lythraceae plant, *Lagerstroemia speciosa*, was used to synthesis Ag-NPs that inhibited biofilm formation against *P. aeruginosa*.[43] There are few studies reporting the MIC values of AgNPs determined using the dilution method technique, a number of studies are based on the disk diffusion method for the determination of the antimicrobial activity of AgNPs. Garibo *et al.* showed that green synthesized AgNPs possess higher antimicrobial potential against *E. coli*, *S. aureus*, *P. aeruginosa*, and *C. albicans* than chemically produced AgNPs.[44] Also, the study conducted by Shu *et al.* confirmed that ampicillin in combination with AgNPs possesses extremely higher antibacterial activity against highly resistant *E. coli*-Amp^{+} compared with ampicillin alone.[7] Using electron microscopy, Xia *et al.* demonstrated that AgNPs destroy the cell wall, infiltrate within the cells, damage organelles, induce chromatin condensation and margination, a sign of apoptotic cell death.[45] Also, it has been confirmed that the size of nanoparticles has an influence on their antimicrobial activity, smaller-sized nanoparticles pass unhindered through the cell membrane, expressing their activity within the cell. According to reported studies, the antimicrobial activity of AgNPs is also attributed to the electrostatic interaction between positively charged silver ions and negatively charged cell walls.[46] Due to a slightly different cell membrane of the fungi composed mostly of fibrous β-1,3 glucan

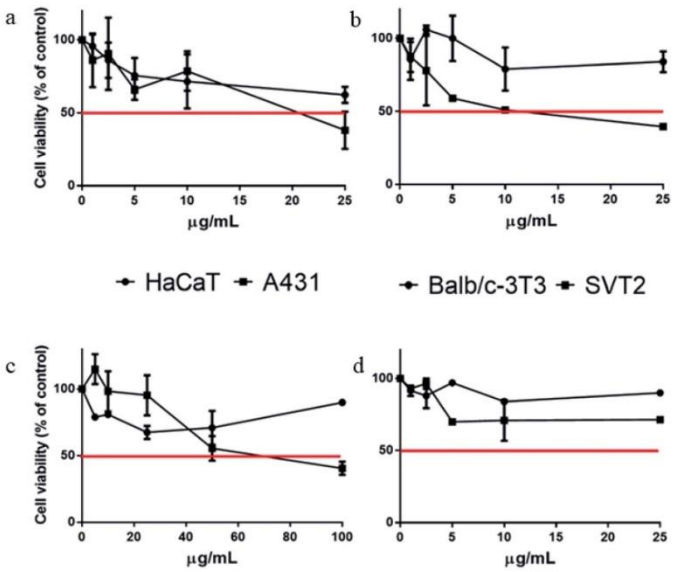

Fig. 4 Cytotoxic activity of synthesized LSA-AgNPs (a and b) and LSR-AgNPs (c and d) against immortalized (HaCaT and Balb/c-3T3) and cancer (A431 and SVT-2) cell lines.

and mannoproteins, interaction with AgNPs is quite different.[47] This fact may be one of the causes for the slightly lower antifungal activity of obtained AgNPs compared with their antibacterial activity.

3.6. Cytotoxic activity

The cytotoxic activity of biosynthesized LSA-AgNPs and LSR-AgNPs was analyzed on two immortalized (murine fibroblasts Balb/c-3T3, and human keratinocytes, HaCaT) cell lines and two cancer cell lines (transformed fibroblast, SVT2, and epidermoid carcinoma, A431). The MTT test was used to determine cell viability after the treatment with different concentrations of LSA-AgNPs and LSR-AgNPs (from 1 to 100 g mL^{-1}) for 48 hours.

As shown in Fig. 4 (panels a and b), LSA-AgNPs present a slight selectivity towards cancer A431 and SVT-2 cells, with IC_{50} values of 20.5 ± 5 and 12,7 ± 6 µg mL^{-1}, respectively. Interestingly, no IC_{50} values were detected on immortalized cells. In a previously published research, the methanolic extract of the *L. salicaria* root showed biocompatibility on the two immortalized cell lines, but only up to 45 µg mL^{-1} for murine cell lines.[15] Interestingly, when roots were used to obtain nanoparticles, LSR-AgNPs exerted toxicity only towards the A431 cell line (62 ± 17 µg mL^{-1}) (panels c and d). Based on the presented results, both nanoparticles LSA-AgNPs and LSR-AgNPs synthesized using *L. salicaria* aqueous extracts, exhibit a selective behavior towards cancer cell lines. Thus, the selective activity may occur due to the acidic pH in cancer cells, leading to greater release of Ag^{+} and phytochemicals from AgNPs in their surroundings compared with the immortalized ones.[48] The cytotoxicity of AgNPs is based on their ability to penetrate into the cells and liberate silver ions which promote ROS generation, causing mitochondrial and DNA damage, as well as cell apoptosis.[49] In addition, the advantage of AgNPs synthesized by plant extracts is based on phytochemicals incorporated

Table 4 Percentage of hemolysis induced by AgNPs synthesized by aerial part (LSA-AgNPs) and root (LSR-AgNPs) extracts

Concentration (µg mL^{-1})	% hemolysis	
	LSA-AgNPs	LSR-AgNPs
150	<negative control	2.77 ± 0.25
120	<negative control	0.50 ± 0.11
90	<negative control	0.28 ± 0.06
60	<negative control	<negative control
30	<negative control	<negative control
10	<negative control	<negative control

Appendix E

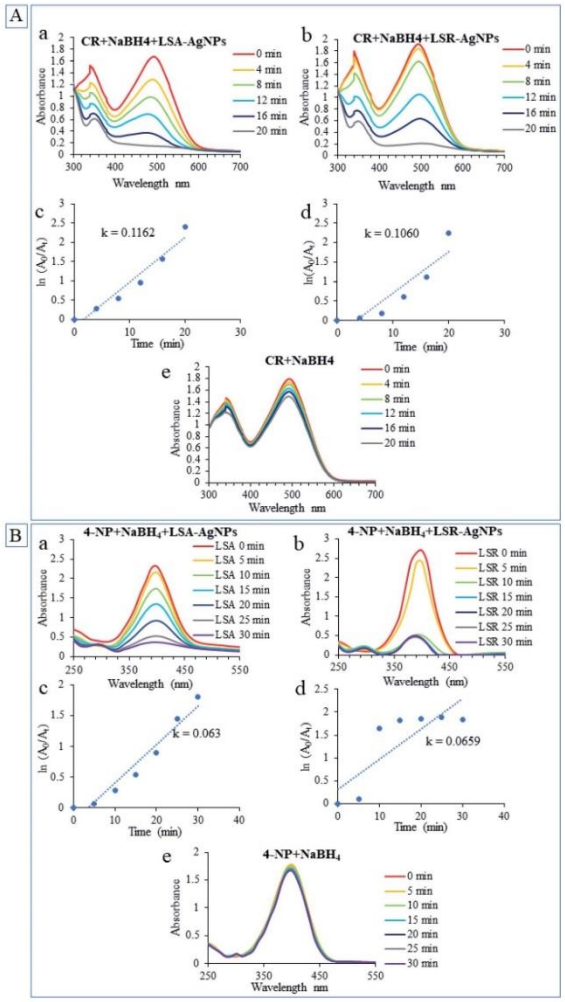

Fig. 5 (A) The catalytic activity of the synthesized LSA-AgNPs (a) and LSR-AgNPs (b) on Congo red (CR) degradation in the presence of $NaBH_4$ and corresponding degradation kinetics of CR (c and d), degradation of CR in absence of nanoparticles (e); (B) the catalytic activity of the synthesized LSA-AgNPs (a) and LSR-AgNPs (b) on reduction 4-NP to 4-AP in the presence of $NaBH_4$ and corresponding degradation kinetics of 4-NP (c and d), degradation of 4-NP in absence of nanoparticles (e).

Appendix E

into the nanoparticle structure, which have well-known biological activity. Various studies concluded that green synthesized AgNPs combined with cancer drugs can elevate anticancer activity, in relation to the drugs attached to chemically synthesized nanoparticles.[50]

3.7. Hemolytic activity of synthesized nanoparticles

Blood is the first contact for nanoparticles to reach their target tissues, so the effect of nanoparticles on blood cells is crucial for further research and potential therapeutic application.[51] The process of hemoglobin release during the interaction of different LSA-AgNPs and LSR-AgNPs concentrations with erythrocytes at 37 °C for 1 h was monitored spectrophotometrically at 540 nm. The hemolytic activity of the sample was calculated based on the hemolytic activity of SDS used as a positive control. It is considered that 1% solution of SDS causes complete (100%) hemolysis of erythrocytes. The examined samples of nanoparticles showed a negligible degree of erythrocytes hemolysis (Table 4). Moreover, LSA-AgNPs at all applied concentrations showed lower hemolytic activity compared with the negative control (erythrocytes in PBS solution), hence LSA-AgNPs may be considered as membrane stabilizing agents. However, LSR-AgNPs showed dose-dependent weak hemolysis when applied in concentrations from 150 to 90 μg mL^{-1}. The highest applied concentration of LSR-AgNPs showed only 2.8% of erythrocytes hemolysis while concentrations lower than 90 μg mL^{-1} had no effect on erythrocyte degradation. Because high hemocompatibility of biosynthesized nanoparticles was observed, it could be safely used in a therapeutic application, moreover, LSA-AgNPs possess the potential for further research as antihemolytic and erythrocytes membrane stabilization agents.

3.8. The catalytic activity of synthesized nanoparticles

Environmental pollution by industrial dyes has a great influence on public health. Many of the synthetic dyes are highly carcinogenic and left in the environment for a long time. As degradation of these compounds requires catalysts that would increase the reaction rate, today, there is great interest in the easy production of environmentally friendly catalysts.[52] Many investigations have confirmed that green synthesis nanoparticles had the potential to catalyze the degradation of numerous organic contaminants. The effectiveness of LSA-AgNPs and LSR-AgNPs for the degradation of CR and the reduction of 4-nitrophenol to 4-aminophenol (4-AP) at room temperature was examined. The reactions of catalytic degradation of CR were monitored spectrophotometrically in the wavelength range between 700 and 300 nm, while the wavelength range for monitoring 4-NP reduction was between 550 and 250 nm. The ability of AgNPs to behave as a catalyst in the degradation of dye is reflected in their property to transfer an electron from donor molecules ($NaBH_4$) to acceptor molecules (azo bond in CR).[53] The catalytic activities of LSA-AgNPs and LSR-AgNPs are presented in Fig. 5 and both types of nanoparticles showed high potential for catalytic degradation of CR (Fig. 5A(a and b)) as well as for catalytic reduction 4-NP to 4-AP in the presence of $NaBH_4$ (Fig. 5B(a and b)). The absorbance of the CR constantly decreased overtime at 338 and 497 nm, and finally, the solution became colorless and absorption maximums in the UV-Vis spectrum disappear. Application of $NaBH_4$ in the absence of AgNPs has no significant effect on the degradation of CR solution and reduction 4-NP (Fig. 5A and B(e)). During the reduction process of CR and 4-NP, $NaBH_4$ has the role of an electron source, however, electron transfer is not possible without the presence of a catalyst. The nanoparticles serve as electron transporters, absorbing BH_4^- and dyes on their surface, allowing electron exchange from BH_4^- to organic dyes.[54] The catalytic rate constant (k) for LSA-AgNPs and LSR-AgNPs was higher for reaction of degradation CR ($k = 0.1162$ and $k = 0.1060$, respectively) compared with k for chemocatalytic reduction of 4-NP to 4-AP ($k = 0.063$ and $k = 0.0659$, respectively). In general, biogenic LSA-AgNPs and LSR-AgNPs exhibited excellent catalytic activity with high efficiency of CR degradation and 4-NP reduction, so they can be successfully applied as catalysts in wastewater treatment.

4. Conclusions

The results of the present study showed that aqueous extracts of *Lythrum salicaria* can be successfully used for the eco-friendly, economically viable, and rapid synthesis of AgNPs. It is concluded that reaction conditions play an important role in the rate of nanoparticles formation. The results of antimicrobial activity demonstrate that newly synthesized AgNPs have promising antimicrobial potential against most of the selected bacteria. Their activity on immortalized and cancer cells indicates a selectivity towards the latter, even if low toxicity was found in the case of LSR-AgNPs towards SVT-2 cells. Contrary LSR-AgNPs which showed a slight degree of red blood cell hemolysis at the highest applied concentration, LSA-AgNPs are completely hemocompatible. The green AgNPs showed clear catalytic potential in Congo red dye and 4-nitrophenol degradation reactions, which possesses well-known harmful effects on the environment. The current study suggested that the invasive potential of this plant in the North American continent may be exploited in the eco-fabrication of AgNPs. Further research will be focused on decreasing size and increasing the cytotoxic selectivity of synthesized nanoparticles. Also, further research may include the incorporation of some drugs into their structure for the development of new pharmaceuticals. Due to the demonstrated antimicrobial activity, future research may be focused on the possible use of biosynthesized nanoparticles in wastewater disinfection as well.

Conflicts of interest

There are no conflicts to declare.

Acknowledgements

This work was supported by the Serbian Ministry of Education, Science and Technological Development (Agreements No. 451-03-9/2021-14/200122 and No. 451-03-9/2021-14/200378).

Appendix E

References

1 A. A. Abdelhamid, M. A. Al-Ghobashy, M. Fawzy, M. B. Mohamed and M. M. S. A. Abdel-Mottaleb, *ACS Sustainable Chem. Eng.*, 2013, **1**, 1520–1529.
2 P. Singh, Y. J. Kim, D. Zhang and D. C. Yang, *Trends Biotechnol.*, 2016, **34**, 588–599.
3 M. Guilger-Casagrande and R. de Lima, *Front. Bioeng. Biotechnol.*, 2019, **7**, 287.
4 Z. Yang, Z. Li, X. Lu, F. He, X. Zhu, Y. Ma, R. He, F. Gao, W. Ni and Y. Yi, *Nano-Micro Lett.*, 2016, **9**, 1–13.
5 M. S. Akhtar, J. Panwar and Y. S. Yun, *ACS Sustainable Chem. Eng.*, 2013, **1**, 591–602.
6 N. Kulkarni and U. Muddapur, *J. Nanotechnol.*, 2014, **2014**, 510246.
7 M. Shu, F. He, Z. Li, X. Zhu, Y. Ma, Z. Zhou, Z. Yang, F. Gao and M. Zeng, *Nanoscale Res. Lett.*, 2020, **15**, 1–9.
8 H. P. Borase, B. K. Salunke, R. B. Salunkhe, C. D. Patil, J. E. Hallsworth, B. S. Kim and S. V. Patil, *Appl. Biochem. Biotechnol.*, 2014, **173**, 1–29.
9 R. Dobrucka, M. Szymanski and R. Przekop, *Int. J. Environ. Sci. Technol.*, 2019, **16**, 8517–8526.
10 A. M. Youssef, H. S. El-Sayed, I. EL-Nagar and S. M. El-Sayed, *RSC Adv.*, 2021, **11**, 22571–22584.
11 D. Rawat, V. Mishra and R. S. Sharma, *Chemosphere*, 2016, **155**, 591–605.
12 N. Kataria and V. K. Garg, *J. Environ. Chem. Eng.*, 2017, **5**, 5420–5428.
13 C. Umamaheswari, A. Lakshmanan and N. S. Nagarajan, *J. Photochem. Photobiol., B*, 2018, **178**, 33–39.
14 J. P. Piwowarski, S. Granica and A. K. Kiss, *J. Ethnopharmacol.*, 2015, **170**, 226–250.
15 N. Srećković, J. S. Katanić Stanković, S. Matić, N. R. Mihailović, P. Imbimbo, D. M. Monti and V. Mihailović, *Ind. Crops Prod.*, 2020, **155**, 112781.
16 S. Mohammadalinejhad, H. Almasi and M. Esmaiili, *Mater. Sci. Eng., C*, 2019, **105**, 110115.
17 V. Mihailović, S. Kreft, E. T. Benković, N. Ivanović and M. S. Stanković, *Ind. Crops Prod.*, 2016, **89**, 141–151.
18 S. D. Sarker, L. Nahar and Y. Kumarasamy, *Methods*, 2007, **42**, 321–324.
19 CLSI, *Reference Method for Broth Dilution Antifungal Susceptibility Testing of Yeasts, Approved Standard — Second Edition Serving the World ' s Medical Science Community Through Voluntary Consensus*, 2008, vol. 22.
20 NCCLS, *Reference Method for Broth Dilution Antifungal Susceptibility Testing of Yeasts; Approved Standard — Second Edition. NCCLS document M27-A2*, NCCLS, 940 West Valley Road, Suite 1400, Wayne, Pennsylvania 19087-1898 USA, 2nd edn, 2002, vol. 22.
21 M. E. Cucciolito, A. D'Amora, G. De Feo, G. Ferraro, A. Giorgio, G. Petruk, D. M. Monti, A. Merlino and F. Ruffo, *Inorg. Chem.*, 2018, **57**, 3133–3143.
22 A. Ullah Khan, Q. Ullah Khan, K. Tahir, S. Ullah, A. Arooj, B. Li, K. Ur Rehman, S. Nazir, M. Ullah Khan and I. Ullah, *Mater. Sci. Eng., C*, 2021, **126**, 112146.
23 M. P. Desai, R. V. Patil and K. D. Pawar, *Process Biochem.*, 2020, **98**, 172–182.
24 A. M. El Badawy, T. P. Luxton, R. G. Silva, K. G. Scheckel, M. T. Suidan and T. M. Tolaymat, *Environ. Sci. Technol.*, 2010, **44**, 1260–1266.
25 G. Liu, X. Ma, X. Sun, Y. Jia and T. Wang, *Adv. Mater. Sci. Eng.*, 2018, 3758161.
26 L. B. Anigol, J. S. Charantimath and P. M. Gurubasavaraj, *Org. Med. Chem. Int. J.*, 2017, **3**(5), 555622.
27 T. N. Jebakumar Immanuel Edison and M. G. Sethuraman, *ACS Sustainable Chem. Eng.*, 2013, **1**, 1326–1332.
28 V. Goodarzi, H. Zamani, L. Bajuli and A. Moradshahi, *Mol. Cell Biol. Res. Commun.*, 2014, **3**, 165–174.
29 S. Firoozi, M. Jamzad and M. Yari, *J. Nanostruct. Chem.*, 2016, **6**, 357–364.
30 S. Pirtarighat, M. Ghannadnia and S. Baghshahi, *Mater. Sci. Eng., C*, 2019, **98**, 250–255.
31 V. Thi Lan Huong and N. T. Nguyen, *Mater. Today: Proc.*, 2019, **42**, 88–93.
32 V. Seerangaraj, S. Sathiyavimal, S. N. Sankar, J. G. T. Nandagopal, P. Balashanmugam, F. A. Al-Misned, M. Shanmugavel, P. Senthilkumar and A. Pugazhendhi, *J. Environ. Chem. Eng.*, 2021, 105088.
33 L. G. Vardanyan and B. S. Ingole, in *Environment International*, Elsevier Ltd, 2006, vol. 32, pp. 208–218.
34 E. Navarro, A. Baun, R. Behra, N. B. Hartmann, J. Filser, A. J. Miao, A. Quigg, P. H. Santschi and L. Sigg, *Ecotoxicology*, 2008, **17**, 372–386.
35 K. L. Kelly, E. Coronado, L. L. Zhao and G. C. Schatz, *J. Phys. Chem. B*, 2003, **107**, 668–677.
36 M. José Yacamán, J. A. Ascencio, H. B. Liu and J. Gardea-Torresdey, *J. Vac. Sci. Technol., B: Microelectron. Nanometer Struct. Process., Meas., Phenom.*, 2001, **19**, 1091–1103.
37 A. A. Bhutto, Ş. Kalay, S. T. H. Sherazi and M. Culha, *Talanta*, 2018, **189**, 174–181.
38 M. Švecová, P. Ulbrich, M. Dendisová and P. Matějka, *Spectrochim. Acta, Part A*, 2018, **195**, 236–245.
39 F. U. Khan, Y. Chen, N. U. Khan, Z. U. H. Khan, A. U. Khan, A. Ahmad, K. Tahir, L. Wang, M. R. Khan and P. Wan, *J. Photochem. Photobiol., B*, 2016, **164**, 344–351.
40 C. Vijilvani, M. R. Bindhu, F. C. Frincy, M. S. AlSalhi, S. Sabitha, K. Saravanakumar, S. Devanesan, M. Umadevi, M. J. Aljaafreh and M. Atif, *J. Photochem. Photobiol., B*, 2020, **202**, 111713.
41 H. Liu, T. H. Taylor, K. Pettus, S. Johnson, J. R. Papp and D. Trees, *Antimicrob. Resist. Infect. Control*, 2016, **5**, 1–6.
42 K. Punjabi, S. Mehta, R. Chavan, V. Chitalia, D. Deogharkar and S. Deshpande, *Front. Microbiol.*, 2018, **9**, 2207.
43 V. Sai Saraswathi, N. Kamarudheen, K. V. BhaskaraRao and K. Santhakumar, *J. Photochem. Photobiol., B*, 2017, **168**, 107–116.
44 D. Garibo, H. A. Borbón-Nuñez, J. N. D. de León, E. García Mendoza, I. Estrada, Y. Toledano-Magaña, H. Tiznado, M. Ovalle-Marroquin, A. G. Soto-Ramos, A. Blanco, J. A. Rodríguez, O. A. Romo, L. A. Chávez-Almazán and A. Susarrey-Arce, *Sci. Rep.*, 2020, (10), 1–11.

Appendix E

45 Z. K. Xia, Q. H. Ma, S. Y. Li, D. Q. Zhang, L. Cong, Y. L. Tian and R. Y. Yang, *J. Microbiol., Immunol. Infect.*, 2016, **49**, 182–188.
46 J. S. Kim, E. Kuk, K. N. Yu, J. H. Kim, S. J. Park, H. J. Lee, S. H. Kim, Y. K. Park, Y. H. Park, C. Y. Hwang, Y. K. Kim, Y. S. Lee, D. H. Jeong and M. H. Cho, *Nanomedicine*, 2007, **3**, 95–101.
47 K. J. Kim, W. S. Sung, B. K. Suh, S. K. Moon, J. S. Choi, J. G. Kim and D. G. Lee, *BioMetals*, 2009, **22**, 235–242.
48 I. F. Tannock and D. Hot, *Acid pH in Tumors and Its Potential for Therapeutic Exploitation1*, 1989.
49 T. Shi, X. Sun and Q.-Y. He, *Curr. Protein Pept. Sci.*, 2018, **19**, 525–536.
50 S. Patra, S. Mukherjee, A. K. Barui, A. Ganguly, B. Sreedhar and C. R. Patra, *Mater. Sci. Eng., C*, 2015, **53**, 298–309.
51 K. M. de la Harpe, P. P. D. Kondiah, Y. E. Choonara, T. Marimuthu, L. C. du Toit and V. Pillay, *Cells*, 2019, **8**(10), 1209.
52 A. Naghizadeh, Z. M. Mizwari, S. M. Ghoreishi, S. Lashgari, S. Mortazavi-Derazkola and B. Rezaie, *Environ. Technol. Innovation*, 2021, **23**, 101560.
53 H. Kolya, P. Maiti, A. Pandey and T. Tripathy, *J. Anal. Sci. Technol.*, 2015, **6**, 1–7.
54 K. Zhang, J. M. Suh, J.-W. Choi, H. W. Jang, M. Shokouhimehr and R. S. Varma, *ACS Omega*, 2019, **4**, 483–495.

Appendix E

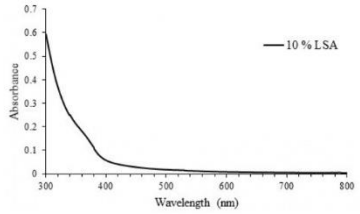

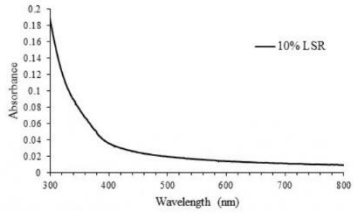

Appendix F

World Journal of Microbiology and Biotechnology (2021) 37:215
https://doi.org/10.1007/s11274-021-03180-6

ORIGINAL PAPER

Thermo resistant antioxidants from photoautotrophic microorganisms: screening and characterization

Luigi D'Elia[1] · Paola Imbimbo[1] · Davide Liberti[1] · Francesco Bolinesi[2] · Olga Mangoni[2] · Antonino Pollio[2] · Giuseppe Olivieri[3,4] · Daria Maria Monti[1]

Received: 27 July 2021 / Accepted: 27 October 2021 / Published online: 11 November 2021

Abstract

The demand for natural antioxidants to be used in food industry is increasing, as synthetic antioxidants are toxic and have high production costs. Specifically, food processing and preservation require antioxidants resistant to thermal sterilization processes. In this study, twenty-five strains among microalgae and cyanobacteria were screened as antioxidants producers. The species *Enallax* sp., *Synechococcus bigranulatus* and *Galdieria sulphuraria* showed the highest content of chlorophyll a and total carotenoids. In vitro stability and antioxidant activity of the ethanolic extracts were performed. The results revealed that pigments present in the extracts, obtained from the previously mentioned species, were stable at room temperature and exhibited in vitro free radical scavenging potential with IC_{50} values of 0.099 ± 0.001, 0.048 ± 0.001 and 0.13 ± 0.02 mg mL^{-1}, respectively. Biocompatibility assay showed that the extracts were not toxic on immortalized cell lines. The antioxidant activity was also tested on a cell-based model by measuring intracellular ROS levels after sodium arsenite treatment. Noteworthy, extracts were able to exert the same protective effect, before and after the pasteurization process. Results clearly indicate the feasibility of obtaining biologically active and thermostable antioxidants from microalgae. Green solvents can be used to obtain thermo-resistant antioxidants from cyanobacteria and microalgae which can be used in the food industry. Thus, the substitution of synthetic pigments with natural ones is now practicable.

Graphical abstract

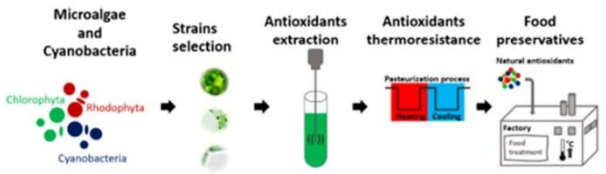

Keywords Microalgae · Pigments · Natural antioxidants · ABTS · H_2_DCFDA · Pasteurization

✉ Giuseppe Olivieri
giuseppe.olivieri@wur.nl

✉ Daria Maria Monti
mdmonti@unina.it

[1] Department of Chemical Sciences, University of Naples Federico II, Via Cinthia 4, 80126 Naples, Italy

[2] Department of Biology, University of Naples Federico II, Via Cinthia 4, 80126 Naples, Italy

[3] Bioprocess Engineering Group, Wageningen University and Research, Droevendaalsesteeg 1, 6700AA Wageningen, The Netherlands

[4] Department of Chemical, Materials and Industrial Engineering, University of Naples Federico II, Piazzale Tecchio 80, 80125 Naples, Italy

Appendix F

Introduction

Due to the toxicity of synthetic antioxidants, natural molecules with antioxidant activity have drawn great attention for their potential use as food preservatives or nutraceuticals (Villalobos-Delgado et al. 2019; Liu et al. 2019). Nowadays, microalgae and cyanobacteria are emerging as an important source of sustainable antioxidants.

These microorganisms can survive in several environments, such as hot terrestrial and marine habitats, considered inhospitable for most life forms (Elleuche et al. 2015; Urbieta et al. 2015). In recent years, several photosynthetic microorganisms have found application in industrial processes and in food industry for two reasons: (i) they can grow in harsh environmental conditions, so they are not susceptible to microbial contamination (Bhandiwad et al. 2013); (ii) they produce molecules resistant to high temperatures, ionic strength and extreme pH values (Patel et al. 2019; Zuccaro et al. 2020; Malavasi et al. 2020; Ferraro et al. 2020). Moreover, high value compounds from algae and cyanobacteria are more effective than synthetic ones in food application (Sidari and Tofalo 2019).

Microalgae and cyanobacteria are photosynthetic single-cell organisms, which are usually classified on the basis of their pigments, photosynthetic storage products and morphology (Metting 1996; Gualtieri 2001; Pulz and Gross 2004). Cyanobacteria, known in the past as blue-green algae, have a prokaryotic cell and produce chlorophyll *a* as well as phycobiliproteins (Watson et al. 2015; Stirbet et al. 2018). Green algae have chlorophylls *a* and *b* (Leliaert et al. 2012). Red algae contain chlorophyll *a* and phycobilisomes that are located on the surface of unstacked thylakoid membranes (Yoon et al. 2002, 2006).

In general, microalgae and cyanobacteria, present in different ecosystems, account for a large part of the total ecosystem biomass and productivity, and can be exploited to generate several added value products of nutraceutical and industrial relevance (Patel et al. 2019). Noteworthy, these microorganisms have the great advantage to be able to grow in wastewaters and on non-arable lands, and to produce a huge number of secondary metabolites endowed with biological activity (Petruk et al. 2018; Imbimbo et al. 2020).

Currently, only few microalgae strains are commercialized. The dry biomass from either *Chlorella* and *Arthrospira* is used as food supplements due to the high content of proteins rich in essential amino acids (Sidari and Tofalo 2019). The biomass of *Nannochloropsis species*, *Isochrysis species*, *Nitzschia species*, *Phaeodactylum species*, and *Porphyridium cruentum*, is rich in ω-3 fatty acids such as eicosapentaenoic (EPA) and docosahexaenoic (DHA), which exert beneficial effects on human health (Sidari and Tofalo 2019; Jiménez Callejón et al. 2020; Derwenskus et al. 2020).

Moreover, microalgae produce a huge array of pigments, whose physiological function is to harvest the light at different wavelengths, and to protect cells from the continuous exposure to high levels of oxygen and radical stress (Sampath-Wiley et al. 2008; Gouveia et al. 2010; Matos et al. 2017; Sun et al. 2018; Koyande et al. 2019). These are mainly carotenoids and phycobiliproteins (Keddar et al. 2020). These pigments can be widely used in the food industry as food colorants to replace synthetic dyes, or as additives to prolong the shelf-life of food products. Nevertheless, to date, Spirulina Blue is the only natural blue food coloring used in the food industry (Böcker et al. 2019).

Unfortunately, several factors need to be considered when developing food products from seaweeds and microalgae: (i) consumer awareness and demand; (ii) bioavailability; (iii) over time stability of bioactive compounds, and (iv) cost-effectiveness of the process. Therefore, the use of the whole algal biomass and extracts for human consumption must be related to food safety regulations, which vary among countries (Pulz and Gross 2004).

To this regard, microalgae have received approval by different regulations. *Chlorella pyrenoidosa*, *Chlorella vulgaris* and *Heterochlorella luteoviridis* are species not subjected to the Novel Foods Regulation, as they have been on the food market before 15 May 1997 (Champenois et al. 2015). Astaxanthin from *Haematococcus pluvialis*, oil from *Schizochytrium* sp., *Nannochloropsis gaditana* and *Phaeodactylum tricornutum* were approved as novel food ingredients between 2004 and 2017 under regulation (EC) No. 258/97 (Regulation (EC) No 258/97 2002; Sidari and Tofalo 2019). In order to simplify the current authorization procedures, a new regulation on novel food has been established with effective validity at the end of 2017 (Sidari and Tofalo 2019). According to this, a novel food category has been proposed, i.e. "food consisting of, isolated from or produced from, microorganisms, fungi or algae" (Sidari and Tofalo 2019). Also, the Food and Drug Administration (FDA, United States), Food Standards Australia New Zealand (FSANZ) and Ministry of health, Labour and Welfare in Japan, approved safe biomasses and extracts of several microalgae as novel food ingredients (Sidari and Tofalo 2019). Today, algae-based food products market is in expansion, as the world population is increasingly aware in the purchase of healthy food with a low environmental impact (Barsanti and Gualtieri 2018). As an example, the global carotenoid market is projected to increase to 2.0 billion USD by 2026 (Harvey and Ben-Amotz 2020). The production of carotenoids, such as β-carotene from *Dunaliella salina*, is 3000 t year $^{-1}$, with a total cost of 104 USD kg^{-1}. This value highlights that microalgal biomass is an expensive material compared to other types of biomasses. As reported by Ruiz et al., in the south of Spain the microalgal biomass cost production is estimated between 3.4 and 5.2 € kg^{-1} (100 ha,

Appendix F

with a productivity of about 27 ton ha^{-1} Yr^{-1} for open ponds and between 34 and 61 ton ha^{-1} Yr^{-1} for photobioreactors). Authors highlighted that the cost of biomass is influenced by light exposure, as the same model in the Netherlands shows a cost of biomass between 6.0 and 11.0 € kg^{-1} (Ruiz et al. 2016). In addition, the procedures employed for the extraction of high value compounds from microalgae represent a bottleneck in the exploitation of an algae-based biorefinery (Slegers et al. 2020). For example, the overall costs for the production of β-carotene from *D. salina* reflect a cost of 27-53 € day^{-1} (Sangiorgio et al. 2020). To make microalgae competitive to other natural sources, it is necessary to develop innovative and sustainable techniques able to reduce the costs of the whole process.

Another important factor to be considered is the potential toxicity and carcinogenic effect of synthetic antioxidants, as they are often obtained by using toxic solvents and some residual contaminants may be found (Villalobos-Delgado et al. 2019; Cheng et al. 2020; Marzorati et al. 2020).

Thus, the idea of using antioxidants from natural sources is mandatory. Here, twenty-five photosynthetic thermotolerant microorganisms were used: 11 Chlorophyta, 4 Rhodophyta and 10 Cyanobacteria strains. Thermotolerant species were used to obtain antioxidants resistant to the high temperatures reached during the sterilization processes. Extracts were obtained with a green solvent (ethanol), according to the Food Safety Regulation (EC 178/2002) and the mentioned-above Novel Food Regulation (EC 258/97), which limit the type of solvent to be used in the extraction processes. Strains were screened for their growth rate and their extracts for carotenoid content and in vitro antioxidant activity. Those endowed with the most promising activity were then evaluated for their biocompatibility and for their antioxidant activity on a cell-based model, before and after pasteurization process.

Materials and methods

Strains and medium

Twenty-five strains, Chlorophyta, Rhodophyta and Cyanobacteria, were selected from the Algal Collection of the University Federico II (ACUF, www.acuf.net) (D'Elia et al. 2018). Chlorophyta strains were: *Chlorella vulgaris* Beij (062); *Chlorella zofingiensis* Dönz (252); *Coelastrella terrestris* (Reisigl) Hegewald et N. Hanagata (271); *Chlorella* sp. (684); *Chlorella sorokiniana* Shihira et Krauss (824); *Scenedesmus* sp. (826); *Chlorella sorokiniana* Shihira et Krauss (830); *Enallax* sp. (833); *Scenedesmus* sp. (839); *Scenedesmus* sp. (840); *Westiellopsis prolifera* (845). Cyanobacteria strains were: *Nodularia sphaerocarpa* Bornet et Flahault (033); *Calothrix membranacea* Shmidle (114); *Gloeotrichia* sp. (115); *Anabaena flos-aquae* Healey (249); *Nostoc commune* Vaucher ex Bornet et Flahault (299); *Fischerella ambigua* (Kützing ex Bornet et Flahault) Gomont (304); *Lyngbya major* Meneghini (633); *Synechococcus bigranulatus* Scuria (680); *Synechocystis fuscopigmentos* Kovácic (683); *Chroococcidiopsis* sp. (831). Rhodophyta strains were: *Galdieria sulphuraria* (Galdieri) Merola (064); *Galdieria phlegrea* Pinto G. (291); *Galdieria partita* Sentsova (627) and *Galdieria maxima* Sentsova (671). Chlorophyta inorganic medium was Bold Basal Medium (BBM) (Bold 1949). Cyanobacteria were grown in Blue-Green medium (BG-11) (Rippka et al. 1979). The culture medium for Rhodophyta was the Allen medium (Allen 1968). Media were sterilized in autoclave (121 °C, 20 min).

Algal growth

Cultures of 50 mL were grown in flasks (100 mL) on a shaking shaker in a climate room at 39 ± 1 °C equipped with fluorescent lamps. Cultures were exposed 24 h with a constant light intensity of 300 Photosynthetic Active Radiations (PAR) $\mu mol_{photons}$ m^{-2} s^{-1} (Pruvost et al. 2012).

The growth and microalgal concentration of each strain was followed for 14 days by measuring the optical density (O.D.) at 730 nm wavelength. The conversion between the O.D. and the biomass dry weight was determined for each strain at the end of the exponential growth phase. The conversion factor was: 1 O.D. corresponded to 0.2 mg dry weight. The conversion between fresh and dry weight was measured for each strain and the ratio was found to be 5:1, which means that 1 g of fresh biomass corresponded to 200 mg ± 18 mg of dry weight.

Division per day (k) is directly related to the ratio between the O.D. of each day (t_2) and the initial time (t_1) and inversely related to Δt (Andersen 2005):

$$k = \frac{log_2(O.D._{t_2}/O.D._{t_1})}{\Delta t}$$

The light yield ($Y_{X/E}$, g $mol_{photons}^{-1}$) was defined as the ratio of the produced biomass and the light energy irradiated over the cultivation time. Thus:

$$\frac{(x_t - x_{t=0}) \cdot V}{A \cdot I \cdot t}$$

where the produced biomass is the product of the culture volume (V, L) and the biomass concentration produced ($x_t - x_{t=0}$, g L^{-1}) during the culture time (t, s). The irradiated energy is the product of the irradiated surface (A, m^{-2}), the irradiance (I, μmol m^{-2} s^{-1}) and of the culture time.

Appendix F

Ethanol extracts

Antioxidants extractions were performed using ethanol as solvent, as reported by Aremu, with some modifications (Aremu et al. 2016). Briefly, for each extraction, 1 g of harvested biomass, which corresponds to 200 mg of dry weight (D.W.), was suspended in 2 mL of pure ethanol and disrupted by ultrasonication (40% amplitude, 4 min on ice, Bandelin SONOPULS HD 3200, tip MS73). The final volume was adjusted to 20 mL and the mixture was shaken for 24 h at 250 rpm in a dark room at 4 °C. The mixture was then centrifuged at 12,000 *g* for 10 min and the supernatant stored at −20 °C. The supernatant, dried under N_2 stream at 30 °C, was solubilized in ethanol (12 mg mL^{-1}) and stored at −20 °C. The extract represents the ethanol extract (EE).

Spectrophotometric characterization

UV-vis absorption spectra of EE were collected at different time (0, 24 and 48 h) using a quartz cuvette of 1 cm path length. Spectra were collected at 25 °C over 400-700 nm wavelength range using a Varian Cary 5000 UV-vis-NIR spectrophotometer.

Determination of pigments concentration

Pigments concentration was determined spectrophotometrically by acquiring the spectra in the range 400–700 nm. The amount of pigments was calculated using formulae (1–3), derived for ethanol extracts (Lichtenthaler 1987):

$$Chla = 13.36 \cdot A_{664nm} - 5.19 \cdot A_{649nm} \quad (1)$$

$$Chlb = 27.43 \cdot A_{649nm} - 8.12 \cdot A_{664nm} \quad (2)$$

$$Carotenoids = (1000 \cdot A_{470nm} - 2.13 \cdot Chla - 97.63 \cdot Chlb)/209 \quad (3)$$

The results were expressed as mg of pigments g^{-1} of biomass D.W.

Antioxidants productivity ($P_{antioxidants}$, mg L^{-1} day^{-1}) was calculated as the product between biomass antioxidants content (A_{ox}) and biomass concentration (X, g L^{-1}), calculated when the antioxidants content reached the maximum level (t_{smax}, day) (Gifuni et al. 2018):

$$P_{antioxidants} = \frac{A_{OX(t_{smax})} \cdot X_{(t_{smax})}}{t_{smax}}$$

Total carotenoid quantification

The total carotenoid content was determined by spectrophotometrical analysis as described by Gilbert-López et al. (Gilbert-López et al. 2015). The ethanolic extracts from *S. bigranulatus, Enallax sp.* and *G. sulphuraria* were dissolved in pure methanol in a concentration range from 0.5 to 0.05 mg mL^{-1}. A standard calibration curve of commercial β-carotene (from 5 to 200 µg mL^{-1}) was used to calculate the concentration of total carotenoids. The absorbance of samples was recorded at 470 nm using a plate reader. The total carotenoid content was expressed as the ratio of mg of carotenoids and g of the extract.

Pigments characterization by HPLC

For pigment determination, extracts were resuspended in 100 % methanol and analyzed using an HPLC Hewlett Packard (1100 Series). 200 µl of sample was injected and pigments were separated by using a C8 column (3 µm Hyperloop MOS, 10 cm, 4.6 mm internal diameter, Shandon), as described in Vidussi et al. (Vidussi et al. 1996) and modified. Briefly, the elution was performed at flow rate of 1 mL min^{-1} using a linear binary gradient between solvent A (MeOH:0.5 N aqueous ammonium acetate, 70:30 v/v) and solvent B (MeOH), with the following gradient: min 0, 25% B; min 1, 50% B; min 15,100% B, min 19, 25% B. For the determination of chlorophylls and carotenoids, a spectrophotometer with a diodes array detector (DAD) was set at 440 nm, making it possible to determine the absorption spectrum of the 350–750 nm interval for each peak, in order to check the purity of each pigment. The column was calibrated using different pigment standards (chlorophyll a, chlorophyll b, chlorophyll c1+c2, alloxanthin, prasinoxanthin, 19′-butanoyloxyfucoxanthin, fucoxanthin, 19′-hexanoyloxyfucoxanthin, peridinin, zeaxanthin, neoxanthin, violaxanthin, b-carotene) with a range of concentrations between 0 and 60 µg/L for carotenoids and 0–250 µg/L for chlorophylls. Standards were provided by the International Agency for 14 C Determination, VKI Water Quality Institute, Copenhagen, Denmark.

ABTS assay

The *in vitro* antioxidant activity of each extract was evaluated by the 2,2'-azinobis-(3-ethylbenzothiazoiline-6-sulfonic acid) ABTS assay, according to Rigano et al. with some modifications (Rigano et al. 2014). Briefly, 7.4 mM $ABTS^{+}$ was mixed with 140 mM $K_2S_2O_8$ and the solution stabilized for 12 h at room temperature in the dark. The mixture was then diluted with ethanol to obtain an absorbance of 0.70 ± 0.02 unit at 734 nm using a spectrophotometer. Ethanolic extracts (50 µL) were allowed to react with 250 µL of diluted $ABTS^{+}$ solution for 7 min, and then the absorbance was read at 734 nm. The standard curve was linear between 0 and 20 µM Trolox. Results are expressed as IC_{50} (mg mL^{-1}), i.e. the concentration required to scavenge 50% of free radical ABTS.

Appendix F

Biocompatibility assay

Human keratinocytes (HaCaT, Innoprot, Derio, Spain) and murine fibroblasts (BALB/c-3T3, ATCC, VA, USA) were cultured in Dulbecco's modified Eagle's medium (DMEM) (Sigma-Aldrich, St Louis, MO, USA) supplemented with 10% foetal bovine serum (HyClone, Logan, UT, USA), 2 mM L-glutamine and antibiotics. Cells were grown in a 5% CO_2 humidified atmosphere at 37 °C and seeded in 96-well plates at a density of 2×10^3 cells per well. Ethanol microalgal extracts were added to the cells 24 h after seeding for dose-dependent cytotoxicity assays. After 48 h incubation, cell viability was assessed by the MTT assay as described in Galano et al. (Galano et al. 2014). Briefly, 3-(4,5-dimethylthiazol-2-yl)-2,5-diphenyltetrazolium bromide (MTT) reagent dissolved in DMEM in the absence of phenol red (Sigma-Aldrich) was added to the cells (0.5 mg mL^{-1} final concentration). Following 4 h incubation at 37 °C, the culture medium was removed and the resulting formazan salts were dissolved by adding isopropanol containing 0.01 N HCl (100 µL per well). Absorbance values were determined at 570 nm using an automatic plate reader (Microbeta Wallac 1420, PerkinElmer, Waltham, MA, USA). Cell survival was expressed as percentage of viable cells in the presence of the ethanol microalgal extract under test compared with control cells grown in the absence of the extract. Three separate analyses were carried out with each sample. Control experiments were performed either by growing cells in the absence of the EE or by adding to the cell cultures identical volumes of ethanol.

Thermal pasteurization

Thermal pasteurization was performed according to the protocol reported by Ferraro et al. (Ferraro et al. 2020). Briefly, EEs were heated at 75 °C in a water bath. After 10 min incubation, samples were transferred to a second water bath at 20 °C and then stored at 4 °C until analysis.

Cellular reactive oxygen species (ROS) assay

The antioxidant activity of EEs before and after pasteurization was determined by measuring intracellular ROS levels, according to the protocol previously reported (Sobeh et al. 2018), with some modifications. HaCaT cells were pre-incubated for 2 h with 80 µg mL^{-1} of raw or pasteurized extract. At the end of incubation, cells were treated with 25 µM 2′,7′-dichlorodihydrofluorescein diacetate (H_2-DCFDA) for 45 min at 37 °C in complete medium without phenol red. Then, cells were incubated with 300 µM $NaAsO_2$ (SA) for 1 h at 37 °C. Finally, cells were washed with warm PBS plus (phosphate buffer saline supplemented with 1 mM $CaCl_2$, 0.5 mM $MgCl_2$, and 30 mM glucose). The fluorescence of DCF was detected at an emission wavelength of 525 nm and an excitation wavelength of 488 nm using a Perkin-Elmer LS50 spectrofluorometer (Shelton, CT, USA). Emission spectra were acquired at a scanning speed of 300 nm min^{-1}, with 5 nm slit width both for excitation and emission. ROS levels were expressed as percentage of fluorescence intensity of the sample under test, compared to untreated cells. Three independent experiments were carried out, each one with three determinations.

Statistical analysis

All the experiments were performed in triplicate. Results are presented as mean of results obtained after three independent experiments (mean ± SD or mean ± SEM) and compared by one-way ANOVA according to the Bonferroni's method (post-hoc) using Graphpad Prism for Windows, version 6.01.

Results

Biomass production

Commercial-scale cultivation of photosynthetic microorganisms is fundamental for the biomass generation process, and photobioreactors (PBRs) are often used as they allow a good control of all the experimental set up. 11 Chlorophyta, 4 Rhodophyta and 10 Cyanobacteria strains were grown at 40 °C for 14 days. Most of the strains showed an adaptation time of 3-5 days, followed by an exponential growth phase and ultimately a stationary phase (Online Resource S1-S3). Strains *Westiellopsis prolifera* (845), *Nodularia sphaerocarpa* (033), *Calothrix membranacea* (114), *Nostoc commune* (299), *Fischerella ambigua* (304) and *Lyngbya major* (633), did not adapt to the chosen experimental conditions and were discarded. For all the other microalgal cells, division per day (k) and light yield were calculated and reported in Fig. 1. Among the three phyla, *Scenedesmus*sp. (826), *Chroococcidiopsis*sp. (831) and *Galdieria phlegrea* (291) showed the lowest division per day (grey bars). On the other hand, the species endowed with the highest division per day and light yield were: *Enallax* sp. (833) (0.59 ± 0.12 day^{-1}; 0.49 ± 0.09 g $mol_{photons}^{-1}$) for Chlorophyta; *Synechococcus bigranulatus* (680) (0.57 ± 0.04 day^{-1}; 0.37 ± 0.03 g $mol_{photons}^{-1}$) for Cyanobacteria, and *Galdieria sulphuraria* (064) (0.57 ± 0.02 day^{-1}; 0.07 ± 0.02 g $mol_{photons}^{-1}$) for Rhodophyta.

Pigment extraction and quantification

Ethanol was used to extract antioxidants from microalgae, as it is considered a safe solvent for humans. Pigments concentration was obtained by using the formulas from Chen

Appendix F

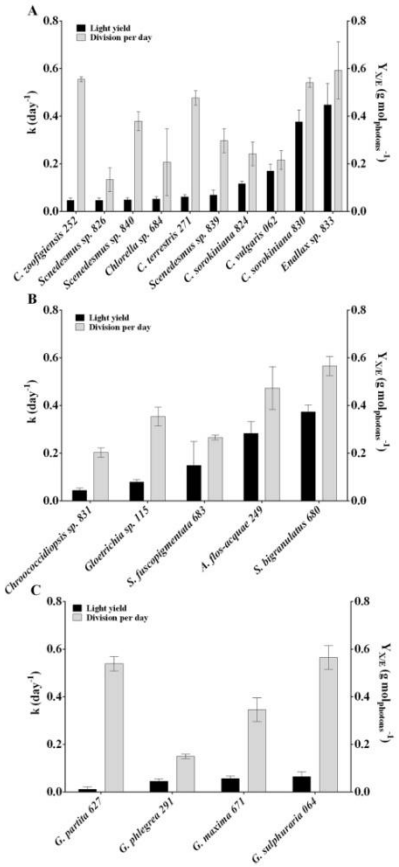

Fig. 1 Analysis of microalgal growth. Divisions per day (k) and light yield (Y) of Chlorophyta (**A**), Cyanobacteria (**B**) and Rhodophyta (**C**) strains. Divisions per day (grey bars) and light yield (black bars) were calculated at exponentially phase. Data expressed as mean ± SD (n = 3)

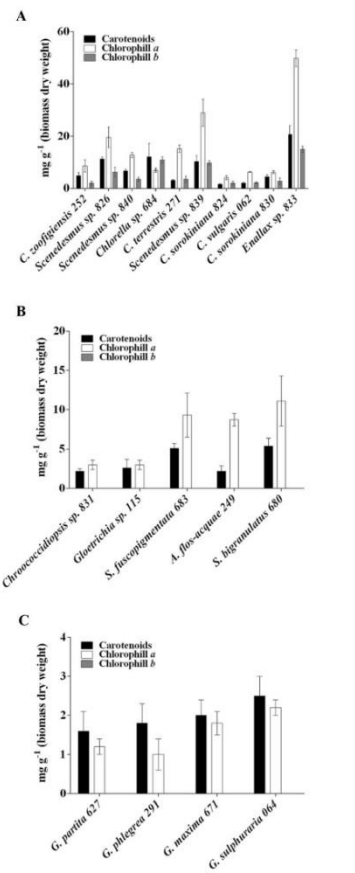

Fig. 2 Analysis of pigments content in different microalgal strains. Chlorophyll a (white bars), chlorophyll b (grey bars) and total carotenoids (black bars) present in the ethanol extracts from Chlorophyta (**A**), Cyanobacteria (**B**) and Rhodophyta (**C**). Each content is expressed as mg of extract pigment per g of biomass dry weight

and Vaidyanathan (Chen and Vaidyanathan 2013) (Online Resource Table S1). In this study, chlorophyll a (Fig. 2, white bars) was higher in *Scenedesmus* sp. (839) and *Enallax* sp. (833) for Chlorophyta species (Fig. 2A), whereas, among Cyanobacteria, *S. bigranulatus* seemed to be the best antioxidants producer (Fig. 2B). In the case of Cyanidiales, instead, the chlorophyll a content was very similar (Fig. 2C).

As for chlorophyll b content (Fig. 2, grey bars), a slight variation in Chlorophyta species was observed, although

Appendix F

no chlorophyll *b* in Cyanobacteria and Rhodophyta was observed (Fig. 2B, C). When total carotenoids were determined, the Chlorophyta with the highest value was *Enallax sp.* (20.7 ± 3.4 mg $g_{d.w.}^{-1}$), whereas in case of Cyanobacteria *S. bigranulatus* showed the highest carotenoid level (5.4 ± 1.0 mg $g_{d.w.}^{-1}$) and *G. sulphuraria* (2.5 ± 0.5 mg $g_{d.w.}^{-1}$) among Rhodophyta.

In vitro determination of the antioxidant activity of ethanol extracts

Then, the ABTS scavenging assay was performed. Even if the reliability of this analysis is controversial, it is widely used to test the antioxidant activity of different molecules. The results of the screening are shown in Table 1. *C. sorokiniana* (824) showed the lowest IC_{50} value, followed by *Enallax* sp. (833) for the Chlorophyta species. In the case of Cyanobacteria, ethanol extracts from *S. bigranulatus* (680) and *Anabaena flos-aquae* (249) showed the highest antioxidant power, whereas *G. sulphuraria* (064) showed the best antioxidant power among Rhodophyta. Thus, on the basis of the division per day, on the total pigments content and on the *in vitro* antioxidant activity, one strain for each phylum was selected for further experiments: *Enallax* sp. (833), *S. bigranulatus* (680) and *G. sulphuraria* (064). The selected strains showed an antioxidant productivity of 6.3 ± 0.9 mg L^{-1} day^{-1} (*Enallax sp.*); 8.0 ± 1.5 mg L^{-1} day^{-1} (*S. bigranulatus*) and 6.0 ± 0.4 mg L^{-1} day^{-1} (*G. sulphuraria*).

Determination of carotenoid content in selected strains

Starting from the ethanolic extract of *Enallax* sp., *S. bigranulatus* and *G. sulphuraria* the total carotenoids content was determined spectrophotometrically. The results are reported in Table 2. The carotenoid content is expressed as mg of carotenoids extracted per g of ethanol dry extract. It is interesting to notice that the conventional extraction allowed obtaining 924 mg of carotenoids per g of dry extract from *Enallax* sp., whereas 565 mg and 394.5 mg of carotenoids were recovered from *S. bigranulatus* and *G. sulphuraria*, respectively.

Pigments characterization by HPLC of selected strains extract

Online Resource Table S2 reports the list of pigments obtained in *Enallax*sp., *S. bigranulatus* and *G. sulphuraria*,

Table 2 Comparison between extract yields and carotenoids content of selected strains

Strain	$mg_{extract}\ g_{d.w.}^{-1}$	$mg_{carotenoids}\ g_{extract}^{-1}$
*Enallax*sp.	256.4 ± 16.7	924.0 ± 39.6
S. bigranulatus	216.6 ± 6.6	565.0 ± 19.8
G. sulphuraria	42.9 ± 0.9	394.5 ± 31.2

Table 1 In vitro antioxidant activity of ethanol extracts, by ABTS assay

Phylum	Species	ACUF N°	IC_{50} (mg mL^{-1})
Chlorophyta	*Chlorella vulgaris*	62	0.10 ± 0.04
	Chlorella zoofigiensis	252	0.22 ± 0.04
	Coelastrella terrestris	271	0.13 ± 0.01
	Chlorella sp.	684	0.13 ± 0.01
	Chlorella sorokiniana	824	0.08 ± 0.02
	Scenedesmus sp.	826	0.12 ± 0.01
	Chlorella sorokiniana	830	0.25 ± 0.01
	Enallax sp.	833	0.099 ± 0.001
	Scenedesmus sp.	839	0.15 ± 0.05
	Scenedesmus sp.	840	0.18 ± 0.03
Cyanobacteria	*Gloetrichia* sp.	115	0.16 ± 0.01
	Anabaena flos-acquae	249	0.05 ± 0.01
	Synechococcus bigranulatus	680	0.048 ± 0.001
	Synechocystis fuscopigmentata	683	0.09 ± 0.04
	Chroococcidiopsis sp.	831	0.035 ± 0.004
Rhodophyta	*Galdieria sulphuraria*	64	0.13 ± 0.02
	Galdieria phlegrea	291	0.19 ± 0.06
	Galdieria partita	627	$>>2$
	Galdieria maxima	671	0.15 ± 0.03

Values are expressed as IC_{50}, i.e. the concentration required to scavenge 50% of free radical ABTS

Appendix F

using the method reported in Vidussi et al. (Vidussi et al. 1996), which does not allow the identification of phycobilins.

As shown in Online Resource Table S2 and in Fig. 3, HPLC analyses allowed to identify, among the eleven pigments eluted, violaxanthin (peak 2), lutein (peak 4), chlorophylls a and b (peaks 6-11), and β-carotene (peak11) in *Enallax*sp. Peaks 1, 3, 5 were xanthophylls not identified. In *S. bigranulatus*, zeaxanthin (peak 3), chlorophyll a - and its isomer - (peaks 7, 8), and β-carotene (peak 10), were identified. Peaks 1, 2, 4, 5, 6, 9 were xanthophylls not identified. In *G. sulphuraria*, among the nine eluted pigment, only two were xanthophylls not identified (peaks 2, 9), whereas zeaxanthin (peak 1), chlorophyll a - and its isomers - (peak 3-5), phaeophytins (peaks 6, 7) and β-carotene (peak 9) were identified.

Ethanol extract biocompatibility on immortalized eukaryotic cells

In order to verify if the ethanol extracts could be used in the food industry, the biocompatibility of the selected strains extracts was verified by MTT assay on eukaryotic immortalized cells: HaCaT (human keratinocytes) and BALB/c-3T3 (murine fibroblasts) cells. Cells were plated, and 24 h after seeding, increasing amount (from 5 μg mL^{-1} to 100 μg L^{-1}) of *S. bigranulatus, Enallax* sp. and *G. sulphuraria* extracts were added to the cells, taking into account that the average of the IC_{50} of the tested samples was lower than 100 μg mL^{-1}. After 48 h incubation, cell viability was assessed by the MTT (3-(4,5-dimethylthiazol-2-yl)-2,5-diphenyltetrazolium bromide) assay and cell survival was expressed as the percentage of viable cells in the presence of the extract compared to that of control samples. Two groups of cells were used as control, i.e. cells untreated with the extract and cells supplemented with identical volumes of buffer. Each sample was tested in two independent analyses, each carried out in triplicates (Fig. 4). MTT assays showed that the molecules extracted in ethanol resulted to be biocompatible with both the cell lines analyzed, up to 100 μg mL^{-1}.

Ethanolic extract thermo-resistance and stability

To assess the stability of ethanolic extracts, spectra of each selected strain were acquired at different time of storage at 4 °C. For each strain, the integral of the area under each spectrum (for each time) was calculated and compared with that obtained at time 0. The UV–Vis absorption spectra of extracts from *Enallax* sp., *S. bigranulatus* and *G. sulphuraria* are reported in Fig. 5. After 48 h storage, a loss of absorbance was found: 33% for *Enallax*sp., 7% for *S. bigranulatus* and 34% for *G. sulphuraria*, thus suggesting an overall stability of all the extracts overtime.

To verify if high temperature treatments affect the bioactivity of ethanol extracts, pasteurization was done (i.e. heated at 75 °C for 10 min). The stability of pasteurized ethanolic extracts was measured spectrophotometrically up to 48 h. The results are reported in Fig. 5 and showed a loss of absorbance of 28%, 17% and 26% for *Enallax* sp., *S. bigranulatus* and *G. sulphuraria*, respectively, thus indicating that pasteurization process does not affect the

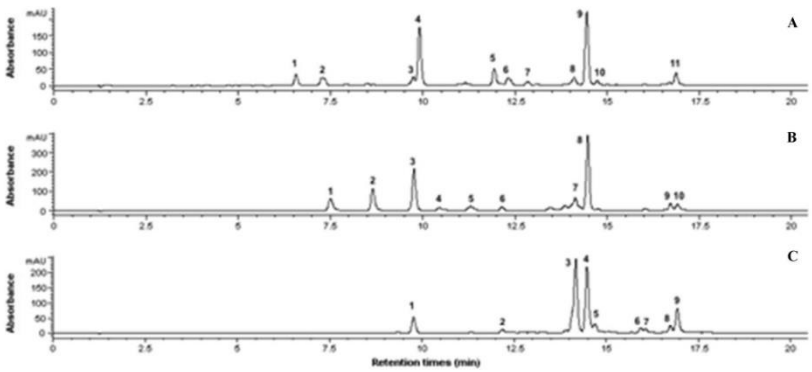

Fig. 3 HPLC analysis. Representative HPLC chromatograms of carotenoids extracted in **A** *Enallax* sp.; **B** *S. bigranulatus*; **C** *G. sulphuraria*. Peak numbers and their identification are reported in Table 2

Appendix F

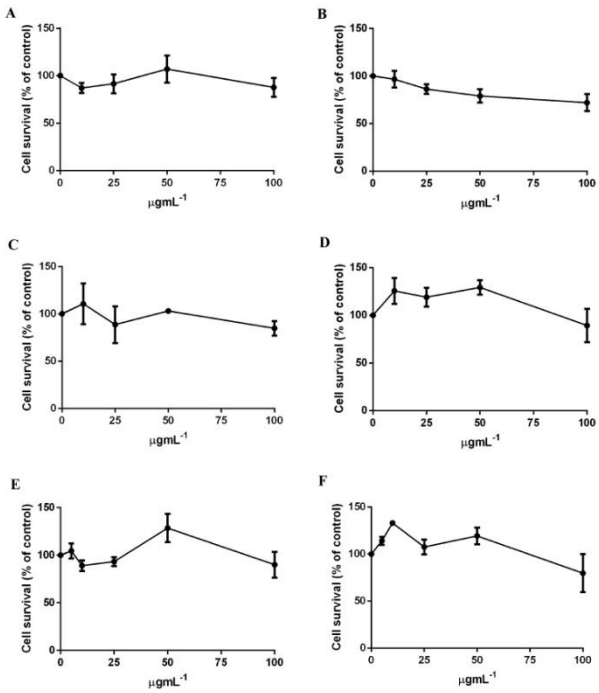

Fig. 4 Effect of ethanol extracts from *S. bigranulatus*, *Enallax* sp. and *G. sulphuraria* on the viability of immortalized cells. Dose–response curve of cells incubated for 48 h in the presence of increasing concentration (5–100 µg mL^{-1}) of each extract. **A**, **C**, **E**, HaCaT cells; **B**, **D**, **F**, BALB/c-3T3 cells. Cells were incubated with *S. bigranulatus* extracts (**A**, **B**); *Enallax sp.* (**C**, **D**); *G. sulphuraria* (**E**, **F**). Cell viability was assessed by the MTT assay and expressed as described in Materials and Methods section. Values are given as means ± SD ($n \geq 3$)

antioxidant activity and the overall stability. Finally, a comparison between the antioxidant activity of raw and of pasteurized extracts was performed. Cells were incubated for 2 h with 80 µg mL^{-1} of either raw or pasteurized extracts prior to SA exposure. At the end of the experiment, ROS levels were measured by using 2,7-dichlorodihydrofluorescein diacetate (H_2-DCFDA). As shown in Fig. 6, no alteration in ROS levels was observed when cells were incubated with the two molecules (white and grey bars), whereas a significant increase in ROS levels was observed when cells were exposed to SA (black bars).

Discussion

The threshold of legally permitted synthetic food additives that can be used in the food industry is decreasing due to their suspected role as promoters of carcinoma, and their toxic effects on liver and kidney (El-Baky et al. 2003). It has been demonstrated that natural β-carotene is superior to the synthetic one. In particular, the so called "natural β-carotene" is a mixture of carotenoids and nutrients, which are absent in synthetic β-carotene (Varfolomeev and Wasserman 2011). Hence, the substitution of synthetic pigments with natural ones is becoming mandatory. Moreover, during the thermal processes applied for food preservation, antioxidant molecules could lose their activity.

The aim of this work was to identify microalgae able to produce antioxidants resistant to thermal stress, to be used in the food industry. For this reason, ethanol was used as solvent (Assunção et al. 2017; Bulut et al. 2019). The growth of several strains from different phyla, able to grow between 40 and 70 °C, was followed overtime (Varshney et al. 2015) and *Enallax* sp., *S. bigranulatus* and *G. sulphuraria* were found to have the highest division per day and light yields. These results well correlate with antioxidant productivity,

Appendix F

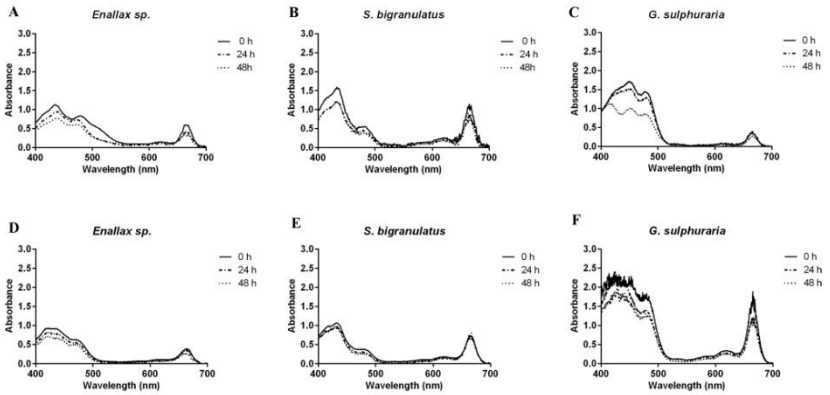

Fig. 5 UV–Vis absorption spectra of *Enallax*sp., *S. bigranulatus* and *G. sulphuraria* extracts. Sample concentration was 0.12 mg mL^{-1}. Spectra were acquired at 25 °C, in the range 400–700 nm. Spectra are reported at time 0 (–), after 24 h (---) and 48 h (···) storage, at 4 °C in dark conditions. **A**–**C** are referred to raw extracts, **D**–**F**, to pasteurized ones. **A**, **D** are referred to *Enallax* sp., **B**, **E** to *S. bigranulatus* and **C**, **F** to *G. sulphuraria*

and can be compared with those obtained by Silva (Silva et al. 2014) for *S. bigranulatus*, and by Graziani (Graziani et al. 2013) for *G. sulphuraria*. The highest content of pigments is observed in *Enallax sp.* and *S. bigranulatus* with a chlorophyll a content of 49.8 ± 3.2 mg $g_{d.w.}{}^{-1}$ and 11.1 ± 3.2 mg $g_{d.w.}{}^{-1}$, and a carotenoid content of 20.7 ± 3.4 mg $g_{d.w.}{}^{-1}$ and 5.4 ± 1.0 mg $g_{d.w.}{}^{-1}$.The average of the carotenoid content found in the used biomass samples was higher than those reported by Spolaore (Spolaore et al. 2006), who found an average carotenoid content of 0.1–0.2% of dry weight biomass. On the other hand, a high pigments content has been reported for *Galdieria* species, when the biomass was broken by French press or bead-beater (Imbimbo et al. 2020). Cyanidiales are known to usually possess a strong cell wall (Merola et al. 2009) which protects cells from most of the extraction techniques used. Thus, in this experimental system, ultrasound treatment may not be sufficient to disrupt the biomass and to release pigments. However, Rubashvili analysed the carotenoid content of various agro-industrial wastes, and found that β-carotene content of tomato skin, tangerine peel and orange peel was 0.083–0.127, 0.256–0.321 and 0.416–0.591 mg $g_{dried\ peel}{}^{-1}$ respectively (Rubashvili et al. 2018). These data clearly indicate that algal and cyanobacterial biomass are more advantageous for the extraction of these antioxidant molecules. Indeed, it has to be considered that these phytochemicals vary in structure and function from vegetable to vegetable and from cultivar to cultivar, and their level is strictly related to the level of maturity, postharvest handling, processing, and geographical position (Jideani et al. 2021).

The ethanol extracts of selected strains were analysed by HPLC, in order to collect more information about the specific pigments (carotenoids and chlorophylls). The main peaks of each species were identified (Moore et al. 1995; Graziani et al. 2013; Goecke et al. 2020; Zimermann et al. 2020). The overall picture showed a high variability of xanthophylls, both identified and not identified, among samples. The amount of pigments, such as xanthophylls, strongly depends on growth conditions, in particular light intensity and temperature (Moore et al. 1995; Kana et al. 1997; Bolinesi et al. 2020). In *G. sulphuraria* we found relatively high amount of chlorophylls and phaeophytin compared to other species, and *Enallax* sp. was the only species lacking zeaxanthin and presenting lutein and violaxanthin.

The biocompatibility results fully agree with those reported in literature. As an example, some authors found that antioxidants were toxic at high concentration, whereas low doses have a protective effect (Rigano et al. 2014; Petruk et al. 2018; Imbimbo et al. 2019). Based on biocompatibility results, 80 μg mL^{-1} of each extract was selected as the optimal concentration to be used to analyse the free radical scavenger activity against oxidative stress induced by SA before and after pasteurizing of extracts. Noteworthy, SA-induced ROS production was strongly inhibited when cells were pre-treated with both raw (30–40% decrease) and pasteurized (40–50% decrease) extracts of selected strains.

Appendix F

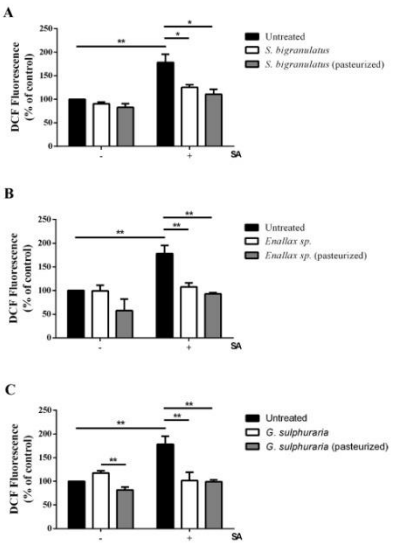

Fig. 6 Comparison of antioxidant activity between raw and pasteurized extracts from *S. bigranulatus*, *Enallax* sp. and *G. sulphuraria* on SA-stressed HaCaT cells. Intracellular ROS levels were determined by DCFDA assay on: **A** *S. bigranulatus*; **B** *Enallax* sp.; **C** *G. sulphuraria*. Cells were pre-incubated in the presence of 80 μg mL^{-1} of unpasteurized (white bars) and 80 μg mL^{-1} of pasteurized extract (grey bars) for 2 h, prior of SA treatment (300 μM, 60 min). Black bars refer to untreated cells in the absence (−) or in the presence (+) of SA. Values are expressed as percentage with respect to control (i.e. untreated) cells. Data are shown as means ± standard deviation (S.D.). Three independent measurements were carried out. * indicates $p < 0.05$; ** indicates $p < 0.01$

Thus, the antioxidants present in *Enallax* sp., *S. bigranulatus* and *G. sulphuraria* can be easily extracted in ethanol, are biologically active and resistant to pasteurization. This opens the way to the use of microalgal and cyanobacteria extracts in food preservation.

Supplementary Information The online version contains supplementary material available at https://doi.org/10.1007/s11274-021-03180-6.

Authors' contributions LDE, PI, DL, FB performed research and analyzed data, OM analyzed data, AP GO and DMM conceived study. All authors contributed to write the paper.

Funding Not applicable.

Data availability Not applicable.

Code availability Not applicable.

Declarations

Conflict of interest The authors declare that they have no conflict of interest.

References

Allen MM (1968) Simple conditions for growth of unicellular blue-green algae on plates. J Phycol 4:1–4. https://doi.org/10.1111/J.1529-8817.1968.TB04667

Andersen R (2005) Algal culturing techniques. J Phycol 41:906–908. https://doi.org/10.1111/j.1529-8817.2005.00114.x

Aremu AO, Masondo NA, Molnár Z et al (2016) Changes in phytochemical content and pharmacological activities of three Chlorella strains grown in different nitrogen conditions. J Appl Phycol 28:149–159. doi: https://doi.org/10.1007/s10811-015-0568-7

Assunção MFG, Amaral R, Martins CB et al (2017) Screening microalgae as potential sources of antioxidants. J Appl Phycol 29:865–877. doi: https://doi.org/10.1007/s10811-016-0980-7

Barsanti L, Gualtieri P (2018) Is exploitation of microalgae economically and energetically sustainable? Algal Res 31:107–115. doi: https://doi.org/10.1016/j.algal.2018.02.001

Bhandiwad A, Guseva A, Lynd L (2013) Metabolic engineering of *Thermoanaerobacterium thermosaccharolyticum* for increased n-butanol production. Adv Microbiol 3:46–51. https://doi.org/10.4236/aim.2013.31007

Böcker L, Ortmann S, Surber J et al (2019) Biphasic short time heat degradation of the blue microalgae protein phycocyanin from *Arthrospira platensis*. Innov Food Sci Emerg Technol 52:116–121. doi: https://doi.org/10.1016/j.ifset.2018.11.007

Bold HC (1949) The morphology of *Chlamydomonas chlamydogama*, sp. nov. Bull Torrey Bot Club 76:101. https://doi.org/10.2307/2482218

Bolinesi F, Saggiomo M, Ardini F et al (2020) Spatial-related community structure and dynamics in phytoplankton of the Ross Sea, Antarctica. Front Mar Sci 7:1092. https://doi.org/10.3389/FMARS.2020.574963

Bulut O, Akın D, Sönmez Ç et al (2019) Phenolic compounds, carotenoids, and antioxidant capacities of a thermo-tolerant *Scenedesmus sp.* (Chlorophyta) extracted with different solvents. J Appl Phycol 31:1675–1683. doi: https://doi.org/10.1007/s10811-018-1726-5

Champenois J, Marfaing H, Pierre R (2015) Review of the taxonomic revision of *Chlorella* and consequences for its food uses in Europe. J Appl Phycol 27:1845–1851. doi: https://doi.org/10.1007/s10811-014-0431-2

Chen Y, Vaidyanathan S (2013) Simultaneous assay of pigments, carbohydrates, proteins and lipids in microalgae. Anal Chim Acta 776:31–40. doi: https://doi.org/10.1016/j.aca.2013.03.005

Cheng S-H, Khoo HE, Kong KW et al (2020) Extraction of carotenoids and applications. Carotenoids: properties, processing and applications. Elsevier, Amsterdam, pp 259–288

D'Elia L, Del Mondo A, Santoro M et al (2018) Microorganisms from harsh and extreme environments: a collection of living strains at ACUF (Naples, Italy). Ecol Quest 29:63–74. https://doi.org/10.12775/EQ.2018.023

Derwenskus F, Schäfer B, Müller J et al (2020) Coproduction of EPA and fucoxanthin with *P. tricornutum*—a promising approach for up- and downstream processing. Chem Ing Tech 92:1780–1789. https://doi.org/10.1002/cite.202000046

Appendix F

El-Baky A, FKEB,. GSE-B (2003) Spirulina species as a source of carotenoids and a-tocopherol and its anticarcinoma factors. Biotechnology 2:222–240. https://doi.org/10.3923/biotech.2003.222.240

Elleuche S, Schäfers C, Blank S et al (2015) Exploration of extremophiles for high temperature biotechnological processes. Curr Opin Microbiol 25:113–119. doi: https://doi.org/10.1016/J.MIB.2015.05.011

Ferraro G, Imbimbo P, Marseglia A et al (2020) A thermophilic C-phycocyanin with unprecedented biophysical and biochemical properties. Int J Biol Macromol 150:38–51. doi: https://doi.org/10.1016/j.ijbiomac.2020.02.045

Galano E, Arciello A, Piccoli R et al (2014) A proteomic approach to investigate the effects of cadmium and lead on human primary renal cells. Metallomics 6:587–597. doi: https://doi.org/10.1039/c3mt00344b

Gifuni I, Olivieri G, Pollio A, Marzocchella A (2018) Identification of an industrial microalgal strain for starch production in biorefinery context: The effect of nitrogen and carbon concentration on starch accumulation. N Biotechnol 41:46–54. doi: https://doi.org/10.1016/J.NBT.2017.12.003

Gilbert-López B, Mendiola JA, Fontecha J et al (2015) Downstream processing of *Isochrysis galbana*: a step towards microalgal biorefinery. Green Chem 17:4599–4609. doi: https://doi.org/10.1039/c5gc01256b

Goecke F, Noda J, Paliocha M, Gislerød HR (2020) Revision of *Coelastrella* (Scenedesmaceae, Chlorophyta) and first register of this green coccoid microalga for continental Norway. World J Microbiol Biotechnol 36:149. doi: https://doi.org/10.1007/s11274-020-02897-0

Gouveia L, Marques AE, Sousa JM et al (2010) Microalgae—source of natural bioactive molecules as functional ingredients. Food Sci Technol Bull Funct Foods 7:21–37. https://doi.org/10.1616/1476-2137.15884

Graziani G, Schiavo S, Nicolai MA et al (2013) Microalgae as human food: chemical and nutritional characteristics of the thermoacidophilic microalga *Galdieria sulphuraria*. Food Funct 4:144–152. https://doi.org/10.1039/c2fo30198a

Gualtieri P (2001) Morphology of photoreceptor systems in microalgae. Micron 32:411–426

Harvey PJ, Ben-Amotz A (2020) Towards a sustainable *Dunaliella salina* microalgal biorefinery for 9-cis β-carotene production. Algal Res 50:102002. doi: https://doi.org/10.1016/j.algal.2020.102002

Imbimbo P, Romanucci V, Pollio A et al (2019) A cascade extraction of active phycocyanin and fatty acids from *Galdieria phlegrea*. Appl Microbiol Biotechnol 103:9455–9464. https://doi.org/10.1007/s00253-019-10154-0

Imbimbo P, Bueno M, Elia LD et al (2020) Green compressed fluid technologies to extract antioxidants and lipids from *Galdieria phlegrea* in a biorefinery approach. ACS Sustain Chem Eng 8:2939–2947. https://doi.org/10.1021/acssuschemeng.9b07505

Jideani AIO, Silungwe H, Takalani T et al (2021) Antioxidant-rich natural fruit and vegetable products and human health. Int J Food Prop 24:41–67. doi: https://doi.org/10.1080/10942912.2020.1866597

Jiménez Callejón MJ, Robles Medina A, González Moreno PA et al (2020) Simultaneous extraction and fractionation of lipids from the microalga *Nannochloropsis* sp. for the production of EPA-rich polar lipid concentrates. J Appl Phycol 32:1117–1128. doi: https://doi.org/10.1007/s10811-020-02037-z

Kana TM, Geider RJ, Critchley C (1997) Regulation of photosynthetic pigments in micro-algae by multiple environmental factors: a dynamic balance hypothesis. New Phytol 137:629–638. https://doi.org/10.1046/J.1469-8137.1997.00857

Keddar MN, Ballesteros-Gómez A, Amiali M et al (2020) Efficient extraction of hydrophilic and lipophilic antioxidants from microalgae with supramolecular solvents. Sep Purif Technol 251:117327. doi: https://doi.org/10.1016/j.seppur.2020.117327

Koyande AK, Chew KW, Rambabu K et al (2019) Microalgae: a potential alternative to health supplementation for humans. Food Sci Hum Wellness 8:16–24. https://doi.org/10.1016/j.fshw.2019.03.001

Leliaert F, Smith DR, Moreau H et al (2012) Phylogeny and molecular evolution of the green algae. CRC Crit Rev Plant Sci 31:1–46. https://doi.org/10.1080/07352689.2011.615705

Lichtenthaler HK (1987) Chlorophylls and carotenoids: pigments of photosynthetic biomembranes. Methods Enzym 148:350–382. https://doi.org/10.1016/0076-6879(87)48036-1

Liu X, Luo G, Wang L, Yuan W (2019) Optimization of antioxidant extraction from edible brown algae *Ascophyllum nodosum* using response surface methodology. Food Bioprod Process 114:205–215. doi: https://doi.org/10.1016/J.FBP.2019.01.003

Malavasi V, Soru S, Cao G (2020) Extremophile microalgae: the potential for biotechnological application. J Phycol 56:559–573

Marzorati S, Schievano A, Idà A, Verotta L (2020) Carotenoids, chlorophylls and phycocyanin from *Spirulina*: supercritical CO2 and water extraction methods for added value products cascade. Green Chem 22:187–196. https://doi.org/10.1039/c9gc03292d

Matos J, Cardoso C, Bandarra NM, Afonso C (2017) Microalgae as healthy ingredients for functional food: a review. Food Funct 8:2672–2685

Merola A, Castaldo R, De Luca P et al (2009) Revision of Cyanidium caldarium. Three species of acidophilicalgae. https://doi.org/10.1080/11263508109428026

Metting FB (1996) Biodiversity and application of microalgae. J Ind Microbiol Biotechnol 17:477–489. doi: https://doi.org/10.1007/bf01574779

Moore LR, Goericke R, Chisholm SW (1995) Comparative physiology of *Synechococcus* and *Prochlorococcus*: influence of light and temperature on growth, pigments, fluorescence and absorptive properties. Mar Ecol Prog Ser 116:259–276. https://doi.org/10.3354/meps116259

Patel A, Matsakas L, Rova U, Christakopoulos P (2019) A perspective on biotechnological applications of thermophilic microalgae and cyanobacteria. Bioresour Technol 278:424–434. doi: https://doi.org/10.1016/J.BIORTECH.2019.01.063

Petruk G, Gifuni I, Illiano A et al (2018) Simultaneous production of antioxidants and starch from the microalga *Chlorella sorokiniana*. Algal Res 34:164–174. doi: https://doi.org/10.1016/j.algal.2018.07.012

Pruvost J, Cornet JF, Goetz V, Legrand J (2012) Theoretical investigation of biomass productivities achievable in solar rectangular photobioreactors for the cyanobacterium *Arthrospira platensis*. Biotechnol Prog 28:699–714. doi: https://doi.org/10.1002/btpr.1540

Pulz O, Gross W (2004) Valuable products from biotechnology of microalgae. Appl Microbiol Biotechnol 65:635–648. doi: https://doi.org/10.1007/s00253-004-1647-x

Regulation HAT (2002) Regulation (EC) No 258/97 of the European Parliament and of the Council of 27 January 1997 concerning novel foods and novel food ingredients. Off J Eur Commun 40:1–7

Rigano MM, Raiola A, Tenore GC et al (2014) Quantitative trait loci pyramiding can improve the nutritional potential of tomato (*Solanum lycopersicum*) fruits. J Agric Food Chem 62:11519–11527

Rippka R, Deruelles J, Waterbury JB (1979) Generic assignments, strain histories and properties of pure cultures of cyanobacteria. J Gen Microbiol 111:1–61. doi: https://doi.org/10.1099/00221287-111-1-1

Appendix F

Rubashvili I, Tsitsagi M, Ebralidze K et al (2018) Extraction and analysis of the major carotenoids of agro-industrial waste materials using sequential extraction techniques and high performance liquid chromatography. Eurasian J Anal Chem 13:em06

Ruiz J, Olivieri G, de Vree J et al (2016) Towards industrial products from microalgae. Energy Environ Sci 9:3036–3043. doi: https://doi.org/10.1039/C6EE01493C

Sampath-Wiley P, Neefus CD, Jahnke LS (2008) Seasonal effects of sun exposure and emersion on intertidal seaweed physiology: Fluctuations in antioxidant contents, photosynthetic pigments and photosynthetic efficiency in the red alga *Porphyra umbilicalis Kützing* (Rhodophyta, Bangiales). J Exp Mar Bio Ecol 361:83–91. doi: https://doi.org/10.1016/j.jembe.2008.05.001

Sangiorgio P, Verardi A, Editors G et al (2020) Natural beta-carotene: a microalgae derivate for nutraceutical applications. Chem Eng Trans 79:200

Sidari R, Tofalo R (2019) A comprehensive overview on microalgal-fortified/based food and beverages. Food Rev Int 35:778–805

Silva CSP, Silva-Stenico ME, Fiore MF et al (2014) Optimization of the cultivation conditions for *Synechococcus* sp. PCC7942 (cyanobacterium) to be used as feedstock for biodiesel production. Algal Res 3:1–7. doi: https://doi.org/10.1016/j.algal.2013.11.012

Slegers PM, Olivieri G, Breitmayer E et al (2020) Design of value chains for microalgal biorefinery at industrial scale: process integration and techno-economic analysis. Front Bioeng Biotechnol 8:1048. https://doi.org/10.3389/fbioe.2020.550758

Sobeh M, Youssef FS, Esmat A et al (2018) High resolution UPLC-MS/MS profiling of polyphenolics in the methanol extract of *Syzygium samarangense* leaves and its hepatoprotective activity in rats with CCl4-induced hepatic damage. Food Chem Toxicol 113:145–153. https://doi.org/10.1016/j.fct.2018.01.031

Spolaore P, Joannis-Cassan C, Duran E, Isambert A (2006) Commercial applications of microalgae. J Biosci Bioeng 101:87–96. doi: https://doi.org/10.1263/jbb.101.87

Stirbet A, Lazár D, Papageorgiou GC (2018) Chlorophyll a fluorescence in cyanobacteria: relation to photosynthesis. Elsevier, Amsterdam, pp 79–130

Sun XM, Ren LJ, Zhao QY et al (2018) Microalgae for the production of lipid and carotenoids: a review with focus on stress regulation and adaptation. Biotechnol Biofuels 11:1–16

Urbieta MS, Donati ER, Chan K-G et al (2015) Thermophiles in the genomic era: biodiversity, science, and applications. Biotechnol Adv 33:633–647

Varfolomeev SD, Wasserman LA (2011) Microalgae as source of biofuel, food, fodder, and medicines. Appl Biochem Microbiol 47:789–807. doi: https://doi.org/10.1134/S0003683811090079

Varshney P, Mikulic P, Vonshak A et al (2015) Extremophilic microalgae and their potential contribution in biotechnology. Bioresour Technol 184:363–372. doi: https://doi.org/10.1016/J.BIORTECH.2014.11.040

Vidussi F, Claustre H, Bustillos-Guzmàn J et al (1996) Determination of chlorophylls and carotenoids of marine phytoplankton: separation of chlorophyll a from divinylchlorophyll a and zeaxanthin from lutein. J Plankton Res 18:2377–2382. doi: https://doi.org/10.1093/plankt/18.12.2377

Villalobos-Delgado LH, Mateo J, Caro I et al (2019) Natural antioxidants in fresh and processed meat. Sustainable meat production and processing. Elsevier, Amsterdam, pp 207–236

Watson SB, Whitton BA, Higgins SN et al (2015) Harmful algal blooms. Freshwater algae of North America. Academic Press, London, pp 873–920

Yoon HS, Hackett JD, Pinto G, Bhattacharya D (2002) The single, ancient origin of chromist plastids. Proc Natl Acad Sci USA 99:15507–15512. https://doi.org/10.1073/pnas.242379899

Yoon HS, Müller KM, Sheath RG et al (2006) Defining the major lineages of red algae (Rhodophyta). J Phycol 42:482–492. doi: https://doi.org/10.1111/j.1529-8817.2006.00210.x

Zimermann JDar, Sydney F, Cerri EB et al (2020) Growth kinetics, phenolic compounds profile and pigments analysis of *Galdieria sulphuraria* cultivated in whey permeate in shake-flasks and stirred-tank bioreactor. J Water Process Eng 38:101598. doi: https://doi.org/10.1016/j.jwpe.2020.101598

Zuccaro G, Yousuf A, Pollio A, Steyer J-P (2020) Microalgae cultivation systems. Microalgae cultivation for biofuels production. Elsevier, Amsterdam, pp 11–29

Appendix F

World Journal of Microbiology and Biotechnology

Thermo resistant antioxidants from microalgae: screening and characterization

Luigi D'Elia[1], Paola Imbimbo[1], Davide Liberti[1], Francesco Bolinesi [2], Olga Mangoni[2], Antonino Pollio[2], Giuseppe Olivieri[3,4]*, Daria Maria Monti[1]*

[1]Department of Chemical Sciences, University of Naples Federico II, via Cinthia 4, 80126, Naples, Italy

[2]Department of Biology, University of Naples Federico II, via Cinthia 4, 80126, Naples, Italy

[3]Bioprocess Engineering Group, Wageningen University and Research, Droevendaalsesteeg 1, 6700AA, Wageningen, the Netherlands

[4]Department of Chemical, Materials and Industrial Engineering, University of Naples Federico II, Piazzale Tecchio 80, 80125, Naples, Italy

*Corresponding Authors: G.O. giuseppe.olivieri@wur.nl; D.M.M. mdmonti@unina.it; tel +39081679150; fax +39 081-674090

Supplementary material

Growth curves of analysed strains

Pigments content of ethanolic extract

Pigments identification

Appendix F

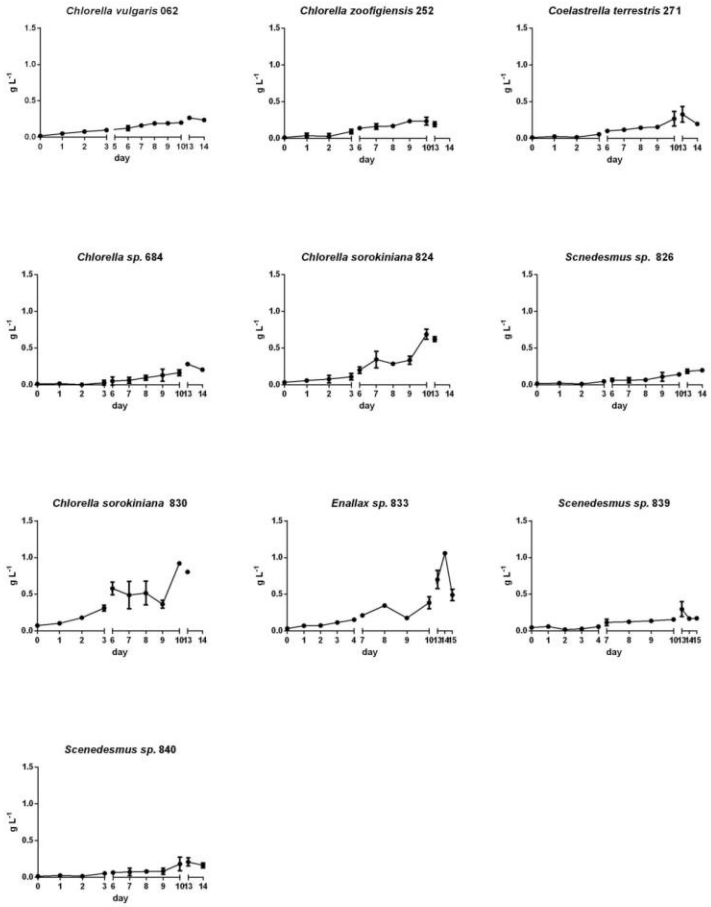

Figure S1. Growth curves of Chlorophyta. Cells were grown in 50 mL of BBM medium at 40°C with a light intensity of 300 $\mu mol_{photons}$ m^{-2} s^{-1} and O.D. was measured every day for 14 day. Growth is expressed as a function of time.

Appendix F

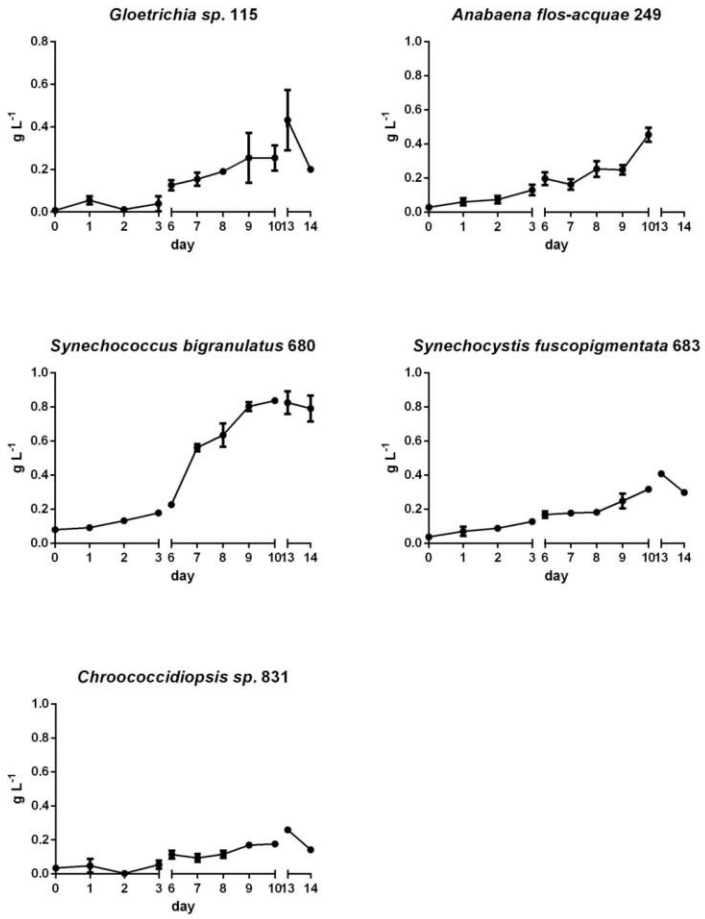

Figure S2. Growth curves of Cyanobacteria. Cells were grown in 50 mL of BG11 medium at 40°C with a light intensity of 300 $\mu mol_{photons}$ m^{-2} s^{-1} and O.D. was measured every day for 14 day. Growth is expressed as a function of time.

Appendix F

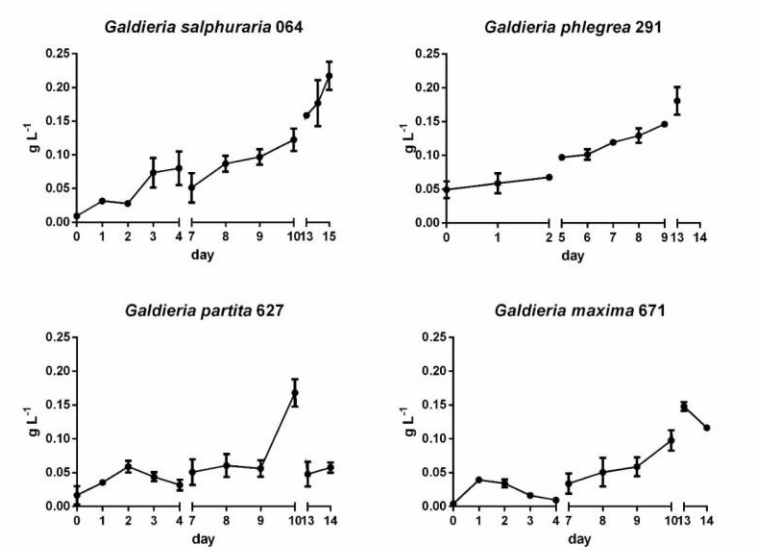

Figure S3. Growth curves of Rhodophyta. Cells were grown in 50 mL of Allen medium at 40°C with a light intensity of 300 $\mu mol_{photons}$ m^{-2} s^{-1} and O.D. was measured every day for 14 day. Growth is expressed as a function of time.

Appendix F

Table S1. Pigments content of all strain expressed as mg of extract on g of dry weight biomass

Microalgal source	Carotenoids (mg g^{-1} D.W. biomass)	Chlorophyll *a* (mg g^{-1} D.W. biomass)	Chlorophyll *b* (mg g^{-1} D.W. biomass)
	Chlorophyta		
C. zoofigiensis 252	4.9 ± 1.1	8.6 ± 2.3	2.0 ± 0.8
Scenedesmus sp. 826	11.3 ± 0.7	19.5 ± 3.9	6.3 ± 1.8
Scenedesmus sp. 840	6.7 ± 0.6	12.8 ± 1.0	3.5 ± 0.8
Chlorella sp. 684	12.1 ± 5.2	6.9 ± 0.8	10.9 ± 1.2
C. terrestris 271	3.1 ± 0.3	15.2 ± 1.4	3.5 ± 1.2
Scenedesmus sp. 839	10.3 ± 2.2	28.9 ± 5.2	9.8 ± 0.8
C. sorokiniana 824	1.6 ± 0.2	4.1 ± 0.8	2.0 ± 0.8
C. vulgaris 062	2.1 ± 0.3	6.3 ± 0.2	2.2 ± 0.4
C. sorokiniana 830	4.5 ± 0.7	6.2 ± 0.6	2.8 ± 1.2
Enallax sp. 833	20.7 ± 3.4	49.8 ± 3.2	15.0 ± 1.1
	Cyanobacteria		
Chroococcidiopsis sp. 831	2.2 ± 0.3	3.0 ± 0.6	n.d.
Gloetrichia sp. 115	2.6 ± 1.1	3.0 ± 0.6	n.d.
S. bigranulatus 680	5.4 ± 1.0	11.1 ± 3.2	n.d.
S. fuscopigmentata 683	5.1 ± 0.6	9.3 ± 2.8	n.d.
A. flos-acquae 249	2.2 ± 0.7	8.7 ± 0.8	n.d.
	Rhodophyta		
G. partita 627	1.6 ± 0.5	1.2 ± 0.2	n.d.
G. phlegrea 291	1.8 ± 0.5	1.0 ± 0.4	n.d.
G. maxima 671	2.0 ± 0.4	1.8 ± 0.3	n.d.
G. sulphuraria 064	2.5 ± 0.5	2.2 ± 0.2	n.d.

Appendix F

Online Resource Table S2 List of pigments identified in *Enallax sp.*, *S. bigranulatus*, *G. sulphuraria*, with related retention time and absorption peak at different wavelength (nm).

Peak number	Pigment	Retention time (min)	λ (nm)		
		Enallax sp.			
1	xanthophyll	6.563	417	**440**	469
2	violaxanthin	7.278	416	**439**	468
3	xanthophyll	9.737	-	**449**	472
4	lutein	9.908	421	**445**	473
5	xanthophyll	11.135	416	**440**	466
6	chlorophyll b	12.313	**467**	601	653
7	chlorophyll b*	12.845	**463**	601	653
8	chlorophyll a*	14.105	**426**	617	664
9	chlorophyll a	14.445	**432**	618	665
10	chlorophyll a*	14.727	**432**	618	666
11	β-carotene	16.872	426	**450**	476
		S. bigranulatus			
1	xanthophyll	7.498	426	**449**	477
2	xanthophyll	8.648	427	**450**	477
3	zeaxanthin	9.758	426	**450**	477
4	xantophyll	10.445	422	**444**	471
5	xanthophyll	11.302	422	**444**	470
6	xanthophyll	12.147	421	**445**	471
7	chlorophyll a*	14.129	428	**618**	647
8	chlorophyll a	14.472	**432**	618	665
9	xanthophyll	16.719	422	**445**	471
10	β-carotene	17.055	426	**450**	476

Appendix F

Peak number	Pigment	Retention time (min)	λ (nm)		
		G. sulphuraria			
1	zeaxanthin	12.184	426	**450**	477
2	xanthophyll	14.174	421	**444**	471
3	chlorophyll a	14.476	**430**	616	664
4	chlorophyll a*	14.696	421	**615**	655
5	chlorophyll a*	15.936	404	**616**	666
6	phaeophytin	16.268	**407**	502, 533, 609	665
7	phaeophytin	16.740	**408**	502, 533, 609	665
8	xanthophyll	16.929	420	**444**	471
9	β-carotene	12.184	427	**450**	477

Values in bold represent the maximum adsorption wavelength for each pigment. The symbol * means isomers. The number of each pigment reflects the sequence of elution on chromatograms (Figure 3).

Appendix G

Journal of Colloid and Interface Science 624 (2022) 400–410

Contents lists available at ScienceDirect

Journal of Colloid and Interface Science

journal homepage: www.elsevier.com/locate/jcis

Non-covalent small molecule partnership for redox-active films: Beyond polydopamine technology

Rita Argenziano [a], Maria Laura Alfieri [a], Youri Arntz [b], Rachele Castaldo [c], Davide Liberti [a], Daria Maria Monti [a], Gennaro Gentile [c], Lucia Panzella [a], Orlando Crescenzi [a], Vincent Ball [b], Alessandra Napolitano [a,*], Marco d'Ischia [a]

[a] Department of Chemical Sciences, University of Naples "Federico II", Via Cintia 21, I-80126 Naples, Italy
[b] Faculté de Chirurgie Dentaire, Université de Strasbourg, 8 rue Sainte Elisabeth, Strasbourg 67000, France
[c] Institute for Polymers, Composites and Biomaterials – National Research Council of Italy, Via Campi Flegrei, 34, Pozzuoli, NA 80078, Italy

GRAPHICAL ABSTRACT

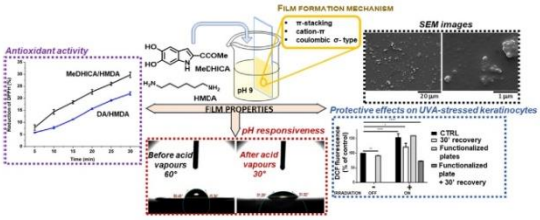

ARTICLE INFO

Article history:
Received 26 March 2022
Revised 12 May 2022
Accepted 19 May 2022
Available online 22 May 2022

Keywords:
Redox active films
UVA absorbing films
Yellowish homogeneous films
pH dependent hydrophobicity
Non-covalent interactions
Methyl 5,6-dihydroxyindole-2-carboxylate
Hexamethylenediamine
Film component structural analysis
Reducing activity
UV stressed HaCaT cells

ABSTRACT

Hypothesis: The possibility to use hexamethylenediamine (HMDA) to impart film forming ability to natural polymers including eumelanins and plant polyphenols endowed with biological activity and functional properties has been recently explored with the aim to broaden the potential of polydopamine (PDA)-based films overcoming their inherent limitations. 5,6-dihydroxyindole-2-carboxylic acid, its methyl ester (MeDHICA) and eumelanins thereof were shown to exhibit potent reducing activity.
Experiments: MeDHICA and HMDA were reacted in aqueous buffer, pH 9.0 in the presence of different substrates to assess the film forming ability. The effect of different reaction parameters (pH, diamine chain length) on film formation was investigated. Voltammetric and AFM /SEM methods were applied for analysis of the film redox activity and morphology. HPLC, MALDI-MS and ^{1}HNMR were used for chemical characterization. The film reducing activity was evaluated in comparison with PDA by chemical assays and using UV stressed human immortalized keratinocytes (HaCat) cells model.
Findings: Regular and homogeneous yellowish films were obtained with moderately hydrophobic properties. Film deposition was optimal at pH 9, and specifically induced by HMDA. The film consisted of HMDA and monomeric MeDHICA accompanied by dimers/small oligomers, but no detectable

* Corresponding author.
E-mail address: alesnapo@unina.it (A. Napolitano).

https://doi.org/10.1016/j.jcis.2022.05.123
0021-9797/

Appendix G

MeDHICA/HMDA covalent conjugation products. Spontaneous assembly of self-organized networks held together mainly by electrostatic interactions of MeDHICA in the anion form and HMDA as the dication is proposed as film deposition mechanism. The film displayed potent reducing properties and exerted significant protective effects from oxidative stress on HaCaT.

1. Introduction

The complex interplay of physical and chemical processes underlying mussels' ability to adhere to rocks underwater has prompted a huge body of research aimed at translating the peculiar structural motifs of catechol- and amine-rich foot proteins in the byssus proteins into viable film forming systems for surface functionalization and other applications in materials science [1–5]. Most of the scientific and technologically-oriented research in the field of wet adhesion in the past decade was driven by the discovery of polydopamine (PDA), a black eumelanin-like polymer produced by autoxidation of dopamine at pH 8.5–9.0 under aerobic conditions [6–11]. Extensive studies have led to the conclusion that the unusual adhesive properties of PDA are due to a combination of cation-π and π-stacking interactions involving protonated amine groups and electron-rich aromatic moieties properly assembled into oligomeric scaffolds of variable molecular size and redox state [12–14].

PDA-based technological and nanotechnological applications have pervaded virtually every area of surface science. Recent studies have further expanded the field of applications of polydopamine films including notably corrosion protection ability of steel surfaces [15–17] and membrane surface modification for filtrations purposes [18–20].

Even more diverse are the use of PDA in biomedicine, ranging from stimulus responsive drug delivery [21,22] to photothermal therapy against cancer [23,24] and enzyme immobilization [25].

Though the technology of PDA-based films is still attracting much attention, studies have appeared in the literature focused on the development of alternate mussel-inspired strategies such as the possibility to impart film forming ability to natural polymers including eumelanins and polyphenol plant materials endowed with important biological activity and functional properties. These strategies aim at overcoming some limitations inherent to the PDA methodology [26] such as the use of a toxic monomer, the need for high dopamine concentrations (>10 mM) and oxidants inducing polymerization, the dark color of the films, the abundant precipitate responsible for massive compound waste, and difficulties in controlling film thickness and properties [27–29].

More convenient options based on use of safer and less expensive polyphenols, such as caffeic acid, gallic acid, 3,4-dihydroxy-L-phenylalanine (DOPA), and other natural or synthetic catechols [30–32] have been explored to obtain functional biocompatible thin films. With most of the catechol precursors, which were generally devoid of intrinsic adhesive properties on polymerization, including dopamine at very low concentrations,[29] film deposition required the addition of hexamethylenediamine (HMDA), a long chain diamine enabling film deposition during catechol polymerization [33–35]. In all these studies, it was suggested or assumed that HMDA gives rise to intermolecular amine-quinone condensation processes leading to highly cross-linked oligomer structures. Interestingly, the copolymerization of varied catechol (amine)s and functional nucleophilic additives was found to give rise to nano-coatings on various surfaces including plastic, metal, glass and polymers with tailored chemical and physical properties, opening new opportunities for the development of novel and versatile functional biomimetic materials for a range of applications [36,37].

A paradigm shift in current concepts of mussel-inspired adhesion was prompted by a report in which the key motifs borrowed from the interfacial adhesive mussel foot proteins were assembled into a low-molecular-weight, one-component adhesive system combining catechol with hydrophobic and electrostatic functional groups [38]. This relatively small molecular system was found to adhere to a range of surfaces generating a smooth thin layer and thus considerably simplifying bio-inspired themes for wet adhesion based on PDA-like systems of huge chemical complexity.

The potential interest of such small tailored molecular systems as prototypes for a novel class of adhesives was corroborated by several observations in the literature including, as a representative example, a most recent one on supramolecular adhesives from low-molecular-weight monomers [39]. This latter featured aromatic catechol ether rings tethered by polyether chains in a star-shaped assembly. Compared with polymeric adhesive materials of the PDA-type, supramolecular adhesive materials had to contend with competing effects from water when applied to wet surfaces or even under water, for which rational design rules are still lacking [39]. The main requirements of a synergistic cation–π and hydrogen bonding interactions of antifouling zwitterions and mussel-inspired binding moieties were exemplified by a recent paper [40] reporting single-molecule force spectroscopy (SMFS) between DOPA and zwitterionic molecules of opposite dipole orientations, such as zwitterionic 2-methacryloyloxyethyl phosphorylcholine (MPC). The strong MPC–DOPA interaction could be attributed to the synergy of cation–π interactions and hydrogen bonding.

Based on preliminary observations indicating that HMDA specifically enables substrate-independent film deposition from 5,6-dihydroxyindole (DHI), a key monomer precursor in the biosynthesis of eumelanin polymers, at pH 9.0 in aqueous buffer, [41] we directed our attention to assessing whether other eumelanin precursors or derivatives could be exploited for film formation compliant to the mussel-inspired adhesion paradigm. In previous studies we reported that eumelanins obtained by oxidation of the other major biosynthetic precursor 5,6-dihydroxyindole-2-carboxylic acid (DHICA) show higher free radical scavenging activity with respect to those prepared from DHI, and that these properties are even more marked in eumelanins from the methyl ester derivative 5,6-dihydroxyindole-2-carboxylic acid methyl ester (MeDHICA) [42,43]. Such differences have been rationalized in terms of the structural and π-electron features of these materials as deduced by spectroscopic analyses [42,44,45].

On this basis we focused on the oxidation of DHICA and its derivative MeDHICA in the presence of HMDA in the perspective of obtaining functional films.

Herein we disclose, to the best of our knowledge, an unprecedented example of mussel-inspired reducing film-forming system hinging on a non-covalent small-molecule partnership between HMDA and 5,6-dihydroxyindole-2-carboxylic acid methyl ester. The present study provides a new strategy overcoming some limitations inherent to the widely used PDA film forming technology

Appendix G

and describes the easy access to films with superior reducing properties. Indeed, the system differs from PDA and other underwater adhesives from catechols in that it does not require extensive polymerization, but only a partial reactivity-controlled conversion of the monomer to low molecular weight oligomers which can produce, in combination with the monomer and HMDA, thin, light-colored films with potent reducing properties and redox responsive behavior.

2. Experimental

2.1. Materials

HMDA, 1,2-ethylenediamine, 1,4-butanediamine, 1,12-dodecanediamine, 1,10-decanediamine, butylamine, lysine, dopamine hydrochloride, pyridine, 6-amino-1-hexanol, tetrabutylammonium hydrogen sulfate, acetic anhydride, 2,2-diphenyl-1-picrylhydrazyl (DPPH), iron chloride (III) hexahydrate, 2,4,6-tri(2-pyridyl)-s-triazine (TPTZ), 2,2′-azino-bis(3-ethylbenzothiazoline-6-sulfonic acid) (ABTS), potassium persulfate and 2′,7′-dichlorofluor escein diacetate (H_2DCFDA) were purchased by Sigma-Aldrich. MeDHICA [43] and DHI [46] were prepared as reported. 4,4′-MeDHICA and 4,7′-MeDHICA dimers were obtained by oxidation of MeDHICA in the presence of copper sulfate and purified by preparative HPLC (see SI for details). Human immortalized keratinocytes (HaCaT) were purchased from Innoprot (Derio, Spain).

2.2. Methods

UV–vis spectra were run on a V-730 Jasco instrument. Quartz substrates were cleaned by soaking in a piranha solution (96% H_2SO_4/30% H_2O_2 5:1 v/v) overnight, rinsed with distilled water and dried under vacuum.

Water contact angle analyses were performed using a contact angle goniometer (Digidrop-gbx, France) equipped with video capture. 1 μL of distilled water was dropped on the air side surface of the substrate.

Quartz Crystal Microbalance measurement were performed with a quartz crystal microbalance-dissipation (QCM-D) system from Q-Sense (Göteborg, Sweden) (see SI for details).

^{1}H/^{13}C NMR spectra were recorded in methanol d_4 or DMSO d_6 at 400/100 MHz on a Bruker spectrometer. ^{1}H,^{1}H COSY, ^{1}H,^{13}C HSQC and ^{1}H,^{13}C HMBC were run at 400 MHz using Bruker standard pulse programs. Chemical shifts are given in ppm.

HPLC analyses were performed on an Agilent 1100 binary pump instrument with UV–vis detector (see SI for details).

Positive Reflectron MALDI spectra were recorded on a AB Sciex TOF/TOF 5800 instrument (see SI for details).

DLS measurements were performed using a home-made instrument, composed of a Photocor compact goniometer, an SMD 6000 Laser Quantum 50 mW light source (Quantum Laser, Heaton Mersey, UK) operating at 532.5 nm, a photomultiplier (PMT-120-OP/B), and a correlator (Flex02-01D) from Correlator.com.

AFM analyses were run with a commercial microscope (BioCATALYST, Bruker, Santa Barbara, CA, USA) by contact mode and in liquid phase (see SI for details).

The electrochemical characterization of the films deposited from solution was performed by cyclic voltammetry and electrochemical impedance spectroscopy using a three-electrode set-up (Chl 604B, CH Instruments, Houston, Texas) (see SI for details).

Bright Field Transmission Electron Microscopy (TEM) analysis was performed by a FEI TECNAI G12 Spirit-Twin (120 kV, LaB6) microscope equipped with a FEI Eagle 4 k CCD camera (Eindhoven, The Netherlands). The specimens were collected by gently dipping holey carbon copper grids into the MeDHICA/HDMA-mixture (1:1.5 M ratio) and into the MeDHICA mixture at 30 min and 4 h reaction time. Prior to observations, the collected specimens were air dried.

Morphological analysis was performed on MeDHICA/HDMA films applied onto glass substrates after 24 h reaction in carbonate buffer. The films were observed by a FEI Quanta 200 FEG scanning electron microscope (SEM) with a secondary electron detector at 10 kV accelerating voltage in high vacuum mode. Before the analysis the samples were sputter coated with a thin Au/Pd layer. SEM micrographs were analysed by means of the public domain software ImageJ (release 1.43u).

DFT calculations were performed as described in the SI.

2.3. Oxidation of MeDHICA in the presence of amines/additives

Procedure for film preparation. MeDHICA dissolved in the minimal amount of DMSO was added to a solution of the appropriate amine, diamine or other additive in 0.05 M carbonate buffer pH = 9.0 to a final concentration of 1 mM, at an indole/additive molar ratio of 1:1.5, and the mixture was taken under vigorous stirring. Quartz substrates or glass substrates were dipped into the reaction mixture and left under stirring for different time periods (6–24 h), then rinsed with distilled water in an ultrasonic bath, dried and analyzed by UV–vis spectrophotometry (only quartz slides). Coating of other materials including plastics, aluminum slides or glass substrates was run under the same conditions. Different MeDHICA/HMDA molar ratios were investigated from 0.5:1 up to 1:5. In control experiments the reaction was run in the absence of amines. In other experiments, the 4,4′-MeDHICA dimer was used instead of MeDHICA using HMDA at an indole/additive molar ratio of 1:1.5 for coating of quartz slides.

Film analysis. For structural analysis of the films the coated quartz slides (around 3 square centimeters) were treated with DMSO (2 mL) with ultrasound treatment and the resulting solutions were subjected to HPLC and MALDI MS analysis. For proton NMR analysis the DMSO solutions are taken to dryness and subjected to acetylation with acetic anhydride /pyridine (1 mL/100 μL) overnight. After addition of methanol and removal of the volatile components the residue was taken up in methanol d_4.

2.4. Reducing property assays

The coated glass substrates were obtained by dipping glass slides into a solution of MeDHICA, DHI or dopamine (DA) in the presence of HMDA at a catechol/amine molar ration of 1:1.5 over 24 h. The slides are then rinsed with distilled water in an ultrasonic bath, and exposed to the assay medium as described below.

Ferric reducing/antioxidant power (FRAP) assay [47]. The glass substrates with the MeDHICA/HMDA films were immersed in 20 mL of a solution containing $FeCl_3$ (20 mM) and 2,4,6-tris(2-pyridyl)-s-triazine (10 mM) in 0.3 M acetate buffer (pH 3.6) at 10:1:1 v/v/v ratios. The absorbance at 593 nm was measured periodically over 1 h.

2,2-diphenyl-1-picrylhydrazyl (DPPH) assay [48]. The glass substrates with the MeDHICA, DHI or DA/HMDA films were immersed in a solution of 50 μM DPPH in methanol (20 mL) and the reducing power was evaluated by UV–vis spectroscopy measuring the absorbance at 515 nm every 5 min over 1 h.

2,2′-Azino-bis(3-ethylbenzthiazoline-6-sulfonic acid) (ABTS) assay [49]. The 2,2′-azino-bis(3-ethylbenzothiazoline-6-sulfonic acid) radical cation ($ABTS^•$) was produced as described by reacting ABTS with potassium persulfate. The $ABTS^•$ solution was diluted with methanol to an absorbance of 0.5 at 745 nm. The glass substrates with the MeDHICA/HMDA film were immersed in this solution and the absorbance at 745 nm was measured periodically over 1 h.

Appendix G

All above-described experiments were run in triplicate.

2.5. UVA irradiation of HaCat cells and ROS levels determination

35 mm eukaryotic cell plates that had previously been rinsed with a 1:1 water/ isopropanol mixture were coated by immersion into a solution of MeDHICA and HMDA at 1:1.5 M ratio as described above. After 24 h, the plates were extensively rinsed with distilled water in an ultrasonic bath and sterilized by exposure to a UV lamp (15 min). Cells were plated onto dishes coated with MeDHICA/HMDA films and uncoated dishes at a density of $3.5x10^4$ cells/cm^2, and irradiated by UVA light for 10 min (100 J/cm^2) [50]. After a recovery time of 30 min, ROS levels were determined by H_2DCFDA assay (for details see SI).

3. Results and discussion

In a first series of experiments, the HMDA-modified dip-coating protocol previously reported for eumelanin film deposition from DHI [41] was extended to the alternate eumelanin precursor DHICA. In this procedure a solution of the indole at 1 mM in 0.05 M carbonate buffer pH = 9.0 is taken under stirring in air in the presence of HMDA. Quartz slides are dipped into the reaction mixture and film formation is monitored periodically by UV–vis analysis. In the case of DHICA no detectable film formation was observed under all the conditions tested despite precipitation of a dark eumelanin-type polymer (Fig. S1A). Notably, when MeDHICA, recently reported as a potent antioxidant, [43,50] was tested at pH 9.0 in the presence of HMDA the formation of a light-colored precipitate with deposition of a yellowish film on the quartz substrate was observed featuring a well-defined absorption maximum centred at 340 nm (Fig. S1A).

A systematic investigation of the reaction conditions (Fig. S1B) based on spectrophotometric analysis of the films obtained with various molar excess of HMDA (up to 5 M equivalents) indicated maximal film deposition from MeDHICA using HMDA at 1.5 M equivalents. Accordingly, 1 mM MeDHICA and 1.5 mM HMDA in 50 mM carbonate buffer at pH 9.0 were selected as optimal reaction conditions.

Under these conditions after 6 h the film showed an intense absorption maximum at 340 nm that increased over time reaching a maximum at 24 h. No UV-detectable species was deposited on quartz in the absence of the diamine (Fig. S1C). Film deposition from MeDHICA/HMDA was observed also on materials other than quartz, including plastic surfaces and metals (Fig. S1D).

Kinetic determination of MeDHICA/HMDA film deposition over 1 h was carried out using the Quartz Crystal Microbalance (QCM-D) methodology. The MeDHICA/HMDA solution was introduced in the cell and let it flow for about 1 h monitoring the frequency changes (Fig. S2A) and the dissipation changes (Fig. S2B) over time. Based on the observation that the frequency change (Δf) of the oscillating quartz should be linearly related to its mass change, provided the film is rigid and assuming a homogeneous mass density for melanin-like material (1.2 g/cm^3), the film thickness was estimated using the Sauerbrey equation from the QCM-D data and was found to be 8.7 nm after 1 h of deposition [51]. This indicated that film deposition starts immediately after mixing of the reagents.

Film deposition from the MeDHICA/HMDA system was found to depend on pH, being maximal under moderately alkaline conditions (pH = 9.0) and markedly lower at pH 7.0 or ~~higher~~ pH 10.0 (Fig. S3A). The marked decrease in the extent of film formation at pH lower than 9.0 could be explained considering the slower rate of MeDHICA oxidation, while at pH higher than 9 HMDA deprotonation and ammonium ion depletion may represent the critical factor. Besides pH, the structural characteristics of the amine component proved also to be critical for film deposition. Either monoamines (butylamine, 6-aminohexanol), ammonium salts (tetrabutylammonium) or diamines with chains shorter or longer than 6 carbons proved to be less effective or ineffective in inducing film deposition (Fig. S3B).

3.1. Morphological, structural and electrochemical characterization

Scanning electron microscopy (SEM) images of the film obtained under the described conditions with 1.5:1 excess HMDA at 24 h reaction time showed a regular and homogeneous morphology (Fig. 1A). Smooth regions characterized by a fine substructure were evident. Nanoparticles with size lower than about 250 nm and sparse aggregates were observed.

Atomic Force Microscopy (AFM) analysis of the MeDHICA/HMDA film allowed to estimate thickness of 37 ± 5 nm and roughness of 13.8 nm (Fig. S4).

Compared to a reference PDA film, the film exhibited a relatively high water-contact angle (WCA) of about 60 ± 1 versus 37.0 ± 0.3, indicating a more hydrophobic character (Fig. 1Bi). After exposure to HCl vapors, the WCA value decreased to 31.2 ± 0.3, suggesting an increase in hydrophilicity (Fig. 1B ii), likely due to an increase of ammonium ion from HMDA with concomitant protonation of MeDHICA-derived catechol components. However, no significant morphological changes were associated to the exposure of the surface of the film to HCl vapors (Fig. S5).

The MeDHICA/HMDA films did not show detectable modification of the UV–vis absorption spectra upon exposure to aqueous sodium borohydride, consistent with the lack of a significant proportion of reducible quinonoid structures. However, ammonia vapors caused an appreciable darkening of the film color accompanied by almost complete loss of the absorption maximum at 340 nm after 48 h and concomitant development of a broad absorption covering the visible region (Fig. S6A), compatible with base-promoted oxidative conversion of film components to polymeric eumelanin-type material. Similar changes in the UV–vis absorption spectrum of MeDHICA/HMDA films were observed by irradiation with a UV lamp at 320 nm over 1 h (Fig. S6B) suggesting a potential application of the films for oxidant and UV sensing. Exposure to HCl vapors caused a hypsochromic shift of the absorption at 340 nm to 320 nm likely resulting from protonation of the ionized catechol function of MeDHICA and related species present in the film (Fig. S6C). By immersing the film deposited on quartz in 2:1 methanol/0.1 M aqueous HCl a significant decrease of the absorbance at 320 nm was rapidly observed (Fig. S6D).

Consistent with the above observations, suggesting a high content of reduced catechol units in the films, cyclic voltammetry (CV) measurements showed an irreversible oxidation–reduction wave in the absence of the external redox probe (Fig. 2A) indicating that the film was electroactive. In addition, the MeDHICA/HMDA film on the electrode surface proved to be virtually impermeable to potassium hexacyanoferrate (Fig. 2B), in agreement with the impedance spectrum (Fig. 2C). In particular, the film displayed a high resistance to diffusion of the redox probe to the electrode in the low frequency domain as shown by the linear part of the Nyquist plot (Fig. 2C) [52].

3.2. Chemical characterization of the film

The chemical composition of the MeDHICA/HMDA films was investigated by dissolving the films deposited on the quartz surface with DMSO with the aid of an ultrasound treatment. After this treatment the quartz slide showed no appreciable absorbance in all UV–Vis range indicating complete dissolution of the film. The chromatographic profile of the resulting DMSO solution, analyzed by

Appendix G

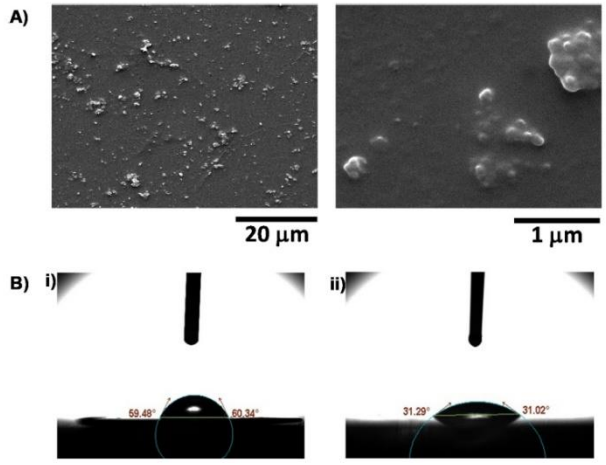

Fig. 1. (A) SEM images of films formed onto glass substrates from MeDHICA/HMDA reaction mixtures. (B) WCA of the MeDHICA/HMDA film (i) before and (ii) after exposure to HCl vapors.

HPLC with UV detection, showed the presence of MeDHICA (R_T = 12-min) in small amounts together with higher amounts of other components, including the 4,4′-MeDHICA dimer (4,4′-biindolyl) and 4,7′-MeDHICA dimer (4,7′-biindolyl) at R_T = 16 and 18 min, respectively, as identified by comparison with authentic standards (Fig. 3A, B). Other more retained components could tentatively be identified as higher oligomers likely tetramers based on comparison with the elution profile of the mixture obtained from oxidation of the 4,4′-biindolyl (Fig. S7). Following 24 h exposure to ammonia vapors, similar washing of the film with DMSO consistently indicated almost complete consumption of the monomer and dimers with increase of higher oligomers (Fig. S8).

MS analysis in the MALDI mode of the film formed on the MALDI plate and extensively washed with water indicated a well detectable pseudomolecular ion peak for the monomer at *m/z* 208 and a pattern of pseudomolecular peaks $[M + Na]^+$ at *m/z* 435, 640, 845 corresponding to MeDHICA oligomers up to tetrameric species. In addition, pseudomolecular ion peaks attributable to HMDA were apparent (Fig. S9, Table S1).

The presence of MeDHICA oligomers and intact HMDA in the mixture was also demonstrated by proton NMR analysis of the film following solubilization in DMSO and acetylation. Signals due the acetylated HMDA at 3.2, 1.90, 1.5 and 1.3 ppm were discernible together with resonances due to methyl groups of MeDHICA oligomers in the 3.8–4.0 ppm region and the relevant aromatic protons in the sp^2 region. The peaks at 6.63 and 7.42 ppm attributable to the 4,4′-biindolyl [43] (Fig. S10) were well discernible, while the other signals confirmed the presence of closely related oligomers (Fig. 3C).

Combined NMR and HPLC analysis allowed to conclude that the MeDHICA-derived pool of species consists of the monomer and of dimers or small oligomers as major components. Apparently, no evidence was obtained for the presence of species derived from coupling of HMDA to MeDHICA or its oligomers. In separate experiments a sample of the 4,4′-dimer of MeDHICA was allowed to autoxidize under the same conditions used for the monomer in the presence of HMDA. A well detectable film was obtained, closely resembling that from the monomer (Fig. S11). This latter observation would support a contribution of the dimers to the processes of self-organization and self-assembly underlying film formation.

3.3 Chemical, kinetic and morphological analysis of the MeDHICA/HMDA interaction

To elucidate the role of HMDA in film deposition, we looked for the presence of covalent conjugates between MeDHICA or its oligomers and the diamine. Analysis of the ethyl acetate-extractable fraction of the MeDHICA/HMDA reaction mixture after 24 h oxidation provided evidence for residual starting material in the organic phase and no other well defined absorbing species in the aqueous layer. Direct analysis of the reaction mixture at shorter reaction times was then attempted by adding sodium dithionite at various times to stop the reaction. Aliquots were then withdrawn, taken to dryness and acetylated with acetic anhydride and pyridine overnight. After removal of the volatiles the residue was analysed by gradient HPLC. Under these conditions, the only detectable species were MeDHICA and dimeric products, as observed also in a control mixture obtained from MeDHICA oxidation in the absence of HMDA. On this basis it can be concluded that the bulk of the MeDHICA/HMDA oxidation mixture reflects that of the film as described above.

In separate experiments HMDA was found to exert a marked slowing effect on the rate of MeDHICA oxidation/consumption and dimer accumulation (Fig. S12A). After 3 h under stirring in air at pH 9.0 in the presence of HMDA a 63% residual MeDHICA was determined while in the absence of the diamine the remaining starting material was around 28% (Fig. S 12A) and the consumption was complete after 6 h. Consistently formation yields of 4,4′-biindolyl and 4,7′-biindolyl was slowed down in the presence of

Appendix G

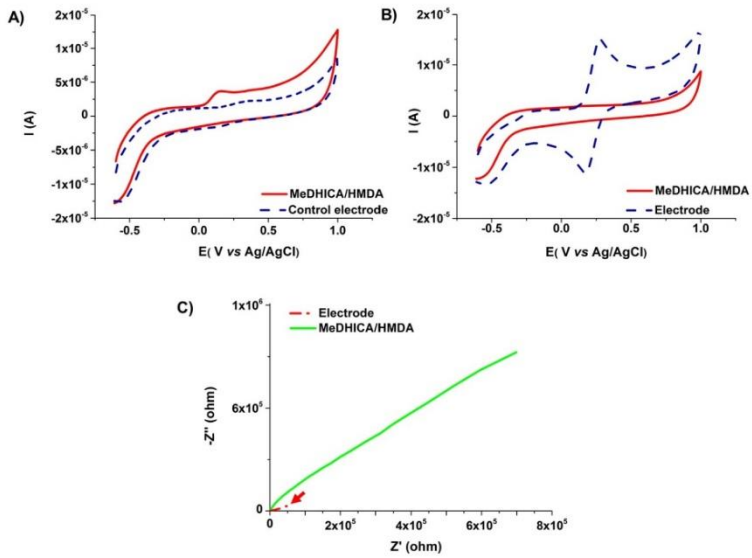

Fig. 2. Electrochemical analysis of the MeDHICA/HMDA film deposited on amorphous carbon working electrodes. (A) Capacitive curves of the film after 1 h dipping of the electrode in the MeDHICA/HMDA mixture in carbonate buffer at pH 9.0. (B) CV curve of potassium hexacyanoferrate as a redox probe on the pristine electrodes (dashed lines) and the same electrodes covered with the MeDHICA/HMDA film. (C). Electrochemical impedance spectra of the MeDHICA/HMDA film deposited on carbon working electrodes vs pristine electrode.

HMDA in the first 3 h after which time their consumption becomes predominant (Fig S12B).

The origin of this effect is unclear, but may be related to non-covalent interactions *e.g.* lowering the oxidation potential of MeDHICA. The relevance of the oxidation kinetics to film deposition was thus investigated by promoting the fast oxidation of MeDHICA in presence of HMDA with potassium ferricyanide. After 30 min no film deposition was detected on quartz by UV–vis spectrophotometer despite complete oxidation of the catechol. It is concluded that a slow rate of oxidative conversion of MeDHICA is crucial to ensure the coexistence of larger pools of intermediates with longer lifetimes and increased availability for non-covalent interactions, self-assembly and cross-linking inducing a high structural and redox diversity of the growing scaffolds. Film deposition would also benefit from the low tendency of MeDHICA to autoxidation compared to DHICA and DHI, ensuring a dominant catechol character of the film associated with chemical control over the oligomer growth process.

In subsequent experiments the effect of HMDA on the species produced by self-assembly of MeDHICA and related oligomers in carbonate buffer, pH 9.0, was investigated by Dynamic Light Scattering (DLS) analyses (Fig.S12C). Time evolution of the hydrodynamic diameter distributions associated to MeDHICA oligomer particles generated by the aerobic oxidation of the indole in the presence of HMDA indicated a higher growth rate of particle size in solution in comparison with that observed for the oxidation mixture of MeDHICA in the absence of HMDA. The hydrodynamic diameter attained the maximum value of 900 nm in 90 min in the presence of HMDA, whereas in the absence of the diamine the particle growth was much slower and did only reach the value of 450 nm after 24 h. This result would apparently suggest that the presence of the diamine favors aggregation possibly through non-covalent interactions with the oligomer species generated by aerobic oxidation of the indole.

Transmission electron microscopy (TEM) analysis of the MeDHICA/HMDA mixture (Fig. 4) clearly showed very good film-forming properties of the system. Indeed, when applied onto the TEM grid, the mixture formed a continuous very thin film embedding large nanoparticles with variable shape, most of them quasi-spherical, whose approximate size was in the range 50–150 nm (Fig. 4A, left panel). TEM observations at higher magnification (Fig. 4A, right panel) revealed the substructure of the film, characterized by the presence of homogeneously distributed domains with size below 5 nm. On the contrary, in absence of HMDA, the MeDHICA mixture produced a discontinuous film, whose thickness is much higher in comparison to that obtained from the MeDHICA/HDMA mixture, as shown by the low transparency of the film to the electron beam (Fig. 4B, left panel). In the small regions characterized by a thickness low enough to allow the analysis of the film at higher magnification (Fig. 4B, right panel), TEM images showed the substructure of the film with the presence of embedded nanodomains with lateral size between 5 and 20 nm, thus higher than that observed at the same magnification on the film obtained from the MeDHICA/HDMA mixture.

Appendix G

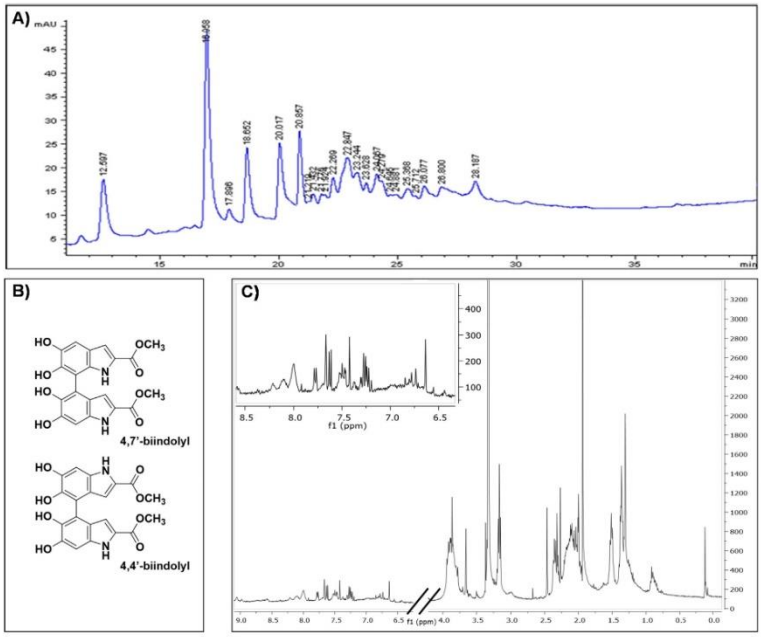

Fig. 3. (A) Elutographic profile of the MeDHICA/HMDA film dissolved in DMSO (Eluent: H_2O/acetonitrile 20–70% gradient, λ = 300 nm). (B) Structures of MeDHICA dimers. (C) ^{1}H NMR spectrum (methanol d_4) of the film dissolved in DMSO and subjected to acetylation treatment. Inset: aromatic resonance region.

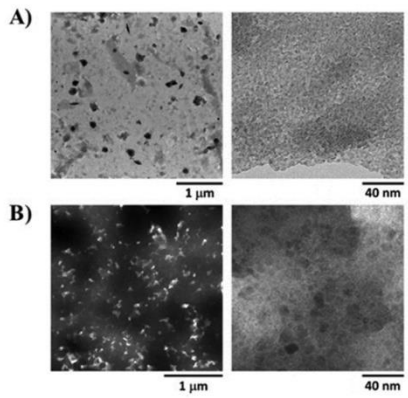

Fig. 4. Bright field TEM images of the reaction mixtures of MeDHICA in the presence (A) and in the absence (B) of HMDA in carbonate buffer pH 9.0 after 4 h.

3.4. Reducing properties of the MeDHICA/HMDA films and cell protection effects

In view of the potent reducing properties of MeDHICA and its polymer,[43,50,53] the films obtained by the MeDHICA/HMDA procedure were investigated for their reducing capacity in a common antiradical reducing assay *i.e.* the DPPH assay in comparison with the films obtained from DA and DHI in the presence of HMDA under the same reaction conditions that is with the catechol system at 1 mM, at pH 9 over 24 h. At this concentration DA and DHI in the absence of HMDA do not give rise to appreciable film formation and could not be included in the evaluation. The assay was run by dipping the coated substrates in the proper solution of DPPH. In all cases well detectable effects of the films were observed in the first 30 min, whereas after 1 h of contact no further discoloration of the DPPH solution was observed. All the films showed a good reducing activity (Fig. 5A) with a consumption of DPPH for the MeDHICA/HMDA system at 30% vs a value of 20% and 10% for DA and DHI, respectively. Moreover, in the case of the MeDHICA/HMDA system manifestation of the reducing activity was apparent from the marked darkening of the exposed film area (Fig. S13), on account of oxidative conversion of the MeDHICA units in the film to melanin-type scaffolds, as noted before.

Based on these results that highlighted a superior reducing potential of the MeDHICA/HMDA film with respect to other films

Appendix G

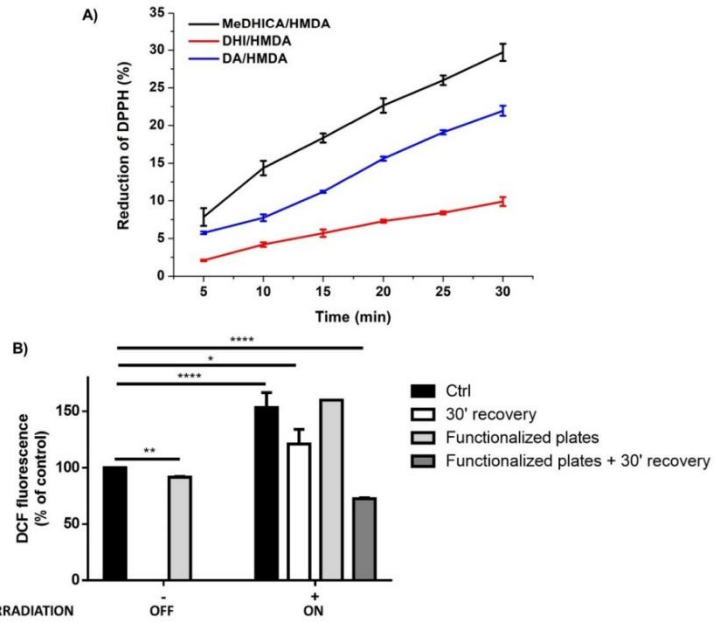

Fig. 5. (A) Kinetics of reduction DPPH (50 μM) of glass substrates coated with MeDHICA/HMDA, DA/HMDA or DHI/HMDA films. Shown are the results of triplicates ± SD. (B) Protection effect of MeDHICA/HMDA films on UVA-stressed HaCaT cells. MeDHICA/HMDA coated plates (grey bars) and unfunctionalized plates (black and white bars) were stressed by UVA radiations (100 J/cm^2) and intracellular ROS levels were measured by 2′,7′-dichlorodihydrofluorescein diacetate (H_2DCFDA). Measurements were taken immediately after irradiation and after 30 min recovery. Top lines indicate the significance of data compared (those connected by the segments) * indicates $p < 0.05$; ** indicates $p < 0.01$; *** indicates $p < 0.005$; **** indicates $p < 0.001$.

previously investigated different electron transfer assays, *i.e.* the FRAP assay, based on Fe (+3) reduction, and the ABTS radical reducing assay were run. Also, in this case the MeDHICA/HMDA film proved active with a well appreciable development of the absorption Fe^{2+}-TPTZ complex at 593 nm for the FRAP assay, and an around 15% reduction of ABTS over 30 min (Fig S14).

The MeDHICA/HMDA film was not toxic for HaCaT cells, as no difference in cell viability was observed between cells grown on coated wells with respect to those grown on unfunctionalized supports (data not shown). In further experiments, the ability of MeDHICA/HMDA films to protect cell cultures from oxidative stress conditions was evaluated. HaCaT cells, grown on either functionalized and unfunctionalized plates, were stressed by UVA, and then ROS levels were evaluated by the 2′,7′-dichlorofluorescin diacetate (H_2DCFDA) assay. Fig. 5B shows that, in the absence of irradiation, functionalization induces a modest, although significant ($p < 0.01$), reduction in ROS basal levels. After irradiation, a significant increase was observed, on both unfunctionalized (black bars, 1.5 fold increase, $p < 0.001$) and functionalized (light grey bars, 1.5 fold increase, $p < 0.005$) plates. Interestingly, after 30 min from stress, the functionalized plates showed a lower ROS level with respect to unfunctionalized plates. In particular, in the case of unfunctionalized plates, a 25% decrease of ROS levels (white bar, $p < 0.05$) was observed with respect to just stressed cells, whereas, in the case of functionalized plates, more than 50% decrease (dark grey bar, $p < 0.005$) was observed. Interestingly, ROS level reached for functionalized plates after irradiation, 30 min from stress, was lower than that obtained with non-irradiated cells (20% decrease, $p < 0.001$). The time needed for recovery of the cells from the irradiation stress (recovery time) was optimized in a preliminary set of experiments (not shown).

This result supports the marked reducing activity of eumelanins from MeDHICA in cell cultures, in agreement with previously reported data,[50] and points to MeDHICA/HMDA films as a valuable system for implementation of devices capable of protecting cells and likely tissues against the damages associated to oxidative stress conditions.

3.5. Computational studies

To test the efficiency of the postulated non-covalent interactions involved during film deposition, the general properties of MeDHICA, its anion as well as its one-electron (semiquinone) and two-electron (quinone) oxidation states in the most stable tautomeric forms were investigated both at the DFT and post Hartree-Fock levels (Table S2-S4). The results indicated predicted

Appendix G

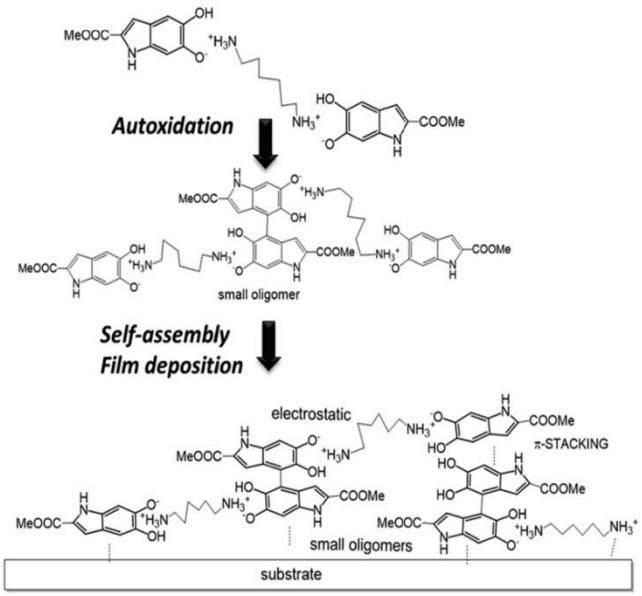

Fig. 6. Schematic outline of the process of MeDHICA/HMDA film deposition. This scheme highlights the proposed interplay of complementary non-covalent interactions between MeDHICA monomer and oligomers and the diprotonated form of HMDA.

pK_a values of 7.5 for MeDHICA at the 6-OH group and of 6.2 for the semiquinone at the 5-O position (average values of the two methods) (Table S5 and S6). Computed oxidation potentials of MeDHICA against catechol gave values incompatible with any significant oxidation by *o*-quinone both *in vacuo* and in water (Table S7).

3.6. Proposed model for MeDHICA-HMDA film deposition

The results so far reported highlighted some structural requirements and experimental factors that appear to be critical for MeDHICA-HMDA film deposition, including: (a) an aliphatic diamine with a sufficiently long and flexible aliphatic chain; (b) the ester derivative of DHICA; and (c) a slightly alkaline pH such as to ensure both the presence of HMDA in the diprotonated form (pK_{a1} = 10.76, pK_{a2} = 11.86)[54] and the extensive deprotonation of the acidic 6-OH group of MeDHICA (pK_a = 7.5) favored by the electronwithdrawing ester function.

The above species can be engaged in a range of non-covalent interactions, such as:

(a) cation- π involving the protonated primary amine groups of HMDA projecting toward the π-electron-rich system of the catechol ring of MeDHICA;[12,14].
(b) π -type (electrostatic), between the MeDHICA anion at the 6-OH group and one protonated primary amine groups of HMDA aligned on the plane of the oxygen lone pairs of the *o*-diphenolic functionality;[55].
(c) π -stacking, involving MeDHICA rings;
(d) hydrophobic, between the flat aromatic moieties and the long aliphatic chains of HMDA.

In addition, anion species from the medium, besides the anion from MeDHICA, may also combine with electron-poor sites of MeDHICA-derived scaffolds, *e.g. o*-quinone moieties or the ester carbonyl groups, via anion-π type interactions as additional contributors [56,57].

Overall, these non-covalent interactions from autoxidizing MeDHICA in the presence of HMDA would give rise to complex networks of self-assembling small-sized molecules held together by the long chain diamine tethers. In this regard, the optimal pH required for adhesion and film, *i.e.* pH 9.0, would be explained by the opportunity to ensure the coexistence of the diprotonated HMDA as tether and the MeDHICA anion as charged aromatic building block providing adhesive and cohesive platforms. Moreover, the chain length ensured by the six methylene groups of HMDA would allow to connect separate MeDHICA-based scaffolds via the efficient binding of the positively-charged ammonium ends to π -electron rich catechol moieties or negatively-charged phenoxide groups. In accord with this hypothesis, analysis of the ^{1}H NMR spectra from the DMSO washings of the MeDHICA/HMDA films invariably showed an approx. 0.5:1 ratio of HMDA versus MeDHICA-derived species, not affected by the initial molar ratio of the reagents (Fig. S15). In this context, the marked decrease in the WCA caused by exposure to gaseous HCl could be due to protonation of basic sites such as MeDHICA anion. Along the same line of reasoning, the absorbance decrease of the coated quartz slides

Appendix G

by acid washings are likely the result of the loss of the electrostatic forces primarily responsible for film adhesion.

A schematic illustration of the proposed model for film deposition from MeDHICA/HMDA is reported in Fig. 6.

4. Conclusions

The present study describes, to the best of our knowledge, the first example of mussel-inspired dip-coating technology based on an ionizable catechol compound, the methyl ester of the natural melanin precursor 5,6-dihydroxyindole-2-carboxylic acid, and a diprotonated adhesion mediator, hexamethylenediamine, for the functionalization of various surfaces with non-polymeric thin films and interfaces. It throws light on the non-covalent self-assembly of the monomer or very small oligomers as specifically mediated by the diamine to form an adhesive network of charged pair system.

Typical mussel-inspired adhesion protocols rely on the extensive oxidative polymerization of catechol compounds in the presence of amine components *via* both covalent cross-linking and non-covalent interactions causing formation in solution of many complex components and abundant precipitation of insoluble products.

The underwater MeDHICA/HMDA film-forming system disclosed herein differs from most of the catechol-based surface functionalization protocols as described also in recent papers [58,59] in a number of respects:

(a) it represents, the first example of mussel-inspired dip-coating technology based on the non-covalent self-assembly of small molecules driven by a catechol compound with a very poor tendency to oxidation; (b) it leads to light-colored and DMSO-washable films that lack some of the undesired properties of typical mussel-inspired films, including PDA films, such as a dark coloration.

The results presented are of both scientific and technological relevance, as they: (a) highlight the importance of electrostatic interactions between the catechol-diamine partners; (b) disclose a new adhesive material devoid of large polymeric aggregates like those that usually deposit on mussel-inspired coatings; (c) support the potential biomedical applications of the novel coatings displaying complete biocompatibility and potent reducing ability and cell protection properties; (d) suggest the potential use of the films for detection of oxidizing media or prolonged UV exposure following spectrophotometric determination of visible absorption changes.

In conclusion, these results extend the classical PDA paradigm for mussel-inspired surface functionalization to a novel tunable, low molecular weight variant based on structure-controlled catechol oxidation, which may stimulate further research aimed at the design of versatile next generation mussel-inspired films.

CRediT authorship contribution statement

Rita Argenziano: Investigation. **Maria Laura Alfieri:** Formal analysis, Validation. **Youri Arntz:** Investigation. **Rachele Castaldo:** Investigation. **Davide Liberti:** Investigation. **Daria Maria Monti:** Validation. **Gennaro Gentile:** Investigation. **Lucia Panzella:** Methodology. **Orlando Crescenzi:** Software. **Vincent Ball:** Validation. **Alessandra Napolitano:** Conceptualization, Writing – original draft. **Marco d'Ischia:** Conceptualization, Writing – original draft.

Declaration of Competing Interest

The authors declare that they have no known competing financial interests or personal relationships that could have appeared to influence the work reported in this paper.

Acknowledgements

This research was financially supported by 2017YJMPZN PRIN project.

Appendix A. Supplementary material

Supplementary data to this article can be found online at https://doi.org/10.1016/j.jcis.2022.05.123.

References

[1] F. Byette, I. Marcotte, C. Pellerin, Covalently crosslinked mussel byssus protein-based materials with tunable properties, Pept. Sci. 111 (2019) 1–8, https://doi.org/10.1002/pep2.24053.
[2] P.P. Anand, Y.S. Vardhanan, Computational modelling of wet adhesive mussel foot proteins (Bivalvia): insights into the evolutionary convolution in diverse perspectives, Sci. Rep. 10 (2020) 1–24, https://doi.org/10.1038/s41598-020-59169-y.
[3] Z. Wang, H.-C. Yang, F. He, S. Peng, Y. Li, L. Shao, S.B. Darling, Mussel-inspired surface engineering for water-remediation materials, Matter. 1 (2019) 115–155, https://doi.org/10.1016/j.matt.2019.05.002.
[4] C. Shao, M. Wang, L. Meng, H. Chang, B. Wang, F. Xu, J. Yang, P. Wan, Mussel-inspired cellulose nanocomposite tough hydrogels with synergistic self-healing, adhesive, and strain-sensitive properties, Chem. Mater. 30 (2018) 3110–3121, https://doi.org/10.1021/acs.chemmater.8b01172.
[5] P. Kord Forooshani, B.P. Lee, Recent approaches in designing bioadhesive materials inspired by mussel adhesive protein, J. Polym. Sci. Part A, Polym. Chem. 55 (2017) 9–33, https://doi.org/10.1002/pola.28368.
[6] J.H. Ryu, P.B. Messersmith, H. Lee, Polydopamine surface chemistry: a decade of discovery, ACS Appl. Mater. Interfaces 10 (2018) 7523–7540, https://doi.org/10.1021/acsami.7b19865.
[7] H. Liu, X. Qu, H. Tan, J. Song, M. Lei, E. Kim, G.F. Payne, C. Liu, Role of polydopamine's redox-activity on its pro-oxidant, radical-scavenging, and antimicrobial activities, Acta Biomater. 88 (2019) 181–196, https://doi.org/10.1016/j.actbio.2019.02.032.
[8] V. Ball, Polydopamine nanomaterials: recent advances in synthesis methods and applications, Front. Bioeng. Biotechnol. 6 (2018) 1–12, https://doi.org/10.3389/fbioe.2018.00109.
[9] M. d'Ischia, A. Napolitano, V. Ball, C.-T. Chen, M.J. Buehler, Polydopamine and eumelanin: from structure–property relationships to a unified tailoring strategy, Acc. Chem. Res. 47 (2014) 3541–3550, https://doi.org/10.1021/ar500273y.
[10] N.F. Della Vecchia, R. Avolio, M. Alfè, M.E. Errico, A. Napolitano, M. d'Ischia, Building-block diversity in polydopamine underpins a multifunctional eumelanin-type platform tunable through a quinone control point, Adv. Funct. Mater. 23 (2013) 1331–1340, https://doi.org/10.1002/adfm.201202127.
[11] Y. Guo, A. Baschieri, F. Mollica, L. Valgimigli, J. Cedrowski, G. Litwinienko, R. Amorati, Hydrogen atom transfer from HOO. to ortho-quinones explains the antioxidant activity of polydopamine, Angew. Chemie Int. Ed. 60 (2021) 15220–15224, https://doi.org/10.1002/anie.202101033.
[12] M.A. Gebbie, W. Wei, A.M. Schrader, T.R. Cristiani, H.A. Dobbs, M. Idso, B.F. Chmelka, J. Herbert Waite, J.N. Israelachvili, Tuning underwater adhesion with cation-π interactions, Nat. Chem. 9 (2017) 473–479, https://doi.org/10.1038/nchem.2720.
[13] S. Hong, Y. Wang, S.Y. Park, H. Lee, Progressive fuzzy cation-π assembly of biological catecholamines, Sci. Adv. 4 (2018) 1–11, https://doi.org/10.1126/sciadv.aat7457.
[14] M. Shin, Y. Park, S. Jin, Y.M. Jung, H.J. Cha, Two faces of amine-catechol pair synergy in underwater cation-π interactions, Chem. Mater. 33 (2021) 3196–3206, https://doi.org/10.1021/acs.chemmater.1c00079.
[15] F. Bahremand, T. Shahrabi, B. Ramezanzadeh, Development of a nanostructured film based on samarium (III)/polydopamine on the steel surface with superior anti-corrosion and water-repellency properties, J. Colloid Interface Sci. 582 (2021) 342–352, https://doi.org/10.1016/j.jcis.2020.08.039.
[16] Z. Chen, W. Yang, Y. Chen, X. Yin, Y. Liu, Smart coatings embedded with polydopamine-decorated layer-by-layer assembled SnO2 nanocontainers for the corrosion protection of 304 stainless steels, J. Colloid Interface Sci. 579 (2020) 741–753, https://doi.org/10.1016/j.jcis.2020.06.118.
[17] L. Cheng, C. Liu, H. Wu, H. Zhao, L. Wang, Interfacial assembled mesoporous polydopamine nanoparticles reduced graphene oxide for high performance of waterborne epoxy-based anticorrosive coatings, J. Colloid Interface Sci. 606 (2022) 1572–1585, https://doi.org/10.1016/j.jcis.2021.08.150.
[18] J. Wang, H. Guo, X. Shi, Z. Yao, W. Qing, F. Liu, C.Y. Tang, Fast polydopamine coating on reverse osmosis membrane: process investigation and membrane performance study, J. Colloid Interface Sci. 535 (2019) 239–244, https://doi.org/10.1016/j.jcis.2018.10.016.
[19] H. Kang, X. Zhang, L. Li, B. Zhao, F. Ma, J. Zhang, Polydopamine and poly (dimethylsiloxane) modified superhydrophobic fiberglass membranes for efficient water-in-oil emulsions separation, J. Colloid Interface Sci. 559 (2020) 178–185, https://doi.org/10.1016/j.jcis.2019.10.016.

Appendix G

[20] R. Li, J. Liu, A. Shi, X. Luo, J. Lin, R. Zheng, H. Fan, S.V. Selasie, H. Lin, A facile method to modify polypropylene membrane by polydopamine coating via inkjet printing technique for superior performance, J. Colloid Interface Sci. 552 (2019) 719–727, https://doi.org/10.1016/j.jcis.2019.05.108.

[21] A.K. Sutanto, Y. Xing, T. Ding, Z. Wang, K. Sun, D. Mo, J. Zhang, K. Cai, Hybrid mesoporous nanoparticles with highly integrated polydopamine for pH-responsive membrane permeation and drug delivery, Colloids Interface Sci. Commun. 41 (2021), https://doi.org/10.1016/j.colcom.2021.100385.

[22] M.L. Alfieri, M. Massaro, M. d'Ischia, G. D'Errico, N. Gallucci, M. Gruttadauria, M. Licciardi, L.F. Liotta, G. Nicotra, G. Sfuncia, S. Riela, Site-specific halloysite functionalization by polydopamine: a new synthetic route for potential near infrared-activated delivery system, J. Colloid Interface Sci. 606 (2022) 1779–1791, https://doi.org/10.1016/j.jcis.2021.08.155.

[23] L.-Y. Guo, Q.-S. Xia, J.-L. Qin, M. Yang, T.-Y. Yang, F.-T. You, Z.-H. Chen, B. Liu, H.-S. Peng, Skin-safe nanophotosensitizers with highly-controlled synthesized polydopamine shell for synergetic chemo-photodynamic therapy, J. Colloid Interface Sci. 616 (2022) 81–92, https://doi.org/10.1016/j.jcis.2022.02.046.

[24] H. Cao, B. Jiang, Y. Yang, M. Zhao, N. Sun, J. Xia, X. Gao, J. Li, Cell membrane covered polydopamine nanoparticles with two-photon absorption for precise photothermal therapy of cancer, J. Colloid Interface Sci. 604 (2021) 596–603, https://doi.org/10.1016/j.jcis.2021.07.004.

[25] V. Ball, Activity of alkaline phosphatase adsorbed and grafted on "polydopamine" films, J. Colloid Interface Sci. 429 (2014) 1–7, https://doi.org/10.1016/j.jcis.2014.05.002.

[26] H.A. Lee, Y. Ma, F. Zhou, S. Hong, H. Lee, Material-independent surface chemistry beyond polydopamine coating, Acc. Chem. Res. 52 (2019) 704–713, https://doi.org/10.1021/acs.accounts.8b00583.

[27] W.-Z. Qiu, H.-C. Yang, Z.-K. Xu, Dopamine-assisted co-deposition: an emerging and promising strategy for surface modification, Adv. Colloid Interface Sci. 256 (2018) 111–125, https://doi.org/10.1016/j.cis.2018.04.011.

[28] V. Ball, D. Del Frari, V. Toniazzo, D. Ruch, Kinetics of polydopamine film deposition as a function of pH and dopamine concentration: insights in the polydopamine deposition mechanism, J. Colloid Interface Sci. 386 (2012) 366–372, https://doi.org/10.1016/j.jcis.2012.07.030.

[29] F. Bernsmann, V. Ball, F. Addiego, A. Ponche, M. Michel, J.J. de Almeida Gracio, V. Toniazzo, D. Ruch, Dopamine-melanin film deposition depends on the used oxidant and buffer solution, Langmuir 27 (2011) 2819–2825, https://doi.org/10.1021/la104981s.

[30] T.S. Sileika, D.G. Barrett, R. Zhang, K.H.A. Lau, P.B. Messersmith, Colorless multifunctional coatings inspired by polyphenols found in tea, chocolate, and wine, Angew. Chemie Int. Ed. 52 (2013) 10766–10770, https://doi.org/10.1002/anie.201304922.

[31] J. Kuang, J.L. Guo, P.B. Messersmith, High ionic strength formation of DOPA-melanin coating for loading and release of cationic antimicrobial compounds, Adv. Mater. Interfaces 1 (2014) 1400145, https://doi.org/10.1002/admi.201400145.

[32] F. Behboodi-Sadabad, S. Li, W. Lei, Y. Liu, T. Sommer, P. Friederich, C. Sobek, P.B. Messersmith, P.A. Levkin, High-throughput screening of multifunctional nanocoatings based on combinations of polyphenols and catecholamines, Mater. Today Bio 10 (2021), https://doi.org/10.1016/j.mtbio.2021.100108.

[33] M.L. Alfieri, L. Panzella, S.L. Oscurato, M. Salvatore, R. Avolio, M.E. Errico, P. Maddalena, A. Napolitano, M. d'Ischia, The chemistry of polydopamine film formation: the amine-quinone interplay, Biomimetics 3 (2018) 26, https://doi.org/10.3390/biomimetics3030026.

[34] S. Chen, J. Zhang, Y. Chen, S. Zhao, M. Chen, X. Li, M.F. Maitz, J. Wang, N. Huang, Application of phenol/amine copolymerized film modified magnesium alloys: anticorrosion and surface biofunctionalization, ACS Appl. Mater. Interfaces 7 (2015) 24510–24522, https://doi.org/10.1021/acsami.5b05851.

[35] M. Iacomino, J.I. Paez, R. Avolio, A. Carpentieri, L. Panzella, G. Falco, E. Pizzo, M. E. Errico, A. Napolitano, A. del Campo, M. d'Ischia, Multifunctional thin films and coatings from caffeic acid and a cross-linking diamine, Langmuir 33 (2017) 2096–2102, https://doi.org/10.1021/acs.langmuir.6b04079.

[36] S. Suárez-García, J. Sedó, J. Saiz-Poseu, D. Ruiz-Molina, Copolymerization of a catechol and a diamine as a versatile polydopamine-like platform for surface functionalization: The case of a hydrophobic coating, Biomimetics 2 (2017) 22, https://doi.org/10.3390/biomimetics2040022.

[37] Q. Lyu, J. Zhang, K.G. Neoh, C. Li Lin Chai, A one step method for the functional and property modification of DOPA based nanocoatings, Nanoscale 9 (2017) 12409–12415, https://doi.org/10.1039/c7nr05293f.

[38] B.K. Ahn, S. Das, R. Linstadt, Y. Kaufman, N.R. Martinez-Rodriguez, R. Mirshafian, E. Kesselman, Y. Talmon, B.H. Lipshutz, J.N. Israelachvili, J.H. Waite, High-performance mussel-inspired adhesives of reduced complexity, Nat. Commun. 6 (2015) 8663, https://doi.org/10.1038/ncomms9663.

[39] X. Li, Y. Deng, J. Lai, G. Zhao, S. Dong, Tough, long-term, water-resistant, and underwater adhesion of low-molecular-weight supramolecular adhesives, J. Am. Chem. Soc. 142 (2020) 5371–5379, https://doi.org/10.1021/jacs.0c00520.

[40] L. Xie, L. Gong, J. Zhang, L. Han, L. Xiang, J. Chen, J. Liu, B. Yan, H. Zeng, A wet adhesion strategy via synergistic cation-π and hydrogen bonding interactions of antifouling zwitterions and mussel-inspired binding moieties, J. Mater. Chem. A 7 (2019) 21944–21952, https://doi.org/10.1039/c9ta08152f.

[41] M.L. Alfieri, L. Panzella, S.L. Oscurato, M. Salvatore, R. Avolio, M.E. Errico, P. Maddalena, A. Napolitano, V. Ball, M. d'Ischia, Hexamethylenediamine-mediated polydopamine film deposition: inhibition by resorcinol as a strategy for mapping quinone targeting mechanisms, Front. Chem. 7 (2019) 407, https://doi.org/10.3389/fchem.2019.00407.

[42] L. Panzella, G. Gentile, G. D'Errico, N.F. Della Vecchia, M.E. Errico, A. Napolitano, C. Carfagna, M. d'Ischia, Atypical structural and π-electron features of a melanin polymer that lead to superior free-radical-scavenging properties, Angew. Chemie Int. Ed. 52 (2013) 12684–12687, https://doi.org/10.1002/anie.201305747.

[43] R. Micillo, M. Iacomino, M. Perfetti, L. Panzella, K. Koike, G. D'Errico, M. d'Ischia, A. Napolitano, Unexpected impact of esterification on the antioxidant activity and (photo)stability of a eumelanin from 5,6-dihydroxyindole-2-carboxylic acid, Pigment Cell Melanoma Res. 31 (2018) 475–483, https://doi.org/10.1111/pcmr.12689.

[44] R. Micillo, L. Panzella, K. Koike, G. Monfrecola, A. Napolitano, M. d'Ischia, "Fifty shades" of black and red or how carboxyl groups fine tune eumelanin and pheomelanin properties, Int. J. Mol. Sci. 17 (2016) 746, https://doi.org/10.3390/ijms17050746.

[45] M. d'Ischia, A. Napolitano, A. Pezzella, P. Meredith, M. Buehler, Melanin biopolymers: tailoring chemical complexity for materials design, Angew. Chemie Int. Ed. 59 (2020) 11196–11205, https://doi.org/10.1002/anie.201914276.

[46] R. Edge, M. d'Ischia, E.J. Land, A. Napolitano, S. Navaratnam, C.A. Ramsden, P.A. Riley, Dopaquinone redox exchange with dihydroxyindole and dihydroxyindole carboxylic acid, Pigment Cell Res. 19 (2006) 443–450, https://doi.org/10.1111/j.1600-0749.2006.00327.x.

[47] I.F. Benzie, J.J. Strain, The ferric reducing ability of plasma (FRAP) as a measure of "'antioxidant power"': the FRAP assay, Anal. Biochem. 239 (1996) 70–76, https://doi.org/10.1006/abio.1996.0292.

[48] P. Goupy, C. Dufour, M. Loonis, O. Dangles, Quantitative kinetic analysis of hydrogen transfer reactions from dietary polyphenols to the DPPH radical, J. Agric. Food Chem. 51 (2003) 615–622, https://doi.org/10.1021/jf025938l.

[49] R. Re, N. Pellegrini, A. Proteggente, A. Pannala, M. Yang, C. Rice-Evans, Antioxidant activity applying an improved ABTS radical cation decolorization assay, Free Radic. Biol. Med. 26 (1999) 1231–1237, https://doi.org/10.1016/S0891-5849(98)00315-3.

[50] D. Liberti, M.L. Alfieri, D.M. Monti, L. Panzella, A. Napolitano, A melanin-related phenolic polymer with potent photoprotective and antioxidant activities for dermo-cosmetic applications, Antioxidants 9 (2020) 270, https://doi.org/10.3390/antiox9040270.

[51] F. Bernsmann, A. Ponche, C. Ringwald, J. Hemmerle, J. Raya, B. Bechinger, J.C. Voegel, P. Schaaf, V. Ball, Characterization of dopamine-melanin growth on silicon oxide, J. Phys. Chem. C. 113 (2009) 8234–8242, https://doi.org/10.1021/jp901188h.

[52] N. Eliaz, E. Gileadi, Physical Electrochemistry: Fundamentals, Techniques and Applications, Wiley-VCH, Weinheim, 2018, pp. 1–480.

[53] M.L. Alfieri, G. Pilotta, L. Panzella, L. Cipolla, A. Napolitano, Gelatin-based hydrogels for the controlled release of 5,6-dihydroxyindole-2-carboxylic acid, a melanin-related metabolite with potent antioxidant activity, Antioxidants 9 (2020) 245, https://doi.org/10.3390/antiox9030245.

[54] D.D. Perrin, Dissociation Constants of Organic Bases in Aqueous Solution, Butterworths, London, 1972, pp. 132–236.

[55] G. Prampolini, M. d'Ischia, A. Ferretti, The phenoxyl group-modulated interplay of cation-π and σ-type interactions in the alkali metal series, PCCP 22 (2020) 27105–27120, https://doi.org/10.1039/d0cp03707a.

[56] Z. Liu, Z. Chen, J. Xi, X. Xu, An accurate single descriptor for ion-π interactions, Natl. Sci. Rev. 7 (2020) 1036–1045, https://doi.org/10.1093/nsr/nwaa051.

[57] D.-X. Wang, M.-X. Wang, Exploring anion-π interactions and their applications in supramolecular chemistry, Acc. Chem. Res. 53 (2020) 1364–1380, https://doi.org/10.1021/acs.accounts.0c00243.

[58] T.-Y. Kuo, Y.-C. Chung, Surface-initiated polymerization of mussel-inspired dopamine for hydrophilic coatings, Mater. Adv. 2 (2021) 5686–5690, https://doi.org/10.1039/D0MA00908C.

[59] Q. Guo, J. Chen, J. Wang, H. Zeng, J. Yu, Recent progress in synthesis and application of mussel-inspired adhesives, Nanoscale 12 (2020) 1307–1324, https://doi.org/10.1039/C9NR09780E.

Appendix G

Supporting information

Non-covalent small molecule partnership for redox-active films: beyond polydopamine technology

Rita Argenziano,[a] Maria Laura Alfieri,[a] Youri Arntz,[b] Rachele Castaldo,[c] Davide Liberti,[a] Daria Maria Monti,[a] Gennaro Gentile,[c] Lucia Panzella,[a] Orlando Crescenzi,[a] Vincent Ball,[b] Alessandra Napolitano,[a] * Marco d'Ischia

[a]*Department of Chemical Sciences, University of Naples Federico II, Via Cintia 21, I-80126 Naples, Italy*
[b]*Faculté de Chirurgie Dentaire, Université de Strasbourg, 8 rue Sainte Elisabeth, Strasbourg, 67000, France*
[c]*Institute for Polymers, Composites and Biomaterials - National Research Council of Italy, Via Campi Flegrei, 34, Pozzuoli (NA), 80078, Italy*

Table of contents

Appendix G

Experimental Section

Methods. *Measurement using quartz crystal microbalance-dissipation (QCM-D) system*. In QCM-D the changes in the resonance frequency (-Δf) of a quartz crystal are measured when material is adsorbed onto it from a solution. The crystal is excited at its fundamental frequency (about 5 MHz), and observations are made at the 3rd, 5th, and 7th overtones ((v) 3, 5, and 7) at 15, 25, and 35 MHz, respectively. For rigid films, -Δf/v is independent of the overtone number v. According to the Sauerbrey relation,[1] -Δf/v can be related directly to the total mass of the film. Before use, the crystal was cleaned with a Plasma Cleaner PDC-32G-2 for 15 min.

HPLC analyses were performed on a Agilent 1100 binary pump instrument equipped with a SPD-10AV VP UV-visible detector using an octadecylsilane-coated column, 250 mm × 4.6 mm, 5 µm particle size (Phenomenex Sphereclone ODS) at 0.7 mL/min. Detection wavelength was set at 300 nm. Eluent system: water – acetonitrile 20 to 70% gradient over 5-45 min. Preparative HPLC was carried out on an Agilent 1200 instrument coupled with a UV detector set at 300 nm using an Econosil C18 column (10 µm, 22 × 250 mm) at 25 mL/min. Eluent: 1 % formic acid – acetonitrile 75:25 v/v.

Positive reflectron MALDI spectra were recorded using 2,5-dihydroxybenzoic acid as the matrix. Spectra represents the sum of 15,000 laser pulses from randomly chosen spots per sample position. Raw data are analyzed using the computer software provided by the manufacturers and are reported as monoisotopic masses.

AFM analyses. The cantilevers used were the Scan-assist Fluid (Bruker) with a nominal spring constant of 0.7 N/m and a type radius of 20 nm. The images were acquired with a resolution of 512 × 512 and a scan rate of 0.5 Hz. The film thickness was determined by measuring the difference in height between the needle scratched area and the native area of the film. The measurement was repeated three times. The roughness (Ra) was estimated on 20 µm × 20 µm, using the freeware software Gwyddion (GNU, Boston, MA, USA), dedicated to SPM microscopy analysis.

Cyclic voltammetry (CV) and electrochemical impedance spectroscopy. The amorphous carbon working electrode (ref. CHI 104, CH Instruments) was polished with a SiC paper, rinsed with distilled water, and polished sequentially with Al_2O_3 pastes (Escil, Villeurbane, France) with 1.0 and 0.1 µm particles size. Finally, the quality of these cleaning steps was tested by performing a cyclic voltammetry scan between -0.6 and +1.0 V *versus* the reference electrode in the presence of 1 mM potassium hexacyanoferrate at a potential sweep rate of 100 mVs^{-1}. The surface state of the amorphous carbon electrode was deemed satisfactory when the oxidation and reduction peak

potentials were separated by less than 80 mV, the theoretical peak separation for a one electron process being 59 mV at 25°C.[2] After film deposition for one hour, the capacitive CV curve of the coatings were acquired in the presence of buffer at a scan rate of 100 mVs^{-1}. After that, the pure buffer was replaced by a buffer containing 1 mM potassium hexacyanoferrate to investigate the film permeability to this redox probe, using the same potential scan rate. Finally, impedance spectra were acquired in the presence of the redox probe (*vs* the reference electrode) at a constant potential corresponding to the oxidation peak potential measured on the pristine electrode with a potential modulation of ± 5 mV with a frequency changing from 10^5 to 10^{-2} Hz.

Analysis of the MeDHICA/HMDA reaction products. The reaction of MeDHICA with HMDA was run under the conditions described in the main text. In brief, the indole (0.05 mmol) dissolved in the minimal amount of DMSO was added to a solution of the HMDA in 0.05 M carbonate buffer pH = 9.0 to a final concentration of 1 mM (50 mL), at an indole/additive molar ratio of 1:1.5, and the mixture was taken under vigorous stirring. After 24 h the mixture was extracted with ethyl acetate (3x 100 mL) and the combined organic phases were taken to dryness. The residue taken up in methanol was analysed by HPLC under the gradient conditions reported above. In other experiments aliquots (5 mL) of the reaction mixture were withdrawn at given time points, extracted with ethyl acetate and analysed by HPLC to quantify residual MeDHICA and 4,4'-biindolyl and 4,7'- biindolyl formation against proper standards (vide infra). Alternatively, the ethyl acetate extractable fraction of the aliquots withdrawn was subjected to acetylation treatment (acetic anhydride (1 mL) /pyridine 100 µL, overnight) and analysed by HPLC after removal of the volatiles.

TEM and DLS analysis MeDHICA/HMDA mixture. For these purposes the reaction was carried out as described in the above paragraph. TEM grids were immersed in the reaction mixture at given time points (30 min- 4 h). For DLS analysis the reaction was carried out into the instrument cell and the reaction was followed over 24 h.

Synthesis of 4,4'-biindolyl and 4,7- biindolyl from MeDHICA. A solution of MeDHICA (200 mg, 0.96 mmol) in 0.5 M Tris buffer (pH 7.5) (60 mL) was treated with copper sulfate pentahydrate (1 molar equivalent) and the reaction mixture was taken under vigorous stirring. After 3 min, the oxidation reaction was stopped by addition of sodium dithionite, acidified to pH 2.0 and rapidly extracted with ethyl acetate. The mixture was fractionated by preparative HPLC (eluant 1 % formic acid – acetonitrile 75:25 v/v) to give 4,4'-biindolyl (R_T 12.9 min, 60 mg, 30% w/w yield, >90% pure), and 4,7'-biindolyl (R_T 16.2 min, 20 mg, 10% w/w yield, >90% pure) that were subjected to

Appendix G

complete spectral analysis (Figure S16-S25). The assignment of the proton and carbon resonances as deduced by 2D NMR analysis is reported in the following:

4,4'- biindolyl. ^{1}H NMR (DMSO-d_6) δ (ppm): 3.74 (s, 3Hx2), 6.38 (s, 1Hx2, H-3 and H-3'), 6.90 (s, 1Hx2, H-7 and H-7'), 11.32 (1Hx2, NH and NH'). ^{13}C NMR (DMSO-d6) δ (ppm): 51.65 (CH_3), 96.27 (CH, C-7 and C-7'), 109.14 (CH, C-3 and C-3'), 114.72 (C, C-4 and C-4'), 120.72 (C, C-9 and C-9'), 124.14 (C, C-2 and C-2'), 132.64 (C, C-8 and C-8'), 139.87 (C, C-5 and C-5'), 147.10 (C, C-6 and C-6'), 162.13 (C, carboxy groups).

4,7'- biindolyl. ^{1}H NMR (DMSO-d6) δ (ppm): 3.73 (s, 3Hx2), 6.37 (1H, s, H-3), 6.89 (1H, s, H-7), 6.98 (1H, s, H-4'), 7.01 (1H, s, H-3'), 9.42 (1H, NH'), 11.32 (1H, NH). ^{13}C NMR (DMSO-d6) δ (ppm): 51.17 (CH_3), 51.63 (CH_3), 96.59 (CH, C-7), 104.0 (CH, C-4'), 107.06 (C, C-7'), 108.90 (CH, C-3'), 109.01 (CH, C-3), 112.14 (C, C-4), 119.46 (C, C-9), 120.60 (C, C-9'), 124.14 (C, C-2), 124.80 (C, C-2'), 132.57 (C, C-8), 132.90 (C, C-8'), 140.61 (C, C-5), 142.88 (C, C-5'), 145.12 (C, C-6'), 147.34 (C, C-6), 161.92 (C, carboxy group), 162.16 (C, carboxy group).

Cell Cultures. Human immortalized keratinocytes (HaCaT, Innoprot, Derio, Spain) were cultured in Dulbecco's modified Eagle's medium (DMEM), supplemented with 10% fetal bovine serum, 2 mM L-glutamine and antibiotics in a 5% CO_2 humidified atmosphere at 37 °C. Every 48 h, cells were refreshed at a 1:5 ratio. The culture medium was removed, and cells were rinsed with PBS and then detached with trypsin-EDTA. After centrifugation (5 min at 1000 rpm), cells were diluted in fresh medium.

2',7'-Dichlorofluorescin diacetate (H_2DCFDA) assay. After irradiation, cells were incubated with the cell permeable, redox-sensitive fluorophore H_2DCFDA (20 μM) for 30 min at 37 °C. Cells were then washed twice with cold PBS, detached by trypsin, centrifuged at 1000 rpm for 10 min and resuspended in PBS containing 30 mM glucose, 1 mM $CaCl_2$, and 0.5 mM $MgCl_2$ (PBS plus) at a cell density of $1x10^5$ cells/mL. H_2DCFDA is nonfluorescent until it is hydrolyzed by intracellular esterases, and in the presence of ROS it is readily oxidized to the highly fluorescent 2',7'-dichlorofluorescein (DCF). DCF fluorescence intensity was measured at an emission wavelength of 525 nm with excitation wavelength set at 488 nm using a Perkin-Elmer LS50 spectrofluorometer (Perkin Elmer, Milano, Italy). Emission spectra were acquired at a scanning speed of 300 nm/min, with 5 slit widths for excitation and emission. ROS production was expressed as percentage of DCF fluorescence intensity of the sample under test, with respect to the untreated sample.

Appendix G

Computational methods. DFT calculations were performed with the Gaussian package of programs.[3] To carry out structural explorations and to compute vibrational-rotational contributions to the free energy, the PBE0[4] functional was adopted in combination with a reasonably large basis set [6-31+G(d,p)]. The M06-2X[5] functional with a much larger basis set [6-311++G(2d,2p)] was adopted for single-point energy evaluations. The spin-unrestricted formulation was used for open-shell species. Calculations were performed either in vacuo, or by adoption of a polarizable continuum medium (PCM)[6-9] to account for the influence of the aqueous environment. The M06-2X single-point calculations also included non-electrostatic contributions to the solvation free energy, employing radii and non-electrostatic terms of the SMD solvation model.[10] Coupled-cluster calculations were carried out with the ORCA package (Version 4.0.1.2)[11] using the cc-pVTZ basis set.[12] For the sake of computational efficiency, the domain-based local-pair natural-orbital coupled-cluster approach with single, double, and perturbative triple excitations, DLPNO-CCSD(T)[13-15] was used to approximate the standard but unfavourably scaled CCSD(T).[16] Computations were carried out using tight thresholds (TightPNO); however, an iterative full local MP2 guess was not used (UseFullLMP2Guess set to "false"), so as to ensure direct comparability of closed-shell species with open-shell species, for which this option is not yet implemented.

Appendix G

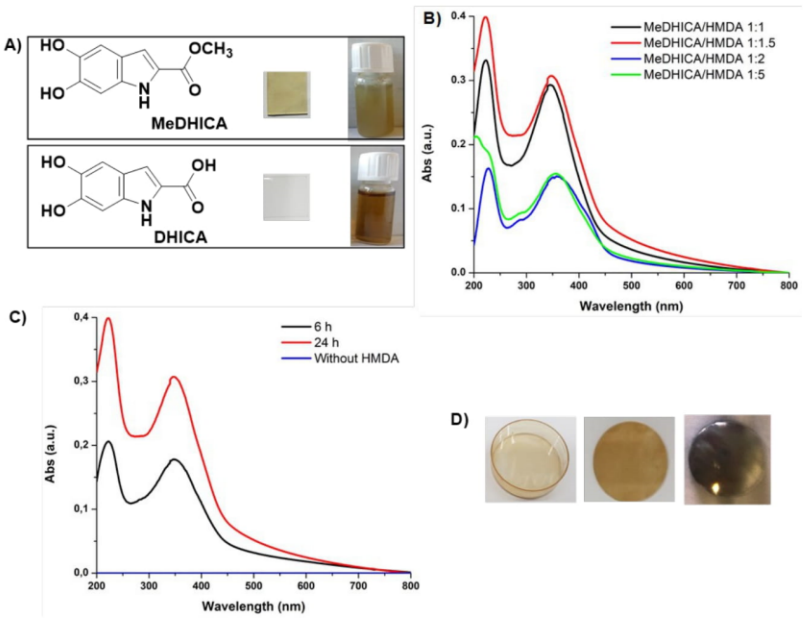

Fig. S1. A) Reaction mixtures of MeDHICA/HMDA (top) and DHICA/HMDA (bottom) and quartz substrates after 24 h dipping in the mixture at pH 9.0; B) UV-vis absorption spectra of the quartz substrates dipped in the MeDHICA/HMDA reaction mixture at different indole to amine molar ratios, taken after 24 h; C) UV-vis spectrum of the quartz substrate dipped in the MeDHICA reaction mixture with or without HMDA at different reaction times; D) MeDHICA/HMDA coatings on various materials from left to right: polycarbonate, polystyrene, aluminium.

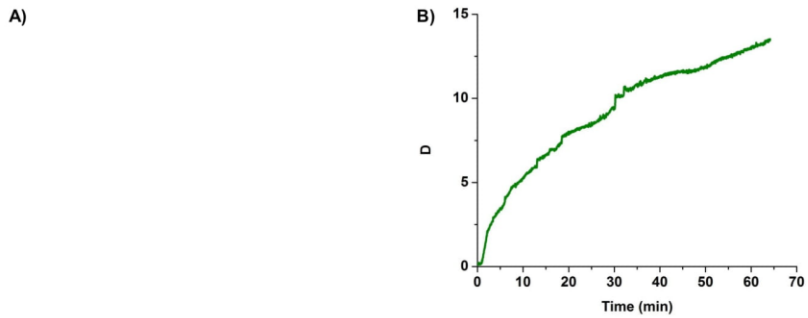

Fig. S2. Kinetics of MeDHICA/HMDA film deposition up to 65 min as monitored by QCM-D experiment with frequency variations (A) and dissipation variations (B) at the 3rd overtone as a function of time.

Appendix G

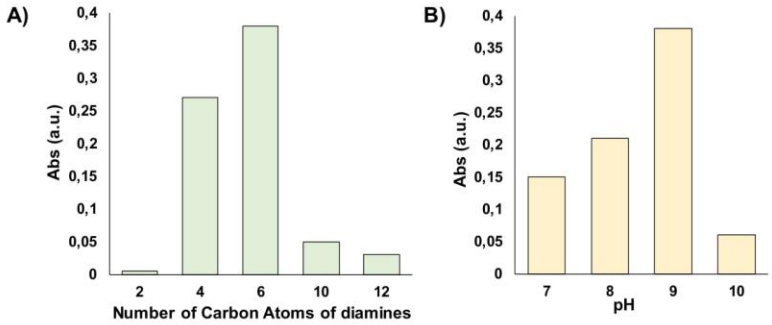

Fig. S3. A) Effect of pH on film deposition MeDHICA/HMDA as measured by absorbance at 340 nm of the quartz slides after 24 h of reaction. B) Effect of chain length of 1,n-diamines on film deposition. Shown is the absorbance at 340 nm of the quartz slides immersed in the MeDHICA solution and the proper diamine at pH 9.0 over 24 h.

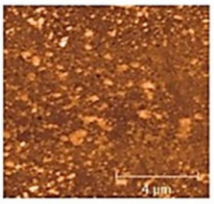

Fig. S4. AFM image of films applied onto glass substrates from MeDHICA/HMDA reaction mixtures.

Appendix G

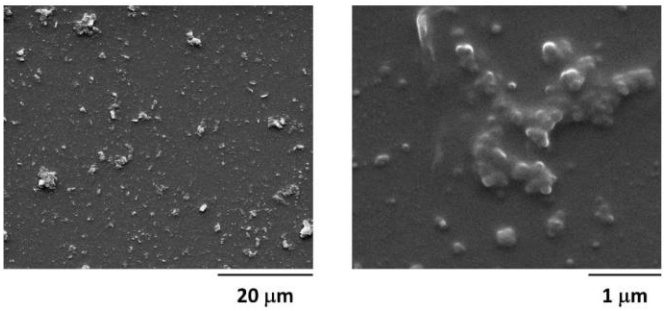

Fig. S5. SEM images of films applied onto glass substrates from MeDHICA/HMDA reaction mixtures at 24 h reaction time after exposure to HCl vapors.

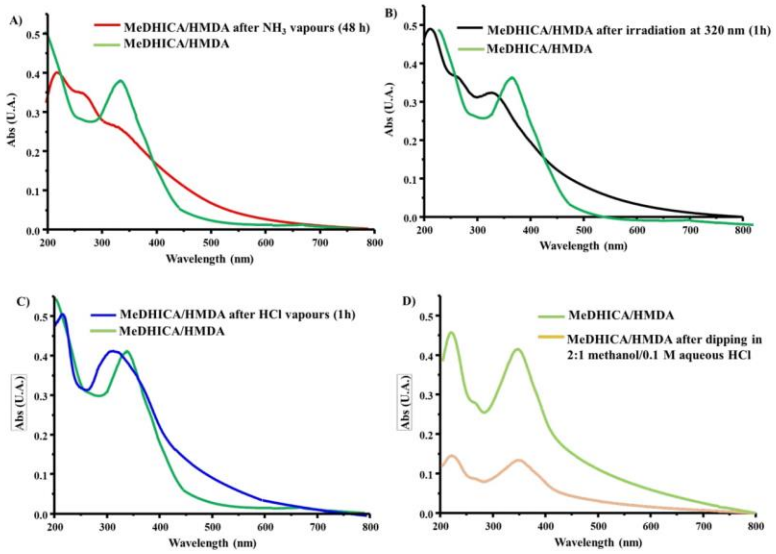

Fig. S6. UV-vis spectra of MeDHICA/HMDA film (A) before and after exposure to ammonia vapors for up to 48 h, (B) following irradiation with a UV lamp at 320 nm over 1 h, (C) before and after exposure to HCl vapors or (D) before and after dipping in 2:1 methanol/0.1 M aqueous HCl.

Appendix G

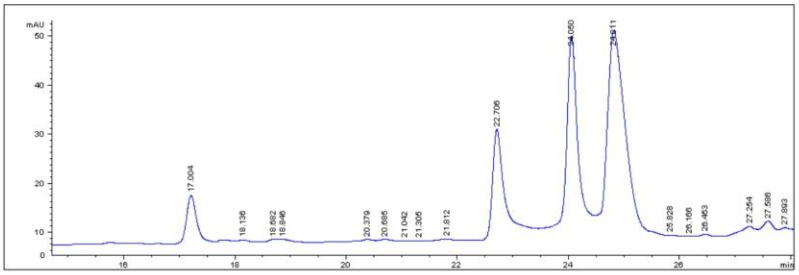

Fig. S7. HPLC profile of the oxidation mixture of 4,4'-biindolyl (R_T 17.0 min) from MeDHICA at 20 min reaction time (Eluant: H_2O/acetonitrile 20-70 % gradient, λ=300 nm).

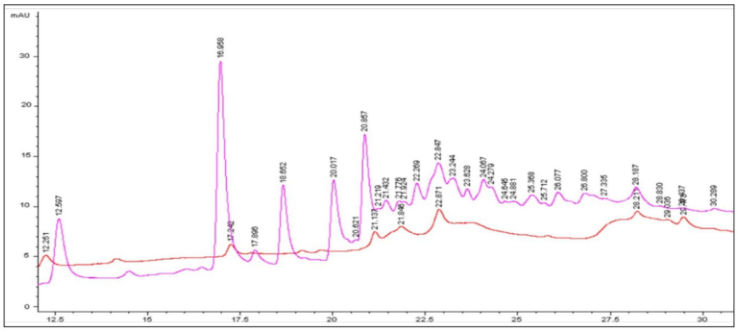

Fig. S8. HPLC profile of the MeDHICA/HMDA film dissolved in DMSO before (magenta trace) and after (red trace) 24 h exposure to ammonia vapors (Eluant: H_2O/acetonitrile 20-70 % gradient, λ=300 nm).

Appendix G

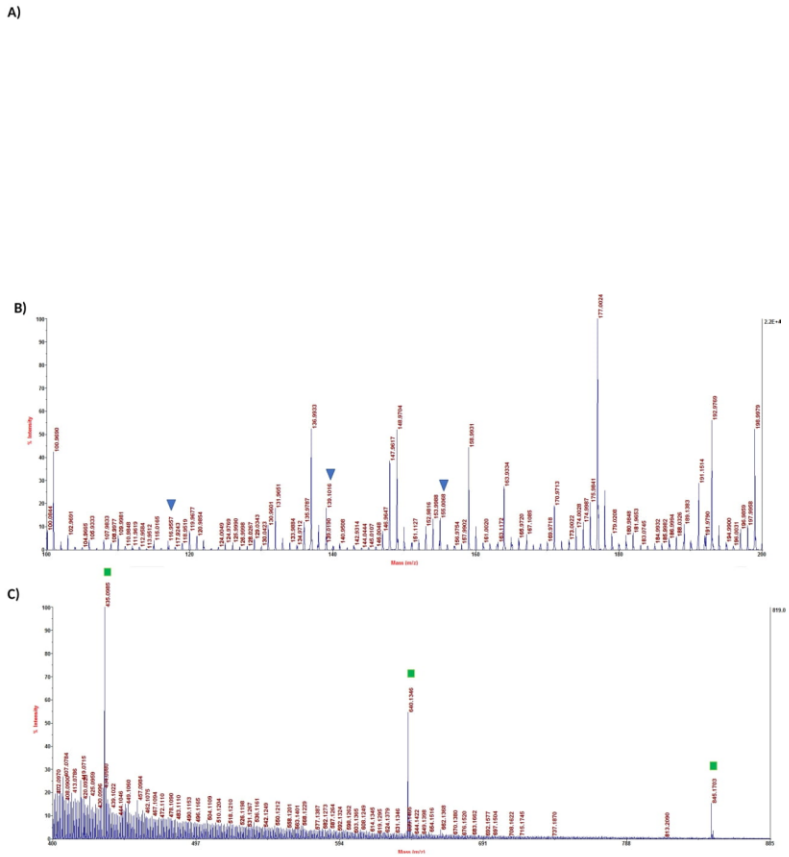

Fig. S9. A) MALDI MS analysis of the film formed on the MALDI plate after extensive rinsing with water. B) Segmental spectrum in the range *m/z* 100-200. Triangles indicate signals due to hexamethylenediamine. C) Segmental spectrum in the range *m/z* 200-885. Squares indicate signals due to MeDHICA oligomers. Other signals are due to matrix or impurities.

Table S1. Pseudomolecular ion peaks observed in the MALDI spectrum of MeDHICA/HMDA film and proposed structural assignment.

MeDHICA/HMDA film		
Observed peaks (clusters)	MW of molecular species (Da)	
116.9 (H^+), 139.1 (Na^+), 155.0 (K^+)	116	HMDA
435 (Na^+)	412	MeDHICA dimer
640 (Na^+)	617	MeDHICA trimer
845 (Na^+)	822	MeDHICA tetramer

Appendix G

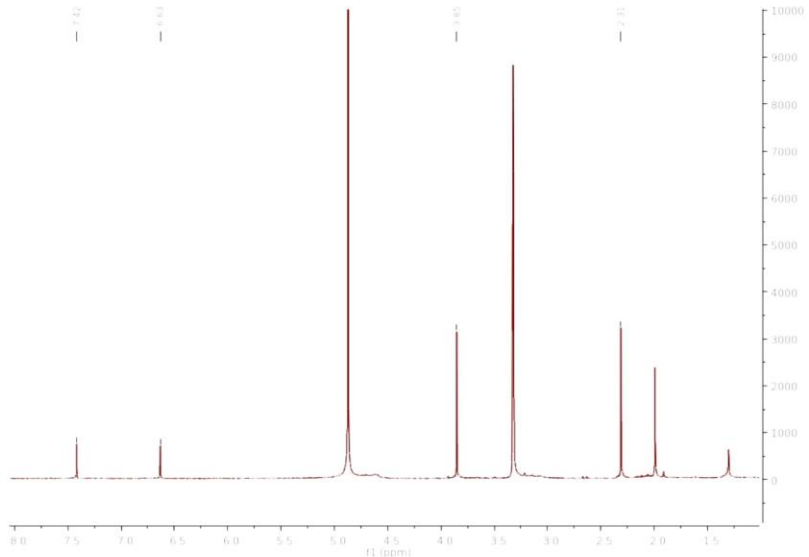

Fig. S10. ^{1}H NMR spectrum of acetylated 4,4'-biindolyl from MeDHICA in methanol-d_4.

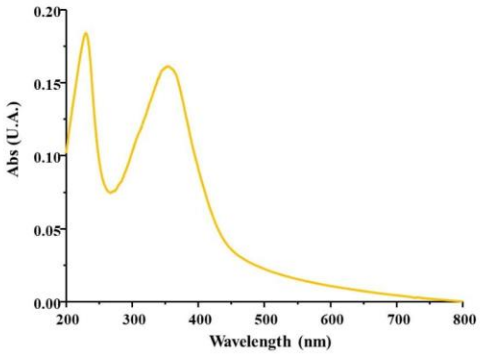

Fig. S11. UV-vis spectrum of the quartz substrate dipped in the 4,4'-biindolyl dimer from MeDHICA /HMDA reaction mixture at 1:1.5 indole to amine molar ratio taken at 24 h.

Appendix G

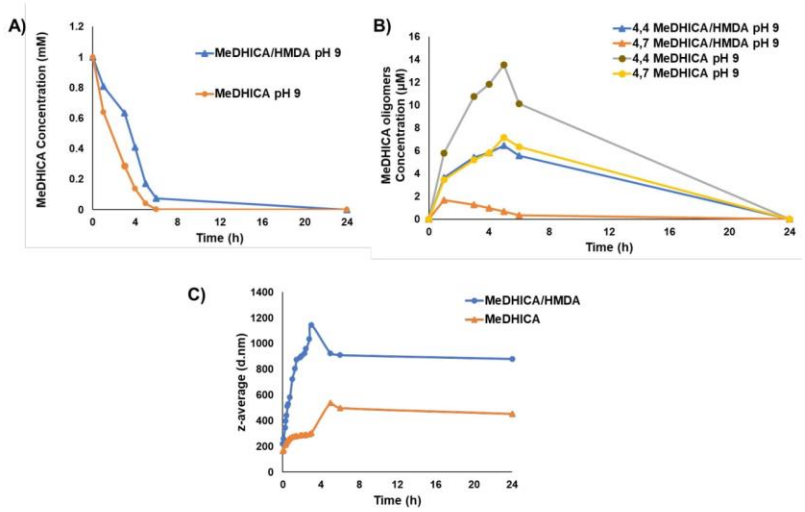

Fig. S12. Effect of HMDA on the kinetics of MeDHICA aerial oxidation at pH 9. A) Consumption of MeDHICA and B) Formation of 4,4' and 4,7' dimers in the reaction carried out with or without HMDA; C) Time evolution of the hydrodynamic diameter distributions of the particles generated by MeDHICA oxidation in presence or in the absence of HMDA.

Fig. S13. Glass substrate coated with MeDHICA/HMDA film after partial immersion in DPPH solution. The reducing activity is manifested by enhanced melanization of the film area exposed to DPPH. The arrow indicates the level at which the glass slide was immersed in the solution.

Appendix G

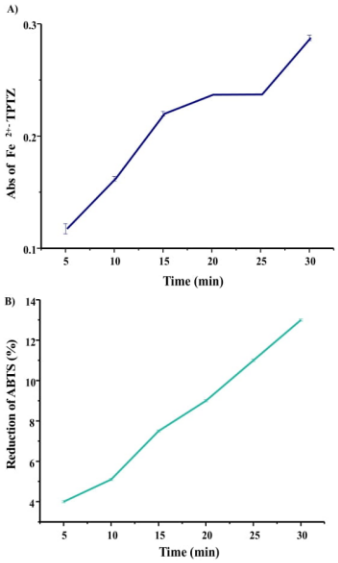

Fig. S14. Kinetics of A) development of the absorption of Fe^{2+}-TPTZ complex, and B) reduction of ABTS (50 µM) over time by immersion of glass substrates coated with MeDHICA/HMDA films. Shown are the results of triplicates ± SD.

Table S2. Neutral forms in vacuo. For each chemical species, energy values (Ha) and relative energies (kcal/mol) of all distinct conformers identified are reported.
E: electronic energy, PBE0/6-31+G(d,p);
G_{RRHO}: Gibbs free energy in the ideal gas / rigid rotor / harmonic oscillator approximation, referred to a temperature of 298.15 K and to a 1 atm standard state;
$E_{M06\text{-}2X,large}$: electronic energy, M06-2X/6-311++G(2d,2p) // PBE0/6-31+G(d,p);
$G_{RRHO,M06\text{-}2X,large} = E_{M06\text{-}2X,large} + G_{RRHO} - E$;
$E_{DLPNO\text{-}CCSD(T)}$: electronic energy, DLPNO-CCSD(T)/cc-pVTZ // PBE0/6-31+G(d,p);
$G_{RRHO,DLPNO\text{-}CCSD(T)} = E_{DLPNO\text{-}CCSD(T)} + G_{RRHO} - E$.

Symm.	E	°E	G_{RRHO}	°G	$E_{M06\text{-}2X,large}$	°G	$G_{RRHO,M06\text{-}2X,large}$	°G	$E_{DLPNO\text{-}CCSD(T)}$	°E	$G_{RRHO,DLPNO\text{-}CCSD(T)}$	°G
Reduced state												
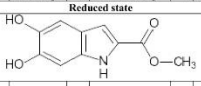												
C_1	-741.34932	14.8	-741.20807	13.9								
C_s	-741.37117	1.1	-741.22872	1.0	-742.09710	1.2	-741.95465	1.0	-740.94875	1.1	-740.80629	0.9
C_s	-741.37000	1.9	Saddle point	2.1	-742.09517	2.4	-741.95217	2.6				
C_s	-741.34726	16.1	Saddle point	16.7								
C_s	-741.35754	9.7	-741.21528	9.4								
C_s	-741.37297	0.0	-741.23028	0.0	-742.09895	0.0	**-741.95626**	0.0	-740.95046	0.0	**-740.80777**	0.0
C_s	-741.37172	0.8	Saddle point	1.1	-742.09699	1.2	-741.95388	1.5				
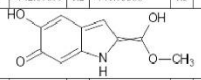												
C_1	-741.31715	35.0	-741.17477	34.8								
C_1	-741.31392	37.1	-741.17014	37.7								
C_1	-741.31711	35.1	-741.17588	34.1								
C_1	-741.31518	36.3	-741.17288	36.0								

C_1	-741.31978	33.4	-741.17872	32.4								
C_1	-741.31786	34.6	-741.17660	33.7								
C_1	-741.31220	38.1	-741.16971	38.0								
C_s	-741.32029	33.1	-741.18011	31.5								
C_s	-741.31978	33.4	-741.17824	32.7								
C_s	-741.31287	37.7	Saddle point	37.3								
C_s	-741.30862	40.4	Saddle point	39.8								
C_s	-741.31817	34.4	Saddle point	34.1								
C_s	-741.31004	39.5	Saddle point	40.0								
C_s	-741.30847	40.5	Saddle point	40.8								
C_s	-741.31384	37.1	Saddle point	36.7								
C_s	-741.31146	38.6	Saddle point	38.2								
C_s	-741.31293	37.7	Saddle point	36.8								
C_s	-741.30876	40.3	Saddle point	39.4								
C_s	-741.31387	37.1	Saddle point	37.1								
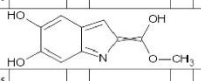												
C_1	-741.30919	40.0	-741.16728	39.5								
C_1	-741.29586	48.4	-741.15513	47.2								
C_1	-741.30117	45.1	-741.15990	44.2								
C_1	-741.29562	48.5	-741.15488	47.3								
C_s	-741.30488	42.7	-741.16378	41.7								
C_s	-741.30116	45.1	Saddle point	45.7								

Appendix G

C_1	-741.29527	48.8	Saddle point	47.9								
C_1	-741.29123	51.3	Saddle point	50.1								
C_1	-741.30285	44.0	Saddle point	42.9								
C_1	-741.30920	40.0	Saddle point	40.5								
C_1	-741.32068	32.8	-741.17743	33.2								
C_1	-741.32390	30.8	-741.18155	30.6								
C_1	-741.32223	31.8	Saddle point	31.9								
C_1	-741.29558	48.6	Saddle point	47.6								
C_1	-741.29171	51.0	Saddle point	49.4								
C_1	-741.31138	38.6	-741.16980	38.0								
One-electron oxidation state												
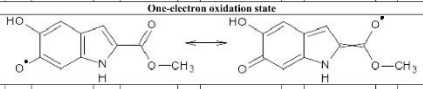												
C_1	-740.72330	15.2	-740.59447	14.3								
C_1	-740.74563	1.2	-740.61569	1.0	-741.46480	1.6	-741.33486	1.1	-740.31763	1.0	-740.18768	0.9
C_1	-740.74445	1.9	Saddle point	2.1	-741.46286	2.8	-741.33236	2.6				
C_1	-740.72105	16.6	Saddle point	17.1								
C_1	-740.73091	10.4	-740.60096	10.3								
C_1	-740.74748	0.0	-740.61733	0.0	-741.46672	0.4	**-741.33657**	0.0	-740.31930	0.0	**-740.18915**	0.0
C_1	-740.74625	0.8	Saddle point	1.1	-741.46478	1.6	-741.33411	1.5				
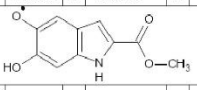												
C_1	-740.72244	15.7	-740.59355	14.9								

C_1	-740.74534	1.4	-740.61493	1.5	-741.46499	1.4	-741.33457	1.3	-740.31691	1.5	-740.18650	1.7
C_1	-740.74420	2.1	Saddle point	2.6	-741.46309	2.6	-741.33211	2.8				
C_1	-740.72020	17.2	Saddle point	18.1								
C_1	-740.73178	9.9	-740.60112	10.2								
C_1	-740.74754	0.0	-740.61684	0.3	-741.46728	0.0	-741.33657	0.0	-740.31889	0.3	-740.18819	0.6
C_1	-740.74632	0.8	Saddle point	1.4	-741.46537	1.2	-741.33421	1.5				
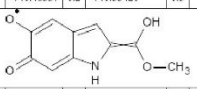												
C_1	-740.66841	49.7	-740.54119	47.8								
C_1	-740.66813	49.8	-740.54255	46.9								
C_1	-740.66604	51.1	-740.53919	49.0								
C_1	-740.66896	49.3	-740.54312	46.6								
C_1	-740.66250	53.4	-740.53558	51.3								
C_1	-740.66429	52.2	-740.53581	51.2								
C_1	-740.67128	47.9	-740.54622	44.6								
C_1	-740.67032	48.5	-740.54383	46.1								
C_1	-740.66464	52.0	Saddle point	49.9								
C_1	-740.66042	54.7	Saddle point	52.4								
C_1	-740.66912	49.2	Saddle point	47.2								
C_1	-740.65957	55.2	Saddle point	53.8								
C_1	-740.65847	55.9	Saddle point	54.4								
C_1	-740.66494	51.8	Saddle point	49.7								
C_1	-740.66257	53.3	Saddle point	51.2								

Appendix G

C_5	-740.66474	52.0	Saddle point	49.6								
C_6	-740.66062	54.5	Saddle point	52.1								
C_7	-740.66444	52.1	Saddle point	50.5								
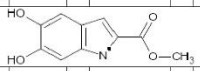												
C_1	-740.70346	27.7	-740.57621	25.8								
C_2	-740.71410	21.0	-740.58627	19.5								
C_3	-740.71273	21.8	Saddle point	20.6								
C_4	-740.70346	27.7	Saddle point	27.3								
C_5	-740.68845	37.1	Saddle point	36.3								
C_6	-740.71183	22.4	-740.58428	20.7								
C_7	-740.71051	23.2	Saddle point	21.8								
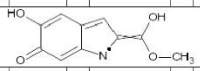												
C_1	-740.68719	37.9	-740.55892	36.7								
C_2	-740.67655	44.5	-740.54861	43.1								
C_3	-740.68057	42.0	Saddle point	42.6								
C_4	-740.68058	42.0	-740.55159	41.3								
C_5	-740.67641	44.6	-740.54841	43.2								
C_6	-740.68449	39.6	-740.55587	38.6								
C_7	-740.68059	42.0	-740.55300	40.4								
C_8	-740.67637	44.7	Saddle point	43.6								
C_9	-740.67241	47.1	Saddle point	46.1								

C_1	-740.68249	40.8	Saddle point	39.9								
C_2	-740.68727	37.8	Saddle point	38.2								
C_3	-740.69659	32.0	-740.56588	32.3								
C_4	-740.70132	29.0	-740.57136	28.8								
C_5	-740.69967	30.0	Saddle point	30.1								
C_6	-740.67646	44.6	Saddle point	43.6								
C_7	-740.67266	47.0	Saddle point	45.7								
C_8	-740.69045	35.8	-740.56140	35.1								
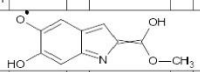												
C_1	-740.68858	37.0	-740.55917	36.5								
C_2	-740.67892	43.1	-740.55087	41.7								
C_3	-740.67868	43.2	-740.55078	41.8								
C_4	-740.68610	38.6	-740.55769	37.4								
C_5	-740.68305	40.5	-740.55443	39.5								
C_6	-740.67842	43.4	Saddle point	42.4								
C_7	-740.67445	45.9	Saddle point	44.7								
C_8	-740.68410	39.8	Saddle point	38.7								
C_9	-740.68858	37.0	Saddle point	37.2								
C_1	-740.69980	30.0	-740.56902	30.3								
C_2	-740.70398	27.3	-740.57397	27.2								
C_3	-740.70230	28.4	Saddle point	28.5								
C_4	-740.67869	43.2	Saddle point	42.0								

Appendix G

C_1	-740.67488	45.6	Saddle point	43.9								
C_s	-740.69259	34.5	-740.56388	33.5								
Two-electron oxidation state												
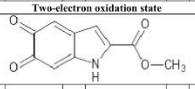												
C_1	-740.08621	15.3	-739.97022	14.1								
C_1	-740.08657	15.0	-739.96992	14.2								
C_s	-740.10860	1.2	-739.99091	1.1	-740.83092	1.3	-740.71322	1.2	-739.69041	1.1	-739.57271	1.0
C_s	-740.10743	2.0	Saddle point	2.2	-740.82899	2.5	-740.71071	2.7				
C_1	-740.08290	17.3	Saddle point	17.7								
C_1	-740.09338	10.8	-739.97577	10.6								
C_s	-740.11055	0.0	-739.99262	0.0	-740.83300	0.0	**-740.71507**	0.0	-739.69219	0.0	**-739.57426**	0.0
C_s	-740.10933	0.8	Saddle point	1.1	-740.83111	1.2	-740.71265	1.5				
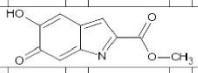												
C_1	-740.09340	10.8	-739.97517	10.9								
C_s	-740.10455	3.8	-739.98620	4.0	-740.83087	1.3	-740.71252	1.6	-739.69164	0.3	-739.57328	0.6
C_s	-740.10320	4.6	Saddle point	5.2	-740.82879	2.6	-740.71000	3.2				
C_1	-740.09316	10.9	Saddle point	12.3								
C_1	-740.07799	20.4	Saddle point	21.8								
C_s	-740.10236	5.1	-739.98405	5.4	-740.82853	2.8	-740.71021	3.1	-739.68949	1.7	-739.57118	1.9
C_s	-740.10103	6.0	Saddle point	6.5	-740.82649	4.1	-740.70771	4.6				
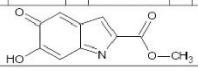												

C_1	-740.08590	15.5	-739.96809	15.4								
C_s	-740.09904	7.2	-739.98088	7.4	-740.82635	4.2	-740.70819	4.3	-739.68697	3.3	-739.56881	3.4
C_s	-740.09767	8.1		8.5								
C_s	-740.08509	16.0		17.1								
C_s	-740.07634	21.5	Saddle point	22.6								
C_s	-740.09764	8.1	-739.97974	8.1								
C_s	-740.09630	8.9	Saddle point	9.2								

Table S3. Neutral forms in water. For each chemical species, energy values (Ha) and relative energies (kcal/mol) of all distinct conformers identified are reported.

G_{PCM}: PCM free energy, PBE0/6-31+G(d,p);

$G_{PCM,RRHO}$: PCM Gibbs free energy in the ideal gas / rigid rotor / harmonic oscillator approximation, referred to a temperature of 298.15 K and to a 1 atm standard state;

$G_{SMD,M06\text{-}2X,large}$: SMD free energy, SMD/M06-2X/6-311++G(2d,2p) // PCM/PBE0/6-31+G(d,p);

$G_{SMD,RRHO,M06\text{-}2X,large} = G_{SMD,M06\text{-}2X,large} + G_{PCM,RRHO} - G_{PCM}$;

$E_{vacuo,M06\text{-}2X,large}$: electronic energy, M06-2X/6-311++G(2d,2p) // PCM/PBE0/6-31+G(d,p);

$E_{vacuo,DLPNO\text{-}CCSD(T)}$: electronic energy, DLPNO-CCSD(T)/cc-pVTZ // PCM/PBE0/6-31+G(d,p);

$G_{SMD,RRHO,DLPNO\text{-}CCSD(T)} = E_{vacuo,DLPNO\text{-}CCSD(T)} + G_{SMD,M06\text{-}2X,large} - E_{vacuo,M06\text{-}2X,large} + G_{PCM,RRHO} - G_{PCM}$.

Symm.	G_{PCM}	°G	$G_{PCM,RRHO}$	°G	$G_{SMD,M06\text{-}2X,large}$	°G	$G_{SMD,RRHO,M06\text{-}2X,large}$	°G	$E_{vacuo,M06\text{-}2X,large}$	°E	$E_{vacuo,DLPNO\text{-}CCSD(T)}$	°E	$G_{SMD,RRHO,DLPNO\text{-}CCSD(T)}$	°G
Reduced state														
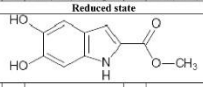														
C_1	-741.37067	10.7	-741.22864	10.6										
C_2	-741.38704	0.4	-741.24542	0.0	-742.11845	0.4	**-741.97682**	0.0	-742.09651	1.3	-740.94825	1.2	**-740.82856**	0.0
C_3	-741.38556	1.4	Saddle point	1.3	-742.11561	2.2	-741.97347	2.1	-742.09464	2.4				
C_4	-741.36948	11.4	Saddle point	12.4										
C_5	-741.37626	7.2	-741.23357	7.5	-742.10933	6.1	-741.96664	6.4	-742.08401	9.1				
C_6	-741.38773	0.0	-741.24548	0.0	-742.11905	0.0	-741.97680	0.0	-742.09851	0.0	-740.95016	0.0	-740.82845	0.1
C_7	-741.38615	1.0	Saddle point	1.0	-742.11626	1.8	-741.97404	1.7	-742.09667	1.2				
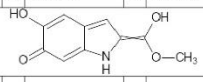														
C_1	-741.33792	31.3	-741.19488	31.7										
C_1	-741.34301	28.1	-741.20108	27.9										
C_1	-741.33878	30.7	-741.19574	31.2										

C_1	-741.34086	29.4	-741.19855	29.4										
C_1	-741.34300	28.1	-741.20199	27.3										
C_1	-741.34275	28.2	-741.20121	27.8										
C_1	-741.34682	25.7	-741.20556	25.0										
C_1	-741.34501	26.8	-741.20235	27.1										
C_2	-741.34279	28.2	-741.20260	26.9										
C_3	-741.33925	30.4	Saddle point	30.3										
C_3	-741.34478	26.9	Saddle point	26.1										
C_3	-741.33709	31.8	Saddle point	32.5										
C_3	-741.33640	32.2	Saddle point	32.8										
C_2	-741.34279	28.2	Saddle point	28.1										
C_3	-741.34055	29.6	Saddle point	29.4										
C_1	-741.34310	28.0	-741.20298	26.7										
C_3	-741.33962	30.2	Saddle point	30.0										
C_2	-741.34072	29.5	-741.19922	29.0										
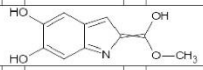														
C_1	-741.32717	38.0	-741.18611	37.3										
C_1	-741.33053	35.9	-741.18930	35.3										
C_1	-741.32704	38.1	-741.18491	38.0										
C_2	-741.32598	38.7	-741.18478	38.1										
C_3	-741.32238	41.0	Saddle point	39.2										
C_4	-741.32845	37.2	Saddle	36.4										

Appendix G

			point											
C_2	-741.32721	38.0	-741.18775	36.2										
C_3	-741.33733	31.6	-741.19449	32.0										
C_4	-741.34017	29.8	-741.19809	29.7										
C_5	-741.33847	30.9	Saddle point	30.9										
C_6	-741.32581	38.9	-741.18488	38.0										
C_7	-741.32224	41.1	Saddle point	40.5										
C_8	-741.32953	36.5	-741.18894	35.5										
One-electron oxidation state														
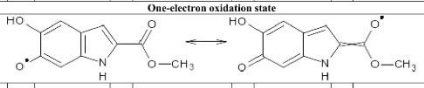														
C_1	-740.74346	10.9	-740.61408	10.8										
C_2	-740.74779	8.2	Saddle point	9.5										
C_3	-740.76016	0.4	-740.63067	0.3	-741.48280	0.9	-741.35332	0.6	-741.46430	1.7	-740.31712	1.2	-740.20614	0.2
C_4	-740.75872	1.3	Saddle point	1.6	-741.48005	2.6	-741.35007	2.6	-741.46241	2.9				
C_5	-740.74175	12.0	Saddle point	12.9										
C_6	-740.74785	8.1	-740.61782	8.4										
C_7	-740.76081	0.0	-740.63123	0.0	-741.48334	0.6	-741.35376	0.3	-741.46639	0.4	-740.31901	0.0	**-740.20638**	0.0
C_8	-740.75931	0.9	Saddle point	1.2	-741.48066	2.3	-741.35066	2.3	-741.46449	1.6				
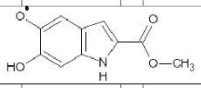														
C_1	-740.74293	11.2	-740.61310	11.4										
C_2	-740.76001	0.5	-740.62997	0.8	-741.48345	0.5	-741.35341	0.5	-741.46455	1.6	-740.31648	1.6	-740.20535	0.6

C_3	-740.75858	1.4	Saddle point	2.0	-741.48073	2.2	-741.35023	2.5	-741.46269	2.7				
C_4	-740.74143	12.2	Saddle point	13.7										
C_5	-740.74888	7.5	-740.61825	8.1	-741.47413	6.4	-741.34349	6.8	-741.45217	9.3				
C_6	-740.76076	0.0	-740.63079	0.3	-741.48425	0.0	**-741.35428**	0.0	-741.46702	0.0	-740.31870	0.2	-740.20596	0.3
C_7	-740.75926	1.0	Saddle point	1.5	-741.48141	1.8	-741.35106	2.0	-741.46515	1.2				
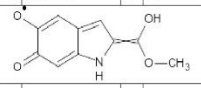														
C_1	-740.69851	39.1	-740.56952	38.7										
C_2	-740.70471	35.2	-740.57676	34.2										
C_3	-740.69953	38.5	-740.57038	38.2										
C_4	-740.70182	37.0	-740.57329	36.4										
C_5	-740.70527	34.9	-740.57751	33.7										
C_6	-740.70494	35.1	-740.57761	33.6										
C_7	-740.70870	32.7	-740.58078	31.7										
C_8	-740.70632	34.2	-740.57759	33.7										
C_9	-740.70494	35.1	Saddle point	33.9										
C_{10}	-740.70161	37.1	Saddle point	36.1										
C_{11}	-740.70677	33.9	Saddle point	32.8										
C_{12}	-740.69732	39.8	Saddle point	39.7										
C_{13}	-740.69693	40.1	Saddle point	39.2										
C_{14}	-740.70439	35.4	Saddle point	34.8										
C_{15}	-740.70226	36.7	Saddle point	36.1										

C_4	-740.70534	34.8	-740.57912	32.7										
C_5	-740.70206	36.9	Saddle point	35.4										
C_6	-740.70169	37.1	-740.57380	36.0										
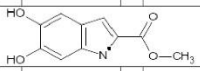														
C_1	-740.72155	24.6	-740.59395	23.4										
C_2	-740.71809	26.8	-740.59047	25.6										
C_3	-740.73216	18.0	-740.60521	16.3										
C_4	-740.73048	19.0	Saddle point	17.6										
C_5	-740.72136	24.8	Saddle point	24.8										
C_6	-740.71538	28.5	Saddle point	28.7										
C_7	-740.73204	18.1	-740.60493	16.5										
C_8	-740.73046	19.0	Saddle point	17.8										
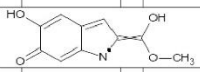														
C_1	-740.70387	35.7	-740.57461	35.5										
C_2	-740.70762	33.4	-740.57831	33.2										
C_3	-740.70771	33.3	Saddle point	33.4										
C_4	-740.70347	36.0	-740.57411	35.8										
C_5	-740.70427	35.5	-740.57544	35.0										
C_6	-740.70089	37.6	Saddle point	37.2										
C_7	-740.70574	34.6	Saddle point	34.7										

C_1	-740.70390	35.7	Saddle point	36.2										
C_2	-740.71191	30.7	-740.58178	31.0										
C_3	-740.71683	27.6	-740.58720	27.6										
C_4	-740.71523	28.6	Saddle point	28.7										
C_5	-740.70403	35.6	-740.57530	35.1										
C_6	-740.70065	37.7	Saddle point	37.2										
C_7	-740.70732	33.6	-740.57864	33.0										
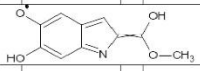														
C_1	-740.70547	34.7	-740.57641	34.4										
C_2	-740.70593	34.4	-740.57725	33.9										
C_3	-740.70977	32.0	-740.58029	32.0										
C_4	-740.70546	34.7	-740.57648	34.4										
C_5	-740.70979	32.0	Saddle point	32.1										
C_6	-740.70647	34.1	-740.57680	34.2										
C_7	-740.70615	34.3	-740.57756	33.7										
C_8	-740.70267	36.5	Saddle point	36.4										
C_9	-740.70786	33.2	Saddle point	33.3										
C_{10}	-740.70550	34.7	Saddle point	35.2										
C_{11}	-740.71511	28.7	-740.58488	29.1										
C_{12}	-740.71884	26.3	-740.58918	26.4										
C_{13}	-740.71720	27.4	Saddle point	27.5										
C_{14}	-740.70608	34.3	-740.57752	33.7										

Appendix G

C_5	-740.70264	36.5	Saddle point	35.8										
C_6	-740.70895	32.5	-740.58050	31.8										
Two-electron oxidation state														
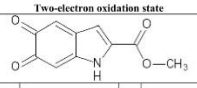														
C_1	-740.11350	10.7	-739.99753	9.6										
C_3	-740.11727	8.4	-739.99954	8.4										
C_5	-740.12981	0.5	-740.01227	0.4	-740.85495	0.4	-740.73740	0.3	-740.82957	1.4	-739.68941	1.2	-739.59724	0.2
C_2	-740.12841	1.4	Saddle point	1.6	-740.85227	2.1	-740.73425	2.3	-740.82769	2.6				
C_4	-740.10999	12.9	Saddle point	14.1										
C_7	-740.11732	8.3	-739.99941	8.5										
C_8	-740.13062	0.0	-740.01289	0.0	-740.85566	0.0	**-740.73792**	0.0	-740.83184	0.0	-739.69140	0.0	**-739.59748**	0.0
C_9	-740.12915	0.9	Saddle point	1.1	-740.85304	1.6	-740.73501	1.8	-740.82997	1.2				
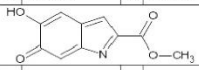														
C_1	-740.10696	14.8	-739.98919	14.9										
C_2	-740.11719	8.4	-739.99988	8.2										
C_3	-740.11560	9.4	Saddle point	9.4										
C_4	-740.10601	15.4	Saddle point	16.7										
C_5	-740.09853	20.1	Saddle point	21.8										
C_7	-740.11700	8.5	-739.99916	8.6										
C_8	-740.11548	9.5	Saddle point	9.9										

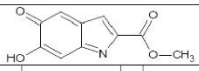														
C_1	-740.10149	18.3	-739.98434	17.9										
C_3	-740.10053	18.9	-739.98277	18.9										
C_5	-740.11325	10.9	-739.99564	10.8										
C_6	-740.11162	11.9	Saddle point	12.1										
C_7	-740.09994	19.3	Saddle point	20.2										
C_8	-740.09850	20.2	Saddle point	21.6										
C_2	-740.11351	10.7	-739.99585	10.7										
C_4	-740.11193	11.7	Saddle point	11.9										

Table S4. Monoanionic forms in water. For each chemical species, energy values (Ha) and relative energies (kcal/mol) of all distinct conformers identified are reported.
G_{PCM}: PCM free energy, PBE0/6-31+G(d,p);
$G_{PCM,RRHO}$: PCM Gibbs free energy in the ideal gas / rigid rotor / harmonic oscillator approximation, referred to a temperature of 298.15 K and to a 1 atm standard state;
$G_{SMD,M06\text{-}2X,large}$: SMD free energy, SMD/M06-2X/6-311++G(2d,2p) // PCM/PBE0/6-31+G(d,p);
$G_{SMD,RRHO,M06\text{-}2X,large} = G_{SMD,M06\text{-}2X,large} + G_{PCM,RRHO} - G_{PCM}$;
$E_{vacuo,M06\text{-}2X,large}$: electronic energy, M06-2X/6-311++G(2d,2p) // PCM/PBE0/6-31+G(d,p);
$E_{vacuo,DLPNO\text{-}CCSD(T)}$: electronic energy, DLPNO-CCSD(T)/cc-pVTZ // PCM/PBE0/6-31+G(d,p);
$G_{SMD,RRHO,DLPNO\text{-}CCSD(T)} = E_{vacuo,DLPNO\text{-}CCSD(T)} + G_{SMD,M06\text{-}2X,large} - E_{vacuo,M06\text{-}2X,large} + G_{PCM,RRHO} - G_{PCM}$.

Symm.	G_{PCM}	°G	$G_{PCM,RRHO}$	°G	$G_{SMD,M06\text{-}2X,large}$	°G	$G_{SMD,RRHO,M06\text{-}2X,large}$	°G	$E_{vacuo,M06\text{-}2X,large}$	°G	$E_{vacuo,DLPNO\text{-}CCSD(T)}$	°G	$G_{SMD,RRHO,DLPNO\text{-}CCSD(T)}$	°G
Reduced state														
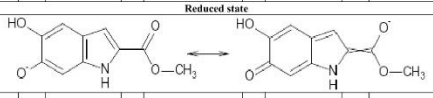														
C_1	-740.90457	10.1	-740.77529	10.1										
C_s	-740.92000	0.4	-740.79088	0.3	-741.65075	0.4	-741.52163	0.2	-741.55957	1.1	-740.40089	1.0	-740.36295	0.1
C_s	-740.91849	1.4	Saddle point	1.5	-741.64784	2.2	-741.51821	2.4	-741.55763	2.3				
C_s	-740.90381	10.6	Saddle point	11.5										
C_s	-740.91052	6.4	-740.78065	6.7	-741.64263	5.5	-741.51277	5.8	-741.55133	6.3				
C_s	-740.92064	0.0	-740.79132	0.0	-741.65132	0.0	**-741.52200**	0.0	-741.56138	0.0	-740.40248	0.0	**-740.36311**	0.0
C_s	-740.91904	1.0	Saddle point	1.2	-741.64846	1.8	-741.51876	2.0	-741.55937	1.3				
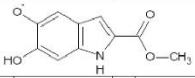														
C_1	-740.90068	12.5	-740.77159	12.4										

C_s	-740.91631	2.7	-740.78723	2.6	-741.64735	2.5	-741.51827	2.3	-741.55266	5.5	-740.39428	5.1	-740.35989	2.0
C_s	-740.91480	3.7	Saddle point	3.8	-741.64449	4.3	-741.51493	4.4	-741.55073	6.7				
C_s	-740.89989	13.0	Saddle point	14.0										
C_s	-740.90647	8.9	-740.77685	9.1										
C_s	-740.91694	2.3	-740.78785	2.2	-741.64790	2.1	-741.51882	2.0	-741.55476	4.2	-740.39633	3.9	-740.36039	1.7
C_s	-740.91535	3.3	Saddle point	3.4	-741.64493	4.0	-741.51546	4.1	-741.55275	5.4				
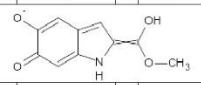														
C_1	-740.85535	41.0	-740.72927	38.9										
C_1	-740.85242	42.8	-740.72494	41.7										
C_1	-740.85346	42.2	-740.72728	40.2										
C_1	-740.85090	43.8	-740.72291	42.9										
C_1	-740.85428	41.6	-740.72629	40.8										
C_1	-740.85368	42.0	-740.72696	40.4										
C_1	-740.84920	44.8	-740.72107	44.1										
C_1	-740.84970	44.5	-740.72124	44.0										
C_s	-740.85543	40.9	Saddle point	39.8										
C_s	-740.85424	41.7	Saddle point	41.3										
C_s	-740.85072	43.9	Saddle point	42.1										
C_s	-740.84660	46.5	Saddle point	45.6										
C_s	-740.85315	42.3	Saddle point	40.9										
C_s	-740.84797	45.6	Saddle point	44.8										
C_s	-740.84651	46.5	Saddle point	44.7										

Appendix G

C_s	-740.85112	43.6	Saddle point	42.5										
C_s	-740.84855	45.2	Saddle point	44.0										
C_s	-740.85110	43.6	Saddle point	41.8										
C_s	-740.84713	46.1	Saddle point	44.4										
C_s	-740.85017	44.2	Saddle point	42.9										
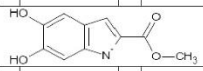														
C_1	-740.88894	19.9	-740.76144	18.7										
C_1	-740.88706	21.1	-740.75900	20.3										
C_s	-740.89927	13.4	-740.77153	12.4										
C_s	-740.89746	14.5	Saddle point	13.9										
C_s	-740.88881	20.0	Saddle point	20.3										
C_s	-740.88621	21.6	Saddle point	22.3										
C_s	-740.89955	13.2	-740.77219	12.0										
C_s	-740.89780	14.3	Saddle point	13.5										
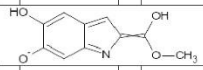														
C_1	-740.86106	37.4	-740.73214	37.1										
C_1	-740.86263	36.4	-740.73478	35.5										
C_1	-740.85845	39.0	-740.73057	38.1										
C_1	-740.85865	38.9	-740.73058	38.1										
C_1	-740.85749	39.6	Saddle point	39.1										

C_s	-740.86346	35.9	-740.73598	34.7										
C_s	-740.86082	37.5	-740.73232	37.0										
C_s	-740.85857	39.0	-740.73076	38.0										
C_s	-740.85452	41.5	Saddle point	41.1										
C_s	-740.86111	37.4	Saddle point	37.3										
C_s	-740.86103	37.4	Saddle point	37.5										
C_s	-740.87159	30.8	-740.74165	31.2										
C_s	-740.87289	30.0	-740.74379	29.8										
C_s	-740.87093	31.2	Saddle point	31.1										
C_s	-740.85836	39.1	Saddle point	38.6										
C_s	-740.85437	41.6	Saddle point	40.1										
C_s	-740.86269	36.4	Saddle point	36.2										
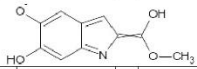														
C_1	-740.85965	38.3	-740.73118	37.7										
C_1	-740.85640	40.3	Saddle point	39.6										
C_1	-740.85646	40.3	-740.72851	39.4										
C_1	-740.85665	40.2	-740.72805	39.7										
C_s	-740.86186	36.9	-740.73431	35.8										
C_s	-740.85880	38.8	-740.73051	38.2										
C_s	-740.85664	40.2	Saddle point	40.0										
C_s	-740.85270	42.6	Saddle point	41.9										

Appendix G

C_5	-740.85954	38.3	Saddle point	36.9										
C_6	-740.85964	38.3	Saddle point	38.5										
C_7	-740.86916	32.3	-740.73932	32.6										
C_8	-740.87077	31.3	-740.74165	31.2										
C_9	-740.86882	32.5	Saddle point	32.4										
C_{10}	-740.85648	40.3	-740.73028	38.3										
C_{11}	-740.85253	42.7	Saddle point	41.8										
C_{12}	-740.86097	37.4	-740.73432	35.8										
One-electron oxidation state														
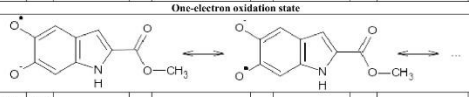														
C_1	-740.27491	10.6	-740.15927	10.4										
C_2	-740.29105	0.5	-740.17545	0.2	-741.02084	0.3	-740.90524	0.1	-740.91856	8.9	-739.75638	11.2	**-739.74306**	0.0
C_3	-740.28955	1.4	Saddle point	1.4	-741.01806	2.1	-740.90206	2.1	-740.91655	10.1				
C_4	-740.27353	11.5	Saddle point	12.4										
C_5	-740.28050	7.1	-740.16415	7.3	-741.01155	6.1	-740.89520	6.4	-740.90972	14.4				
C_6	-740.29179	0.0	-740.17583	0.0	-741.02134	0.0	**-740.90539**	0.0	-740.92053	7.6	-739.75807	10.1	-739.74293	0.1
C_7	-740.29020	1.0	Saddle point	1.1	-741.01855	1.8	-740.90237	1.9	-740.91848	8.9				
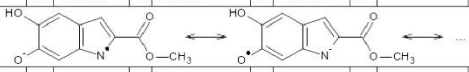														
C_8	-740.27667	9.5	-740.16102	9.3										

C_1	-740.27385	11.3	-740.15774	11.4										
C_2	-740.28708	3.0	-740.17108	3.0	-741.01663	3.0	-740.90064	3.0	-740.93268	0.0	-739.77423	0.0	-739.74219	0.5
C_3	-740.28532	4.1	Saddle point	4.3	-741.01360	4.9	-740.89729	5.1	-740.93037	1.4				
C_4	-740.27653	9.6	Saddle point	10.8										
C_5	-740.27192	12.5	Saddle point	14.1										
C_6	-740.28712	2.9	-740.17054	3.3	-741.01681	2.8	-740.90024	3.2	-740.93057	1.3	-739.77218	1.3	-739.74185	0.8
C_7	-740.28543	4.0	Saddle point	4.7	-741.01378	4.7	-740.89678	5.4	-740.92837	2.7				
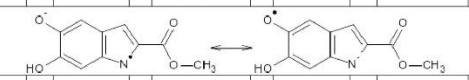														
C_1	-740.27510	10.5	-740.15906	10.5										
C_1	-740.27362	11.4	-740.15697	11.8										
C_2	-740.28603	3.6	-740.17032	3.5	-741.01606	3.3	-740.90035	3.2	-740.93212	0.4	-739.77335	0.6	-739.74158	0.9
C_3	-740.28428	4.7	Saddle point	4.9	-741.01299	5.2	-740.89681	5.4	-740.92982	1.8				
C_4	-740.27471	10.7	Saddle point	11.8										
C_5	-740.27262	12.0	Saddle point	13.7										
C_6	-740.28634	3.4	-740.17000	3.7	-741.01642	3.1	-740.90007	3.3	-740.93057	1.3	-739.77194	1.4	-739.74144	1.0
C_7	-740.28469	4.5	Saddle point	5.0	-741.01352	4.9	-740.89671	5.4	-740.92843	2.7				
Two-electron oxidation state														
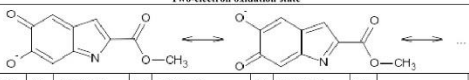														
C_1	-739.64806	6.4	-739.54592	5.9	-740.37606	6.8	-740.27392	6.2	-740.29451	3.6				
C_2	-739.65800	0.1	-739.55538	0.0	-740.38637	0.3	**-740.28376**	0.0	-740.30022	0.0	-739.14675	0.0	**-739.13029**	0.0
C_3	-739.65626	1.2	Saddle point	1.4	-740.38343	2.1	-740.28033	2.2	-740.29786	1.5				
C_4	-739.64577	7.8	Saddle point	8.4	-740.37213	9.2	-740.26830	9.7	-740.29352	4.2				

Appendix G

C_s	-739.64238	9.9	Saddle point	11.5										
C_s'	-739.65820	0.0	-739.55484	0.3	-740.38684	0.0	-740.28348	0.2	-740.29833	1.2	-739.14505	1.1	-739.13019	0.1
C_s	-739.65651	1.1	Saddle point	1.5	-740.38391	1.8	-740.28037	2.1	-740.29605	2.6				

Appendix G

Table S5. pK_a Values computed at two different theory levels for reference acids, and corresponding experimental values. For each chemical species, the G value of the most stable conformer identified was used in the calculation. At each theory level, a linear fitting with respect to the experimental values was used to correct the raw pK_a values.

Species	$G_{SMD,RRHO,M06\text{-}2X,large}$ / Ha		pK_a[a]	$G_{SMD,RRHO,DLPNO\text{-}CCSD(T)}$ / Ha		pK_a[b]	Exptl. pK_a[c]
	Neutral form	Deprotonated form		Neutral form	Deprotonated form		
2-Chlorophenol	-766.98129	-766.52471	8.60	-766.00933	-765.54140	7.87	8.56
2-Nitrophenol	-511.86777	-511.41850	6.15	-511.09495	-510.63193	6.20	7.23
3-Chlorophenol	-766.98389	-766.52506	9.36	-766.01231	-765.54190	8.71	9.12
3-Nitrophenol	-511.86979	-511.41373	8.43	-511.09724	-510.62861	8.10	8.36
4-Chlorophenol	-766.98362	-766.52218	10.23	-766.01165	-765.53867	9.59	9.41
4-Nitrophenol	-511.87346	-511.42400	6.21	-511.10027	-510.63591	6.65	7.15
Acetic acid	-229.04790	-228.60117	5.30	-228.72562	-228.26458	5.52	4.756
Acetone	-193.07805	-192.59222	18.42	-192.78580	-192.28458	19.20	19.1[d]
Acetylacetone	-345.68236	-345.22468	8.97	-345.16075	-344.68772	9.60	8.9[e]
Formic acid	-189.75375	-189.31168	3.73	-189.49983	-189.04135	4.65	3.75
Phenol	-307.36938	-306.90558	11.03	-306.86571	-306.39053	10.34	9.99

[a] R^2 = 0.970; mean absolute error = 0.50; maximum absolute error = 1.08.
[b] R^2 = 0.974; mean absolute error = 0.52; maximum absolute error = 1.03.
[c] All values from the *CRC Handbook of Chemistry and Physics*.[17]
[d] Guthrie *et al., J. Am. Chem. Soc.,* 1982.[18]
[e] Bordwell, *Acc. Chem. Res.,* 1988.[19]

Appendix G

Table S6. pK_a values computed at two different theory levels for MeDHICA in its reduced, one-electron (semiquinone) and two-electron (quinone) oxidation states. For each chemical species, the G value of the most stable tautomer / conformer identified (see Tables S2-S4) was used in the calculation. The linear fitting constants obtained from the data in Table S5 were used to correct the raw pK_a values.

Species	$G_{SMD,RRHO,M06\text{-}2X,larger}$ / Ha		pK_a	$G_{SMD,RRHO,DLPNO\text{-}CCSD(T)}$ / Ha		pK_a
	Neutral form	Deprotonated form		Neutral form	Deprotonated form	
Reduced state	-741.97682	-741.52200	8.01	-740.82856	-740.36311	7.02
One-electron oxidation state	-741.35428	-740.90539	6.02	-740.20638	-739.74306	6.30
Two-electron oxidation state	-740.73792	-740.28376	7.79	-739.59748	-739.13029	7.62

Table S7. Energetics of redox reactions of MeDHICA (neutral forms in vacuo and in water), computed at two different theory levels. For each chemical species, the *G* value of the most stable tautomer / conformer identified (see Tables S2-S4) was used in the calculation. In order to (partially) compensate for systematic errors, half-reaction energies are referred to the corresponding half-reaction of 4-methyl-1,2-dihydroxybenzene, computed at the same level, and taken as zero (*i.e.*, each one-electron oxidation step of MeDHICA is referred to the corresponding one-electron oxidation step of 4-methyl-1,2-dihydroxybenzene, computed at the same level).

Half-reaction	$^{\circ}_{r}G_{RRHO,M06\text{-}2X,Jarge}$ / **kcal/mol**	$^{\circ}_{r}G_{SMD,RRHO,M06\text{-}2X,Jarge}$ / **kcal/mol**	$^{\circ}_{r}G_{RRHO,DLPNO\text{-}CCSD(T)}$ / **kcal/mol**	$^{\circ}_{r}G_{SMD,RRHO,DLPNO\text{-}CCSD(T)}$ / **kcal/mol**
	In vacuo	**In water**	**In vacuo**	**In water**
Reduced → one-electron oxidized (semiquinone)	-0.5	-0.5	-1.0	-0.6
One-electron oxidized (semiquinone) → two-electron oxidized (quinone)	5.9	5.8	6.1	5.7

Appendix G

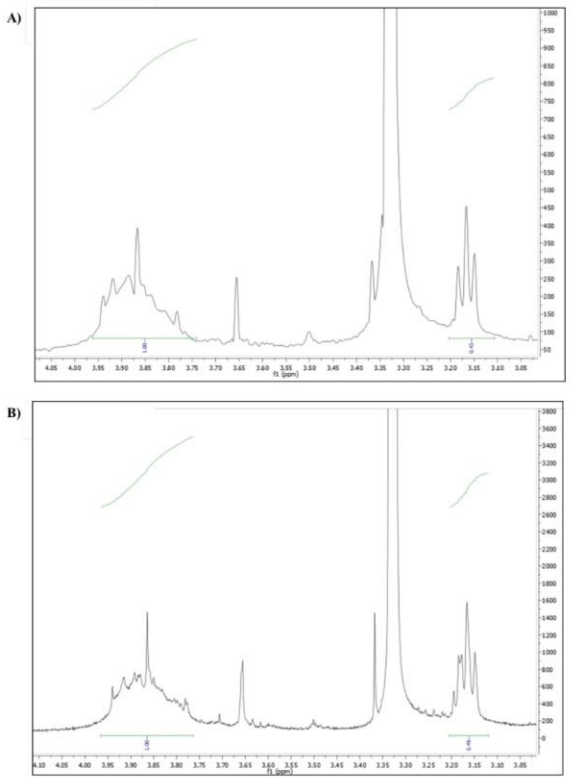

Fig. S15. [1]H NMR spectra of the films dissolved in DMSO and subjected to acetylation treatment from the oxidation mixtures of MeDHICA/HMDA at different indole to diamine molar ratios. Shown are peak area integration of signals due to the methyl group of the ester functionality of MeDHICA and its oligomers at 3.9-3.7 ppm and the methylene group alpha to the amino groups in HMDA at 3.15 ppm. A) Films from mixtures at 1: 1.5 and B) 1:0.5 indole to amine molar ratio.

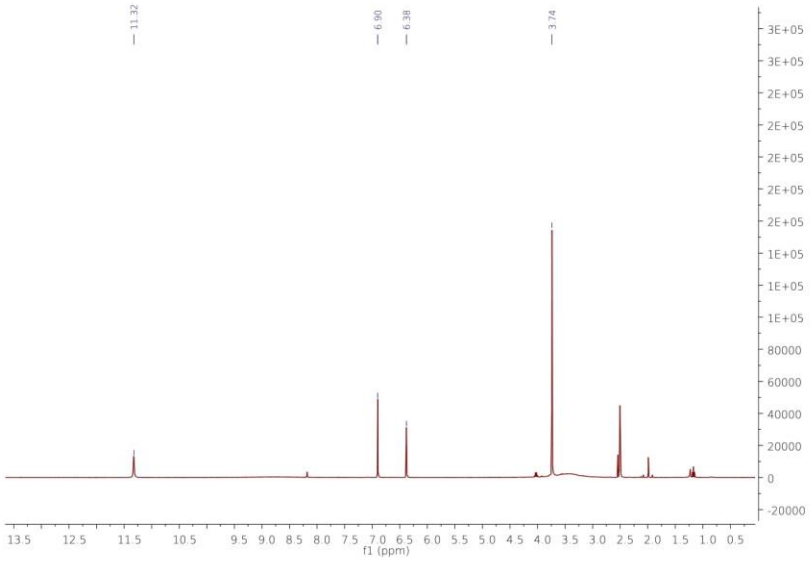

Fig. S16. ^{1}H NMR spectrum of 4,4'-biindolyl from MeDHICA in DMSO-d6.

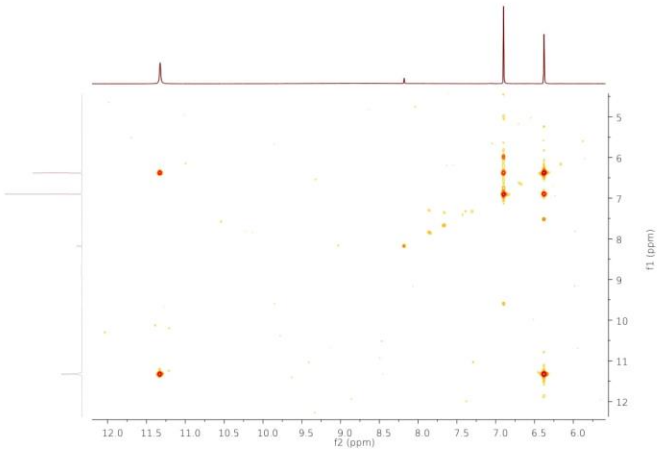

Fig. S17. ^{1}H,^{1}H COSY spectrum of 4,4'-biindolyl from MeDHICA (selected region).

Appendix G

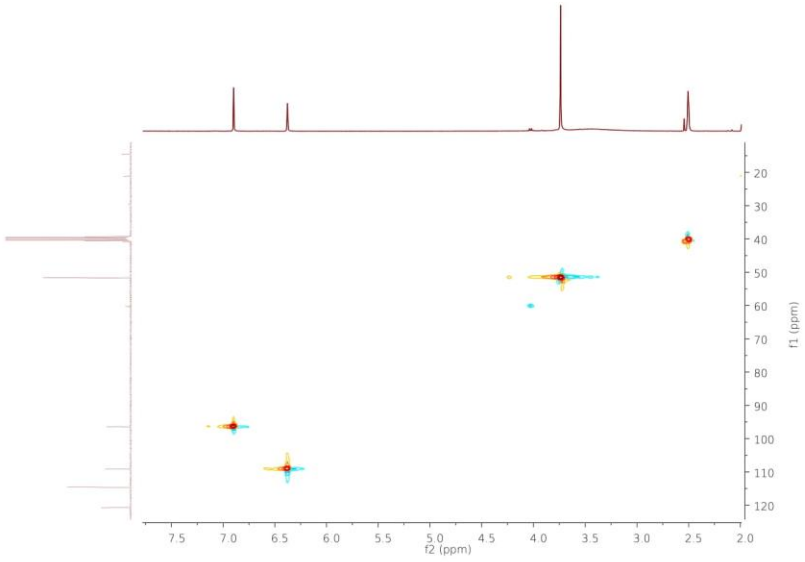

Fig. S18. $^{1}H,^{13}C$ HSQC spectrum of 4,4'-biindolyl from MeDHICA (selected region).

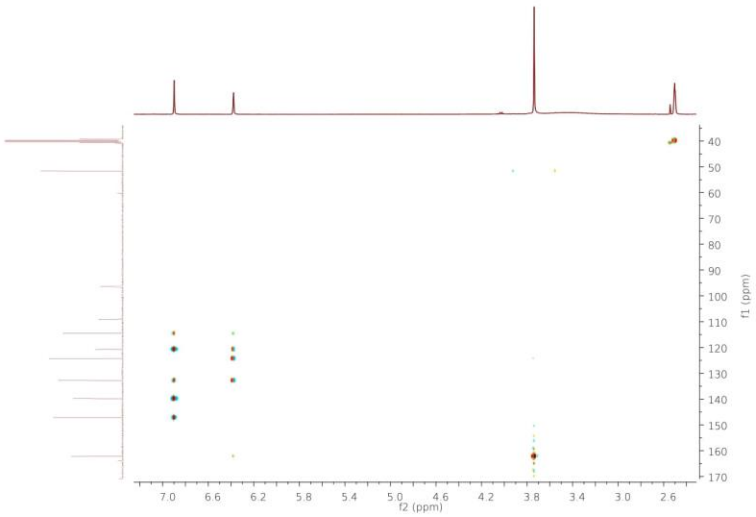

Fig. S19. $^{1}H,^{13}C$ HMBC spectrum of 4,4'-biindolyl from MeDHICA (selected region).

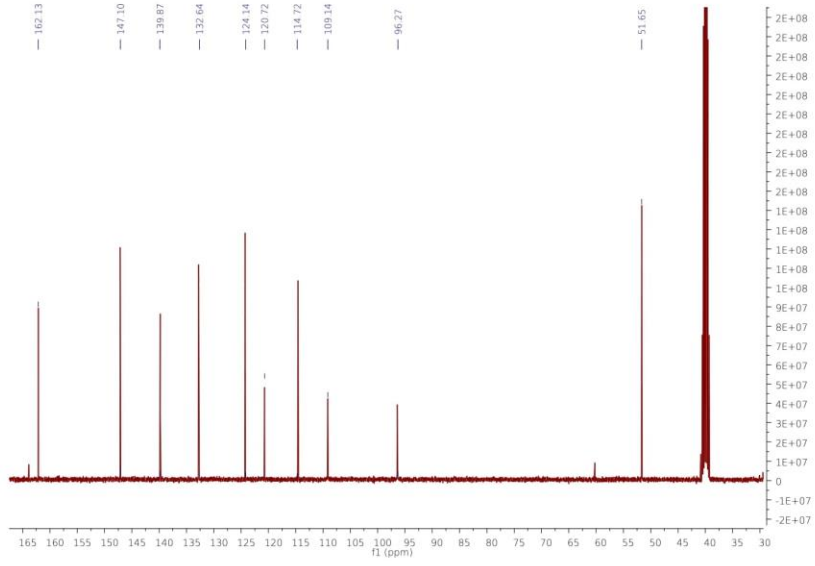

Fig. S20. ^{13}C NMR spectrum of 4,4'-biindolyl from MeDHICA in DMSO-d6 (selected region).

Appendix G

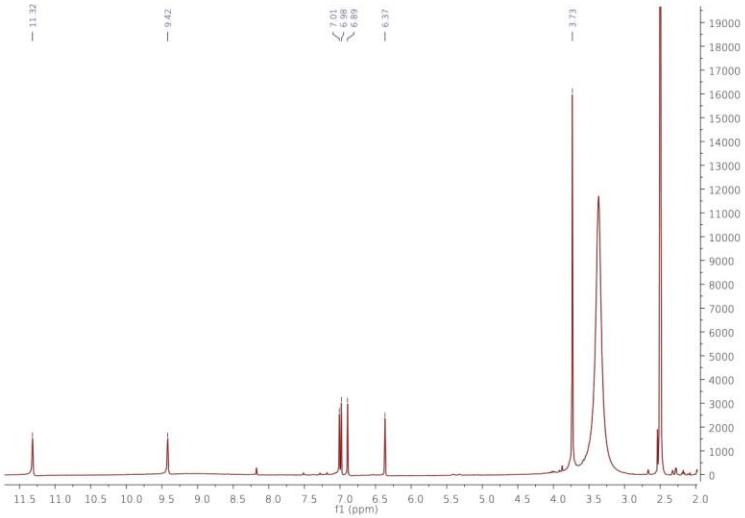

Fig. S21. ^{1}H NMR spectrum of 4,7'-biindolyl from MeDHICA in DMSO-d6.

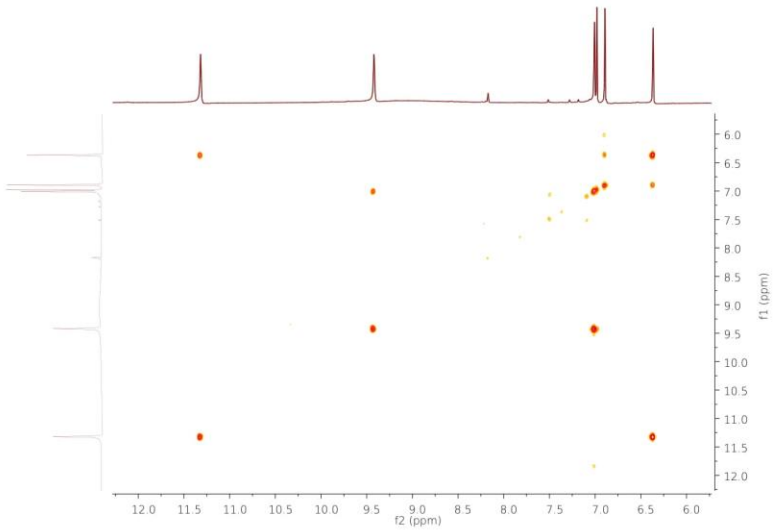

Fig. S22. ^{1}H,^{1}H COSY spectrum of 4,7'-biindolyl from MeDHICA (selected region).

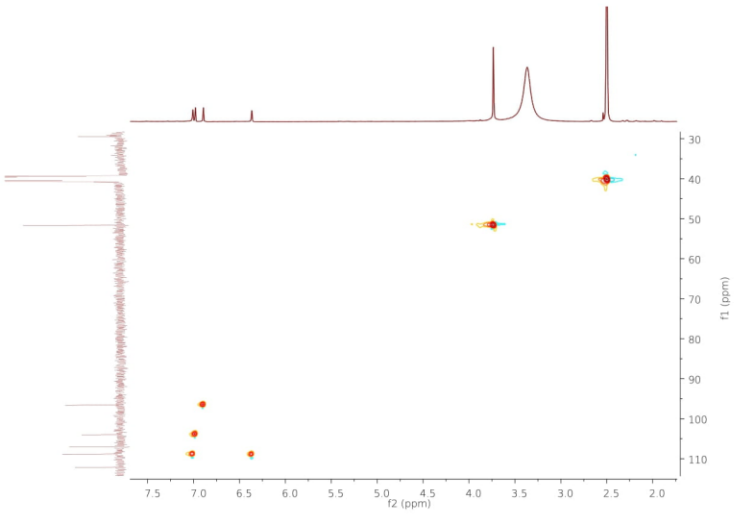

Fig. S23. $^{1}H,^{13}C$ HSQC spectrum of 4,7'-biindolyl from MeDHICA (selected region).

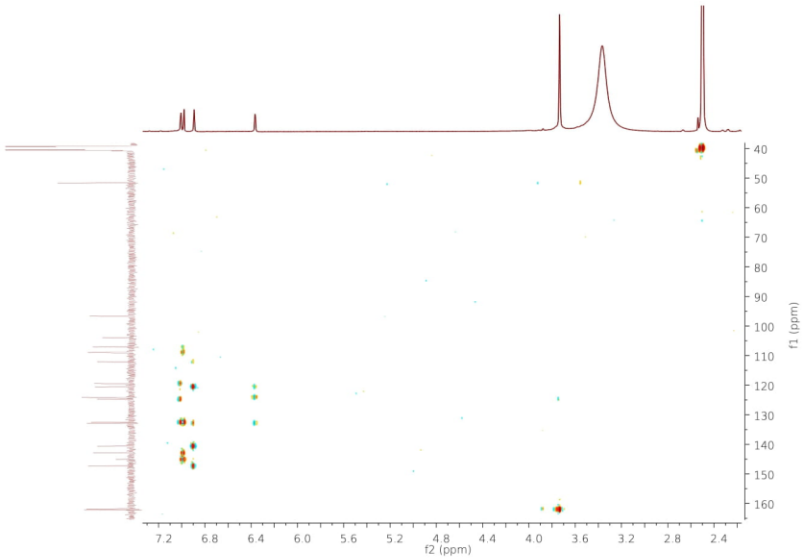

Fig. S24. $^{1}H,^{13}C$ HMBC spectrum of 4,7'-biindolyl from MeDHICA (selected region).

Appendix G

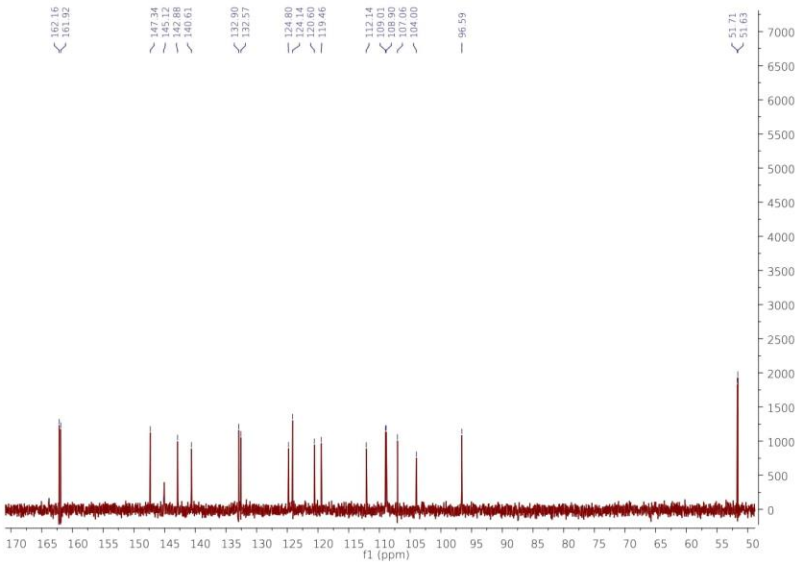

Fig. S25. ^{13}C NMR spectrum of 4,7'-biindolyl from MeDHICA in DMSO-d6 (selected region).

Appendix G

References

[1] G. Sauerbrey, The use of quartz oscillators for weighing thin layers and for microweighing, Z. Phys. 155 (1959) 206-222. DOI: 10.1007/BF01337937.

[2] P.T. Kissinger, W.R. Heineman, Cyclic voltammetry, J. Chem. Educ. 60 (1983) 702–706. DOI: 10.1021/ed060p702.

[3] M.J. Frisch, G.W. Trucks, H.B. Schlegel, G.E. Scuseria, M.A. Robb, J.R. Cheeseman, G. Scalmani, V. Barone, B. Mennucci, G.A Petersson, H. Nakatsuji,M. Caricato, X. Li, H.P. Hratchian, A.F. Izmaylov, J. Bloino, G. Zheng, J. L. Sonnenberg, M. Hada, M. Ehara, K. Toyota, R. Fukuda, J. Hasegawa, M. Ishida, T. Nakajima, Y. Honda, O. Kitao, H. Nakai, T. Vreven, J.A. Jr. Montgomery, J.E. Peralta, F. Ogliaro, M. Bearpark, J.J. Heyd, E. Brothers, K.N. Kudin, V. N. Staroverov, R. Kobayashi, J. Normand, K. Raghavachari, A. Rendell, J.C. Burant, S.S. Iyengar, J. Tomasi, M. Cossi, N. Rega, J.M. Millam, M. Klene, J.E. Knox, J.B. Cross, V. Bakken, C. Adamo, J. Jaramillo, R. Gomperts, R.E. Stratmann, O. Yazyev, A.J. Austin, R. Cammi, C. Pomelli, J.W. Ochterski, R.L. Martin, K. Morokuma, V.G. Zakrzewski, G.A. Voth, P. Salvador, J.J. Dannenberg, S. Dapprich, A.D. Daniels, Ö. Farkas, J.B. Foresman, J.V. Ortiz, J. Cioslowski, Fox, D.J. in Gaussian 09, Revision D.01; Gaussian, Inc., Wallingford CT, 2013.

[4] C. Adamo, V. Barone, Toward reliable density functional methods without adjustable parameters: the PBE0 model, J. Chem. Phys. 110 (1999) 6158-6170. DOI:10.1063/1.478522.

[5] Y. Zhao, D.G. Truhlar, The M06 suite of density functionals for main group thermochemistry, thermochemical kinetics, noncovalent interactions, excited states, and transition elements: two new functionals and systematic testing of four M06-class functionals and 12 other function, Theor. Chem. Acc. 120 (2008) 215-241. DOI: 10.1007/s00214-007-0310-x.

[6] S. Miertuš, E. Scrocco, J. Tomasi, Electrostatic interaction of a solute with a continuum. A direct utilizaion of AB initio molecular potentials for the prevision of solvent effects, Chem. Phys. 55 (1981) 117-129. DOI: 10.1016/0301-0104(81)85090-2.

[7] M. Cossi, N. Rega, G. Scalmani, V. Barone, Energies, structures, and electronic properties of molecules in solution with the C-PCM solvation model, J. Comput. Chem. 24 (2003) 669-681. DOI: 10.1002/jcc.10189.

[8] G. Scalmani, V. Barone, K.N. Kudin, C.S. Pomelli, G.E. Scuseria, M.J. Frisch, Achieving linear-scaling computational cost for the polarizable continuum model of solvation, Theor. Chem. Acc. 111 (2004) 90-100. DOI: 10.1007/s00214-003-0527-2.

[9] J. Tomasi, B. Mennucci, R. Cammi, Quantum mechanical continuum solvation models, Chem. Rev. 105 (2005) 2999-3093. DOI: 10.1021/cr9904009.

[10] A. V. Marenich, C.J. Cramer, D.G. Truhlar, Universal solvation model based on solute electron density and on a continuum model of the solvent defined by the bulk dielectric constant and atomic surface tensions, J. Phys. Chem. B 113 (2009) 6378-6396. DOI: 10.1021/jp810292n.

[11] F. Neese, The ORCA Program System. WIREs Comput. Mol. Sci. 2 (2012), 73-78. DOI: 10.1002/wcms.81.

[12] T.H. Dunning, Gaussian basis sets for use in correlated molecular calculations. I. The atoms boron through neon and hydrogen, J. Chem. Phys. 90 (1989) 1007-1023. DOI: 10.1063/1.456153.

[13] C. Riplinger, B. Sandhoefer, A. Hansen, F. Neese, Natural triple excitations in local coupled cluster calculations with pair natural orbitals, J. Chem. Phys. 139 (2013) 134101. DOI: 10.1063/1.4821834.

[14] C. Riplinger, P. Pinski, U. Becker, E.F. Valeev, F. Neese, Sparse maps - a systematic infrastructure for reduced-scaling electronic structure methods. II. Linear scaling domain based pair natural orbital coupled cluster theory, J. Chem. Phys. 144 (2016) 024109. DOI: 10.1063/1.4939030.

Appendix G

[15] C. Riplinger, F. Neese, An efficient and near linear scaling pair natural orbital based local coupled cluster method, J. Chem. Phys. 138 (2013) 034106. DOI: 10.1063/1.4773581.

[16] K. Raghavachari, G.W. Trucks, J.A. Pople, M. Head-Gordon, Chem. Phys. Lett. 157 (1989) 479-483. DOI: 10.1016/S0009-2614(89)87395-6.

[17] D.R. Lide, in CRC Handbook of Chemistry and Physics, 83rd Edition, CRC Press: Boca Raton, 2002.

[18] J.P. Guthrie, J. Cossar, A. Klym, The pK_a of acetone: a kinetic method for determining the pKas of ketones in aqueous solution, J. Am. Chem. Soc. 104 (1982) 895-896. DOI: 10.1021/ja00367a061.

[19] F.G. Bordwell, Equilibrium acidities in dimethyl sulfoxide solution, Acc. Chem. Res. 21 (1988) 456-463. DOI: 10.1021/ar00156a004.

antioxidants

MDPI

Article

Chestnut Wood Mud as a Source of Ellagic Acid for Dermo-Cosmetic Applications

Federica Moccia [1], Davide Liberti [1], Samuele Giovando [2], Carla Caddeo [3], Daria Maria Monti [1], Lucia Panzella [1,*] and Alessandra Napolitano [1]

[1] Department of Chemical Sciences, University of Naples "Federico II", Via Cintia 4, I-80126 Naples, Italy
[2] Centro Ricerche per la Chimica Fine Srl for Silvateam Spa, Via Torre 7, I-12080 San Michele Mondovì, Italy
[3] Department of Scienze della Vita e dell'Ambiente, Sezione di Scienze del Farmaco, University of Cagliari, Via Ospedale 72, I-09124 Cagliari, Italy
* Correspondence: panzella@unina.it; Tel.: +39-081674131

Abstract: Ellagic acid (EA) has long been recognized as a very active antioxidant, anti-inflammatory, and antimicrobial agent. However, its low bioavailability has often hampered its applications in health-related fields. Here, we report a phospholipid vesicle-based controlled release system for EA, involving the exploitation of chestnut wood mud (CWM), an industrial by-product from chestnut tannin production, as a largely available and low-cost source of this compound. Two kinds of CWM with different particle size distributions, indicated as CWM-A and CWM-B (<100 and 32 μm, respectively), containing 5 ± 1% *w*/*w* EA, were incorporated into transfersomes. The latter were small in size (~100 nm), homogeneously dispersed, and negatively charged. 2,2-Diphenyl-1-picrylhydrazyl (DPPH) and ferric reducing/antioxidant power (FRAP) assays indicated up to three-fold improvement in the antioxidant properties of CWM upon incorporation into transfersomes. The kinetics of EA released under simulated physiological conditions were evaluated by UV-Vis spectroscopy and HPLC analysis. The best results were obtained with CWM-B (100% of EA gradually released after 37 days at pH 7.4). A stepwise increase in the antioxidant properties of the released material was also observed. Cell-based experiments confirmed the efficacy of CWM-B transfersomes as antioxidant agents in contrasting photodamage.

Keywords: ellagic acid; chestnut wood; antioxidant; controlled release; transfersomes; HaCaT; 2,2-diphenyl-1-picrylhydrazyl (DPPH) assay; ferric reducing/antioxidant power (FRAP) assay; UVA; reactive oxygen species

Citation: Moccia, F.; Liberti, D.; Giovando, S.; Caddeo, C.; Monti, D.M.; Panzella, L.; Napolitano, A. Chestnut Wood Mud as a Source of Ellagic Acid for Dermo-Cosmetic Applications. *Antioxidants* **2022**, *11*, 1681. https://doi.org/10.3390/antiox11091681

Academic Editor: Stanley Omaye

Received: 22 July 2022
Accepted: 25 August 2022
Published: 28 August 2022

1. Introduction

Ellagic acid (EA) is a phenolic compound naturally present in many red fruits and berries. Apart from being the main product of ellagitannin hydrolysis, it is endowed with remarkable biological properties, including antioxidant [1–3], anti-inflammatory [4], antimicrobial [5], antidiabetic [6], antiviral [7], antidegenerative [8], and anticancer activities [9]. In addition to systemic uses, topical applications of EA have been widely described [10]. Several studies have reported the potential use of EA for the prevention or treatment of skin disorders. For example, EA was found to be effective against skin tumors [11], contact dermatitis [12], or cutaneous leishmaniasis [13]. It can be used in wound bandaging [14], or as a photoprotective [15] and antiaging agent [16]. Furthermore, EA is considered a useful compound in the treatment of skin pigmentation disorders, such as hyperpigmentation, melasma, and other dyschromia [17].

Despite its remarkable properties, the wide application of EA is limited by its low permeability and low solubility in aqueous solvents. To overcome these drawbacks, several approaches have been proposed, involving modulation of EA solubility properties through encapsulation or chemical derivatization [18–23], and different type of

Appendix H

formulations based on e.g., pectins [24,25], chitosan [25–27], chitin [28], zein [5], cellulose [29], cyclodextrins [30–32], poly(lactide-co-glycolide) (PLGA) [33], graphene oxide [34], alginate [35], and microalgae [36] have been designed for the controlled release of this compound.

In this context, liposomes (spherical vesicles composed of one or more bilayers formed by dispersion of phospholipids in aqueous medium) have been largely utilized as a drug delivery vehicle for administration of nutrients and pharmaceutical drugs in biomedical, food, and agricultural industries, and have also been exploited for enhancing the biological effects [37–39], improving skin permeation [40], and guaranteeing a sustained release [41] of EA. In particular, over the last few years, liposomes have been the target of reformulating studies aimed at producing vesicles capable of delivering active compounds to the deeper skin layers. A number of additives have been explored in combination with conventional components of liposomes, producing new classes of vesicles, such as transfersomes. Transfersomes are composed of phospholipids and an edge activator, which is a membrane-softening agent (e.g., Tween 80, Span 80, or sodium cholate) that makes the vesicle ultra-deformable and capable of penetrating the skin more efficiently than conventional liposomes [42–45].

In addition to the development of novel formulations to improve its bioavailability, another primary aim of the recent scientific research on EA is the discovery of sustainable, low cost and easily available sources of this compound, prompted by the global increasing demand for green products and processes. Among these sources, a prominent role is occupied by agri-food by-products such as pomegranate peel [46–50], although other ellagitannin-rich wastes have recently emerged as possible sources of EA. A noticeable example is represented by chestnut shell [51–53] as well as chestnut wood fiber, which is the residual exhausted material from chestnut tannin industrial production [54,55].

Within this scenario, we report herein the exploitation of chestnut wood mud (CWM) as an easily available source of EA for dermo-cosmetic applications upon incorporation into transfersomes. CWM is an industrial by-product of the chestnut tannin production, deriving from exhausted chestnut wood subjected to a natural fermentation process. The antioxidant properties of the samples were investigated by chemical assays and the protective effects on UVA-induced oxidative photodamage were evaluated on immortalized human keratinocytes (HaCaT). Finally, the controlled-release profile of EA under simulated physiological conditions was investigated by UV-Vis spectroscopy and HPLC.

2. Materials and Methods

2.1. Materials

CWM was provided by Silvateam (S. Michele Mondovì, Cuneo, Italy). CWM was first dried in an oven at 35 °C for one week, then ground in a common blender and finally passed through sieves to obtain two fractions with particle sizes lower than 100 and 32 μm, indicated as CWM-A and CWM-B, respectively.

Lipoid S75 (S75), a mixture of soybean phospholipids (70% phosphatidylcholine, 9% phosphatidylethanolamine and 3% lysophosphatidylcholine), triglycerides and fatty acids, was purchased from Lipoid GmbH (Ludwigshafen, Germany). Tween 80 (polysorbate 80, polyoxyethylene sorbitan monooleate; non-ionic hydrophilic surfactant, HLB 15) was supplied by Galeno (Carmignano, Prato, Italy).

2,2-Diphenyl-1-picrylhydrazyl (DPPH), iron(III) chloride (97%), phosphate buffer saline (PBS) 10×, 2,4,6-tris(2-pirydyl)-s-triazine (TPTZ) (≥98%), and (±)-6-hydroxy-2,5,7,8-tetramethylchromane-2-carboxylic acid (Trolox) (97%) were obtained from Sigma-Aldrich (Milan, Italy).

2.2. Methods

UV–Vis spectra were recorded on a Jasco (Lecco, Italy) V-730 Spectrophotometer.

HPLC analysis was performed with an Agilent (Cernusco sul Naviglio, Milan, Italy) instrument equipped with a UV-Vis detector; a Phenomenex (Castel Maggiore, Bologna, Italy)

Appendix H

Sphereclone ODS column (250 × 4.60 mm, 5 µm) was used at a flow rate of 1.0 mL/min. A gradient elution using 0.1% formic acid in water (solvent A) and methanol (solvent B) was performed as follows: 5% B, 0–10 min; from 5 to 80% B, 10–57.5 min. The detection wavelength was set at 254 nm.

2.3. Preparation and Characterization of Transfersomes

CWM (A or B) was weighed in a glass vial along with S75; thereafter, Tween 80 and water were added (Table 1). To obtain the transfersomes, the dispersion was sonicated (5 s on and 2 s off, 10 cycles; 13 microns of probe amplitude) with an ultrasonic disintegrator (Soniprep 150 plus; MSE Crowley, London, UK).

For comparative purposes, empty transfersomes (i.e., those without CWM) were also prepared under the same conditions as CWM transfersomes (Table 1).

The mean diameter, polydispersity index, and zeta potential of the transfersomes were determined by dynamic and electrophoretic light scattering using a Zetasizer nano-ZS (Malvern Panalytical, Worcestershire, UK). Samples ($n > 10$) were diluted with water (1:100) and analyzed at 25 °C.

The above three parameters were monitored for 90 days to assess the long-term stability of the formulations.

Table 1. Composition of the transfersome formulations.

Formulation	S75	CWM	Tween 80	H_2O
Empty transfersomes	120 mg	-	0.05 mL	0.95 mL
CWM-A transfersomes	120 mg	2 mg	0.05 mL	0.95 mL
CWM-B transfersomes	120 mg	2 mg	0.05 mL	0.95 mL

2.4. Antioxidant Properties of CWM Samples

2.4.1. DPPH Assay

CWM or CWM transfersomes (0.02–0.15 mg/mL final dose) (concentrations are referred to as CWM content in the formulations) were added to 3 mL of a 0.2 mM ethanolic solution of DPPH [56], and after 10 min under stirring at room temperature, the absorbance at 515 nm was measured. Experiments were run in triplicate.

2.4.2. Ferric Reducing/Antioxidant Power (FRAP) Assay

CWM and CWM transfersomes were added (0.001–0.1 mg/mL final dose) (concentrations are referred to as CWM content in the formulations) to 3 mL of 0.3 M acetate buffer (pH 3.6) containing 1.7 mM $FeCl_3$ and 0.83 mM TPTZ [57], and after 10 min of stirring at room temperature, the absorbance of the solutions at 593 nm was measured. Results were expressed as Trolox equivalents (eqs). Experiments were run in triplicate.

2.5. Release Experiments from CWM Transfersomes

Each CWM transfersome formulation (3 g) was placed in a dialysis membrane (MWCO 100–500 Da) and dialyzed against 30 mL of PBS 1×. The samples were kept at 37 °C in a water bath. Next, 0.5 mL of release medium was periodically withdrawn and replaced with an equal volume of corresponding fresh medium and analyzed using UV-Vis spectroscopy or HPLC. Each experiment was run in triplicate.

2.6. Antioxidant Properties of Released Fractions from CWM Transfersomes

Aliquots (150 µL) of the released fractions from CWM transfersomes were added to 2 mL of FRAP reagent prepared as described in Section 2.4.2. After 10 min under stirring, the mixtures were centrifuged (3 min at 5000 rpm) and the absorbance of the supernatants at 593 nm was measured.

Appendix H

2.7. Analysis of Cell Viability

Immortalized human keratinocytes (HaCaT, Innoprot, Derio, Spain) were cultured in 10% fetal bovine serum in Dulbecco's Modified Eagle's Medium, in the presence of 1% antibiotics and 2 mM L-glutamine, in a 5% CO_2 humidified atmosphere at 37 °C. To verify the biocompatibility of each sample, cells were seeded in 96-well plates at a density of $2 \times 10^3/cm^2$ and 24 h after seeding. Cells were incubated in the presence of increasing concentration of EA (up to 10 µM) or transfersome samples (up to 25 µL/mL) for 24 and 48 h. At the end of incubation, cell viability was assessed by the 3-(4,5-dimethylthiazol-2-yl)-2,5-diphenyltetrazoliumbromide (MTT) assay. Cell survival was expressed as the percentage of viable cells in the presence of each sample and compared with control cells (represented by the average obtained between untreated cells and cells supplemented with the highest concentration of buffer). Each sample was tested in three independent analyses, each carried out in triplicate.

2.8. UVA Irradiation and Dichlorofluorescein Diacetate (DCFDA) Assay

The protective effect of each sample was measured by determining the intracellular reactive oxygen species (ROS) levels. A previously reported protocol [58] was followed, with some modifications. Briefly, HaCaT cells were preliminarily exposed for 2, 6, and 16 h to 10 µM EA to define the proper incubation time. After that, cells were incubated with the samples (10 µM EA or 25 µL/mL transfersomes, providing a 10 µM EA concentration) for 6 h in the absence or presence of 10 min UVA irradiation (100 J/cm^2). At the end of the irradiation, H_2-DCFDA was added to measure intracellular ROS level. Fluorescence intensity of the probe was measured at an emission wavelength of 525 nm and an excitation wavelength of 488 nm using a Perkin-Elmer (Milan, Italy) LS50 spectrofluorometer. Emission spectra were acquired at a scanning speed of 300 nm/min, with 5 slit widths for both excitation and emission. ROS production was expressed as percentage of DCF fluorescence intensity of the sample under test, compared to the untreated sample. Results are presented as mean of results obtained after three independent experiments (mean ± SD) and compared by one-way ANOVA according to Bonferroni's method (post hoc) using Graphpad Prism for Windows, version 6.01.

3. Results and Discussion

3.1. Determination of the EA Content in CWM Samples

To gain information about the amount of EA contained in the two CWM samples, DMSO solutions of CWM-A and CWM-B were prepared and then analyzed using UV-Vis spectroscopy and HPLC after proper dilution in methanol. DMSO was chosen as the solvent based on its ability to dissolve a wide range of most polar and non-polar natural phenolic compounds, including EA [50,54,59].

As an example, the UV-Vis spectrum and elutographic profile of CWM-A are reported in Figure 1. The UV-Vis spectrum was characterized by absorption maxima at around 280 and 360 nm, as expected based on the presence of EA [60]. In agreement with this observation, HPLC analysis showed the presence of a single chromatographable compound eluted at ca. 38 min, identified as EA by comparison with an authentic standard. Quantitative analysis indicated content of EA of 5 ± 1% *w*/*w* for both CWM-A and CWM-B.

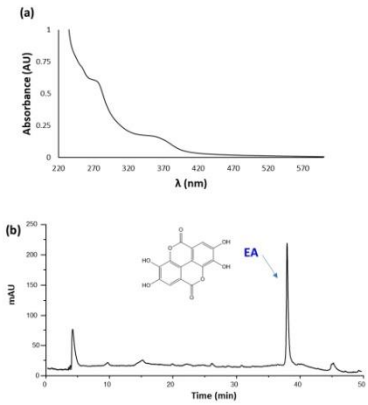

Figure 1. (**a**) UV-Vis spectrum (recorded at 0.02 mg/mL) and (**b**) HPLC profile (recorded at 1 mg/mL) of CWM-A.

3.2. Incorporation of CWM Samples into Transfersomes

Transfersomes—that is, phospholipid vesicles modified with Tween 80 to promote skin penetration—containing CWM were produced and characterized in terms of size, homogeneity, and surface charge. To evaluate the CWM effect on the vesicles, the CWM transfersomes were compared with the empty transfersomes.

The light scattering results, as reported in Table 2, showed that the empty transfersomes had a mean diameter of 106 nm, and were homogeneously dispersed (polydispersity index 0.27) and highly negatively charged (−71 mV). CMW-A incorporation significantly increased the mean diameter of the vesicles, although they remained small (around 120 nm); the polydispersity index was unaltered, and the zeta potential value became less negative (Table 2), but it was still high enough to allow particle repulsion and prevent aggregation. On the other hand, CMW-B incorporation did not affect the vesicle size, nor the homogeneity of the dispersion, but produced less negative surface charge, as much as CMW-A.

The stability of the transfersome formulations was evaluated by monitoring the mean diameter, the polydispersity index, and the zeta potential during a 90-day storage period at 4 °C. No significant alterations (<10%) were detected.

Table 2. Characteristics of empty and CWM transfersomes: mean diameter (MD), polydispersity index (PI), and zeta potential (ZP). Each value represents the mean ± SD ($n > 10$). * values statistically different ($p < 0.05$) with respect to empty transfersomes.

Formulation	MD (nm)	PI	ZP (mV)
Empty transfersomes	106 ± 3.1	0.27 ± 0.01	−71 ± 5.8
CWM-A transfersomes	* 121 ± 7.8	0.27 ± 0.01	* −56 ± 5.7
CWM-B transfersomes	105 ± 2.9	0.27 ± 0.03	* −58 ± 9.4

The physicochemical characteristics of the herein described transfersomes are in line with those reported in literature for other EA-incorporating nanosystems [20]. As an example, Tween 80-coated chitosan-based nanoformulations exhibited an average hydrodynamic diameter of 155 nm and a PI of 0.37, although a lower ZP (−9.7 mV) compared to CWM transfersomes was determined. These nanoformulations led to a sustained release of EA

Appendix H

(47% after 24 h) at pH 7.4 and exhibited more efficient anticancer effects in tumor-bearing mice compared to EA alone [27]. EA-loaded schizophyllan and chitin nanoparticles showed size distributions of 217.8 and 39.82 nm, and ZP of +27 and −9.14 mV, respectively. The chitin nanoparticles in particular led to a rapid release of EA (ca. 50%) after 8 h at pH 7.4, followed by a gradual release (up to 63%) that continued up to 50 h. MTT assay indicated that both nanoformulations effectively inhibited the growth of breast cancer cell lines, with IC_{50} values of 60 and 115 μg/mL, respectively [28]. Zein nanoparticles containing EA showed a mean size between 260 and 370 nm and a PI lower than 0.3. These formulations were found to be positively charged, with ZP ranging from +24 to + 37 mV, and showed inhibitory and bactericide activity against *S. aureus* and *P. aeruginosa* (MIC <72 μg/mL) [5]. Finally, poly(ε-caprolactone)-based EA nanoparticles formulated by applying various stabilizing agents exhibited average diameters ranging from 193 to 1252 nm, PI of 0.36–0.98 and ZP of −25–+62 mV. A fast release followed by a linear release period with a slower rate was observed at pH 7.4, with a cumulative release ranging from 25% to 48% after 8 days. These nanoparticles enhanced the cytotoxicity of EA up to 6.9-fold against colon adenocarcinoma cells, as well as the absorption extent of orally taken EA in rabbits [61].

3.3. Antioxidant Properties of CWM Transfersomes

The antioxidant properties of the CWM transfersomes were initially investigated with respect to the starting CWM samples by widely used chemical assays; that is, the DPPH and FRAP assays. Standard EA was also tested for comparison. The results are shown in Table 3. Both CWM-A and CWM-B exhibited antioxidant properties in line with what was expected based on a 5% *w*/*w* EA content. Notably, incorporation into transfersomes induced an about 2.5-fold decrease in the EC_{50} values determined in the DPPH assay for the CWM samples, and an even higher improvement in the reducing properties was observed in the FRAP assay. Since empty transfersomes were not found to exhibit significant antioxidant properties, these results clearly suggest a larger availability of the antioxidant compound EA following incorporation into the vesicles.

Table 3. Antioxidant properties of CWM samples. Reported are the mean ± SD values of at least three experiments. Data for CWM transfersomes have been normalized based on the CWM content in the formulation.

	DPPH Assay EC_{50} (mg/mL)	**FRAP Assay (mg of Trolox/mg of Sample)**
CWM-A transfersomes	0.0389 ± 0.0005	0.36 ± 0.06
CWM-B transfersomes	0.0375 ± 0.0004	0.39 ± 0.04
Empty transfersomes	-	0.00015 ± 0.00002
CWM-A	0.103 ± 0.001	0.047 ± 0.002
CWM-B	0.106 ± 0.001	0.050 ± 0.001
EA	0.0051 ± 0.0004	1.04 ± 0.02

3.4. Release of EA from CWM Transfersomes and Antioxidant Properties of the Released Fractions under Simulated Physiological Conditions

The release of EA from the CWM transfersomes in PBS at 37 °C was followed by UV-Vis spectroscopy and HPLC over 5 weeks. No significant release of EA was observed in the case of CWM-A, probably as a result of the higher particle size of the sample, whereas very promising results were obtained with the CWM-B transfersomes. Indeed, the UV-Vis spectra of the released fractions from the latter exhibited absorption maxima at ca. 280 and 360 nm, which linearly increased over time (Figure 2a). HPLC analysis confirmed a controlled release of EA, which was complete after 30 days, reaching a concentration of ca. 56 μM (Figure 2b).

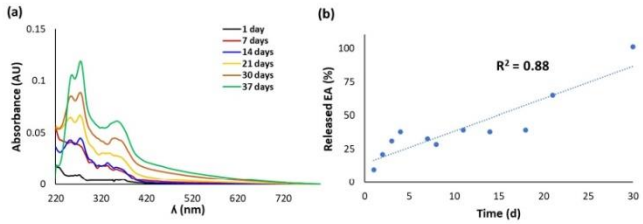

Figure 2. (**a**) UV-Vis spectra of fractions released over time from CWM-B transfersomes in PBS at 37 °C. (**b**) Kinetics of release of EA, determined by HPLC analysis. Reported are the mean values of at least three experiments (SD ≤ 10%).

The released fractions from CWM-B transfersomes were also evaluated for their antioxidant properties by chemical assays. Actually, it was not possible to perform the DPPH assay due to interference of the released material with the assay medium. On the other hand, the reducing properties evaluated by the FRAP assay (Figure 3a) linearly increased over time on account of the progressive release of EA from the transfersomes. A good linear correlation (R^2 = 0.91) of the antioxidant properties with the amount of total released EA was indeed observed (Figure 3b).

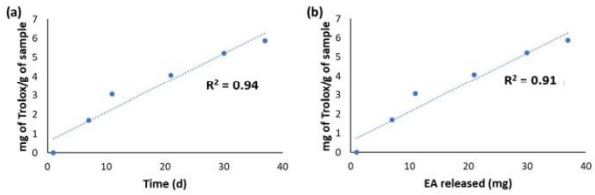

Figure 3. (**a**) Results of the FRAP assay on the fractions released over time from CWM-B transfersomes in PBS at 37 °C. (**b**) Correlation between the Fe^{3+}-reducing properties of the released fractions and the amount of released EA.

3.5. Cell Viability of CWM Transfersomes

Based on the encouraging results of the release experiments, and with the aim of further probing the potential of CWM transfersomes for dermo-cosmetic applications, in subsequent experiments the sample biocompatibility was evaluated on HaCaT, since these cells are normally present in the outermost layer of the skin. EA was also tested for comparison in a range of concentrations corresponding to those provided by the CWM transfersome samples. MTT assay (not shown) showed that both EA (up to 10 μM) and the transfersomes (up to 25 μL/mL) were biocompatible under all the experimental conditions.

3.6. Protective Effect of CWM Transfersomes on Photoinduced Oxidative Stress

The antioxidant cytoprotective properties of CWM-A and CWM-B transfersomes were evaluated on UVA-irradiated HaCaT. Preliminary experiments (data not shown) were performed to define the optimal time (2, 6, or 16 h) for cell preincubation with 10 μM EA (corresponding to a non-cytotoxic concentration of 25 μL/mL CWM transfersomes), and 6 h incubation was chosen for further experiments. As shown in Figure 4, UVA irradiation induced a significant increase in intracellular ROS levels (150–200%) with respect to untreated cells. When cells were pretreated with 10 μM EA (Figure 4a, gray bars) prior to UVA exposure, a significant lowering of intracellular ROS levels was observed. As

Appendix H

expected, empty transfersomes did not exert any protective effect against oxidative stress. Interestingly, when cells were treated with 25 μL/mL CWM-B transfersomes (providing an EA concentration of 10 μM) (Figure 4b, gray bars) prior to UVA exposure, a significant reduction ($p \leq 0.05$) in intracellular ROS levels, compared to untreated UVA-exposed cells, was observed. On the other hand, CWM-A transfersomes (Figure 4b, white bars) were unable to protect cells from UVA-induced oxidative stress injury. Thus, these results, combined with those from the release experiments, suggest that the particle size of the CWM incorporated into transfersomes is fundamental to allow EA to be active as an antioxidant in cellular models.

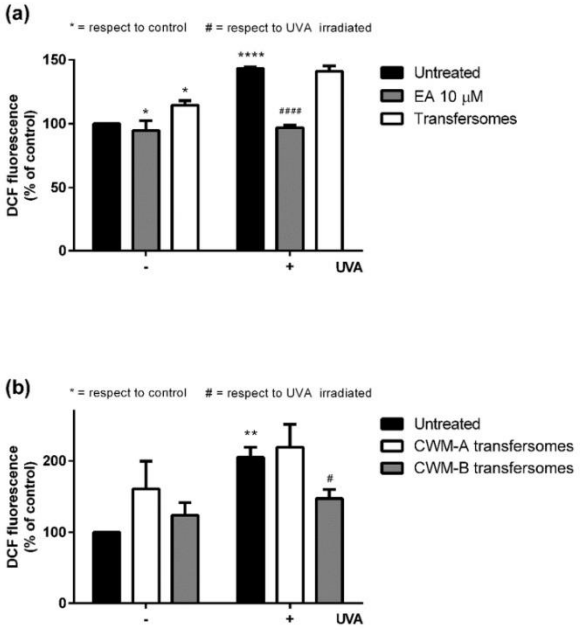

Figure 4. Protective effects of EA and transfersome samples on UVA-stressed HaCaT cells. Intracellular ROS levels were determined by DCFDA assay. Cells were preincubated with (**a**) 10 μM EA (gray bars) or 25 μL/mL empty transfersomes (white bars), or (**b**) 25 μL/mL of CWM-A (white bars) or CWM-B (gray bars) transfersomes (both providing a 10 μM EA concentration). Black bars refer to untreated cells in the absence (-) or in the presence (+) of UVA stress. Values are expressed as percentage with respect to untreated cells. Data shown are means ± SD of three independent experiment. *, # indicate $p < 0.05$; ** indicates $p < 0.01$; ****, #### indicate $p < 0.001$ with respect to control cells and UVA treated cells, respectively.

4. Conclusions

In conclusion, the present work reports the efficacy of transfersomes as carriers for the controlled release of the biologically active compound EA from CWM, an industrial by-product deriving from tannin extraction. The incorporation into the transfersomes induced a significant improvement of the antioxidant properties of CWM, likely as a

Appendix H

result of the larger availability of EA. Moreover, the transfersomal CWM-B was found to be able to decrease ROS production in UVA-irradiated keratinocytes and to provide a complete and controlled release of EA in pseudophysiological conditions at pH 7.4, a result of interest in dermo-cosmetic applications. For example, open wounds are characterized by a neutral or alkaline pH ranging from 6.5 to 8.5, whereas chronic wounds exhibit a pH in the range of 7.5–8.5 [62,63]. All together, these results highlight nanoformulated CWM of proper particle size as an easily accessible and biocompatible material that could warrant a sustained release of the water-insoluble bioactive EA under physiologically relevant conditions; for example for the treatment and protection of damaged skin.

Author Contributions: Conceptualization, C.C., D.M.M. and L.P.; Data curation, F.M., D.L., C.C., D.M.M. and L.P.; Investigation, F.M., D.L. and C.C.; Methodology, F.M., D.L., C.C., D.M.M. and L.P.; Resources, S.G.; Supervision, D.M.M., L.P. and A.N.; Validation, C.C., D.M.M., L.P. and A.N.; Writing—original draft, F.M., C.C. and D.M.M.; Writing—review and editing, L.P. and A.N. All authors have read and agreed to the published version of the manuscript.

Funding: This research received no external funding.

Data Availability Statement: The data are contained within the article.

Acknowledgments: The authors wish to thank the European Union (FSE, PON Ricerca e Innovazione 2014–2020, Azione I.1 "Dottorati Innovativi con caratterizzazione Industriale") for funding a PhD grant to Federica Moccia. Financial support to Lucia Panzella by Italian MIUR, PRIN 2017 2017YJMPZN is acknowledged.

Conflicts of Interest: The authors declare no conflict of interest.

References

1. Tošović, J.; Bren, U. Antioxidative action of ellagic acid—A kinetic DFT study. *Antioxidants* **2020**, *9*, 587. [CrossRef]
2. Xiao, Y.; Huang, R.; Wang, N.; Deng, Y.; Tan, B.; Yin, Y.; Qi, M.; Wang, J. Ellagic acid alleviates oxidative stress by mediating Nrf2 signaling pathways and protects against paraquat-induced intestinal injury in piglets. *Antioxidants* **2022**, *11*, 252. [CrossRef]
3. Kim, D.H.; Sim, Y.; Hwang, J.H.; Kwun, I.S.; Lim, J.H.; Kim, J.; Kim, J.I.; Baek, M.C.; Akbar, M.; Seo, W.; et al. Ellagic acid prevents binge alcohol-induced leaky gut and liver injury through inhibiting gut dysbiosis and oxidative stress. *Antioxidants* **2021**, *10*, 1386. [CrossRef]
4. Romeo, I.; Vallarino, G.; Turrini, F.; Roggeri, A.; Olivero, G.; Boggia, R.; Alcaro, S.; Costa, G.; Pittaluga, A. Presynaptic release-regulating alpha2 autoreceptors: Potential molecular target for ellagic acid nutraceutical properties. *Antioxidants* **2021**, *10*, 1759. [CrossRef]
5. de Souza Tavares, W.; Pena, G.R.; Martin-Pastor, M.; de Sousa, F.F.O. Design and characterization of ellagic acid-loaded zein nanoparticles and their effect on the antioxidant and antibacterial activities. *J. Mol. Liq.* **2021**, *341*, 116915. [CrossRef]
6. Amor, A.J.; Gómez-Guerrero, C.; Ortega, E.; Sala-Vila, A.; Lázaro, I. Ellagic acid as a tool to limit the diabetes burden: Updated evidence. *Antioxidants* **2020**, *9*, 1226. [CrossRef]
7. Umar, A.K.; Zothantluanga, J.H.; Aswin, K.; Maulana, S.; Sulaiman Zubair, M.; Lalhlenmawia, H.; Rudrapal, M.; Chetia, D. Antiviral phytocompounds "ellagic acid" and "(+)-sesamin" of *Bridelia retusa* identified as potential inhibitors of SARS-CoV-2 3CL pro using extensive molecular docking, molecular dynamics simulation studies, binding free energy calculations, and bioactivity prediction. *Struct. Chem.* **2022**, *10*, 1–21. [CrossRef]
8. Javaid, N.; Shah, M.A.; Rasul, A.; Chauhdary, Z.; Saleem, U.; Khan, H.; Ahmed, N.; Uddin, M.S.; Mathew, B.; Behl, T.; et al. Neuroprotective effects of ellagic acid in Alzheimer's disease: Focus on underlying molecular mechanisms of therapeutic potential. *Curr. Pharm. Des.* **2021**, *27*, 3591–3601. [CrossRef]
9. Mohammadinejad, A.; Mohajeri, T.; Aleyaghoob, G.; Heidarian, F.; Oskuee, R.K. Ellagic acid as a potent anticancer drug: A comprehensive review on in vitro, in vivo, in silico, and drug delivery studies. *Biotechnol. Appl. Biochem.* 2021; *in press*. [CrossRef]
10. Ríos, J.L.; Giner, R.M.; Marín, M.; Recio, M.C. A pharmacological update of ellagic acid. *Planta Med.* **2018**, *84*, 1068–1093. [CrossRef]
11. Korkina, L.G.; Pastore, S.; Dellambra, E.; De Luca, C. New molecular and cellular targets for chemoprevention and treatment of skin tumors by plant polyphenols: A critical review. *Curr. Med. Chem.* **2013**, *20*, 852–868. [CrossRef]
12. Mo, J.; Panichayupakaranant, P.; Kaewnopparat, N.; Songkro, S.; Reanmongkol, W. Topical anti-inflammatory potential of standardized pomegranate rind extract and ellagic acid in contact dermatitis. *Phyther. Res.* **2014**, *28*, 629–632. [CrossRef]
13. De Moraes Alves, M.M.; Arcanjo, D.D.R.; Figueiredo, K.A.; De Sousa Macêdo Oliveira, J.S.; Viana, F.J.C.; De Sousa Coelho, E.; Lopes, G.L.N.; Gonçalves, J.C.R.; Carvalho, A.L.M.; Dos Santos Rizzo, M.; et al. Gallic and ellagic acids are promising adjuvants to conventional amphotericin B for the treatment of cutaneous leishmaniasis. *Antimicrob. Agents Chemother.* **2020**, *64*, e00807–e00820. [CrossRef]

Appendix H

14. Tavares, W.S.; Tavares-Júnior, A.G.; Otero-Espinar, F.J.; Martín-Pastor, M.; Sousa, F.F.O. Design of ellagic acid-loaded chitosan/zein films for wound bandaging. *J. Drug Deliv. Sci. Technol.* **2020**, *59*, 101903. [CrossRef]
15. Lembo, S.; Balato, A.; Di Caprio, R.; Cirillo, T.; Giannini, V.; Gasparri, F.; Monfrecola, G. The modulatory effect of ellagic acid and rosmarinic acid on ultraviolet-B-induced cytokine/chemokine gene expression in skin keratinocyte (HaCaT) cells. *Biomed Res. Int.* **2014**, *2014*, 346793. [CrossRef] [PubMed]
16. Moon, N.R.; Kang, S.; Park, S. Consumption of ellagic acid and dihydromyricetin synergistically protects against UV-B induced photoaging, possibly by activating both TGF-β1 and wnt signaling pathways. *J. Photochem. Photobiol. B Biol.* **2018**, *178*, 92–100. [CrossRef]
17. Panzella, L.; Napolitano, A. Natural and bioinspired phenolic compounds as tyrosinase inhibitors for the treatment of skin hyperpigmentation: Recent advances. *Cosmetics* **2019**, *6*, 57. [CrossRef]
18. Muráth, S.; Szerlauth, A.; Sebok, D.; Szilágyi, I. Layered double hydroxide nanoparticles to overcome the hydrophobicity of ellagic acid: An antioxidant hybrid material. *Antioxidants* **2020**, *9*, 153. [CrossRef]
19. Li, Y.; Mei, L.; Guan, X.; Hu, Y. Ellagic acid solid dispersion: Characterization and bioactivity in the hydroxyl radical oxidation system. *Food Res. Int.* **2021**, *142*, 110184. [CrossRef]
20. Ceci, C.; Graziani, G.; Faraoni, I.; Cacciotti, I. Strategies to improve ellagic acid bioavailability: From natural or semisynthetic derivatives to nanotechnological approaches based on innovative carriers. *Nanotechnology* **2020**, *31*, 382001. [CrossRef]
21. Nyamba, I.; Lechanteur, A.; Semdé, R.; Evrard, B. Physical formulation approaches for improving aqueous solubility and bioavailability of ellagic acid: A review. *Eur. J. Pharm. Biopharm.* **2021**, *159*, 198–210. [CrossRef]
22. Elbehairi, S.E.I.; Alfaifi, M.Y.; Shati, A.A.; Fahmy, U.A.; Gorain, B.; Md, S. Encapsulation of ellagic acid in di-block copolymeric micelle for non-small cell lung cancer therapy. *Sci. Adv. Mater.* **2021**, *13*, 66–72. [CrossRef]
23. Villalgordo, J.M.; Trulli, L.; García-Villalba, R.; García, V.; Althobaiti, Y.; Tomás-Barberán, F.A. Novel regioselective synthesis of urolithin glucuronides–human gut microbiota cometabolites of ellagitannins and ellagic acid. *J. Agric. Food Chem.* **2022**, *70*, 5819–5828. [CrossRef] [PubMed]
24. Ortenzi, M.A.; Antenucci, S.; Marzorati, S.; Panzella, L.; Molino, S.; Rufián-Henares, J.Á.; Napolitano, A.; Verotta, L. Pectin-based formulations for controlled release of an ellagic acid salt with high solubility profile in physiological media. *Molecules* **2021**, *26*, 433. [CrossRef]
25. Karakas, C.Y.; Ordu, H.R.; Bozkurt, F.; Karadag, A. Electrosprayed chitosan-coated alginate–pectin beads as potential system for colon-targeted delivery of ellagic acid. *J. Sci. Food Agric.* **2022**, *102*, 965–975. [CrossRef] [PubMed]
26. Ahlawat, J.; Neupane, R.; Deemer, E.; Sreenivasan, S.T.; Narayan, M. Chitosan-ellagic acid nanohybrid for mitigating rotenone-induced oxidative stress. *ACS Appl. Mater. Interfaces* **2020**, *12*, 18964–18977. [CrossRef]
27. Kaur, H.; Ghosh, S.; Kumar, P.; Basu, B.; Nagpal, K. Ellagic acid-loaded, tween 80-coated, chitosan nanoparticles as a promising therapeutic approach against breast cancer: In-vitro and in-vivo study. *Life Sci.* **2021**, *284*, 119927. [CrossRef]
28. Pirzadeh-Naeeni, S.; Mozdianfard, M.R.; Shojaosadati, S.A.; Khorasani, A.C.; Saleh, T. A comparative study on schizophyllan and chitin nanoparticles for ellagic acid delivery in treating breast cancer. *Int. J. Biol. Macromol.* **2020**, *144*, 380–388. [CrossRef]
29. Li, B.; Harich, K.; Wegiel, L.; Taylor, L.S.; Edgar, K.J. Stability and solubility enhancement of ellagic acid in cellulose ester solid dispersions. *Carbohydr. Polym.* **2013**, *92*, 1443–1450. [CrossRef]
30. Savic, I.M.; Jocic, E.; Nikolic, V.D.; Popsavin, M.M.; Rakic, S.J.; Savic-Gajic, I.M. The effect of complexation with cyclodextrins on the antioxidant and antimicrobial activity of ellagic acid. *Pharm. Dev. Technol.* **2019**, *24*, 410–418. [CrossRef]
31. Sharma, K.; Kadian, V.; Kumar, A.; Mahant, S.; Rao, R. Evaluation of solubility, photostability and antioxidant activity of ellagic acid cyclodextrin nanosponges fabricated by melt method and microwave-assisted synthesis. *J. Food Sci. Technol.* **2022**, *59*, 898–908. [CrossRef]
32. Gontijo, A.V.L.; G Sampaio, A.D.; Koga-Ito, C.Y.; Salvador, M.J. Biopharmaceutical and antifungal properties of ellagic acid-cyclodextrin using an *in vitro* model of invasive candidiasis. *Future Microbiol.* **2019**, *14*, 957–967. [CrossRef] [PubMed]
33. Das, J.; Debbarma, A.; Lalhlenmawia, H. Formulation and in vitro evaluation of poly-(D,L-lactide-co-glycolide) (PLGA) nanoparticles of ellagic acid and its effect on human breast cancer, MCF-7 cell line. *Int. J. Curr. Pharm. Res.* **2021**, *13*, 56–62. [CrossRef]
34. Kakran, M.; Sahoo, N.G.; Bao, H.; Pan, Y.; Li, L. Functionalized graphene oxide as nanocarrier for loading and delivery of ellagic acid. *Curr. Med. Chem.* **2011**, *18*, 4503–4512. [CrossRef] [PubMed]
35. Ichiura, H.; Konishi, T.; Morikawa, M. Alginate film prepared on polyethylene nonwoven sheet and its function for ellagic acid release in response to sodium ions. *J. Mater. Sci.* **2009**, *44*, 992–997. [CrossRef]
36. Yağmur, N.; Şahin, S.; Korkmaz, E. Microencapsulation of ellagic acid extracted from pomegranate peel onto Spirulina: Characterization, loading, and storage stability properties. *J. Food Process. Preserv.* **2021**, *45*, e15086. [CrossRef]
37. Wei, Y.; Wang, Y.; Xia, D.; Guo, S.; Wang, F.; Zhang, X.; Gan, Y. Thermosensitive liposomal codelivery of HSA-paclitaxel and HSA-ellagic acid complexes for enhanced drug perfusion and efficacy against pancreatic cancer. *ACS Appl. Mater. Interfaces* **2017**, *9*, 25138–25151. [CrossRef]
38. Najafi, A.; Taheri, R.A.; Mehdipour, M.; Martinez-Pastor, F.; Rouhollahi, A.A.; Nourani, M.R. Improvement of post-thawed sperm quality in broiler breeder roosters by ellagic acid-loaded liposomes. *Poult. Sci.* **2019**, *98*, 440–446. [CrossRef]
39. Stojiljković, N.; Ilić, S.; Stojanović, N.; Janković-Veličković, L.; Stojnev, S.; Kocić, G.; Radenković, G.; Arsić, I.; Stojanović, M.; Petković, M. Nanoliposome-encapsulated ellagic acid prevents cyclophosphamide-induced rat liver damage. *Mol. Cell. Biochem.* **2019**, *458*, 185–195. [CrossRef]

Appendix H

40. Gonçalves, M.M.; Carneiro, J.; Döll-Boscardin, P.M.; Justus, B.; Budel, J.M.; Farago, P.V.; de Paula, J.P. Preparation of ellagic acid-loaded vesicles and method validation to quantify encapsulation efficiency. *Lat. Am. J. Pharm.* **2018**, *37*, 1000–1004.
41. Madrigal-Carballo, S.; Lim, S.; Rodriguez, G.; Vila, A.O.; Krueger, C.G.; Gunasekaran, S.; Reed, J.D. Biopolymer coating of soybean lecithin liposomes via layer-by-layer self-assembly as novel delivery system for ellagic acid. *J. Funct. Foods* **2010**, *2*, 99–106. [CrossRef]
42. Rai, S.; Pandey, V.; Rai, G. Transfersomes as versatile and flexible nano-vesicular carriers in skin cancer therapy: The state of the art. *Nano Rev. Exp.* **2017**, *8*, 1325708. [CrossRef] [PubMed]
43. Cevc, G. Material transport across permeability barriers by means of lipid vesicles. In *Handbook of Biological Physics*; Lipowsky, R., Sackmann, E., Eds.; Elsevier B.V.: Amsterdam, The Netherlands, 1995; pp. 465–490.
44. Sguizzato, M.; Ferrara, F.; Hallan, S.S.; Baldisserotto, A.; Drechsler, M.; Malatesta, M.; Costanzo, M.; Cortesi, R.; Puglia, C.; Valacchi, G.; et al. Ethosomes and transethosomes for mangiferin transdermal delivery. *Antioxidants* **2021**, *10*, 768. [CrossRef] [PubMed]
45. Kocbek, P.; Baumgartner, S.; Kristl, J. Preparation and evaluation of nanosuspensions for enhancing the dissolution of poorly soluble drugs. *Int. J. Pharm.* **2006**, *312*, 179–186. [CrossRef]
46. Magangana, T.P.; Makunga, N.P.; Fawole, O.A.; Opara, U.L. Processing factors affecting the phytochemical and nutritional properties of pomegranate (*Punica granatum* L.) peel waste: A review. *Molecules* **2020**, *25*, 4690. [CrossRef] [PubMed]
47. Verotta, L.; Panzella, L.; Antenucci, S.; Calvenzani, V.; Tomay, F.; Petroni, K.; Caneva, E.; Napolitano, A. Fermented pomegranate wastes as sustainable source of ellagic acid: Antioxidant properties, anti-inflammatory action, and controlled release under simulated digestion conditions. *Food Chem.* **2018**, *246*, 129–136. [CrossRef]
48. Panzella, L.; Moccia, F.; Nasti, R.; Marzorati, S.; Verotta, L.; Napolitano, A. Bioactive phenolic compounds from agri-food wastes: An update on green and sustainable extraction methodologies. *Front. Nutr.* **2020**, *7*, 60. [CrossRef] [PubMed]
49. Moccia, F.; Flores-Gallegos, A.C.; Chávez-González, M.L.; Sepúlveda, L.; Marzorati, S.; Verotta, L.; Panzella, L.; Ascacio-Valdes, J.A.; Aguilar, C.N.; Napolitano, A. Ellagic acid recovery by solid state fermentation of pomegranate wastes by *Aspergillus Niger* and *Saccharomyces cerevisiae*: A comparison. *Molecules* **2019**, *24*, 3689. [CrossRef]
50. Moccia, F.; Agustin-Salazar, S.; Verotta, L.; Caneva, E.; Giovando, S.; D'Errico, G.; Panzella, L.; d'Ischia, M.; Napolitano, A. Antioxidant properties of agri-food byproducts and specific boosting effects of hydrolytic treatments. *Antioxidants* **2020**, *9*, 438. [CrossRef]
51. An, J.Y.; Wang, L.T.; Lv, M.J.; Wang, J.D.; Cai, Z.H.; Wang, Y.Q.; Zhang, S.; Yang, Q.; Fu, Y.J. An efficiency strategy for extraction and recovery of ellagic acid from waste chestnut shell and its biological activity evaluation. *Microchem. J.* **2021**, *160*, 105616. [CrossRef]
52. Husanu, E.; Mero, A.; Rivera, J.G.; Mezzetta, A.; Ruiz, J.C.; D'Andrea, F.; Pomelli, C.S.; Guazzelli, L. Exploiting deep eutectic solvents and ionic liquids for the valorization of chestnut shell waste. *ACS Sustain. Chem. Eng.* **2020**, *8*, 18386–18399. [CrossRef]
53. Lameirão, F.; Pinto, D.; Vieira, E.F.; Peixoto, A.F.; Freire, C.; Sut, S.; Dall'Acqua, S.; Costa, P.; Delerue-Matos, C.; Rodrigues, F. Green-sustainable recovery of phenolic and antioxidant compounds from industrial chestnut shells using ultrasound-assisted extraction: Optimization and evaluation of biological activities in vitro. *Antioxidants* **2020**, *9*, 267. [CrossRef] [PubMed]
54. Moccia, F.; Gallucci, N.; Giovando, S.; Zuorro, A.; Lavecchia, R.; D'Errico, G.; Panzella, L.; Napolitano, A. A tunable deep eutectic solvent-based processing for valorization of chestnut wood fiber as a source of ellagic acid and lignin. *J. Environ. Chem. Eng.* **2022**, *10*, 107773. [CrossRef]
55. Panzella, L.; Moccia, F.; Toscanesi, M.; Trifuoggi, M.; Giovando, S.; Napolitano, A. Exhausted woods from tannin extraction as an unexplored waste biomass: Evaluation of the antioxidant and pollutant adsorption properties and activating effects of hydrolytic treatments. *Antioxidants* **2019**, *8*, 84. [CrossRef] [PubMed]
56. Goupy, P.; Dufour, C.; Loonis, M.; Dangles, O. Quantitative kinetic analysis of hydrogen transfer reactions from dietary polyphenols to the DPPH radical. *J. Agric. Food Chem.* **2003**, *51*, 615–622. [CrossRef] [PubMed]
57. Benzie, I.F.F.; Strain, J.J. The ferric reducing ability of plasma (FRAP) as a measure of "'antioxidant power"': The FRAP assay. *Anal. Biochem.* **1996**, *239*, 70–76. [CrossRef] [PubMed]
58. Imbimbo, P.; Romanucci, V.; Pollio, A.; Fontanarosa, C.; Amoresano, A.; Zarrelli, A.; Olivieri, G.; Monti, D.M. A cascade extraction of active phycocyanin and fatty acids from *Galdieria phlegrea*. *Appl. Microbiol. Biotechnol.* **2019**, *103*, 9455–9464. [CrossRef]
59. Garcia-Villalba, R.; Espín, J.C.; Kroon, P.A.; Alasalvar, C.; Heinonen, M.; Voorspoels, S.; Tomas-Barberan, F. A validated method for the characterization and quantification of extractable and non-extractable ellagitannins after acid hydrolysis in pomegranate fruits, juices, and extracts. *J. Agric. Food Chem.* **2015**, *63*, 6555–6566. [CrossRef]
60. Tokutomi, H.; Takeda, T.; Hoshino, N.; Akutagawa, T. Molecular structure of the photo-oxidation product of ellagic acid in solution. *ACS Omega* **2018**, *3*, 11179–11183. [CrossRef]
61. Mady, F.M.; Shaker, M.A. Enhanced anticancer activity and oral bioavailability of ellagic acid through encapsulation in biodegradable polymeric nanoparticles. *Int. J. Nanomed.* **2017**, *12*, 7405–7417. [CrossRef]
62. Dissemond, J.; Witthoff, M.; Brauns, T.C.; Haberer, D.; Goos, M. pH values in chronic wounds. Evaluation during modern wound therapy. *Der Hautarzt* **2003**, *54*, 959–965. [CrossRef]
63. Jones, E.M.; Cochrane, C.A.; Percival, S.L. The effect of pH on the extracellular matrix and biofilms. *Adv. Wound Care* **2015**, *4*, 431–439. [CrossRef]

Appendix I

ACS Sustainable Chemistry & Engineering

pubs.acs.org/journal/ascecg

Research Article

Inside out *Porphyridium cruentum*: Beyond the Conventional Biorefinery Concept

Davide Liberti, Paola Imbimbo, Enrica Giustino, Luigi D'Elia, Giarita Ferraro, Angela Casillo, Anna Illiano, Gabriella Pinto, Maria Chiara Di Meo, Gerardo Alvarez-Rivera, Maria Michela Corsaro, Angela Amoresano, Armando Zarrelli, Elena Ibáñez, Antonello Merlino, and Daria Maria Monti*

Cite This: *ACS Sustainable Chem. Eng.* 2023, 11, 381−389

Read Online

ACCESS | Metrics & More | Article Recommendations | Supporting Information

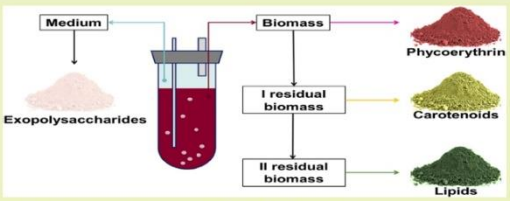

ABSTRACT: Here, an unprecedented biorefinery approach has been designed to recover high-added value bioproducts starting from the culture of*Porphyridium cruentum*. This unicellular marine red alga can secrete and accumulate high-value compounds that can find applications in a wide variety of industrial fields. 300 ± 67 mg/L of exopolysaccharides were obtained from cell culture medium; phycoerythrin was efficiently extracted (40% of total extract) and isolated by single chromatography, with a purity grade that allowed the crystal structure determination at 1.60 Å; a twofold increase in β-carotene yield was obtained from the residual biomass; the final residual biomass was found to be enriched in saturated fatty acids. Thus, for the first time, a complete exploitation of*P. cruentum*culture was set up.

KEYWORDS: *microalgae, cascade approach, high-added-value molecules, phycoerythrin, sulfated exopolysaccharides*

INTRODUCTION

Microalgae capture carbon dioxide during their growth to perform photosynthesis. This implies the production of oxygen and the reduction of carbon dioxide emissions.[1] It is noteworthy that microalgae are used as a reliable source of food and high-added value products.[2] Microalgae can be considered perfect candidates for their use in biorefinery approaches,[3] as they can grow in lands which do not compete with food production, and with a higher growth rate with respect to conventional crops. From a theoretical point of view, a biorefinery is a combination of multiple integrated processes able to convert the biomass into a variety of high-added value products, in an economical and environmentally sustainable approach.[4] This is in line with the principles of circular economy, fostered by international organizations and promoted by European Union (https://eur-lex.europa.eu/legal-content/EN/ALL/?uri=CELEX%3A52015DC0614). Unfortunately, in the microalgae field, a real biorefinery has been demonstrated only for few strains,[5] and most of the present literature is focused on the extraction of one or two classes of molecules, thus suggesting that the process is not economically feasible.

Porphyridium cruentum is a red marine microalga, reservoir of potentially high-added value molecules, such as carotenoids, sulfated exopolysaccharides (EPSs), B-phycoerythrin (PE), and lipids.[6−9] Carotenoids are well-known antioxidants, also able to counteract many disorders, from type 2 diabetes, to degenerative diseases or cancer.[10] Sulfated EPSs have a chemical structure which confer them peculiar rheological properties[11] and many biological activities,[12] such as antimicrobial, anti-inflammatory,[13] hypocholesterolemic,[14] antiviral activities,[15] and skin protective activity.[16] PE, the main protein found in*P. cruentum*, has a good market value for different reasons: (i) in biomedical and molecular applications for its natural fluorescence; (ii) as a natural red-colored protein to be used as a dye for food and cosmetics, and (iii) in the

Received: September 30, 2022
Revised: November 10, 2022
Published: November 29, 2022

Appendix I

pharmaceutical industry thanks to its antioxidant activity.[17] Finally, recent literature exploited the use of saturated fatty acids as antimicrobial agents and as drug delivery systems.[18,19]

Thus, taking advantage of the chemical composition of *P. cruentum*, here we propose a real biorefinery. For the first time, not only the biomass but also the exhausted medium was fully exploited to recover: EPSs from the medium and PE, carotenoids and lipids from the biomass. Molecules were extracted sequentially, starting from the most valuable one, without affecting the activity of the molecules in the residual biomass.

MATERIALS AND METHODS

Reagents. All chemicals, solvents, and reagents, unless differently specified, were from Sigma-Aldrich (St Louis, MO, USA).

Microalgal Strain and Dry Weight Determination. *Porphyridium cruentum* strain was acquired from Culture Collection of Autotrophic Organism (CCALA, Centre for Phycology, Institute of Botany of the AS CR, Dukelská 135, TŘEBOŇ CZ-379 82, Czech Republic). Preculture (50 mL, 0.09 ± 0.01 O.D./mL) of *P. cruentum* was inoculated in *Porphyridium* medium[20] in a 1 L bubble column photobioreactor (working volume 800 mL) in a room with constant temperature (25 ± 1 °C) and light (fluorescent lamps with an intensity of 13 ± 1 PAR $\left[\frac{\mu mol_{Photons}}{m^2}/s\right]$) in autotrophic conditions, without CO_2. The culture was mixed by bubbling through a sintered glass tube placed at the bottom of each culture tube. Algal growth was monitored by measuring the absorbance at 730 nm. The O.D. values were converted into biomass amount by correlating O.D. and dry cell weight.

Exopolysaccharide Isolation and Quantization. To process a high volume of medium, the latter was concentrated 10 times by lyophilization, prior to addition of pure ethanol (1:2 v/v); EPSs were then recovered by centrifugation (12,000 g, 30 min, 4 °C), collected and lyophilized. Total carbohydrates were quantified by the phenol−sulfuric acid method, according to Geresh et al.,[21] with some modifications, as reported in Gallego.[4] A reference curve was obtained by using glucose (0.03−1.0 mg/mL).

Determination of Monosaccharide Composition. Lyophilized EPSs (2 mg) were solubilized with 1 mL of HCl/CH_3OH (1.25 M) for 16 h at 80 °C.[22] Then, the sample was dried and acetylated with 25 μL of acetic anhydride and 25 μL of pyridine and kept at 100 °C for 30 min. The mixture was analyzed by gas chromatography−mass spectrometry (GC−MS) by using an Agilent Technologies instrument (GC 7820A, MS 5977B), equipped with a HP-5MS 30 m, 0.25 mm, 0.25 μm capillary column. The following temperature program was used to analyze acetylated methyl glycosides: 140 °C for 3 min, 140 °C → 240 °C at 3 °C/min.

Total Carbon, Hydrogen, Nitrogen, and Sulfur. The determination of total carbon (C), hydrogen (H), nitrogen (N), and sulfur (S) in EPSs recovered from *P. cruentum* medium was carried out by performing total combustion, using the FlashSmart Elemental Analyzer, according to Álvarez-Gómez and colleagues.[23] Elements (C, H, N, S) were expressed as % with respect to the sample's total weight.

Protein Extraction and Quantification. Fresh biomass was harvested by centrifugation at 1200*g* for 30 min at room temperature and resuspended at 10 $mg_{D.W.}$/mL in PBS pH 7.4. Cell disruption was done by: (i) maceration; (ii) freeze and thaw; (iii) French Press, and (iv) sonication. For the maceration, the biomass was kept at 4 °C in agitation for 24 h. For the freeze and thaw method, the biomass was frozen (−80 °C) and then thawed (37 °C) for five cycles. For the French Press, two cycles were performed at a pressure of 2 kbar. The ultrasound method was performed by operating with MS73 tip at 40% amplitude of the instrument (Bandelin Sonoplus HD 3200) for different lengths of time, from 4 to 20 min, (30″ on, 30″ off), on ice. At the end of each step, samples were centrifuged at 5000 *g* at 4 °C for 30 min, proteins were recovered in the supernatant, total proteins were determined by BCA Protein Assay Kit (Thermo Scientific) and then SDS-PAGE analysis followed by Coomassie staining was performed. Phycobiliprotein concentration was determined by the Bennet and Bogorad equations:[24]

$$C_{PC} = \frac{[Abs_{615nm} - (0.474 \times Abs_{652})]}{5.34} \quad (1)$$

$$C_{Apc} = \frac{[Abs_{652nm} - (0.208 \times Abs_{620nm})]}{5.09} \quad (2)$$

$$C_{Pc} = \frac{[Abs_{562nm} - (2.41 \times C_{Pc}) - (0.849 \times C_{Apc})]}{9.62} \quad (3)$$

The reported wavelengths (562, 615, and 652 nm) correspond to the maximum of absorption of phycoerythrin, phycocyanin, and allophycocyanin, respectively.

Phycoerythrin Purification. PE purification was performed by comparing three techniques: anion-exchange chromatography, gel filtration, and ultrafiltration. Anion-exchange chromatography was carried out by using a Nuvia-Q resin equilibrated with PBS pH 7.4, and elution was performed using 0.25 M NaCl. Gel filtration was performed by using a Sephadex G-75 equilibrated in PBS pH 7.4. Ultrafiltration was carried out with a 10 kDa molecular weight cut-off membrane, and the process was performed at 4 °C. The fractions obtained by anion-exchange and gel filtration, as well as the retentate obtained by ultrafiltration, were collected and analyzed by SDS-PAGE followed by Coomassie staining and PE purity grade was calculated by measuring the ratio Abs_{562nm}/Abs_{280nm}.

Crystallization, Data Collection, Structure Solution, and Refinement of Phycoerythrin. PE crystals were grown by the hanging drop vapor diffusion method[25] using a drop containing 10 mg/mL PE in 0.25 M ammonium sulfate, 25 mM potassium phosphate at pH 5.0, equilibrated with a reservoir containing 0.5 M ammonium sulfate, and 50 mM potassium phosphate at pH 5.0. Red crystals were visible after 1 week (Figure S1, Supporting Information).

The crystals were soaked in a cryoprotectant solution containing 30% (v/v) glycerol in the reservoir solution and cooled at −173 °C. Starting from one crystal, a high-resolution data set was collected at the XRD2 beamline at the Elettra synchrotron in Trieste, Italy, at −173 °C. Data were processed and scaled using Autoproc.[26] The crystal was trigonal, space group R3, with unit cell parameters $a = b = 186.59$ Å, $c = 59.19$ Å, $\alpha = \beta = 90°$, and $\gamma = 120°$. For data collection statistics, see Table S1 (Supporting Information). The structure of PE was solved by molecular replacement using PHASER,[27] and the PE structure deposited in the Protein Data Bank under the accession 3V58,[28] as a starting model. The structure shows the presence of two ($\alpha\beta$) dimers in the asymmetric unit. Visual inspection and model improvements were carried out using Coot.[29] Refinements were carried out using Refmac 5.0.[30] *R* factor and *R* free values were used to optimize the refinement strategy. The final model, which has good geometries and refinement statistics (Table S1, Supporting Information), was deposited in the Protein Data Bank under the accession code 8B4N. Pymol (www.pymol.org) was used to obtain molecular-graphics figures.

In Situ Digestion. A single PE crystal was solubilized in water and analyzed by SDS-PAGE. For in-gel hydrolysis, SDS-PAGE bands were excised from the gel lane, destained by consecutive cycles of 0.1 M NH_4HCO_3 at pH 8.0 and acetonitrile (ACN), followed by reduction (10 mM DTT in 100 mM NH_4HCO_3, 45 min, at 56 °C) and alkylation (55 mM IAM in 100 mM NH_4HCO_3, 30 min, at room temperature). The gel pieces were washed with 0.1 M NH_4HCO_3 of pH 8.0 and ACN and subjected to the enzymatic hydrolysis by covering them with 40 μL sequencing grade modified trypsin (10 ng/μL trypsin; 10 mM NH_4HCO_3) overnight at 37 °C. Peptide mixtures were eluted, vacuum-dried, and resuspended in 2% ACN acidified with 0.1% HCOOH. Tryptic peptide mixtures were analyzed by MALDI-TOF (AB SCIEX, Milan, Italy) to reveal the amino acid sequence of the three phycoerythrin chains.

https://doi.org/10.1021/acssuschemeng.2c05869
ACS Sustainable Chem. Eng. 2023, 11, 381−389

Appendix I

Mass Spectrometry Analyses. Matrix-assisted laser desorption/ionization (MALDI) mass spectrometry (MS) experiments were performed on a 5800 MALDI-TOF-TOF ABSciex equipped with a nitrogen laser (337 nm) (AB SCIEX, Milan, Italy). Starting from each band, aliquots of peptide mixture (0.5 μL) were mixed (1:1, v/v) with alphacyano hydroxycinnamic acid (10 mg/mL) in acetonitrile: 55 mM citric acid (70:30) solution. Calibration was done by using a calibration mixture from AB SCIEX (Monoisotopic (M + nH)$^{n+}$: 904.46 Da des-Arg-Bradykinin, 1296.68 Da Angiotensin I, 1570.67 Da Glu-Fibrinopeptide B, 2093.08 Da ACTH (clip 1−17), 2465.19 Da ACTH (clip 18−39), 3657.92 Da ACTH (clip 7−38)). Peptides were identified by MS spectra, acquired using a mass (m/z) range of 400−4000 Da. Peptide mass fingerprinting was performed by MS digest of homologue phycoerythrin sequences. MALDI MS experiments were performed on a 5800 MALDI-TOF-TOF ABSciex equipped with a nitrogen laser (337 nm) (AB SCIEX, Milan, Italy). The instrument operated with an accelerating voltage of 20 kV, a grid voltage at 66% of the source voltage, and a delay time at 200 ns. Laser power was set to 3500 V for the spectra acquisition. Each spectrum represents the sum of 10,000 laser pulses from randomly chosen positions on the same target place. The data were reported as monoisotopic masses.

Carotenoid Extraction and Characterization. Carotenoids were extracted from the dry biomass, either raw or after protein extraction. Extractions were performed in ethanol, as reported by Aremu, with some modifications.[31] Briefly, for each extraction, 200 mg of freeze-dried biomass was suspended in pure ethanol (4 mL) and sonicated (40% amplitude, 4 min on ice, Bandelin Sonoplus HD 3200, tip MS73). The mixture volume was then adjusted to 20 mL and shaken for 24 h at 250 rpm in a dark room at 4 °C. The supernatant was collected by centrifugation at 12,000g for 10 min, dried under nitrogen stream, and then stored at −20 °C. Carotenoid identification was performed by HPLC-DAD-APCI-QTOF-MS/MS, whereas quantization was done by calibration curves obtained by using commercial zeaxanthin and β-carotene, according to a method previously described,[5] with some modifications. The analysis of the extracts was carried out in an Agilent 1290 UHPLC system (Ultrahigh Performance Liquid Chromatography) equipped with a diode-array detector (DAD), coupled to an Agilent 6540 quadrupole-time-of-flight mass spectrometer (q-TOF MS) equipped with an atmospheric pressure chemical ionization (APCI) source, all from Agilent Technologies (Santa Clara, CA, USA). Extracts were solubilized in ethanol (5 mg/mL), filtered through 0.45 μm nylon filters, and then analyzed under positive ionization mode, using the following parameters: capillary voltage, 3.5 kV; drying temperature, 350 °C; vaporizer temperature, 400 °C; drying gas flow rate, 8 L/min; nebulizer gas pressure, 40 psi; corona current (which sets the discharge amperage for the APCI source), 4000 nA. The mass spectrometer was operated in MS and tandem MS modes for the structural analysis of all compounds. The MS and Auto MS/MS modes were set to acquire m/z values ranging between 50 and 1100 and 50 and 800, respectively, at a scan rate of 5 spectra per second.

Lipids Extraction and Characterization. Lipids were extracted on the dried biomass. Both the raw and the two residual biomasses (I and II residual biomass) were dried at 60 °C for 24 h. Lipids were obtained as reported by Bligh and Dyer.[32] Nitrogen flux was used to dry, recover, and weigh lipids. Lipid fractionation was performed by solubilizing them in chloroform and using a commercial prepacked column containing a stationary phase made of Florisil. Neutral lipids were eluted with chloroform:methanol (2:1, v/v), fatty acids with 2% acetic acid in diethyl-ether, whereas phospholipids were eluted with 100% methanol. The recovered fatty acids were then characterized by GC−MS, as previously reported.[33]

Statistical Analyses. Results are reported as mean of results obtained after three independent experiments (mean ± SD) and compared by one-way analysis of variance according to Bonferroni's method (post hoc) using Graphpad Prism for Windows, version 6.01.

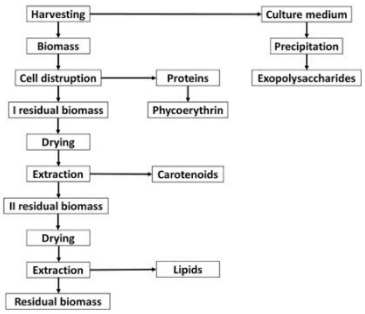

Figure 1. Schematic representation of the applied process.

RESULTS AND DISCUSSION

Exopolysaccharide Recovery and Characterization. Figure 1 reports the extraction strategy used to recover different molecules from *P. cruentum*. At the end of cell growth, medium, generally regarded as waste, was collected and polysaccharides were isolated by precipitation using ethanol or 2-propanol. The EPS content was measured by the phenol−sulfuric acid method and no difference between the two applied solvents was observed (ethanol yield 0.100 ± 0.020 and 2-propanol 0.116 ± 0.020 mg/mL); thus ethanol was selected because of its wide range of applications.[34] The EPS yield was found to be 300 ± 67 mg/L of culture medium, which corresponds to an EPS yield of 0.53 g/$g_{d.w.biomass}$. The monosaccharide composition was achieved by GC−MS analysis, after derivatization as acetylated methyl glycosides (AMGs). The GC−MS chromatogram disclosed the presence of mainly xylose (Xyl), galactose (Gal), and glucose (Glc). Finally, traces of rhamnose (Rha), glucuronic acid (GlcA), and glucosamine (GlcN) were detected (Figure 2).

Because the EPSs from *P. cruentum* are known to be sulfated, the elemental composition analysis was performed. Results, reported in Table 1, indicate that the % of sulfur present in the sample is similar to that reported in the literature (7.4% ± 0.2%).[35,36] No proteins were detected.

Biomass Exploitation. *Phycoerythrin Extraction Optimization.* To extract PE, different extraction procedures were evaluated, as described in Materials and Methods. Total protein concentration was determined by colorimetric assay (BCA), whereas PE, phycocyanin (PC), and allophycocyanin (APC) concentrations were obtained using the Bennet and Bogorad equations (reported in the Material and Methods section). As shown in Table 2, the amount of PE was similar in all the analyzed samples, whereas PC and APC were found to be most abundant only in the extract obtained by French Press. Indeed, the presence of APC and PC in the French Press extract halved the purity grade of the extract with respect to those obtained for the other three extracts.

Supernatants were also analyzed by SDS-PAGE followed by Coomassie staining (Figure S2A, Supporting Information) and UVA light exposure, taking advantage of chromophores present in PE (Figure S2B, Supporting Information). The analyses revealed two major bands, whose molecular weights corresponded to α and β subunits (17 kDa) and γ subunit (30

https://doi.org/10.1021/acssuschemeng.2c05869
ACS Sustainable Chem. Eng. 2023, 11, 381−389

Appendix I

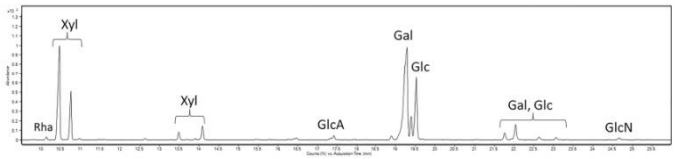

Figure 2. GC–MS chromatogram of the AMG of *P. cruentum* exopolysaccharides recovered from the culture medium. In the graph, the relative ion current abundance is reported as a function of retention time (min).

Table 1. Elemental Composition and Protein Content of EPS[a]

O (%)	N (%)	H (%)	C (%)	S (%)	protein content (mg/mL)
76.0 ± 2.4	1.1 ± 0.6	2.6 ± 0.4	13.1 ± 1.3	7.4 ± 0.2	N.D.

[a]Elements were measured by an elemental analyzer. Oxygen % was calculated by subtracting the % of the other elements from 100%. % are expressed as mg of each element/mg of analyzed EPS. Protein content was measured by colorimetric assay.

Table 2. Total Protein and Phycobiliprotein Concentration, Extraction Yield, and Phycoerythrin Purity Grade Obtained for Each Extraction Protocol[a]

	maceration	sonication	freeze and thaw	French press
protein yield (%)	44 ± 5	35 ± 4	35 ± 3	37 ± 6
PE yield (%)	1.8 ± 0.1	1.8 ± 0.8	1.8 ± 0.5	1.4 ± 0.7
PE purity grade (Abs_{562nm}/Abs_{280nm})	0.8 ± 0.1	0.9 ± 0.1	1.1 ± 0.1	0.4 ± 0.2
PC yield (%)	0.14 ± 0.02	0.48 ± 0.1	0.21 ± 0.1	1.4 ± 0.5
APC yield (%)	0.13 ± 0.1	0.2 ± 0.1	0.5 ± 0.02	1.1 ± 0.2

[a]Total protein concentration was obtained by BCA assay and total PE, PC, and APC concentration by Bennett and Bogorad equations. Yields are expressed as $g_{protein}/g_{d.w.biomass}$. The PE purity grade was calculated from the Abs_{562nm}/Abs_{280nm} ratio.

kDa) of PE, in each lane. Results suggested ultrasound as the most promising method. As biomass storage is a crucial step in industrial-scale processes, also from a logistically point of view,[37] extractions were performed by ultrasound on either fresh or frozen biomass (stored at −80 °C) for different lengths of time (from 4 to 20 min). At the end of each extraction, the disrupted biomass was analyzed by SDS-PAGE (Figure S2C,D, Supporting Information). Supernatants obtained after 20 min extraction seemed to be the best choice for fresh biomass, as 4 min extraction allowed to recover a PE content of 1.8% (Table 2) with a purity grade of 0.9 (Table 2), whereas 20 min of sonication on fresh biomass allowed to recover a PE content of 3.0 ± 0.4% with a purity grade of 1.5 ± 0.3. These extraction values are higher with respect to those obtained, after 20 min of sonication, from the frozen biomass: PE content of 2.2 ± 0.2 to 3.0 ± 0.4% for frozen and fresh biomass, respectively, and a PE purity grade of 1.0 ± 0.2 and 1.5 ± 0.3 for frozen and fresh biomass, respectively.

Phycoerythrin Purification and Structure Determination. PE purification was performed by comparing three techniques: anion-exchange chromatography, gel filtration, and ultrafiltration. The results of the different techniques are reported in the Supporting Information (Figure S2E–G, Supporting Information). Only the size-exclusion chromatography allowed obtaining pure PE; in particular, this purification step allowed to recover about 80% of PE and to reach a purity grade of 4.0. It is known that a purity grade ≥4.0 indicates a protein to be used in analytical grade.[38] According to the overall results, this approach allowed obtaining high-purity grade PE by only one step extraction and purification. To the best of our knowledge, this is the first time that PE was extracted and purified with such a purity grade by using only a single purification step.[39−42] To determine the protein identity and purity, PE was crystallized, and its X-ray structure was determined at 1.60 Å resolution. The X-ray structure is constituted by 5990 atoms, including five phycoerythrobilin (PEB) chromophores for each $\alpha\beta$ dimer, one methylated Asn in position β72 (Figure 3A) for each β subunit, two sulfate ions, and 324 water molecules and refines to *R* factor/*R*free values of 0.222/0.256. The structure confirms the formation of the $(\alpha\beta)_3$ hexamer (Figure 3C,D) but does not allow to identify the exact location of the γ subunit (Figure 3E). Similar results were obtained in previous studies[43,44] and were attributed to rotational disorder of the γ subunit within the protein crystal and to the finding that the electron density of this subunit is averaged out by the threefold crystallographic symmetry. The α subunit contains 164 residues, the β subunit 177 residues. The overall structure of the protein is very similar to that previously reported and deposited in the Protein Data Bank under accession code 3VS8, obtained from crystals grown under different experimental conditions, but at the same pH. After superposition, the 164 CA atoms of the α subunit have a root-mean-square (r.m.s.) deviation of 0.146 Å, and the 177 CA atoms of β subunit have an r.m.s. deviation of 0.142 Å. Each $\alpha\beta$ dimer has five PEBs in position α82, α139, β61, β82, and β158. The first PEB, which adopts two alternate conformations in our structure, is covalently attached to the side chain of Cys82 of the α subunit by ring A. The second PEB is bound to Cys139 of the same subunit. The other three PEBs are found in the β subunit. They are bound to the side chains of Cys61, Cys82, and Cys158. The stereochemistry of the chromophores and their interaction with protein residues are basically identical to that observed in the starting model[28] and previously described. An example of the well-defined electron density maps of the

https://doi.org/10.1021/acssuschemeng.2c05869
ACS Sustainable Chem. Eng. 2023, 11, 381−389

Appendix I

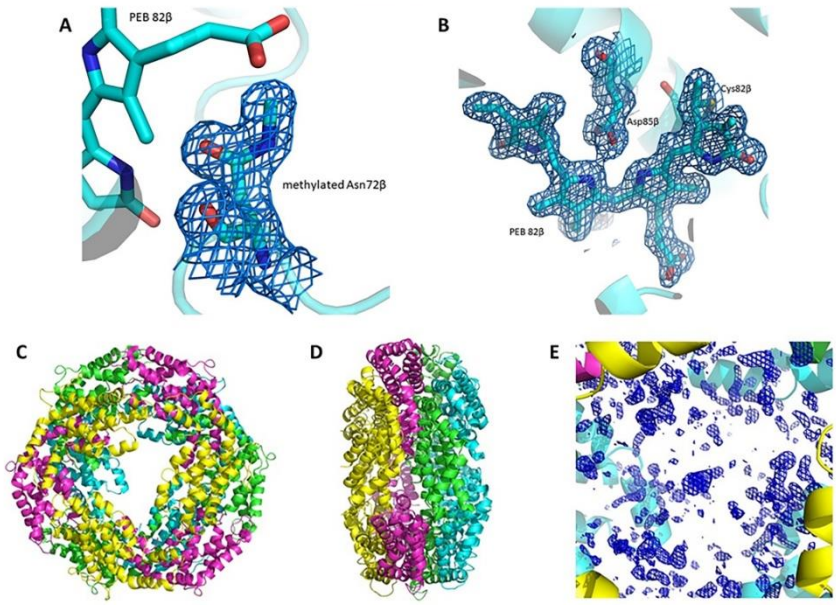

Figure 3. PE crystal structure. (A) 2Fo-Fc electron density map (1.0σ) of the methylated Asn72β in the structure of PE. (B) 2Fo-Fc electron density maps contoured at 1.0σ of one of the five PEB chromophores found in the structure of PE. (C) $(\alpha\beta)_3$ hexamer shown from the upper view and the lateral view (D). Electron density of the central cavity is shown in panel E. This segment of electron density should contain information on the location of the γ subunit.

chromophores is reported in Figure 3B. To verify the presence of a γ subunit, PE crystals were dissolved and analyzed by UV−vis absorption spectroscopy, SDS-PAGE analyses, and mass spectrometry. The UV−vis absorption spectrum (Figure S3A, Supporting Information) showed a peculiar shoulder at 498 nm, ascribed to the phycourobilin chromophore of the γ subunit. SDS-PAGE analysis (Figure S3B, Supporting Information) showed the presence of two molecular species, whose molecular mass was compatible with α and β subunits (double bands at about 17 kDa) and with the γ subunit (30 kDa). In situ digestion was performed on the bands and the peptide mixtures were analyzed by MALDI-TOF; peptide mass fingerprinting was performed by MS digest of homologue phycoerythrin sequences. The assignment of each mass spectrometry signal allowed highlighting the peptide sequence along the entire protein sequence. As shown in Figure 4,BA, the MS analysis of lower band enabled tracing the peptide sequence (labeled in bold and underlined) for the α and β chains, displaying a sequence coverage of 64 and 61%, respectively. The MS analysis of the higher band, on the other hand, revealed that the signals were attributed to two γ-chains with comparable sequence coverage (59.3 and 43.5%), as shown in Figure 4C,D. The presence of the two γ subunits has been previously found in the structure of the entire phycobilisome solved by electron microscopy (PDB code 6KGX).[45] The heptameric structures of PE, with the two different γ subunits, extracted from PDB code 6KGX are reported in Figure 5, with the same orientation.

Carotenoid Extraction and Characterization. Carotenoid extraction was performed by using a conventional method on both residual biomass (herein referred as I residual biomass) and on the raw one, used as benchmark (as reported in the Materials and Methods section). HPLC analyses (Figure 6) revealed that zeaxanthin and β-carotene were the major pigments present in the two extracts. Quantification analyses for the two carotenoids are reported in Table 3 and indicate that all the zeaxanthin isoforms present in the I residual biomass represented about 55% of those present in the raw biomass, whereas β-carotene isoform recovery was about 210% with respect to the raw biomass. It is important to point out that the carotenoids yield obtained from the I residual biomass was comparable to the one obtained by innovative green extractions performed on the residual biomass of the same species,[4] thus suggesting the feasibility of the proposed process.

Lipid Extraction and Characterization. According to the strategy described in Figure 1, lipid extraction represented the last class of the proposed process, after a drying step. To verify

https://doi.org/10.1021/acssuschemeng.2c05869
ACS Sustainable Chem. Eng. 2023, 11, 381−389

Appendix I

Figure 4. α, β, and γ chain sequences of *P. cruentum* detected by MALDI-TOF analysis. (A) α chain sequence displaying the different peptides (bold and underlined) compared to P11392 (PHEA_PORPP) sequence on UniProt. (B) β chain sequence displaying the different peptides (bold and underlined) compared to P11393 (PHEB_PORPP) sequence on UniProt. (C) γ chain sequence displaying the different peptides (bold and underlined) compared to A0A5J4YX19 (PHEB_PORPP) sequence on UniProt. (D) γ chain sequence displaying the different peptides (bold and underlined) compared to A0A5J4YZM7 (PHEB_PORPP) sequence on UniProt.

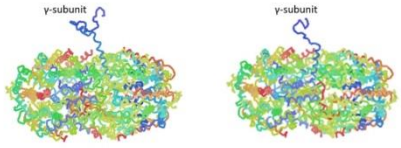

Figure 5. Heptameric $(\alpha\beta)_3\gamma$ structures observed in the phycobilisome from *P. cruentum*.

if the previous extractions could affect lipid composition, control experiments were performed by determining the composition of the lipid fraction obtained after PE extraction (I residual biomass) and after PE and carotenoid extraction (II residual biomass). The extractions were performed according to Bligh and Dyer,[32] followed by a solid phase extraction (SPE). As shown in Table 4, a 14% yield of total lipids was obtained from the raw biomass, whereas about 29% were extracted from the I residual biomass (i.e., after protein extraction). Nevertheless, when lipids were extracted from the II residual biomass (i.e., after protein and carotenoid extractions), the yield (14.1%) was comparable to those calculated for the raw biomass. Interestingly, the gas chromatography analysis of the fatty acid fraction revealed a clear trend: while polyunsaturated fatty acids (PUFAs) decreased during the cascade extractions (from 26 to 14 to 4%), a clear increase in the yield of saturated fatty acids (SFAs) was observed (from 72 to 76 to 93%). SFAs are considered now as an interesting new class of molecules, thanks to their chemical stability, responsible for their well-defined melting points and biocompatibility. Thus, they have been proposed as new materials for drug-controlled release or simply as antibacterial molecules.[18,19]

■ CONCLUSIONS

The strategy proposed in Figure 1 was found to be effective, because an innovative and reliable strategy was set up to sequentially recover high-added-value products from *P. cruentum* culture. In particular, (i) *P. cruentum* culture is completely employed to recover intra- and extracellular class of high-added-value molecules; (ii) the yield of each extracted class of molecules is similar to those obtained when extractions are performed to recover single class of molecules; and (iii) according to the biorefinery principles, all the class of molecules have been recovered starting from the one with the highest market value. Simultaneous microalgae culture valorization and carbon capture can contribute to the sustainable expansion of the microalgae market.

■ ASSOCIATED CONTENT

Supporting Information

The Supporting Information is available free of charge at https://pubs.acs.org/doi/10.1021/acssuschemeng.2c05869.

Crystallographic data; PE extraction and purification analyses; carotenoid identification (PDF)

https://doi.org/10.1021/acssuschemeng.2c05869
ACS Sustainable Chem. Eng. 2023, 11, 381−389

Appendix I

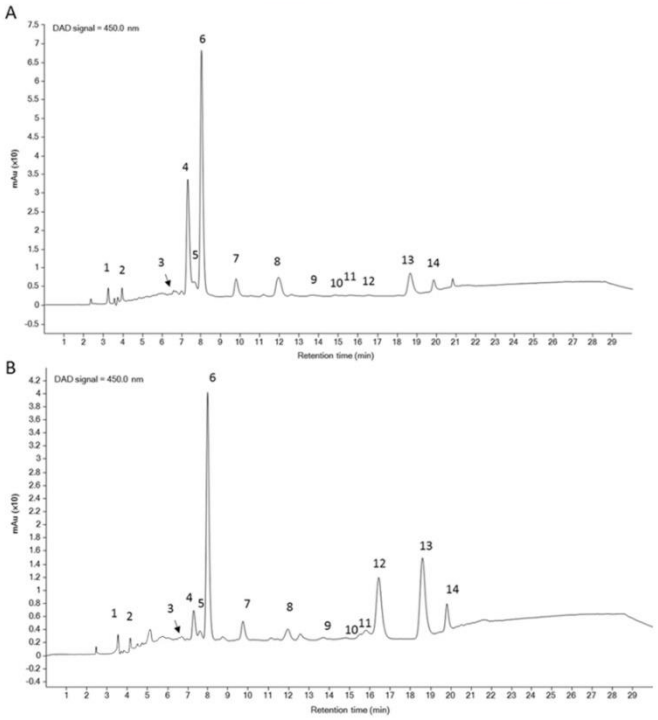

Figure 6. Representative HPLC–DAD chromatograms of carotenoids extracted from *P. cruentum* biomass. (A) Raw biomass; (B) I residual biomass (after PE extraction). Peak numbers and their identification are reported in Table S2, Supporting Information.

Table 3. Comparison between Zeaxanthin, β-Carotene, and Their Isomers in the Raw and I Residual Extracts

peak number	retention time (min)	peak identification	raw biomass ($mg/g_{extract}$)	I residual biomass ($mg/g_{extract}$)
5	7.668	zeaxanthin isomer I	1.03	0.64
6	8.057	zeaxanthin	21.37	11.79
7	9.826	zeaxanthin isomer II	2.84	1.69
13	18.701	β-carotene	0.20	0.44
14	18.892	β-carotene isomer	0.04	0.07

Table 4. Total Lipid Yields[a]

	lipid yield (%)	neutral lipids (%)	phospholipids (%)	fatty acids (%)	PUFA (%)	SFA (%)
raw biomass	14.0 ± 2.6	11.2 ± 1.5	12.0 ± 4.0	3.7 ± 0.3	25.8 ± 4.6	71.7 ± 13.6
I residual biomass	28.8 ± 1.5	10.2 ± 0.3	10.6 ± 0.3	2.5 ± 0.2	14.4 ± 1.9	76.3 ± 5.8
II residual biomass	14.1 ± 0.4	9.1 ± 0.6	3.8 ± 0.4	1.6 ± 0.2	4.3 ± 0.8	92.8 ± 7.2

[a]Lipids mean yields are reported as the percentage of the ratio between each lipidic class after SPE and dried raw biomass.

https://doi.org/10.1021/acssuschemeng.2c05869
ACS Sustainable Chem. Eng. 2023, 11, 381−389

Appendix I

AUTHOR INFORMATION

Corresponding Author

Daria Maria Monti − *Department of Chemical Sciences, University of Naples Federico II, Naples 80126, Italy;* orcid.org/0000-0002-1136-0576; Email: mdmonti@unina.it

Authors

Davide Liberti − *Department of Chemical Sciences, University of Naples Federico II, Naples 80126, Italy;* orcid.org/0000-0003-1255-5030

Paola Imbimbo − *Department of Chemical Sciences, University of Naples Federico II, Naples 80126, Italy*

Enrica Giustino − *Department of Chemical Sciences, University of Naples Federico II, Naples 80126, Italy*

Luigi D'Elia − *Department of Chemical Sciences, University of Naples Federico II, Naples 80126, Italy;* orcid.org/0000-0002-6557-1715

Giarita Ferraro − *Department of Chemical Sciences, University of Naples Federico II, Naples 80126, Italy*

Angela Casillo − *Department of Chemical Sciences, University of Naples Federico II, Naples 80126, Italy*

Anna Illiano − *Department of Chemical Sciences, University of Naples Federico II, Naples 80126, Italy;* orcid.org/0000-0003-1491-8966

Gabriella Pinto − *Department of Chemical Sciences, University of Naples Federico II, Naples 80126, Italy;* orcid.org/0000-0001-9169-3452

Maria Chiara Di Meo − *Department of Sciences and Technologies (DST), University of Sannio, Benevento 82100, Italy*

Gerardo Alvarez-Rivera − *Laboratory of Foodomics, Institute of Food Science Research, CIAL, CSIC, Madrid 28049, Spain;* orcid.org/0000-0003-1657-8141

Maria Michela Corsaro − *Department of Chemical Sciences, University of Naples Federico II, Naples 80126, Italy;* orcid.org/0000-0002-6834-8682

Angela Amoresano − *Department of Chemical Sciences, University of Naples Federico II, Naples 80126, Italy*

Armando Zarrelli − *Department of Chemical Sciences, University of Naples Federico II, Naples 80126, Italy;* orcid.org/0000-0001-7866-821X

Elena Ibáñez − *Laboratory of Foodomics, Institute of Food Science Research, CIAL, CSIC, Madrid 28049, Spain*

Antonello Merlino − *Department of Chemical Sciences, University of Naples Federico II, Naples 80126, Italy;* orcid.org/0000-0002-1045-7720

Complete contact information is available at: https://pubs.acs.org/10.1021/acssuschemeng.2c05869

Author Contributions

D.L. and D.M.M. designed the concept and supervised the experiments. D.L., P.I., E.G., and L.D.E. performed the experimental work with microalgae. G.F. grew the crystals of PE and performed the X-ray diffraction data collection and data processing. A.M. solved and refined the structure of PE. A.C. and M.M.C. analyzed EPSs. A.I., G.P., and A.A. analyzed PE sequence. M.C.D.M. and A.Z. analyzed lipid composition. G.A.-R. and E.I. analyzed carotenoids. D.L. P.I, E.G., and D.M.M. wrote the manuscript. Both G.F. and A.M. analyzed the structure and wrote the crystallographic sections of the paper. All authors have read and agreed to the published version of the manuscript.

Notes

The authors declare no competing financial interest.

ACKNOWLEDGMENTS

P.I. would like to acknowledge ALGAE4IBD project (FROM NATURE TO BEDSIDE-ALGAE BASED BIO COMPOUND FOR PREVENTION) funded by the European Union's Horizon 2020 Research and Innovation program under grant agreement N° 101000501. This work was supported by the Ministry of Science and Innovation of Spain (Grant No. PID2020-113050RB-I00). G.A.-R. would like to acknowledge the Ministry of Science and Innovation (MICINN) for his "Juan de la Cierva-Incorporación" postdoctoral grant IJC2019-041482-I. A.M. and G.F. thank Elettra Synchrotron of Trieste staff for their help during X-ray diffraction data collection.

REFERENCES

(1) Zhang, S.; Liu, Z. Advances in the Biological Fixation of Carbon Dioxide by Microalgae. *J. Chem. Technol. Biotechnol.* **2021**, *96*, 1475−1495.

(2) Bhalamurugan, G. L.; Valerie, O.; Mark, L. Valuable Bioproducts Obtained from Microalgal Biomass and Their Commercial Applications: A Review. *Environ. Eng. Res.* **2018**, *23*, 229−241.

(3) Yen, H. W.; Hu, I. C.; Chen, C. Y.; Ho, S. H.; Lee, D. J.; Chang, J. S. Microalgae-Based Biorefinery - From Biofuels to Natural Products. *Bioresour. Technol.* **2013**, *135*, 166−174.

(4) Gallego, R.; Martínez, M.; Cifuentes, A.; Ibáñez, E.; Herrero, M. Development of a Green Downstream Process for the Valorization of *Porphyridium Cruentum* Biomass. *Molecules* **2019**, *24*, 1564.

(5) Imbimbo, P.; Bueno, M.; D'Elia, L.; Pollio, A.; Ibañez, E.; Olivieri, G.; Monti, D. M. Green Compressed Fluid Technologies To Extract Antioxidants and Lipids from *Galdieria Phlegrea* in a Biorefinery Approach. *ACS Sustainable Chem. Eng.* **2020**, *8*, 2939−2947.

(6) Feller, R.; Matos, Â. P.; Mazzutti, S.; Moecke, E. H. S.; Tres, M. V.; Derner, R. B.; Oliveira, J. V.; Junior, A. F. Polyunsaturated ω-3 and ω-6 Fatty Acids, Total Carotenoids and Antioxidant Activity of Three Marine Microalgae Extracts Obtained by Supercritical CO_2 and Subcritical N-Butane. *J. Supercrit. Fluids* **2018**, *133*, 437−443.

(7) Di Lena, G.; Casini, I.; Lucarini, M.; Lombardi-Boccia, G. Carotenoid Profiling of Five Microalgae Species from Large-Scale Production. *Food Res. Int.* **2019**, *120*, 810−818.

(8) Rebolloso Fuentes, M. M.; Acién Fernández, G. G.; Sánchez Pérez, J. A.; Guil Guerrero, J. L. Biomass Nutrient Profiles of the Microalga *Porphyridium Cruentum*. *Food Chem.* **2000**, *70*, 345−353.

(9) Gaignard, C.; Gargouch, N.; Dubessay, P.; Delattre, C.; Pierre, G.; Laroche, C.; Fendri, I.; Abdelkafi, S.; Michaud, P. New Horizons in Culture and Valorization of Red Microalgae. *Biotechnol. Adv.* **2019**, *37*, 193−222.

(10) Rodriguez-Concepcion, M.; Avalos, J.; Bonet, M. L.; Boronat, A.; Gomez-Gomez, L.; Hornero-Mendez, D.; Limon, M. C.; Meléndez-Martínez, A. J.; Olmedilla-Alonso, B.; Palou, A.; Ribot, J.; Rodrigo, M. J.; Zacarias, L.; Zhu, C. A Global Perspective on Carotenoids: Metabolism, Biotechnology, and Benefits for Nutrition and Health. *Prog. Lipid Res.* **2018**, *70*, 62−93.

(11) Xiao, R.; Zheng, Y. Overview of Microalgal Extracellular Polymeric Substances (EPS) and Their Applications. *Biotechnol. Adv.* **2016**, *34*, 1225−1244.

(12) De Jesus Raposo, M. F.; De Morais, R. M. S. C.; De Morais, A. M. M. B. Bioactivity and Applications of Sulphated Polysaccharides from Marine Microalgae. *Mar. Drugs* **2013**, *11*, 233−252.

(13) Mišurcová, L.; Škrovánková, S.; Samek, D.; Ambrožová, J.; Machů, L. Health Benefits of Algal Polysaccharides in Human Nutrition. *Adv. Food Nutr. Res.* **2012**, *66*, 75−145.

(14) Dvir, I.; Stark, A. H.; Chayoth, R.; Madar, Z.; Arad, S. M. Hypocholesterolemic Effects of Nutraceuticals Produced from the Red Microalga *Porphyridium Sp.* in Rats. *Nutrients* **2009**, *1*, 156−167.

Appendix I

(15) Huheihel, M.; Ishanu, V.; Tal, J.; Arad, S. Activity of *Porphyridium Sp.* Polysaccharide against Herpes Simplex Viruses *in Vitro* and *in Vivo*. *J. Biochem. Biophys. Methods* **2002**, *50*, 189−200.
(16) Meléndez-Martínez, A. J.; Mapelli-Brahm, P.; Stinco, C. M. The Colourless Carotenoids Phytoene and Phytofluene: From Dietary Sources to Their Usefulness for the Functional Foods and Nutricosmetics Industries. *J. Food Compos. Anal.* **2018**, *67*, 91−103.
(17) Qiu, J.; Madoz-Gurpide, J.; Misek, D. E.; Kuick, R.; Brenner, D. E.; Michailidis, G.; Haab, B. B.; Omenn, G. S.; Hanash, S. Development of Natural Protein Microarrays for Diagnosing Cancer Based on an Antibody Response to Tumor Antigens. *J. Proteome Res.* **2004**, *3*, 261−267.
(18) Yoon, B.; Jackman, J.; Valle-González, E.; Cho, N. J. Antibacterial Free Fatty Acids and Monoglycerides: Biological Activities, Experimental Testing, and Therapeutic Applications. *Int. J. Mol. Sci.* **2018**, *19*, 1114.
(19) Xue, K.; Lv, S.; Zhu, C. Bringing Naturally-Occurring Saturated Fatty Acids into Biomedical Research. *J. Mater. Chem. B* **2021**, *9*, 6973−6987.
(20) Brody, M.; Emerson, R. The Effect of Wavelength and Intensity of Light on the Proportion of Pigments in *Porphyridium Cruentum*. *Am. J. Bot.* **1959**, *46*, 433−440.
(21) Geresh, S.; Adin, I.; Yarmolinsky, E.; Karpasas, M. Characterization of the Extracellular Polysaccharide of *Porphyridium Sp.*: Molecular Weight Determination and Rheological Properties. *Carbohydr. Polym.* **2002**, *50*, 183−189.
(22) Ricciardelli, A.; Casillo, A.; Vergara, A.; Balasco, N.; Corsaro, M. M.; Tutino, M. L.; Parrilli, E. Environmental Conditions Shape the Biofilm of the Antarctic Bacterium *Pseudoalteromonas Haloplanktis* TAC125. *Microbiol. Res.* **2019**, *218*, 66−75.
(23) Álvarez-Gómez, F.; Korbee, N.; Casas-Arrojo, V.; Abdala-Díaz, R. T.; Figueroa, F. L. UV Photoprotection, Cytotoxicity and Immunology Capacity of Red Algae Extracts. *Molecules* **2019**, *24*, 341.
(24) Bennett, A.; Bogobad, L. Complementary chromatic adaptation in a filamentous blue-green alga. *J. Cell Biol.* **1973**, *58*, 419−435.
(25) Russo Krauss, I.; Merlino, A.; Vergara, A.; Sica, F. An Overview of Biological Macromolecule Crystallization. *Int. J. Mol. Sci.* **2013**, *14*, 11643.
(26) Vonrhein, C.; Flensburg, C.; Keller, P.; Sharff, A.; Smart, O.; Paciorek, W.; Womack, T.; Bricogne, G. Data Processing and Analysis with the autoPROC Toolbox. *Acta Crystallogr. Sect. D Biol. Crystallogr.* **2011**, *67*, 293−302.
(27) McCoy, A. J.; Grosse-Kunstleve, R. W.; Adams, P. D.; Winn, M. D.; Storoni, L. C.; Read, R. J. Phaser Crystallographic Software. *J. Appl. Crystallogr.* **2007**, *40*, 658−674.
(28) Camara-Artigas, A.; Bacarizo, J.; Andujar-Sanchez, M.; Ortiz-Salmeron, E.; Mesa-Valle, C.; Cuadri, C.; Martin-Garcia, J. M.; Martinez-Rodriguez, S.; Mazzuca-Sobczuk, T.; Ibañez, M. J.; Allen, J. P. PH-Dependent Structural Conformations of B-Phycoerythrin from *Porphyridium Cruentum*. *FEBS J.* **2012**, *279*, 3680−3691.
(29) Emsley, P.; Cowtan, K. Coot: Model-Building Tools for Molecular Graphics. *Acta Crystallogr. Sect. D Biol. Crystallogr.* **2004**, *60*, 2126−2132.
(30) Murshudov, G. N.; Vagin, A. A.; Dodson, E. J. Refinement of Macromolecular Structures by the Maximum-Likelihood Method. *Acta Crystallogr. Sect. D Biol. Crystallogr.* **1997**, *53*, 240−255.
(31) Aremu, A. O.; Masondo, N. A.; Molnár, Z.; Stirk, W. A.; Ördög, V.; Van Staden, J. Changes in Phytochemical Content and Pharmacological Activities of Three Chlorella Strains Grown in Different Nitrogen Conditions. *J. Appl. Phycol.* **2016**, *28*, 149−159.
(32) Bligh, E. G.; Dyer, W. J. A Rapid Method of Total Lipid Extraction and Purification. *Can. J. Biochem. Physiol.* **1959**, *37*, 911−917.
(33) Imbimbo, P.; Romanucci, V.; Pollio, A.; Fontanarosa, C.; Amoresano, A.; Zarrelli, A.; Olivieri, G.; Monti, D. M. A Cascade Extraction of Active Phycocyanin and Fatty Acids from *Galdieria Phlegrea*. *Appl. Microbiol. Biotechnol.* **2019**, 9455−9464.
(34) Melo, T.; Figueiredo, A. R. P.; da Costa, E.; Couto, D.; Silva, J.; Domingues, M. R.; Domingues, P. Ethanol Extraction of Polar Lipids from *Nannochloropsis Oceanica* for Food, Feed, and Biotechnology Applications Evaluated Using Lipidomic Approaches. *Mar. Drugs* **2021**, *19*, 593.
(35) Bernaerts, T. M. M.; Kyomugasho, C.; Van Looveren, N.; Gheysen, L.; Foubert, I.; Hendrickx, M. E.; Van Loey, A. M. Molecular and Rheological Characterization of Different Cell Wall Fractions of *Porphyridium Cruentum*. *Carbohydr. Polym.* **2018**, *195*, 542−550.
(36) Ben Hlima, H.; Smaoui, S.; Barkallah, M.; Elhadef, K.; Tounsi, L.; Michaud, P.; Fendri, I.; Abdelkafi, S. Sulfated Exopolysaccharides from *Porphyridium Cruentum*: A Useful Strategy to Extend the Shelf Life of Minced Beef Meat. *Int. J. Biol. Macromol.* **2021**, *193*, 1215−1225.
(37) Gruber-Brunhumer, M. R.; Jerney, J.; Zohar, E.; Nussbaumer, M.; Hieger, C.; Bromberger, P.; Bochmann, G.; Jirsa, F.; Schagerl, M.; Obbard, J. P.; Fuchs, W.; Drosg, B. Associated Effects of Storage and Mechanical Pre-Treatments of Microalgae Biomass on Biomethane Yields in Anaerobic Digestion. *Biomass Bioenergy* **2016**, *93*, 259−268.
(38) Fernández-Rojas, B.; Hernández-Juárez, J.; Pedraza-Chaverri, J. Nutraceutical Properties of Phycocyanin. *J. Funct. Foods* **2014**, *11*, 375−392.
(39) Nguyen, H. P. T.; Morançais, M.; Déléris, P.; Fleurence, J.; Nguyen-Le, C. T.; Vo, K. H.; Dumay, J. Purification of R-Phycoerythrin from a Marine Macroalga *Gracilaria Gracilis* by Anion-Exchange Chromatography. *J. Appl. Phycol.* **2020**, *32*, 553−561.
(40) Serucňik, M.; Vicente, F. A.; Brecko, Ž.; Coutinho, J. A. P.; Ventura, S. P. M.; Žnidaršič-Plazl, P. Development of a Microfluidic Platform for R-Phycoerythrin Purification Using an Aqueous Micellar Two-Phase System. *ACS Sustainable Chem. Eng.* **2020**, *8*, 17097−17105.
(41) Vicente, F. A.; Cardoso, I. S.; Martins, M.; Gonçalves, C. V. M.; Dias, A. C. R. V.; Domingues, P.; Coutinho, J. A. P.; Ventura, S. P. M. R-Phycoerythrin Extraction and Purification from Fresh *Gracilaria Sp.* Using Thermo-Responsive Systems. *Green Chem.* **2019**, *21*, 3816−3826.
(42) Ulagesan, S.; Nam, T. J.; Choi, Y. H. Extraction and Purification of R-Phycoerythrin Alpha Subunit from the Marine Red Algae *Pyropia Yezoensis* and Its Biological Activities. *Molecules* **2021**, *26*, 6479.
(43) Ficner, R.; Huber, R. Refined Crystal Structure of Phycoerythrin from *Porphyridium Cruentum* at 0.23-Nm Resolution and Localization of the Gamma Subunit. *Eur. J. Biochem.* **1993**, *218*, 103−106.
(44) Ritter, S.; Hiller, R. G.; Wrench, P. M.; Welte, W.; Diederichs, K. Crystal Structure of a Phycourobilin-Containing Phycoerythrin at 1.90-Å Resolution. *J. Struct. Biol.* **1999**, *126*, 86−97.
(45) Ma, J.; You, X.; Sun, S.; Wang, X.; Qin, S.; Sui, S. F. Structural Basis of Energy Transfer in *Porphyridium Purpureum* Phycobilisome. *Nature* **2020**, *579*, 146−151.

Appendix I

Inside out *Porphyridium cruentum*: beyond the conventional biorefinery concept

Davide Liberti[a], Paola Imbimbo[a], Enrica Giustino[a], Luigi D'Elia[a], Giarita Ferraro[a], Angela Casillo[a], Anna Illiano[a], Gabriella Pinto[a], Maria Chiara Di Meo[b], Gerardo Alvarez-Rivera[c], Maria Michela Corsaro[a], Angela Amoresano[a], Armando Zarrelli[a], Elena Ibanez[c], Antonello Merlino[a], Daria Maria Monti[a*]

[a] Department of Chemical Sciences, University of Naples Federico II, via Cinthia 4, 80126, Naples, Italy.

[b] Department of Sciences and Technologies (DST), University of Sannio, 82100 Benevento, Italy.

[c] Laboratory of Foodomics, Institute of Food Science Research, CIAL, CSIC, Nicolás Cabrera 9, 28049 Madrid, Spain.

*corresponding author: mdmonti@unina.it

Appendix I

Table of contents:

Table S1. Data collection and refinement statistics.

Data collection	
Space group	R3
a=b, c (Å)	186.590, 59.190
α=β, γ (°)	90.0, 120.0
Molecules for asymmetric unit	Two αβ dimers
Observed reflections	925709 (44973)
Unique reflections	100909 (5012)
Resolution (Å)	46.65– 1.60 (1.62– 1.60)
Completeness (%)	99.0 (98.3)
Rmerge (%)	0.101 (1.028)
Average I/σ(I)	12.9 (2.2)
Multiplicity	9.2 (9.0)
$CC_{1/2}$	0.997 (0.595)
Refinement	
Resolution (Å)	46.65 -1.60
N° reflections	95441
N° reflections in working set	6986
Rfactor/Rfree	0.223/0.256
N° non-H atoms in the refinement	5990
B-factor overall ($Å^2$)	18.1
Average B-factor	23.93
Ramachandran values (%)	
Most favoured/ Additional allowed	97.19
Outliers	0.62
R.m.s.d. from ideality	
R.m.s.d. bonds (Å)	0.010
R.m.s.d. angles (°)	1.602

Appendix I

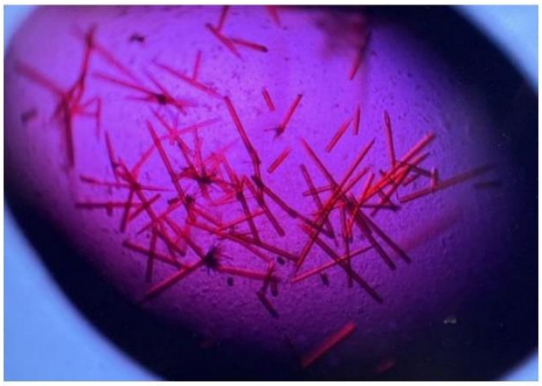

Figure S1. PE crystals. Crystals were grown by hanging drop vapor diffusion method using a drop containing 10 mg/mL PE in 0.250 M ammonium sulphate, 0.025 M potassium phosphate at pH 5.0, equilibrated with a reservoir containing 0.500 M ammonium sulphate, 0.050 M potassium phosphate at pH 5.0.

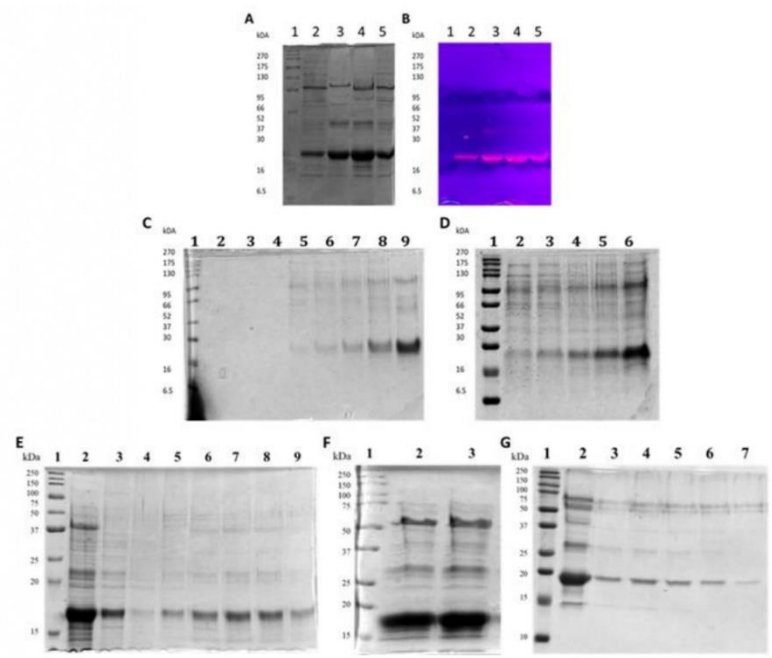

Figure S2. PE extraction and purification. Coomassie stained (**A**) and UVA light exposed unstained (**B**) SDS-PAGE analysis of total proteins extracted with different techniques. Lane 1: protein molecular weight markers; lane 2: Freeze & thaw extract; lane 3: Ultrasound extract; lane 4: Maceration extract; lane 5: French Press extract. 30 µg of total proteins were loaded in each lane. **C, D,** Coomassie staining of SDS-PAGE. Proteins were extracted by ultrasounds for different times. **(C)** fresh biomass and **(D)** frozen biomass. **C:** Lane 1: protein molecular weight markers; lanes 2-4: empty lanes; lanes 5-9: proteins extracted for 4, 8, 12, 16, and 20 minutes, respectively. **D:** Lane 1: protein molecular weight markers; lanes 2-6: proteins extracted for 4, 8, 12, 16, and 20 minutes, respectively. **E-G.** SDS-PAGE analysis of different procedures to isolate PE from *P. cruentum*. **E**: Anion-exchange. Lane 1: molecular weight markers; lane 2: total protein extract, lane 3: unbound; lane 4: washing fraction 1; lane 5: washing fraction 3; lane 6-9: samples eluted by 0.25 M NaCl. **F**: Ultrafiltration. Lane 1: molecular weight markers; lane 2: total protein extract; lane 3: ultrafiltration retentate. **G**: Size exclusion chromatography. Lane 1: molecular weight markers; lane 2: total protein extract; lanes 3-7: samples eluted from gel filtration. In all lanes, 30 µg of total proteins were analyzed.

Appendix I

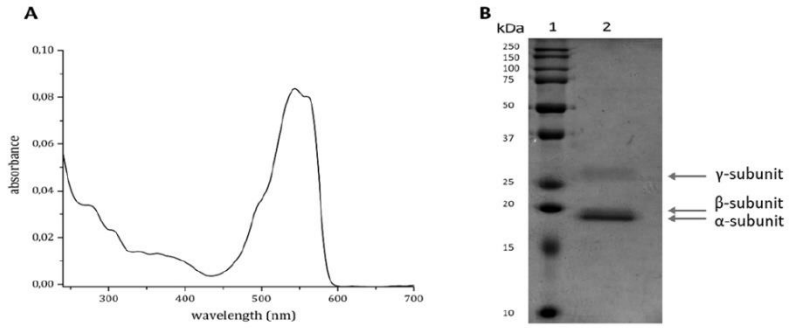

Figure S3. Analyses of PE dissolved crystals. A: UV-vis spectrum obtained from PE dissolved crystals. Spectrum was acquired at 25 °C, in the range 400–700 nm. **B**: SDS-PAGE analyses of PE dissolved crystals. Lane 1: molecular weight markers; lane 2: 20 µL of PE dissolved crystals.

Table S2. Tentatively identified compounds from *P. cruentum* extracts by HPLC-DAD-APCI-QTOF-MS/MS analysis, including peak annotation, high-resolution mass spectrometry features and UV–Vis maxima.

Peak	RT (min)	Identification	Experimental $[M+H]^+$ *m/z*	UV–Vis maxima (nm)	MS/MS product ions
1	3.471	Chlorophyll derivative I	549.4875	340s, 380s, 428	307.1400, 97.1048
2	4.177	Chlorophyll derivative II	549.4871	340s, 380s, 428	305.1354, 255.0720
3	6.658	Phaeophorbid B, methyl ester	623.2851	420	565.2795, 499.2056
4	7.347	Pheophytin derivative	909.5374	340s, 380s, 428	631.2374, 559.2071
5	7.668	Zeaxanthin isomer I	569.4357	422, 446, 474	464.8067, 281.2215, 175.1480
6	8.057	Zeaxanthin	569.4342	420s, 445, 476	423.3309, 338.2549, 175.1480
7	9.826	Zeaxanthin isomer II	569.4365	422, 446, 474	539.4249, 175.1480
8	11.920	3-Acetylpheophytin a	887.5709	410	609.2687, 549.2495
9	13.621	Divinyl pheophytin a	869.5547	410	592.2652, 487.1950
10	14.656	Plastoquinone	749.6235	420	551.3212, 495.2654, 151.0743
11	14.862	Pheophytin b	885.5527	420	607.2536, 503.2403
12	16.500	Pheophytin a	871.5739	420	594.2828, 533.2567
13	18.701	β-Carotene	537.4441	420s, 450, 480	375.2935, 173.1293
14	18.892	β-Carotene isomer	537.4456	420s, 450, 480	261.1637, 146.1004

Appendix L

antioxidants

MDPI

Article

Shedding Light on the Hidden Benefit of *Porphyridium cruentum* Culture

Davide Liberti [1], Paola Imbimbo [1,*], Enrica Giustino [1], Luigi D'Elia [1], Mélanie Silva [2], Luísa Barreira [2] and Daria Maria Monti [1,*]

[1] Department of Chemical Sciences, University of Naples Federico II, Via Cinthia 4, 80126 Naples, Italy
[2] Centre of Marine Sciences, University of Algarve, 8005-139 Faro, Portugal
* Correspondence: paola.imbimbo@unina.it (P.I.); mdmonti@unina.it (D.M.M.)

Abstract: Microalgae can represent a reliable source of natural compounds with different activities. Here, we evaluated the antioxidant and anti-inflammatory activity of sulfated exopolysaccharides (s-EPSs) and phycoerythrin (PE), two molecules naturally produced by the red marine microalga *Porphyridium cruentum* (CCALA415). *In vitro* and cell-based assays were performed to assess the biological activities of these compounds. The s-EPSs, owing to the presence of sulfate groups, showed biocompatibility on immortalized eukaryotic cell lines and a high antioxidant activity on cell-based systems. PE showed powerful antioxidant activity both *in vitro* and on cell-based systems, but purification is mandatory for its safe use. Finally, both molecules showed anti-inflammatory activity comparable to that of ibuprofen and helped tissue regeneration. Thus, the isolated molecules from microalgae represent an excellent source of antioxidants to be used in different fields.

Keywords: microalgae; exopolysaccharides; phycoerythrin; antioxidant activity; anti-inflammatory activity; biocompatibility; wound healing

check for updates

Citation: Liberti, D.; Imbimbo, P.; Giustino, E.; D'Elia, L.; Silva, M.; Barreira, L.; Monti, D.M. Shedding Light on the Hidden Benefit of *Porphyridium cruentum* Culture. *Antioxidants* **2023**, *12*, 337. https://doi.org/10.3390/antiox12020337

Academic Editors: Antonella D'Anneo and Marianna Lauricella

Received: 9 January 2023
Revised: 25 January 2023
Accepted: 26 January 2023
Published: 31 January 2023

1. Introduction

Microalgae are ubiquitous eukaryotic photosynthetic microorganisms that are able to live in different environments, in single colonies, chains, or groups; depending on the species, their size can vary from a few to hundreds of micrometers [1–3]. The biodiversity of microalgae is mainly due to their unique ability to adapt and grow even under unfavorable growth conditions (e.g., extreme temperatures, variable salinity, and low or high light intensity) and to produce a wide range of interesting chemical compounds with novel structures and biological activities [4,5]. Among the microalgae, the red marine microalga *Porphyridium cruentum* could be pointed to as a commercial source of various high-value bioproducts [1], to be recovered from the same culture, in order to make the whole process economically feasible [6–10]. In particular, *P. cruentum* produces sulfated exopolysaccharides (s-EPSs) that are accumulated in a layer surrounding the cytoplasmic membrane. These exopolysaccharides act as a mucilage, because *P. cruentum* is without a well-defined cell wall [11]. They are composed of glucuronic acid and several major neutral monosaccharides, such as D- and L-Gal, D-Glc, D-Xyl, D-GlcA, and sulfate groups. S-EPSs from *P. cruentum* have antioxidant [12], immunomodulatory, anti-inflammatory, hypocholesterolemic, antimicrobial, and antiviral activity [13,14]. S-EPSs from *P. cruentum* also exhibit specific rheological properties that can be exploited in food applications [12,15]. In addition to exopolysaccharides, *P. cruentum* produces a broad range of colored pigments, including chlorophylls, carotenoids, and phycobilins, which are commercially utilized in the food, pharmaceutical, and cosmetic industries [16]. Amongst them, phycoerythrin (PE) is a light-harvesting protein with a structure of $(\alpha\beta)_6\gamma$ complex and a MW ranging from 240 to 260 kDa. Due to its unique biological properties, PE has gained much attention from the food and pharmaceutical industries and in the molecular biology field [17–22]. Here, starting from our recent results [10], a comprehensive study on the biological activities

Appendix L

of s-EPSs and purified phycoerythrin was carried out in order to verify if the extraction techniques could affect their biological activities.

2. Materials and Methods

2.1. Reagents

All solvents, reagents, and chemicals were purchased from Sigma-Aldrich (St Louis, MO, USA).

2.2. Biocompounds Isolation

S-EPSs and PE were isolated and purified from the culture of *Porphyridium cruentum* (CCALA415) as previously described [10]. Briefly, at the end of cell growth, the culture was centrifuged to recover s-EPSs in the supernatant. The s-EPSs were precipitated by adding pure ethanol (1:2 v/v) and centrifuging the sample (12,000× g, 30 min, and 4 °C). The supernatant was discarded, and the precipitate was freeze-dried. S-EPSs yield was 300 ± 67 g/L, which corresponds to 0.53 $g/g_{d.w.\ biomass}$. In the case of PE, a crude aqueous extract was obtained *via* sonication (40% amplitude; 20 min, 30 s on and 30 s off) from the harvested biomass. PE was then isolated *via* a one-step purification procedure as reported by Liberti, up to a purity grade of 4 [10].

2.3. Eukaryotic Cell Culture and Biocompatibility Assay

Immortalized human keratinocytes (HaCaT, Innoprot, Derio, Spain) and immortalized murine fibroblasts Balb/c-3T3 (ATCC, Virginia, USA) were cultured in 10% foetal bovine serum in Dulbecco's modified Eagle's medium, in the presence of 1% penicillin/streptomycin and 2 mM L-glutamine, in a 5% CO_2 humidified atmosphere at 37 °C. To verify the biocompatibility of the crude extract of s-EPSs and of purified PE, cells were seeded in 96-well plates at a density of 2×10^3/well and, 24 h after seeding, were incubated with increasing concentrations of the extract/compounds (5 to 75 µg/mL for EPS, 5 to 500 µg/mL of total proteins for crude extracts, and 5 nM to 100 nM for purified PE) for 72 h. At the end of the incubation period, cell viability was assessed with the MTT assay. Cell survival is expressed as the percentage of viable cells in the presence of compounds compared with control cells (represented by the average obtained between untreated cells and cells supplemented with the highest concentration of buffer).

2.4. In Vitro Antioxidant Assays

The antioxidant activity of the extract/compounds was tested by measuring their ability to scavenge the free radicals 1,1-diphenyl-2-picrylhydrazyl radical and 2,2′-azinobis-[3-ethylbenzthiazoline-6-sulfonic acid] (DPPH and ABTS, respectively) and to reduce or chelate redox active iron and copper (ferric-reducing antioxidant power (FRAP); iron-chelating activity (ICA), and copper-chelating activity (CCA), respectively). DPPH and FRAP assays were performed following the procedure reported by Rodrigues et al. [23], and ascorbic acid and butylhydroxytoluene (BHT), respectively, were used as positive controls at the same concentrations of the sample under test. The ability of the extract/compounds to scavenge the ABTS radical was assessed as previously reported [24]. The results were compared to a calibration curve obtained using Trolox (6-hydroxy-2,5,7,8-tetramethylchromane-2-carboxylic acid) as the standard. ICA and CCA were determined by measuring the formation of the Fe^{2+}-ferrozine complex and by using pyrocatechol violet, respectively, according to the method reported by Megias [25]. EDTA was used as a standard at a final concentration of 100 µg/mL. S-EPS or purified PE was tested between 0.05 and 120 µg/mL and 0.2 and 270 nM, respectively. The results are expressed as IC_{50}, i.e., the concentration required to scavenge 50% of the free radical or as the highest percentage achieved.

Appendix L

2.5. Determination of Intracellular ROS Levels on Eukaryotic Cell Lines by DCFDA Assay

The protective effect of s-EPSs (from 5 to 75 µg/mL) or purified PE (10 nM) against oxidative stress was measured by determining the intracellular reactive oxygen species (ROS) levels, following the protocol used by Imbimbo [26].

2.6. Determination of Intracellular Glutathione Levels (DTNB Assay) and Lipid Peroxidation Levels (TBARS Assay) on Eukaryotic Cell Lines

Intracellular GSH levels and lipid peroxidation levels were measured by following the procedure described by Petruk [27] using 12 µg/mL of s-EPSs or 10 nM of purified PE.

2.7. Anti-Inflammatory Activity

The anti-inflammatory activity of the compounds was tested by their ability to inhibit cyclooxygenase-2 (COX-2). S-EPS or purified PE was tested at different concentrations (4 and 167 µg/mL for s-EPSs or 10 and 27 nM for purified PE) using a commercial inhibitory screening assay kit, Cayman test kit-560131 (Cayman Chemical Company, Ann Arbor, MI, USA). Ibuprofen was used as a positive control. Results are expressed as a percentage of inhibition of COX-2.

2.8. Wound Healing Assay

Wound healing was assessed with a scratch assay. HaCaT cells were seeded at a cell density of 3×10^5 cells/cm^2 for 24 h, to allow cells to reach about 95% of confluence. Then, cells were washed with PBS, scratched manually with a 200 µL pipet tip, and incubated with 12 µg/mL of s-EPSs or 10 nM of purified PE. The scratch size was monitored at 0 h and 24 h by acquiring images using optical microscopy (Zeiss LSM 710, Zeiss, Germany) at 10× magnification. The width of the wound was measured by using Zen Lite 2.3 software (Zeiss, Germany). Results are expressed as a reduction of the area (fold) compared with untreated cells.

2.9. Statistical Analyses

All the experiments were performed in triplicate. Results are presented as the mean of results obtained after three independent experiments (mean ±SD) and compared by one-way ANOVA according to Bonferroni's method (post hoc) using GraphPad Prism for Windows, version 6.01 (Dotmatics, California, USA).

3. Results

3.1. s-Exopolysaccharides Characterization

3.1.1. s-EPSs Biocompatibility on Cell-Based Model

s-EPSs were tested for their biocompatibility on two eukaryotic immortalized cell lines: HaCaT (human keratinocytes) and Balb/c-3T3 (murine fibroblasts). Twenty-four hours after seeding, cells were incubated with increasing amounts of s-EPSs (from 5 to 75 µg/mL). After 72 h of incubation, cell viability was assessed by the MTT assay; cell survival is expressed as the percentage of viable cells in the presence of s-EPSs compared with that of control samples (i.e., untreated cells). The results in Figure 1 show that, under all the experimental conditions, the s-EPSs were fully biocompatible on both the cell lines analyzed.

Appendix L

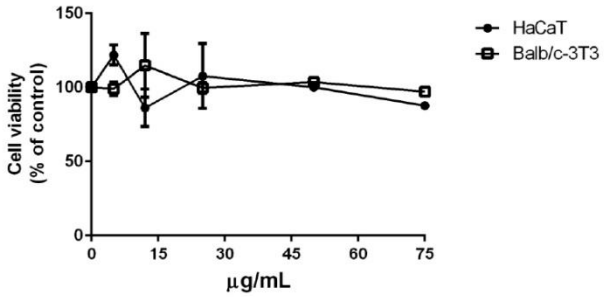

Figure 1. Effect of s-EPSs from *P. cruentum* on cell viability. Dose–response curves of HaCaT (black dots) and Balb/c-3T3 (empty squares) cells after 72 h of incubation with increasing concentrations of exopolysaccharides (5–75 µg/mL). Cell viability is reported as a function of s-EPS concentration.

3.1.2. s-EPSs *In Vitro* Antioxidant Activity

The antioxidant activity of s-EPS was evaluated with different *in vitro* analyses: ABTS, DPPH, FRAP, and iron and copper chelating assays. As shown in Table 1, s-EPSs were not able to scavenge the ABTS and DPPH radicals, whereas a slight but significant activity was observed for the chelation of iron and for ferric ion reduction assays. Both tests are based on the ability to act on iron: the former measures the ability of the compounds under test to bind Fe^{2+}, whereas the latter analyzes the ability to reduce Fe^{3+} to Fe^{2+}. As for the copper chelating assay, the highest activity reached, at the highest concentration tested, was $9 \pm 3\%$, a value much lower than the one obtained by testing the positive control molecule at the same concentration.

Table 1. *In vitro* antioxidant and chelating activity of s-EPSs. Results are expressed as percentage of inhibition. The concentration evaluated is referred to the final concentration of s-EPSs or positive control used in the well.

Test	Concentration (µg/mL)	s-EPSs Activity (%)	C+ Activity (%)
FRAP	120	34 ± 3	97 ± 1
ABTS	25	2 ± 2	98 ± 2
DPPH	50	1 ± 1	52 ± 1
ICA	55	66 ± 3	91 ± 1
CCA	45	9 ± 3	91 ± 2

3.1.3. s-EPSs Antioxidant Activity on a Cell-Based Model

The antioxidant activity of s-EPSs was also evaluated on HaCaT cells. For this purpose, cells were incubated with increasing concentrations of s-EPSs (from 5 to 50 µg/mL) for 2 h, and then oxidative stress was induced by UVA irradiation (100 J/cm^2). Immediately after irradiation, the intracellular ROS levels were measured by using H_2DCFDA as a probe. For each set of experiments, untreated cells were used as a control. As shown in Figure 2, UVA treatment significantly increased the DCF fluorescence (black bars, $p < 0.001$). In the absence of stress, s-EPSs induced a slight but significant increase in the intracellular ROS level (Figure 2, white, dashed grey, and dark grey bars on the left part of the graph). Interestingly, when cells were preincubated with s-EPSs prior to being stressed, only 5 and 12 µg/mL were able to protect the cells from ROS formation (Figure 2, light grey and white bars on the right part of the graph), whereas the higher concentrations had no protective effect. This result is in agreement with those of Giordano et al. [28], as antioxidants act at low

Appendix L

concentrations, whereas, at high concentrations, they may work as pro-oxidants. Based on these results, s-EPSs were used at 12 μg/mL for further experiments.

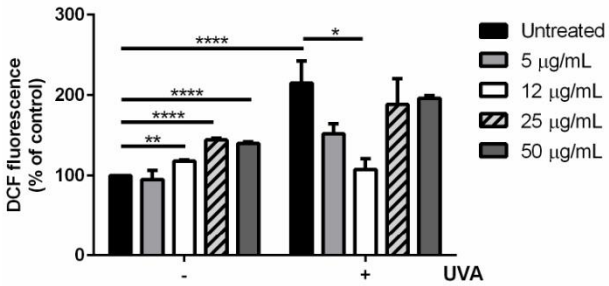

Figure 2. Antioxidant activity of s-EPSs on UVA-stressed HaCaT cells. Intracellular ROS levels were determined with DCFDA assay. Cells were preincubated in the presence of increasing amounts (from 5 to 50 μg/mL) of s-EPSs for 2 h prior to UVA irradiation (100 J/cm^2). Results are expressed as percentages compared with untreated cells. Black bars refer to untreated cells; light grey bars refer to cells incubated with 5 μg/mL of s-EPSs; white bars refer to cells incubated with 12 μg/mL; dashed bars refer to cells incubated with 25 μg/mL; dark grey bars refer to cells incubated with 50 μg/mL of s-EPSs in the absence (−) or presence (+) of UVA stress. Data shown are means ± S.D. of three independent experiments. * indicates $p < 0.05$, ** indicates $p < 0.01$, and **** indicates $p < 0.001$.

To deeply analyze the protective effect of s-EPSs, the intracellular glutathione levels and lipid peroxidation levels were determined with DTNB and TBARS assays, respectively. In the absence of any treatment, a significant decrease ($p < 0.01$) in GSH levels was observed after UVA exposure (Figure 3A), and s-EPSs (grey bars) were able to inhibit GSH oxidation, thus confirming a protective effect against oxidative stress. As for the TBARS assay, a significant increase ($p < 0.05$) in lipid peroxidation levels was observed after UVA treatment (black bars, Figure 3B), but, notably, this effect was inhibited upon pretreatment with s-EPSs (grey bars). Treatment of the cells with exopolysaccharides did not significantly alter either glutathione or lipid peroxidation levels in the absence of UVA treatment (−). Taken together, the results clearly indicate that s-EPSs are able to protect cells from oxidative damage.

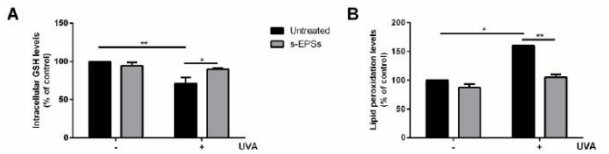

Figure 3. Protective effect of s-EPSs on HaCaT cells. Intracellular GSH levels were determined with a DTNB assay (**A**) and lipid peroxidation levels were determined with a TBARS assay (**B**). Cells were preincubated in the presence of 12 μg/mL of s-EPSs for 2 h prior to UVA irradiation (100 J/cm^2). GSH and lipid peroxidation levels were measured 90 min after UVA irradiation. Black bars refer to untreated cells, and grey bars refer to cells incubated with s-EPSs, in the absence (−) or in the presence (+) of UVA stress. Values are expressed as percentages compared with untreated cells. Data shown are means ± S.D. of three independent experiments. * Indicates $p < 0.05$; ** indicates $p < 0.01$.

Appendix L

3.1.4. *In Vitro* Anti-Inflammatory Activity of s-EPSs

As inflammation is a condition strictly linked to oxidative stress, the anti-inflammatory activity of s-EPSs was measured by evaluating their capacity to inhibit the enzyme COX-2. When inflammation occurs, COX-2 is able to enhance the prostanoid production [29]. As reported in Table 2, surprisingly, s-EPSs showed no significant differences compared with ibuprofen used as positive control when tested at the same concentration, thus suggesting a new role of s-EPSs in inflammation control.

Table 2. *In vitro* s-EPSs anti-inflammatory activity.

	Concentration (µg/mL)	Inhibition (%)
s-EPSs	167	77 ± 8
Ibuprofen	167	99 ± 1

3.2. Phycoerythrin Characterization

3.2.1. Phycoerythrin Biocompatibility on Immortalized Eukaryotic Cells

Following biomass lysis, phycoerythrin (PE) had a purity grade of 1.5 [10]. This value is considered as reagent-grade, thus indicating that the protein can be used as it is for food applications [30]. In order to verify the safety of the protein on eukaryotic cells, an MTT assay was performed by comparing the crude extract with the purified protein (purity grade of four). The results of the MTT assay, reported in Figure 4, clearly show that only pure PE was fully biocompatible with both cell lines (Figure 4B), while the crude extract exerted a dose-dependent toxicity (Figure 4A). These results clearly indicate that PE needs to be purified to a higher purity grade before being used on cell-based models, or, at least, that it cannot be applied when present in the extract at concentrations higher than a certain threshold (100 µg/mL).

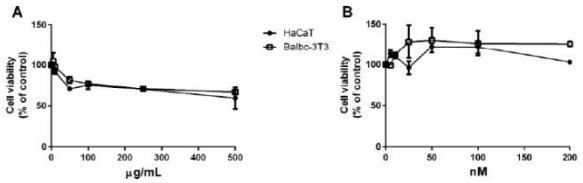

Figure 4. Biocompatibility of total extract (**A**) and purified PE (**B**) on eukaryotic cells. Dose–response curves of HaCaT (black dots) and Balb/c-3T3 cells (empty squares) after 72 h of incubation with increasing concentrations of total extract (**A**) and purified PE (**B**). Cell viability was assessed with an MTT assay and is reported as a function of extract/protein concentration.

3.2.2. *In Vitro* Antioxidant Activity

In vitro analysis of the antioxidant activity of purified PE was carried out with the abovementioned experimental procedures. As reported in Table 3, purified PE was not able to scavenge the DPPH radical or chelate copper ions. However, it demonstrated a high capacity to scavenge the ABTS radical ion and to reduce ferric iron or chelate iron with considerably low IC_{50} values (0.072 ± 0.004 and 0.084 ± 0.012 µM, 0.084 ± 0.004 µM, respectively). Noteworthy, the purified PE IC_{50} values were about 160, 1000, and 600 times lower than the IC_{50} values obtained with the positive control molecules (Trolox, 12 ± 1 µM in the ABTS; BHT, 90 ± 4 µM in the FRAP; and EDTA, 51 ± 3 µM in the ICA).

Appendix L

Table 3. *In vitro* antioxidant and chelating activity of purified PE. Results are expressed as IC_{50} values, μM.

Test	Purified PE	Positive Control
	IC_{50} (μM)	
ABTS	0.072 ± 0.004	12 ± 1
DPPH	>0.27	29 ± 2
FRAP	0.084 ± 0.012	90 ± 4
ICA	0.084 ± 0.004	51 ± 3
CCA	>0.1	63 ± 2

3.2.3. Cell-Based Antioxidant Activity of PE

Starting from the encouraging results obtained *in vitro*, purified PE was tested on the UVA-stressed HaCaT experimental system used for s-EPSs. Cells were treated with 2.5 μg/mL (10 nM) of purified PE for 2 h, and then oxidative stress was induced by UVA irradiation (100 J/cm^2). At the end of irradiation, the intracellular ROS levels were evaluated. As shown in Figure 5, UVA induced a significant increase in intracellular ROS levels (black bars, 200%) compared with untreated cells ($p < 0.001$). When cells were treated with purified PE (grey bars), no increase in intracellular ROS levels was observed. Interestingly, when cells were incubated with purified PE prior to UVA exposure, an inhibition of the intracellular ROS production was observed.

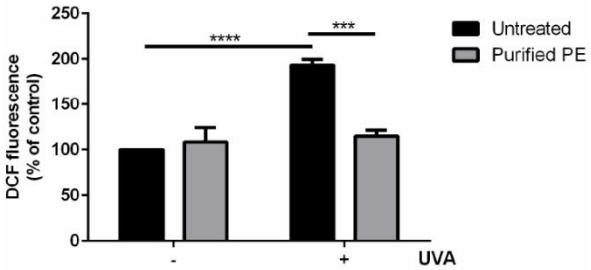

Figure 5. Protective effect of purified PE on UVA-stressed HaCaT cells. Intracellular ROS levels were determined with DCFDA assay. Cells were preincubated in the presence of 10 nM of purified PE (grey bars) for 2 h prior to UVA irradiation (100 J/cm^2). Black bars refer to untreated cells in the absence (−) or in the presence (+) of UVA stress. Values are expressed as percentages compared with untreated cells. Data shown are means ± S.D. of three independent experiments. *** indicates $p < 0.005$; **** indicates $p < 0.001$ with respect to UVA-treated cells.

The effect of purified PE on GSH and lipid peroxidation was also assessed. As shown in Figure 6, PE was able to fully protect cells from oxidative stress, as no alteration in either the GSH levels (Figure 6A) or in the lipid peroxidation levels (Figure 6B) was found when the cells were pretreated with purified PE prior to stress, thus confirming the protective effect of the protein against oxidative stress.

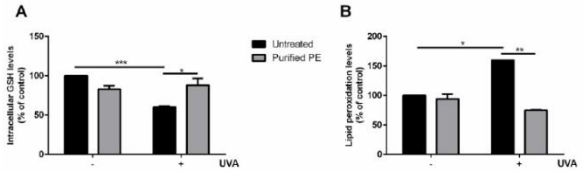

Figure 6. Analysis of intracellular GSH and lipid peroxidation levels on HaCaT cells. Cells were preincubated with 10 nM of purified PE for 2 h before UVA irradiation (100 J/cm^2). (**A**) determination of intracellular GSH levels; (**B**) analysis of lipid peroxidation levels. In both experiments, measurements were recorded 90 min after UVA-induced stress. Values are expressed as a percentage compared with control (i.e., untreated) cells. Data shown are means ± S.D. of three independent experiments. * indicates $p < 0.05$, ** indicates $p < 0.01$, and *** indicates $p < 0.005$.

3.2.4. *In Vitro* PE Anti-Inflammatory Activity

Purified PE was also able to inhibit COX-2 (Table 4) by about 75%, although the level of inhibition attained with ibuprofen 24 nM could not be achieved at any of the analyzed concentrations.

Table 4. COX-2 inhibition by purified PE.

Sample	Concentration (nM)	Inhibition (%)
Phycoerythrin	27	75 ± 8
	10	72 ± 8
Ibuprofen	24	96 ± 1

3.3. Effect of s-EPSs and Purified PE on Wound Healing

Finally, a scratch assay was carried out on HaCaT cells to test the ability of s-EPSs and purified PE to induce cell migration related to wound repairing. The results are reported in Figure 7 and in Table 5. In the absence of any treatment, the cells spontaneously migrated to induce the re-epithelialization. Interestingly, when the cells were treated with either s-EPSs or purified PE, a significant enhancement in the wound closure was observed after 24 h. Indeed, s-EPSs reduced the scratched area by 2.5 ± 0.17-fold and purified PE by 2.4 ± 0.1317-fold compared with untreated cells (1.80 ± 0.02-fold reduction).

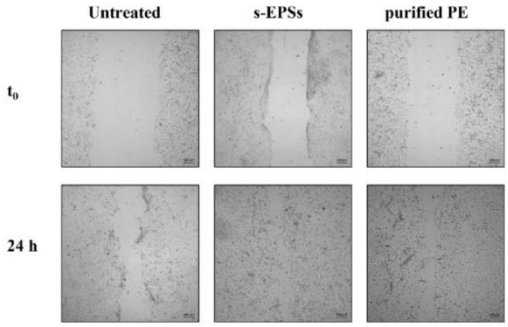

Figure 7. Effect of s-EPSs and purified PE on wound healing. Confluent HaCaT cells were scratched and treated with either 12 µg/mL s-EPSs or 10 nM purified PE for 24 h. Optical microscopy images were acquired at 10× magnification at the beginning (t_0) and end (24 h) of the incubation.

Appendix L

Table 5. Reduction of area (fold) of wound closure upon 24 h of incubation with either s-EPSs or purified PE. Data shown are means ± S.D. of three independent experiments. For each experiment, at least 10 images were acquired. * indicates $p < 0.05$.

Sample	Reduction in Area (Fold)
Untreated	1.80 ± 0.02
s-EPSs	2.50 ± 0.17 *
Purified PE	2.40 ± 0.13 *

* = $p < 0.05$.

4. Discussion

As the use of synthetic molecules is known to be harmful in the long run, the search for new natural compounds endowed with beneficial properties is urgent [31]. In this context, antioxidants from microalgae could represent an excellent alternative, but the costs of microalgae upstream and downstream processes are still too high [32].

We recently set up a cascade approach to recover four classes of molecules from *P. cruentum* culture: s-EPSs, PE, carotenoids, and saturated fatty acids. Among them, here, we evaluated the biological activity of s-EPSs and PE. S-EPSs were chosen as it is generally thought that polysaccharides with a high sulfated content have biological activities [33], such as antioxidant action [34]. It is known that antioxidant molecules can bind metal ions, forming metal–ion complexes. The presence of sulfate groups could increase the metal-binding capacity of the carbohydrates by donating an electron pair or by losing a proton, thus stabilizing the complex [35,36].

In agreement with the findings of Wang et al., we found that s-EPSs had no radical scavenging activity against DPPH, whereas they showed antioxidant activity in the ABTS assay, with IC_{50} values ranging from 6.59 to 8.92 mg/mL [37]. Interestingly, despite the low antioxidant activity observed *in vitro*, s-EPSs were active on a cell-based system at a concentration almost 600 times lower than that measured *in vitro*. This result is in agreement with literature, as it is well known that *in vitro* assays should not be compared with cell-based ones. Indeed, antioxidants provide their function by different mechanisms of action, so that bioavailability, stability, retention, or reactivity of the compound under test in a complex system, such as that of eukaryotic cells, cannot be either mimicked or evaluated *in vitro* [38]. Our results indicated that s-EPSs were able not only to inhibit the intracellular ROS production but also to prevent GSH depletion and lipid peroxidation.

Different is the case of PE, which was found to be a very powerful antioxidant agent *in vitro* and on a cell-based system. The ABTS assay was in line with that observed by Sonani on a PE from a different source (IC_{50} of 72 ± 4 nM vs. 101 nM, respectively) [39], whereas the PE prepared by this author had lower DPPH-scavenging (IC_{50} of 930 nM) and iron-chelating abilities (IC_{50} of 484 nM) than the purified PE prepared in this study. We hypothesize that the higher antioxidant activity measured in our experimental system may rely on the source or strain used. A different source may also affect the biocompatibility results: indeed, we found that only pure PE was biocompatible with eukaryotic cells, strongly suggesting the importance of purification of the protein for all the potential applications. Pure PE protected cells from UVA irradiation at a concentration in the low nanomolar range (10 nM). Generally, antioxidants prevent the generation of free radicals, which can significantly affect some physiological processes, including wound healing. In particular, ROS generation can damage tissues and slow down the regeneration process. The presence of antioxidants should counteract chronic inflammation and at the same time contribute to promoting tissue regeneration [40]. Considering that both s-EPSs and PE were able to inhibit one of the key enzymes in the inflammation process (COX-2) and to induce a significantly faster scratch closure compared with untreated cells, we can conclude that the bioproducts obtained by *P. cruentum* represent an excellent ingredient for new biomaterials, such as medical patches.

Appendix L

5. Conclusions

In this study, s-EPSs and PE, obtained from *P. cruentum* culture by a cascade approach described in a previous work [10], showed a remarkable antioxidant activity in a cell-based system, higher than that obtained by *in vitro* assays, thus suggesting that the reliability of *in vitro* assays has to be overhauled. Moreover, both molecules showed anti-inflammatory characteristics comparable with ibuprofen and a significant ability to promote cell proliferation.

Author Contributions: D.L., P.I. and D.M.M. designed the concept and supervised the experiments. D.L., P.I., E.G. and L.D. performed the experimental work with microalgae. D.L., P.I., E.G. and D.M.M. wrote the manuscript. L.B. supervised M.S. on the in vitro experiments. All authors have read and agreed to the published version of the manuscript.

Funding: This work was carried out with funding from the Portuguese Foundation for Science and Technology (FCT) through UIDB/04326/2020, UIDP/0436/2020, LA/P/0101/2020.

Institutional Review Board Statement: Not applicable.

Informed Consent Statement: Not applicable.

Data Availability Statement: The data presented in this study are available in the article.

Acknowledgments: P.I. would like to acknowledge the ALGAE4IBD project (From Natura to Bedside-Algae Based Bio Compound for Prevention) funded by the European Union's Horizon 2020 Research and Innovation program under grant agreement No. 101000501.

Conflicts of Interest: The authors declare no conflict of interest.

References

1. Mobin, S.; Alam, F. Some Promising Microalgal Species for Commercial Applications: A Review. *Energy Procedia* **2017**, *110*, 510–517. [CrossRef]
2. Alam, F.; Date, A.; Rasjidin, R.; Mobin, S.M.A.; Moria, H.; Baqui, A. Biofuel from Algae: Is It a Viable Alternative? In *Advances in Biofuel Production: Algae and Aquatic Plants*; Apple Academic Press: New York, NY, USA, 2014; pp. 32742–33487.
3. Suganya, T.; Varman, M.; Masjuki, H.H.; Renganathan, S. Macroalgae and Microalgae as a Potential Source for Commercial Applications along with Biofuels Production: A Biorefinery Approach. *Renew. Sustain. Energy Rev.* **2016**, *55*, 909–941. [CrossRef]
4. Herrero, M.; Mendiola, J.A.; Plaza, M.; Ibañez, E. Screening for Bioactive Compounds from Algae. In *Advanced Biofuels and Bioproducts*; Springer: New York, NY, USA, 2013; pp. 833–872.
5. Anbuchezhian, R.; Karuppiah, V.; Li, Z. Prospect of Marine Algae for Production of Industrially Important Chemicals. In *Algal Biorefinery: An Integrated Approach*; Springer: Cham, Switzerland, 2015; pp. 195–217.
6. Feller, R.; Matos, Â.P.; Mazzutti, S.; Moecke, E.H.S.; Tres, M.V.; Derner, R.B.; Oliveira, J.V.; Junior, A.F. Polyunsaturated ω-3 and ω-6 Fatty Acids, Total Carotenoids and Antioxidant Activity of Three Marine Microalgae Extracts Obtained by Supercritical CO_2 and Subcritical n-Butane. *J. Supercrit. Fluids* **2018**, *133*, 437–443. [CrossRef]
7. Di Lena, G.; Casini, I.; Lucarini, M.; Lombardi-Boccia, G. Carotenoid Profiling of Five Microalgae Species from Large-Scale Production. *Food Res. Int.* **2019**, *120*, 810–818. [CrossRef]
8. Rebolloso Fuentes, M.M.; Acién Fernández, G.G.; Sánchez Pérez, J.A.; Guil Guerrero, J.L. Biomass Nutrient Profiles of the Microalga *Porphyridium cruentum*. *Food Chem.* **2000**, *70*, 345–353. [CrossRef]
9. Gaignard, C.; Gargouch, N.; Dubessay, P.; Delattre, C.; Pierre, G.; Laroche, C.; Fendri, I.; Abdelkafi, S.; Michaud, P. New Horizons in Culture and Valorization of Red Microalgae. *Biotechnol. Adv.* **2019**, *37*, 193–222. [CrossRef]
10. Liberti, D.; Imbimbo, P.; Giustino, E.; D'elia, L.; Ferraro, G.; Casillo, A.; Illiano, A.; Pinto, G.; Di Meo, M.C.; Alvarez-Rivera, G.; et al. Inside out *Porphyridium Cruentum*: Beyond the Conventional Biorefinery Concept. *ACS Sustain. Chem. Eng.* **2023**, *11*, 381–389. [CrossRef]
11. Dvir, I.; Stark, A.H.; Chayoth, R.; Madar, Z.; Arad, S.M. Hypocholesterolemic Effects of Nutraceuticals Produced from the Red Microalga *Porphyridium* sp. in Rats. *Nutrients* **2009**, *1*, 156–167. [CrossRef]
12. Ben Hlima, H.; Smaoui, S.; Barkallah, M.; Elhadef, K.; Tounsi, L.; Michaud, P.; Fendri, I.; Abdelkafi, S. Sulfated Exopolysaccharides from *Porphyridium cruentum*: A Useful Strategy to Extend the Shelf Life of Minced Beef Meat. *Int. J. Biol. Macromol.* **2021**, *193*, 1215–1225. [CrossRef]
13. Mišurcová, L.; Škrovánková, S.; Samek, D.; Ambrožová, J.; Machů, L. Health Benefits of Algal Polysaccharides in Human Nutrition. *Adv. Food Nutr. Res.* **2012**, *66*, 75–145.

Appendix L

14. Gallego, R.; Martínez, M.; Cifuentes, A.; Ibáñez, E.; Herrero, M. Development of a Green Downstream Process for the Valorization of *Porphyridium cruentum* Biomass. *Molecules* **2019**, *24*, 1564. [CrossRef]
15. Medina-Cabrera, E.V.; Gansbiller, M.; Rühmann, B.; Schmid, J.; Sieber, V. Rheological Characterization of *Porphyridium sordidum* and *Porphyridium purpureum* Exopolysaccharides. *Carbohydr. Polym.* **2021**, *253*, 117237. [CrossRef]
16. Sudhakar, M.P.; Jagatheesan, A.; Perumal, K.; Arunkumar, K. Methods of Phycobiliprotein Extraction from *Gracilaria crassa* and Its Applications in Food Colourants. *Algal Res.* **2015**, *8*, 115–120. [CrossRef]
17. Kannaujiya, V.K.; Kumar, D.; Pathak, J.; Sinha, R.P. Phycobiliproteins and Their Commercial Significance. In *Cyanobacteria*; Elsevier: Amsterdam, The Netherlands, 2019; pp. 207–216.
18. Hsieh-Lo, M.; Castillo, G.; Ochoa-Becerra, M.A.; Mojica, L. Phycocyanin and Phycoerythrin: Strategies to Improve Production Yield and Chemical Stability. *Algal Res.* **2019**, *42*, 101600. [CrossRef]
19. Manirafasha, E.; Ndikubwimana, T.; Zeng, X.; Lu, Y.; Jing, K. Phycobiliprotein: Potential Microalgae Derived Pharmaceutical and Biological Reagent. *Biochem. Eng. J.* **2016**, *109*, 282–296. [CrossRef]
20. Simovic, A.; Combet, S.; Velickovic, T.C.; Nikolic, M.; Minic, S. Probing the Stability of the Food Colourant R-Phycoerythrin from Dried Nori Flakes. *Food Chem.* **2022**, *374*, 131780. [CrossRef]
21. Ganesan, A.R.; Subramani, K.; Shanmugam, M.; Seedevi, P.; Park, S.; Alfarhan, A.H.; Rajagopal, R.; Balasubramanian, B. A Comparison of Nutritional Value of Underexploited Edible Seaweeds with Recommended Dietary Allowances. *J. King Saud Univ.* **2020**, *32*, 1206–1211. [CrossRef]
22. García, A.B.; Longo, E.; Murillo, M.C.; Bermejo, R. Using a B-Phycoerythrin Extract as a Natural Colorant: Application in Milk-Based Products. *Molecules* **2021**, *26*, 297. [CrossRef]
23. Rodrigues, M.J.; Neves, V.; Martins, A.; Rauter, A.P.; Neng, N.R.; Nogueira, J.M.F.; Varela, J.; Barreira, L.; Custódio, L. In Vitro Antioxidant and Anti-Inflammatory Properties of *Limonium algarvense* Flowers' Infusions and Decoctions: A Comparison with Green Tea (*Camellia sinensis*). *Food Chem.* **2016**, *200*, 322–329. [CrossRef]
24. Re, R.; Pellegrini, N.; Proteggente, A.; Pannala, A.; Yang, M.; Rice-Evans, C. Antioxidant Activity Applying an Improved ABTS Radical Cation Decolorization Assay. *Free Radic. Biol. Med.* **1999**, *26*, 1231–1237. [CrossRef]
25. Megías, C.; Pastor-Cavada, E.; Torres-Fuentes, C.; Girón-Calle, J.; Alaiz, M.; Juan, R.; Pastor, J.; Vioque, J. Chelating, Antioxidant and Antiproliferative Activity of *Vicia sativa* Polyphenol Extracts. *Eur. Food Res. Technol.* **2009**, *230*, 353–359. [CrossRef]
26. Imbimbo, P.; Romanucci, V.; Pollio, A.; Fontanarosa, C.; Amoresano, A.; Zarrelli, A.; Olivieri, G.; Monti, D.M. A Cascade Extraction of Active Phycocyanin and Fatty Acids from *Galdieria phlegrea*. *Appl. Microbiol. Biotechnol.* **2019**, *103*, 9455–9464. [CrossRef] [PubMed]
27. Petruk, G.; Di Lorenzo, F.; Imbimbo, P.; Silipo, A.; Bonina, A.; Rizza, L.; Piccoli, R.; Monti, D.M.; Lanzetta, R. Protective Effect of *Opuntia ficus-indica* L. Cladodes against UVA-Induced Oxidative Stress in Normal Human Keratinocytes. *Bioorg. Med. Chem. Lett.* **2017**, *27*, 5485–5489. [CrossRef] [PubMed]
28. Giordano, M.E.; Caricato, R.; Lionetto, M.G. Concentration Dependence of the Antioxidant and Prooxidant Activity of Trolox in Hela Cells: Involvement in the Induction of Apoptotic Volume Decrease. *Antioxidants* **2020**, *9*, 1058. [CrossRef] [PubMed]
29. Landa, P.; Kokoska, L.; Pribylova, M.; Vanek, T.; Marsik, P. In Vitro Anti-Inflammatory Activity of Carvacrol: Inhibitory Effect on COX-2 Catalyzed Prostaglandin E2 Biosynthesisb. *Arch. Pharm. Res.* **2009**, *32*, 75–78. [CrossRef]
30. Fernández-Rojas, B.; Hernández-Juárez, J.; Pedraza-Chaverri, J. Nutraceutical Properties of Phycocyanin. *J. Funct. Foods* **2014**, *11*, 375–392. [CrossRef]
31. Montégut, L.; de Cabo, R.; Zitvogel, L.; Kroemer, G. Science-Driven Nutritional Interventions for the Prevention and Treatment of Cancer. *Cancer Discov.* **2022**, *12*, 2258–2279. [CrossRef]
32. Coulombier, N.; Jauffrais, T.; Lebouvier, N. Antioxidant Compounds from Microalgae: A Review. *Mar. Drugs* **2021**, *19*, 549. [CrossRef]
33. Wang, Y.; Xing, M.; Cao, Q.; Ji, A.; Liang, H.; Song, S. Biological Activities of Fucoidan and the Factors Mediating Its Therapeutic Effects: A Review of Recent Studies. *Mar. Drugs* **2019**, *17*, 183. [CrossRef]
34. de Souza, M.C.R.; Marques, C.T.; Dore, C.M.G.; da Silva, F.R.F.; Rocha, H.A.O.; Leite, E.L. Antioxidant Activities of Sulfated Polysaccharides from Brown and Red Seaweeds. *J. Appl. Phycol.* **2007**, *19*, 153–160. [CrossRef]
35. Bhunia, B.; Uday, U.S.P.; Oinam, G.; Mondal, A.; Bandyopadhyay, T.K.; Tiwari, O.N. Characterization, Genetic Regulation and Production of Cyanobacterial Exopolysaccharides and Its Applicability for Heavy Metal Removal. *Carbohydr. Polym.* **2018**, *179*, 228–243. [CrossRef]
36. Andrew, M.; Jayaraman, G. Structural Features of Microbial Exopolysaccharides in Relation to Their Antioxidant Activity. *Carbohydr. Res.* **2020**, *487*, 107881. [CrossRef]
37. Wang, W.-N.; Li, Y.; Zhang, Y.; Xiang, W.-Z.; Li, A.-F.; Li, T. Comparison on Characterization and Antioxidant Activity of Exopolysaccharides from Two Porphyridium Strains. *J. Appl. Phycol.* **2021**, *33*, 2983–2994. [CrossRef]
38. López-Alarcón, C.; Denicola, A. Evaluating the Antioxidant Capacity of Natural Products: A Review on Chemical and Cellular-Based Assays. *Anal. Chim. Acta* **2013**, *763*, 1–10. [CrossRef]

Appendix L

39. Sonani, R.R.; Singh, N.K.; Kumar, J.; Thakar, D.; Madamwar, D. Concurrent Purification and Antioxidant Activity of Phycobiliproteins from *Lyngbya* sp. A09DM: An Antioxidant and Anti-Aging Potential of Phycoerythrin in Caenorhabditis Elegans. *Process Biochem.* **2014**, *49*, 1757–1766. [CrossRef]
40. Alvarez, X.; Alves, A.; Ribeiro, M.P.; Lazzari, M.; Coutinho, P.; Otero, A. Biochemical Characterization of *Nostoc* sp. Exopolysaccharides and Evaluation of Potential Use in Wound Healing. *Carbohydr. Polym.* **2021**, *254*, 117303. [CrossRef]